ALFRED-WEGENER-INSTITUT
HELMHOLTZ-ZENTRUM FÜR POLAR- UND MEERESFORSCHUNG

770
2023

Berichte
zur Polar- und Meeresforschung
Reports on Polar and Marine Research

The Expedition PS131 of the Research Vessel POLARSTERN to the Fram Strait in 2022

Edited by

Torsten Kanzow

with contributions of the participants

HELMHOLTZ

Die Berichte zur Polar- und Meeresforschung werden vom Alfred-Wegener-Institut, Helmholtz-Zentrum für Polar- und Meeresforschung (AWI) in Bremerhaven, Deutschland, in Fortsetzung der vormaligen Berichte zur Polarforschung herausgegeben. Sie erscheinen in unregelmäßiger Abfolge.

Die Berichte zur Polar- und Meeresforschung enthalten Darstellungen und Ergebnisse der vom AWI selbst oder mit seiner Unterstützung durchgeführten Forschungsarbeiten in den Polargebieten und in den Meeren.

Die Publikationen umfassen Expeditionsberichte der vom AWI betriebenen Schiffe, Flugzeuge und Stationen, Forschungsergebnisse (inkl. Dissertationen) des Instituts und des Archivs für deutsche Polarforschung, sowie Abstracts und Proceedings von nationalen und internationalen Tagungen und Workshops des AWI.

Die Beiträge geben nicht notwendigerweise die Auffassung des AWI wider.

Herausgeber
Dr. Horst Bornemann

Redaktionelle Bearbeitung und Layout
Susan Amir Sawadkuhi

Alfred-Wegener-Institut
Helmholtz-Zentrum für Polar- und Meeresforschung
Am Handelshafen 12
27570 Bremerhaven
Germany

www.awi.de
www.awi.de/reports

Der Erstautor bzw. herausgebende Autor eines Bandes der Berichte zur Polar- und Meeresforschung versichert, dass er über alle Rechte am Werk verfügt und überträgt sämtliche Rechte auch im Namen seiner Koautoren an das AWI. Ein einfaches Nutzungsrecht verbleibt, wenn nicht anders angegeben, beim Autor (bei den Autoren). Das AWI beansprucht die Publikation der eingereichten Manuskripte über sein Repositorium ePIC (electronic Publication Information Center, s. Innenseite am Rückdeckel) mit optionalem print-on-demand.

The Reports on Polar and Marine Research are issued by the Alfred Wegener Institute, Helmholtz Centre for Polar and Marine Research (AWI) in Bremerhaven, Germany, succeeding the former Reports on Polar Research. They are published at irregular intervals.

The Reports on Polar and Marine Research contain presentations and results of research activities in polar regions and in the seas either carried out by the AWI or with its support.

Publications comprise expedition reports of the ships, aircrafts, and stations operated by the AWI, research results (incl. dissertations) of the Institute and the Archiv für deutsche Polarforschung, as well as abstracts and proceedings of national and international conferences and workshops of the AWI.

The papers contained in the Reports do not necessarily reflect the opinion of the AWI.

Editor
Dr. Horst Bornemann

Editorial editing and layout
Susan Amir Sawadkuhi

Alfred-Wegener-Institut
Helmholtz-Zentrum für Polar- und Meeresforschung
Am Handelshafen 12
27570 Bremerhaven
Germany

www.awi.de
www.awi.de/en/reports

The first or editing author of an issue of Reports on Polar and Marine Research ensures that he possesses all rights of the opus, and transfers all rights to the AWI, including those associated with the co-authors. The non-exclusive right of use (einfaches Nutzungsrecht) remains with the author unless stated otherwise. The AWI reserves the right to publish the submitted articles in its repository ePIC (electronic Publication Information Center, see inside page of verso) with the option to "print-on-demand".

Titel: Untersuchung der Schmelzprozesse des Meereises in der Eisrandzone nördlich von Spitzbergen (Foto: Mario Hoppmann, AWI)

Cover: Scientists studying sea-ice melt processes in the marginal ice zone north of Svalbard (Photo: Mario Hoppmann, AWI)

The Expedition PS131 of the Research Vessel POLARSTERN to the Fram Strait in 2022

Edited by

Torsten Kanzow

with contributions of the participants

Please cite or link this publication using the identifiers

https://hdl.handle.net/10013/epic.2f58b395-b7ce-4cd8-bf37-1be5b3896017
https://doi.org/10.57738/BzPM_0770_2023

ISSN 1866-3192

PS131 – ATWAICE

27 June 2022 – 17 August 2022

Bremerhaven – Bremerhaven

Chief scientist
Torsten Kanzow

Coordinator
Ingo Schewe

Contents

APPENDIX

1. ÜBERBLICK UND FAHRTVERLAUF

Torsten Kanzow AWI

Die Expedition PS131 **AT**lantic **WA**ter pathways to the **ICE** in the Nansen Basin and Fram Strait (**ATWAICE**) nahm sich zentralen Zielen des POF-IV Programms des Forschungsbereichs “Erde und Umwelt” der Helmholtz-Gemeinschaft mit einem Fokus auf den Themen “Ocean and Cryosphere in Climate” and “Marine and Polar Life” an. Unsere Arbeit war vier Zielen zugeordnet. Der Schwerpunkt lag auf einer Prozessstudie bzgl. der ozeanischen Kontrolle der Meereis-Schmelze in der Eisrandzone nördlich von Spitzbergen sowie deren Kopplung zur Biogeochemie, Biologie und Atmosphäre. Das zweite Ziel stellte eine Fortführung des verankerungsbasierten Langzeit-Monitorings der Austauschzirkulation in der Fram Straße als Teil der interdisziplinären Infrastruktur FRAM des AWI dar – als Beitrag zu dringend benötigen Langzeitbeobachtungsprogrammen in Schlüsselregionen im Ozean, um anthropogene Änderungen quantifizieren zu können. Darüber hinaus erforschte die ATWAICE Expedition die ozeanischen Einflüsse auf marine Gletscher in Nordostgrönland. Eine lithosphärische Studie im Aurora Vent-Field, am westlichen Ende des Gakkelrückens, stellte schließlich die vierte Aufgabe der Expedition dar. Unsere Arbeiten zu den Zielen eins, zwei sowie vier waren äußerst erfolgreich, jedoch führten ein massiver Festeisgürtel und Nebel an der grönländischen Küste zu großen Einschränkungen unserer Arbeiten hinsichtlich Ziel 3. Zur nachfolgenden Orientierung, ist der Expeditionsverlauf in Abbildung 1.1 dargestellt.

28. Juni bis 04. Juli: Am 28. Juni verließ die *Polarstern* Bremerhaven bei sommerlichen Bedingungen mit 47 wissenschaftlichen Teilnehmerinnen und Teilnehmern. Für die ersten vier Tage war es aufgrund der Corona-Vorsorgebestimmungen Pflicht, Masken zu tragen und große Menschenansammlungen zu meiden. Nach einer zweiten Runde von negativen Antigentests wurden diese Maßnahmen eingestellt. Der Transit in die östliche Framstraße fand bei ruhigen Bedingungen statt, wodurch die Vorbereitungen und Tests für die anschließende Feldarbeit reibungslos verliefen. Am 1. Juli wurden vor der Küste Norwegens Tests der CTD und des LOKI durchgeführt.

05. bis 10. Juli: Bei angenehmen Wetterbedingungen wurden die Arbeiten in der östlichen Framstraße durchgeführt, einem Gebiet, das von der Advektion warmen, salzhaltigen Wassers (im Folgenden als Atlantikwasser bezeichnet) im Westspitzbergenstrom (WSC) dominiert wird. Die Arbeiten wurden hauptsächlich im Rahmen des AWI-Observatoriums FRAM (Frontiers in Arctic Marine Monitoring) durchgeführt. Das Verankerungsprogramm unterstützt integrierte langfristige, ganzjährige physikalische, biochemische und biologische Zeitreihenmessungen. Alle 8 Verankerungen wurden erfolgreich geborgen, wobei sich einige von ihnen bis 20 m unter die Meeresoberfläche erstreckten. Die Anforderung bzgl. Zeitserienmessungen nahe der Oberfläche stellt eine Herausforderung dar, da die Verankerungen in Wassertiefen zwischen 700 und 2600 m ausgelegt waren. Anschließend wurden die Verankerungen wieder ausgelegt. Starke Strömungen im WSC machten es bisweilen schwer, die exakten Tiefen der

obersten Elemente jeder Verankerung unter der Meeresoberfläche abzuschätzen. Neben Verankerungsarbeiten deckten wir in den Nachtstunden die drei Langzeit-Hausgartenstationen S3, HG4 und N4 mit gefierten Messungen von Hydrographie, Geschwindigkeit, biologischen und chemischen Wasserproben, Plankton-Imaging (LOKI) und Unterwasserstrahlung (RAMSES) sowie Plankton- und Quallen-Multinetzfänge ab. Eine zweite nächtliche Aktivität war die Vervollständigung eines hydrographischen Schnitts durch den WSC bei 79°N. Ein Helikopterflug nach Ny Alesund wurde zudem durchgeführt (6. Juli), um unsere Vorräte an Blitzknallmunition (freundlicherweise vom AWIPEV-Stationsmanagement zur Verfügung gestellt) zu erhöhen, die für die Eisbärenschutzwachen im nachfolgenden Arbeitsgebiet benötigt würden. Auf demselben Flug wurde auch ein wichtiges Ersatzteil für die MSS-Winde an Bord gebracht. Außerdem setzten wir einen Gleiter (Universität Bergen) aus, der anschließend entlang des WSC die MIZ nördlich von Svalbard ansteuern sollte – dem zweiten Arbeitsbereich unserer Expedition. Des Weiteren führten wir Tests für verschiedene Systeme durch, deren Betrieb in der MIZ geplant war, darunter die geschleppte Sensorplattform Triaxus und helikopterbasierte Fernerkundungsanwendungen (Kameras, EM-Bird).

11. – 15. Juli: Nach dem erfolgreichen Abschluss der Arbeiten in der Framstraße erreichten wir am 11. Juli die eisfreien Gewässer am Kontinentalhang nördlich von Svalbard, um den Schwerpunkt der Expedition – eine interdisziplinäre Studie zur sommerlichen Meereisschmelze in der MIZ – zu starten. Hierbei konzentrierten wir uns konzeptionell auf zwei Skalen. Erstens beabsichtigten wir, die ozeanischen, biologischen und Meereisgradienten über die MIZ hinweg aufzulösen, hauptsächlich basierend auf schiffsgestützten Messungen (einschließlich der geschleppten Triaxus-Sensorplattform), Driftereinsätzen und Helikopteruntersuchungen. Das Abschmelzen und Zerfallen einzelner Eisschollen bildete den zweiten Schwerpunkt. Bezüglich letzterem fanden Untersuchungen auf drei Eisschollen mit unterschiedlichen Abständen zur Eiskante statt. Es sollte dabei jede Scholle mit Meereis- und ozeanografischen Bojen instrumentiert werden, um Zeitreihen für die Dauer von 3 Wochen zu erhalten. Außerdem sollten auf jeder der drei Schollen dreimal Meereis-, ozeanografische und biologische Untersuchungen durchgeführt werden, um Veränderungen im Laufe der Zeit zu dokumentieren. Wir begannen die MIZ Arbeiten mit einem kurzen Triaxus-Survey im offenen Wasser, das sich der Eiskante von Süden näherte, gefolgt von einem schiffsgestützten Hydrographie-Nährstoffschnitt mit einem Stationsabstand von 8 Seemeilen entlang eines Transekts durch die MIZ zum Packeis. Die Gesamtlänge des Transekts (Triaxus im offenen Wasser und CTD im Eis) betrug 84 sm. Nachfolgend wurden zwischen dem 13. und 15. Juli drei Eisstationen entlang des Transekts absolviert, die die Installation von eisphysikalischen und ozeanographischen Bojen sowie eine Reihe von Mess- und Probennahmeaktivitäten (Eisdicke, Eisbohrkerne, Eigenschaften der Eisoberfläche, biologische Proben des Eises, Untereisturbulenz, Untereis-Hydrographie) umfassten. Die erste Scholle befand sich am nördlichen Ende des Transekts („Nordscholle“) in einem Gebiet mit relativ großen Schollen. Die zweite Scholle („Südscholle“) befand sich etwa 28 sm südlich davon. Während unserer Arbeit an dieser Scholle kam von Süden her Dünung heran, und die Scholle zerbrach in mehrere kleine Stücke. Wir hatten ursprünglich geplant, die dritte Eisstation noch weiter südlich in Richtung Eisrand anzusiedeln. Es wurde dann jedoch entschieden, nicht weiter nach Süden zu ziehen, da das Dünungsereignis alle Eisschollen weiter zur Eiskante hin zerschlagen hatte, was eine Arbeit auf dem Eis und die Installation von Bojen unmöglich gemacht hätte. Stattdessen wurde die dritte Eisschollenstation (Mittelscholle) etwa in der Mitte zwischen Nord- und Südscholle angesiedelt.

16. – 19. Juli (offenes Wasser und südlicher Teil der MIZ): Nach Abschluss der ersten Runde der Eisschollenstationen kehrten wir ins offene Wasser am südlichen Endpunkt des MIZ-Schnitts zurück. Wir setzten zwei vom BSH (Hamburg) freundlicherweise zur Verfügung

gestellte Argo Floats östlich des Yermak-Plateaus in eisfreien Bedingungen im tiefen Wasser aus. Anschließend wurde das allererste Survey vom Triaxus unter dem Meereis mit einem Depressorgewicht über das südliche Ende des vorher absolvierten MIZ Schnitts bei lockeren Eisbedingungen durchgeführt. Die hydrographisch-biogeochemischen Sensordaten des Triaxus wurden sofort analysiert, um die angestrebten sogenannten Bio-Superstationen festzulegen. Letztere bestanden aus CTD-Casts (für biogeochemische und biologische Wasserproben), Ramses Unterwasserlicht-Profilmessungen, zwei Multinet-Fängen (einer für Plankton und der andere für Quallen), LOKI (Zooplankton-Fotografie) und Mikrostruktur-Turbulenzprofilen (zur Ableitung von vertikalen Flüssen). Eine der Stationen war durch ein tiefes Chlorophyllmaximum gekennzeichnet, eine von Atlantikwasserstation bis zur Meeresoberfläche dominiert und eine von Polarwasser bedeckt (Schmelzwasser an der Oberfläche, flaches Chlorophyllmaximum). Entlang des Transekts wurden Verankerungen ausgelegt, um oberflächennahe Eigenschaften in verschiedenen Meereisbedeckungsregimen abzudecken. Das Verankerungspaar Y1 und Y2 wurde in einem Gebiet von größtenteils ganzjährig offenem Wasser ausgelegt (mit Top-Elementen, die sich 20 m unter der Oberfläche befinden). Das Verankerungspaar Y3 und Y4 wurde weiter nördlich in saisonal eisbedeckten Gewässern ausgelegt (eines mit einem Rohr als Top-Element, das bis zu 6 m unter die Meeresoberfläche reicht – eine wahre High-Risk Verankerung).

19.–22. Juli (nördlicher Teil der MIZ): Ein weiteres erfolgreiches Triaxus-Survey durch dichtes Eis (Eisbedeckung größer als 90 %) zum nördlichen Ende des MIZ-Transekts legte den Grundstein für die nachfolgenden Arbeiten. Kurz bevor wir das nördliche Ende des Transekts erreichten, beschlossen wir, die Plattform zu bergen, da die Eisschollen groß wurden und Presseisrücken aufwiesen. Auch hier wurden die Triaxus Daten unmittelbar verwendet, um repräsentative Standorte für zwei Bio-Superstationen zu definieren (eine am nördlichen Ende der Linie und eine andere, die durch ein oberflächennahes Dichteminimum gekennzeichnet war). Darauf folgte der Einsatz der Verankerung Y5 am nördlichen Ende des Schnitts in einem größtenteils ganzjährig eisbedeckten Gebiet (Top-Element 20 m unter der Oberfläche). Anschließend besuchten wir die Nordscholle, die Mittelscholle und die Südscholle erneut, um eine ähnliche Reihe von Messungen wie bei der ersten Runde durchzuführen. Alle drei Schollen waren seit dem ersten Besuch recht kohärent etwa 20 sm nach Westen gedriftet. Es war offensichtlich, dass seitdem Oberflächenschmelze stattgefunden hatte. Für den Nordschollen-Besuch war der Zugang mit der Gangway möglich. Die Eisscholle war weitgehend intakt, aber ein Teil der Eisscholle (relativ nahe an der Bojenstelle) war abgebrochen. Alle Bojen waren allerdings noch vorhanden. Die Südscholle hingegen hatte sich in mehrere Schollen aufgeteilt. Für den Zugang war eine Mummychair-Operation notwendig. Alle Bojen standen noch zusammenhängend auf einem (recht kleinen) Stück Eis. Für das Messprogramm auf Eis griffen wir hier dann auf ein anderes (größeres) Stück der ursprünglichen Scholle zurück. Die Mittelscholle erwies sich als weitgehend intakt und mit allen Bojen present. Trotz nebliger Bedingungen konnten wir zwischen dem 13. und 22. Juli eine Reihe von Helikopter-Vermessungen durchführen, sowohl kamerabasiert (Eisoberflächeneigenschaften) als auch EM Bird-basiert (Eisdicke).

23.–26. Juli (Aurora): Nachdem wir dichtes Eis mit Presseisrücken durchquert hatten, erreichten wir am 24. Juli das Hydrothermalfeld Aurora, das einzige derzeit bekannte aktive Hydrothermalfeld des Arktischen Ozeans. Es befindet sich nahe dem westlichen Ende des Gakkelrückens. Hierbei handelt es sich eine aktive Spreizungszone. Hier legten wir acht Ozeanbodenseismometer (OBS) aus, anhand derer wir untersuchen werden, wie sich Magma im Untergrund bewegt und wie Wasser entlang von Verwerfungen tief in den Untergrund

eindringen kann. Da eine genaue Positionierung der OBS auf dem Meeresboden in diesem zerklüfteten Terrain erforderlich ist, erwies sich die Auslegung der OBS auf Grund der Präsenz großer Eisschollen als zeitaufwändige Aufgabe. Die OBS sollen ein ganzes Jahr lang am Meeresboden verbringen und winzige Erdbeben in der Nähe des Aurora-Hydrothermalfelds aufzeichnen. Wir führten einen tiefen (4000 m) CTD Cast durch und legten eine Verankerung in direkter Nähe des Hydrothermalfeldes aus, anhand deren Daten sich die Plume-Signatur hydrothermalen Ursprungs in der Wassersäule charakterisieren lassen soll.

27. Juli bis 02. August (Yermak-Plateau): Am 27. Juli kehrten wir an die Westflanke des Yermak-Plateaus bei 81°20' N zurück. Anschließend führten wir in hangaufwärtiger Richtung eine topographische Kartierung durch und legten basierend auf den Messungen die Verankerungen Y7 und Y8 in 1450 m bzw. 800 m Wassertiefe aus. Zwischen diesen Aktivitäten wurde eine 24-Stunden-Eisstation durchgeführt, deren Hauptziel darin bestand, eine kontinuierliche Aufzeichnung von Mikrostruktur-Turbulenzmessungen zum Studium gezeiteninduzierter Vermischung zu erhalten. Am 29. Juli wurde ein Triaxus-Survey von der Nordscholle zur Mittelscholle und weiter zur Südscholle durchgeführt. Letzteres war seit den letzten Besuchen etwa 25 sm nach Südwesten verdriftet. Basierend auf der Erhebung wurden zwei Super-Biostationen durchgeführt. Am nächsten Tag machten wir unseren dritten Probennahmebesuch auf der Nordscholle, bei dem zudem alle Bojen erfolgreich geborgen wurden. Aufgrund der nebligen Bedingungen konnten wir im angegebenen Zeitraum nur ein sehr begrenztes Helikopter-Vermessungsprogramm durchführen, um die Eigenschaften der Eisoberfläche zu untersuchen. Nach Abschluss eines zusätzlichen Triaxus-Surveys von der Südscholle in Richtung Eiskante führten wir eine weitere Super-Biostation durch. Am 31. Juli besuchten wir dann zum jeweils dritten Mal die Süd- und Mittelscholle zur Durchführung von abschließenden in situ Messungen und konnten dabei erneut unsere gesamte Bojen-Instrumentierung bergen. Es folgte eine weitere Super-Biostation. Am 01. August richteten wir unsere Aufmerksamkeit schließlich auf den äußeren Rand des MIZ und schleppten das Triaxus durch eine mesoskalige Eisformation, die nach Süden in das eisfreie Wasser hineinragte. Begleitet wurde dies von einer Wasserprobennahme entlang des Triaxus-Weges. Am 02.August, nachdem die Bergung des UiB-Glider erfolgt war, starteten wir einen Transit zum Ostgrönlandstrom. Am Abend erwartete uns bei ruhiger Transitfahrt das verspätete Bergfest.

03.–07. August (Nordostgrönland): Nach der Ankunft im Ostgrönlandstrom wurde die Bergung und anschließende Wiederauslegung der FRAM EGC-Verankerung sowie eine klassischen Hausgarten-Station (s. Arbeiten in der östlichen Framstraße) durchgeführt. Anschließend fuhren wir weiter westwärts zum inneren grönländischen Schelf, wo die Festeisbarriere der Norske Oer unser Fortkommen entscheidend einschränkte. Das Ziel der nachfolgenden Arbeiten sollte es sein, ozeangetriebenes Abschmelzen der 79N Gletschers und des Zachariae Isstroem zu erforschen und glaziologische Arbeiten auf den Gletschern durchzuführen. Da ein Durchbrechen der Eisbarriere gen 79N Gletscher mit dem Schiff nicht machbar schien, entschieden wir uns, mögliche glaziologische und ozeanographische Flugziele von Südwesten her anzufliegen. Wir konnten uns der Insel Franske Oer nähern, da eine kleine Region im südlichen Teil des Festeises im Norsketrog tatsächlich eine Dicke von weniger als 80 cm aufwies. Da der Nebel unser stetiger Begleiter blieb und einen Langstreckenflug zu den Gletschern unmöglich machte, entschieden wir uns, weiter nach Westen zu versetzen und zu versuchen, die Flugreichweite zu verkürzen. Am Abend des 05. August waren wir in die Passage zwischen den Inseln Parisoerne und Franske Oer vorgedrungen, einem möglichen Tor für warmes Atlantikwasser in die Joekelbugten, in die der mächtige Auslassgletscher Zachariae Isstroem mündet. Unsere hydrographischen und bathymetrischen Kartierungen

zeigten jedoch, dass sich dieser Kanal zusehends verengte und zu flach wurde (weniger als 280 m), um einen nennenswerten Durchstrom warmen Wassers zu gewährleisten. Da zu diesem Zeitpunkt die Wettervorhersage für die kommenden zwei Tage noch schlechtere Flugbedingungen prognostizierte, beschlossen wir dann, das Programm für Nordostgrönland vorzeitig zu beenden. Wir führte eine Super-Biostation in der Nähe der oben genannten Inseln durch, gefolgt von zwei Eisstationen in unterschiedlichen Eisbedingungen (festes vs. rottes Festeis) auf dem Rückweg nach Osten im Norsketrog. Um zumindest rudimentär das Zeitserienprogramm bzgl. ozeanbedingter Gletscherschmelze aufrecht zu erhalten, legten wir am 7. August eine Verankerung am nördlichen Ende des Ile-de-France Schnitts im Norsketrog aus. Zwischen 2016 und 2017 hatte hier schon einmal eine AWI-Verankerung im Atlantikwasserzustrom in Richtung des 79N Gletschers gelegen. Nach diesem insgesamt eher wenig erfolgreichen Programm zur Ozean-Gletscher Wechselwirkung in Nordostgrönland begaben wir uns auf einen Transit entlang der grönländischen Küste zum Scoresbysund nahe 70°N.

09. – 17. August: Nach einer kurzen, zufälligen Begegnung mit FS *Maria S. Merían* an der Mündung des Scoresbysundes machten wir uns gegen Mitternacht des 9. August direkt zum inneren Fjord am Übergang zum Nordvestfjord auf. Hier bargen wir erfolgreich zwei Verankerungen, die vier Jahre lang im Wasser gewesen waren, und führten ein reduziertes hydrographisches Programm durch, um das Einströmen von warmem Atlantikwasser in das tiefe Becken des Nordvest Fjords zu dokumentieren - der Heimat des Daugaard-Jensen-Gletschers, der mit einer hohen Rate Eisberge produziert. Auf dem Weg aus dem Fjord hinaus wurde ein letztes Triaxus-Survey durchgeführt. Nach mehreren fehlgeschlagenen Versuchen des regulären Auslösens der an der Fjordmündung liegenden Verankerung SCO3 wurde abschließend versucht, sie am Morgen des 11. August per Dretschen zu bergen. Wir konnten den oberen Teil der Verankerung an Bord nehmen, während die unteren Elemente einschließlich eines ADCPs auf dem Meeresboden verblieben. Anschließend kehrten wir bei ruhiger See quer über das Europäische Nordmeer – nördlich von Island, den Färöer-Inseln und den Shetlandinseln – in die Nordsee zurück und erreichten Bremerhaven am Morgen des 17. August.

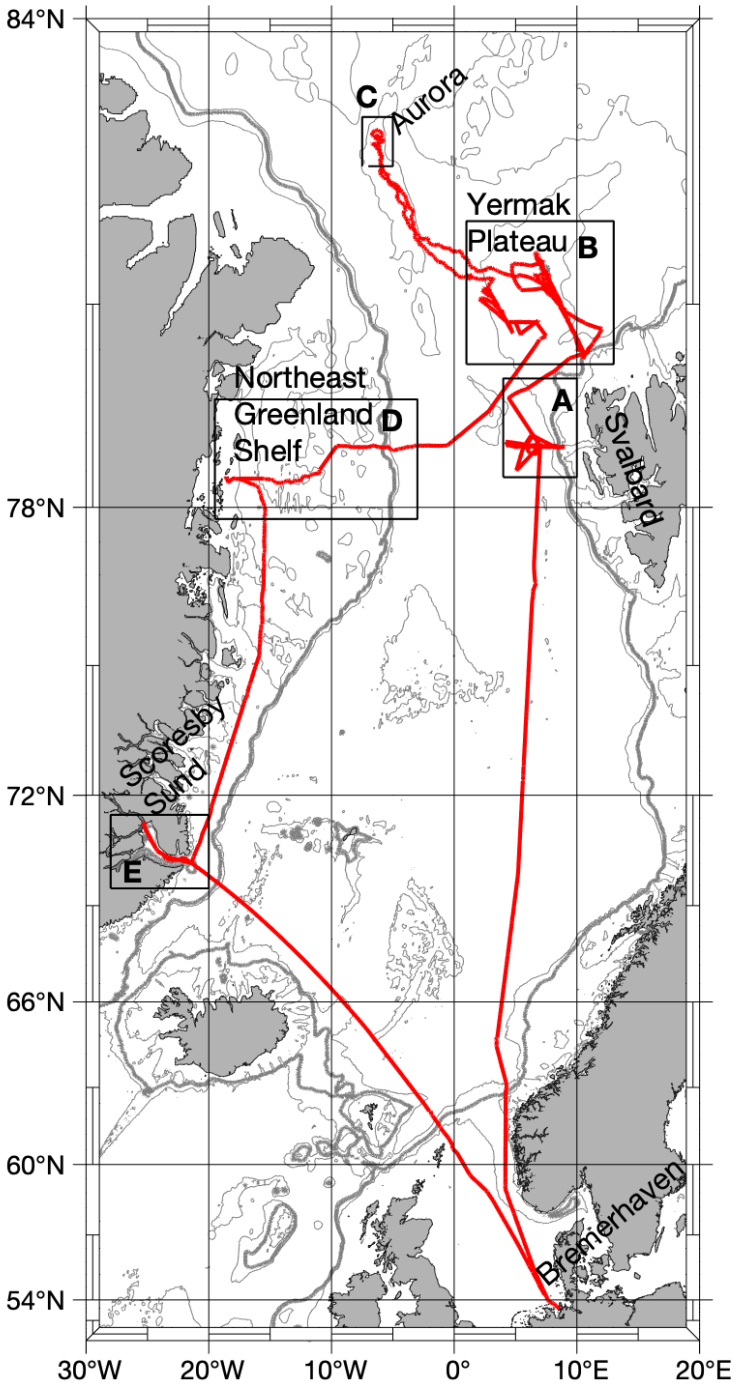

Abb. 1: Route der Expedition PS131. Die Arbeitsgebiete: Östliche Framstraße, Eisrandzone, Aurora Hydrothermalfeld, Nordostgrönlandshelf bzw. Scoresbysund sind durch die Rechtecke A, B, C, D und E gekennzeichnet. Siehe https://doi.pangaea.de/10.1594/PANGAEA.95100 für eine Darstellung des master tracks in Verbindung mit der Stationsliste der Expedition PS131.

Fig 1.1: Track of expedition PS131. The boxes A, B, C, D and E mark the different work areas of Eastern Fram Strait, the marginal ice zone, Aurora vent field, Northeast Greenland and Scoresby Sund, respectively. See https://doi.pangaea.de/10.1594/PANGAEA.95100 to display the master track in conjunction with the station list of expedition PS131.

SUMMARY AND ITINERARY

The expedition PS131 **AT**lantic **WA**ter pathways to the **ICE** in the Nansen Basin and Fram Strait (**ATWAICE**) addressed important goals defined in the new programme POF IV of the research field "Earth and Environment" of the Helmholtz Association with a focus on Topic 2: "Ocean and Cryosphere in Climate" and Topic 6: "Marine and Polar Life". Our work was divided into four major aims. The prime objective 1 was a multidisciplinary process study of ocean controls on sea ice melt and the couplings to biogeochemistry, biology and the atmosphere in the marginal ice zone (MIZ) north of Svalbard. Objective 2 of ATWAICE represents the continuation of the mooring-based long-term monitoring of the exchange flows in Fram Strait (as part of AWI's interdisciplinary FRAM infrastructure in the Arctic Ocean) – realizing the strong need for long-term year-round monitoring programmes at key ocean sites in order to quantify anthropogenically-introduced changes. Objective 3 targeted ocean impacts on major marine-terminating glaciers in (North)east Greenland. Objective 4 constituted a lithospheric study in the Aurora vent field at the western end of Gakkel Ridge. We were very successful with objective 1, 2 and 4, while a fast ice area and foggy conditions at the Greenlandic coast impeded our work towards objective 3 severely. For subsequent orientation, the expedition track is shown in Figure 1.1.

28 June to 4 July: On 28 June *Polarstern* left Bremerhaven in summerly conditions with a science party consisting of 47 participants. For the first four days, Corona precaution regulations made it mandatory to wear masks and avoid large gatherings. After a second round of all negative antigen tests, the measures were abandoned. The transit to Eastern Fram Strait took place during calm conditions which made the preparations and tests for the subsequent fieldwork go smoothly. On 1 July tests of the CTD and LOKI were performed off the coast of Norway.

5 to 10 July: During pleasant weather conditions the first block of field work was carried out in eastern Fram Strait, an area dominated by the advection of warm, saline waters (hereafter referred to as Atlantic Waters) in the West Spitsbergen Current (WSC). The work was mainly carried out in the framework of AWI's FRAM observatory (Frontiers in Arctic Marine Monitoring). The mooring programme supports integrated long-term, year-round physical, biochemical and biological time series measurements. All of the 8 moorings were successfully recovered, with some of them extending through the water column to up to 20 m below the sea surface, which is challenging when deployed in water depth between 700 and 2,600 m. The moorings were subsequently redeployed. Strong currents in the WSC made it a difficult task to estimate the depth of the top elements of each of the moorings below the sea surface. Besides mooring work, during the night hours we covered three long-term Hausgarten stations S3, HG4 and N4 with lowered measurements of hydrography, velocity, biological and chemical water samples, plankton imaging (LOKI) and underwater radiation (RAMSES) and plankton and jellyfish multinets. A second nighttime activity was the completion of a hydrographic section across the WSC at 79N. A helicopter flight to Ny Alesund was additionally accomplished (6

July) to increase our supplies of flashbang ammunition (kindly made available by the AWIPEV station management) needed for polar bear guarding activities. On the same flight important spare parts for the MSS winch was also brought on board. Also, we deployed a glider (Bergen University) which subsequently would travel north along the WSC toward the MIZ north of Svalbard – the second work area of our expedition. We further accomplished tests for various systems whose operation was planned in the MIZ, including the towed sensor platform Triaxus and helicopter-based remote sensing applications (cameras, ice thickness, etc).

11 – 15 July: After the very successful completion of the work Fram Strait on 11 July we arrived in the ice-free waters on the continental slope north of Svalbard, to start the main focus of the expedition – an interdisciplinary study of the MIZ. The idea behind the work on summertime melt of sea ice in the MIZ had been to focus on two scales. Firstly, we intended to resolve the oceanic, biological and sea ice gradients across the MIZ, primarily based on ship-based measurements (including the towed Triaxus sensor platform), drifter deployments and helicopter surveys. In addition, the melt and decay of individual ice floes represented a second focus. The heart of the latter was work on three ice floes having different distances from the ice edge. We envisioned to instrument each floe with sea ice and oceanographic buoys to obtain time series for the duration of 3 week. Also, sea ice, oceanographic and biological surveys were to be conducted three times on each of the three floes to document changes over time. We started with a short Triaxus tow in open water approaching the ice edge from the south, continued by a ship-based hydrography / nutrient survey with 8 nm station spacing along a transect across MIZ into the pack ice. The total length of the transect (Triaxus open water and CTD in ice) was 84 nm. After its completion, between 13 and 15 July three ice station along the transect were made, which included the installation of ice physics and oceanographic buoys and a suite of measurement and sampling activities (ice thickness, ice coring, ice surface properties, ice biological samples, under ice turbulence, under ice CTD). The first floe was targeted was on the northern end of the line (North Floe) in an area of relatively large floes. The second floe (South Floe) was located some 28 nm south of Floe North. During our work of the floe, swell came in from the south, and the floe broke up into several small pieces. We had initially planned to have the next ice station further south toward the ice edge. Yet, the decision made not to move further south, because the swell event had effectively smashed all floes further south toward the ice edge, making on ice work and buoy installation impossible. Instead, the third ice floe station (Middle Floe) was chosen roughly in the middle between North Floe and South Floe.

July (open water and southern part of MIZ): After completion of the first round of ice floe stations, we returned to the open water area at the southern end point of the cross-MIZ transect. We deployed two Argo Floats kindly provided by BSH (Hamburg) east of Yermak Plateau in ice-free deep waters. Subsequently the first ever tow of Triaxus under sea ice using a depressor weight was conducted across southern end of MIZ in loose ice conditions. The hydrographic-biogeochemical sensor data was then instantly analysed to define the targeted so-called Bio-Superstations. The latter consisted of CTD casts (for biogeochemical and biological water sampling), Ramses (underwater light) profiling, two multinet catches (one for zooplankton and the other for jellyfish), LOKI (zooplankton photography) and microstructure turbulence profiles (for the derivation of vertical fluxes). One of the stations was characterized by a deep subsurface chlorophyl maximum, one being an Atlantic Water station (up to the sea surface) and one covering polar water (meltwater at surface, shallow chlorophyll max without warm water near the surface). Moorings were deployed along transect to cover near surface properties in different sea ice coverage regimes. The pair of moorings Y1 and Y2 was deployed in mostly year-round open water (with mooring top elements residing 20m below surface). The mooring pair Y3 and Y4 was deployed further north in seasonally ice-covered waters (one having a surface tube element reaching up to 6 m below the sea surface).

19-22 July (northern part of MIZ): A successful Triaxus trawl through dense ice (ice cover larger than 90%) toward northern end of MIZ transect lay the foundation for the subsequent work. Shortly before reaching the northern end of the transect, we decided to recover the platform as ice floes became large and ridged. Again, the trawl was used to define representative locations for two Bio-Superstations (one at the northern end of the line and another one characterized by a subsurface density minimum). This was followed by the deployment of mooring Y5 on northern end of line in mostly perennial ice cover (mooring top 20 m below surface). Subsequently we revisited North Floe, Middle Floe and South Floe to conduct a similar suite of measurements as during the first round of visits. All three floes had drifted in a quite coherent way about 20 nm to the west since the first visit. Surface melt was apparent to have taken place. For the North Floe revisit the access with the gangway was possible. The floe was largely intact, but a part of the floe (relatively close to the buoy site) had broken off. All buoys were still in place. South Floe Ice had split up into several floes. A mummy chair operation was necessary for access. All buoys were still together on one piece of ice. For the on-ice measurement programme we accessed another (larger) piece of the original floe. The middle floe turned out to be largely intact with all buoys in place. Despite foggy conditions we managed to accomplish a number of helicopter surveys between 13 and 22 July, both camera-based (ice surface properties) and EM Bird-based (ice thickness).

23-26 July: After passing through dense, ridged ice we arrived on 24 July at the Aurora hydrothermal vent field, the only currently known active vent field of the Arctic Ocean located near the western end of Gakkel Ridge. It is an active spreading zone. Here we deployed eight ocean bottom seismometers (OBSs), based on which we will investigate, how magma moves in the subsurface and how water can penetrate along faults deep into the subsurface. As precise positioning of the OBSs on the sea floor is required, the deployment of the OBSs was a time-consuming task in the field of large ice floes. The OBSs will spend an entire year at the seafloor, recording tiny earthquakes in the vicinity of the so-called Aurora hydrothermal vent field. We further took a deep (4,000 m) CTD and deployed one mooring in direct vicinity of the vent that may hopefully detect the plume signature of hydrothermal origin in the water column.

27 July - 2 August (Yermak Plateau): On 27 July we had returned to the western flank of Yermak plateau near 81°20‘N. We subsequently prepared the deployment of two moorings with a bathymetric cross-isobath survey, and subsequently deployed Y7 and Y8 at 1450 and 800 m water depth. In between, a 24 hours ice station was accomplished, whose main task was to obtain a continuous record of MSS turbulence measurements. On 29 July a Triaxus survey was conducted from North Floe to Middle Floe and further to South floe (staying slightly east of the floes). The latter had drifted roughly 25 nm to the southwest since the last visits. Based on the survey two Super-Biostations were carried out. The next day made our third sampling visit to North Floe which involved the successful recovery of all buoys. Due to foggy conditions we only managed to accomplish a very limited camera-based helicopter survey programme to study ice surface properties. After completing a additional Triaxus survey from South Floe toward the ice edge, we conducted another Super-Biostation. On 31 July we re-visited South Floe and Middle Floe, and again were able to retrieve all our instrumentation. This was followed by another Super-Biostation. On 1 August we finally turned our attention to the outer margin of the MIZ, towing Triaxus across a mesoscale ice feature protruding into the ice-free waters to the south. This was accompanied by a water sampling programme along the Triaxus path. On 2 August, after the recovery of the UiB glider purposefully steered toward the feature, we started a transit to the East Greenland Current. In the evening the delayed Bergfest waited for us during a calm transit.

3-7 August: Upon arrival in the East Greenland Current, the recovery and subsequent re-deployment of the FRAM EGC mooring was accomplished plus a classical Hausgarten Bio-Station. We subsequently headed to the inner shelf where the Norske Oer fast ice barrier was waiting for us. The aim of the subsequent work should have been to study the ocean-driven melt of the 79N Glacier and Zachariae Isstroem, combined with glaciological measurements on the glaciers. As breaking though the ice barrier toward the 79N Glacier with the vessel seemed unlikely, we decided to approach possible glaciological and oceanographic flight targets from the South. We were able to move close to Franske Oer, as patches in the Southern part of the fast ice in Norske Trough were actually less than 80 cm thick and melting. With fog being our close company, making any long-range flight to the glaciers impossible we decided to go further west, trying to shorten any flight ranges. By the evening of 5 August we had moved into the passage between islands of Parisoerne and Franske Oer, a possible gateway for warm Atlantic Water from the Greenland Shelf into Joekelbugten, into which the massive outlet glacier Zachariae Isstroem terminates. Our hydrographic and bathymetry charting however revealed this channel to narrow down and become too shallow (less than 280 m) to support any sizable flow. The weather prediction for the coming two days revealed even worse flight conditions. ee then decided to stop the program for Northeast Greenland, conducted a biostation close to the abovementioned islands, and two ice stations in different ice conditions (solid vs rotten fast ice) on the way back east in Norske Trough. On 7 August we deployed a mooring on the northern end of the Ile de France section, in a place previously covered by an AWI mooring in the Atlantic Water inflow branch toward the glaciers on the coast of Greenland. After this rather unsuccessful programme we set sail to Scoresby Sund near 70°N.

August 9-17: After a short, fortuitous encounter with RV *Maria S. Merían* at the mouth of Scoresby Sund, near midnight of 09 August, we sailed straight into the inner fjord toward the transition to Nordvest Fjord. Here we recovered two moorings that had been in the water for four years, and conducted a small hydrographic programme to document the cascading of warm Atlantic Water into the deep basin of Nordvest Fjord, home of the heavily iceberg producing Daugaard Jensen Glacier. On the way out of the fjord a final Triaxus trawl was conducted before (after a number of failed attempts of regular release) mooring SCO3 at the fjord mouth was subject of a dredging operation in the morning of 11 August. We managed to retrieve the top part of the mooring, while the bottom elements including an ADCP remained on the sea floor. Subsequently we sailed back straight across the North Atlantic in calm seas – passing north of Iceland, Faroe Islands and Shetland - into North Sea, and arrived in Bremerhaven in the morning of 17 August.

WEATHER CONDITIONS DURING PS131

Patrick Suter DE.DWD

Atlantic Water pathways to the ICE in the Nansen Basin and Fram Strait, ATWAICE for short, was the main focus of the *Polarstern*-expedition PS131 and was dedicated to the development of a process study on ocean-driven ice melt in the ice margin zone north of Svalbard. In addition, the FRAM mooring array, which the AWI has been operating west of Svalbard since 1997, was partly renewed, and ocean-bottom seismometers and moorings were deployed on the Gakkel Ridge (AURORA-vent-fields) northwest of the main research area. A final focus led the expedition to the vicinity of the 79N-Glacier on the northeast coast of Greenland. There, the glacier retreat caused by the ocean was to be investigated. However, weather and ice conditions close the glacier made this impossible, so the remaining time was used to recover three moorings in Greenland's Scoresby-Sound about 500 nautical miles to the south.

Bremerhaven - Fram Strait

The Arctic expedition PS131 started from Bremerhaven on 28 June 2022. The weather conditions at departure were calm and dominated by high pressure. A high-pressure zone lay from northern Germany over southern Norway to the Norwegian Sea. In the early afternoon, *Polarstern* set off for the North Sea via the lock system of the Weser with light winds. The departure was accompanied by quite sunny and pleasantly warm conditions, as well as, shallow cumulus clouds. During the journey northwestwards through the North Sea, *Polarstern* lay on the southwestern flank of a large high-pressure zone that was slowly shifting towards Scandinavia. Thus, the current turned to southeast and reached mostly moderate strength on 29 and 30 June. With mostly sunny weather and quite dry air, the coast of southwest Norway was passed. The swell, initially from south to southwest and later also from northeast, reached a maximum of 1 m.

In the area of the southern Norwegian Sea, a first test station for various scientific measuring instruments was scheduled for 1st of July. At the same time, a low-pressure system moved from the North Sea to the Shetland Islands. The wind from the east increased from 3 to 5-6 Bft and shallow cumulus and overlying altocumulus and cirrus clouds developed in the afternoon. In the second half of the night on 2 July, *Polarstern* crossed the Arctic Circle. It was also the first night without a sunset. This was the start of the polar day, which meant that the day light will remain permanently. On 2 July, the low continued to move northwards to the east of Iceland, intensifying. As a result, a frontal system formed with the confluence of warm and humid air with its origin over Scandinavia and cooler sea air from the south just south of the driving area. By the evening, the first rain showers had fallen and the easterly flow had decreased to 4 Bft. On 3 July, *Polarstern* was stuck in the middle of the now occluded frontal system. The wind shifted to southwest and increased to 5 Bft, temporarily also 6 Bft. Within the high-up-reaching nimbostratus cloud cover, there was intermittent visibility below 1 km (fog) and precipitation. Meanwhile, temperatures dropped into the single digits. On 4 July, a low-pressure system east of Iceland extended northeastwards to southern Svalbard. *Polarstern*, sailing in the Greenland Sea, temporarily came to the front of the slowly northward moving frontal system. As a result,

the wind shifted to the east in the afternoon and decreased to 2 to 3 Bft. When another test station was held, the southwesterly wind field caught up with the ship again. Again, fog and intermittent light drizzle occurred.

Eastern Fram Strait ("Hausgarten")

By the morning of 5 July, *Polarstern* had reached the research area "Hausgarten" in the eastern Fram Strait at around 79° North. The working program included initially mooring- and various test work. The remnants of the now stationary frontal system still lay over the centre of Svalbard, southeast of the research area. A high-pressure system over the western Fram Strait started to take over. This led the wind to shift to north to northeast by the morning and increase to 6 Bft. Embedded in this current, significantly drier and cooler air flowed in. This led to significantly improved weather conditions and a transition to mostly sunny conditions and excellent visibility. The mountains of Northwest Svalbard were visible from a distance of over 50 nm. The wind sea temporarily increased to somewhat over 2 m.

On 6 July, the high-pressure system and a fresh to strong northeasterly current remained predominant. In addition to station work on the ship, a resupply flight to the AWI research station in Ny Alesund could be carried out as planned in mostly sunny conditions after morning fog patches. At the ship, somewhat aggravating for the scientific equipment to be lowered into the water was the wind sea, which was over 2 m high at times.

The station work in the eastern Fram Strait continued on 7 July. A high-pressure system continued to lie to the east of *Polarstern*. The northeasterly wind decreased to 4 Bft during the day and veered slightly back to the north, as *Polarstern* approached Svalbard. As a result, the wave height also gradually decreased to around 1 m. The first half of the day was characterised by slowly descending Stratocumulus clouds, which dissipated after midday. Subsequently, the high slowly moved southwards, resulting in a wind shift over north to northwest, later west with 4 to 5 Bft on 8 July. The air mass continued to be dry, but in the afternoon a local humidity field with low-lying stratus clouds overran the research area.

On 9 July, there happened a change in the weather situation. The high-pressure system moved southwards and the Fram Strait came to the front of a stationary trough over northeast Greenland. In the course of the day, the current turned to southwest with 4 to 5 Bft. This started the transport of cool, humid air originating over the ice of the western Fram Strait. This air took up moisture over the water and reached *Polarstern* near Hausgarten Station IV in the form of dense and fog/stratus, vertically reaching up to 900 m. The temperature dropped to around 0°C in the fog. By the evening, swell with 1 m could also be observed, approaching from the southwest. On 10 July, a fresh southwesterly current continued to prevail, which, however, turned somewhat to the south near the ground by morning. This meant that the air at the surface, which was no longer flowing in from the ice to the southwest, was somewhat drier. The fog lifted off the ground and temporarily turned into stratocumulus clouds. During the course of the day, *Polarstern* sailed northwest to the ice edge of Hausgarten Station Nord. As a result, the ship again came under the influx of cool and foggy air from the ice. This time evolution of the different air masses was also visible in the temperature development. While 4 to 5°C prevailed outside the fog, the temperature in the fog air dropped abruptly to 1°C.

Transition zone sea ice - open water and ice-floe-work northwest of Svalbard

By 11 July, the research area had shifted northeast to just north of Svalbard near 80°30'N 10°30'E. Embedded in the fresh southwesterly flow, a shortwave trough moved northeast over

the research area. In connection with this, the wind slightly increased to 6 Bft in the morning and the sea with swell from the southwest temporarily reached 1.5 to 2 m. The passage of the trough was accompanied by a strong wind. The passage of the trough was accompanied by moist air and some rain. Some drier air flowed in from at the rear side. Because *Polarstern* moved northwest in the afternoon, however, the dryer could never really reached to the ground directly at the ice edge. With the cooling underlay of the loose ice and the cold water, the humidity condensed just above the surface. This led to misty conditions again in the afternoon.

On 12 July, *Polarstern* continued slowly northwestwards in occasionally denser ice. This brought the ship just southeast of a weak high-pressure ridge, and low wind prevailed. A shallow layer of fog remained present in the moistened boundary layer, through which the sun shone through at times. In the evening a first suitable ice floe near 81°36'N 06°41'E was found for ice work.

On 13 Juli, *Polarstern* still was under the influence of small air pressure contrasts. On the eastern side of a filling up low-pressure system over the southern Fram Strait, mild and humid air was advected into the research area with upper-level southerly winds. This led to upward gliding motions and the cloud layer grew upwards. There were repeated time periods with fog, intermittent drizzle and also rain. Two short windows, in which the otherwise very low stratus clouds broke up and the visibility increased significantly, were optimally used for helicopter flights to explore and measure the floes. On 14 July, *Polarstern* was on the northwestern edge of a low-pressure zone with a former gale south of Fram Strait and a secondary low northeast of Svalbard. Meanwhile, ice work on a second ice floe more to the southeast near 81°11'N 07°35'E was on the schedule. The near-bottom current became northeasterly and increased to 4 to 5 Bft. Continuous warm air advection and oversaturated air led to foggy conditions with occasional light drizzle. In addition, a subdued but clearly noticeable swell from southwest to south could be observed. This caused numerous cracks and movement on the ice floe.

On 15 July, further ice work was started on a third ice floe, which was located between the two other floes, near 81°21'N 06°39'E. This third floe remained on the northern edge of a low-pressure zone within a moderate northeasterly flow. While the air in the mid and upper levels of the troposphere had become drier somewhat, cool and moist air remained trapped under a capping inversion near the ground. With temperatures slightly below the freezing point, this resulted in freezing fog, intermittent supercooled drizzle and correspondingly poor visibility.

On 16 July, *Polarstern* temporarily left the ice to the southeast. With a low-pressure system moving from south of Svalbard into Fram Strait, the northeasterly current increased to 5 to 6 Bft by the morning. However, as the low weakened at the same time, the winds from northeast also decreased to 3 to 4 Bft by the evening. After a warm front moved over the research area from the southeast, the clouds and fog temporarily dissipated with lee effects downstream of Svalbard. As a result, several helicopter flights were carried out. A flight in the evening over ice was again accompanied by widespread stratus and fog, some of which had a vertical thickness of 150 to 200 m. With the lee effects and the drive out of the ice, the air temperature rose to 8°C by the evening and the swell from the south reached 1.5 m at times.

In the night of 17 July, *Polarstern* went back into the ice before sailing southeast out of the ice again by midday. The low described above slowly dissipated over the Fram Strait. After a brief increase in the southwesterly wind to 5-6 Bft during the night, the wind slowed down by morning and subsequently shifted slowly to northeast. Shallow fog was present over the ice, mostly reaching only 30 to 50 m high. In the afternoon, the fog grew briefly to 150 m with a temporary drop in temperature. As *Polarstern* moved southeast out of the ice, the fog lifted and visibility consequently increased.

By evening, a powerful low-pressure system approached south of Svalbard. The swell at the ice edge from southeast to south increased to 2 to 2.5 m, which, triggered by the low, indicated strong foehn winds in the north of Svalbard. On 18 July, mooring work was planned outside of the sea ice. The powerful low moved northwestwards into the Fram Strait. During the night, its warm front crossed *Polarstern* from southeast to northwest. In connection with this, the moisture content reached values very untypical for polar regions. The total water vapour content (PPW) measured with radiosonde ascents reached values of over 30 mm during the night, with a maximum of 35 mm during the weather balloon ascent on 17.07.22 at 21 UTC. Comparable values are normally found on a sultry summer day in Central Europe. A masked cold front followed in the morning. Behind it, a lee-side low formed north of Svalbard. The initial wind from the northeast with 5 Bft, shifted over east to southeast by the morning and briefly reached 6 Bft. The foehn-like winds brought in drier air, with which the cloud coverage decreased. The cold and humid foggy boundary layer over the ice was also cleared out after midday and pushed away to the northwest. The air mass was exceptionally mild. The morning radiosonde ascent from 03:00 UTC near 80°24'N 10°18'E recorded 18.4°C at about 700 m altitude. On the ship, the highest temperature of the expedition was measured with 10.3°C at noon. Meanwhile, the low moved further northeast from Fram Strait. As a result, the wind decreased to 2 to 3 Bft with a temporary westerly rotation until the evening. In the meantime, *Polarstern* moved slightly northwest towards the ice edge. The swell from southeast to east reached 1.5 to 2 metres.

On 19 July, the weakening low was located on the northeast coast of Greenland. A large high-pressure system was located in the northern Laptev Sea. From this, a weak ridge slowly spread southwestwards into the research area. The easterly current temporarily increased to 5 Bft at night. As the ridge approached, northerly winds of 4 Bft set in. The air continued to be relatively mild, and the somewhat increased humidity was visible in the form of mist fields in the boundary layer near the ground. Above this, increasingly dense altocumulus and cirrus clouds moved in from the southeast during the course of the day. The swell from south decreased to 1 m. By the evening, the mooring work at the ice edge was completed and the research vessel headed northwest again into the sea ice. On 20 July, weak high-pressure influence continued to prevail. The current turned southwest to south and weakened. With the southerly winds, more moisture was brought in by upslope motion in the form of lower stratocumulus clouds. From early afternoon, the cloudiness changed to stratus and fog. After renewed mooring work near 81°30'N 07°00'E, work on the first ice floe was again on the schedule from the evening.

On 21July, after a short transit, ice work continued on the third ice floe. In the evening, station work with a focus on biological measurements (bio-station) was scheduled a little east of the third ice floe. The work was carried out under the continuing influence of light high pressure. This led to light wind conditions and it was persistently foggy, cloudy and grey. On 22 July, *Polarstern* again reached the second ice floe, which the scientists again used for ice work. Meanwhile, the small high-pressure zone lay in the northern Fram Strait. South of Svalbard, on the other hand, there was a low-pressure zone. In between, a moderate north to northwest flow resulted in the research area. The upper limit of the fog layer grew to 1,300 to 1,500 m with persistent warm air advection and upslope motion close to the ground. Light drizzle also fell repeatedly out of the supersaturated air mass.

Transit and station work at the Gakkel-Ridge (AURORA-vent-fields)

On the evening of 22 July, the ice work was completed and *Polarstern* headed northwest to the underwater Gakkel Ridge (AURORA station). The transit through the thickening ice followed the northwestern edge of a shallow low-pressure zone with a core near Novaya Zemliya and

was accompanied by weak northerly to northeasterly winds. With frontogenetic processes, the cloud layer continued to grow towards 23 July and nimbostratus formed, which, according to the morning radiosonde ascent, reached up to 4,500 m and caused intermittent weak rain and drizzle. Visibility remained poor at due to fog. From the evening hours, drier air slowly flowed in and the air mass dried from above. From midnight onwards, this drier air made its way down to the ground and displaced the fog. Due to the continuous brightness, these improved conditions were immediately used for helicopter flights to explore the ice for the further transit, as well as for scientific measurements. By the morning of 24 July, the fog returned, although the vertical thickness was only about 100 m. The inflow of slightly milder air and temperatures slightly above the freezing point resulted in fog-free and thus very favourable flying conditions from midday onwards. Shortly after reaching the desired position near 82°54'N 06°25'W, another wall of fog rolled in. The research area around the AURORA thermal fields was under weak air pressure differences on 25 July, resulting in weak northerly winds. A thin and supercooled stratus layer had formed directly above the ice, its vertical extent varied between 100 and 250 m. This repeatedly led to mist or foggy conditions. Especially in the afternoon, the stratus clouds were repeatedly breaking up with longer time intervals where good visibility prevailed. With temperatures below 0°C all day, a so-called ice day was recorded. On 25 July, the most northerly position of this expedition was reached at 82°58'15.7''N 06°11'26.2''W.

On 26 July, station work near the Gakkel Ridge was completed and *Polarstern* began the return transit southeast to the three ice floes and the ice edge. Light-wind conditions continued to prevail with only weak pressure differences. The weather was similar to that of the previous day, with shallow stratus clouds and fog at times, as well as periods of clearing with better visibility. In addition, light snow grains and freezing rain fell out of the supercooled clouds in the afternoon. From the east, however, the humidity increased somewhat overall, which led to cloud fields in the middle and upper layers.

Ice-floe-work and measurements in ice-open-water-transition-zone northwest of Svalbard

In the afternoon of 27 July, the return transit ended with mooring work near 81°20'N 01°09'E. The station was located at the western edge of a low-pressure zone within highly humid air. During this, *Polarstern* was on the western edge of a shallow low-pressure zone within high-up-reaching humid air. This led to nimbostratus clouds, repeated precipitation and fog. Different types of precipitation were observed: Ice pellets, frozen drizzle and rain, wet snowflakes and liquid but supercooled drizzle. The north to northwest flow reached 4 Bft.

On 28 July, a new floe was searched for and found near 81°19'N 01°13'E for a 24-hour ice station. Starting from the low-pressure zone in the east, a small-scale low moved westward until the evening with its core just north of *Polarstern*. The northerly winds decreased to 3 Bft. This meant that warm air advection and nimbostratus clouds continued to prevail. At times, this resulted in supercooled drizzle with all-day temperatures below the freezing point. Visibility was repeatedly below 1 km (fog) and never exceeded 5 km (mist) throughout the day.

On 29 July, the small low north of *Polarstern* moved further west, weakening. The weak wind slowly shifted back over northwest to west and finally to southwest by the evening. The air still was humid, which was reflected by an overcast sky. However, the stratus clouds lifted from the surface and increasingly cleared. As a result, visibility also increased somewhat and there was only sporadic supercooled drizzle of light intensity. Above, several layers of dense stratocumulus clouds remained. After mooring work and a trip with the Triaxus, a so-called bio-station was on the programme in the evening on the ice. This continued during the night into 30th of July and was again accompanied by fog.

During the day, the third and last visit to the three ice floes began, which in the meantime had drifted to the southwest. As before, the measurement on the ice began at the northernmost

floe. In the meantime, a strengthening high had moved from the North Cape to Novaja Semlja. On the other hand, starting from a low between Iceland and Jan Mayen, a warm front extended northeastwards across Fram Strait to Svalbard. *Polarstern* was initially still north of the frontal system, which meant that drier air initially prevailed with weak southerly winds. The compact fog turned into fog patches by the morning of 30 July. The stratus/stratocumulus clouds above with varying ceilings between 120 and 600 m dissipated with a break-off edge coming from the south shortly after noon. This was followed by a mostly sunny afternoon. After several days without helicopter flights, the improvement in the weather made it possible to fly again from the morning hours. By the evening, the ice floe work was completed and all the measuring equipment was packed away.

From the evening onwards, a trip with Triaxus to the southeast followed. *Polarstern* drove directly into the above-mentioned warm front, which lay northwest of Svalbard. The initial stratocumulus clouds quickly turned into stratus and fog. With the proximity to the ice edge, a subdued but clearly noticeable swell from the southeast was also observed. On 3 July, ice work took place also for the third time on the second floe, located furthest to the southeast. Within a quasi-stationary warm front, it was cloudy, grey and foggy with light winds. By evening, *Polarstern* had also reached the third floe, which lay between the two others. During the night, the measurements on the third floe were also completed and all scientific equipment was packed up. There was little or no change in the weather and visibility conditions.

At the turn of the month, the next bio-station was on the agenda until midday near 80°46'N 03°45'E. A small high had formed just northeast of *Polarstern*. In the meantime, the frontal system had begun to dissipate, which was noticeable in that the vertical thickness, or cloud top, dropped to 700 to 900 m. At the surface, the expedition members only noticed almost nothing of this and the fog once again proved to be very persistent. The intermittent drizzle also did not necessarily make the outdoor work more pleasant. In addition, there was still a subdued, weak swell from the south. From the afternoon onwards, another trip with the Triaxus followed to the east/southeast towards a mesoscale ice formation at the boundary.

On 2 August, measurements and scientific work continued on a mesoscale ice formation near 80°45'N and between 05°-07°E. North of the working area, a high-pressure area continued to form a high-pressure bridge to another high-pressure area over the Kara Sea. South of Svalbard lay a low-pressure zone. In between, humid air continued to prevail in the lower layers with a fresh northeasterly current. This initially manifested itself in dense fog and intermittent light drizzle. However, the thickness of the stratus clouds decreased by the afternoon and at times the sky and the sun shining through were visible. In these conditions, the transit started south-westwards into Fram Strait, with the 79N-Glacier on the coast of northeast Greenland as a further stopover. The sea with swell from south to southwest increased to 1.5 m in the open water.

East-Greenland Current - 79N-Glacier

On 3 August, there was a high-pressure zone north of Fram Strait. Just west of Svalbard, on the other hand, there was a low. This formed a low-pressure zone with another low east of Svalbard. This resulted in a most of the time fresh northerly current. After sailing southwest in the eastern Fram Strait, *Polarstern* reached again the ice edge in the morning, which represents the transition to the western Fram Strait and the East-Greenland Current. This transition was approximately at the zero meridian. From then on, the ship sailed west along 79°N latitude, while mooring work was still being carried out near 05°23'W. Fog and poor visibility were also constant companions here at first. Shortly after noon, drier air started to prevail near the

ground, which led to the dissipation of fog and a slight increase of the ceiling, as well as a temporary break-up of the stratus clouds.

On 4 August, a high-pressure zone remained north of *Polarstern*, while a low-pressure zone was located towards the east and southeast. This slowly shifted to the east. As a result, the air pressure gradient over Fram Strait decreased and the northerly flow weakened. After repeated fog periods, a new weather state with numerous shallow fog patches and also repeated sunshine set in from the afternoon onwards. These conditions were used for ice reconnaissance flights to ensure optimal travel to the west through the ice of varying thickness. Due to these flights, the scientific interest, as well as the weather forecast, it was decided to take a south-south-westerly route. Thus, after a southerly detour to 78°30'N, *Polarstern* continued west. Temperatures dropped to -1.7 to -1°C, which meant that an ice day was recorded again for a long time. The -1.7°C was the lowest temperature of the expedition PS131. On 5 August, *Polarstern* fought its way west through thick ice and by the evening had reached the area just east of the Qeqertaq-Prins-Henrik-Island chain (former Île-de-France), about 30 nm southeast of the 79N-Glacier. Towards the northeast was a high-pressure zone. From this, a ridge extended to just north of the ship. This led to a weak current from southeasterly directions. With this, the cold and humid boundary layer had regained vertical thickness, which manifested itself in the form of persistent fog.

On 6 August, the high-pressure ridge slowly moved northwards. At the same time, a small low developed south of the ship directly on the coast. This caused the initially weak winds from different directions to turn north with a slight increase. Once again, the bad weather conditions with only short windows of time in which the fog cleared to fog patches put a spanner in the planned helicopter flights to the 79N-Glacier. At the same time, the glacier was mostly covered in clouds coming from the sea and sliding up the glacier. An ice station was set up from the ship to take measurements and samples of the sea ice, which varied in thickness over a small area. In the course of the afternoon, the low in the south became noticeable. With the onset of warm air advection, more moisture was brought in, which led to the onset of supercooled drizzle in the evening. For reasons of time, and also as a result of the further weather development, which did not promise any flight conditions to the 79N-Glacier in the near future, it was decided in the evening to leave the area close to the 79N-Glacier on the following 7 August. Until the morning of 7 August, mooring work and measurements of the water column were carried out. Afterwards, the transit to the south to the Greenlandic Scoresby Sound began. The aforementioned low moved directly over the research area from the south during the course of the day and provided a lot of moisture. Warm-front-like nimbostratus clouds prevailed in the supersaturated air mass, causing fog and repeated supercooled drizzle at temperatures around 0°C, as well as a little bit of wet snow. The weak winds shifted the southeast to west, as *Polarstern* moved south and crossed the low core.

East-Greenland current - Scoresby Sound (Kangertittivaq)

In the night of 8 August, *Polarstern* came under the influence of dry air south of the low on its rear side. At the same time, a light inflow of intermediate high-pressure became noticeable from the south. This led to the dissipation of fog and mostly sunny conditions. During the day, residual moisture remained directly above the ground, which at times turned into shallow fog patches and caused misty conditions. Nevertheless, helicopter flights could be made to explore the ice conditions to the south. By evening, a low-pressure system was moving north along the coast from Scoresby Sound. The preceding frontal system provided a textbook like approach of frontal cloud cover until the evening. This caused the mid- and upper-level altocumulus and cirrus fields to become denser during the day. By evening, descending stratocumulus was

also added, bringing a little bit of rain. In the evening, in the now almost ice-free driving area, nimbostratus clouds followed, which changed into fog. This was accompanied by prolonged precipitation. As the low approached, a northeasterly current set in, which reached 5 to 6 Bft by the evening. A low-pressure trough had formed from the aforementioned low north of Scoresby Sound. *Polarstern* moved southwards within this trough for some time on 9 August. The wind calmed down temporarily in the trough. The low-level cloud cover on the back side of the frontal system remained mostly dense at first and it was repeatedly foggy. In the afternoon, visibility increased and the cloud ceiling was slowly lifted.

From the evening onwards, a gale moved northeastwards from Iceland. As it approached, the northerly flow gain again strength from the afternoon hours of 9 August. By midnight, *Polarstern* had reached the entrance of Scoresby Sound and the northerly wind briefly reached 7 Bft, which was also the wind maximum on this expedition with a 10-minute wind speed average of 14.4 m/s. By coincidence, a short meeting with the German research vessel *Maria S. Merian* took place before entering Scoresby Sound. The sea with swell from northeast and southeast reached 1.5 to 2 metres. In the meantime, the cloud cover had also broken up. On the night of 10th of August, the sun also sank below the horizon for the first time since 2 July, ending the polar day.

As *Polarstern* moved into the world's largest fjord system, the wind abruptly dropped in the second half of the night of 10 August, because the entrance area of the Sound, which runs from east to west and is about 20 nm wide, was protected from the strong northerly current by high mountainous terrain to the north. On 10 August, the gale (core pressure around 986 hPa at 06:00 UTC) was located near Jan Mayen and moved further northeastwards, deepening slightly. Due to the more favourable wind and weather conditions, *Polarstern* first steamed to the north of the Sound to recovery two moorings near 71°15'N 25°12'W. The wind in the shelter of the sound came from different directions with around 2 Bft. Weather conditions with dry air close to the ground, as well as initially high stratocumuls clouds, which changed to altocumulus clouds as *Polarstern* moved northwest, also allowed several helicopter flights to the surrounding mountain glaciers throughout the day. The isolated showers that were present in the morning with a snowfall-line of 300 to 500 m also disappeared in the morning hours. As the water temperature increased, so did the air temperature, which reached 7 to 8°C by the evening.

During the night of 11 August, the boat returned to the mouth of the Sound, where further mooring work had to be done. Meanwhile, the gale northeast of Jan Mayen continued to move northeast. A small-scale low had formed in the northern part of the Sound. At the same time, an intermediate high-pressure ridge moved northeastwards from the Denmark Strait over the eastern part of Scoresby Sound. Thus, the small-scale low sucked in air from the Greenland Sea, which, with additional channelling-effects, triggered a strong easterly flow by morning. This decreased to 5 Bft at the mooring position at the entrance area of the Sound. The wind sea reached 1 to 1.5 m. With this current, colder air from the Greenland Sea was also brought in, causing temporary fog patches. Otherwise, the sky was mostly covered with stratocumulus clouds during the day. By the early evening of 11 August, the work in the Scoresby Sound was completed. This marked the start of the last leg of the expedition with the return transit to Bremerhaven.

Scoresby-Sound - Bremerhaven

In the night of 12 August, a low moved from the Denmark Strait to northwest Iceland. When *Polarstern* left Scoresby Sund, the wind, which shifted from east to northeast, increased again slightly to 5 to 6 Bft, before the wind temporarily slowed down with a shift to southeast to

south. Meanwhile, the low moved eastwards towards northeast Iceland during the day. With its movement, a fresh easterly current set in again. Moisture in the Greenland Sea increased rapidly with the low-pressure influence, which was once again reflected in repeated stratus, fog and intermittent precipitation. During the course of the day*, Polarstern* passed through the low and its frontal system, heading southeast. The sea with swell from northeast and also south to southwest reached around 1.5 m.

In the night of 13 August, *Polarstern* reached the rear side of northeastward moving low. As a result, drier air slowly flowed in with an initially westerly current from the second half of the night, which led to quite sunny conditions from the morning onwards. In the meantime, a swell of around 2 m arrived from the southwest. After a brief decrease in wind, a moderate south to southwest flow established itself by noon. In the afternoon, the cloud cover in the area east of Iceland increased again.

On 14 August, another low moved from the Irminger Sea to southeast Iceland. This formed an elongated low-pressure zone to another low over northern France. At the same time, there was a large high-pressure zone over Scandinavia and northwest Russia. However, the pressure opposites in the Norwegian Sea north of the Shetland Islands were initially small. As a result, the winds decreased at first. During the course of the day, the low over northern France moved to southern England, while extending to the north of Scotland with a trough. As a result, a moderate southeasterly to southerly flow developed from noon onwards. At the same time, the air mass became increasingly humid as *Polarstern* moved into a forming warm front, leading to fog and some drizzle from the morning hours. Visibility and weather conditions improved on the back side of the front in the afternoon. During the night of 15 August, the southeasterly wind weakened and again at times fog and some light drizzle occurred, while the research vessel reached the North Sea.

On 15 August, a fresh southeasterly flow resulted between a low over England and a high over Eastern Europe. Towards morning, the boundary layer close to the surface dried up somewhat and visibility increased to 10 to 20 km. Due to an unstable stratification in the mid-levels, isolated showers occurred. During the course of the day, the low- and mid-level clouds became less and less, and the sun was able to appear repeatedly next to occasionally denser cirrus fields. The wave heights with wind seas and initially swell from southwest to west, later from southeast, reached 1 to 1.5 m. By 16 August, the low had moved northeastwards into the North Sea and during the day further towards southern Norway. In the morning, *Polarstern* was sailing on its southeast flank, where the wind temporarily slowed down. In the afternoon, the ship sailed south of the depression and a weak to moderate westerly current developed. The sky showed a mixture of mid- and high-level clouds with repeated sunshine. The tendency to showers that came to life in the morning was only temporary. After a steady rise in temperature during the return transit, pleasantly warm values around 20 degrees were reached in the afternoon. Westerly winds of 3 to 4 Bft also blew in the German Bight. For the last section in the Weser, the wind speed dropped and turned clockwise to northerly directions. With the inflow of humid North Sea air and the nocturnal emission of long-wave radiation, locally very dense fog patches formed until the morning, which accompanied the arrival of *Polarstern*. On the morning of 17 August, *Polarstern* docked in Bremerhaven, bringing the ATWAICE expedition PS131 to an end.

2. PHYSICAL OCEANOGRAPHY

Wilken-Jon von Appen[1], Torsten Kanzow[1], Mario Hoppmann[1], Rebecca McPherson[1], Zerlina Hofmann[1], Laura Mathieu[1], Simon Reifenberg[3], Hauke Becker[1], Matthias Monsess[1], Rainer Graupner[1], Normen Lochthofen[1], Jacob Allerholt[1], Ilker Fer[2], Fiona Ellliot[2], Christian Haas[1], Mara Neudert[1]
not on board: Maren Walter[3], Janine Ludszuweit[1], Olivier Desprez de Gesincourt[4], Sébastien Péré[4], Yusuke Kawaguchi[5], Takehiko Nose[5], Jean Rabault[6], Tomotaka Katsuno[5], Takuji Waseda[5], Tsubasa Kodaira[5], Ignatius Rigor[7]

[1]DE.AWI
[2]NO.Uni Bergen
[3]DE.Uni Bremen
[4]FR.SHOM
[5]JP.Uni Tokyo
[6]Norwegian Meteorological Institute
[7]UW

Grant-No. AWI_PS131_07

Objectives

The physical oceanography group carried out work in five distinct areas during the cruise. The objectives in the different areas were complementary but also partially independent.

Area 1 (FRAM): Long-term monitoring of the WSC and in the Hausgarten observatory

The monitoring programme of the Atlantic Water (AW) inflow into the Arctic via the West Spitsbergen Current (WSC) started in 1997. ATWAICE contributed to maintaining this long-standing time series observatory, as the AW inflow conditions drive the changing physical (and also biogeochemical and biological) properties of the Arctic Ocean. Hence, our key question was: How do the properties of the AW inflow change at one of the main Arctic Ocean gateways and how do changes influence the wider Arctic environment? What is the long-term evolution in the transport of those properties into the Arctic Ocean?

The Frontiers in Arctic Marine Monitoring (FRAM) Helmholtz infrastructure initiative has increased the ability to observe the temporal evolution of the coupled physical-chemical-biological system in the upper water column and throughout the water column to the sea floor. Continuing these interdisciplinary time series allows for the evaluation of interannual variations in addition to shorter-term interactions on mesoscale to seasonal timescales. Two main multidisciplinary time series locations were pursued in the framework of FRAM and its continuation: the F4 site at 1,000 m water depth in the inflowing Atlantic Water boundary current (West Spitsbergen Current) and the EG4 site at 1,000 m water depth in the outflowing Polar Water boundary current (East Greenland Current). By being embedded in very different water masses representing end points of Arctic conditions, they allow for a better prediction of what conditions and changes are to be expected in the future Arctic Ocean.

Area 2 (MIZ): Ocean-sea ice coupling in the MIZ

This objective represented the major focus of ATWAICE related to key mechanisms of rapid Arctic sea ice decline and Arctic Amplification. These include processes affecting heat fluxes in the air-ice-ocean system, ocean mixed layer-halocline coupling, ice melt, and ice edge

dynamics in the MIZ. We posited that oceanic eddies, fronts, and tidal mixing shape the sea ice distribution in the MIZ which leads to locally enhanced ice melting as well as to the generation of stratified areas with suppressed melting. These processes result in sea ice characteristics that can be distinguished by different gradients of sea ice floe size, concentration, roughness, and thickness. Our study also aimed to understand the complex physical-chemical-biological interactions that control biogeochemical cycling and ecosystem functioning. Our guiding questions in the MIZ were:

Q1: What are the pathways and processes in the inflow regions of warm AW to the Arctic Ocean that transport heat and nutrients to the sea ice and into the euphotic layer in the MIZ?

Q2: How does the dynamic structure (stratification, mixing rates, (sub-) mesoscale activity) of the upper ocean change spatially from the open ocean across the MIZ to the pack ice? How does it change seasonally with strongly varying atmospheric forcing?

Q3: What is the fate of sea ice in the summer melting season? And how does it change over time as oceanic mixing and atmospheric fluxes change over time?

Q4: How do the physical (sub-) mesoscale structures (fronts, ice-edge, eddies, etc.) and sea ice properties (e.g. melt ponds, light transmission) impact biological production?

Area 3 (79NG): Ocean impacts on marine-terminating glaciers in Northeast Greenland

In terms of Greenland, the North-East Greenland Ice Stream (NEGIS) system shows signs of significant ocean-driven thinning of its major outlet glaciers, the Nioghalvfjerdsfjorden Glacier (79NG) and Zachariæ Isstrøm (ZI). Ocean and ice-based studies were supposed to establish the trajectory of the NEGIS system. We aimed to implement sustained monitoring capacities for investigating ocean-driven melt of the 79NG and ZI to answer the question: What are the sensitivities of present-day ocean-driven melt to changing environmental conditions at 79NG and ZI?

Area 4 (Aurora): Plume monitoring at the Aurora vent field

The ultra-slow spreading Gakkel Ridge presents a source of chemical elements washed out by the hydrothermal fluids to the Arctic Ocean. Little is known about the plume's temporal variability and its interaction with tectonic and oceanographic events (e.g. current reversals). We aimed to cover a whole seasonal cycle of plume properties.

Area 5 (Scoresby): Flow of Atlantic Water to glaciers in central Greenland

Analogously to the much larger NEGIS, the Scoresby Sund in central Greenland is a complex fjord system that features the interaction of warm Atlantic Water with glaciers. The warm water thereby affects the glacier flow rates and the vertical distribution of meltwater in the water column. During MSM76 (2018) three moorings were placed at the mouth of Scoresby Sund and at the Scoresby Sund-Nordvest Fjord transition to retrieve information on the long-term variability of the fjord system.

Work at sea

The cruise covered the five working areas along the cruise track as shown in Figure 2.1.

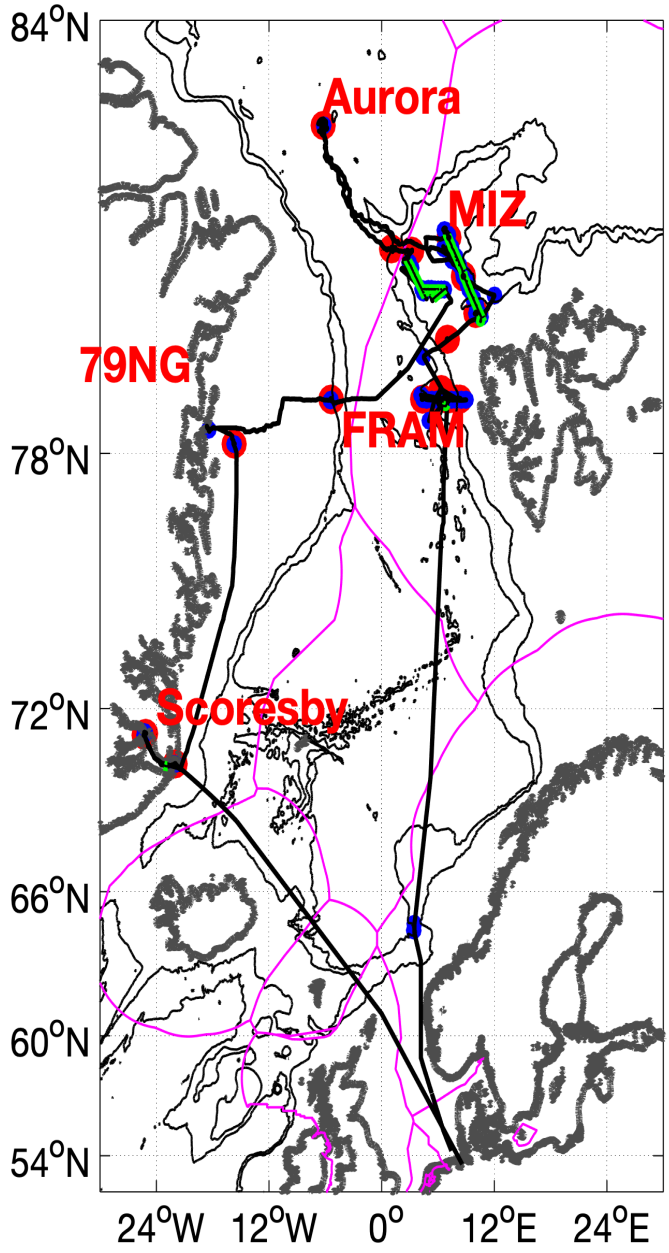

Fig. 2.1: Cruise track (black) with locations of mooring recoveries and deployments (red), CTD stations (blue), and Triaxus tows (green); the boundaries of the exclusive economic zones are shown in magenta. The coast line is shown in gray as well as the 1,000 m and 2,000 m isobaths.

Moorings (areas 1, 2, 4, 5)

Recoveries

A total of 12 ocean moorings were recovered over the course of PS131 (Fig. 2.1). This included the 9 planned recoveries in the original expedition programme and an additional 3 moorings from a fjord in Northeast Greenland, Scoresby Sund. There was only one major complication during all the recoveries which occurred at the mouth of Scoresby Sund (SCO3-1, further details are found below). The moorings contained observations for physical water properties (e.g., temperature, density, ocean currents), and some also targeted biogeochemical and biological parameters.

The total mooring recoveries included the 9 moorings from the long-term LTER HAUSGARTEN observatory in the eastern Fram Strait, including the western East Greenland Current location (HG-EGC-7) (Fig. 2.2). The FRAM multidisciplinary observatory attempts to improve the observations and understanding of the connection between marine biodiversity and environmental conditions using long-term observations of both – physical oceanic properties and benthic and pelagic environments. The mooring observations span the whole water column with an emphasis on the upper euphotic zone.

All of the HAUSGARTEN moorings were recovered without any major complications or losses, comprising a total of 116 sensors. This included the successful recovery of one profiling winch system, designed to measure profiles in the top 100 m of the water column (F4-W-3). Only one temperature logger (SBE56) on F2-20 was lost. A total of 5 of the moorings recovered on PS131 were originally deployed during PS126 in 2021, and 4 were deployed on MSM93 in 2020 (Table 2.1). Almost all the recovered instruments also recorded data for the duration of the deployments. Two of the SBE37s recorded data for shorter periods of time, for 32 days (F2-20) and 5 months (F4-20) respectively. The reason for this remains unclear.

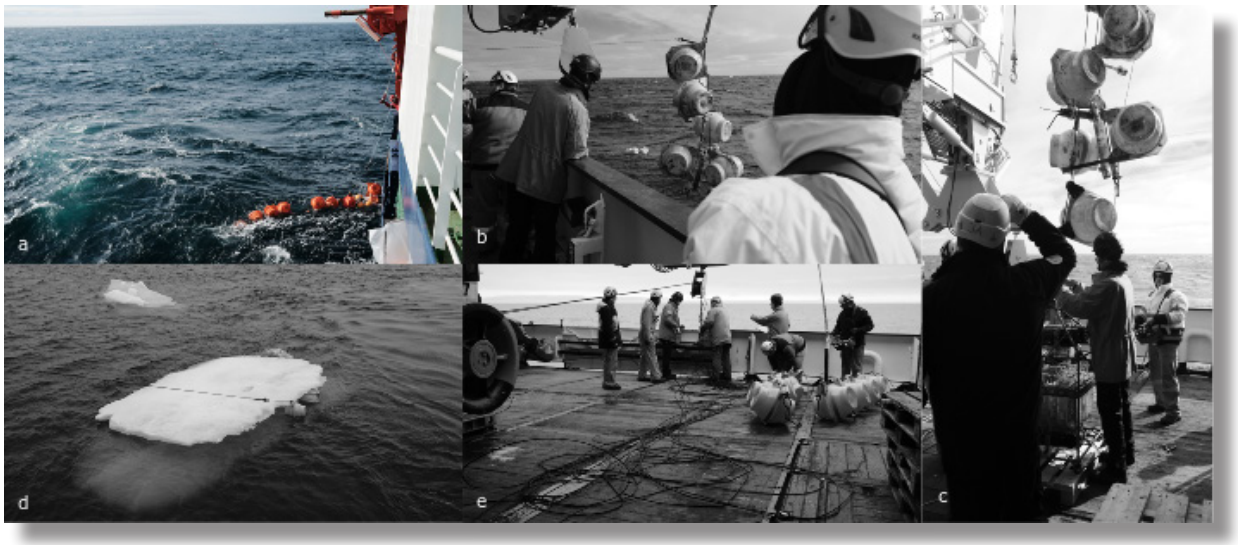

Fig. 2.2: Examples from mooring recoveries: (a) The surface floats and ADCP (300 kHz) from F4-20 are hooked onto from the deck and being brought on board, where the line will run through the crane and onto the capstan and cable drum for the rest of the mooring recovery, (b) the recovery of surface floats and an SBE37 CTD, with the remaining line and floats in the water (F4-S-5), (c) a recovered McLane RAS 500 on deck, with floats and an SBE37 above and being lowered by the crane (F4-S-5), (d) buoys under an ice floe (HG-EGC-7), (e) entanglement of the line during the recovery of HG-IV-FEVI-42. Photos: Mario Hoppmann

Tab. 2.1: Table of details of recovered and deployed moorings

Name	Longitude			Latitude			Depth	Top	Deployment time UTC					Recovery time UTC					Deployment station	Recovery station
	Degrees	Minutes		Degrees	Minutes		Meters	Meters	Year	Month	Day	Hour	Minute	Year	Month	Day	Hour	Minute		
Recoveries																				
F2-20	8	19,77	E	78	59,97	N	787	17	2020	7	4	15	2	2022	7	6	16	2	MSM93/013-5	PS131_9-1
F3-19	7	59,79	E	79	0,01	N	1078	39	2020	7	6	16	2	2022	7	6	13	34	MSM93/025-1	PS131_8-1
F4-20	6	59,97	E	79	59,97	N	1241	53	2021	6	8	15	3	2022	7	5	6	28	PS126/014-1	PS131_2-1
F4S-5	6	57,81	E	79	0,71	N	1260	17	2021	6	8	17	29	2022	7	5	8	44	PS126/014-2	PS131_3-1
F4W-3	7	2,05	E	79	0,71	N	1241	114	2021	6	8	19	37	2022	7	6	9	23	PS126/014-3	PS131_7-1
F4-OZA-2	6	19,96	E	79	10,02	N	1422	108	2020	7	6	13	12	2022	7	8	6	1	MSM93/024-2	PS131_22-1
F5-19	5	40,01	E	79	0,02	N	2084	48	2020	7	6	9	36	2022	7	5	15	31	MSM93/023-1	PS131_5-1
FEVI-42	4	19,89	E	78	59,98	N	2556	56	2021	6	3	11	21	2022	7	9	7	41	PS126/003-23	PS131_28-1
EGC-7	5	21,59	W	78	59,28	N	1041	33	2021	6	16	9	11	2022	8	3	13	18	PS126/021-17	PS131_105-1
SCO1-1	25	9,25	W	71	16,98	N	638	405	2018	8	22	16	13	2022	8	10	15	38	MSM76/127-1	PS131_115-1
SCO2-1	25	17,94	W	71	13,86	N	806	590	2018	8	22	17	45	2022	8	10	11	2	MSM76/128-1	PS131_114-1
SCO3-1	21	59,78	W	70	21,25	N	416	242	2018	8	23	12	25	2022	8	11	13	5	MSM76/132-1	PS131_118-1
Deployments																				
F2-21	8	19,91	E	79	0,01	N	786	20	2022	7	8	15	52						PS131_25-1	
F3-20	7	59,93	E	78	59,98	N	1074	38	2022	7	8	13	42						PS131_24-1	
F4-21	7	0,03	E	79	0,02	N	1224	50	2022	7	7	8	54						PS131_15-1	
F4-S-6	6	57,76	E	79	0,70	N	1231	16	2022	7	10	8	13						PS131_34-1	
F4-W-4	7	1,95	E	79	0,73	N	1249	132	2022	7	7	12	8						PS131_16-1	
F4-OZA-3	6	19,91	E	79	10,00	N	1416	89	2022	7	8	9	33						PS131_23-1	
F5-20	5	39,97	E	79	0,02	N	2091	34	2022	7	7	16	25						PS131_17-1	
FEVI-44	4	19,94	E	78	59,99	N	2568	38	2022	7	9	15	25						PS131_30-1	
Y1-1	10	3,66	E	80	24,08	N	691	23	2022	7	18	7	52						PS131_58-2	
Y2-1	10	3,65	E	80	25,00	N	693	128	2022	7	18	9	53						PS131_59-1	
Y3-1	8	43,30	E	80	56,95	N	768	6	2022	7	19	9	28						PS131_62-2	
Y4-1	8	42,18	E	80	57,95	N	790	16	2022	7	19	12	51						PS131_63-1	
Y5-1	7	9,13	E	81	30,08	N	485	17	2022	7	20	11	47						PS131_66-1	
Y7-1	1	4,34	E	81	20,97	N	1548	22	2022	7	27	18	12						PS131_83-1	
Y8-1	3	10,27	E	81	18,82	N	800	16	2022	7	29	5	34						PS131_85-1	
Aurora-1	6	15,04	W	82	53,87	N	3906	96	2022	7	25	15	49						PS131_77-1	
EGC-8	5	23,74	W	78	59,78	N	1011	47	2022	8	3	17	37						PS131_106-1	
IdF3-2	15	43,12	W	78	10,73	N	361	135	2022	8	7	6	44						PS131_112-1	

The sea state was generally very calm during all recoveries, and while sea ice was present during the work at the western mooring, on the East Greenland continental shelf, (HG-EGC-7), the ice conditions were favorable. There were large floes near the ship and some of the floats and instruments (such as the sediment traps) had to be pulled around or under (Fig. 2.2d) however, there was no damage to the instruments.

Upon recovery, there were also some line entanglements, particularly for HG-IV-FEVI-42, F2-20, and F4-W-3 (e.g., Fig. 2.2e). This did not damage the instruments, merely slowed down the recovery process.

Due to inclement weather conditions (fast ice and fog which prevented flying), the planned work at the 79 North Glacier (including a mooring deployment) was unable to be conducted. Instead, *Polarstern* sailed to Scoresby Sund (69°N, 10°W) to recover three moorings that were deployed on MSM76 in 2018 (Fig. 2.3). Two of these moorings, close to the Daugaard Jensen glacier (SCO1-1, SCO2-1), were recovered successfully. However the third, positioned at the mouth of the fjord, did not release using either the ship-board Posedonia acoustic release system or the deck-unit. The ship's echosounder confirmed its location, where it was observed to be intact and still standing vertically in the water. A line of approximately 1 km in length with various hooks and weights attached was then deployed from the starboard side and stern of the ship to trawl for the mooring. This process resulted in the successful recovery of the upper 50 m of the mooring which comprised a steel buoy and a total of 3 instruments (1 x SBE16, 1 x SBE56, and 1 x SBE37). The remaining line and instruments (1 x ADCP, 1 x SBE16, 1 x SBE37, 1 x SBE56) were not recovered.

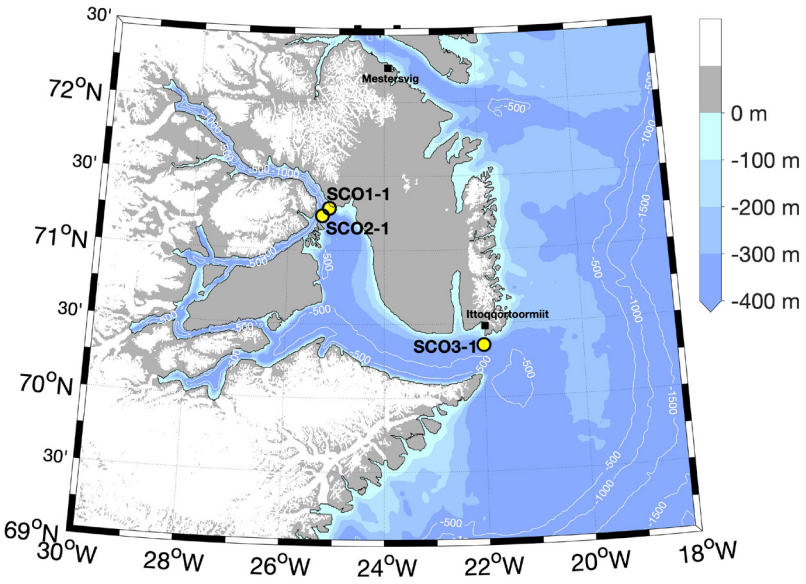

Fig. 2.3: Map of Scoresby Sund and the location of the three moorings, deployed in 2018 and recovered on PS131

The recovered instruments at the three Scoresby Sund mooring locations all recorded data. However, the sampling frequency was not consistent. The recovered ADCP at the glacier (SCO2-1) recorded data hourly for the first 3 months, as initially programed, then jumped to a recording once per 5 and a half days. The reason for this remains unclear. All the SBE37s recorded data for approximately one year, from 08/2018 to the mid/end of 2019 (from 06 to 12/2019). The sample rate was set to 10 seconds thus this premature end was presumably due to the batteries running out. One of the 7 SBE16s recovered was unable to connect to the

computer used to download the data, despite new batteries; the rest appears to have sampled hourly until mid-2022.

Deployments

Throughout PS131, a total of 18 moorings were deployed (Table 2.1). All deployments were successful, with calm ocean conditions occurring throughout the expedition. The 9 recovered LTER HAUSGARTEN moorings were all redeployed with a similar configuration of both physical and biological sensors; including 2 profiling winch systems, each carrying a sensor package (F4-W4, Y2-1) (Fig. 2.4b). In the marginal ice zone, 5 moorings were deployed from 80 – 82°N, including a mooring with a 28 m plastic tube at its top, extending to only 6 m under the surface (Y3-1) (Fig. 2.4c).

These mooring deployments ran smoothly, losing only one anchor near the beginning of the deployment of Y3-1 as the releaser unexpectedly opened (the reason for this is unknown). The mooring was subsequently recovered, a new anchor was attached, and it was successfully deployed thereafter.

One mooring at the Aurora vent field at western Gakkel Ridge (83°N, 6.2°W) was also deployed (AURORA-1), equipped with temperature sensors to record the temperature anomaly from the hydrothermal heat flux into the plume, as well as current meters to record the flow field. The ice at this northern mooring location was very thick and hours were required for the ship to create a field large enough for a safe and smooth mooring deployment.

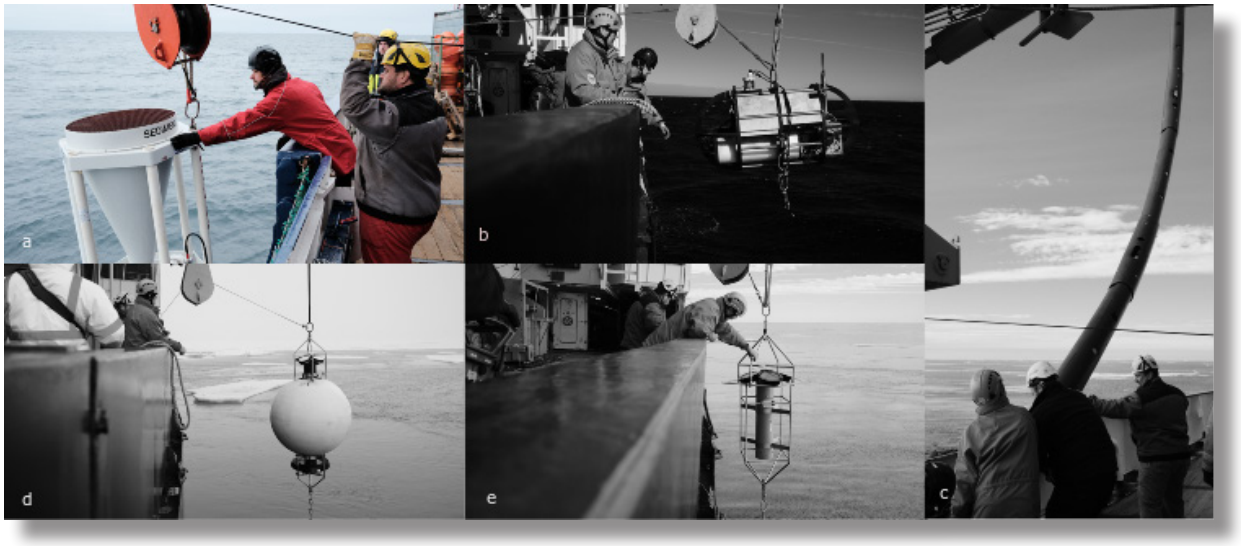

Fig. 2.4: *Examples of mooring deployments: (a) Deployment of sediment trap (HG-IV-FEVI-44), (b) deployment of the profiling winch (F4-W4), (c) the 28 m tube at the top of Y3-1, (d) a steel float with two ADCPs, one upwards and one downwards facing, deployed for University Bergen, (e) the deployment of an ADCP (75kHz, Y5-1). Photos: Mario Hoppmann*

Two moorings were deployed at the shelf edge of the Yermak Plateau for colleagues from the University of Bergen (on board), configured to quantify both the near-surface properties and the intense mixing caused by tidal interactions with the bathymetry. Due to the configuration of these moorings with both bottom and surface-intensified instrumentation, a precise location and depth were required. The required depth had not been reached when >400 m of the mooring had been deployed, thus the ship drifted for over one hour before the correct depth was reached (confirmed by manually measuring the length of line required to reach the surface – this practice was also used for almost all of the moorings deployments) and the remainder of the mooring could be deployed. The deployment, though it took almost 4 hours from start to finish, was successful.

One mooring was also deployed in Northeast Greenland, close to Isle de France in the Norske Trough (IdF2-3) (Fig. 2.1). This was in lieu of the deployment planned for the 79 North glacier front (79N2-3) which could not be reached due to the ice/weather conditions (details above). The purpose of this mooring is to measure the flow of warm sub-surface Atlantic water through the trough system on the northeast continental shelf and towards the glaciers.

CTD (areas 1, 2, 3, 4, 5)

Hydrographic measurements during PS131 were conducted using a Seabird SBE911+ CTD rosette system equipped with 24 x 12l OTE bottles (Fig. 2.5). The sensors and rosette were provided by the physical oceanography group from DE.AWI ("OZE rosette"). In the following, we describe the technical setup of the CTD rosette, followed by a description of the general procedure of performing CTD casts during the cruise. We then present further information on the actual deployments, including a description of initial test casts and an overview of technical issues throughout the cruise. Please note the summarizing table for all casts (Table 2.3).

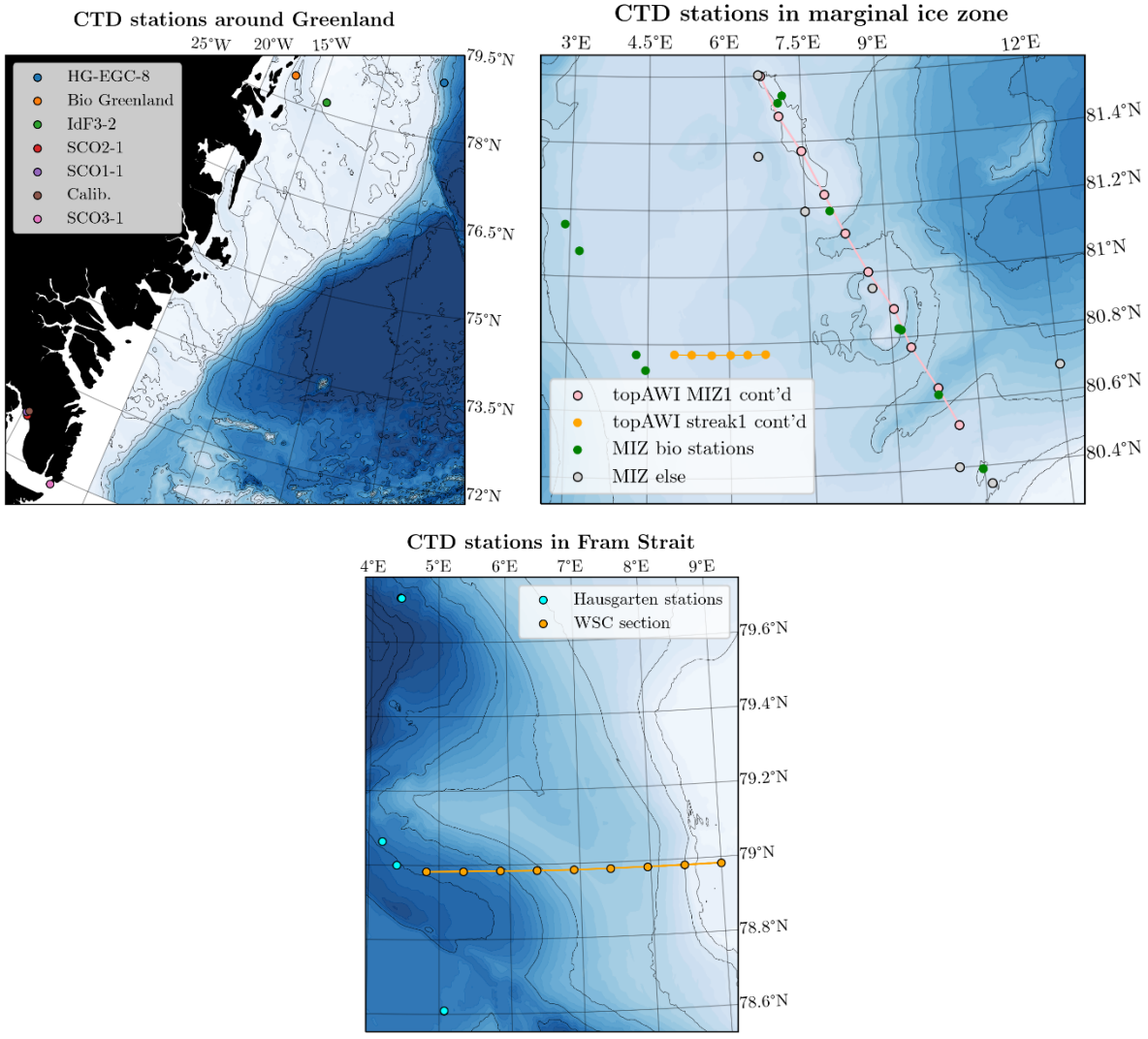

Fig. 2.5: Maps showing the CTD stations in the three main study regions (excluding cast 075_01 at the Aurora site). Only the top left plot includes information on deployed/recovered moorings. For more information on the biological stations and mooring locations, please see the corresponding sections of this report.

The standard sensor configuration (*conf1*) of the CTD system throughout the cruise consisted of two temperature sensors, two conductivity cells, a pressure sensor, two oxygen sensors, two fluorescence sensors, a transmissometer, and a photosynthetically active radiation (PAR) sensor, see Table 2.2 for more details. Only for a single cast at the Aurora vent site, the configuration was changed (*conf2*), in such that the PAR sensor was replaced with a Seapoint Turbidity sensor for the detection of the hydrothermal plume (Chapter 7). After the respective cast (075_01) the configuration was changed back to *conf1*.

Tab. 2.2: Sensor configurations for the CTD system used during PS131. The configuration *conf1* consisted of all sensors listed above (grey shading). For configuration *conf2*, which was only used for cast 075_01 in the Aurora vent region, the PAR sensor on channel V6 was replaced by the turbidity sensor listed last.

	SN	**Calibration Date**	**Channel**	**Description**
CTD				SBE 911plus
Temperature (primary)	5115	2021-11-18	F1	SBE3plus
Conductivity (primary)	2618	2021-11-18	F2	SBE4c
Pressure	0937	2017-11-14	F3	SBE9
Temperature	4127	2021-11-18	F4	SBE3plus
Conductivity	3290	2021-11-18	F5	SBE4c
Oxygen (primary)	4016	2021-07-21	V0	SBE43
Oxygen	4019	2021-07-21	V1	SBE43
Altimeter	46466	--	V2	Teledyne Benthos PSA916
Fluorescence	7239	2021-12-09	V3	WETLabs ECO CDOM Fluorometer
Fluorescence	1853	2021-11-16	V4	WETLabs ECO Chlorophyll Fluorometer
Beam Transmission	1198	2022-01-19	V5	WETLabs C-Star
Photosynthetically Active Radiation (PAR)	2197	2021-11-30	V6	SEA-BIRD PAR-LOG
--	--	--	--	--
Turbidity	14143	unknown	V6	Seapoint Turbidity Meter

Two Acoustic Doppler Current Profilers were attached to the rosette as well; more information can be found in the respective section down below.

Furthermore, a Satlantics/SeaBird SUNA nitrate sensor (SN 1318) was installed on the rosette during most casts. As this sensor has a depth rating of 2,000 m, it was only attached during casts shallower than that. The device was programmed to start sampling – and recording the data internally – as soon as power is supplied. Power was supplied by the SBE911, so that data acquisition starts when the CTD is turned on. The nitrate measurements were not processed by the finalization of this report so that no preliminary results are available here.

Also, an Underwater Vision Profiler (UVP) was attached to the rosette. More details on the UVP measurements can be found in Chapter 10. The UVP starts automatically when it is

lowered more than 20 m and stops recording when it is heaved for more than 30 m. Therefore, the usual procedure for a CTD deployment was as follows: lowering the rosette to 22 m, waiting up to two minutes for the UVP and the CTD pump to turn on, and heaving back at the surface. Then the downcast starts by lowering the rosette with 0.5 m s^{-1} for the first 150 m, after which the lowering speed increases to 1 m s^{-1}. For maximum depths close to the sea floor, the lowering speed got reduced to 0.5 m s^{-1} approximately 100 m above the depth obtained from the ship's system, with a further reduction closer to the bottom, especially when the altimeter did not show a meaningful signal. When the altimeter worked, full-depth casts were stopped 10 m above ground.

During virtually all scientific profiles (Table 2.3), water samples were taken. The Niskin bottles were fired on the upcast, after waiting for 60 s at each target depth for both, sampling the 'true' ambient water mass, and also allowing for lagging sensors to adjust. These water samples are partly used for calibrating the salinity and oxygen observations. Results from on-board salinometry are presented in the subsequent section; please see Chapter 6 for the oxygen titration.

During the initial test station, only nine out of 24 Niskin bottles closed after being fired, likely an effect of the carousel not being used for some time. In two subsequent test casts (down to 100 and 1,648 m) all bottles closed. On top of that, there were problems with the conductivity sensors in the first cast, such that the primary sensor exhibited increased variability compared to the secondary. This was fixed by aligning the T-piece at the respective inlet properly. After that, the high-passed (20 m cut-off frequency) salinity data derived from the two sensors matched well again, so the issue was considered solved after cast 001_01.

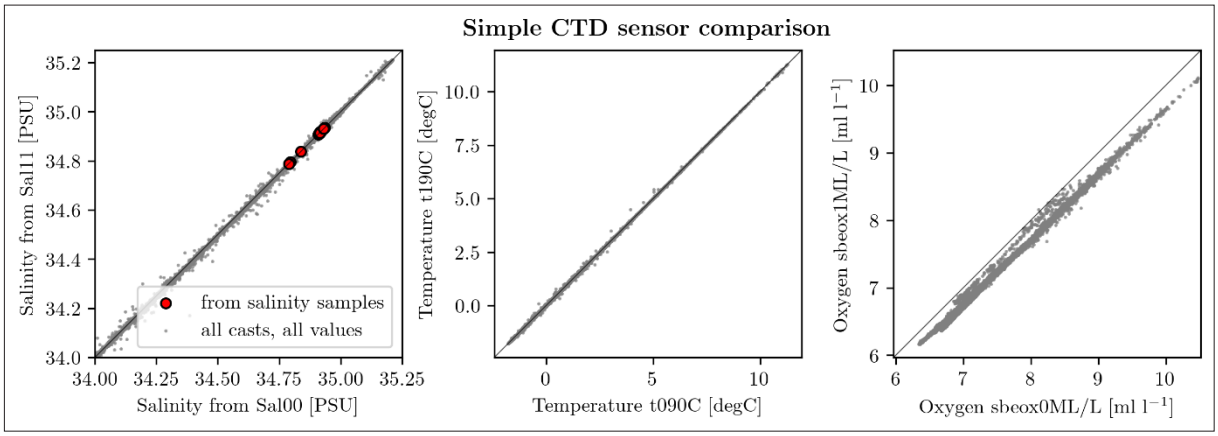

Fig. 2.6: Scatter plots of salinity, temperature, and oxygen (from left to right) with the respective primary sensors on the horizontal axis, and the secondary sensor on the vertical axis. The salinity scale is capped at 34 PSU although some surface observations were much smaller than that. The red dots in the salinity plot show the values for the water samples used for salinometry. Please note the changing offset of the oxygen sensors.

Water sampling for the biological working groups was sometimes targeting the chlorophyll maximum in the water column. It was not uncommon that the shape, intensity, and location

of this maximum changed between downcast and upcast. Particularly during cast 056_02, where there was swell of about 2 m present, identifying and probing the correct depth of the chlorophyll maximum was problematic.

For some stations, the station and cast numbers differ from the logged names recorded by the ship. This was not corrected in file names and header information yet. A list of the respective file names and correct station numbers is provided in Table 2.4.

Tab. 2.3: Meta-data of all CTD stations from PS131. The station names refer to the file numbers and headers of the CTD data. There are a few stations that were logged differently in the ship's dship system (see also Table 2.4).

Station	Time (UTC)	Lat (°N)	Lon (°E)	Depth [dbar]	Description	Comments
001_01	2022-07-01 07:08	64.5150	3.4317	2030	Test station	problem with bottle 6, see also text body
001_03	2022-07-01 12:14	64.7655	3.4843	102	Test station	
001_06	2022-07-01 13:41	64.7653	3.4838	1671	Test station	
006_01	2022-07-05 20:36	78.6092	5.0655	2315	Hausgarten S3	calibration cast, 10 min stops at 2,000 and 1,000m, bottle 17 did not close, issues with oxygen sensor at 2,000m depth, offset changed over time, conductivity difference increased during upcast
006_05	2022-07-06 04:39	78.6095	5.0667	253	Hausgarten S3	salinity and oxygen look fine again
010_02	2022-07-06 19:54	78.9833	7.9548	1098	WSC Section	011_01 in ActionLog, temperature difference up to 0.1 sometimes
012_01	2022-07-06 22:55	78.9833	9.0003	200	WSC Section	Niskin #6 broken
013_01	2022-07-07 00:27	78.9837	8.4772	503	WSC Section	Niskin #6 replaced before cast
014_01	2022-07-07 02:55	78.9833	7.4305	1236	WSC Section	
019_01	2022-07-07 21:12	78.9830	6.9092	1248	WSC Section	
020_01	2022-07-07 23:45	78.9835	6.3847	1581	WSC Section	
021_01	2022-07-08 02:25	78.9838	5.8650	2032	WSC Section	
027_01	2022-07-08 22:46	79.0638	4.1898	2442	Hausgarten HG4	HG-IV-FEVI-42 & HG-IV-FEVI-43

Station	Time (UTC)	Lat (°N)	Lon (°E)	Depth [dbar]	Description	Comments
029_01	2022-07-09 10:59	79.0000	4.3945	254	Hausgarten HG4	HG-IV-FEVI-42 & HG-IV-FEVI-43
032_02	2022-07-09 19:45	78.9832	4.8163	2509	WSC Section	
033_01	2022-07-09 23:00	78.9833	5.3397	2387	WSC Section	
035_01	2022-07-10 13:49	79.7210	4.4217	2724	Hausgarten N4	
035_06	2022-07-10 23:32	79.7195	4.4330	253	Hausgarten N4	10 min calibration stop at 185m
037_01	2022-07-11 08:35	80.3453	10.6097	547	prior to topAWI depl.	036_01 in ActionLog
037_02	2022-07-11 14:06	80.5265	10.1145	405	topAWI MIZ1 section cnt'd	037_01 in ActionLog
038_01	2022-07-11 16:56	80.6417	9.7820	404	topAWI MIZ1 section cnt'd	
039_01	2022-07-11 19:41	80.7682	9.3417	405	topAWI MIZ1 section cnt'd	
040_01	2022-07-11 22:16	80.8858	9.0770	405	topAWI MIZ1 section cnt'd	
041_01	2022-07-12 00:49	81.0002	8.6375	405	topAWI MIZ1 section cnt'd	
042_01	2022-07-12 03:46	81.1187	8.2447	404	topAWI MIZ1 section cnt'd	CTD stopped before going in water bc of passing ice floe, the respective files were moved to folder "iceproblems"
043_01	2022-07-12 07:28	81.2380	7.8785	405	topAWI MIZ1 section cnt'd	
044_01	2022-07-12 10:27	81.3710	7.4678	416	topAWI MIZ1 section cnt'd	
045_02	2022-07-12 13:19	81.4780	7.0388	407	topAWI MIZ1 section cnt'd	
046_01	2022-07-12 17:31	81.6010	6.7053	405	topAWI MIZ1 section cnt'd	
047_02	2022-07-13 17:55	81.6028	6.6568	503	after Floe North Visit 1	
048_02	2022-07-14 18:20	81.1905	7.4932	802	after Floe South Visit 1	oxygen diff -0.3, ship moved a lot bc of the ice
049_02	2022-07-15 18:07	81.3590	6.6217	765	after Floe Middle Visit 1	
053_01	2022-07-16 11:23	80.6785	12.0280	1301	after depressor test	Calibration stops 5min

Station	Time (UTC)	Lat (°N)	Lon (°E)	Depth [dbar]	Description	Comments
056_02	2022-07-17 09:58	80.6202	9.7832	507	Bio-Superstation MIZ2a section	
056_08	2022-07-17 16:33	80.6202	9.7852	153	Bio-Superstation MIZ2a section	
057_02	2022-07-17 19:38	80.3908	10.4713	478	Bio-Superstation MIZ2a section	
057_07	2022-07-18 00:07	80.3900	10.4720	152	Bio-Superstation MIZ2a section	
058_01	2022-07-18 02:23	80.4015	10.0608	688	before Y1-1 & Y2-1 deployment	
061_02	2022-07-18 16:28	80.8208	9.1888	507	Bio-Superstation	
061_07	2022-07-18 21:49	80.8262	9.1392	152	Bio-Superstation	
062_01	2022-07-19 00:28	80.9520	8.6957	768	before Y3-1 & Y4-1 deployment	
065_01	2022-07-19 23:41	81.5170	7.0380	482	Bio-Superstation	Superstation after topAWI
065_05	2022-07-20 05:09	81.5390	7.1250	152	Bio-Superstation	5min calibration stops at 60 and 150 m
069_08	2022-07-22 02:40	81.1880	7.9700	506	Bio-Superstation	problems with CTD cable connection to deck unit prior to cast
075_01	2022-07-25 04:29	82.8998	-5.8053	4023	Aurora Site	oxygen difference jumps at some depths
087_01	2022-07-29 13:41	81.0760	3.1852	506	Bio-Superstation	Superstation after topAWI
088_01	2022-07-29 22:17	81.1547	2.8992	506	Bio-Superstation	
091_01	2022-07-31 01:36	80.7223	4.4590	506	Bio-Superstation	Superstation after topAWI
094_01	2022-08-01 06:42	80.7690	4.2852	506	Bio-Superstation	fairly large C,T differences
096_01	2022-08-01 22:15	80.7697	4.9883	253	CTD Transect Filament	
097_01	2022-08-01 23:56	80.7687	5.3070	253	CTD Transect Filament	
098_01	2022-08-02 01:44	80.7670	5.6750	253	CTD Transect Filament	

Station	Time (UTC)	Lat (°N)	Lon (°E)	Depth [dbar]	Description	Comments
099_01	2022-08-02 03:19	80.7670	6.0237	253	CTD Transect Filament	100_01 in ActionLog
101_01	2022-08-02 04:49	80.7667	6.3363	253	CTD Transect Filament	
102_01	2022-08-02 06:11	80.7668	6.6668	254	CTD Transect Filament	
107_01	2022-08-03 18:28	78.9830	-4.5942	969	HG-EGC-8	
107_05	2022-08-04 00:02	78.9768	-4.5247	253	HG-EGC-8	
108_01	2022-08-05 23:48	78.4463	-17.5828	459	Bio-Station Greenland	
108_05	2022-08-06 03:30	78.4463	-17.5828	463	Bio-Station Greenland	first meters likely completely mixed by ship
111_01	2022-08-07 05:09	78.1785	-14.2787	355	before IdF3-2 deployment	15 min stop at depth
114_03	2022-08-10 12:40	71.2315	-24.6993	806	after SCO2-1 recovery	
115_02	2022-08-10 16:56	71.2807	-24.8360	639	after SCO1-1 recovery	
116_01	2022-08-10 19:17	71.3150	-24.7175	1196		Calibration stops, drift in oxygen sensor
118_02	2022-08-11 14:55	70.3532	-21.9940	414	after SC03-1 recovery	

Tab. 2.4: Overview of stations that need to be renamed for matching the ActionLog of the ship

Station number in CTD protocols and header	Station number as logged by the ship
010_02	011_01
037_01	036_01
037_02	037_01
099_01	100_01

Salinometry (areas 1-5)

We obtained high-precision salinity measurements with an Optimare Precision Salinometer (OPS, SN 007) for potential recalibration of the conductivity sensors. On overview of all taken samples as well as the results from the salinometry can be found in Table 2.5. The samples were taken from the Niskin bottles. Before taking the actual sample, the bottles were filled twice until the water spilled over to rinse them, and the rubber cap was rinsed while the bottles emptied in between. Then the bottles were closed, rinsed with fresh water, sealed with an aluminum cap and stored.

We measured these samples in three batches of 15, 25, and 6 bottles, i.e. 46 samples in total. The day before each session, the salinity bottles were heated in a water bath to approximately

30° C, and then cooled down at room temperature for about 20 h. For the first two batches, the pressure within the bottles was released with an injection needle directly after the warm bath, unfortunately, this had been forgotten for the third batch, so the pressure was released only before putting the samples into the salinometer. Before using the OPS, the samples were shaken thoroughly for overcoming any stratification in the bottle. While sampled by the OPS, the opening of the bottles was sealed with parafilm to inhibit evaporation. The metal inlet tube of the OPS was cleaned with a Kim-wipe between the samples.

A salinometry session starts with the standardization of the OPS using standard seawater. The respective bottle was sealed with the original cap and regularly sampled at the end of each session again. The salinity of the standard increased slightly in all sessions (if this was not the case, it would be a hint to some faults in the process).

Overall, our preliminary analysis suggests that the absolute differences of both salinity measurements from the CTD compared to the OPS salinity were generally smaller than 0.003, with two exceptions. For cast 006_05 there was a considerably (likely faulty) large difference between Sal00 (primary) and Sal11 (secondary) in the bottle file, yet not in the processed .cnv-file. This issue would need to be addressed in future processing steps. The other problem was the occurrence of large differences in the double samples in the third OPS session. It is unclear whether this was due to undocumented mistakes when drawing the water from the Niskin bottles, dirt in the bottles, or developing stratification within the Niskin bottles, as one of the casts was a calibration cast with longer stops, so that the time between firing and sampling the Niskin bottle was exceptionally large. Excluding these outliers, the salinity measurements seem to be of appropriate quality for the planned studies and analyses. The mean absolute errors (MAE) are 0.0011 for the primary sensor and 0.0013 for the secondary (see Fig. 2.7).

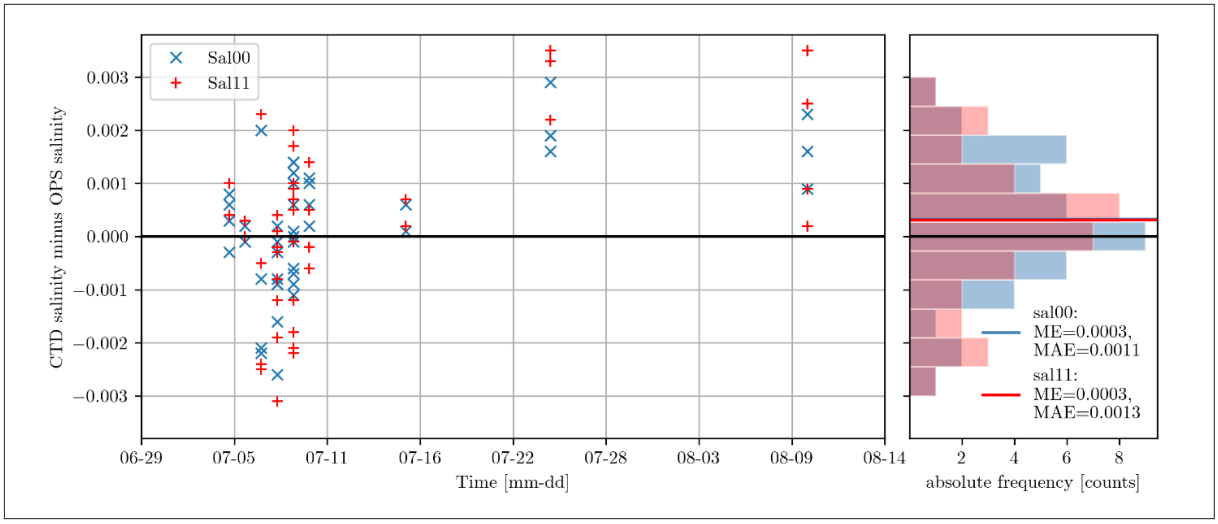

Fig. 2.7: Timeseries (left) and histogram (right) of the difference of the CTD salinity measurements from the primary sensor (Sal00, red) and the secondary sensor (Sal11, blue). The right panel includes lines for the mean error ME and also the numerical value of the mean absolute error MAE. Four outliers were not included, as mentioned in the main text body.

As most of the samples were taken early in the cruise, and few samples were available from later times and at deeper depths, it is not trivial to determine whether there was a temporal drift or a pressure dependency of the sensors.

Tab. 2.5: Results from OPS salinity measurements. The date of the OPS standardization and the corresponding value of the standard after the session is only given for the first occurrence of each batch. The sample with an asterisk under “Remarks” needed to be sampled twice with the OPS, as some leftover Parafilm had clogged the inlet, which led to constantly decreasing salinity. The inlet was cleaned and the salinometer was pumped before continuing measuring, the value was stable afterward.

Station	Date of water sampling	OPS salinity [PSU]	Sal00 salinity [PSU]	Sal11 Salinity [PSU]	OPS standardization	Remarks
006_01	2022-07-05	34.9212	34.9209	34.9216	2022/08/05 34.9957 PSU	Batch 2
006_01	2022-07-05	34.9206	34.9209	34.9216		Batch 2
006_01	2022-07-05	34.9136	34.9144	34.7299		Batch 2
006_01	2022-07-05	34.9138	34.9144	34.7299		Batch 2
010_02	2022-07-06	34.9137	34.9136	34.9137		Batch 2
010_02	2022-07-06	34.9134	34.9136	34.9137		Batch 2
014_01	2022-07-07	34.9112	34.9132	34.9135	2022/08/04 34.9963 PSU	Batch 1
014_01	2022-07-07	34.9140	34.9132	34.9135		Batch 1
019_01	2022-07-07	34.9154	34.9132	34.9129		Batch 1
019_01	2022-07-07	34.9153	34.9132	34.9129		Batch 1
020_01	2022-07-08	34.9141	34.9143	34.9145		Batch 2
020_01	2022-07-08	34.9144	34.9143	34.9145		Batch 2
020_01	2022-07-08	34.9138	34.9135	34.9130		Batch 2
020_01	2022-07-08	34.9161	34.9135	34.9130		Batch 1
021_01	2022-07-08	34.9154	34.9145	34.9151		Batch 1*
021_01	2022-07-08	34.9153	34.9145	34.9151		Batch 2
021_01	2022-07-08	34.9156	34.9140	34.9137		Batch 1
021_01	2022-07-08	34.9149	34.9140	34.9137		Batch 1
027_01	2022-07-09	34.9152	34.9166	34.9172		Batch 2
027_01	2022-07-09	34.9173	34.9166	34.9172		Batch 1
027_01	2022-07-09	34.9118	34.9112	34.9100		Batch 1
027_01	2022-07-09	34.9121	34.9112	34.9100		Batch 1
032_02	2022-07-09	34.9144	34.9150	34.9154		Batch 1
032_02	2022-07-09	34.9149	34.9150	34.9154		Batch 2
032_02	2022-07-09	34.9171	34.9160	34.9149		Batch 1
032_02	2022-07-09	34.9161	34.9160	34.9149		Batch 1
033_01	2022-07-09	34.9159	34.9169	34.9176		Batch 2
033_01	2022-07-09	34.9169	34.9169	34.9176		Batch 2
033_01	2022-07-09	34.9131	34.9143	34.9138		Batch 2
033_01	2022-07-09	34.9129	34.9143	34.9138		Batch 2
035_01	2022-07-10	34.9095	34.9101	34.9089		Batch 2

Station	Date of water sampling	OPS salinity [PSU]	Sal00 salinity [PSU]	Sal11 Salinity [PSU]	OPS standardization	Remarks
035_01	2022-07-10	34.9091	34.9101	34.9089		Batch 2
035_01	2022-07-10	34.9185	34.9196	34.9199		Batch 2
035_01	2022-07-10	34.9194	34.9196	34.9199		Batch 2
053_01	2022-07-16	34.9145	34.9146	34.9147		Batch 2
053_01	2022-07-16	34.9140	34.9146	34.9147		Batch 2
075_01	2022-07-25	34.9318	34.9337	34.9351		Batch 2
075_01	2022-07-25	34.9318	34.9337	34.9351		Batch 2
075_01	2022-07-25	34.9283	34.9312	34.9318		Batch 2
075_01	2022-07-25	34.9296	34.9312	34.9318		Batch 1
114_03	2022-08-10	34.7924	34.7947	34.7949		Batch 3
114_03	2022-08-10	34.7885	34.7947	34.7949	2022/08/12 34.9956 PSU	Batch 3
116_01	2022-08-10	34.8272	34.8384	34.8380		Batch 3
116_01	2022-08-10	34.8345	34.8384	34.8380		Batch 3
116_01	2022-08-10	34.7878	34.7887	34.7880		Batch 3
116_01	2022-08-10	34.7871	34.7887	34.7880		Batch 3

Noble gases

We took 34 water samples in copper tubes from five stations (see Table 2.6) and 29 samples in plastic bottles for Tritium at the same stations (see Table 2.7). The water samples for helium isotopes were stored from the CTD/water bottle system into gas-tight copper tubes, which are clamped of at both sides. As Helium is very volatile and the concentrations are generally low, the samples were taken before any other sampling, e.g., for oxygen or salinity, at the rosette. Tritium samples were taken after all the other groups were done taking water samples. The noble gas samples are analyzed later in the IUP Bremen noble gas mass spectrometry lab and are to be shipped there after the cruise. It was planned to take up to 144 helium and 80 Tritium samples, however, the difficult sea ice conditions close to the Aurora vent site and 79NG did not allow for that. The potential scientific outcome of the trace gas sampling is unclear at this point.

Tab. 2.6: Overview of the Helium sampling. As the time and location for the respective stations are provided in Table 2.3, they are omitted here. If there is "(*bot)"* written after a depth, the Niskin bottle was fired 10 m above the seafloor.

Station	Niskin bottle	Depth [m]	Helium tube
014_01	16	2	#1
021_01	23	2	#2
029_01	24	2	#3
075_01	1	3943 (bot)	#4
075_01	2	3700	#5
075_01	3	3599	#6
075_01	4	3500	#7

Station	Niskin bottle	Depth [m]	Helium tube
075_01	5	3400	#8
075_01	5	3400	#9
075_01	6	3200	#10
075_01	6	3200	#11
075_01	7	3100	#12
075_01	8	3000	#13
075_01	9	2800	#14
075_01	10	2600	#15
075_01	24	2	#16
108_05	1	457 (bot)	#17
108_05	1	457 (bot)	#18
108_05	3	400	#19
108_05	4	350	#20
108_05	5	300	#21
108_05	6	270	#22
108_05	7	240	#23
108_05	8	210	#24
108_05	9	180	#25
108_05	10	150	#26
108_05	11	120	#27
108_05	13	90	#28
108_05	15	60	#29
108_05	17	45	#30
108_05	19	30	#31
108_05	21	15	#32
108_05	23	2	#33
108_05	23	2	#34

Tab. 2.7: Overview of the Tritium sampling. As time and location for the respective stations are provided in Table 2.3, they are omitted here. If there is "(*bot)"* written after a depth, the Niskin bottle was fired 10 m above the seafloor.

Station	Niskin bottle	Depth [m]	Tritium bottle	Comments
075_01	1	3943 (bot)	#1	Niskin empty, no sample
075_01	2	3700	#2	
075_01	3	3599	#3	
075_01	4	3500	#4	
075_01	5	3400	#5	
075_01	5	3400	#6	
075_01	6	3200	#7	
075_01	6	3200	#8	
075_01	7	3100	#9	

Station	Niskin bottle	Depth [m]	Tritium bottle	Comments
075_01	8	3000	#10	
075_01	9	2800	#11	
075_01	10	2600	#12	
075_01	24	2	#13	
108_05	1	457 (bot)	#14	
108_05	3	400	#15	
108_05	4	350	#16	
108_05	5	300	#17	
108_05	6	270	#18	
108_05	7	240	#19	
108_05	8	210	#20	
108_05	9	180	#21	
108_05	10	150	#22	
108_05	11	120	#23	
108_05	13	90	#24	
108_05	15	60	#25	
108_05	17	45	#26	
108_05	19	30	#27	
108_05	21	15	#28	
108_05	23	2	#29	

Lowered ADCP (areas 1-5)

A lowered ADCP system (LADCP), consisting of two RDI 300 kHz ADCPs and a battery container, was mounted on the rosette and operated during PS131. Communication was established to a computer in the winch room via two cables (for master and slave) that were attached before and after each cast to the ADCPs. The ADCPs were operated using the GUI of the LADCP tool V1.7 from GEOMAR. The LADCP computer time was synchronized with the ship's NTP server directly.

During the entire cruise, the settings documented in Tables 2.8 and 2.9 were used. Specifically, they use a bin size of 10 m, a maximum range of 200 m, beam coordinates, no blanking after transmission, narrow band processing, and timing of the master and slave such that the acoustic energy of the master is separated by 0.55 seconds from the acoustic energy of the slave.

The Master (downward-looking) and Slave (upward-looking) data file names consist of the station number (three digits), an abbreviation indicating the viewing direction (UP for upward and DN for downward) and a running number with three digits beginning with 000, representing the file number, in case there are multiple files (e.g., 001DN000.000 and 001UP000.000). These files were stored in a folder named according to the station number. Sometimes also log files documenting all actions conducted as starting (with configurations), stopping, and downloading was kept, but since the files were not downloaded after every cast and sometimes multiple times, these log files are not available for all stations.

The LADCP cable went into the water without dummy plugs on one occasion, after which there were major issues with the connection of the ADCPs and the computer in the winch room. This resulted in a frequent inability to send start, stop, and download commands to the ADCPs. During several CTD casts only one ADCP was recording, during one CTD cast (069_08) neither recorded, and data was downloaded intermittently and often multiple times, all of which is documented in Table 2.10. Since it was often necessary to connect and disconnect the cables multiple times, many profile numbers only contain small amounts of data from on-board testing (marked as “test” in Table 2.10). The cable (COM1 to Master) between the rosette and the wall connection box was exchanged at the end of the cruise and the connection between the ADCPs and the computer appears to be in working order for the next application.

Data processing was carried out with the GEOMAR LADCP Software Version 10.0-10.2 beta which is executed in Matlab. The software combines, if available, data from the LADCP, CTD, navigational data, and vessel-mounted ADCP to conduct the velocity inversion method.

The CTD data were prepared with SBEDataProcessing, specifically with the routines datcnv_forLADCP, celltm, binavg_forLADCP, and trans. The resulting file has a 1 s resolution. Furthermore, a CTD data file is needed with a gridded resolution of 1 dbar that was provided through the software ManageCTD run on the CTD computer. Navigational information was obtained from the CTD data as it is possible to save the NMEA navigational data string during the cast via Seasave. This was not done during the first three casts (002, 003, and 004) and the single cast of the second CTD configuration (057), and the two subsequent casts of the original configuration (058, 059). The data processing revealed a prevalent large up-down compass difference between the ADCPs in the highest latitudes of the cruise (mostly >79.5°N). Data was repeatedly reprocessed when additional information was available (e.g., reprocessed VMADCP data).

Tab. 2.8: Start protocol of the Master LADCP used during PS131

[BREAK Wakeup A]

WorkHorse Broadband ADCP Version 50.40

Teledyne RD Instruments (c) 1996-2010

All Rights Reserved.

SB0 Writing Channel B Break State [DISABLED].

CR1

[Parameters set to FACTORY defaults]

SB0 Writing Channel B Break State [DISABLED].

TS yy/mm/dd,hh:MM:ss

WM15	*; LADCP water ping mode 15*
WV250	*; ambiguity velocity*
WN20	*; 20 bins*
WS1000	*; 10 m bins*

WF0 ; no blank after transmit

WB1 ; narrow band

EZ0111101 ; fixed speed of sound

EX00111 ; beam coordinates, use pitch/roll, 3 beam solution, bin mapping

CF11101 ; allow serial output

WP1 ; single ping data

TP 00:00.00 ; ping length of <0.00 seconds

TE 00:00:01.20 ; ensemble length of 1.2 seconds

SM1 ; Master

SI0 ; sync pulse on every ping, n/a for Slave, but needs ST0200

SA011 ; sync pulse before every ensemble

SW5500 ; wait 0.55 seconds, n/a for Slave

CQ255 ;

RN (three-digit cast no.)DN ; file name

CK

[Parameters saved as USER defaults]

SA = 011 ---------- Synch Before/After Ping/Ensemble Bottom/Water/Both

SI = 00000 ---------- Synch Interval (0-65535)

SM = 1 ---------- Mode Select (0=OFF,1=MASTER,2=SLAVE,3=NEMO)

SS = 0 ---------- RDS3 Sleep Mode (0=No Sleep)

ST = 00000 ---------- Slave Timeout (seconds,0=indefinite)

SW = 05500 ---------- Synch Delay (1/10 msec)

T?

Available Commands:

TB 00:00:00.00 ---------- Time per Burst (hrs:min:sec.sec/100)

TC 00000 ---------- Ensembles Per Burst (0-65535)

TE 00:00:01.20 ---------- Time per Ensemble (hrs:min:sec.sec/100)

*TF **/**/**,**:**:** ---------- Time of First Ping (yr/mon/day,hour:min:sec)*

*TG ****/**/**,**:**:** ---------- Time of First Ping (CCYY/MM/DD,hh:mm:ss)*

TP 00:00.00 ---------- Time per Ping (min:sec.sec/100)

TS yy/mm/dd,hh:MM:ss ---------- Time Set (yr/mon/day,hour:min:sec)

TT yyyy/mm/dd,hh:MM:ss ---------- Time Set (CCYY/MM/DD,hh:mm:ss)

TX 00:00:00 ---------- Buffer Output Period: (hh:mm:ss)

T? ---------- Display Time Help

W?

Available Commands:

WD 111100000 ---------- Data Out (Vel;Cor;Amp PG;St;P0 P1;P2;P3)

WF 0000 ---------- Blank After Transmit (cm)

WG 000 ---------- Percent Good Minimum (1-100%)

WN 020 ---------- Number of depth cells (1-255)

WP 00001 ---------- Pings per Ensemble (0-16384)

WS 1000 ---------- Depth Cell Size (cm)

WV 250 ---------- Mode 1 Ambiguity Vel (cm/s radial)

WZ 010 ---------- Mode 5 Ambiguity Velocity (cm/s radial)

W? ---------- Display Water-Profile Help

E?

EA = +00000 ---------- Heading Alignment (1/100 deg)

EB = +00000 ---------- Heading Bias (1/100 deg)

ED = 00000 ---------- Transducer Depth (0 - 65535 dm)

ES = 35 ---------- Salinity (0-40 pp thousand)

EX = 00111 ---------- Coord Transform (Xform:Type; Tilts; 3Bm; Map)

EZ = 0111101 ---------- Sensor Source (C;D;H;P;R;S;T)

CS ; start pinging

Tab. 2.9: Start protocol of the Slave LADCP used during PS131

[BREAK Wakeup A]

WorkHorse Broadband ADCP Version 50.40

Teledyne RD Instruments (c) 1996-2010

All Rights Reserved.

SB0 Writing Channel B Break State [DISABLED].

CR1

[Parameters set to FACTORY defaults]

SB0 Writing Channel B Break State [DISABLED].

TS yy/mm/dd,hh:MM:ss

WM15 ; LADCP water ping mode 15

WV250 ; ambiguity velocity

WN20 ; 20 bins

WS1000 ; 10 m bins

WF0 ; no blank after transmit

WB1 ; narrow band

EZ0111101 ; fixed speed of sound

EX00111 ; beam coordinates, use pitch/roll, 3 beam solution, bin mapping

CF11101 ; allow serial output

WP1 ; single ping data

TP 00:00.00 ; ping length of <0.00 seconds

TE 00:00:01.20 ; ensemble length of 1.2 seconds

SM2 ; Slave

SA011 ; sync pulse before every ensemble

ST200 ; slave timout 200 seconds, n/a for Master, but needs SI0

CQ255 ;

RN (three-digit cast no.)UP ; file name

CK

[Parameters saved as USER defaults]

S?

SA = 011 ---------- Synch Before/After Ping/Ensemble Bottom/Water/Both

SI = 00000 ---------- Synch Interval (0-65535)

SM = 2 ---------- Mode Select (0=OFF,1=MASTER,2=SLAVE,3=NEMO)

SS = 0 ---------- RDS3 Sleep Mode (0=No Sleep)

ST = 00200 ---------- Slave Timeout (seconds,0=indefinite)

SW = 00000 ---------- Synch Delay (1/10 msec)

T?

Available Commands:

TB 00:00:00.00 ---------- Time per Burst (hrs:min:sec.sec/100)
TC 00000 ---------- Ensembles Per Burst (0-65535)
TE 00:00:01.20 ---------- Time per Ensemble (hrs:min:sec.sec/100)
*TF **/**/**,**:**:** ---------- Time of First Ping (yr/mon/day,hour:min:sec)*
*TG ****/**/**,**:**:** ---------- Time of First Ping (CCYY/MM/DD,hh:mm:ss)*
TP 00:00.00 ---------- Time per Ping (min:sec.sec/100)
TS yy/mm/dd,hh:MM:ss ---------- Time Set (yr/mon/day,hour:min:sec)
TT yyyy/mm/dd,hh:MM:ss ---------- Time Set (CCYY/MM/DD,hh:mm:ss)
TX 00:00:00 ---------- Buffer Output Period: (hh:mm:ss)
T? ---------- Display Time Help

W?

Available Commands:

WD 111100000 ---------- Data Out (Vel;Cor;Amp PG;St;P0 P1;P2;P3)
WF 0000 ---------- Blank After Transmit (cm)
WG 000 ---------- Percent Good Minimum (1-100%)
WN 020 ---------- Number of depth cells (1-255)
WP 00001 ---------- Pings per Ensemble (0-16384)
WS 1000 ---------- Depth Cell Size (cm)
WV 250 ---------- Mode 1 Ambiguity Vel (cm/s radial)
WZ 010 ---------- Mode 5 Ambiguity Velocity (cm/s radial)
W? ---------- Display Water-Profile Help

E?

EA = +00000 ---------- Heading Alignment (1/100 deg)
EB = +00000 ---------- Heading Bias (1/100 deg)
ED = 00000 ---------- Transducer Depth (0 - 65535 dm)
ES = 35 ---------- Salinity (0-40 pp thousand)
EX = 00111 ---------- Coord Transform (Xform:Type; Tilts; 3Bm; Map)
EZ = 0111101 ---------- Sensor Source (C;D;H;P;R;S;T)
CS

Tab. 2.10: LADCP profile no. with corresponding CTD cast no. and availability of DN/UP files

LADCP profile no.	CTD cast no.	DN	UP	Comments
001	-	x	x	test
002	001_01	x	x	not processed due to missing NMEA data in CTD profile
003	001_03	x	x	not processed due to missing NMEA data in CTD profile
004	001_06	x	x	not processed due to missing NMEA data in CTD profile
005	-	x	x	test
006	006_01	x	x	
007	006_05	x	x	
008	-	x	x	test
009	010_02	x	x	station name in ActionLog is 011_01, was saved as 010_02; not processed due to error in processing routine
010	012_01	x	x	
011	013_01	x	x	
012	014_01	x	x	
013	019_01	x	x	
014	020_01	x	x	
015	021_01	x	x	
016	027_01	x	x	
017	029_01	x	x	
018	032_02	x	x	
019	033_01	x	x	
020	035_01	x	x	large up-down compass difference (19.5582), first station north of 79.5°N
021	035_06	x	x	
022	037_01	x	x	station name in ActionLog is 036_01, was saved as 037_01; large up-down compass difference (17.6519)
023	-	-	-	test, not downloaded
024	037_02	x	-	station name in ActionLog is 037_01, was saved as 037_02
025	038_01	x	x	large up-down compass difference (17.7967)
026	039_01	x	x	large up-down compass difference (19.1546)
027	040_01	x	x	large up-down compass difference (39.5208)
028	041_01	-	x	not processed due to missing down file
029	042_01	x	-	
030	043_01	x	-	
031	044_01	x	-	
032	045_02	x	x	large up-down compass difference (33.6399)
033	046_01	x	-	
034	047_02	x	x	large up-down compass difference (18.9537)
035	048_02	x	x	
036	-	x	-	test
037	-	x	x	test

LADCP profile no.	CTD cast no.	DN	UP	Comments
038	049_02	x	x	large up-down compass difference (16.7402)
039	053_01	x	x	
040	-	x	-	test
041	056_02	-	x	
042	-	x	x	test
043	056_08	x	x	large up-down compass difference (18.9158)
044	057_02	x	x	
045	-	x	-	test
046	057_07	x	x	large up-down compass difference (20.5956)
047	-	x	-	test
048	058_01	x	-	
049	061_02	x	x	large up-down compass difference (42.2621)
050	061_07	x	x	large up-down compass difference (21.514); not fully processed due to error in processing routine
051	-	x	-	test
052	062_01	x	-	
053	065_01	x	x	
054	065_05	x	x	not fully processed due to error in processing routine
055	-	x	-	test
056	-	x	x	test
057	075_01	x	x	not processed due to missing NMEA data in CTD profile
058	087_01	x	x	second, very large down file – ADCP did not receive stop command for some time; not processed due to missing NMEA data in CTD profile
059	088_01	x	-	not processed due to missing NMEA data in CTD profile
060	-	-	x	test
061	091_01	x	-	
062	-	x	-	test
063	094_01	-	x	not processed due to missing down file
064	096_01	x	x	large up-down compass difference (19.4137)
065	097_01	x	x	
066	098_01	x	-	
067	099_01	x	x	station name in ActionLog is 100_01, was saved as 099_01
068	101_01	x	-	
069	102_01	x	-	second and third, very large down file – ADCP did not receive stop command until next cast; not processed due to error in processing routine
070	107_01	-	x	not processed due to missing down file
071	107_05	x	-	change of batteries after cast
072	-	x	-	test
073	-	x	x	test
074	-	x	-	test
075	-	x	-	test

LADCP profile no.	CTD cast no.	DN	UP	Comments
076	-	x	-	test
077	-	x	-	test
078	108_01	x	x	
079	108_05	-	-	not downloaded
080	111_01	x	-	
081	-	-	-	test, not downloaded
082	-	x	-	test
083	-	-	x	test
084	-	x	-	test
085	114_03	x	x	
086	115_02	x	x	
087	116_01	x	x	
088	118_02	x	x	

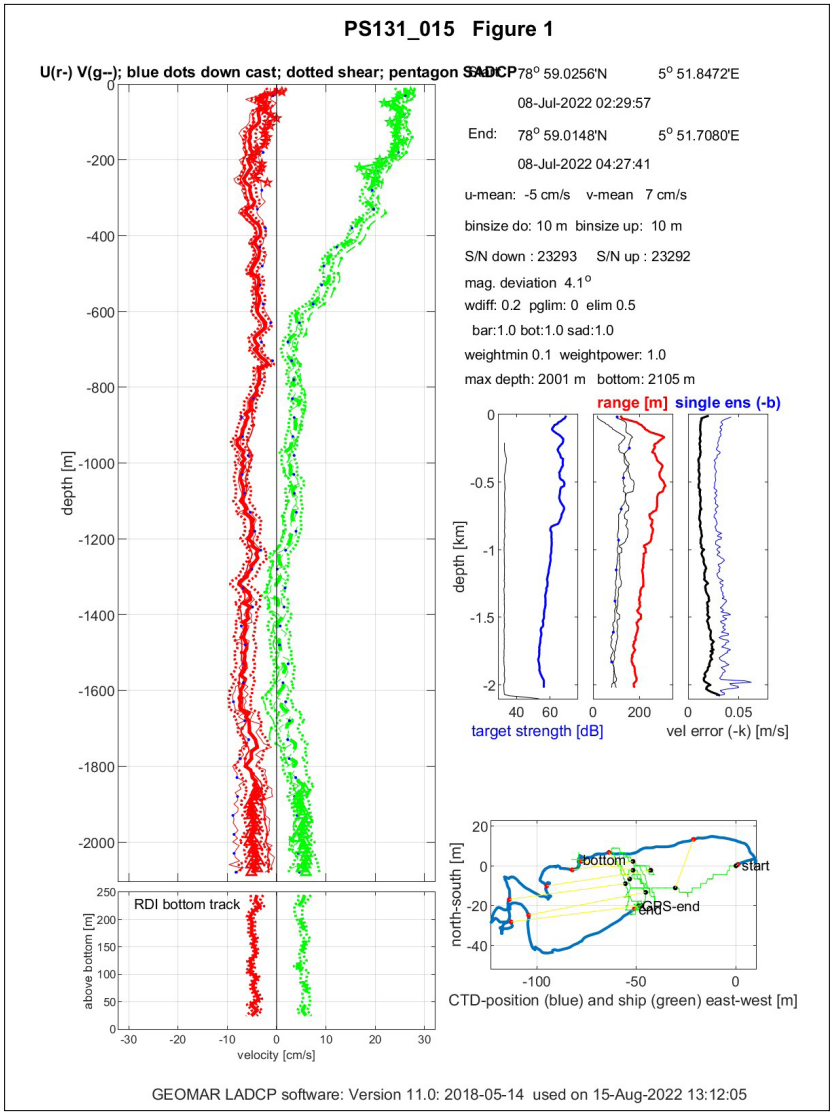

Fig. 2.8: Exemplary output of the processing routine for profile 015

Thermosalinograph (Danish and Norwegian EEZs including transit and areas 1-5)

The thermosalinograph was continuously operated for the part of the cruise where working permits existed: all of the Danish and Norwegian EEZ which included the transit to and from the working areas as well as areas 1 – 5. Standard settings were used. The data was screened in near real-time during the cruise and no remarkable problems were identified.

Vessel-mounted ADCP (areas 1-5)

From 30 June 2022 06:39 to 10 August 2022 15:59 we measured profiles of ocean current velocity in the upper 300 m while underway with a vessel-mounted Acoustic Doppler Current Profiler (VMADCP). The RDI Ocean Surveyor instrument (150 kHz) was mounted at an angle of 45 degrees in the 'Kastenkiel' of *Polarstern.* The instrument was configured in narrowband mode and set up to use a 4 m bin size (configuration file cmd_OS150NB_trigger_off.txt as shown in Table 2.11), covering a range from 15 m to about 200 – 300 m depending on sea state, ice conditions, ship's speed and backscatter signals.

Overall, the system functioned without any issues and all data was collected entirely in data files 11 (file format: PS131011_000 (three-digit file number).ENX, *.ENR, *.ENS, *.N1R, *.N2R, *.NMS, *.STA, *.LTA, *.VMO, *.LOG), as we did not apply any changes to the instrument configuration and there was no need to stop it at any time.

The setup of navigational input was used from the vessel's GPS system. Problems to resolve velocities potentially occurred due to low backscatters, low water depths, and/or sea ice in front of the beams. The multibeam echosounder HYDROSWEEP (15.5 kHz) and acoustic signals to release moorings might also affect the velocity data.

The software VmDas (Teledyne RD Instruments) was used to set the ADCP's operating parameters and to record the data. Finally, the data conversion was done using Matlab routines of the Ocean Surveyor Sputum Interpreter (OSSI) version 1.9 (osheader.m, osdatasip.m, osrefine.m, osbottom.m). Hereby the VMADCP data was corrected by using a misalignment angle of 0.8015° and an amplitude factor of 1.014001 (Fig. 2.9 and 2.10).

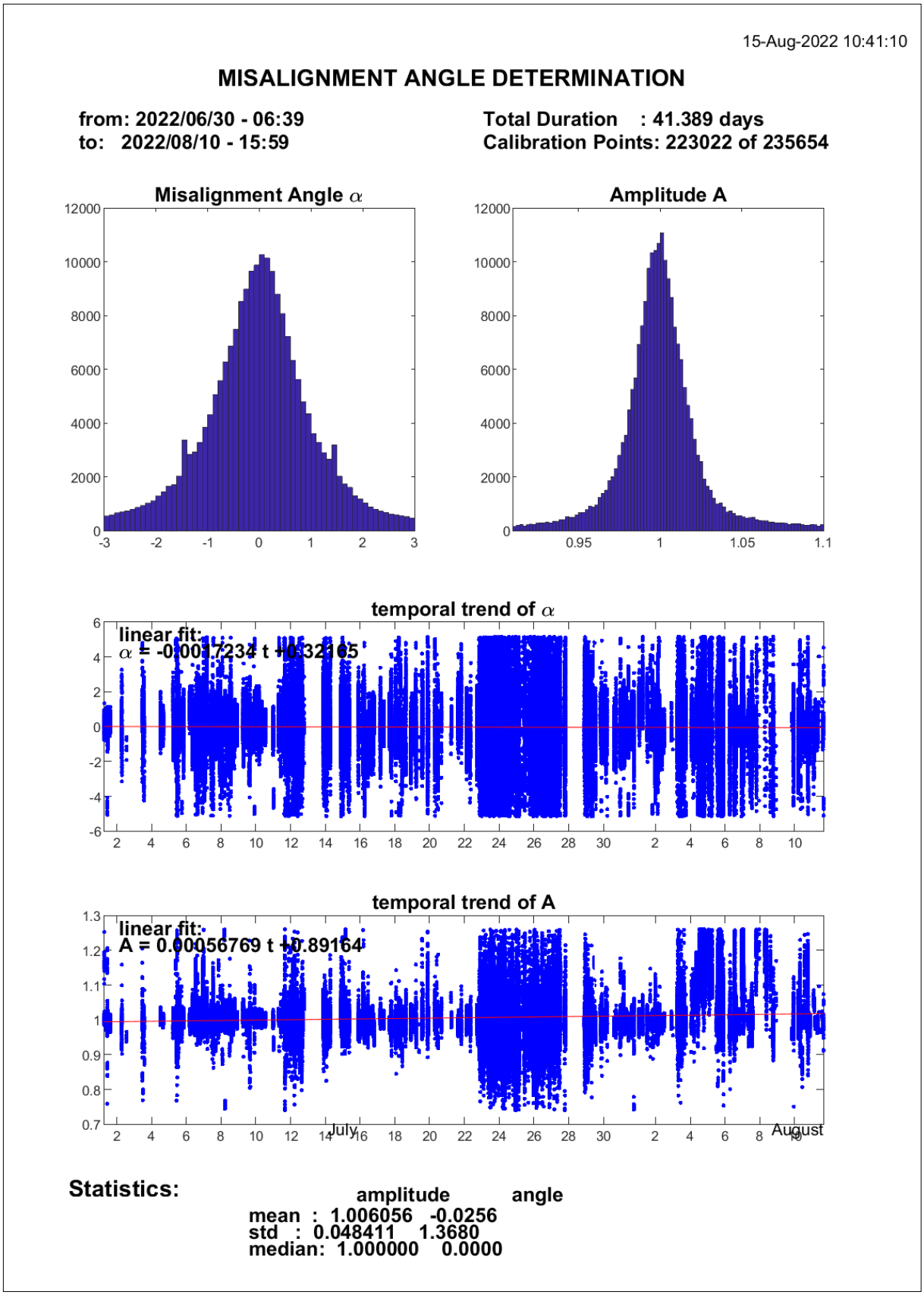

Fig. 2.9: Misalignment determination of the OSSI software

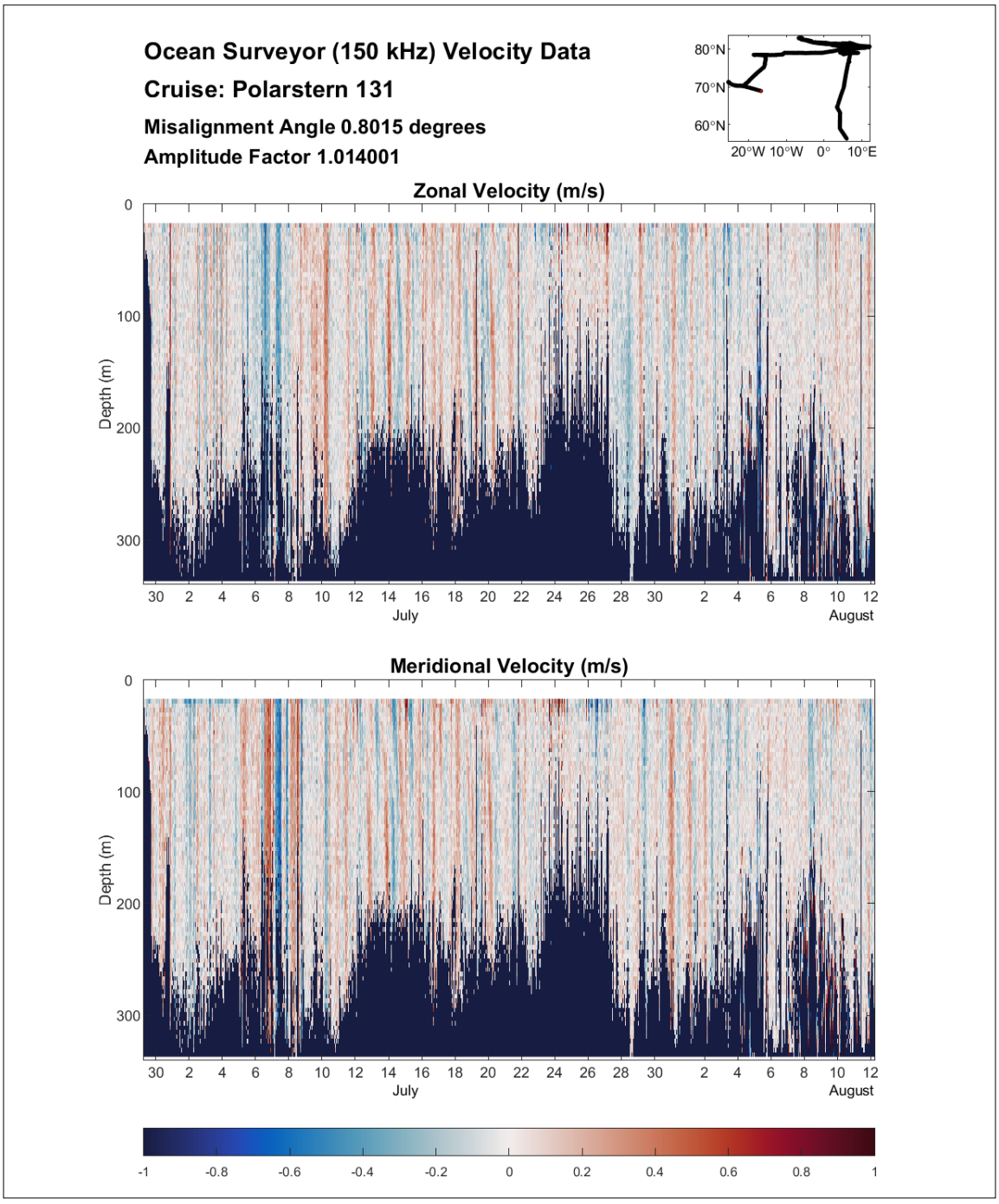

Fig. 2.10: Resulting ocean velocities [m s^{-1}] during PS131

Tab. 2.11: VMADCP command file cmd_OS150NB_trigger_off.txt

;----------

; ADCP Command File for use with VmDas software.

;

; ADCP type: 150 Khz Ocean Surveyor

; Setup name: for Polarstern in 6/2014

```
; Setup type:    Low resolution, long range profile (Narrowband)
;
; NOTE:  Any line beginning with a semicolon in the first
;        column is treated as a comment and is ignored by
;        the VmDas software.
;
; NOTE:  This file is best viewed with a fixed-point font (e.g. courier).
; Modified Last: 12Jun2014
;-------------------------------------------------------------------------/

; Restore factory default settings in the ADCP
cr1

; set the data collection baud rate to 9600 bps,
; no parity, one stop bit, 8 data bits
; NOTE:  VmDas sends baud rate change command after all other commands in
; this file, so that it is not made permanent by a CK command.
cb411

; Set for narrowband single-ping profile mode (NP), 100 (NN) 4 meter bins (NS),
; 2 meter blanking distance (NF), 390 cm/s ambiguity vel (WV)
WP000
NP001
NN080
NS0400
NF0400
;WV390

; Disable single-ping bottom track (BP),
; Set maximum bottom search depth to 1200 meters (BX)
BP000
;BX12000
```

; output velocity, correlation, echo intensity, percent good

ND111100000

; Ping as fast as possible

TP000000

; Since VmDas uses manual pinging, TE is ignored by the ADCP

; and should not be set.

;TE0000000

; Set to calculate speed-of-sound, no depth sensor, external synchro heading

; sensor, pitch or roll being used, no salinity sensor, use internal transducer

; temperature sensor

EZ1011101

; Output beam data (rotations are done in software)

EX00000

; Set transducer misalignment (hundredths of degrees).

; Ignored here but set in VmDAS options.

;EA00000

; Set transducer depth (decimeters)

ED00110

; Set Salinity (ppt)

ES35

;set external triggering and output trigger; no trigger

CX0,0

;set external triggering and output trigger

;CX1,3

; save this setup to non-volatile memory in the ADCP

CK

Triaxus towed ocean profiler of the AWI (topAWI) (area 2)

The remotely operated towed vehicle Triaxus from MacArtney serves as a platform for multiple instruments and allows to gather high-resolution datasets. The system is towed behind the ship either in a saw-tooth pattern or at a constant depth. The main aim of the Triaxus work on PS131 was to support the research in the marginal ice zone, allowing both the gathering of a multidisciplinary dataset and the decision support for the location of the biological sampling stations. Notable new features were: a new method of acquiring data in an ice-covered area with the use of a depressor, the inclusion of a measuring instrument for turbulence (Microrider), and a high-resolution optical system for plankton (LOKI). Another feature study took place at the very edge of the MIZ, where a streak of ice had been spotted on the satellite images. In addition to this scientific work, a deeper deployment test was carried out in the Scoresby Sund fjord.

LOKI:

The optical plankton recorder LOKI (Lightframe On-sight Key species Investigations) was attached to the Triaxus during the cruise. It was operated from 29 July 2022 onwards in a semi-manual data acquisition mode.

Microrider:

During PS131, we attached a MicroRider turbulence instrument package from Rockland Scientific, Canada, in the Triaxus to test its performance. The instrument used is a MicroRider-1000LP (MR, SN060), equipped with shear probes and fast thermistors. Although it is expected that platform vibrations and relatively fast flow past the sensors (2 – 3 m/s) will substantially limit the performance of turbulence measurements, this particular instrument was modified to the tidal energy configuration and recently tested successfully in an AUV deployment (Kolås et al, 2022). This motivated the trials here. Relative to standard MRs, MR SN060 has an increased sampling rate (1024 Hz, instead of 512 Hz), a modified circuit board with an anti-aliasing filter of 196 Hz (instead of 98 Hz), and reduced gain of the shear channel by a factor of 10 from about 1 to 0.1 s. This modification allows reaching wavenumbers high enough to resolve the shear spectrum at flow past sensor speeds reaching 2 m s^{-1}. Furthermore, MR SN060 is fitted with a two-axis vibration sensor (a pair of piezo-accelerometers), and a high-accuracy dual-axis inclinometer (ADIS 16209, pitch and roll angles accurate to 0.18), a low-power six-axis motion sensor (O-Navi, Gyrocube 3F), and an integrated low-power three-axis magnetic field sensing module (MicroMag3).

The instrument was attached mechanically to the lower cargo rail on the port side, with firm brackets to constrain eventual vibrations to narrow frequency bands. The MR was externally powered using a rechargeable battery, installed in the lower port tube. The planned method was to remove vehicle vibrations at distinct frequencies using coherency analysis between the shear probe record and the accelerometer signal measured in multiple directions (Goodman et al., 2006).

Unfortunately, the wavenumber spectra of shear, even after removing the vehicle vibrations using the Goodman algorithm, are substantially contaminated, especially in the bulk of the wavenumber range where the shear spectra must be resolved for dissipation rate estimates. This is demonstrated using an arbitrary, and representative, subset of the data collected on 19 July 2022 (Fig. 2.11). The average vibration spectrum along segment 5 shows large contaminations in the frequency range of 20 to 100 Hz (Fig. 2.12). Average shear spectra from a portion of segment 5, extracted between 50 and 70 m demonstrate the contamination of the shear probe data (Fig. 2.13). Despite cleaning the shear spectra by removing signals coherent with the vibrations, the spectra from both probes are severely contaminated and cannot be used for dissipation rate estimates.

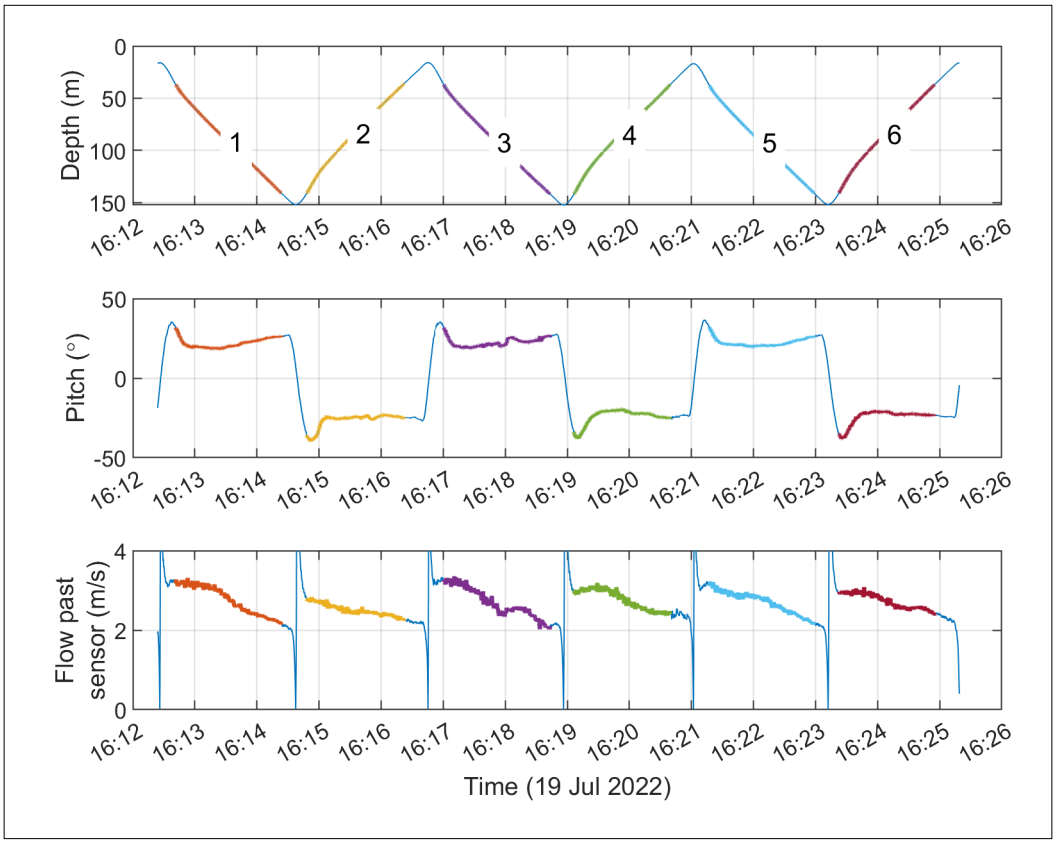

Fig. 2.11: A subset of 6 sections (down and upcasts marked 1 to 6), showing the depth, pitch angle and the relative flow past the sensors estimated from rate of change of pressure and the pitch; the segments of data selected for analysis (marked by bold lines) typically exclude the turning regions and have flow past sensor of 2.5 to 3.5 m/s.

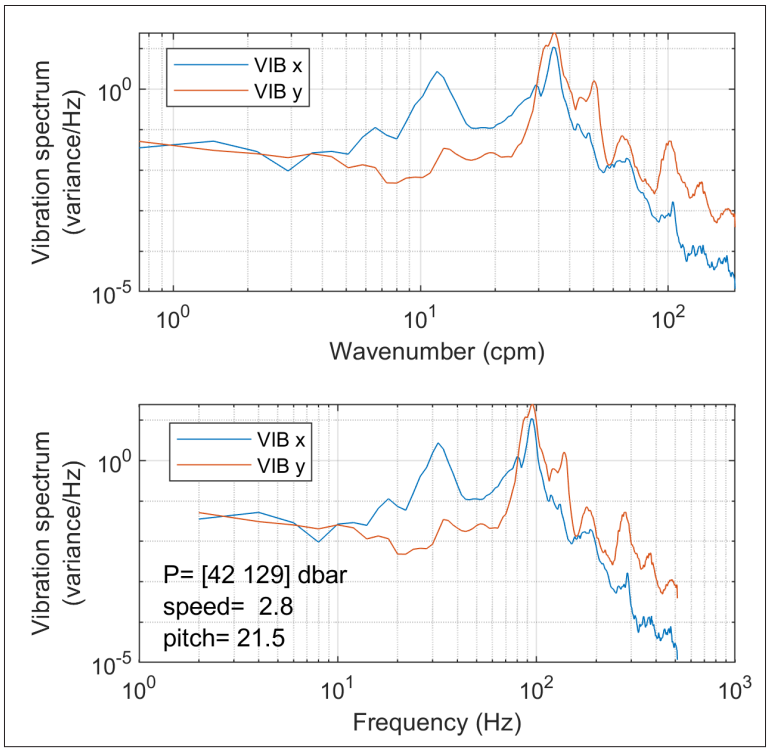

Fig. 2.12: Average wavenumber and frequency spectra of vibration along two axes along segment 5, averaged between 42 and 129 dbar; average speed (in m/s) and pitch angle (degrees) are indicated. The unit of the vibration is arbitrary.

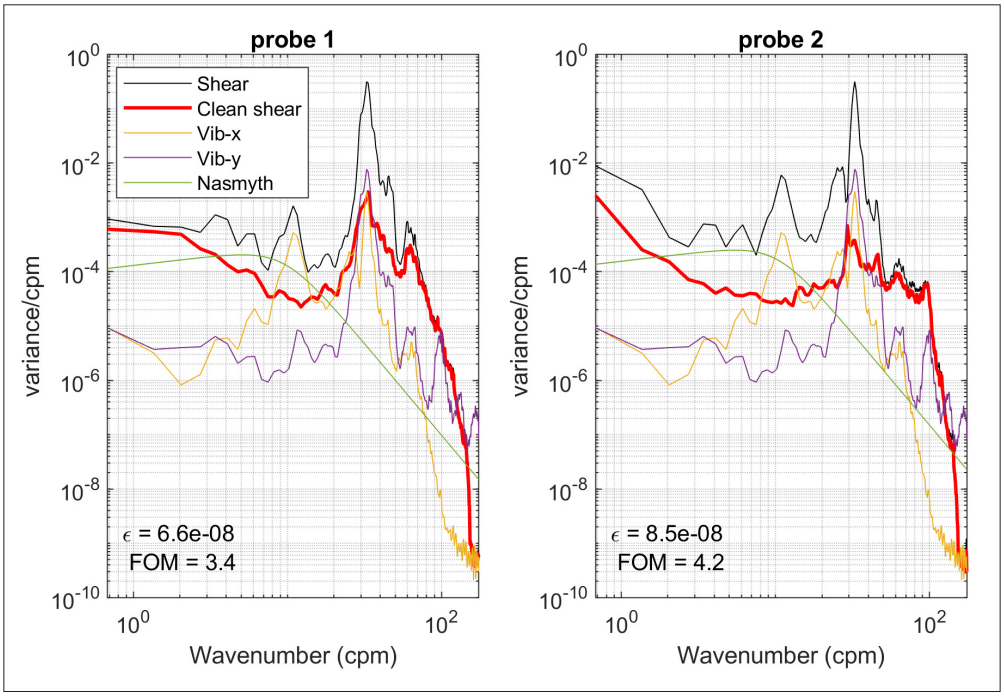

Fig. 2.13: Average wavenumber spectra along segment 5, averaged between 50 and 70 dbar; left panel is for shear probe 1. Right panel is for shear probe 2 (orthogonal to probe 1). The unit of the vibration is arbitrary (here divided by 3,000). Shear spectra (in units of (s^{-2}/cpm) are shown as the measured (black) and cleaned (red, using the Goodman algorithm). The empirical spectra (Nasmyth) are for the estimated dissipation rates indicated on panels (in W/kg) together with figure of merit (FOM; FOM>1 is a poor and unacceptable fit to the empirical shape).

Chronological timeline of deployments:

7 July 2022:

Deployment without depressor, aiming for a general check of the system, including an auto-depth and auto-undulation test.

The communication with the ADCP 1 up could not be established.

During this first test, we learned a few relevant items for a successful dive, such as:

The ROTV software has to be started with admin rights.

The altimeter has to be turned on for the auto-undulation to work.

Minus values of the battery and main supply ampere are usual.

11 July 2022:

Deployment without depressor, undulation between 10 and 200 meters, then 5 and 200 meters. Towards the ice edge.

We still had no communication with the ADCP 1 up.

A time delay of 22 seconds was found between the Triaxus and CTD computers. This is due to the Triaxus computer not being directly connected to the ship's server, in comparison to the other sensors.

16 July 2022:

First depressor test deployment without the Triaxus.

The depressor has to first be lifted before the Triaxus can be picked up and deployed. The depressor is then lowered in the water afterward. Less cable length is needed due to the whole system being lowered in the water. A CTD was mounted on the depressor to be able to know its depth.

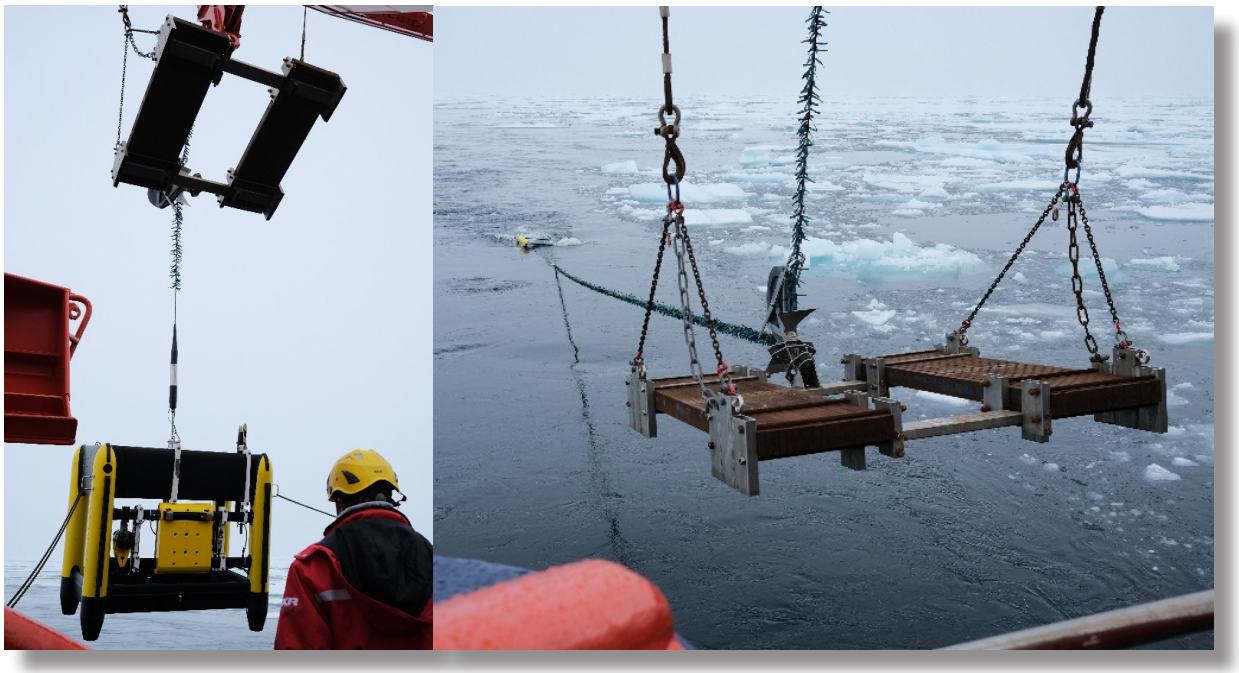

Fig. 2.14: Deployment of the Triaxus with the depressor, credits to Mario Hoppmann

Deployment with depressor. Auto undulation between 11 and 150 meters. First time in ice.

We still had no communication with ADCP 1 up, the microcontroller on the main electronic board was broken and therefore the serial connection to the sensor was not working.

This dive was separated into two sections as follows, also see Table 2.12.

19:25 UTC: Triaxus set to parking depth, change course + CTD new start

19:36 UTC: The new transect start PS131_055_01_02

A change from Atlantic water to fresher polar water accompanied by fluorescence peaks (up to 30 mg/m^3) was observed. The salinity was increasing and decreasing many times – as the ice concentration was varying outside.

19 July 2022:

Deployment with depressor and CTD on the depressor. Auto undulation between 15 to 150 meters, then 20 to 150 meters because of a first altimeter alarm after 45 minutes.

The first occurrence of the yaw flaps issue is found during the pre-dive check. The yaw flaps appear to be moving independently from each other, as also depicted in the software, i.e. the port side flap is first going in the opposite direction as the command and then coming back to the desired value. The flap also got blocked once at one position, which could be solved by moving both of the flaps in that direction and then back to their neutral position.

The serial connection from ADCP 1 up was moved to the port arriving on the computer from the ADCP 2 down. No communication with ADCP 2 down could be established.

After the 3rd altitude alarm, we stopped the undulation and got the Triaxus back on Deck.

22 July 2022:

Maintenance work was done, with the exchange of the fiber optic weak link.

29 July 2022:

Deployment with depressor. Auto undulation between 19 and 150 meters, then soon after from 15 to 150 meters.

The serial connection from ADCP 2 down was moved to the port arriving on the computer from the ADCP 1 up (sensor port 4, previously ACS). Therefore, the ACS was moved to sensor port number 9, because the sensor is also able to work with 24V. The ADCP 1 up was still recorded on the ADCP 2 down computer. This setup will remain for the rest of the deployments (beware of the corresponding naming of the files).

LOKI first measurements with a net size of 150 microns (86_01 files).

Resistance issues down to 54 kOhm, decision to take it back on deck.

30 July 2002

We searched for the reason for the resistance issue in the Termination Bottle and the Connection Cable to the Main Bottle. No Problem was found in the Termination Bottle. The connection cable to the Main Bottle was exchanged.

30 July 2022:

Deployment with depressor. Auto undulation between 15 and 150 meters (going out of the ice?).

LOKI measurements with a new net size of 300 microns (90_01 files).

We ignored the altitude alarms. Only a low chlorophyll value is left in the water column.

1 August 2022:

Deployment with depressor. First auto undulation was chosen to be from 10 to 50 meters, which was directly changed for a 5 to 50 meters undulation, to get measurements from under the ice.

LOKI measurements with a net size of 300 microns and two pumps (95_01 files).

Crossing the ice "filament"? After going out of the ice, the chlorophyll decreases and the temperature gets a bit higher.

This dive was separated into two sections as follows, also see Table 2.12:

16:47 UTC: End of first undulation

17:05 UTC: Second transect with undulation between 6 and 200 meters.

A first leak alarm from the main bottle popped up after around 45 minutes during the downturn. Drifters were deployed during the second transect section. A total of 11 leak alarms occurred. During the dive, we estimated that the amount of water could not reach the leak sensor the whole time. This was confirmed after the inspection of the bottle back on deck. However, after the 9th alarm, the decision was taken to undulate until 150 meters only, which stopped the alarms for some time. After going out of the ice streak, the Triaxus was recovered, this time with the leak alarm staying on.

At some point, the Triaxus didn't rise regularly (went slightly down during the upcast).

5 August 2022:

Repair of the Main Bottle leakage by exchanging the O-ring, and the damage of the sensor port 6 (TriOS RAMSES). We exchanged the motor controller for the port yaw motor (LP), in order to solve the yaw flap issue. But this didn't take away the problem.

8 August 2022:

The port yaw motors (LP) were exchanged, however, the issue with the yaw motors behaving strangely remained.

11 August 2022:

Deployment without depressor. Auto undulation from 10 to 300 meters (from the protocol, Hauke told me 350?).

The aim of this last Triaxus deployment was to test both the cable behavior and the waterproofness of the main bottle for undulations to 350 meters depth. for the next *Polarstern* cruise planned in the Southern Ocean.

At the beginning of the deployment, the Triaxus first had to be lifted to uncross a cable due to a wrong connection order. During the payout of the cable, we experienced short-time resistance issues for unknown reasons, but the values went back to normal after a while. The automatic spooling function was running smoothly.

However, at the end of the operation the winch oil had a burn smell which we couldn't explain. No metal parts were found in the oil.

13 August 2022:

Two deck tests happened, to be found in the Pre-Dive Checklists 1 and 2.

At first, a new issue with the fiber optic cable arose, the default was found in the BCR connector: the ceramic aligning the fiber optic was broken. The connection could be achieved on deck by wiggling it for further deck tests.

During the second deck test, the cable from the main bottle to the yaw motor was changed and the issue didn't rise up again. After experiencing some issues with the ship's power supply (fuse of the top side unit power supply), the old cable from the main bottle to the yaw motor was tested again and the same flap issue happened again. Based on this, we are quite confident that the yaw motor problem came from the cable and is therefore now solved.

Tab. 2.12: Overview of the Triaxus transects during PS131 – for further information see Table 2.12 at the end of the Chapter.

Tab. 2.13: Overview of the recording sensors for the different transect numbers – for further information see Table 2.13 at the end of the Chapter.

Microstructure (area 2)

We conducted ocean microstructure measurements from ice floes as well as during ship stations. Profiles from the ship were obtained using an MSS90L (Sea&Sun Technology, Germany) system. On-ice deployments were made using the same MSS system, as well as using an uVMP ("upriser" Vertical Microstructure Profiler, Rockland Scientific, Canada).

Instrument descriptions

The MSS used was MSS90L SN 095 (except the first four profiles with SN 075). It is a loosely-tethered free-fall instrument equipped with two airfoil probes aligned parallel to each other, a fast-tip thermistor (FP07, with a small sensor guard), an acceleration sensor (for body vibration measurements), conventional CTD sensors for precision measurements, a Turner Design Cyclops-7 in Vivo Chlorophyll/Blue sensor for ChlA fluorescence and an SST-DO, fast optical dissolved oxygen sensor. All channels sampled at 512 Hz. We also note that the sensor guard of the FP07 will further limit the size of the eddies resolved by this sensor. The instrument is ballasted for a typical fall speed of 0.5 m s^{-1} and is decoupled from operation-induced tension by paying out cable at sufficient speed to keep it slack. Data are transmitted in real-time to a ship-board data acquisition system. The shear probes used were type PNS6, serial numbers C6258 (sensitivity 3.54e-04 at 21C, SHE1) and C6259 (sensitivity 3.99e-4 at 21C, SHE2). The same sensors were used throughout the cruise and the sensors point downward when the instrument profiles vertically.

The uVMP is an ascending, uprising profiler, described in detail in Fer et al. (2022). The aim of using the uprising vertical microstructure profiler was to obtain dissipation rate estimates in the upper 50 – 80 m up to the ice-water interface and to resolve the under-ice boundary layer. The uVMP is a VMP250-IR (SN104) from Rockland Scientific, Canada, modified for upward profiling measurements. It is an internally-logging instrument fitted with rechargeable batteries. It is equipped with two shear probes (oriented orthogonally), a fast response temperature (FP07, no guard on the sensor), micro conductivity (SBE7) sensors, as well as pressure,

tilt, and vibration sensors. A probe guard allows profiling until the guard hits the ice surface. Turbulence channels are sampled at a rate of 512 Hz, and the slow channels at 64 Hz. Up to 4 brushes at the rear end provide a drag. We profiled using 3 brushes, giving a rise speed of about 0.6 m s^{-1}. Data acquisition starts and stops by attaching and removing a magnet. The system has two lines, one rope attached to the tail of the profiler and an electric cable with 10 kg ballast, and a mechanical release mechanism. The robe has a stopper at about 2 m from the tail, accessible from the ice when the instrument is in water. The release mechanism is attached here. The instrument is lowered by feeding both lines simultaneously down to 80 – 100 m depth, taking care to avoid entanglement of the lines. At target depth, we wait up to 5 minutes for the turbulence in the wake of the instrument to dissipate or advect away. The weight is then released by sending an electric signal and the instrument ascends. We wait 2 – 3 minutes until the profiler reaches the ice surface and then retrieve the electric cable with ballast using a battery-driven line-puller. Next, the instrument is brought back to the hole by retrieving the recovery line using the same line puller. To avoid dragging the buoyant instrument under sea ice, we send a 5 kg recovery weight along the line to force the instrument down to about 1 m below the ice. As the line is retrieved, the stopper arrives first, the recovery weight is removed, and the weight-release system is re-attached to start a new cast, without having to recover the instrument.

Profiling from the ship

The original plan was to use an RSI VMP-500 profiler with its 1,800 m cable length. This system has a large electric winch and a separate cable thrower system to ensure paying out slack cable. However, the cable thrower did not function and after several trials with alternative setup configurations, we abandoned the VMP system and profiled using the MSS system. The MSS profiler used is MSS90L SN097, the same as the on-ice deployments. The motorized winch used by the ship was different from the on-ice deployment, had an 800 m cable length and a guide arm.

The deployment of the MSS from the ship was done from the starboard side (Fig. 2.15a). A motor-driven winch was mounted on the railing with the bottom plate of the winch welded onto the railing. An arm was used to extend the cable from the winch to the outside. Because of the keel of the ship, the upper 15 m of each cast were excluded from dissipation estimates. A summary of MSS measurements from the ship is given in Table 2.14.

Tab. 2.14: Summary of microstructure sampling from the ship. Cast refers to the file number, CASTXXX.MRD. Comments include corresponding ship-CTD profiles at the station.

Cast	Station Name	Date-UTC	Time (UTC)	Comments
34	56_01	2022-07-17	09:15	before ctd 56_02; aborted at 50 m
35	56_01	2022-07-17	09:20	CTD 056_02
36	057_01	2022-07-17	18:53	CTD 057_02
37	057_08	2022-07-18	00:43	
38	061_01	2022-07-18	15:49	CTD 061_02
39	061_08	2022-07-18	22:25	CTD 061_07
40	065_07	2022-07-20	06:55	about 1h after the CTD 065_05.
57	069_01	2022-07-21	20:23	Aborted at 115 m
58	069_01	2022-07-21	20:41	
59	069_06	2022-07-22	01:37	

Cast	Station Name	Date-UTC	Time (UTC)	Comments
141	087_02	2022-07-29	15:03	CTD 087_01
142	087_08	2022-07-29	20:34	
143	088_03	2022-07-30	01:10	CTD 088_01
166	091_03	2022-07-31	03:28	CTD 091_01
167	091_03	2022-07-31	03:34	CTD 091_01
168	091_07	2022-07-31	07:23	CTD 091_01
190	094_03	2022-08-01	08:20	CTD 094_01
191	094_07	2022-08-01	11:51	aborted cast after ~10 m
192	094_07	2022-08-01	12:01	CTD 094_01

Profiling during ice stations

The MSS was operated from the sea ice during all ice stations. During Floe North Visits 1 and 2, and Floe Middle Visit 2, the MSS and uVMP were alternated, using the same hole. In Floe North Visit 3, Floe Middle Visit 3, and the 24-h stations, the uVMP was deployed from a separate hole, allowing for repeat sampling by both instruments.

A typical MSS deployment was by using a Nansen sledge, through a hole opened by joining 4–5 augered holes. The hole was located approximately 100–250 m away from the ship. When it precipitated, a pop-up tent was used during one station. We collected a profile down to 250–350 m, as frequently as possible.

During the station, the MSS profiler was left in the water between casts. During all stations, an RDI WH-300 kHz was suspended through another hole, typically 10–20 m away from the microstructure profiling hole, sampling continuously through the ice station, at 1-s intervals, and with a 2-m vertical bin size. A GPS receiver recorded the floe position continuously.

Fig. 2.15: Setup of the MSS measurements. Top left, from the side of the ship with a motorized winch with 800 m cable. Top right, from the side of the ice flow, from a hole in the ice without (bottom left) and with (bottom right) tent. The small, motorized winch attached to the Nansen sledge has 400 m cable. The power unit for the motor, a data acquisition unit, and cables are protected in an aluminium box.

The uVMP was deployed only in selected stations (Table 2.15, all three visits of Floe North, the second and third visits of Floe Middle, and at the 24-h station). In Floe North Visits 1 and 2, and Floe Middle Visit 2, uVMP was deployed from the same hole as the MSS, hence the two instruments were deployed in alternating order. In Floe North Visit 3, Floe Middle Visit 3, and the 24-h stations, the uVMP was deployed from a separate hole, allowing for repeat sampling by both instruments. Occasionally the two lines of the uVMP system entangled while lowering the instrument, resulting in bad data, see comments in the detailed log, Table 2.16. A detailed log for the MSS measurements is given in Table 2.17.

Tab. 2.15: Summary of microstructure sampling during ice stations

Station name	Duration	MSS file numbers CAST---.MRD	uVMP file numbers/ number of profiles DAT_---.P	WH-300 files	Ice thickness / Freeboard [m]
Floe North, Visit 1	13 July, 0900-1730	4-7	3-11 / 6	20220713/15085002.000	1.85 / 0.16
Floe South, Visit 1	14 July, 1200-1700	8-20	N/A	20220714/15085000.000	1.97 / 0.14
Floe Middle, Visit 1	15 July, 1230-1700	21-33	N/A	20220715/15085000.000	1.30 / 0.10
Floe North, Visit 2	20 July, 1800-2400	41-48	17-19 / 7	20220720/DPL20000.000	1.69 / 0.19

Station name	Duration	MSS file numbers CAST---.MRD	uVMP file numbers/ number of profiles DAT_---.P	WH-300 files	Ice thickness / Freeboard [m]
Floe South, Visit 2	21 July, 1200-1500	49-56	N/A	20220721/21JUL000.000	1.73 / 0.13
Floe Middle, Visit 2	22 July, 1100-1730	60-66	22-24 / 10	20220722/22JUL000.000	0.87 / 0.13
Floe 24-h	27 July, 2200- 28 July, 2100	67-140	27-37 / 56	20220727/27JUL000.000	1.32 / 0.13
Floe North, Visit 3	30 July, 0830 - 1430	144-165	40-45 / 21	20220730/30JUL000.000	1.60 / 0.20
Floe South, Visit 3	31 July, 1300-1500	169-173	N/A	20220731a/31JUL000.000	1.30 / 0.23
Floe Middle, Visit 3	31 July, 2000, 2400	174-189	48-52 / 14	20220731b/32JUL000.000	1.05 / 0.14
Floe Fast Ice	6 Aug, 0830-1200	193-199	N/A	20220806/6AUG_000.000	1.20 / 0.10

Dissipation rate was measured using two airfoil shear probes. The dataset is processed and prepared following the SCOR Working Group 160, ATOMIX (https://wiki.uib.no/atomix) guidelines and recommendations.

Tab. 2.16: VMP250 log

For further information see Table 2.16 at the end of the Chapter.

Tab. 2.17: MSS log

For further information see Table 2.17 at the end of the Chapter.

Glider (areas 1, 2)

We deployed an ocean glider equipped with turbulence sensors to provide hydrographic and turbulence properties south and southeast of the Marginal Ice Zone study site throughout the cruise duration.

The glider “Odin” is a 1,000-m electric Teledyne Webb Slocum glider (G3, SN 775). It was deployed on 6 July 2022 18:00 UTC with a payload including a pumped SBE CT and a Rockland Scientific (RSI) MicroRider (MR, SN324) turbulence package. Ocean microstructure measurements were obtained from the MicroRider. The glider was operated close to the marginal ice zone, west of Spitsbergen, during the cruise. The track of Odin is shown in Figure 2.16.

The glider data were processed using the SOCIB toolbox. Additionally, a hydrodynamic flight model was applied (Merckelbach et al., 2010) to estimate the angle of attack and flow past the sensor, needed for the processing of the MicroRider data. Dissipation rate was measured using two airfoil shear probes. The dataset is processed and prepared following the SCOR Working Group 160, ATOMIX (https://wiki.uib.no/atomix) guidelines and recommendations.

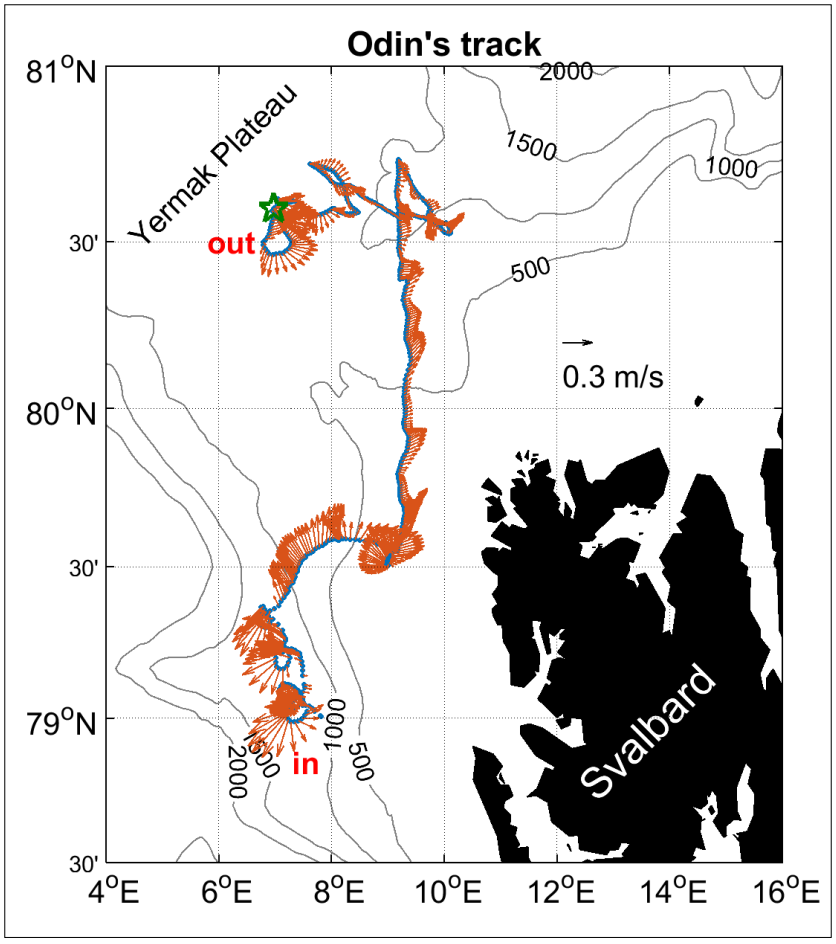

Fig. 2.16: Map with Odin’s track and depth-averaged currents between surfacings; approximate locations of deployment (in), recovery (out), and the impact with sea ice (green pentagram) are indicated. Tides are not removed from the ocean current estimates.

Summary of incidents

Aborts

MS_ABORT_NO_HEAP

2022-07-06T20:41:29

2022-07-06T20:49:06

2022-07-06T21:00:20

2022-07-07T17:53:31

2022-07-09T17:05:03

Several device aborts of this type occurred near the start of the deployment. This has been a known issue for persistor processor G3's running MicroRiders over the last couple of years where insufficient memory is available to the processor. This is yet to be resolved in the latest firmware revisions

The issue was worked around by setting the abort behavior argument reqd_spare_heap to 30,000, subsequent aborts forced us to lower this further to 15,000. It is possible that not sampling the microrider during the inflection may help to ease the load on the persistor. The same abort time was also experienced during 'emergency' missions. Pilots should remember to set the behaviour for every glider mission that could be run.

MS_ABORT_DEVICE_ERROR

2022-07-07T16:10:05

Known issue where if glider is on surface sending data from science bay and iridium call drops science_super driver throws an error resulting in abort

MS_ABORT_BEH_ERROR

2022-07-07T16:31:35

Pilot error, typo in mission file

MS_ABORT_UNDERVOLTS

2022-07-09T15:05:17

Oil pump running at near maximum displacement of 700 c, inflection at 1,000 m and running the microrider led to a voltage drop below 12 V during the gliders inflection that triggered an abort due to low voltage. The microrider was subsquently turned off for several hours to monitor the battery response in case batteries were defective. Microrider sampling was cautiously resumed, and pump displacement was limited to 450 cc, this was gradually increased to a maximum of 650 cc

MS_ABORT_DEVICE_ERROR

2022-07-25T04:56:43

Digifin taken out of service, possible debris in rudder that was cleared by the time pilots tested rudder movement on the surface. Pilots were not able to respond to the abort for 3 hrs

Damage to glider

Glider grounded twice during the segment on 18 July afternoon, due to altimeter being set too deep (200m), this was corrected during next surfacing. The glider did not ground during any subsequent surfacings.

The glider hit the sea ice on 31 July, approximately 11:50 UTC (by the end of DAT_217.P), when all probes of the MicroRider were broken.

Example data

Selected segments of the glider's track are presented in four figures, showing the portion of the track on map and the depth-time distribution of temperature and practical salinity. The first segment (Fig. 2.17) is early in the deployment when the glider was caught in strong southerly currents. The second segment (Fig. 2.18) is a transect across the West Spitsbergen Current. The third segment (Fig. 2.19) is during transit to northern study site, and the last segment (Fig. 2.20) is the work in the MIZ.

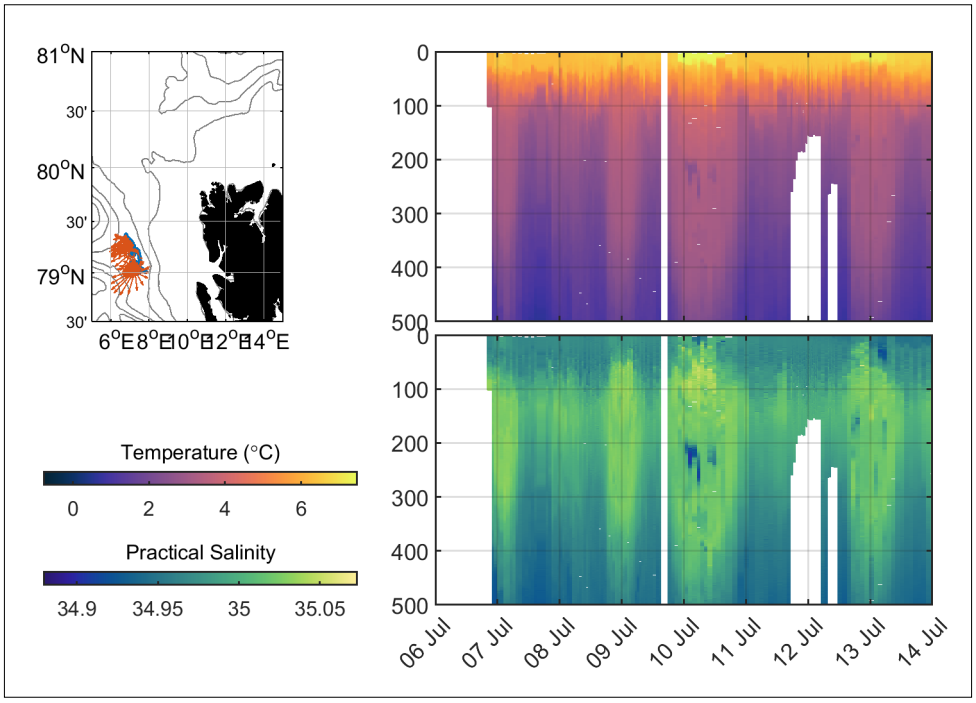

Fig. 2.17: Example glider data showing the segment of the track on the map with depth-average currents, and the time-depth structure of temperature and practical salinity

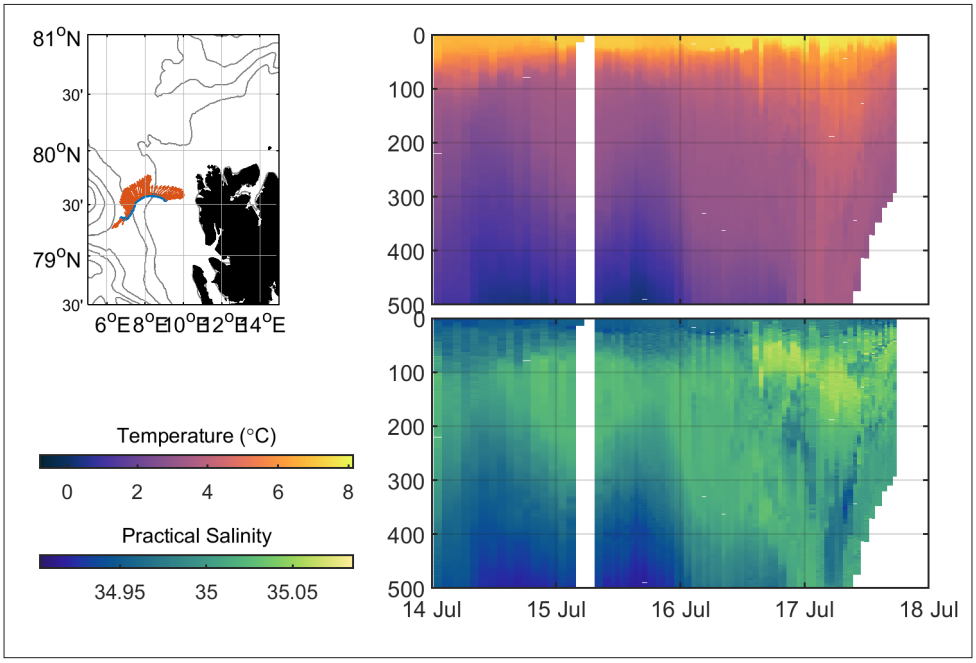

Fig. 2.18: As in Fig. 2.17 but across the WestSpitsbergen Current

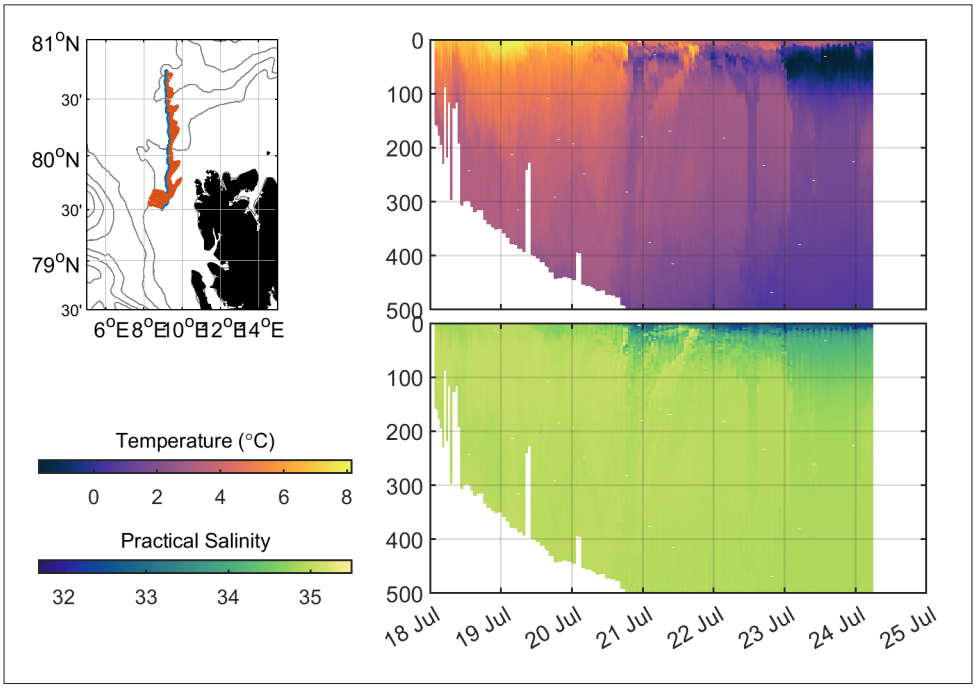

Fig. 2.19: As in Fig. 2.17 but during transit to northern study site

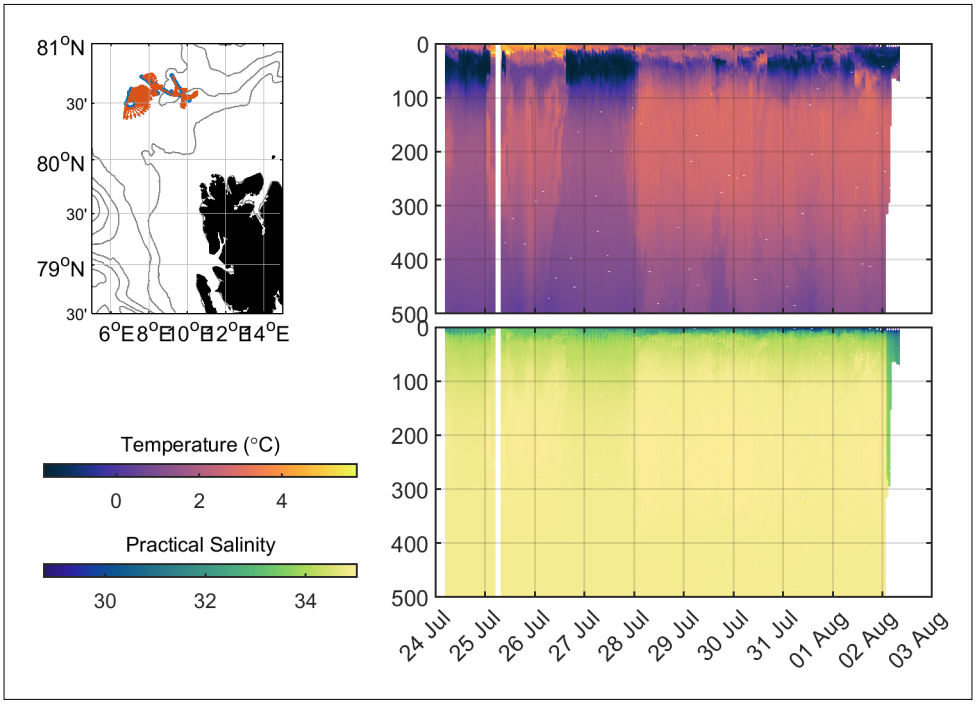

Fig. 2.20: As in Fig. 2.17 but in the MIZ

The glider with the MicroRider performed well and delivered good-quality dissipation rate measurements from the shear probes. Spectral calculations and dissipation rate estimates were made using half-overlapping 24-s records using 6-s fft length (corresponding to about 2 m length with the typical flow past sensor speeds). Figure 2.21 (upper panel) shows the combined best estimate of ε from the two shear probes throughout the mission until the end of the climb when all sensors broke upon impact with sea ice. The time-depth presentation of the temperature is from the glider's pumped SBE-CT sensor.

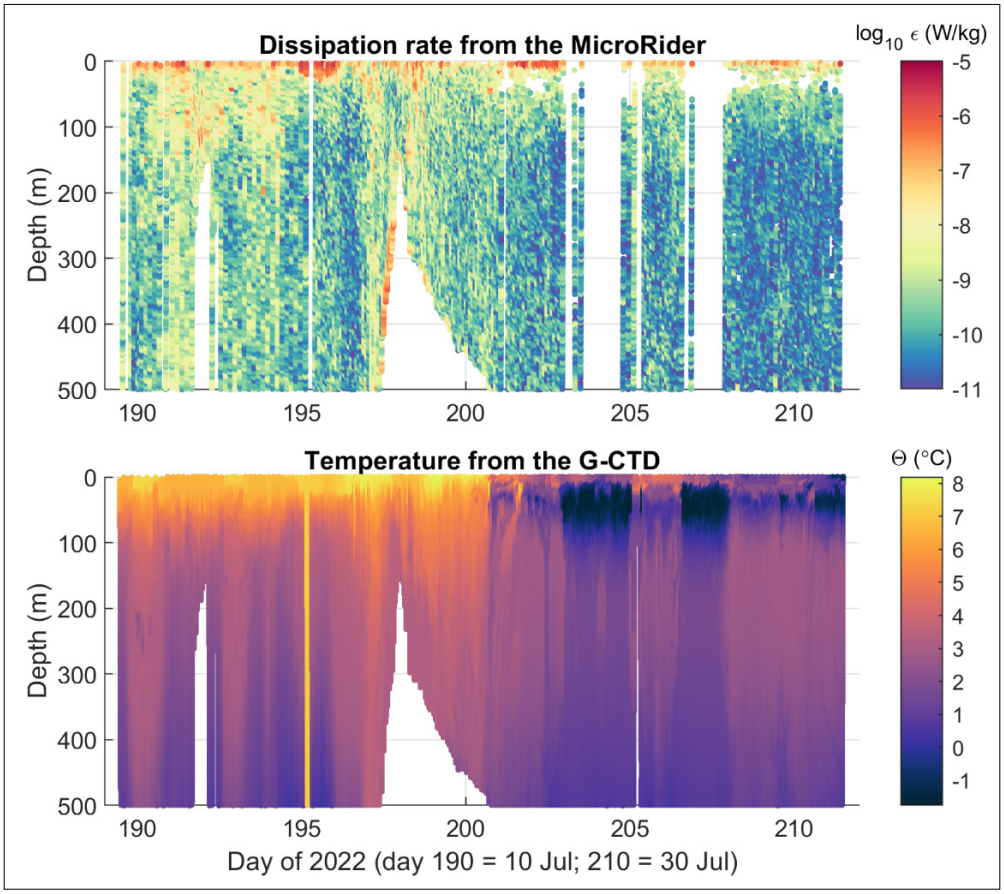

Fig. 2.21: Depth-time evolution of dissipation rate of turbulent kinetic energy (upper panel) and Conservative Temperature (lower panel). Time is a day of 2022.

GPS Drifters (areas 2, 3, 4)

44 Southtek Iridium GPS drifters of type Offshore NOMAD-T V3 (33) and Offshore NOMAD V2 (11) were deployed on PS131, in a total of 48 individual deployments (including 4 redeployments of recovered instruments), to either provide a means to recover expensive instruments (6), to mark important sites (2), to track individual ice floes (1), or to elucidate the surface ocean currents as a complement to measurements obtained by the towed Triaxus system (31) or the ship-based CTD (8). The drifter data were displayed in the ship's Mapviewer software in near-real time, to facilitate navigation and to support the scientific programme in decision-making.

In addition, five MetOcean iSVPs measuring GPS position, surface temperature, and especially barometric pressure were deployed on ice floes (4) or in open water (1) along the cruise track, at maximal distance from each other (which was mostly dependent on logistical constraints). The aim of these deployments, which were done for MeteoFrance and the EUMETNET/E-SurfMAR programme, was to obtain measurements of barometric pressure in a vastly undersampled region of the Arctic. The buoy data is fed into the WMO's Global Telecommunications System (GTS) in near-real time, being immediately available to numerical weather models and thereby contributing to enhanced global weather forecasts.

Tab. 2.18: Overview of Southtek Nomad deployments

ID	AWI ID	IMEI	Type	Date	Latitude	Longitude	Location	Context
603	2022P10010	300534062176030	Nomad T V3	20220713T15:47	81° 35.602‘N	006° 42.428‘E	Floe_ North	Utokyo ADCP
608	2022P10015	300534062174040	Nomad T V3	20220713T13:47	81° 35.411‘N	006° 44.454‘E	Floe_ North	1200kHz ADCP SN14458
610	2022P10017	300534062171040	Nomad T V3	20220713T13:47	81° 35.602‘N	006° 42.428‘E	Floe_ North	UiB ADCP
618	2022P10025	300534062177000	Nomad T V3	20220713T15:47	81° 35.602‘N	006° 42.428‘E	Floe_ North	Radiation Station
631	2022P10038	300534062076090	Nomad T V3	20220720T18:58	81° 29.995‘N	004° 46.584‘E	Floe_ North_ visit2	Incubation site
604	2022P10011	300534062177020	Nomad T V3	20220714T16:36			Floe_ South	Meltpond Site
612	2022P10019	300534062175050	Nomad T V3	20220714T15:50	81° 10.973‘N	007° 40.942‘E	Floe_ South	1200kHz ADCP SN9208
615	2022P10022	300534062171030	Nomad T V3	20220715T14:10	81° 21.018‘N	006° 44.788‘E	Floe_ Middle	1200kHz ADCP SN14456
597	2022P10006	300534062078080	Nomad T V3	20220716T19:43	80° 21.332‘N	010° 34.965‘E	Triaxus Transect1	transect start
595	2022P10004	300534062071120	Nomad T V3	20220716T20:41	80° 26.160‘N	010° 20.439‘E	Triaxus Transect1	5nm along transect
611	2022P10018	300534062171010	Nomad T V3	20220716T21:44	80° 31.129‘N	010° 05.468‘E	Triaxus Transect1	10nm along transect
613	2022P10020	300534062070970	Nomad T V3	20220716T22:45	80° 36.118‘N	009° 50.408‘E	Triaxus Transect1	15nm along transect
600	2022P10009	300534062072110	Nomad T V3	20220716T23:43	80° 40.592‘N	009° 36.527‘E	Triaxus Transect1	20nm along transect
598	2022P10007	300534062074080	Nomad T V3	20220717T00:42	80° 45.153‘N	009° 21.224‘E	Triaxus Transect1	25nm along transect
614	2022P10021	300534062172030	Nomad T V3	20220717T01:44	80° 50.232‘N	009° 06.752‘E	Triaxus Transect1	30nm along transect
630	2022P10037	300534062071110	Nomad T V3	20220717T03:25	80° 59.124‘N	008° 42.650‘E	Triaxus Transect1	35nm along transect
633	2022P10040	300534062079210	Nomad T V3	20220717T04:36	81° 02.450‘N	008° 38.219‘E	Triaxus Transect1	39nm along transect, end
622	2022P10029	300534062177030	Nomad T V3	20220718T11:17	80° 32.744‘N	009° 55.187‘E	MIZ Transect	7nm along transect
621	2022P10028	300534062074960	Nomad T V3	20220718T13:54	80° 38.455‘N	009° 40.083‘E	MIZ Transect	15nm along transect

ID	AWI ID	IMEI	Type	Date	Latitude	Longitude	Location	Context
619	2022P10026	300534062075960	Nomad T V3	20220718T15:03	80° 46.247‘N	009° 18.048‘E	MIZ Transect	20nm along transect
623	2022P10030	300534062078100	Nomad T V3	20220718T23:33	80° 53.944‘N	008° 52.012‘E	MIZ Transect	25nm along transect
617	2022P10024	300534062177040	Nomad T V3	20220719T15:43	81° 05.338‘N	008° 27.521‘E	MIZ Transect	35nm along transect
632	2022P10039	300534062075110	Nomad T V3	20220719T16:41	81° 10.384‘N	008° 10.925‘E	MIZ Transect	40nm along transect
609	2022P10016	300534062172050	Nomad T V3	20220719T17:44	81° 15.965‘N	007° 52.293‘E	MIZ Transect	45nm along transect

Tab. 2.19: Overview of MetOcean iSVP deployments

ID	IMEI	WMO ID	Datetime	Latitude	Longitude	Location
2022P239	300534062833790		20220724T10:55	82° 51.650‘N	006° 52.690‘W	Pack ice
2022P238	300534062831790		20220726T18:25	81° 53.999‘N	003° 13.829‘W	Pack ice
2022P240	300534062835800		20220807T07:00	78° 10.433‘N	015° 44.456‘W	EGC ice floe
2022P241	300534062836780	6401589	20220713T11:30	81° 35.573‘N	006° 47.682‘E	Floe_North
2022P242	300534062839770	6401591	20220808T16:48	74° 55.073‘N	016° 16.050‘W	EGC open water

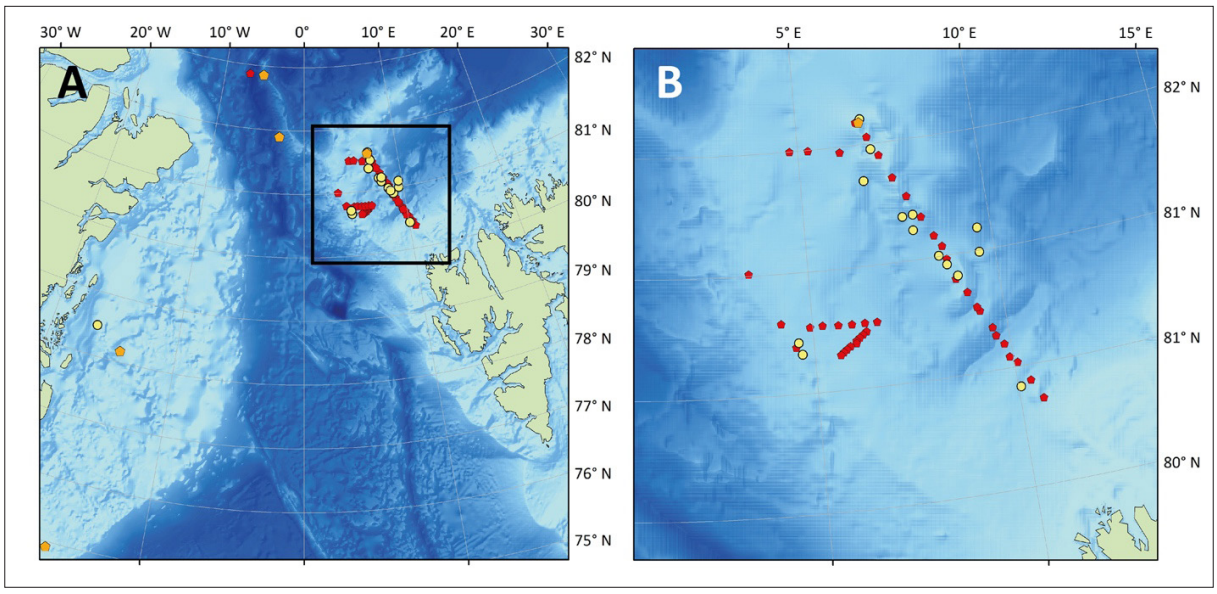

Fig. 2.22: Map of deployment locations of iSVPs (orange), OpenMetBuoys (yellow) and Southtek Nomad drifters (red)

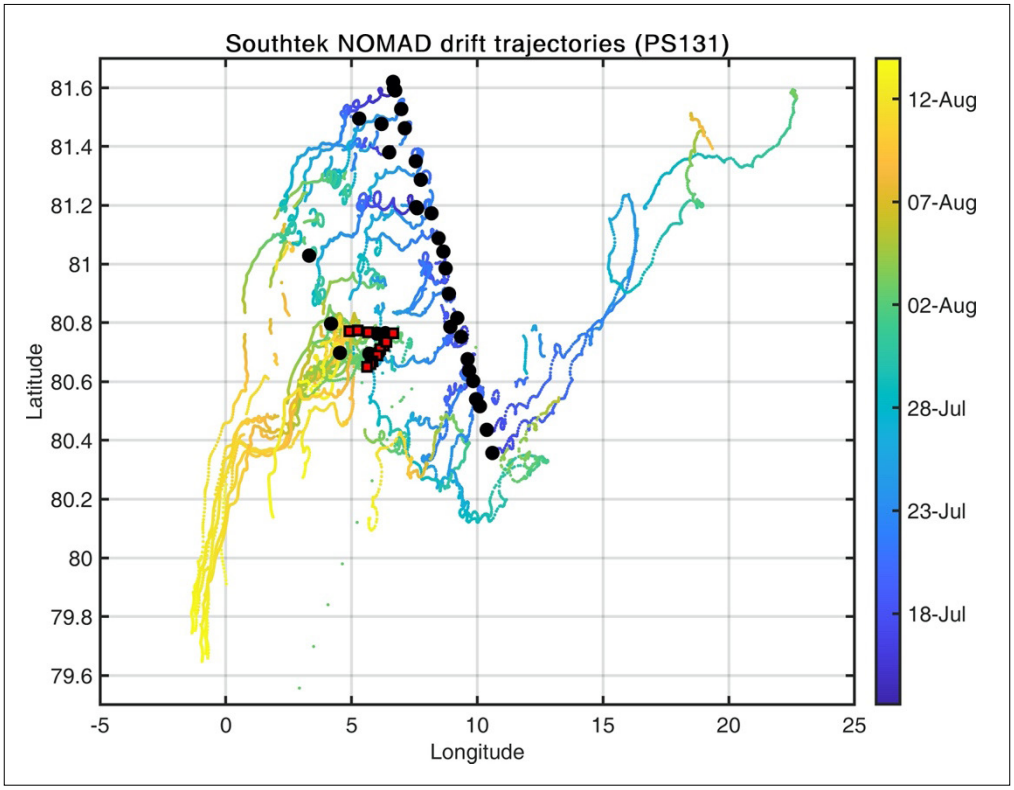

Fig. 2.23: Deployment locations and drift trajectories of Southtek Nomad-T V3 (starting points: black circles) and Nomad V2 (red squares) drifting buoys between deployment and 13 August 2022, close to the end of the expedition

Sea ice drift forecasts (area 2)

Targeted ice drift forecasts were provided by the Sea Ice Drift Forecast Experiment (SIDFEx 2022). SIDFEx is a community effort to collect and analyze Arctic sea ice drift forecasts at lead times from days to a year, based on arbitrary methods, for a number of sea-ice buoys on a regular basis. Prior to the MIZ work, SIDFEx collected and sent forecasts for two fixed positions at 81.5° N 10° E and 81.5° N 15° E, which were used for selecting target areas for the ice floe work. Later on, forecasts for three GPS drifters (one on each floe, with IMEIs 300534062174040, 300534062175050, and 300534062171030), were collected, yet not systematically analyzed. During the cruise, one forecasting group provided forecasts in near real-time; there will be retrospective forecasts submitted after the cruise. Especially the wind and ocean current observations at Floe North enable a thorough case study of forecast errors from different forecasting systems for ice drift in the MIZ.

Autonomous Instruments during Ice stations (area 2)

A total of 66 autonomous instruments were deployed on the three main ice floes for more than 2 weeks (Floe North: 33, Floe Middle: 17, Floe South: 16 instruments). Table 2.20 provides an overview of all instruments, while Figures 2.24 – 2.26 show aerial photographs of the three main buoy sites, where most of the instruments were clustered. Figure 2.27 provides a photograph of the main buoy site on Floe North, where a majority of the instruments were installed.

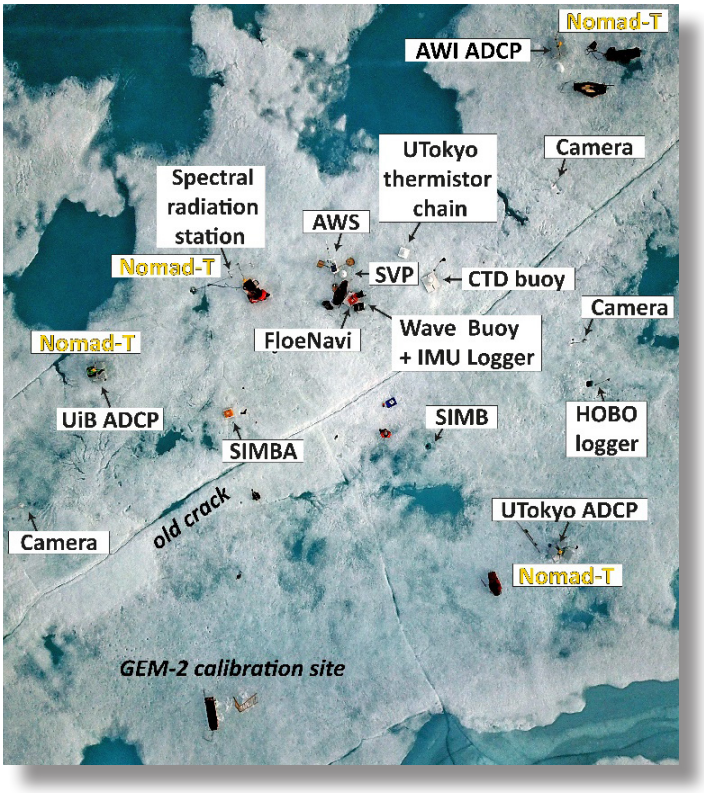

Fig. 2.24: Aerial photo of the buoy site on Ice Floe North

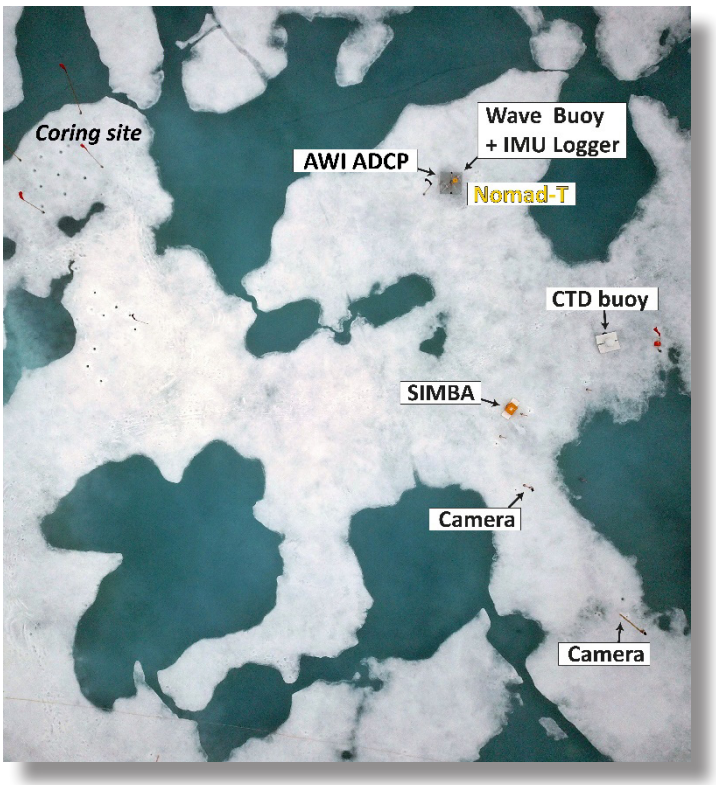

Fig. 2.25: Aerial photo of the buoy site on Ice Floe Middle

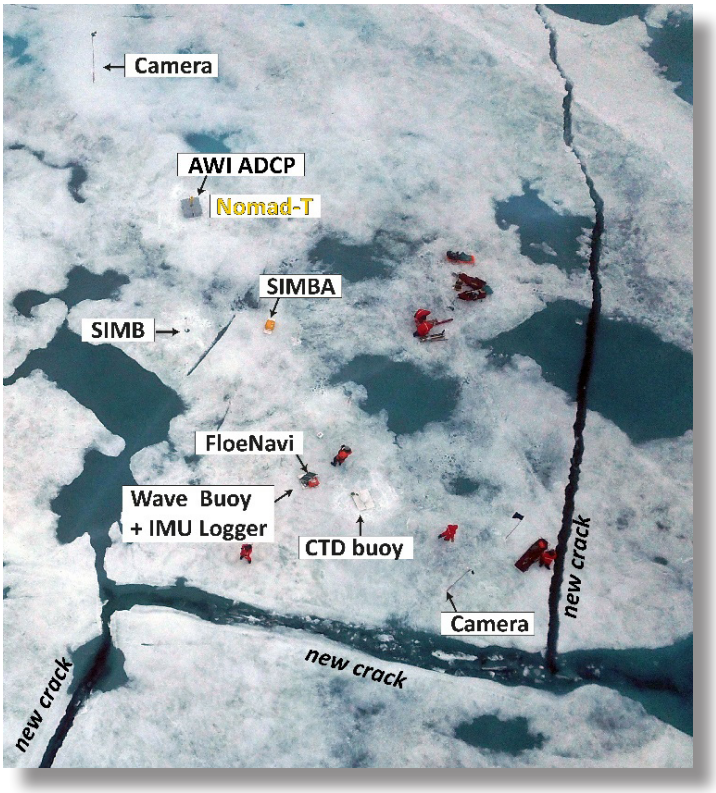

Fig. 2.26: Aerial photo of the buoy site on Ice Floe South

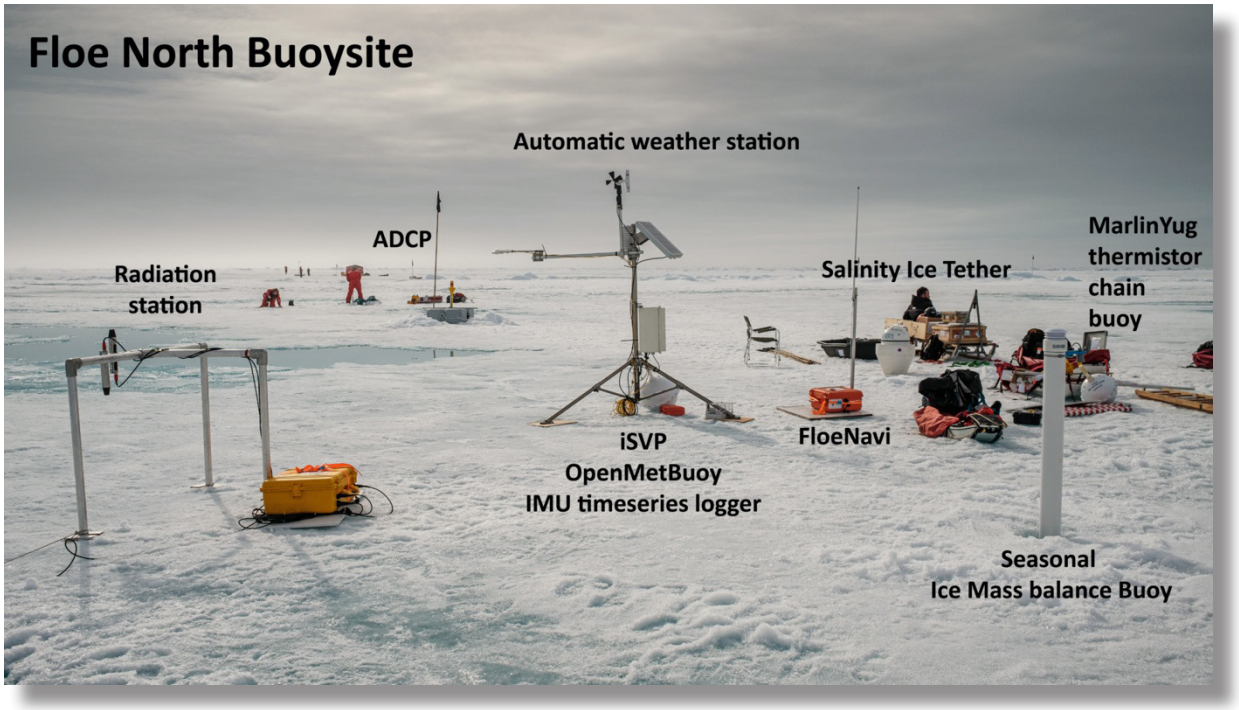

Fig. 2.27: Photo of the different autonomous instruments deployed at the main buoy site on Floe North

Tab. 2.20: Overview of autonomous instruments deployed on the three main ice floes

IceStation	Type	SN	Depth
Floe_North	UTokyo IMU Logger	2022IMU1	on ice
	RDI 1200kHz WH ADCP	14458	2 m
	AWI Radiation Station		on ice
	Automatic Weather Station		on ice
	PacificGyre Salinity Ice Tether (SIT)	300534060151880	
	Seabird SBE37 (on SIT)	22547	5 m
	Seabird SBE37 (on SIT)	22548	10 m
	Seabird SBE37 (on SIT)	22549	20 m
	Seabird SBE37 (on SIT)	22552	50 m
	Seabird SBE37 (on SIT)	22553	75 m
	Seabird SBE37 (on SIT)	22554	100 m
	Wetlabs ECO Triplet (on SIT)	6504	4.3 m
	Hobo CondLogger (rope, top)	21308995	1.8 m
	Hobo CondLogger (rope, middle)	21309009	2.5 m
	Hobo CondLogger (rope, bottom)	21309010	3.2 m
	Hobo PresLogger (rope, bottom)	21248543	3.2 m
	SIMBA thermistor chain buoy	FMI0510	4.8 m
	Reolink Eco Argus Camera	SEAICE3	on ice
	Reolink Eco Argus Camera	SEAICE4	on ice
	Reolink Eco Argus Camera	SEAICE6	on ice
	Reolink Eco Argus Camera	SEAICE7	on ice
	Nortek S1000 ADCP HighRes Burst (UiB)	154	2 m
	OpenMetBuoy	702	on ice
	FloeNavi		on ice
	MarlinYug thermistor chain buoy		2 m
	Cryosphere Inoovations S-IMB		
	MetOcean iSVP	2022P241	on ice
	Nortek S1000 ADCP (UTokyo)		1.8
	Southtek Nomad-T V3 (Utokyo ADCP)	LCF00603	on ice
	Southtek Nomad-T V3 (1200kHz ADCP)	LCF00608	on ice
	Southtek Nomad-T V3 (UiB ADCP)	LCF00610	on ice
	Southtek Nomad-T V3 (Radiation Station)	LCF00618	on ice
	Southtek Nomad-T V3 (Incubation Site)	LCF00631	on ice

IceStation	Type	SN	Depth
Floe_Middle	UTokyo IMU Logger (+Iridium)	2022IMU3	on ice
	RDI 1200kHz WH ADCP	14456	2
	Reolink Eco Argus Camera	SEAICE2	on ice
	Reolink Eco Argus Camera	SEAICE8	on ice
	Reolink Eco Argus Camera	SEAICE9	on ice
	PacificGyre Salinity Ice Tether (SIT)	300234068166760	
	Seabird SBE37 (on SIT)	21093	5
	Seabird SBE37 (on SIT)	21094	10
	Seabird SBE37 (on SIT)	21095	20
	Seabird SBE37 (on SIT)	21099	50
	Seabird SBE37 (on SIT)	21083	100
	Seabird SBE56 (on SIT)	7082	2
	Seabird SBE56 (on SIT)	8479	1
	Seabird SBE56 (on SIT)	8482	0.5
	SIMBA thermistor chain buoy	PRIC0903	4.8 m
	OpenMetBuoy	710	on ice
	Southtek Nomad-T V3 (RDI ADCP)	LCF00615	on ice
Floe_South	UTokyo IMU Logger	2022IMU2	on ice
	RDI 1200kHz WH ADCP	9208	2
	Reolink Eco Argus Camera	SEAICE1	on ice
	Reolink Eco Argus Camera	SEAICE5	on ice
	PacificGyre Salinity Ice Tether (SIT)	300234068514740	
	Seabird SBE37 (on SIT)	21108	10
	Seabird SBE37 (on SIT)	21112	20
	Seabird SBE37 (on SIT)	21115	50
	Seabird SBE37 (on SIT)	21116	75
	Seabird SBE37 (on SIT)	21117	100
	SIMBA thermistor chain buoy	PRIC1007	4.8 m
	Southtek Nomad-T V3 (Pondsite)	LCF00604	on ice
	Southtek Nomad-T V3 (RDI ADCP)	LCF00612	on ice
	OpenMetBuoy	707	on ice
	FloeNavi		on ice

The instruments generally performed as expected, with a few exceptions. One of the two Nortek Signature S1000 ADCPs on Floe North failed due to low batteries. One camera was knocked over by a polar bear. A few CTDs had initial issues with conductivity, which only lasted for a short period of time. Most instruments were placed on ablation shields to prevent them from sinking in. The melting conditions were generally challenging, especially for the ice mass balance buoys, since the deployment holes didn't refreeze. On the other hand, these conditions facilitated the recovery of most in- and under-ice instruments at the end of the study.

The second S1000 (SN 100154) was provided by the University of Bergen, Norway, and was set up with an external 540 Wh Alkaline battery in a storm case. It was deployed pointing downwards, attached to a rod, protruding approximately 0.5 m below the ice under surface. It was secured with buoyancy as in the other installations. The instrument was deployed in water 13 July 2022, 15:25 UTC, and recovered on 30 July 2022, 08:05 UTC. The instrument has 5 beams (4 in Janus configuration and one vertical beam) and is equipped with the high-resolution (HR) feature giving high-quality pulse-to-pulse coherent profiles for turbulence measurements. We used a concurrent plan with average profiles and burst using 5 beams. Average profiles were obtained as 60 s averages every 5 minutes with 20 % measurement load, starting from 0.2 m from the transducer to 18 m, with 1 m cell sizes. The HR profiles were obtained with 5 cm cell sizes between 0.1 to 2.5 m from the transducers, with 2.85 m pulse distance at maximum power level. Bursts were obtained every 30 minutes at 4 Hz as 4096 (about 17 min) samples, in beam coordinate system. In this configuration horizontal precision is 0.99 cm/s, and vertical precision is 0.33 cm/s for the average profiles. The estimated maximum length of using the provided battery was 67 days. During the visit of the floe on 20 June evening, the instrument was removed from the hole for cleaning the hole and placed back in a similar heading orientation. This action is visible in the time series of pressure, pitch, and heading.

Preliminary data from selected autonomous instruments are shown in Figures 2.28 – 2.35 and more results are presented in Chapter 3.

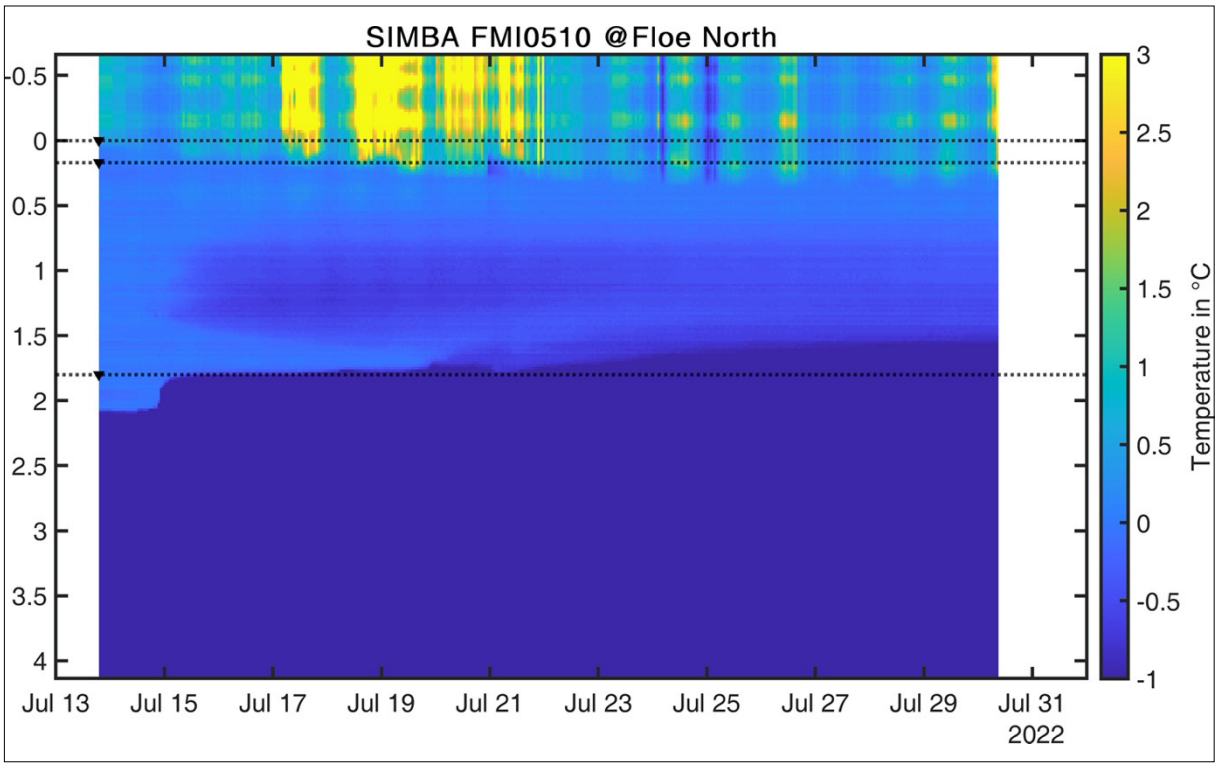

Fig. 2.28: Temperature as a function of vertical distance (0 = initial ice surface) and time from the SIMBA on Floe North

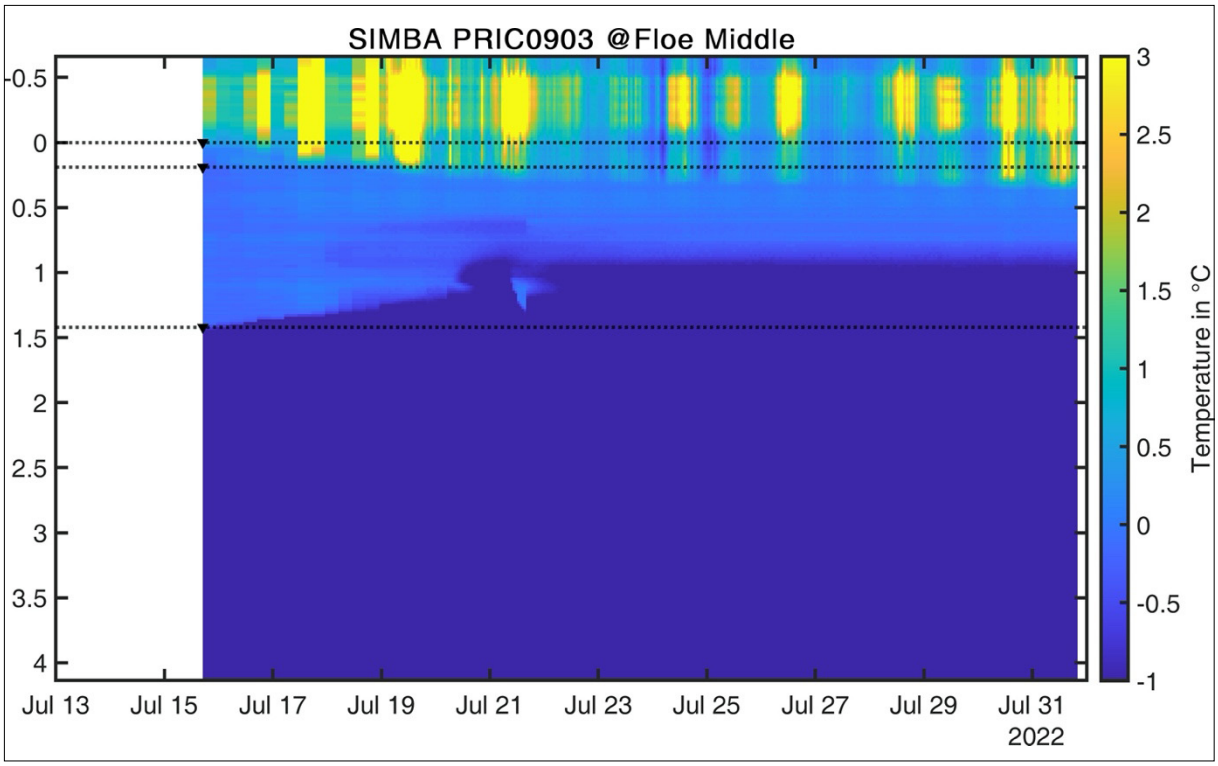

Fig. 2.29: Temperature as a function of vertical distance (0 = initial ice surface) and time from the SIMBA on Floe Middle

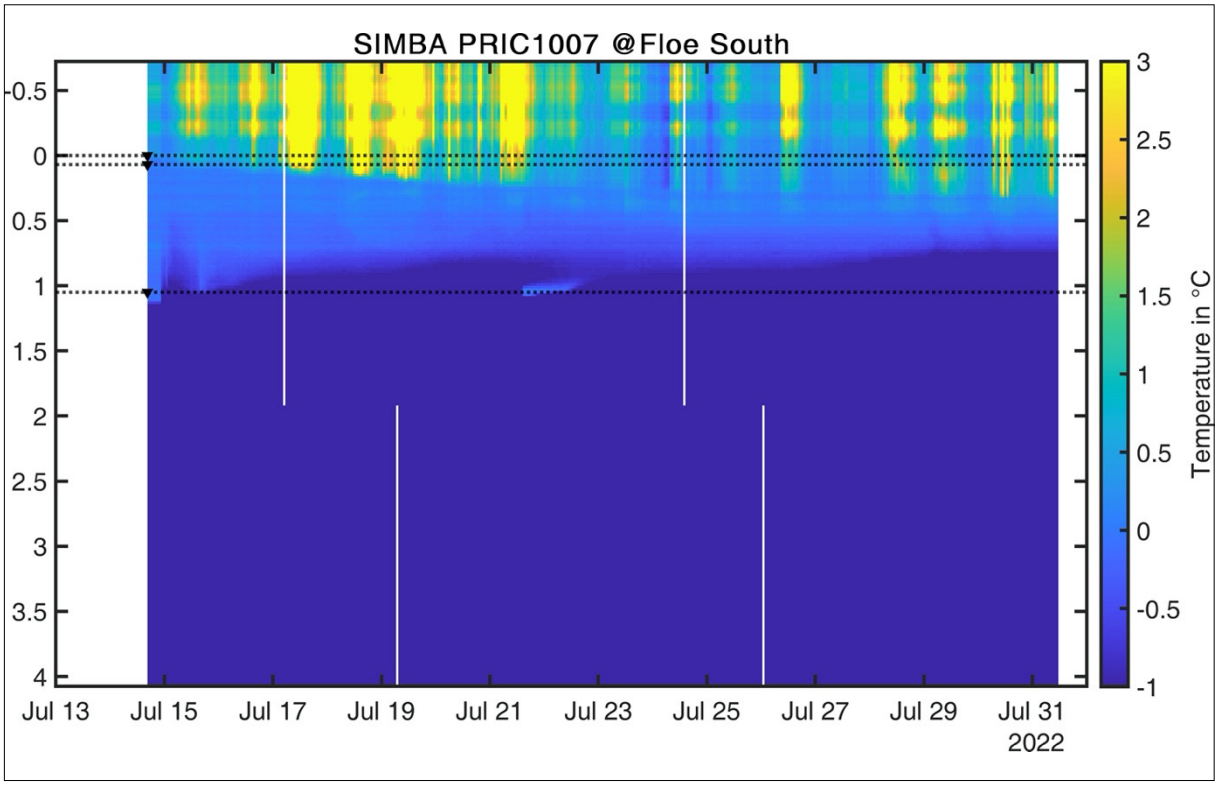

Fig. 2.30: Temperature as a function of vertical distance (0 = initial ice surface) and time from the SIMBA on Floe South

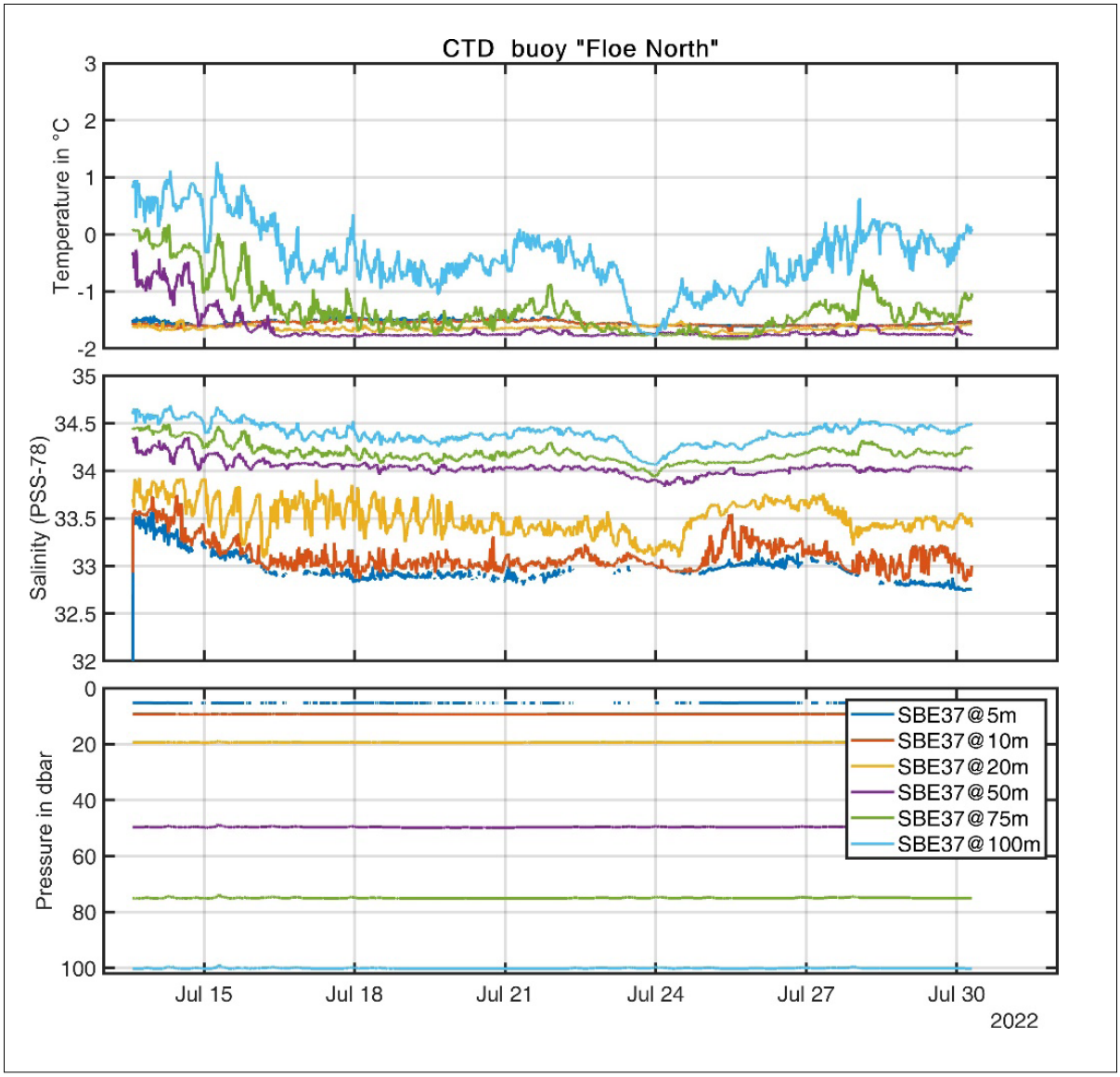

Fig. 2.31: Time series of temperature, salinity, and pressure obtained by CTD buoy 2022016 on Floe North. The colours indicate CTD measurements (Seabird SBE37IMP) at different depths.

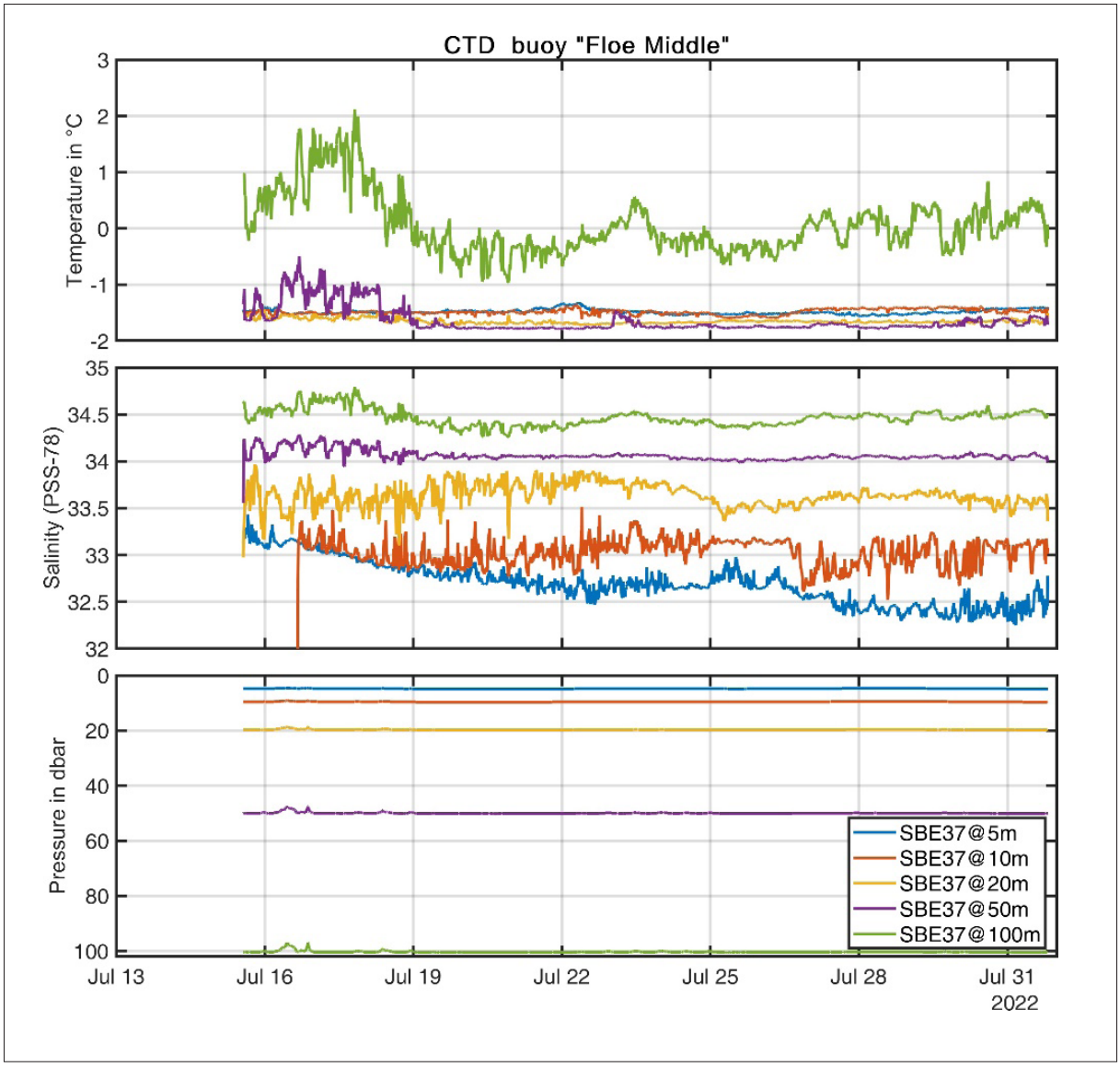

Fig. 2.32: Time series of temperature, salinity, and pressure obtained by CTD buoy 2022012 on Floe Middle. The colours indicate CTD measurements (Seabird SBE37IMP) at different depths.

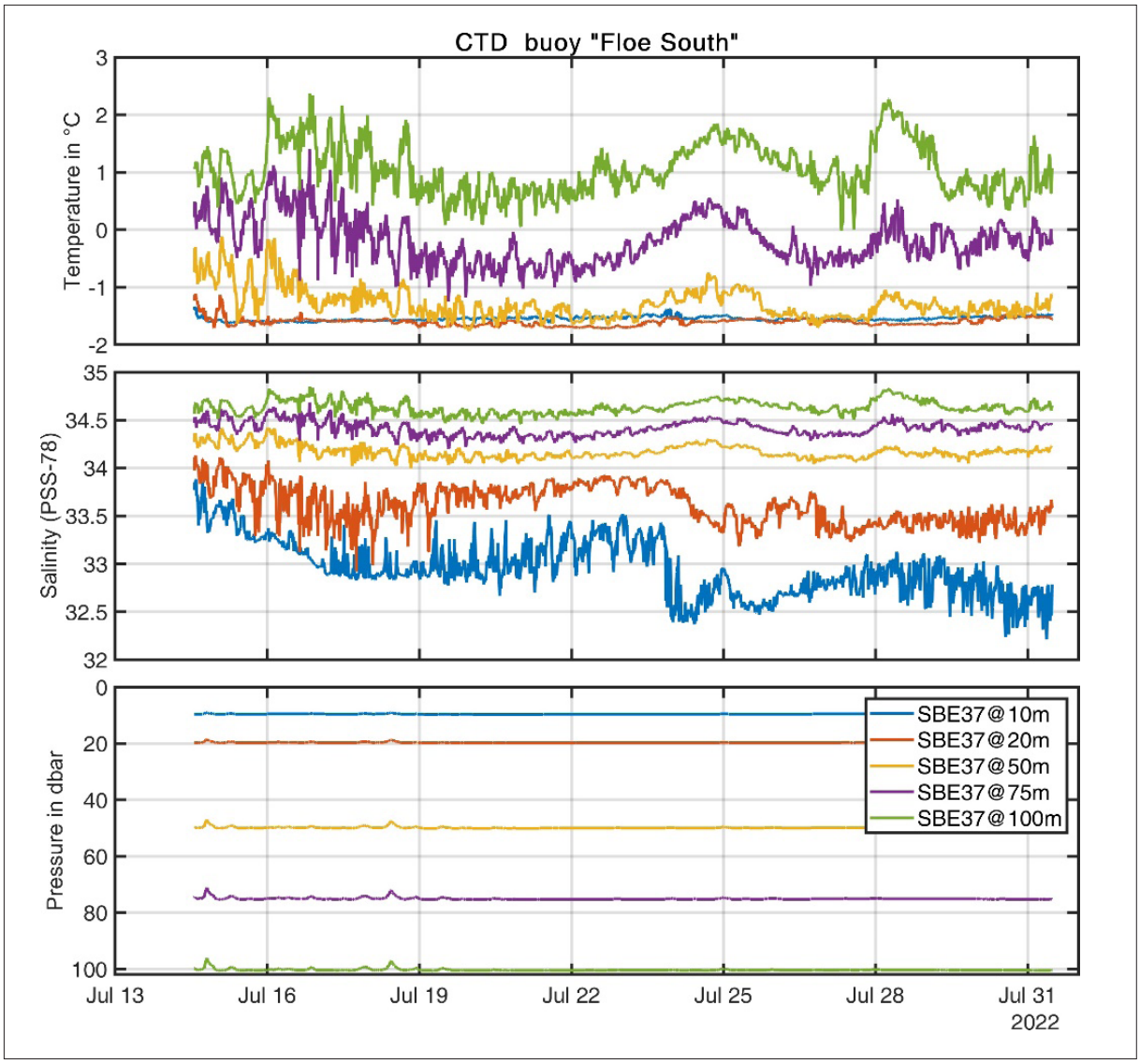

Fig. 2.33: Time series of temperature, salinity, and pressure obtained by CTD buoy 2022O13 on Floe South. The colours indicate CTD measurements (Seabird SBE37IMP) at different depths.

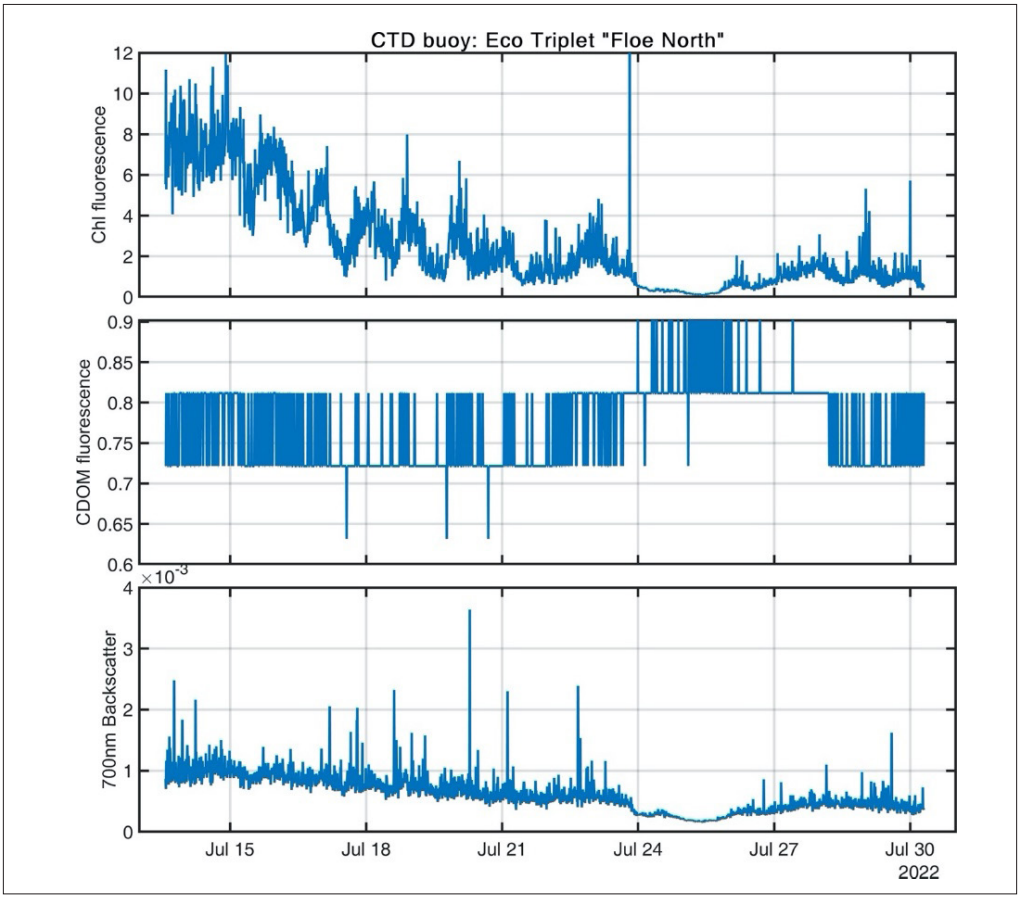

Fig. 2.34: Timeseries from the ECO Triplet at 4.3 m depth on Floe North

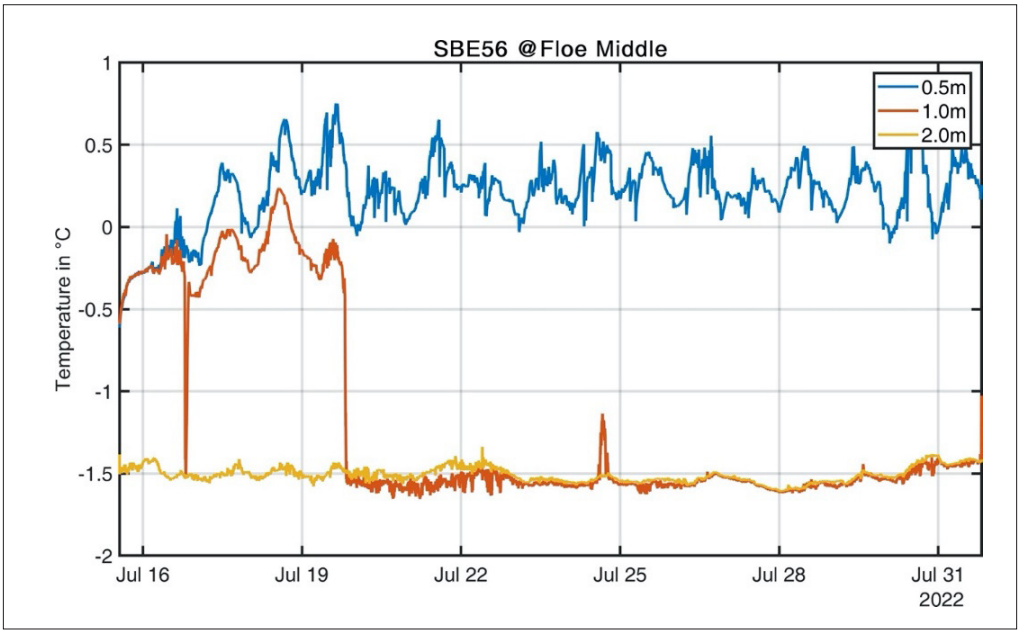

Fig. 2.35: Temperature time series from 3 SBE56 installed on the CTD buoy tether at 0.5 m, 1.0 m, and 2.0 m below the ice surface on Floe North

OpenMetBuoys (“Wavebuoys”)

The dynamic interaction between sea ice and waves especially in the marginal ice zone of the Arctic pack ice region is generally only poorly understood, leading to a significant discrepancy between numerical models and observations, which is even higher in a warming world. Sea ice conditions on small spatial scales impacted by waves can have a significant impact on weather prediction skills even hundreds of kilometers away from the sea-ice edge (Batrak and Müller, 2018), while at the same time sea ice conditions in the Arctic have an impact on medium range weather forecasts over Northern Europe. Even more importantly, waves in ice, sea ice, and open water areas in the Arctic and Antarctic are coupled through a close-loop feedback system: the less sea ice, the more fetch and the higher the waves in the Arctic basin become, which leads to even more sea ice breakup and melting (Thomson and Rogers, 2014). As a consequence, large datasets of high temporal and spatial resolution direct observations of waves in ice are key elements to improving both small-scale wave-ice interaction parametrization, large-scale coupled wave-ice models, and our understanding of the weather and climate dynamics in the polar regions.

In total, 14 OpenMet(wave)Buoys (OMBs) were deployed in the marginal ice zone (MIZ) northwest of Svalbard, and one buoy, OMB-744, was deployed in the fast ice off Greenland (Tab. 2.21). These buoys report GPS position and 20-minute inertial motion averages at hourly intervals via the iridium satellite network (sbd protocol). Two of the 14 buoys ceased transmission within days of the deployment (OMB-722 and 726). OMB-722 was deployed in open water and likely failed because the enclosure may not be suitable for such conditions. The reason for OMB-726 stopping transmission is unknown. OMB-702 experienced intermittent Iridium transmission issues and stopped transmitting data for several days between 8 and 11 Aug, but came back to life on 12 Aug. In addition, three Inertial Motion Unit (IMU) timeseries loggers were deployed on the main MIZ ice floes, which continuously recorded inertial motion and GPS data as a complement to the periodic measurements of the OpenMetBuoys (Tab. 2.22). Two of these loggers only recorded data internally and had to be recovered to obtain the data. All three loggers were successfully retrieved at the end of the MIZ experiment, along with the other instruments, and data were recorded as planned. The only iridium-enabled timeseries logger was later redeployed closer to the ice edge, and also remained deployed beyond the duration of the expedition.

Fig. 2.36: OpenMetBuoy closeup (left) and visitor (right)

Tab 2.21: Overview of OpenMetBuoy (OMB) deployments during PS131

ID	Short-name	IMEI	Date	Latitude	Longitude	Location	Conditions
699	2022X1	300434066013390	20220712T13:45	81° 28.671‘N	007° 02.652‘E		200 x 200 m, 2.6 m ice thickness
702	2022X2	300434066014410	20220713T08:45	81° 36.339‘N	006° 50.540‘E	Floe_N	see Chapter 3
707	2022X3	300434066017380	20220714T15:55	81° 10.973‘N	007° 40.942‘E	Floe_S	see Chapter 3
709	2022X4	300434066015400	20220714T23:54	81° 07.373‘N	007° 55.743‘E		field of small floes, ~1.5m ice thickness
710	2022X5	300434066016350	20220715T14:01	81° 21.011‘N	006° 44.884‘E	Floe_M	see Chapter 3
716	2022X6	300434066018140	20220716T04:45	81° 00.210‘N	008° 30.786‘E	SIMB3	see Chapter 3
717	2022X7	300434066012150	20220716T06:30	80° 54.631‘N	008° 55.896‘E		60 x 30m floe
719	2022X8	300434066013170	20220716T07:45	80° 59.610‘N	009‘ 35.627‘E		40 x 30m floe, >2m ice thickness
720	2022X9	300434066018150	20220716T08:00	81° 05.603‘N	009‘ 38.200‘E		25 x 25m floe, 1m ice thickness
722	2022X10	300434066013160	20220718T10:00	80° 25.011‘N	010‘ 04.107‘E		open water
724	2022X11	300434066017150	20220719T11:45	80° 57.761‘N	008° 41.555‘E		15m, 1.6m ice thickness
726	2022X12	300434066016160	20220722T02:21	81° 11.241‘N	007° 58.342‘E		50 x 40m, 2m ice thickness
729	2022X13	300434066012160	20220731T00:03	80° 39.773‘N	004° 40.976‘E		30x20m, swell 1.5m
732	2022X14	300434066015170	20220731T08:10	80° 42.667‘N	004° 36.544‘E		50x30m, 2m ice thickness
744	2022X15	300434066312520	20220806T18:00	78° 28.497‘N	017° 30.925W	Green-land fast ice	on ridge between 1m FYI and 2m SYI

Tab 2.22: Overview of other wave logger deployments during PS131 (*=redeployment)

Shortname	Date	Latitude	Longitude	Location	Conditions
2022IMU1	20220713T08:45	81° 36.339’N	006° 50.540’E	Floe_North	see Chapter x
2022IMU2	20220714T15:55	81° 10.973’N	007° 40.942’E	Floe_South	see Chapter x
2022IMU3	20220715T14:01	81° 21.011’N	006° 44.884’E	Floe_Middle	see Chapter x
2022IMU3*	20220801T12:45	80° 45.787’N	004° 19.151’E	~15nm from ice edge	50x50m floe, 2m ice thickness

The wave buoys were deployed on ice floes of various dimensions ranging from 15 m to as large as ~2 km. As the ice breaks up/melts, the floe dimensions are also changing. This is interesting and challenging at the same time; ice floes the buoys were deployed on effectively serve as a floating platform for the wave buoys and their dimensions are changing with time.

The scale of ice floes (including horizontal dimension and ice thickness) and incoming wave wavelengths are an important considerations to the wave-ice interaction, so the data obtained during PS131 are interesting to study in detail (i.e. in combination with satellite imagery for example). Figure 2.37 shows an overview of the wave buoy trajectories. Their positions on the 16 and 30 July, and 9 August and their corresponding sea ice concentration (AMSR2 data available from JAXA) and the ECMWF forecast wind fields are also shown. The retreating sea ice edge from the time of deployment and 9 August is apparent. All buoys are located right near the ice edge by 9 Aug while some buoys appear to be in waters where sea ice concentration is 0 according to the AMSR2 data.

To give an overview of the measured wave data, significant wave height and peak wave period time series from all buoys between 12 July and 12 August are shown in Figures 2.38 and 2.39. Figure 2.38 shows primarily the July data when the buoys measured small wave signals unless there was a solid wave event. Figure 2.39 shows the buoy data when the buoys drifted closer to the ice edge as it receded, and many of the buoys measured wave signals. As will be discussed in the last paragraph, the wave height from 10 August may be affected by spectral noise and may be overestimated. We can apply an ideal filter to remove these noise signals to obtain more representative wave heights from these data with noise. The first event that was captured by the buoys occurred on 14 and 15 July as shown in Figure 2.40. The waves that propagated to these buoys located farther in the MIZ were likely generated by the low-pressure system over the Greenland and Norwegian seas (see the mean sea level pressure and wind field on 13 July in Fig. 2.41). The waves that arrived at the ice edge, and subsequently to the wave buoys, were primarily southerly (i.e., traveling from south to north), and the significant wave height at the ice edge was roughly 1.8 m according to the ECMWF wave forecast (see Fig. 2.42). See Fig. 2.43 for further examples.

The second event was captured during the short-lived life of OMB-722 in the open water on around 19 July. At the same time, the buoys close to the ice edge measured waves, however, despite the open water wave reaching over 1.5 m significant wave height, the waves did not reach the buoys deployed farther in the MIZ (like OMB-702,710, etc) as they were attenuated by the ice field. Contrasting these 2 events show that the incoming wave conditions are an important consideration to how the waves propagate into the ice field.

Due to the combination of the buoys drifting southwest and the retreating ice edge, many of the buoys began to measure waves with a peak period around 10 s from 30 July onwards (see Fig. 2.39). From 9, 10 August onwards, all buoys are located close to the ice edge and some even appear to be in open water. By this time, some buoys are showing signs of elevated noise floor in the wave spectra that seem to accompany IMU-based wave buoys on a small floating platform (compared to the conventional ocean wave buoys). This implies, assuming some buoys are still ice floes, we may have captured the wave records as the ice floes melt from large floes into small pieces. With these data, a more in-depth analysis of the wave spectra is necessary to filter noise. Confirming whether they are still on ice floes via satellite imagery if possible will help our analysis and would be an interesting exercise to understand how different ice floe sizes respond to ocean wave forcing.

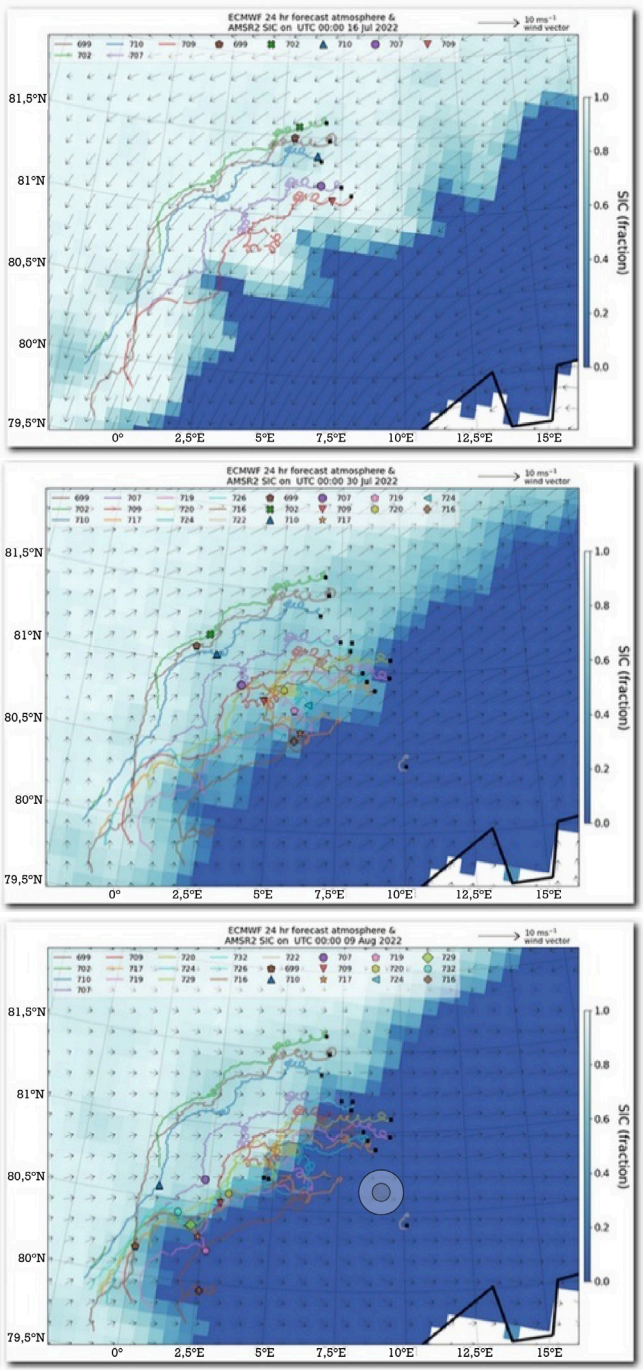

Fig. 2.37:
Wave buoy trajectories between 12 July and 12 August overlaid on AMSR2 sea ice concentration fields on 10 July (top), 30 July (middle), and 9 August (bottom). The black markers depict the deployment locations and markers along each trajectory indicate the respective positions

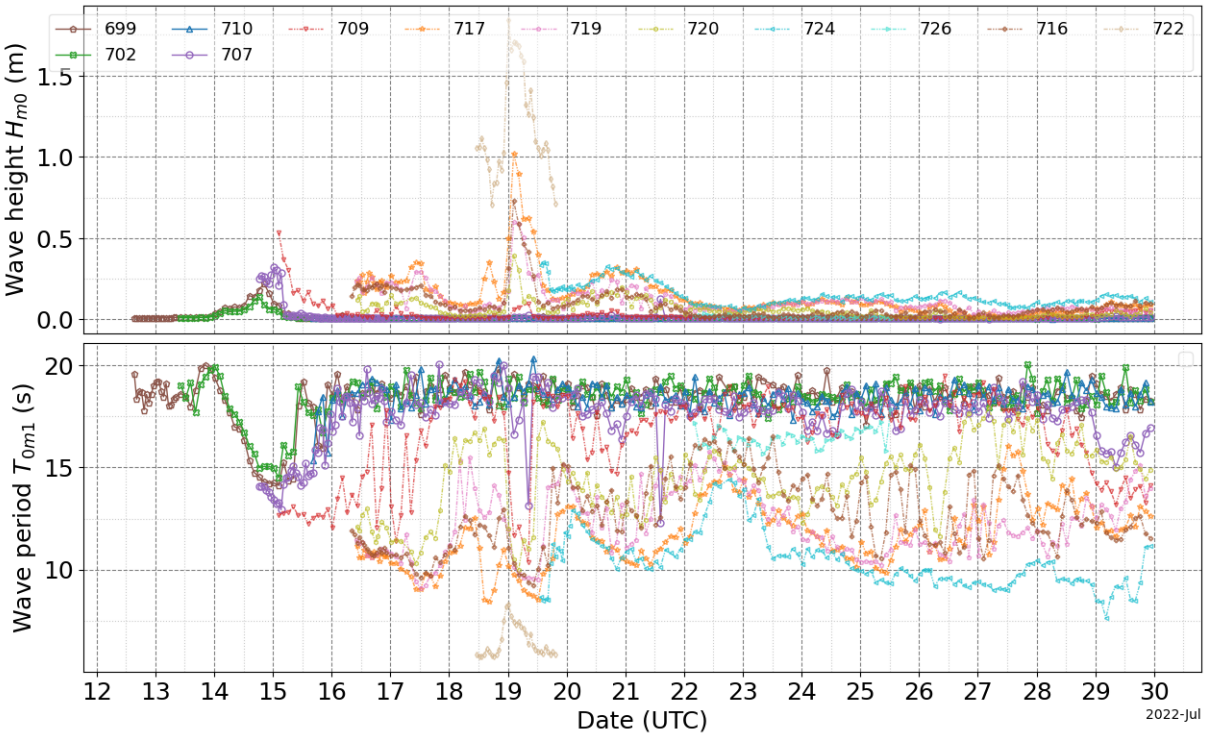

Fig. 2.38: Significant wave height (top) and peak wave period (bottom) from 12 to 29 July

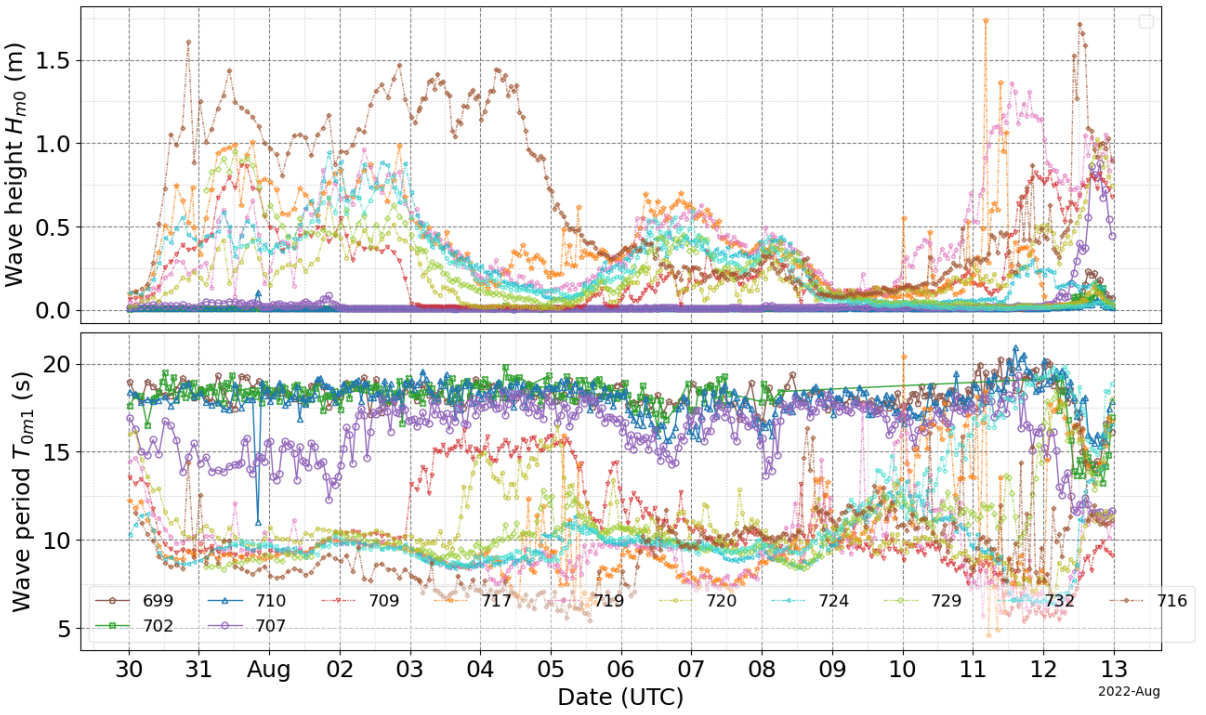

Fig. 2.39: Significant wave height (top) and peak wave period (bottom) from 30 July to 12 August

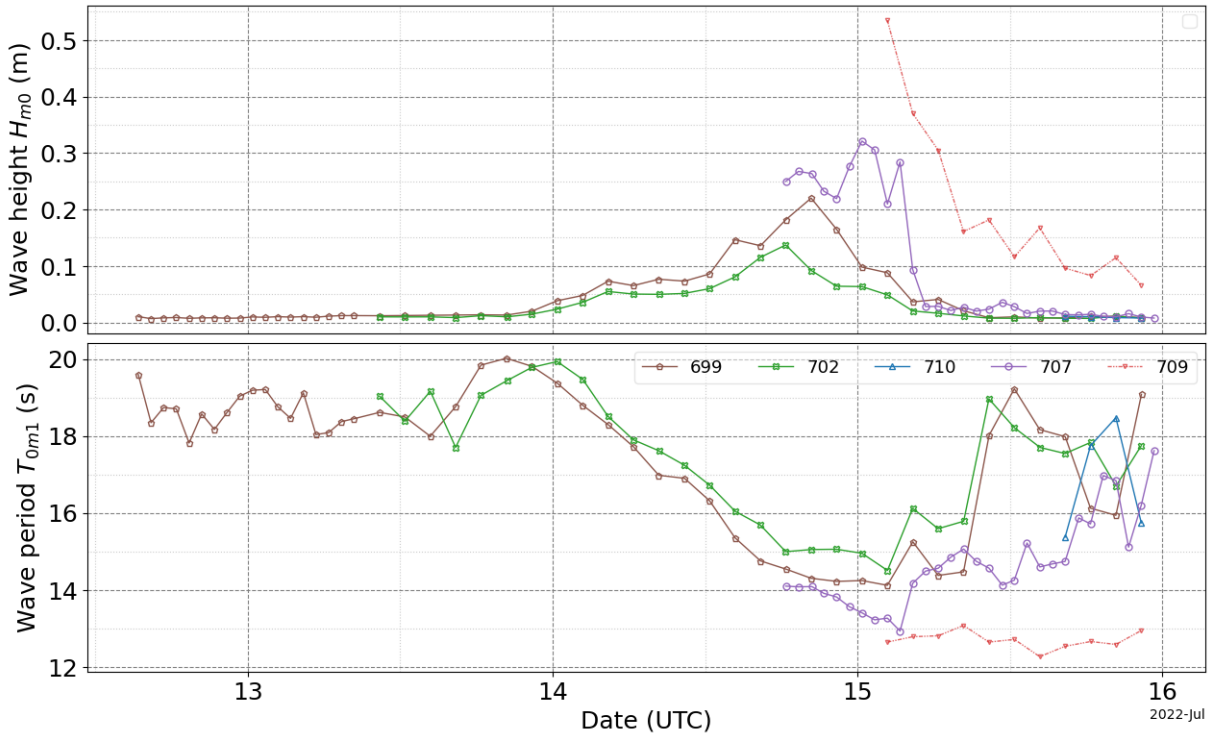

Fig. 2.40: Close-up view of the significant wave height (top) and peak wave period (bottom) during the first wave event that reached the buoys farther in the marginal ice zone between 12 and 15 July

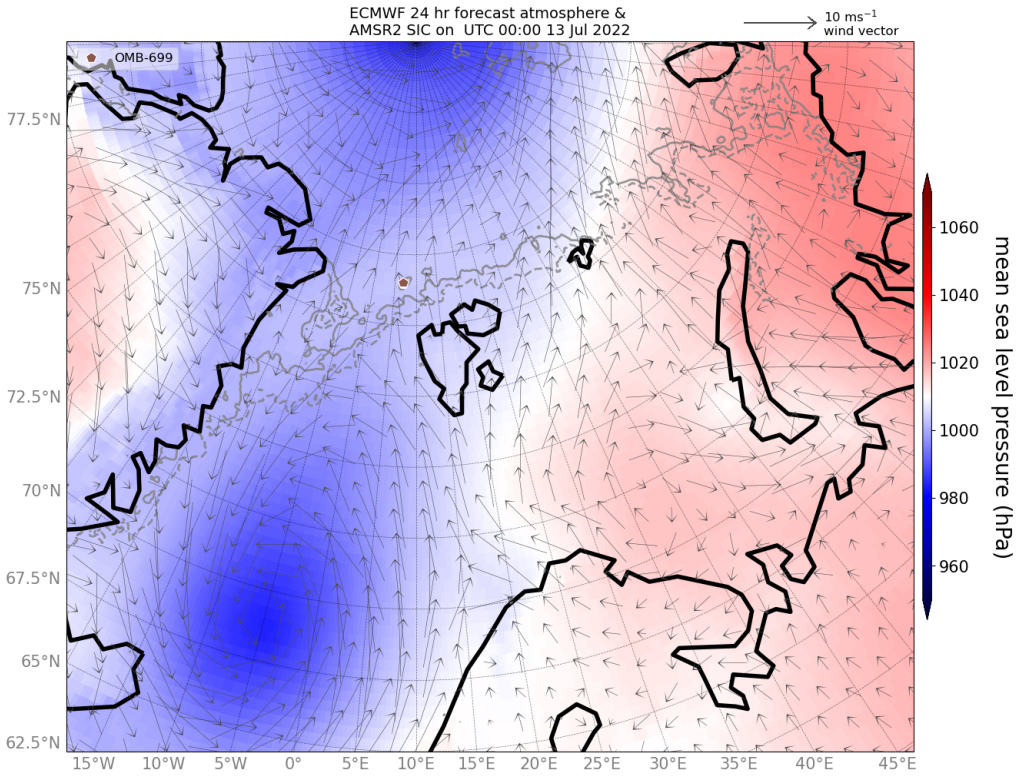

Fig. 2.41: ECMWF mean sea level pressure fields and surface wind field vectors on 13 July when the low pressure system likely generated waves that propagated to the wave buoys; the marker shows the 699 location.

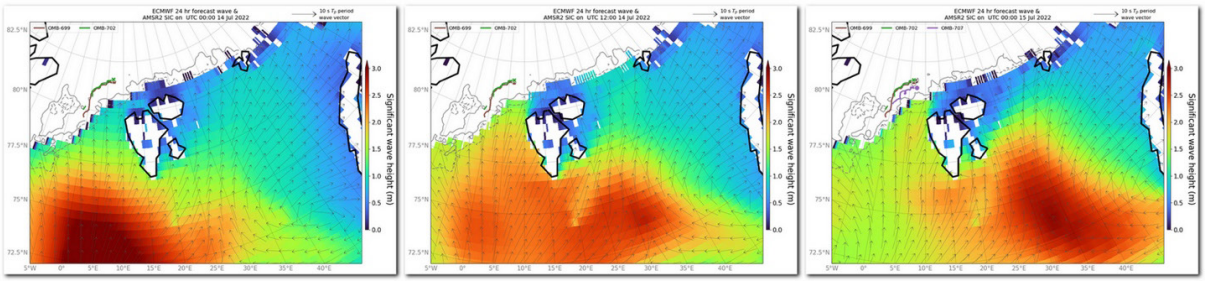

Fig. 2.42: ECMWF wave height field and mean wave direction vectors scaled by the peak period on 00:00 14 July (left), 12:00 14 July (middle), and 00:00 15 July (right) showing the wave propagation from the wave source to the ice edge. The trajectories for 699, 702, and 707 buoys that were already deployed are also shown.

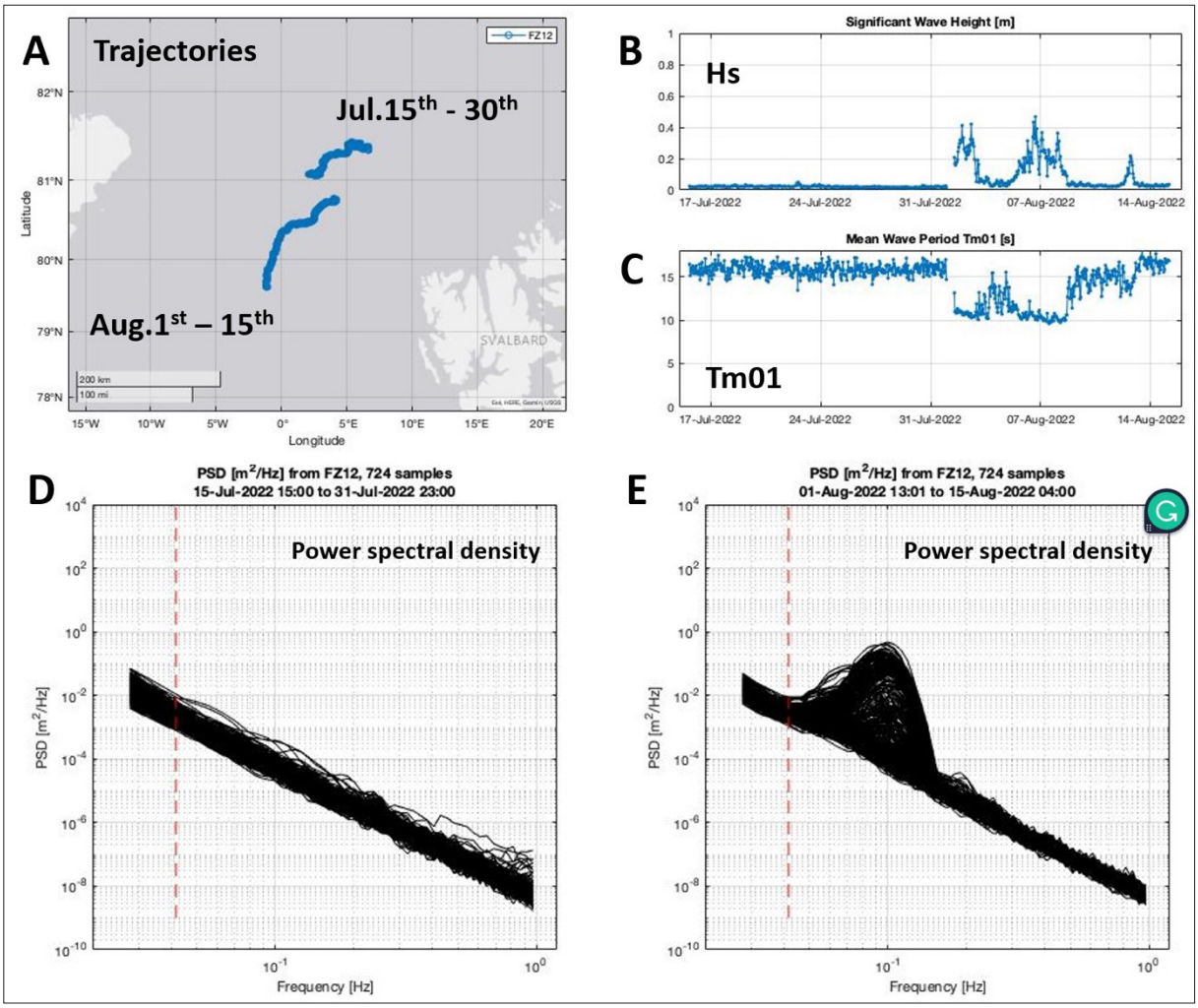

Fig. 2.43: Exemplary results from IMU logger 2022IMU3, which was relocated from Floe Middle to a location closer to the ice edge on 1 August 2022 a) Drift trajectories; b) significant wave height; c) mean wave period; d) power spectral density (PSD) during first deployment and e) PSD during second deployment further south

Ice CTD

In the northern Fram Strait, intense interactions between the warm, nutrient-enriched Atlantic Water (AW) and sea ice occur. The marginal ice zone (MIZ) found in this area features pronounced frontal zones that exert strong controls on the melt and formation of sea ice, biology, biogeochemistry, and air-sea heat exchange. To better understand the physical processes at the ocean-sea-ice interface throughout the MIZ, and how they vary with different ice conditions, high-resolution conductivity-temperature-depth (CTD) profiles of the upper 10 m were taken on ice floes at different locations throughout the region.

At the beginning of the MIZ work programme, three representative ice floes (RIFs) were identified, where several hours-long ice stations were conducted for intensive sampling. The floes represented the idealized ice conditions at different locations in the region: from the pack ice, across the MIZ, and into the open ocean. Each floe was then returned to a total of three times, in approximately weekly intervals (Tab. 2.23), in order to repeat measurements and track the changing floe conditions over time.

Floe North represented pack-ice conditions (Fig. 2.44a) and was also heavily instrumented with other autonomous instruments (Fig. 2.24 and 2.27). Floe South was smaller and further south in the MIZ, where the pack-ice breaks up (Fig. 2.44b). Due to the sudden disintegration of Floe South during the first visit, and its subsequent deterioration (Fig. 2.44c), Floe Middle was chosen to be further north, between Floe North and Floe South, where the ice floes were more stable (Fig. 2.44d). This choice increased the likelihood of repeat measurements and instrument recovery. More details are given in Chapter 3.

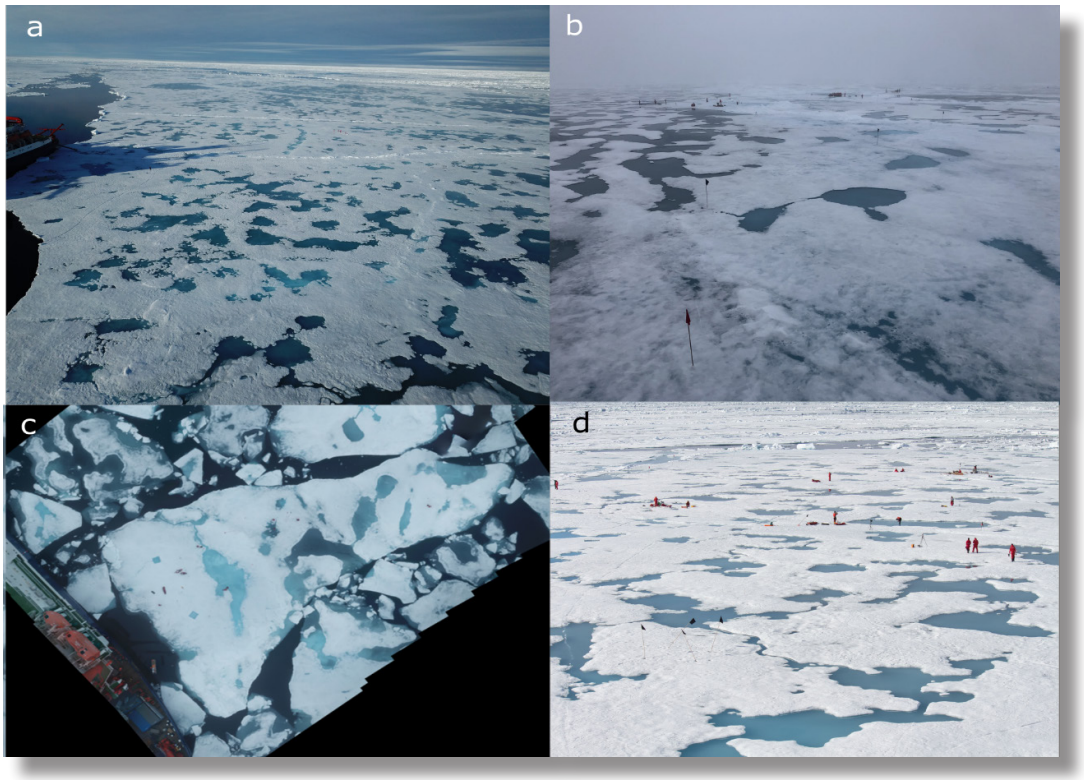

Fig. 2.44: Photographs illustrating the characteristics of each ice floe during different visits; Floe North (Visit 1) (upper left), Floe South (Visit 1) (upper right), Floe South (Visit 3), after its disintegration (lower left), Floe Middle (Visit 3) (lower right); photo credits to Christian Rohleder, Rebecca McPherson, and Christian Haas

Instrumentation

The first visit to Floe North (13.07.2022, Tab. 2.23) was used primarily to test the sampling strategy and two different CTD instruments (Sea and Sun CTD48; RBRconcerto) (Fig. 2.45). The results from repeated profiles from the two sensors were compared, each having measured the upper 10 m in the same drilled hole (not shown). Both instruments were deployed in 'real-time' mode, connected by a data cable to a laptop (Toughook), and sent real-time CTD data to the computer during each profile.

After analyzing the results, it was clear that the small-scale structure of the upper water column was better and more accurately represented by the RBRconcerto (Fig. 2.45, right). This CTD was used in all subsequent measurements. Furthermore, the real-time set-up was abandoned in favor of an internally recording mode. There was no clear benefit of using the real-time mode in this setting: the vertical scales of interest (i.e., potential freshwater surface layer) were not clearly observed from the on-screen data that the real-time mode provided. Using the internal recorder also reduced the time required to set up the instrument before and after each profile, requiring only a 'twist' action to turn the profiler on and off, and minimized the risk of instrument malfunction.

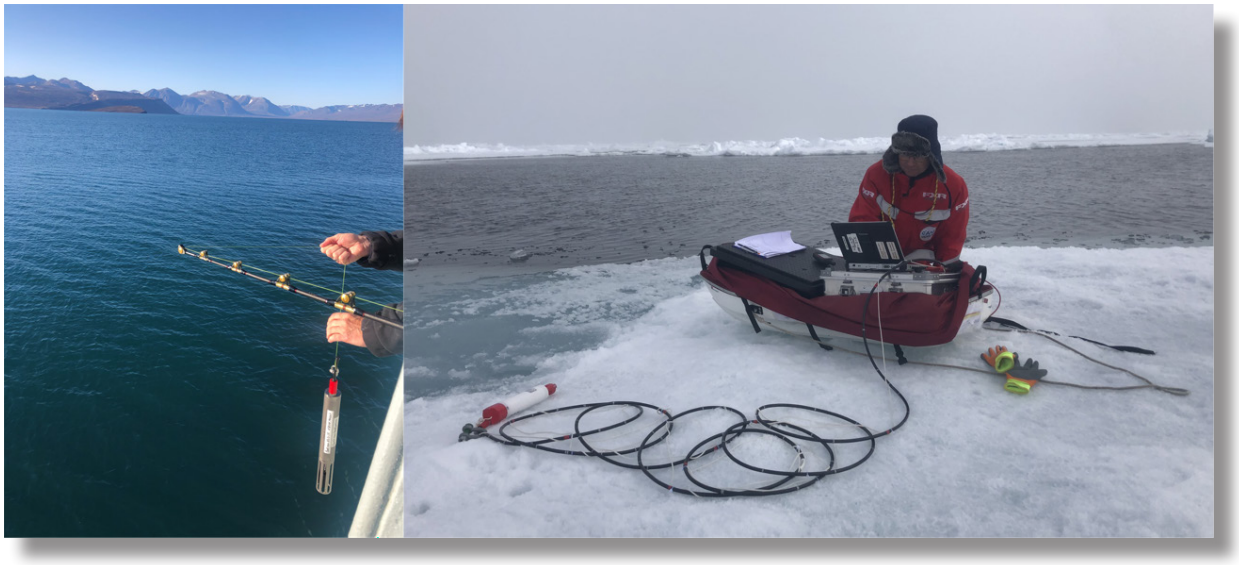

Fig. 2.45: (left) the Sea & Sun CTD48 deployed from the ship (HDMS Triton, 2021) using a fishing rod set-up for deployment, and (right) the RBRconcerto in real-time profiling mode, connected to a laptop (Toughbook) and secondary weight-bearing line; the laptop is operated from a stable position at the top of the pulca. Photo credit: R. McPherson

Sampling Strategy

The sampling strategy using the RBRconcerto was also improved over time. Ultimately, an idealized across-floe transect was followed once the drift of the ice floe had been established using a handheld GPS device (Garmin). One end of the transect was in the lead at the leading edge of the floe, and holes were drilled through the ice at consistent intervals across the floe to the opposite lead, at the trailing edge of the floe. By recording the GPS location at the beginning and end of each site, the direction and speed of the drift of the ice floe could also be determined (Fig. 2.46). This sampling strategy provided an overview of how the under-ice stratification and structure changed spatially across the ice floe, in relation to its drift.

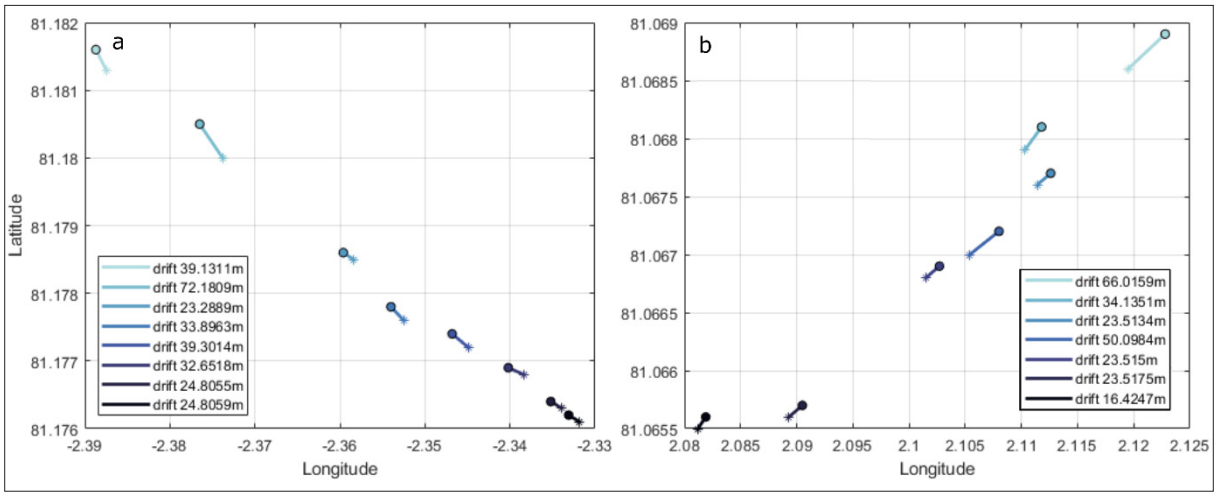

Fig. 2.46: The location of the sites on (left) Floe North during visit 3 (30.07.2022) and (right) Floe Middle during visit 3 (31.07.2022) at the beginning (circle) and end (star) of the profiling conducted there; the drift distance was then calculated over the duration of profiling at each site and included in the legend. The location of the sites show the across-floe sampling strategy

Influence of drilling on under-ice hydrographic structure

The instrument set-up and deployment strategy were also amended after analyzing the results from the second visit to each of the 3 floes. It was not clear from the beginning of the experiment to which extent the drilling holes through the ice (between 1 – 2 m thick), and the proceeding removal of ice from the holes, was changing any under-ice melt water layer that may have existed. Furthermore, the origin and effect of the water that flooded the hole during the drilling process were also unknown. To better examine these impacts, a second experiment was conducted during the second visit to each floe. After drilling a hole at the chosen location, two profiles were taken immediately, following the original sampling strategy. This hole was then returned to after 2+ hours, in which time the water column could stabilize and re-stratify (if relevant), and a second set of profiles was taken.

There was a significant difference in the surface properties of the water over this time. This is demonstrated in the profiles taken on Floe North during visit 2, when this secondary experiment was first conducted (Fig. 2.47). The first profiles taken immediately after the hole was drilled show that the water in the hole (above 1.5 m) was relatively well-mixed, cold, and salty (< –1.5° C and > 30 psu) (Fig. 2.47). These surface waters were warmer than their corresponding freezing point temperatures, with the difference decreasing from over 0.3° C at the bottom of the ice to 0.1° C at the water surface (Fig. 2.47, left).

There is also high variability in these surface properties over the 6 minutes that the first three profiles were taken, with temperature differences of over 0.2° C and salinity varying by over 2 psu. Over two and a half hours later, when the measurements were repeated in the same hole, the surface properties displayed a strong gradient from the bottom of the ice to the surface, increasing from –1.5 to –0.6° C, and freshening from 30 to 11 psu. The water in the hole was at the freezing point (Fig. 2.37, left) and very little variability was seen between the two later profiles.

Greater temperature variability was also observed in the earlier profiles below the ice, down to 10 m (Fig. 2.47, left). On the return visit at 20:00, the temperatures between 2 – 10 m had stabilized at a constant –1.5° C. Less variability was observed in the salinity profiles over time, showing a well-mixed water column below 2 m of 33 psu across the 5 profiles. The water below 2 m was consistently 0.4° C warmer than the freezing point temperature.

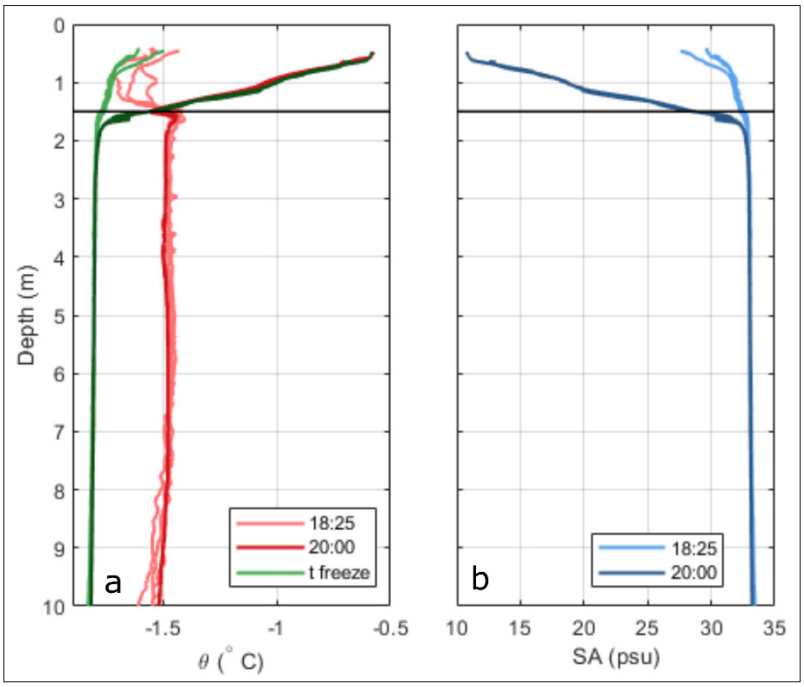

Fig. 2.47: Profiles of (left) potential temperature (red) and corresponding freezing point temperatures (green) and (right) absolute salinity of 5 individual profiles taken at Site 1 on Floe North during Visit 2; the first 3 profiles were taken consecutively at 18:25 UTC (lighter colours), and two further profiles were taken later at 20:00 (dark). The horizontal black lines represent the ice thickness. The profiles are plotted such that 0 m is the top of the water in the hole (calculated by subtracting the freeboard from the ice-thickness).

There was also a change in under-ice properties and structure over time. For the first profiles, there was no clear under-ice stratification. The cold water in the hole warmed with depth, reaching a temperature maximum of –1.4° C below the ice at 1.7 m and decreased to –1.5° C below 2 m (Fig 2.47, left). These under-ice measurements were over 0.4° C warmer than the freezing point temperature. Salinities increased steadily with depth to a stable 33 psu at 1.7 m (Fig. 2.47, right). The later repeated measurements show a colder, fresher layer had developed under the ice between 1.5 – 2 m. Strong gradients showed temperatures increasing from a minimum of 1.56° C at 1.5 m to –1.44° C at 1.6 m, and cooling to –1.5° C below 2 m, and an equivalent increase in salinities, from 28 to 32.8 psu, below which the properties were well-mixed.

Development of the ‘Uprising’ CTD

Due to these significant differences in water properties and structure over time, an alternative deployment strategy was developed to minimize the impact on the results of drilling through the ice. The RBRconcerto was modified so the instrument rises freely upwards from the bottom of the profile, aided by buoyancy, and uses the under-ice current to measure the water properties away from the freshly drilled hole. Another advantage of this setup is the collection of data up to 0.02 m below the ice, and to the very surface in a lead (Fig. 2.49, right) as the temperature and salinity sensors pointed upwards as the instrument rises to the surface. This follows a similar methodology used by the uprising microstructure profile (VMP250, Rockland Scientific) (see Microstructure section, Fig. 2.15).

In order for the instrument to rise freely, a collar of plastic nitrogen sampling bottles was strapped to the top of the CTD which acted as buoyancy (Fig 2.48, left). The rising rate of the CTD was then adjusted by partly filling these bottles with water until a rate of ~0.6 m/s was achieved. A 2 kg weight was attached to the line, approximately 2 m from the instrument, to pull the CTD down through the water column, and a steel shackle attached to the bottom of the CTD for stability as it rose. The whole system was lowered through the ice hole to 10m and, after waiting 30 seconds at the bottom, the line and weight were retrieved at a rate that kept slack on the line attached to the CTD as it freely rose to the surface. The current pushed the instrument away from the ice hole so the instrument stopped against the bottom of the ice farther downstream, and could be easily retrieved by pulling the line. This strategy was tested in a lead before being deployed under ice (Fig. 2.48, right).

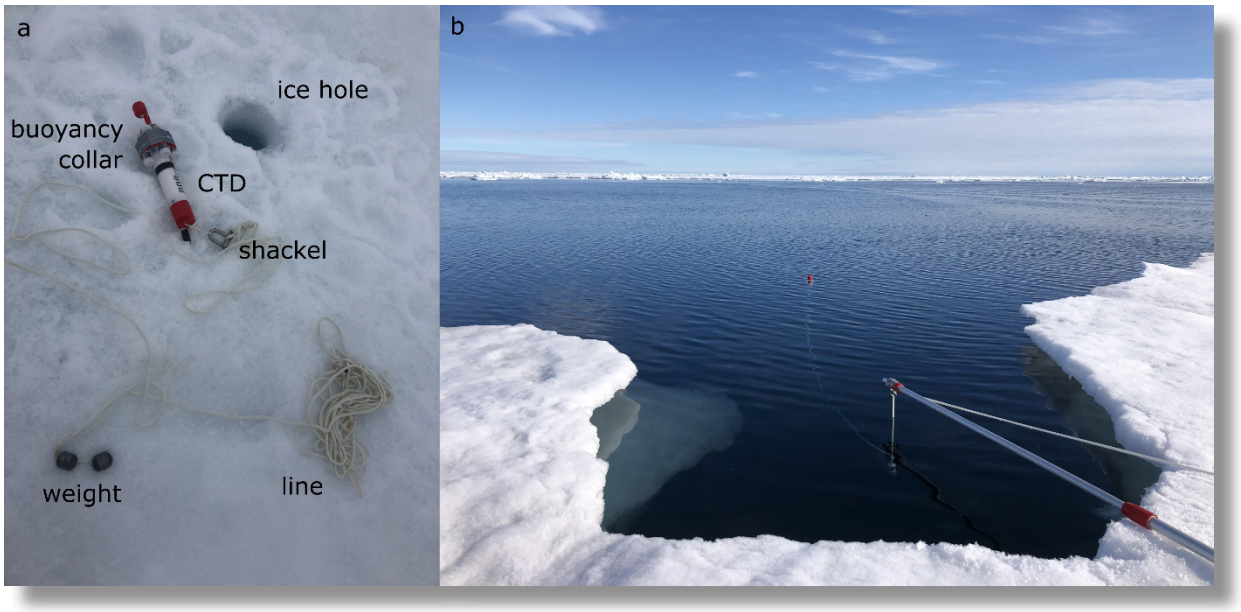

Fig. 2.48: The uprising setup of the CTD with all components labeled (left) and the CTD at the surface in a lead, held away from the ice edge by an adapted boat hook (right)

Tab. 2.23: Summary of ice CTD sampling for the different ice floes. The shaded grey boxes indicate profiles when the uprising CTD was used (instead of the standard 'downwards' profiling mode). In these cases, the 'location' is an under-ice profile instead of an 'ice' profile, which includes measurements in the ice hole itself. Profiles taken in leads are noted accordingly.

Ice Floe	Visit	Site	# Profiles	Latitude	Longitude	Date	Time (UTC)	Location
North	1	1	3	81.5922	6.7970	13.07.2022	11:02:13	Ice
		2	3	81.5919	6.7188	13.07.2022	14:51:10	Ice
	2	1	3	81.5013	4.7789	20.07.2022	18:25:48	Ice
			2	81.4977	4.7566	20.07.2022	19:59:00	Ice
		2	2	81.4995	4.7627	20.07.2022	18:59:22	Ice
		3	2	81.5004	4.7620	20.07.2022	19:21:13	Ice
		4	2	81.5006	4.7621	20.07.2022	19:35:58	Lead
		5	2	81.4971	4.7419	20.07.2022	20:24:18	Ice

Ice Floe	Visit	Site	# Profiles	Latitude	Longitude	Date	Time (UTC)	Location
	3	1	2	81.1816	2.3887	30.07.2022	09:30:18	Lead
		2	3	81.1805	2.3765	30.07.2022	09:47:18	Lead
			2	81.1738	2.2936	30.07.2022	12:53:53	Lead
		3	2	81.1786	2.3596	30.07.2022	10:41:53	Under-ice
			2	81.1742	2.2932	30.07.2022	13:06:47	Under-ice
		4	2	81.1778	2.3540	30.07.2022	11:05:54	Under-ice
			2	81.1742	2.2931	30.07.2022	13:15:51	Under-ice
		5	2	81.1774	2.3468	30.07.2022	11:29:26	Under-ice
			2	81.1746	2.2927	30.07.2022	13:25:00	Under-ice
		6	2	81.1769	2.3402	30.07.2022	11:51:10	Under-ice
			2	81.1749	2.2933	30.07.2022	13:33:46	Under-ice
		7	2	81.1764	2.3352	30.07.2022	12:07:41	Under-ice
			2	81.1749	2.2900	30.07.2022	13:49:13	Under-ice
		8	2	81.1762	2.3331	30.07.2022	12:19:46	Lead
			2	81.1749	2.2915	30.07.2022	13:56:30	Lead
South	1	1	2	81.1828	7.7278	14.07.2022	12:52:43	Ice
		2	2	81.1860	7.6835	14.07.2022	13:44:02	Ice
		3	2	81.1875	7.6416	14.07.2022	14:53:51	Ice
		4	2	81.1883	7.6273	14.07.2022	15:28:02	Ice
		5	2	81.1889	7.6108	14.07.2022	16:01:22	Ice
	2	1	2	81.1891	5.4250	21.07.2022	12:11:39	Ice
			2	81.1817	5.4274	21.07.2022	14:41:40	Ice
		2	2	81.1881	5.4321	21.07.2022	12:32:40	Lead
		3	2	81.1870	5.4352	21.07.2022	13:03:40	Ice
		4	2	81.1858	5.4372	21.07.2022	13:21:14	Ice
		5	3	81.1842	5.4356	21.07.2022	13:41:06	Ice
		6	2	81.1839	5.4363	21.07.2022	13:55:24	Lead
		7	2	NaN	NaN	21.07.2022	14:18:46	Lead
		8	2	81.183	5.4325	21.07.2022	14:26:15	Ice
	3	1	2	80.9276	3.8174	31.07.2022	13:26:00	Lead
			2	80.9267	3.7734	31.07.2022	14:39:10	Lead
		2	2	80.9274	3.8146	31.07.2022	13:33:45	Lead
		3	2	80.9268	3.8036	31.07.2022	13:53:10	Lead
		4	2	80.9266	3.7953	31.07.2022	14:05:05	Under-ice
		5	2	80.9266	3.7836	31.07.2022	14:25:02	Under-ice
Middle	1	1	2	81.3499	6.7939	15.07.2022	12:34:26	Ice
		2	2	81.3514	6.7665	15.07.2022	13:27:45	Ice
		3	2	81.3514	6.7591	15.07.2022	13:50:43	Ice
		4	2	81.3514	6.7377	15.07.2022	14:37:12	Ice
		5	2	81.3518	6.7267	15.07.2022	15:05:24	Ice
		6	2	81.3520	6.7044	15.07.2022	15:40:00	Ice
	2	1	2	81.3513	5.1265	22.07.2022	12:56:59	Ice
			2	81.3419	5.1007	22.07.2022	15:58:39	Ice
		2	2	81.3512	5.1271	22.07.2022	13:43:47	Lead

Ice Floe	Visit	Site	# Profiles	Latitude	Longitude	Date	Time (UTC)	Location
		3	2	81.3508	5.1156	22.07.2022	13:53:41	Lead
		4	2	81.3496	5.1171	22.07.2022	14:14:56	Ice
		5	2	81.3482	5.1080	22.07.2022	14:36:21	Ice
		6	2	81.3460	5.1026	22.07.2022	15:00:09	Ice
		7	2	81.3448	5.0963	22.07.2022	15:23:22	Ice
		8	2	81.3436	5.0876	22.07.2022	15:42:08	Lead
		9	2	81.3425	5.0874	22.07.2022	13:13:48	Ice
	3	1	2	81.0689	2.1228	31.07.2022	21:07:41	Under-ice
		2	2	81.0681	2.1118	31.07.2022	21:23:43	Lead
		3	2	81.0677	2.1126	31.07.2022	21:33:07	Under-ice
		4	2	81.0672	2.1080	31.07.2022	21:52:11	Under-ice
		5	2	81.0669	2.1027	31.07.2022	22:15:02	Under-ice
		6	2	81.0657	2.0905	31.07.2022	22:58:02	Under-ice
		7	2	81.0656	2.0819	31.07.2022	23:21:24	Lead

Preliminary Results: Pronounced variability in the under-ice water properties across the ice floe can be seen on Floe North during visit 3 (Fig. 2.49). The lead at the leading edge of the ice floe is characterized by strong near-surface temperature and salinity gradients. A warm (> 0° C) and fresh (10 psu) surface layer (0 – 0.34 m) overlay a well-mixed cold (–1.6° C) and saline (34 psu) layer below 0.5 m. This surface layer displays temperature variability both within and between profiles, suggesting there is mixing in this layer. The water in the surface layer and ambient below are consistently warmer than the freezing point temperature by 0.2° C.

Across the ice floe, from the leading to the trailing edge, the under-ice water properties become increasingly cold and fresh. At the site closest to the leading edge, there are strong gradients over the upper 0.2 m, where the water directly under the ice is –0.8° C and 10 psu (Fig. 2.49b). These under-ice gradients weaken to where the ambient layer is directly under the ice, at –1.5° C and 33 psu (Fig. 2.49f). The lead at the trailing edge also displays different characteristics from the leading edge. There is a greater variability in the near-surface properties between the 4 profiles, showing a warm, fresh surface layer than deepens over time, from 0.1 m for the first profile to 0.3 m (Fig. 2.49g). Near-surface temperatures reached over 1.5° C before decreasing to –1.6° C below 0.5 m, and salinities also decreased with depth from 0 psu at the water surface, to 33 psu in the ambient below. The first two profiles show similar structure however, the second set of profiles taken on transect 2 shows large variability over the ~5 minutes between the measuring of both profiles.

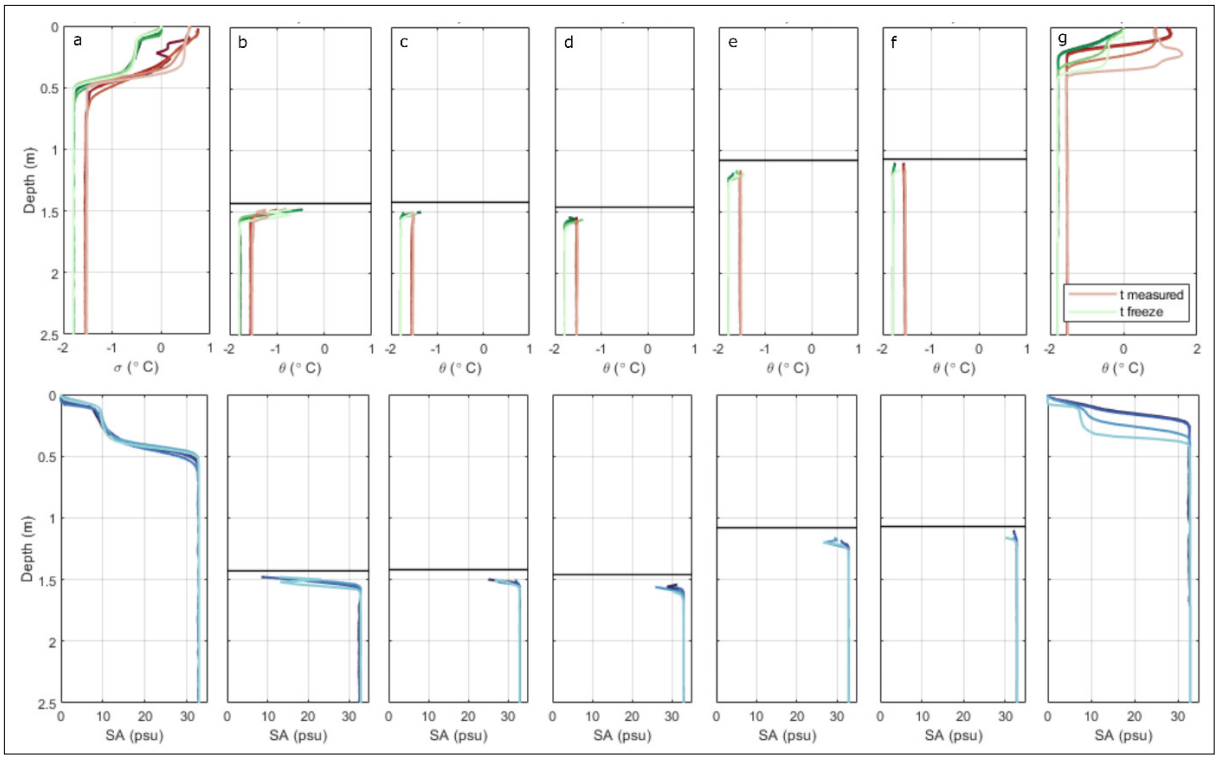

Fig.2.49: Profiles of (top) measured (red) and freezing point (green) temperatures and (bottom) salinity, from the across-floe transect taken on Floe North during visit 3 (Fig. 2.44, upper left). The darker colours represent profiles from transect 1 and lighter colours are from transect 2. The horizontal black lines represent the ice thickness at each site. The vertical scale shows only the surface 2.5 m, and the horizontal scales are constant across each site for comparison. The profiles on the far left-hand side are from the lead at the leading edge of the floe, and the far right-hand side is in the lead at the trailing edge.

These changes in water properties and structure spatially, across the width of the ice floe, suggest that the direction of the drift of the floe impacts the under-ice conditions. Furthermore, the variability in the near-surface in both leads, at the leading and trailing edge of the floe, implies that strong mixing occurs in the upper water column. Further analysis is required to better understand the under-ice properties and behaviours, and quantify the processes that drive the variability.

Physical oceanography at the 79 North Glacier and Zachariae Isstrom (areas 4) and Scoresby Sund (area 5)

The aim of the work should have been to study the ocean-driven melt of the 79N Glacier and Zachariae Isstroem. We were able to move close to Franske Oer, as patches in the Southern part of the fast ice in Norske Trough were less than 80 cm thick and melting (Fig. 2.50). We moved into the passage between the islands of Parisoerne and Franske Oer, a possible gateway for warm Atlantic Water from the Greenland Shelf into Joekelbugten, into which the massive outlet glacier Zachariae Isstroem terminates. Our hydrographic and bathymetry (multibeam) charting however revealed this channel to narrow down and become too shallow (less than 280 m) to support any sizable flow. We conducted a minor hydrographic programme and deployed a mooring on the northern end of the Ile de France section, in a place previously covered by an AWI mooring in the Atlantic Water inflow branch toward the glaciers on the coast of Greenland (Fig. 2.50).

The ship then headed south for Scoresby Sund (area 5). We sailed straight into the inner fjord toward the transition to Nordvest Fjord. Here we recovered two moorings that had been in the water for four years and conducted a small hydrographic programme to document the cascading of warm Atlantic Water into the deep basin of Nordvest Fjord, home of the heavily iceberg-producing Daugaard Jensen Glacier. Mooring SCO3 at the fjord mouth was subject to a dredging operation. We managed to retrieve the top part of the mooring, while the bottom elements including an ADCP remained on the sea floor.

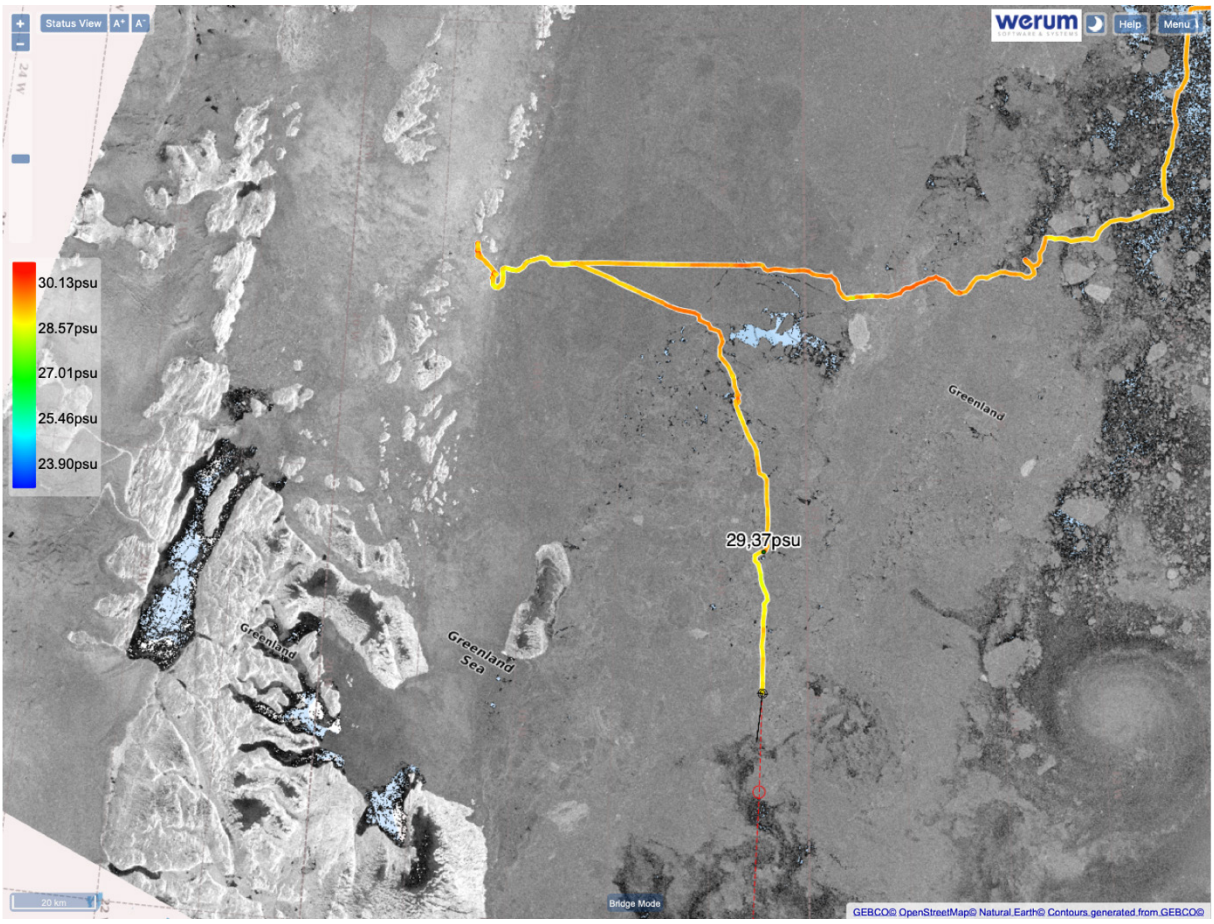

Fig. 2.50: Cruise track marked as surface salinity overlaid on radar image of sea ice; the transition from darker gray to lighter gray near the island (white) marks the transition from fast ice with an age of a few months to older fast ice

Preliminary (expected) results

Preliminary example plots of the data have been shown above e.g. the LADCP, VMADCP, Glider, and ice floe instruments.

Data management

Environmental data will be archived, published, and disseminated according to international standards and FAIR principles by the World Data Center PANGAEA Data Publisher for Earth & Environmental Science (https://www.pangaea.de) within two years after the end of the expedition. By default, the CC-BY license will be applied.

Most buoy data are transmitted via the iridium satellite network, and decoded and stored on dedicated servers of the respective buoy manufacturer. Additionally, selected buoy data is fed

into the database of the International Arctic Buoy Programme (IABP) and the WMO's Global Telecommunications System (GTS), from where they are immediately available for public use.

Any other data will be submitted to an appropriate long-term archive that provides unique and stable identifiers for the datasets and allows open online access to the data.

Molecular data (DNA and RNA data) will be archived, published, and disseminated within one of the repositories of the International Nucleotide Sequence Data Collaboration (INSDC, www.insdc.org) comprising EMBL-EBI/ENA, GenBank, and DDBJ).

Any other data will be submitted to an appropriate long-term archive that provides unique and stable identifiers for the datasets and allows open online access to the data.

This expedition was supported by the Helmholtz Research Programme "Changing Earth – Sustaining our Future" Topic 2, Subtopic 2.1.

We acknowledge financial support by the USIABP and Ignatius Rigor for covering some of the buoy's iridium costs.

In all publications based on this expedition, the **Grant No. AWI_PS131_07** will be quoted.

References

Fer I, Baumann T, Koenig Z, Muilwijk M, Tippenhauer S (2022) Upper-ocean turbulence structure and ocean-ice drag coefficient estimates using an ascending microstructure profiler during the MOSAiC drift. Journal of Geophysical Research- Oceans, accepted.

Goodman L, Levine ER, and Lueck RG (2006) On Measuring the Terms of the Turbulent Kinetic Energy Budget from an AUV, Journal of Atmospheric and Oceanic Technology, 23:977–990, https://doi.org/10.1175/JTECH1889.1.

Kolås EH, Mo-Bjørkelund T, Fer I (2022) Technical note: Turbulence measurements from a light autonomous underwater vehicle. Ocean Sci., 18:1–12, https://doi.org/10.5194/os-18-1-2022.

Merckelbach L, Smeed D and Griffiths G (2010) Vertical water velocities from underwater gliders. J. Atmos. Oceanic Technol., 27:547–563, https://doi.org/10.1175/2009JTECHO710.1.

SIDFEx Team (2022) The Sea Ice Drift Forecast Experiment: Rationale, Implementation, and Selected Results, in preparation.

Thomson J and Rogers WE (2014) Swell and sea in the emerging Arctic Ocean, Geophys. Res. Lett., 41:3136 – 3140, https://doi.org/10.1002/2014GL059983.

Tab. 2.12: Overview of the Triaxus transects during PS131

number	dive	section	name	Syear	Smonth	Sday	Shour	Sminute	Ssecond	Eyear	Emonth	Eday	Ehour	Eminute	Esecond	Sx	Ex	xyar	cable	minz	maxz	station	comment
1	1	1	WSC_ test	2022	7	7	19	23	0	2022	7	7	20	3	0	6,016	6,889	lon				018_01	not really a straight section
2	2	2	MIZ1	2022	7	11	10	17	40	2022	7	11	12	35	20	80,274	80,525	lat	810	10	200	036_02	stopped at ice edge
3	3	3	MIZ_test	2022	7	16	18	43	40	2022	7	16	19	26	30	11,039	10,649	lon	500	10	150	055_01	depressor first time in ice; short section in deployment direction
4	3	4	MIZ2a	2022	7	16	19	36	50	2022	7	17	3	49	0	80,340	81,055	lat	500	10	150	055_01	drifters deployed
5	4	4	MIZ2b	2022	7	19	15	5	20	2022	7	19	20	58	0	81,011	81,572	lat	500	20	150	064_01	insulation alarm; drifters deployed
6	5	5	MIZ3a	2022	7	29	8	23	50	2022	7	29	10	49	45	81,212	80,968	lat	500	15	150	086_01	considerable overlap with MIZ3b
7	6	5	MIZ3b	2022	7	30	18	2	0	2022	7	30	23	10	0	81,091	80,623	lat	500	10	150	090_01	
8	7	6	streak1	2022	8	1	13	19	10	2022	8	1	16	47	50	4,222	6,890	lon	350	5	50	095_01	altitude alarms every couple of minutes
9	7	7	streak2	2022	8	1	17	10	45	2022	8	1	19	28	10	6,856	5,455	lon	750	5	200	095_01	leak alarm; drifters deployed
10	8	8	Scoresby	2022	8	11	5	26	35	2022	8	11	6	26	20	-23,470	-22,900	lon	2000	10	350	117_01	insulation alarm; oil leak winch

Tab. 2.13: Overview of the Triaxus transects during PS131

number	dive	section	name	Syear	Smonth	Sday	Shour	Sminute	Ssecond	Eyear	Emonth	Eday	Ehour	Eminute	Esecond	Sx	Ex	xvar	cable	minz	maxz	station	comment
1	1	1	WSC_ test	2022	7	7	19	23	0	2022	7	7	20	3	0	6,016	6,889	lon				018_01	not really a straight section
2	2	2	MIZ1	2022	7	11	10	17	40	2022	7	11	12	35	20	80,274	80,525	lat	810	10	200	036_02	stopped at ice edge
3	3	3	MIZ_test	2022	7	16	18	43	40	2022	7	16	19	26	30	11,039	10,649	lon	500	10	150	055_01	depressor first time in ice; short section in deployment direction
4	3	4	MIZ2a	2022	7	16	19	36	50	2022	7	17	3	49	0	80,340	81,055	lat	500	10	150	055_01	drifters deployed
5	4	4	MIZ2b	2022	7	19	15	5	20	2022	7	19	20	58	0	81,011	81,572	lat	500	20	150	064_01	insulation alarm; drifters deployed
6	5	5	MIZ3a	2022	7	29	8	23	50	2022	7	29	10	49	45	81,212	80,968	lat	500	15	150	086_01	considerable overlap with MIZ3b
7	6	5	MIZ3b	2022	7	30	18	2	0	2022	7	30	23	10	0	81,091	80,623	lat	500	10	150	090_01	
8	7	6	streak1	2022	8	1	13	19	10	2022	8	1	16	47	50	4,222	6,890	lon	350	5	50	095_01	altitude alarms every couple of minutes
9	7	7	streak2	2022	8	1	17	10	45	2022	8	1	19	28	10	6,856	5,455	lon	750	5	200	095_01	leak alarm; drifters deployed
10	8	8	Scoresby	2022	8	11	5	26	35	2022	8	11	6	26	20	-23,470	-22,900	lon	2000	10	350	117_01	insulation alarm; oil leak winch

Tab. 2.16: VMP250 log

TAB 2.16 VMP250 IR, LOG-SHEET							
Vessel: *Polarstern* **Cruise: PS131, ATWAICE Date: 28 Jun – 14 Aug 2022**							
File number DAT_XXX	Station name	Date (dd. mm.yyyy)	Magnet ON (HH:MM UTC)	Magnet OFF (HH:MM UTC)	Number of casts	probes SN	Comments
3	Floe North, Visit 1	7/13/2022	9:50	10:10	1	N/A	Test probes. Lines entangled. Not free rise. Start approx 50 m
4	Floe North, Visit 1	7/13/2022	10:30	10:45	1		test probes. Rear end first. Worked fine. Start approx 70m
5		7/13/2022	10:50	10:52	0		do not process
6	Floe North, Visit 1	7/13/2022	12:18	12:49	1	sh1: M835; sh2: M2432; T:2185; C:206	entangled during recovery. Probes look ok. Start 85 m
7	Floe North, Visit 1	7/13/2022	12:55	13:10	1		start 75 m
8,9		7/13/2022	14:29		0		do not process
10	Floe North, Visit 1	7/13/2022	15:48	16:06	1		
11	Floe North, Visit 1	7/13/2022	16:08	16:50	3		first and last profiles entangled
12 to 16		7/19/2022					do not process. Some files opened in lab
17	Floe North, Visit 2	7/20/2022	20:19	22:03	5		Start at 58m, 78m, 60m, 65m, 50m
18	Floe North, Visit 2	7/20/2022			0		do not process. A file opened on ice. On ice, average P=1.8dbar
19	Floe North, Visit 2	7/20/2022	23:03	23:40	2		first cast, start 40m, a step at 30m-free ascent 30 to 5m; 2nd cast start 45m. Looks good
20,21		7/21/2022			0		on ice. Do not process. On ice, average P=1.8dbar
22	Floe Middle, Visit 2	7/22/2022	12:06	12:53	3		All clean profiles. 62m, 42m and 70 m

TAB 2.16 VMP250 IR, LOG-SHEET							
		Vessel: *Polarstern*	**Cruise: PS131, ATWAICE**		**Date: 28 Jun – 14 Aug 2022**		
23	Floe Middle, Visit 2	7/22/2022	14:00	14:56	3		All clean
24	Floe Middle, Visit 2	7/22/2022	15:58	17:05	4		70m, 65m, 60, 70m. Entire last profile, cables were entangled.
25, 26					0		Do not process
27	Floe 24h	7/27/2022	22:53	00:10	4	sh1: M835; sh2: M2308; T:2185; C:206	Changed SH2. Profiles from 37, 47, 45 and 47 m. Last cast entangled
28	Floe 24h	7/28/2022	1:07	03:22	0		Do not process
29	Floe 24h	7/28/2022	3:22	07:22	14		First 10 starts at about 40 m, rest 80m
30	Floe 24h	7/28/2022	7:22	08:36	4		all 80m, last entagled
31	Floe 24h	7/28/2022	8:36	10:21	6		all 80m
32	Floe 24h	7/28/2022	11:53	13:05	4		all 80m
33	Floe 24h	7/28/2022	13:10	13:58	2		all 80m
34	Floe 24h	7/28/2022	14:44	15:26	3		50m, last 2 entangled
35	Floe 24h	7/28/2022	15:30	17:56	9		all 80m, some entanglement in 3, 4, 6 and possibly 9
36	Floe 24h	7/28/2022	17:59	20:17	8		all 70-80m. (2 and) 5 and 8 not free rise
37	24h	7/28/2022	20:19	20:57	2		first is 90m, second is not free rise
38, 39	Floe 24h	7/29/2022			0		Do not process
40	Floe North, Visit 3	7/30/2022	8:16	08:55	2		80m, 60m (last not free rise)
41	Floe North, Visit 3	7/30/2022	8:55	12:37	12		all 70-80m.
42	Floe North, Visit 3	7/30/2022	12:48	13:20	2		80m. Last not free rise
43	Floe North, Visit 3	7/30/2022	13:23	13:38	1		60m
44	Floe North, Visit 3	7/30/2022	13:38	14:07	2		80m, 2nd entangled
45	Floe North, Visit 3	7/30/2022	14:08	14:35	2		80m, 2nd entangled
46, 47	Floe North, Visit 3	7/30/2022	16:48	16:48	0		Do not process

TAB 2.16 VMP250 IR, LOG-SHEET							
		Vessel: *Polarstern*	**Cruise: PS131, ATWAICE**		**Date: 28 Jun – 14 Aug 2022**		
48	Floe Middle, Visit 3	7/31/2022	20:31	21:43	4		80m, all entangled? Ice thick=104, freeboard=20cm
49	Floe Middle, Visit 3	7/31/2022	21:44	23:31	6		80-90m
50	Floe Middle, Visit 3	7/31/2022	23:32	23:48	1		60m
51	Floe Middle, Visit 3	7/31/2022			0		Do not process
52	Floe Middle, Visit 3	7/31/2022	23:48	00:39	3		90,85,60m. Forgot to remove magnet (long record of rubbish, 41k s). Reduced the P file to 3000s and overwrote.
53	Floe Middle, Visit 3	7/31/2022			0		Do not process

Tab. 2.17: MSS log

Cast	Station Name	Date-UTC	Time (UTC)	LAT	LON	Comments
1	Floe North, Visit 1	2022-07-13	11:08	81N35.50	06E47.00	MSS90L SN075; P=2 dbar when hair at surface
2	Floe North, Visit 1	2022-07-13	11:28	81N35.50	06E47.00	
3	Floe North, Visit 1	2022-07-13	11:47	81N35.50	06E47.00	Realized after cast3 that the two shear probes were NOT installed. Probe holders were exposed to seawater. Cannot fix on ice. Changed to SN097.
4	Floe North, Visit 1	2022-07-13	14:49	81N35.46	06E42.41	MSS90L SN097
5	Floe North, Visit 1	2022-07-13				stopped a 4m. Do not process
6	Floe North, Visit 1	2022-07-13	15:09	81N35.51	06E42.01	
7	Floe North, Visit 1	2022-07-13	15:29	81N35.56	06E41.58	End of ice station
8	Floe South, Visit 1	2022-07-14	12:22	81N10.99	07E45.26	p=1.4 dbar, hair at surface; ice thickness = 1.9m
9	Floe South, Visit 1	2022-07-14	12:43	81N10.96	07E44.16	
10	Floe South, Visit 1	2022-07-14	13:05	81N10.96	07E43.00	
11	Floe South, Visit 1	2022-07-14	13:27	81N10.98	07E41.93	
12	Floe South, Visit 1	2022-07-14	13:53	81N11.02	07E40.73	recorded both down & upcast (stop didn't work), dented mount on upcast
13	Floe South, Visit 1	2022-07-14				stopped because winch didn't work
14	Floe South, Visit 1	2022-07-14	14:29	81N11.32	07E39.25	refueled generator, everything works
15	Floe South, Visit 1	2022-07-14	14:47	81N11.18	07E38.55	
16	Floe South, Visit 1	2022-07-14	15:07	81N11.25	07E37.87	wind 7-8m/s, fog
17	Floe South, Visit 1	2022-07-14	15:27	81N11.32	07E37.24	
18	Floe South, Visit 1	2022-07-14	15:47	81N11.39	07E36.68	
19	Floe South, Visit 1	2022-07-14	16:06	81N11.45	07E36.16	
20	Floe South, Visit 1	2022-07-14	16:25	81N11.51	07E35.66	
21	Floe Middle, Visit 1	2022-07-15	12:38	81N20.98	06E47.35	Ice thickness 1.3m, P=1.3 dbar when at surface
22	Floe Middle, Visit 1	2022-07-15	12:58	81N20.96	06E46.70	
23	Floe Middle, Visit 1	2022-07-15	13:17	81N20.96	06E46.06	
24	Floe Middle, Visit 1	2022-07-15	13:34	81N20.96	06E45.55	

Cast	Station Name	Date-UTC	Time (UTC)	LAT	LON	Comments
25	Floe Middle, Visit 1	2022-07-15	13:51	81N20.97	06E45.13	
26	Floe Middle, Visit 1	2022-07-15	14:09	81N20.98	06E44.78	
27	Floe Middle, Visit 1	2022-07-15	14:32	81N21.01	06E44.06	
28	Floe Middle, Visit 1	2022-07-15	14:50	81N21.04	06E43.44	
29	Floe Middle, Visit 1	2022-07-15	15:07	81N21.06	06E42.90	
30	Floe Middle, Visit 1	2022-07-15	15:27	81N21.09	06E42.31	
31	Floe Middle, Visit 1	2022-07-15	15:45	81N21.12	06E41.77	
32	Floe Middle, Visit 1	2022-07-15	16:02	81N21.14	06E41.25	
33	Floe Middle, Visit 1	2022-07-15	16:20	81N21.18	06E40.64	
34	56_01	2022-07-17	09:15	80N37.20	09E47.06	before ctd 56_02; problem with winch; Recovered from 50m. Will repeat
35	56_01	2022-07-17	09:20	80N37.21	09E46.97	CTD 056_02
36	057_01	2022-07-17	18:53	80N23.51	10E27.78	CTD 057_02
37	057_08	2022-07-18	00:43	80N23.40	10E28.69	Forgot stopping recording in the upcast (to 45m). Downcast OK but winch problems during recovery.
38	061_01	2022-07-18	15:49	80N48.93	09E12.25	CTD 061_02
39	061_08	2022-07-18	22:25	80N49.47	09E07.56	CTD 061_07
40	065_07	2022-07-20	06:55	81N32.42	07E11.02	after a shallow (150m) CTD LOKI was deployed, about 1h after the CTD 065_05.
41	Floe North, Visit 2	2022-07-20	18:33	81N30.05	04E46.62	P=1.4dbar when the hair is at the surface
42	Floe North, Visit 2	2022-07-20	18:52	81N30.00	04E46.41	
43	Floe North, Visit 2	2022-07-20	19:13	81N29.94	04E46.14	
44	Floe North, Visit 2	2022-07-20	19:31	81N29.90	04E45.87	
45	Floe North, Visit 2	2022-07-20	19:58	81N29.85	04E45.38	
46	Floe North, Visit 2	2022-07-20	22:08	81N29.74	04E42.29	
47	Floe North, Visit 2	2022-07-20	22:25	81N29.75	04E41.90	
48	Floe North, Visit 2	2022-07-20	22:43	81N29.78	04E41.48	
49	Floe South, Visit 2	2022-07-21	12:26	81N11.34	05E25.96	1.5 dbar (hair at surface), 20 cm below ice edge
50	Floe South, Visit 2	2022-07-21	12:48	81N11.27	05E25.93	lost power ~ 280 m.

Cast	Station Name	Date-UTC	Time (UTC)	LAT	LON	Comments
51	Floe South, Visit 2	2022-07-21	13:15	81N11.20	05E25.86	
52	Floe South, Visit 2	2022-07-21	13:36	81N11.14	05E25.82	
53	Floe South, Visit 2	2022-07-21	14:01	81N11.06	05E25.77	
54	Floe South, Visit 2	2022-07-21	14:21	81N10.99	05E25.73	
55	Floe South, Visit 2	2022-07-21				stop 25m - entangled to ice. Do not process
56	Floe South, Visit 2	2022-07-21	14:41	81N10.93	05E25.69	
57	069_01	2022-07-21	20:23	81N11.90	08E06.17	cable entangled on ice floe. Recovery around 115m.
58	069_01	2022-07-21	20:41	81N11.83	08E06.26	No CTD cast associated because CTD broken
59	069_06	2022-07-22	01:37	81N11.17	07E59.07	No CTD cast associated because CTD broken
60	Floe Middle, Visit 2	2022-07-22	11:46	81N21.25	05E08.34	at surface p=1.5; ice thickness=87cm; freeboard=13cm
61	Floe Middle, Visit 2	2022-07-22	12:54	81N21.09	05E07.57	after 3x VMP
62	Floe Middle, Visit 2	2022-07-22	13:20	81N21.02	05E07.30	
63	Floe Middle, Visit 2	2022-07-22	13:38	81N20.97	05E07.12	
64	Floe Middle, Visit 2	2022-07-22	14:55	81N20.74	05E06.39	
65	Floe Middle, Visit 2	2022-07-22	15:20	81N20.66	05E06.22	Tent, low current, cable straight
66	Floe Middle, Visit 2	2022-07-22	15:38	81N20.59	05E06.10	
67	Floe 24h	2022-07-27	22:20	81N21.31	01E23.64	goal 250 m; ice thick=132cm; freeboard=13cm
68	Floe 24h	2022-07-27				stopped at 26m because of cable entangled with winch
69	Floe 24h	2022-07-27	22:40	81N21.25	01E23.32	
70	Floe 24h	2022-07-27	22:59	81N21.19	01E23.01	
71	Floe 24h	2022-07-27	23:42	81N21.11	01E22.36	
72	Floe 24h	2022-07-28	00:13	81N21.07	01E21.96	
73	Floe 24h	2022-07-28	00:30	81N21.06	01E21.80	
74	Floe 24h	2022-07-28	00:47	81N21.06	01E21.65	
75	Floe 24h	2022-07-28	01:13	81N21.06	01E21.47	
76	Floe 24h	2022-07-28	01:27	81N21.06	01E21.40	
77	Floe 24h	2022-07-28	02:07	81N21.07	01E21.33	

Cast	Station Name	Date-UTC	Time (UTC)	LAT	LON	Comments
78	Floe 24h	2022-07-28	02:23	81N21.08	01E21.34	
79	Floe 24h	2022-07-28				
80	Floe 24h	2022-07-28	02:53	81N21.10	01E21.41	
81	Floe 24h	2022-07-28	03:07	81N21.11	01E21.46	
82	Floe 24h	2022-07-28	03:22	81N21.12	01E21.53	
83	Floe 24h	2022-07-28	03:37	81N21.12	01E21.60	
84	Floe 24h	2022-07-28	03:51	81N21.12	01E21.68	
85	Floe 24h	2022-07-28	04:08	81N21.12	01E21.79	
86	Floe 24h	2022-07-28	04:28	81N21.11	01E21.90	
87	Floe 24h	2022-07-28	04:46	81N21.10	01E22.00	
88	Floe 24h	2022-07-28	05:06	81N21.08	01E22.10	
89	Floe 24h	2022-07-28	05:34	81N21.03	01E22.21	
90	Floe 24h	2022-07-28				
91	Floe 24h	2022-07-28	06:16	81N20.94	01E22.33	
92	Floe 24h	2022-07-28				
93	Floe 24h	2022-07-28	06:40	81N20.87	01E22.34	
94	Floe 24h	2022-07-28				aborted at 10m, rope entangled
95	Floe 24h	2022-07-28	07:00	81N20.81	01E22.31	
96	Floe 24h	2022-07-28	07:17	81N20.75	01E22.26	
97	Floe 24h	2022-07-28	07:34	81N20.69	01E22.18	
98	Floe 24h	2022-07-28	07:49	81N20.62	01E22.09	
99	Floe 24h	2022-07-28	08:04	81N20.56	01E21.98	
100	Floe 24h	2022-07-28	08:20	81N20.49	01E21.83	
101	Floe 24h	2022-07-28	08:35	81N20.42	01E21.67	
102	Floe 24h	2022-07-28	08:51	81N20.35	01E21.48	
103	Floe 24h	2022-07-28	09:07	81N20.28	01E21.27	
104	Floe 24h	2022-07-28	09:23	81N20.20	01E21.02	small problem with cable at ~42m, should not be visibile in profile

Cast	Station Name	Date-UTC	Time (UTC)	LAT	LON	Comments
105	Floe 24h	2022-07-28				aborted, probe fell too slow in top 20m
106	Floe 24h	2022-07-28	09:43	81N20.11	01E20.70	ice thickness: 132 cm, freeboard: 13 cm (Gunnar)
107	Floe 24h	2022-07-28	09:58	81N20.05	01E20.44	
108	Floe 24h	2022-07-28	10:13	81N19.99	01E20.17	
109	Floe 24h	2022-07-28	10:31	81N19.92	01E19.82	ice thickness: 127 cm, freeboard: 11 cm
110	Floe 24h	2022-07-28	10:52	81N19.84	01E19.43	
111	Floe 24h	2022-07-28	11:10	81N19.78	01E19.10	
112	Floe 24h	2022-07-28	11:28	81N19.72	01E18.76	
113	Floe 24h	2022-07-28	12:09	81N19.61	01E17.91	
114	Floe 24h	2022-07-28	12:26	81N19.58	01E17.54	
115	Floe 24h	2022-07-28	12:51	81N19.53	01E16.99	
116	Floe 24h	2022-07-28	13:07	81N19.50	01E16.67	
117	Floe 24h	2022-07-28	13:22	81N19.47	01E16.37	
118	Floe 24h	2022-07-28	13:42	81N19.45	01E16.00	
119	Floe 24h	2022-07-28	13:57	81N19.43	01E15.72	
120	Floe 24h	2022-07-28	14:12	81N19.41	01E15.43	
121	Floe 24h	2022-07-28	14:26	81N19.40	01E15.18	
122	Floe 24h	2022-07-28	15:04	81N19.37	01E14.52	
123	Floe 24h	2022-07-28	15:23	81N19.36	01E14.22	
124	Floe 24h	2022-07-28	15:40	81N19.34	01E13.93	
125	Floe 24h	2022-07-28	15:55	81N19.32	01E13.67	
126	Floe 24h	2022-07-28	16:10	81N19.29	01E13.43	
127	Floe 24h	2022-07-28	16:27	81N19.27	01E13.19	
128	Floe 24h	2022-07-28	17:14	81N19.18	01E12.51	
129	Floe 24h	2022-07-28	17:33	81N19.13	01E12.25	
130	Floe 24h	2022-07-28	17:50	81N19.09	01E12.03	
131	Floe 24h	2022-07-28	18:06	81N19.04	01E11.80	

Cast	Station Name	Date-UTC	Time (UTC)	LAT	LON	Comments
132	Floe 24h	2022-07-28	18:24	81N18.99	01E11.56	
133	Floe 24h	2022-07-28	18:41	81N18.94	01E11.34	
134	Floe 24h	2022-07-28	18:56	81N18.90	01E11.19	
135	Floe 24h	2022-07-28	19:10	81N18.85	01E11.04	
136	Floe 24h	2022-07-28	19:24	81N18.80	01E10.88	
137	Floe 24h	2022-07-28	19:38	81N18.76	01E10.72	
138	Floe 24h	2022-07-28	19:52	81N18.71	01E10.54	
139	Floe 24h	2022-07-28	20:08	81N18.66	01E10.36	
140	Floe 24h	2022-07-28	20:22	81N18.61	01E10.23	
141	087_02	2022-07-29	15:03	81N04.58	03E09.29	CTD 087_01
142	087_08	2022-07-29	20:34	81N05.20	03E05.74	
143	088_03	2022-07-30	01:10	81N09.56	02E58.34	CTD 088_01
144	Floe North, Visit 3	2022-07-30	08:16	81N11.30	02E23.49	brushes at surface: 1.44 dbar; ice thickness: 160 cm, freeboard: 20 cm
145	Floe North, Visit 3	2022-07-30	08:35	81N11.22	02E23.40	
146	Floe North, Visit 3	2022-07-30	08:50	81N11.16	02E23.33	
147	Floe North, Visit 3	2022-07-30	09:05	81N11.10	02E23.22	
148	Floe North, Visit 3	2022-07-30	09:19	81N11.04	02E23.08	several readings of ~700 dbar around (“true”) 127-130 dbar, also high ACC (>20 m/s2), the rest of the cast (150-250dbar) were fine again
149	Floe North, Visit 3	2022-07-30	09:41	81N10.95	02E22.81	
150	Floe North, Visit 3	2022-07-30	09:58	81N10.90	02E22.50	
151	Floe North, Visit 3	2022-07-30	10:15	81N10.84	02E22.14	
152	Floe North, Visit 3	2022-07-30	10:50	81N10.75	02E21.38	
153	Floe North, Visit 3	2022-07-30	11:07	81N10.71	02E21.02	
154	Floe North, Visit 3	2022-07-30	11:23	81N10.66	02E20.64	
155	Floe North, Visit 3	2022-07-30	11:37	81N10.63	02E20.29	ice thickness: 160 cm, freeboard: 20 cm
156	Floe North, Visit 3	2022-07-30	11:52	81N10.59	02E19.86	
157	Floe North, Visit 3	2022-07-30	12:12	81N10.55	02E19.30	
158	Floe North, Visit 3	2022-07-30	12:27	81N10.52	02E18.87	

Cast	Station Name	Date-UTC	Time (UTC)	LAT	LON	Comments
159	Floe North, Visit 3	2022-07-30	12:43	81N10.51	02E18.41	
160	Floe North, Visit 3	2022-07-30	12:58	81N10.50	02E17.97	
161	Floe North, Visit 3	2022-07-30	13:13	81N10.50	02E17.58	
162	Floe North, Visit 3	2022-07-30	13:37	81N10.50	02E16.98	
163	Floe North, Visit 3	2022-07-30				aborted
164	Floe North, Visit 3	2022-07-30	13:53	81N10.51	02E16.61	
165	Floe North, Visit 3	2022-07-30	14:08	81N10.53	02E16.28	around 200dbar lost connection to MSS
166	091_03	2022-07-31	03:28	80N43.31	04E29.88	CTD 091_01
167	091_03	2022-07-31	03:34	80N43.32	04E30.39	CTD 091_01
168	091_07	2022-07-31	07:23	80N43.05	04E34.73	CTD 091_01
169	Floe South, Visit 3	2022-07-31	13:31	80N55.65	03E49.01	ice thick: 130 cm, freeboard: 23 cm
170	Floe South, Visit 3	2022-07-31	13:49	80N55.62	03E48.39	
171	Floe South, Visit 3	2022-07-31	14:06	80N55.61	03E47.79	
172	Floe South, Visit 3	2022-07-31	14:22	80N55.60	03E47.23	
173	Floe South, Visit 3	2022-07-31	14:36	80N55.61	03E46.67	
174	Floe Middle, Visit 3	2022-07-31	20:21	81N04.27	02E08.56	1,5dbar with hair at surface
175	Floe Middle, Visit 3	2022-07-31	20:35	81N04.23	02E08.25	P>600 and # in various channels on upcast
176	Floe Middle, Visit 3	2022-07-31	20:52	81N04.19	02E07.87	Ice thick: 105cm, freeboard:14 cm
177	Floe Middle, Visit 3	2022-07-31	21:07	81N04.16	02E07.53	
178	Floe Middle, Visit 3	2022-07-31	21:27	81N04.11	02E07.07	
179	Floe Middle, Visit 3	2022-07-31	21:42	81N04.07	02E06.72	
180	Floe Middle, Visit 3	2022-07-31	22:00	81N04.03	02E06.31	
181	Floe Middle, Visit 3	2022-07-31	22:17	81N03.99	02E05.93	
182	Floe Middle, Visit 3	2022-07-31				went long (what does it mean?)
183	Floe Middle, Visit 3	2022-07-31	22:47	81N03.94	02E05.26	
184	Floe Middle, Visit 3	2022-07-31	23:01	81N03.92	02E04.97	
185	Floe Middle, Visit 3	2022-07-31				many comm errors

Cast	Station Name	Date-UTC	Time (UTC)	LAT	LON	Comments
186	Floe Middle, Visit 3	2022-07-31	23:28	81N03.89	02E04.42	
187	Floe Middle, Visit 3	2022-07-31	23:49	81N03.88	02E04.01	
188	Floe Middle, Visit 3	2022-08-01	00:03	81N03.88	02E03.78	
189	Floe Middle, Visit 3	2022-08-01	00:17	81N03.88	02E03.55	
190	094_03	2022-08-01	08:20	80N46.06	04E18.05	CTD 094_01
191	094_07	2022-08-01	11:51	80N45.72	04E14.30	aborted cast after ~10m due to bad ice conditions
192	094_07	2022-08-01	12:01	80N45.65	04E13.89	CTD 094_01
193	Floe, Fast-ice	2022-08-06	08:38	78N26.12	19W33.33	Fast ice, ice thickness 120 cm
194	Floe, Fast-ice	2022-08-06				
195	Floe, Fast-ice	2022-08-06	09:27	78N26.12	19W33.35	
196	Floe, Fast-ice	2022-08-06	09:50	78N26.12	19W33.35	
197	Floe, Fast-ice	2022-08-06	10:13	78N26.12	19W33.34	
198	Floe, Fast-ice	2022-08-06	10:34	78N26.12	19W33.34	
199	Floe, Fast-ice	2022-08-06	10:59	78N26.12	19W33.35	

3. SEA ICE GEOPHYSICS AND REMOTE SENSING

Christian Haas[1], Gunnar Spreen[2],
Mara Neudert[1], Lena Buth[1], Hannah Niehaus[2],
Victor Lion[3], Mario Hoppmann[1]
Not on board: Gerit Birnbaum[1], Natascha Oppelt[3], Jan Rohde[1]

[1]DE.AWI
[2]DE.UNI-Bremen
[3]DE.CAU

Grant-No. AWI_PS131_02

Objectives

In line with the main objectives of PS131, the main objective of the sea ice geophysics and remote sensing programme was to study ice melt processes across the MIZ in dependence of oceanic and atmospheric boundary layer conditions. Oceanic eddies, fronts and tidal mixing shape the sea ice distribution in the MIZ which leads to locally enhanced ice melting as well as to the generation of stratified areas with suppressed melting. These processes result in sea ice characteristics that can be distinguished by different gradients of sea ice floe size, concentration, roughness and thickness. Our activities were therefore highly interdisciplinary and collaborative, and were carried out particularly closely with the physical oceanographic buoy and underway observations (Chapter 2).

There have been numerous studies of ice melt of individual floes (e.g., Sirevag et al., 2011), but up to now there are only few observations of ice thinning across the MIZ (e.g., Rabenstein et al., 2010; Provost et al., 2017; Duarte et al., 2020), in relation to ocean heat, current or wave, or melt pond gradients between the open water and close pack ice zones. These were not even achieved during the Multidisciplinary drifting Observatory for the Study of Arctic Climate (MOSAiC) in 2020 (Nicolaus et al., 2022; Rabe et al., 2022).

The presence of melt ponds on the surface of Arctic sea ice significantly reduces its albedo, which has implications for the energy and mass budget of the ice and for primary productivity in the upper ocean, and accelerates melt by way of ice-albedo feedback processes. Melt pond coverage is also indicative of the amount of surface melt and freshwater released to the ocean which contributes to upper ocean stratification.

Satellite remote sensing is an important complement to *in-situ* field studies, and can provide information over longer time periods and larger regions than feasible with direct observations. We will therefore use extensive remote sensing data to improve and validate algorithms for retrievals of ice concentration, thickness, floe size, melt pond coverage, and ice drift. The satellite retrieval of parameters, such as the spectral behaviour of sea ice and melt ponds, relies on spectral information, which requires a retrieval of their optical properties (e.g. König et al., 2019; Malinka et al., 2018). PS131 provided unique opportunities for microwave and optical field measurements in the MIZ. They will also support atmospheric corrections and help to calibrate and validate remote sensing products of sea ice albedo, melt pond depth and distribution, as well as tracking of (individual) drifting floes.

Apart from studying the MIZ, our objectives also were to obtain opportunistic ice thickness and melt pond data during the transits to and from the Aurora vent field and the 79 North Glacier

to continue our long-term ice thickness observations in the Arctic Ocean and Transpolar Drift (e.g., Haas et al., 2008; Belter et al., 2021).

More objectives and details of the work programmes and preliminary results are presented in the following Chapters 3.1 – 3.6.

3.1 General ice conditions

Mara Neudert[1], Gunnar Spreen[2], Christian Haas[1]
Additional Ice Observer: Arun Babu, Katie Bartek, Lena Buth, Henning Kirk, Victor Lion, Sabine Lüchtrath, Hannah Niehaus, Philipp Oehlke, Janna Rückert, Vera Schlindwein, Johanna Schüttler, Andreas Walbröl

[1]DE.AWI
[2]DE.UNI-Bremen

Objectives

Ice Watch

General ice conditions during the cruise were monitored by visual observations from the *Polarstern* bridge. Such observations of sea ice from the bridge of ice-going vessels are an integral part of sea ice monitoring since the beginning of Arctic exploration. In this tradition, all ice-going research vessels are asked to carry out standardized Ice Watch observations to enlarge the existing database. The Ice Watch programme for the Arctic (Hutchings et al., 2018) is based on and is compatible with the ASPeCt protocol developed for the Antarctic (Worby & Allison, 1999).

Visual observations are a fast and low-cost possibility to regularly obtain a broad range of sea ice, biological, and meteorological parameters extended with photographs and comments about distinctive features. They have the advantage of discriminating different ice types and specific features like ridge distribution and stages of surface melt, which are hard to obtain by other methods. Besides being a valuable dataset on its own, these observations can be used as *in-situ* comparison to otherwise obtained measurements like remote sensing data. In addition, the Ice Watch observations serve as a reference record for the cruise. They provide an easy way to revisit the specific sea ice and meteorological condition at hourly frequency throughout the cruise.

Nevertheless, it has to be considered that all observations strongly depend on the personal view and training of each individual observer and therefore the absolute accuracy can be low. Additionally, *Polarstern* often favours open water and thin ice areas for steaming, which may bias, e.g., ice thickness observations.

Cameras

Three cameras (360° Panomax camera on the crow's nest, a thermal infrared (IR) and visual camera on Peildeck looking starboard) were continuously observing the sea ice in the surrounding and next to *Polarstern*. From this the general ice conditions can be inferred manually to provide context for other measurements. Sea ice concentration and potentially also melt pond fraction will be extracted automatically from the IR and visual cameras using digital image processing and classification. This will provide continuous and less biased estimates of ice properties compared to the human Ice Watch bridge observations.

Work at sea

Ice Watch

To obtain a continuous record of the sea ice state, all cruise participants were invited to perform standardized visual observations from the ship's bridge, with the goal to obtain one observation every full hour, if the ship was not on station. However, not all night time shifts got covered by volunteers and thus on most days observations start early in the morning and last until late evening. Observations were started when *Polarstern* approached the ice 11 July 2022 and continued until the ice was finally left on 9 August 2022.

The observations were recorded using the standardized protocol of the Ice Watch programme (https://icewatch.met.no/assist). Ice Watch provides the ASSIST software tool, which is a Java application that was installed on a notebook placed on the bridge. ASSIST version 4.1 was used for recording the data, a Canon Powershot GT-X camera was used for the three photographs per observation (see example in Fig. 3.1.1). The Ice Watch Manual (Hutchings et al., 2018) and WMO sea ice nomenclature (WMO, 1989) helped conducting the observations. ASSIST can record 110 different parameters per observation. Only a small subset, however, is recorded always: time, location, ship movement, total ice concentration, ice types, ice thickness, and meteorological conditions. Snow, ice topography, melt state and other parameters were added if observed.

The observations were carried out by 15 members of the scientific parties of the cruise. Every observer had one to three fixed hours during the day for taking ice observations, and observers jumped in spontaneously if needed. In total 259 observations from the bridge were taken, out of 696 possible observations during the time in ice (not accounting for station time), i.e., at about 40 % of the time.

Fig. 3.1.1: Typical photographs taken from the bridge to port side (left,) bow (middle) and starboard side (right) on 20 July 2022

Panomax camera

A Panomax 360° line scanner camera was mounted in the ship's mast and obtained an image every 10 minutes, during the complete time in the ice (Fig. 3.1.2). Panomax images were affected by the ship's roll during steaming or crane operations, distorting the horizon and horizontal features in the images. Note that the Panomax server time setting was not set to UTC. Times were between 45 or 46 minutes ahead of UTC i.e., at 12 UTC the Panomax time was between 12:45 and 12:46.

Fig. 3.1.2: Example of Panomax view of the ice edge, 18 July, 20:30 camera time (19:45 UTC)

Infrared camera and visual camera

On the highest deck on top of the bridge (Peildeck) a thermal infrared (Infratec VarioCAM) and visual camera (GoPro Hero) were installed close to the deck rail to observe the sea ice and ocean next to the ship. Sea ice parameters like ice concentration, melt pond fraction, and ocean and ice temperatures can be inferred after automatic surface classification during post-processing. The cameras also provide supporting information for the surface microwave radiometer observations discussed in Chapter 8. Therefore, a more detailed description of the measurement setup, data availability, and preliminary results are presented in Section 8.2.

Preliminary results

Ice Watch

The first observation was carried out on 11 July 2022, 08:06 UTC and the last 9 August 2022, 08:04 UTC.

Figure 3.1.3 shows the map of all ice thickness observations of the primary ice type observed during the cruise and the ice thickness and ice concentrations histograms of all obtained observations. Most observations were taken in high ice concentration regimes (≥ 9/10) and a smaller fraction of intermediate ice concentrations were observed. This reflects that the PS131 expedition was located in three different sea ice regimes:

In the first regime of the marginal ice zone ice thicknesses were 1.10 m or less, with intermediate sea ice concentrations. The second regime of thicker and high-concentration ice was observed during the transit to and work at the Aurora vent field. The third regime was fast ice of less than 1.0 m thickness close to East Greenland. All observed sea ice was covered by open melt ponds but especially the fast ice near Greenland showed exceptionally high melt pond fractions.

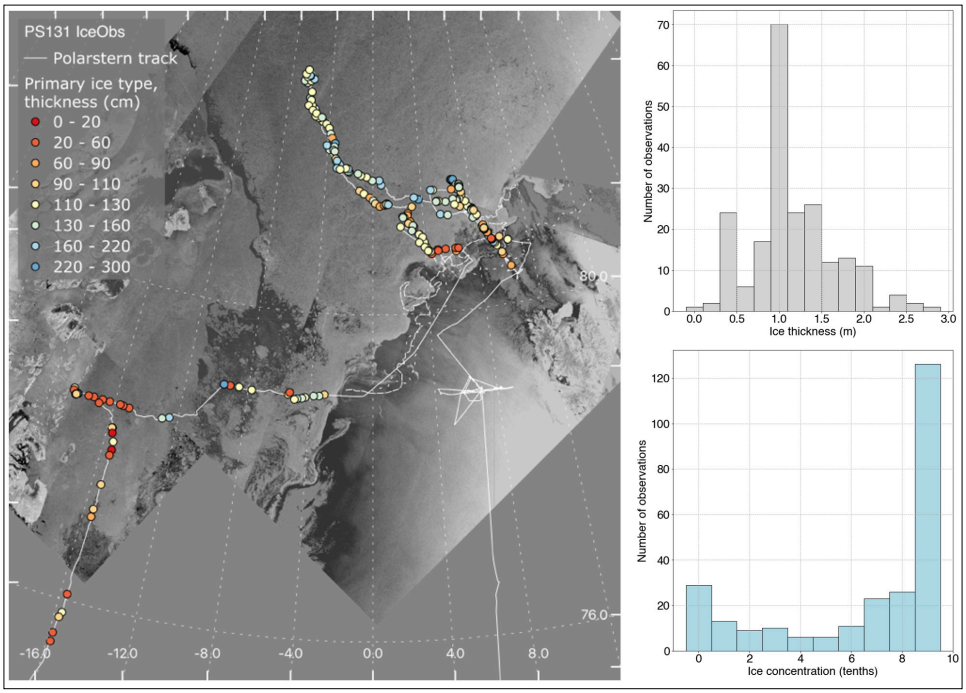

Fig. 3.1.3: Map of all ice observation of the primary ice type thickness (background are Sentinel-1 scenes from 21 July 2022) (left), and the accordant histogram of sea ice thickness (top right) and sea ice concentration (bottom right)

3.2 Overview of revisited ice floes

Christian Haas[1], Gunnar Spreen[2],
Mara Neudert[1], Lena Buth[1], Hannah Niehaus[2],
Victor Lion[3], Mario Hoppmann[1]

[1]DE.AWI
[2]DE.UNI-Bremen
[3]DE.CAU

Objectives

In order to observe temporal sea ice and ocean changes across the MIZ, three ice floes were selected for repeat visits and measurements, and were equipped with various autonomous measurement systems to obtain full descriptions of the surface energy balance, with atmospheric and oceanographic boundary conditions. The aim of this work is to better understand governing processes and to quantify ice melt and the relevant terms of the surface energy balance, while ship-based measurements could only provide snapshot information of met-ice-ocean conditions moving in time and space.

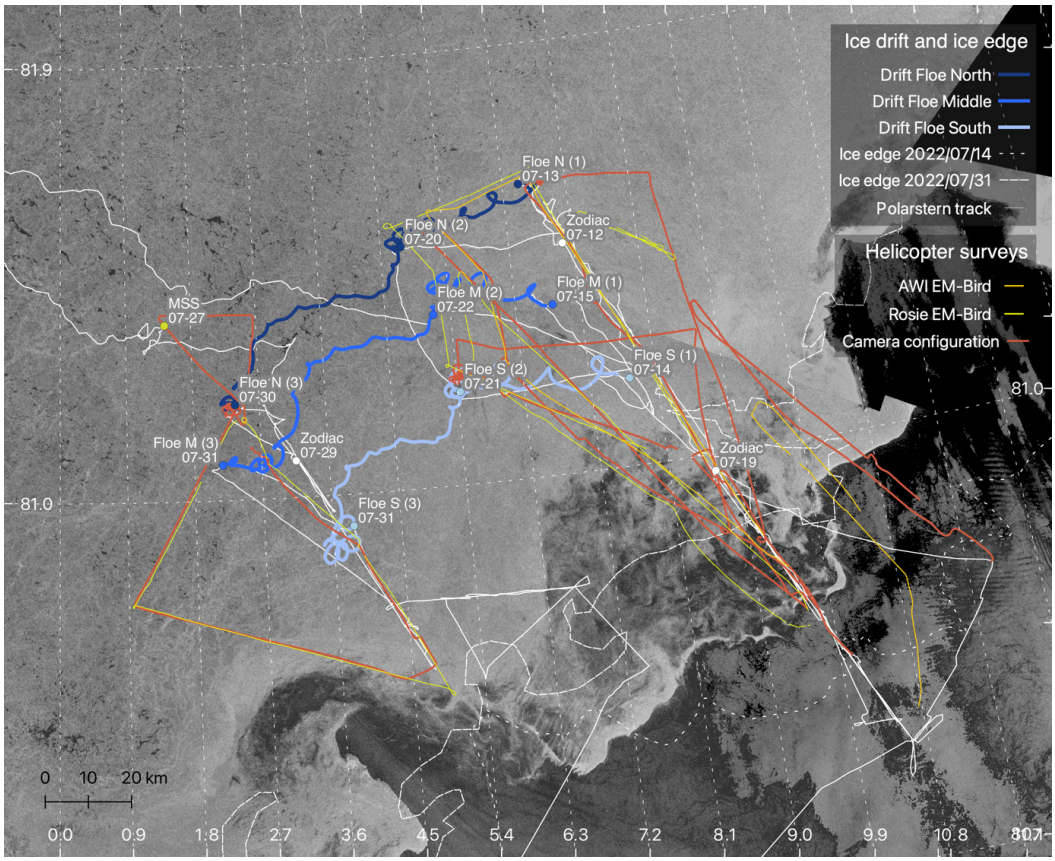

Fig. 3.2.1: Overview map of the marginal ice zone north of Svalbard, showing the drift tracks of the three ice floes N, M, and S studied during ATWAICE (blue lines), and the locations and dates of their three visits (1-3). Locations of additional floes sampled only once (MSS, Zodiac) are also shown. Warm colours show helicopter EM (HEM) ice thickness survey flight tracks and IR and optical camera flight tracks. Solid white line shows Polarstern cruise track. Dashed white lines show representative ice edge locations at the beginning and end of observations. Background shows satellite radar images representing typical ice conditions (21 July 2022).

Work at sea

Three ice floes were selected during a first transect across the MIZ between 12 and 15 July 2022, as shown in Figure 3.2.1. Floes were chosen far enough from the ice edge to have good

chances for survival during the anticipated 2.5 week observational period. In the prevailing foggy conditions during the floe search, the floes were identified with support of the ship's radar to select larger floes while most floes were rather small. Table 3.2.1 gives a summary of sampling dates and approximate sizes of the three floes.

Floes were first visited between 12 and 15 July. They were then revisited between 20 and 22 July and on 30 and 31 July (Tab. 3.2.1), i.e. the total observational period ranged between 16 and 17 days. Each visit lasted between 6 and 8 hours.

Floes were termed N (north), M (middle), and S (south) according to their relative position. Note that the order of their visits was N, S, and M during each observational campaign.

Floe N was a large floe surrounded by several other large floes which were even partially larger. A few days after the first visit the floe experienced a break up near the buoy deployment site which reduced its size to approximately 1 km x 0.6 km which it maintained until the third visit (Fig. 3.2.2, left). The breakup can be seen in the Reolink SeaIceCam footage (*cf.* Fig. 2.44c).

Floe M was a larger floe surrounded by smaller floes. It maintained its size of approximately 0.3 km x 0.3 km throughout the observational period (Fig. 3.2.2, middle column).

Floe S was quite large (>1 km x 1 km) when it was first visited on 14 July, however, under the effect of feelable swell it actually broke during the work on the ice (cracks are visible in top right panel of Fig. 3.2.2). During the two subsequent visits no piece was larger than 100 m any more, with many smaller floes. During the second visit on 21 July it was still possible to traverse over the individual fragments, and in particular to the buoy and melt pond study sites. However, floe parts were too far apart and separated by water during the third visit, such that the buoy and melt pond sites were visited separately by the ship for buoy recovery and a minimal observational program.

Figure 3.2.3 shows snapshots of details of each floe with an indication of the sites of the main activities on the ice, i.e. melt pond and buoy sites, coring and optical (RAMSES) measurements, albedo line, GEM ice thickness measurements, and MSS casts and biological ice coring.

The three floes were equipped with numerous autonomous observation systems summarized in Table 2.20 and described in individual Chapters (2. and 3.3). Figure 3.2.4 presents detailed views of each site.

In addition to the three main ice floes which were visited three times, other ice floes were visited only once. These included a short BIO station in the Aurora region, a 24 h ice station on 27 July primarily in support of continuous turbulence measurements (MSS site in Fig. 3.2.1), and small ice floes visited briefly by zodiac (on 12 July, 1 floe; 19 July, 7 floes; 29 July, 2 floes). In addition, two sites on fast ice near the Greenlandic coast were studied.

Tab. 3.2.1: Overview of the sampling dates and approximate sizes of the three ice floes visited three times to observe ice changes. See map in Figure 3.2.1 and Tables 3.3.2 – 3.3.4 for more information, and Figure 3.2.2 for some visual documentation.

	Visit 1 and size	**Visit 2 and size**	**Visit 3 and size**
Floe N	12./13.7., 2 km x 2 km	20.7., 1 km x 0.6 km	30.7., 1 km x 0.6 km
Floe M	15.7., 0.3 km x 0.3 km	22.7., 0.3 km x 0.3 km	31.7., 0.3 km x 0.3 km
Floe S	14.7., > 1 km x 1 km	21.7., 0.1 km x 0.06 km	31.7., 0.1 km x 0.06 km

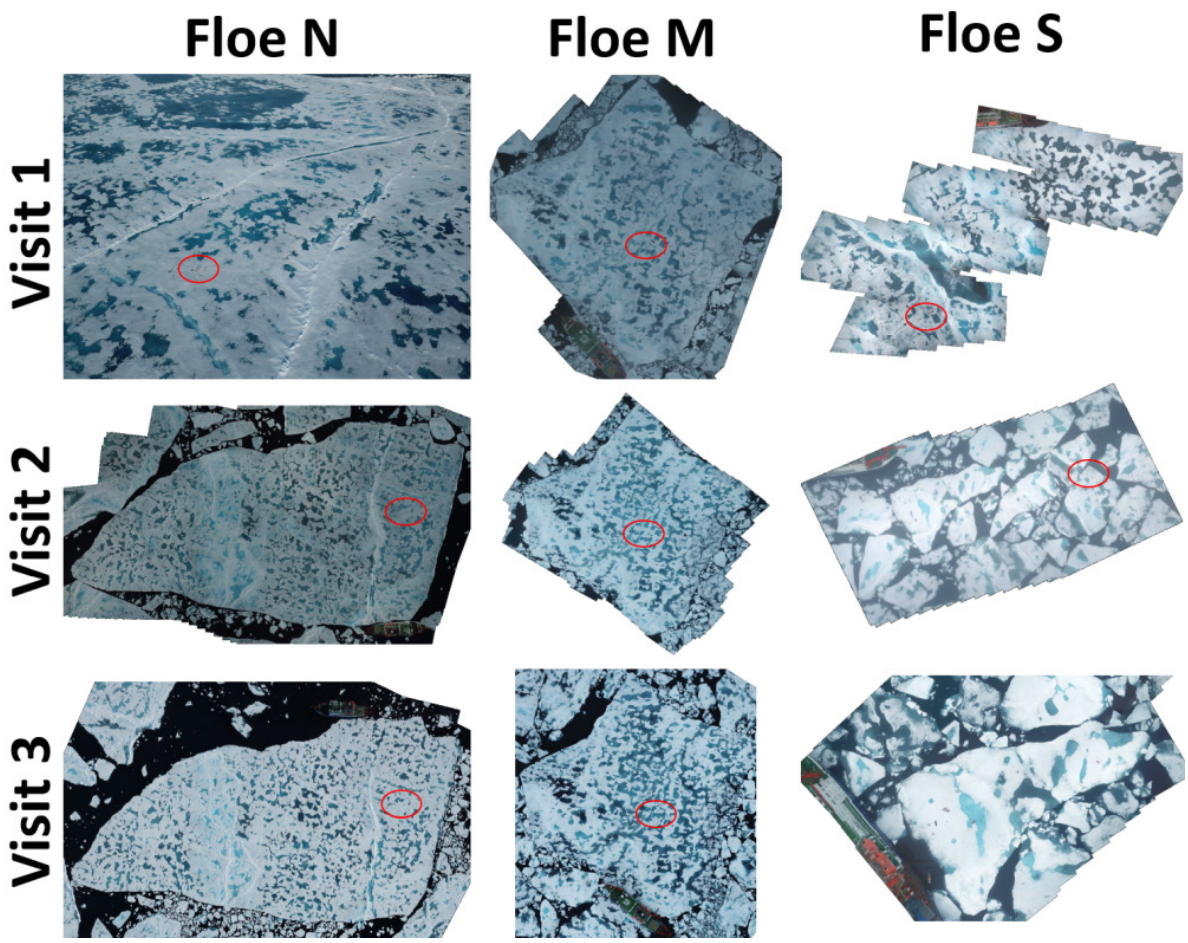

Fig. 3.2.2: Aerial photo mosaics (from drone flights, Section 3.3) of the three floes during each of three visits (cf. Tab. 3.2.1 and map in Fig. 3.2.1). Only top left photo shows an oblique view of the buoy site area of floe N including the heavily ponded ice behind the first pressure ridge where the floe broke shortly after the first visit. Photos are not to scale (but the Polarstern is visible on some) and floes N and M are approximately aligned northwards (up). Red circle shows approximate location of buoy site (see Fig. 3.2.4).

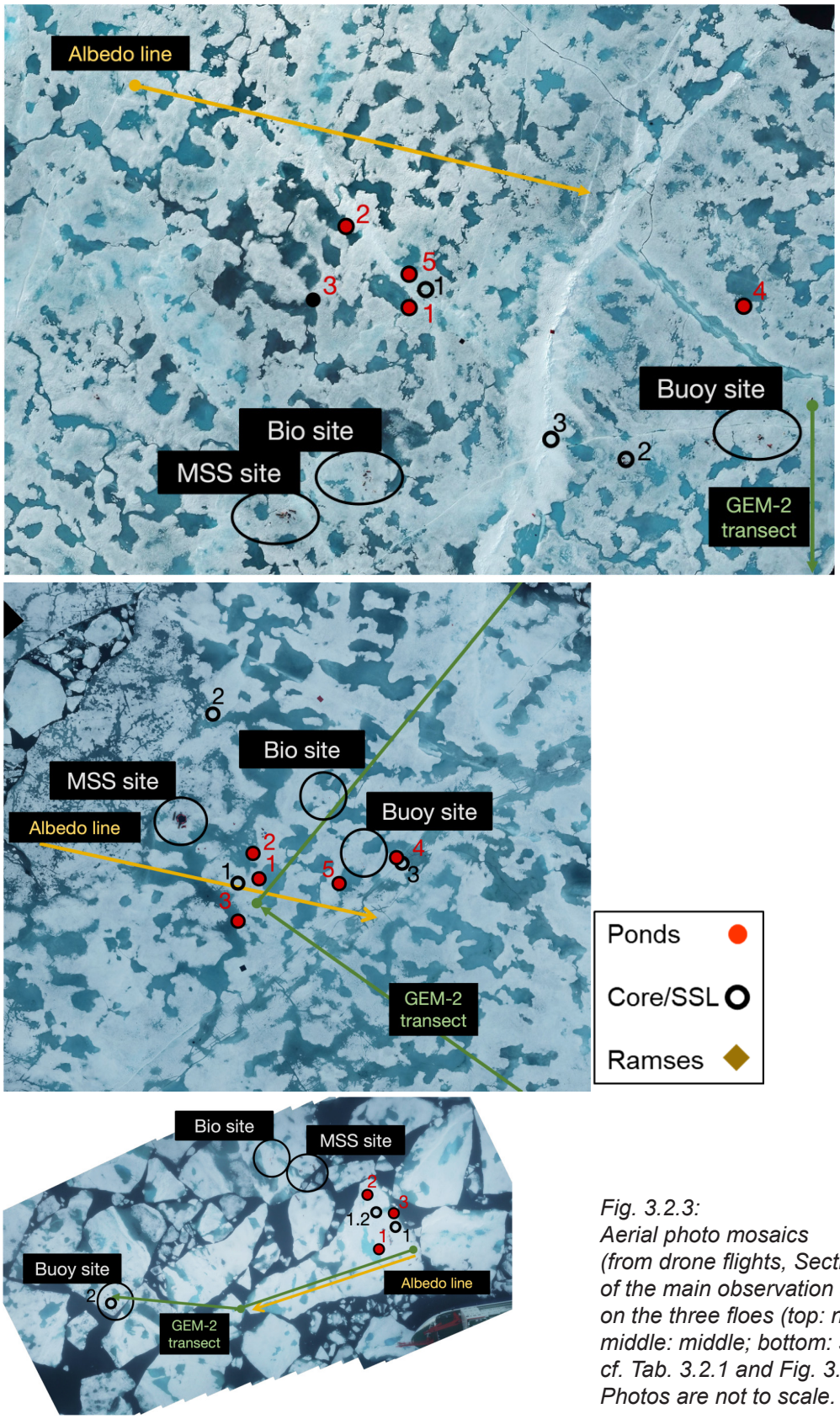

Fig. 3.2.3:
Aerial photo mosaics (from drone flights, Section 3.3) of the main observation sites on the three floes (top: north; middle: middle; bottom: south; cf. Tab. 3.2.1 and Fig. 3.2.1). Photos are not to scale.

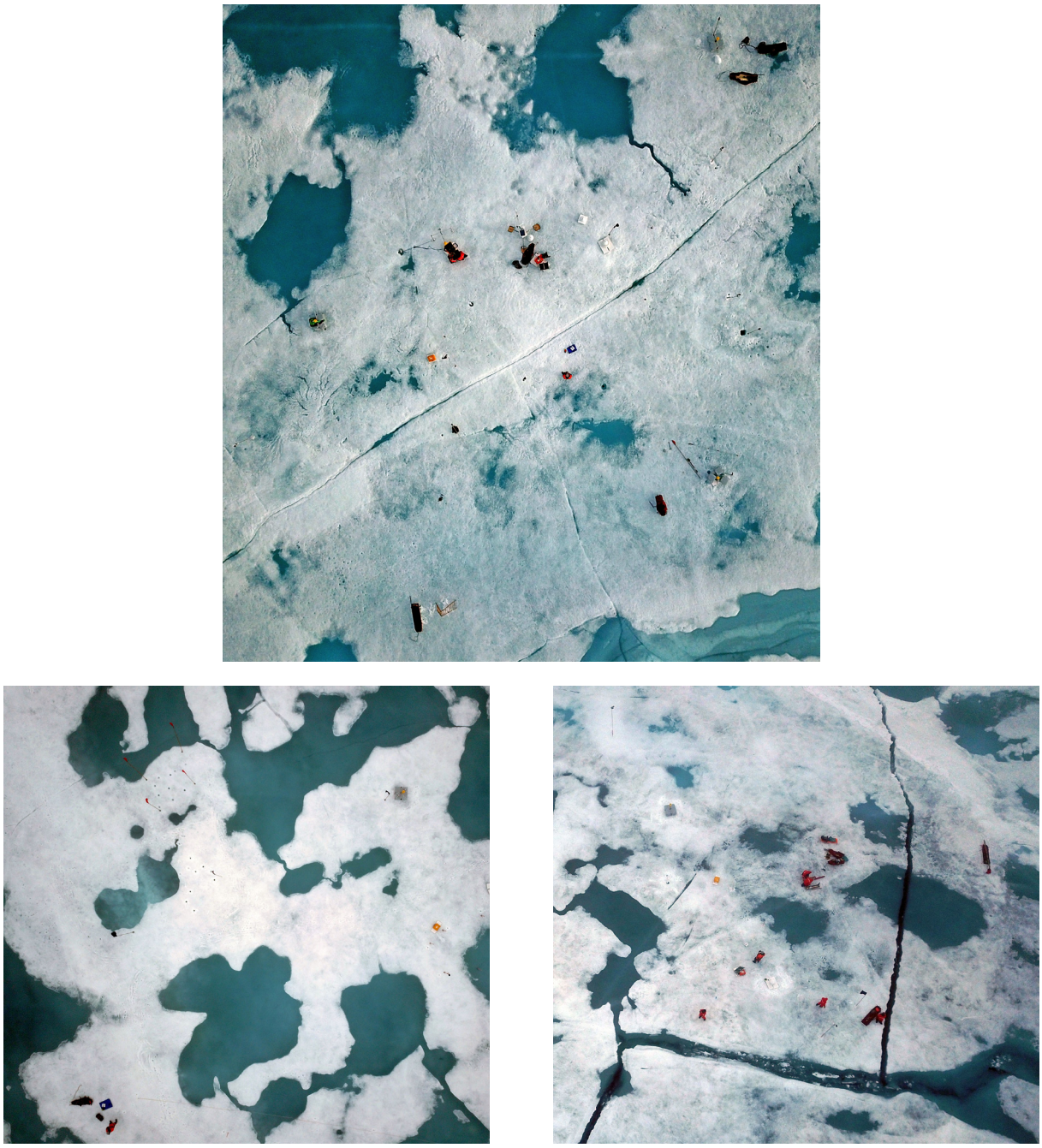

Fig. 3.2.4: Overview of buoy sites on floe N (top), M (bottom left), and S (bottom right). Cf. Table 2.20 for a list of instruments deployed at each site. Figures 2.24 - 2.26 are annotated versions of this figure with all buoy details marked.

Preliminary results

Preliminary results are presented in the respective Chapters about ice mass balance and melt pond studies (3.3 and 3.4), and oceanography (2.).

3.3 Sea ice thickness and mass balance

Christian Haas[1], Mara Neudert[1], Mario Hoppmann[1] [1]DE.AWI
not on board: Jan Rhode[1]

Objectives

Thickness is one of the most important properties of sea ice, and the state of sea ice and any changes can only be well understood if it's thickness is known as well. This is particularly true for the main goals of PS131, as the effect of ocean and atmosphere heat flux and ice melt on sea ice can only be observed with thickness measurements. As ice thickness is very variable at many different spatial scales, the objective was to carry out large-scale ice thickness measurements, small scale measurements to characterize individual floes and their change, and local measurements to continuously observe temporal scales. For the large-scale, we have carried out helicopter electromagnetic induction (HEM) sea ice surveys. Individual ice floes were surveyed with a ground-based multifrequency EM instrument. Observations of temporal changes were carried out with autonomous sensors on, in, and below the ice. All these methods and preliminary results are described in this Chapter.

A particular goal of our work was the application and improvement of multifrequency measurements to retrieve not only ice thickness but also other information about the porosity and salinity of the ice. Therefore, we also measured the salinity and depth of melt ponds, and gathered extensive drill-hole validation data. Under summer conditions sea ice is both highly porous and permeable. However, measurements of sea ice porosity and their influence on EM sensors and on the total ice volume are spatially and temporally limited. Attempts to quantify porosity have been made during earlier cruises (e.g., PS94, MOSAiC). We aim to retrieve ice porosity by geophysical inversion of the EM sensor that is used for the ice thickness surveys.

The primary objectives of the ground-based measurements during floe (re-)visits were therefore to extend the record of sea ice thickness in the MIZ and to retrieve time series of melt rates, melt pond concentration, depth and salinity.

The tasks for this objective can be broken down as following:

- Gather ice thickness drill hole measurements and ablations stake readings to assess the influence of surface and bottom melt over time and the small-scale variability across each floe.
- Obtain high resolution ice thickness data of individual floes
- Collect measurements of depth, conductivity and temperature of melt ponds and their evolution as they are a key feature of sea ice in summer and influence the EM sensor response.
- Assess retrieval of sea ice porosity by geophysical inversion of the EM sensor data using conductivity measurements and reference drill hole lines.

Work at sea

Helicopter ice thickness surveys

We carried out helicopter-borne frequency-domain electromagnetic induction (HEM) sounding surveys to measure total sea-ice thickness (ice thickness plus snow depth) along helicopter flight tracks (Haas et al., 2009). During ATWAICE we used two different EM systems, the Canadian "Rosie" EM Bird and a new EM Bird built by Jan Rohde at AWI. The 4-m long

instruments are towed on a 20 m long cable underneath the helicopter and measure the sea-ice thickness in a height of 10-15m above the surface. A laser altimeter and laser scanner (only in Rosie) are integrated in the EM-Bird system, measuring the distance to the surface in a 30 m wide, 2D swath along the flight. Besides its role for sea ice thickness calculation, the laser data and accompanying DGPS receivers allow the retrieval of snow freeboard and surface roughness and accordingly ridge density and distribution.

Ice conditions were also documented by hand-held, oblique photography.

In total, we carried out 7 EM flights, six over sea ice and one test flight over open water. Flights aimed to pass over the three main ice floes and to cover parts of the oceanographic/biological ship transects, and to cross the ice edge. However, only three surveys were successful in doing so due to marginal weather conditions otherwise. The weather only allowed two periods of helicopter surveying in the MIZ study region, one between 16 – 20 July, and one on 30 July. Therefore, the maximum time difference between repeat flights was only 10 – 13 days. All HEM surveys are summarized in Table 3.3.1 and in Figure 3.2.1.

Tab. 3.3.1: Overview of all conducted EM-Bird flights

Flight ID	Date	Time (UTC)	Description
HEM1	2022-07-08	07:49	Test of AWI EM Bird over open water
HEM2	2022-07-16	15:19	Survey with AWI EM Bird across ice edge, only short due to fog
HEM3	2022-07-17	07:45	Good survey with AWI EM Bird passing over buoy sites and along ship track. Have seen flags of the northern floe.
HEM4	2022-07-18	12:10	Survey with EM Bird Rosie over floe S and M, not enough fuel to extend.
HEM5	2022-07-19	07:12	Good survey with EM Bird Rosie, over all three floes and along ship track.
HEM6	2022-07-20	07:21	Short survey towards ice edge aborted due to fog.
HEM7	2022-07-30	08:55	Good survey with EM Bird Rosie, over all three floes and along ship track.

Aerial photography with Mavic Pro Drone

At each ice station ice conditions and melt pond coverage was documented by flights with a Mavic Pro Drone. During most flights, nadir photos were taken in intervals of 2 seconds, from altitudes ranging between 40 and 400 m depending on weather and cloud conditions. There was sufficient overlap for generating photo mosaics of each floe using the PTGui software. During each flight, also few oblique photos were taken for a better view of the wider surroundings. In Greenland, videos of the ship and ice floes were taken and provided to AWI's communication department.

Drone flights encountered severe problems with weather conditions and magnetic interference from the ship, possibly enhanced by the ship's radar. Low cloud often led to strong moisture accumulation on the drone and the camera lens. In foggy conditions communication between the remote control and drone was often lost. Therefore the drone was only flown with full manual control, and apps for automatic surveying were not used.

Drone data were shared with all cruise participants and examples of drone footage can be found throughout this report, and in particular in Chapter 3.2.

Ship-based underway measurements

a. SIMS

In order to resolve the ice thickness variability and gradients and their temporal change across the MIZ, we used an EM sounder deployed by the bow crane (Sea Ice Monitoring System SIMS, Haas (1998)) to measure ice thickness continuously along the ship's track (Figure 3.3.1). Of particular interest were the joint, coincident surveys with the towed underwater TRIAXUS CTD system to relate ice thickness variability and change to ocean properties and processes.

The SIMS was operated from the first day of entering the MIZ over the Yermak Plateau on 11 July to the last moment leaving it on 2 August. It obtained an almost continuous ice thickness record along the cruise track, including the transits to and from the Aurora Vent Field, with the exception of a few hours when the instrument had stopped due to unknown technical issues. In particular, coincident data were obtained with TRIAXUS surveys MIZ2a&b (16 – 19 July), MIZ3a&b (29 – 30 July), and Streak1&2 (1 August).

b. Laser scanner

In addition to the SIMS measurements, a Velodyne HDL-32E laser scanner was operated from the bow crane to measure sea ice freeboard and roughness in front of the ship. This is a 903 nm NIR laser scanner with 32 lasers arranged with viewing angles from 10.67° to −30.67° with respect to the normal viewing direction perpendicular to the rotating axis (Fig. 3.3.2). The HDL-32E was mounted forward of the crane with the rotating axis oriented horizontally ahead, at a height of approximately 15 m above water, scanning a swath across the ship's track (Fig. 3.3.3). The field of view was limited to +/- 70 degrees from nadir, resulting in a swath width of approximately 70 m. The objective of these measurements is to provide spatial context for the SIMS measurements, to help understanding how much of the SIMS footprint is covered by ice. In addition, as the swath is wider than the hull of the ship, the data will help better understand ship-ice interaction than is possible with the SIMS alone.

The Velodyne measurements were carried out as a pilot project, as the electronic set-up and real-time data acquisition were developed in a student project and were not suitable for week-long, continuous operation. Therefore, it was only operated intermittently during day times between 25 July and 1 August. In order to keep file sizes reasonably small individual surveys were only 0.5 to 1 hour long. However, often they are much shorter because the real-time data acquisition system stalled.

c. Cameras

In addition to the Panomax and IR and GoPro cameras operated throughout the cruise to observe general ice conditions (Chapter 3.1, Fig. 3.1.2), dedicated surveillance cameras were operated directly at the ship's bow overlooking the SIMS and the ice underneath and ahead in order to document general ice conditions and to relate thickness measurements and ship motions to actual ice conditions immediately at the bow. Between 12 and 22 July a photograph was taken every 30 seconds. Unfortunately, operations were affected by power outages from insufficient charging by the associated solar panel, and images are often blurred by sleet or rain drops on the lens. In order to obtain more reliable photos, another Reolink camera with a sampling interval of 5 minutes was used from 30 July to 2 August, however experiencing the same environmental challenges.

Fig. 3.3.1: Photograph of the Sea Ice Monitoring System (SIMS) suspended from the bow crane of the Polarstern and continuously measuring ice thickness along the cruise track by means of EM sounding. Over open water an ice thickness of zero is obtained. Foreground shows ground-based EM measurements using the same method with the GEM (see Section In-situ observations of ice thickness)

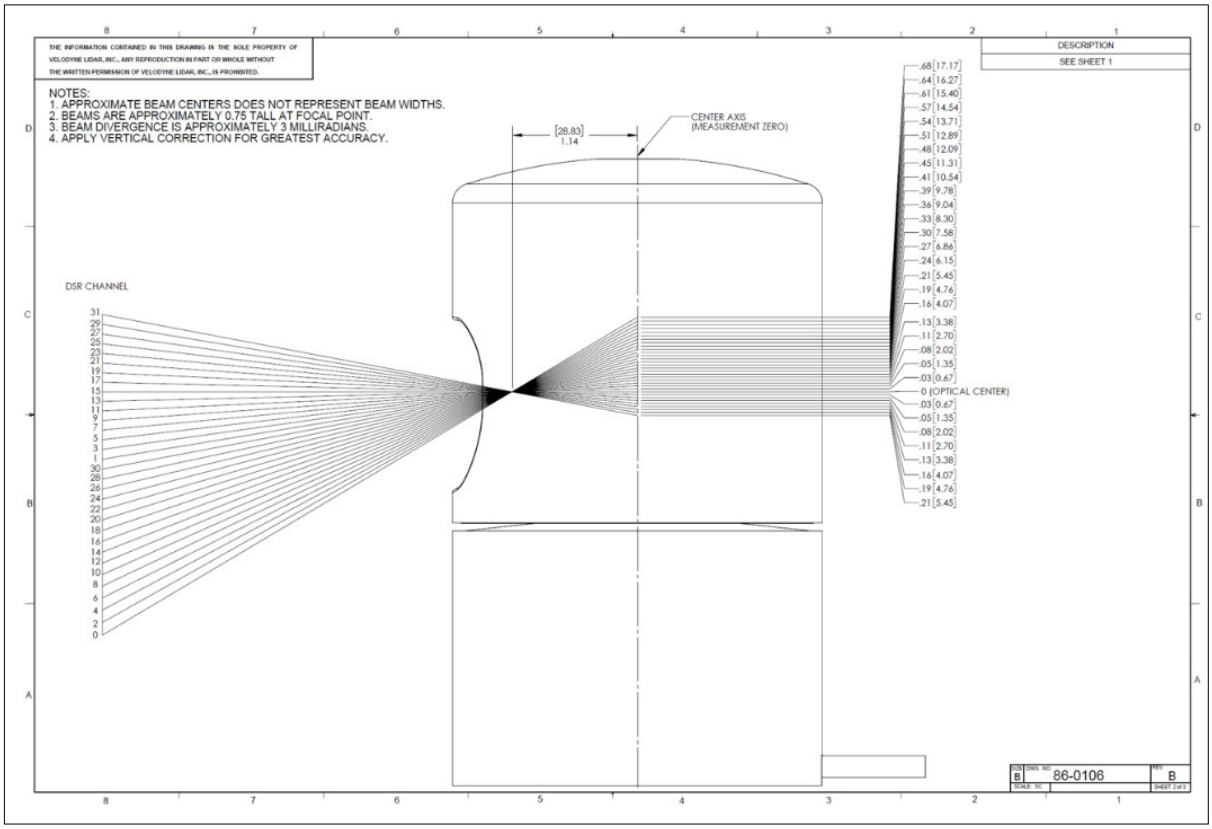

Fig. 3.3.2: Schematics of the Velodyne HDL-32E laser scanner operated from the ship's bow crane, mounted horizontally with the rotating axis pointing forward

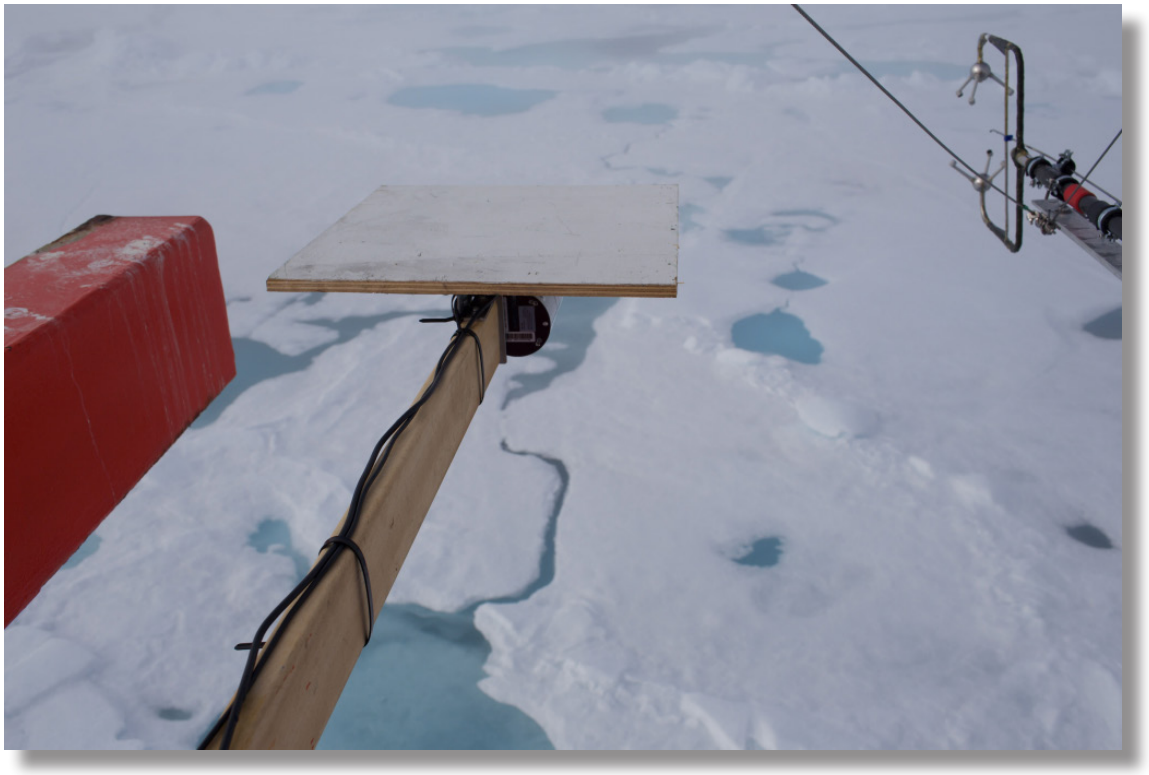

Fig. 3.3.3: Photograph of the Velodyne HDL-32E laser scanner mounted at the bow crane and scanning the ice below the bow, perpendicularly to the steaming direction

In-situ observations of ice thickness

Direct observations of ice thicknesses and surface ablation conducted during ATWAICE were performed with the following methods

- Ice thickness drilling and ablation stake readings
- GEM-2 transects

An overview of ice thickness drill hole measurements and ablation stake readings can be found in Table 3.3.2 – Table 3.3.4. More ice thickness drill holes are reported in Chapter 2 in conjunction with the under-ice CTD measurements. For all drill holes the following additional parameters are available: longitude, latitude, timestamp, draft. For most drill holes, the weathered layer thickness, as well as presence, type and thickness of potential false bottoms were recorded.

Tab.3.3.2: Overview of drill hole and ablation stake measurements at the buoy sites of every floe (cf. Chapter 3.2)

Floe name	Visit #	Date, 2022	Buoy site				Ablation stakes
			Nr. drill holes	Mean TT [m]	Min/Max TT [m]	Comment	Nr. stake readings
FloeN	1	07/13	9	1.93	1.89/1.95	AWIRad, 3 ADCP, 1 SIMB, 4 GEM calibartion; 6 drill holes with false bottoms with and without gaps	6

Floe name	Visit #	Date, 2022	Buoy site				Ablation stakes
			Nr. drill holes	Mean TT [m]	Min/Max TT [m]	Comment	Nr. stake readings
	2	07/20	6	1.77	1.67/1.82	5 GEM calibration, 1 SIMBA; 1 false bottom (hard interface) at SIMB hole	3
	3	07/30	13	1.52	1.34/1.70	AWIRad, 1 SIMBA, 5 GEM calibration, 6 ablation stakes; 4 drill holes with false bottoms (no gap)	6
FloeM	1	07/15	0				3
	2	07/22	10	1.11	0.94/1.22	7 with false bottom without gap (hard interface)	3
	3	07/31	5	1.02	0.94/1.08	No false bottoms	2
FloeS	1	07/14	6	1.52	1.30/1.65	1 SIMB, 5 GEM calibration	3
	2	07/21	3	0.87	0.85/0.90	3 Ablation stakes	3
	3	07/31	3	0.88	0.68/1.39	3 ablation stakes	3

Tab.3.3.3: Overview of drill hole and ablations stake measurements at the other sites

Floe name	Visit #	Date, 2022	Other sites				Ablation stakes
			Nr. drill hole	Mean TT [m]	Min/Max TT [m]	Comment	Ablation stakes
FloeN	1	07/13	—	—	—		3
	2	07/20	—	—	—		5
	3	07/30	—	—	—		6
FloeM	1	07/15	7	1.32	1.20/1.39	5 GEM calibration site (between pond and buoy site), 2 close by in drained melt pond	3
	2	07/22	10	1.21	1.18/1.24	5 at old GEM cal site, 5 at new cal site (50 m from buoy site); 7 with fasle bottoms hard, 1 with false bottom with gap	7
	3	07/31	10	1.05	1.02/1.08	5 at old GEM cal site, 5 at new cal site (50 m from buoy site); 2 with false bottoms hard	3
FloeS	1	07/14	1	2.03	2.03/2.03	RAMSES hole, close to ship	1
	2	07/21	5	2.72	2.60/2.86	GEM calibration at Pond site	1
	3	07/31	5	2.47	2.24/2.68	GEM calibration at Pond site	1

Tab.3.3.4: Overview of drill hole measurements along the drill hole lines

Floe name	Visit #	Date, 2022	Drill hole line			
			Nr. drill holes	Mean TT [m]	Min/Max TT [m]	Comment
FloeM	1	07/15	21	1.31	1.18/1.50	5/21 in ponds, 13 with false bottoms with gap
	2	07/22	21	1.00	0.80/1.22	8/21 in ponds, 5 with false bottoms (hard interface, no gaps)
	3	07/31	21	0.84	0.69/1.13	14/21 in ponds, 1 false bottom (hard interface)

At the main ice stations, GEM-2 thickness transects were established in order to represent the variability across the floe and to be repeated easily. The Geophex GEM-2 is a broadband electromagnetic induction sensor. It was towed in a pulka and measuring the total thickness. For calibration purpose a wooden ladder was used to carry out measurements at stepwise increasing distances to the conductive water. Along the GEM transects we also collected data about melt pond depth and salinity using a WTW Cond3110 conductivity probe and a ruler stick.

The transects on Floe North and Floe South were not accessible in full length at visit 2 and 3 due to floe break-up, however it was possible to repeat them partially.

In addition to the repeat transects, we established a 100 m long line with drill holes spaced 5 m on Floe Middle that was repeated on every visit.

We also carried out GEM-2 transects by floe visits by zodiac, at the 24h MSS ice station and at the ice stations East Greenland 1 and East Greenland 2. Table 3.3.5 provides an overview of GEM-2 operations and auxiliary data.

Tab.3.3.5: Overview of GEM-2 operations and auxiliary data

Floe name	Visit #	Date, 2022	Main GEM-2 transect				Drill hole line	Other activities
			Distance [m]	Nr. ponds	Nr. pond salinities	Comment	Distance	
FloeN	1	07/13	1036	24	—		—	Calibration; Initial survey of the floe on 2022/07/12
	2	07/20	892	24	15		—	Calibration
	3	07/30	878	26	15		—	Calibration; Long transect across entire floe and albedo line
FloeM	1	07/15	930	18	11		100	Calibration; Survey around buoy site
	2	07/22	886	29	24		100	Calibration
	3	07/31	934	34	24		100	Calibration
FloeS	1	07/14	1586	11	5		—	Calibration
	2	07/21	904	14	11		—	Calibration

Floe name	Visit #	Date, 2022	Main GEM-2 transect				Drill hole line	Other activities
			Distance [m]	Nr. ponds	Nr. pond salinities	Comment	Distance	
	3	07/31	94 & 214	12	8	Separate transects on buoy site floe and pond site floe	—	Calibration
MSS	—	07/28	370	5	4	Data of first part lost	50	Calibration; Grid line survey around MSS site (about 2 km in total)
EG 1	—	08/06	3810	—	—		100	Calibration
EG 2	—	08/06	1204	—	—		—	Calibration
Zodiac 1	—	07/12	293	—	—	1 floe	—	Calibration
Zodiac 2	—	07/19	620	—	—	9 floes,10-50 m size	—	
Zodiac 3	—	07/29	140	—	—	3 floes, from 20-50 m size	—	

Continuous autonomous measurements

In order to observe sea ice changes and boundary conditions, several autonomous measurements were performed by our group in addition to the extensive autonomous observations carried out by the oceanography group (*cf*. Chapter 2).

a. Automatic Weather Station (AWS)

On the northern floe, an automatic weather station (AWS) was operated to observe air temperature, humidity, and pressure, 2 m wind speed and direction, and incoming and outgoing short- and longwave radiation (Fig. 3.3.4). Measurements were carried out every 10 minutes and logged with a Campbell CR3000 data logger. The station was recharged by a solar panel. The AWS was placed on weathered ice, with the radiometer mount pointing south (determined by GPS tracking) and reference for wind direction taken. Note that the orientation may have shifted as the floe has rotated in due course which will be determined by GPS data after the cruise.

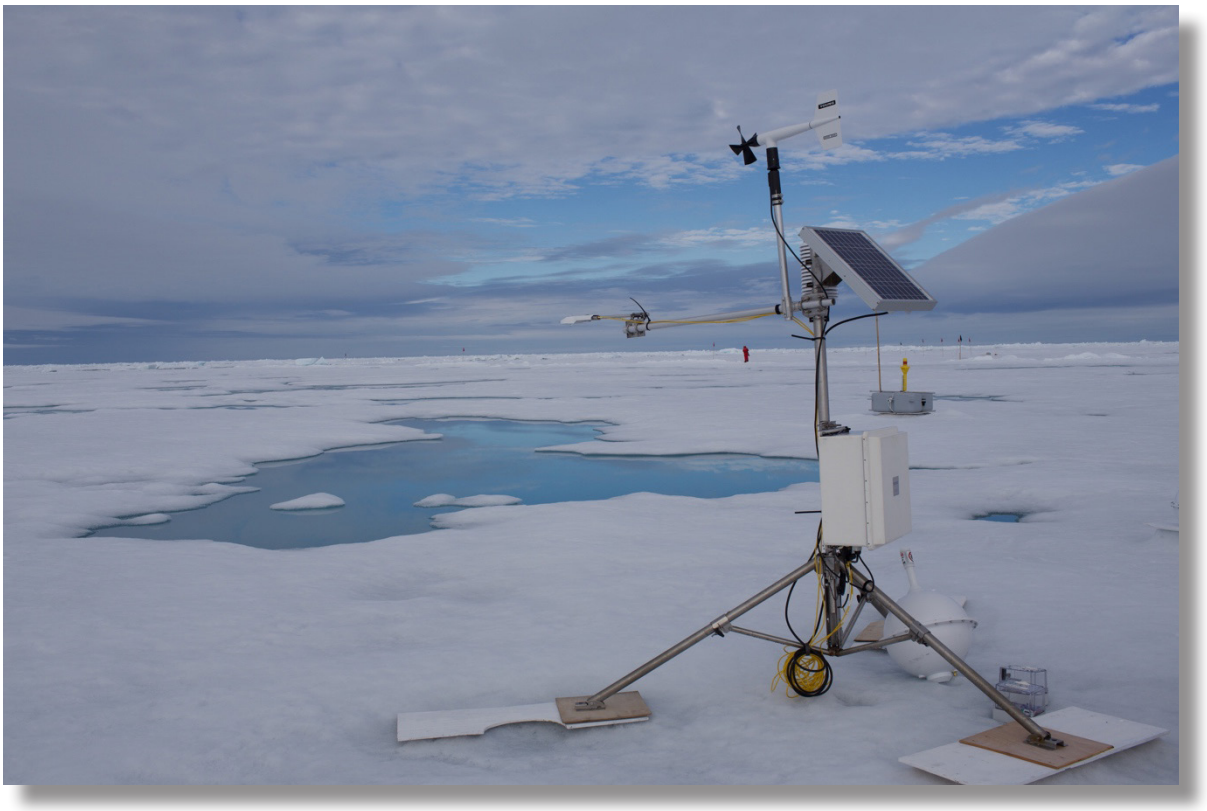

Fig. 3.3.4: Photo of the AWS on the northern floe, taken during the first revisit on 20 July. Radiometers are mounted to point south. Note sinking of wooden feet due to preferential melt. The photo also shows two wave buoys and one SVP placed at the same location, and an ADCP on a float in the background (cf. Chapter 2.)

b. Radiation station

On the northern floe we also deployed a radiation station to fully observe the radiative fluxes onto and through the sea ice. The station was equipped with RAMSES-ACC-VIS hyperspectral radiometers, measuring spectral irradiance from 320 to 950 nm with a resolution of 3.3 nm (Nicolaus et al., 2010) every 10 minutes. Two sensors were mounted above the ice, looking up and down, and one was hung 1 m below the ice, looking up (Fig. 3.3.5).

Fig. 3.3.5: Photo of the radiation station on the northern floe, taken during the first revisit on 20 July; the up- and downlooking radiometers and the yellow power and data logging unit can be seen. Note tilt due to surface ablation. In the bottom left corner the deployment hole for the up-looking, underwater radiometer can be seen. Yellow cone is a Southtek GPS drifter (cf. Chapter 2.).

c. Seasonal Ice Mass Balance Buoys (SIMB)

We operated three SIMB-3 seasonal ice mass balance buoys manufactured by Cryosphere Innovation. They were deployed on the northern floe on 13 July, the southern floe on 14 July, and another, 30 m x 30 m small, 1.84 m thick floe at 81.0014 N, 8.5156 E on 16 July (Tab. 3.3.6; Fig. 3.3.6). Every 4 hours, the SIMBs measured GPS position as well as the distance between two sonic range finders above and below the ice and the ice surface and bottom, allowing calculation of ice thickness and observation of ice thickness change. The SIMBs also measured air temperature and pressure, and water temperature. An innovative feature was a CTD integrated within the hull of the SIMB near the bottom sonar. Unfortunately the location of the CTD was not well ventilated and the sensors were not well calibrated, such that measurements are to be used with care.

The SIMBs were deployed through 10 inch drill holes (Fig. 3.3.6). Under the prevailing summer conditions those drill holes did not refreeze completely, such that the SIMBs remained freely floating. Therefore, it was not possible to observe changes of freeboard or draft separately. Due to continuous motion and rotation of the SIMB'3s in their drill holes measurements are also more noisy than they would be otherwise, in particular in the presence of swell which was experienced by the southernmost device. However, under the impression of melt water stratification within the drill holes they did refreeze somewhat, such that recovery of the two northern SIMBs became difficult and required widening of the holes.

Table 3.3.6: Overview of SIMB deployments

ID	IMEI	Deployment	Operating period	Total thickness and draft at deployment [m]
SIMB#1	300434064564590	Southern floe	July 14-31	1.30, 1.18
SIMB#2	300434064565670	Northern floe	July 13-30	1.92, 1.74
SIMB#3	300434064564600	Small floe in outer MIZ 81.0014N, 8.5156E	July 16-ongoing	1.84, 1.66

Fig. 3.3.6: Photograph of the southernmost SIMB deployed on a small floe; the deployment drill hole and the upper surface-sensing sonic rangefinder can be seen, as well as the radiation shield of the air temperature sensor and barometer on top. Note wave buoy SN 206716 (IMEI 300434066018140) deployed nearby, to the left (cf. Chapter 2)

Preliminary results

Helicopter ice thickness surveys

The map in Figure 3.2.1 shows an overview of all carried out HEM flights (orange and yellow). These showed the gradients from thin ice near the ice edge to thick ice in the north. Figure 3.3.7 shows an example of a 40 km long survey from the north (left) to the ice edge (right) carried out on 30 July. The thickness gradient can be well seen. However, there as also a region of thinner ice around a distance of 10 km, in the vicinity of the middle floe. The thickness distribution shows various peaks indicative of strongly changing conditions along the profile. The mode was at 1.3 m, in good general agreement with other measurements.

All HEM surveys suffered from a lack of sufficient laser returns from open water which are needed for accurate calibration of the measurements. This affected both, measurements with the AWI bird and measurements with EM Bird Rosie which possessed different lasers. Therefore the issue is most likely not due to technical problems but to properties of the water which was very smooth in the calm wind conditions experienced, and which was probably very clear due to it's strong meltwater stratification with little plankton growth in the uppermost layers.

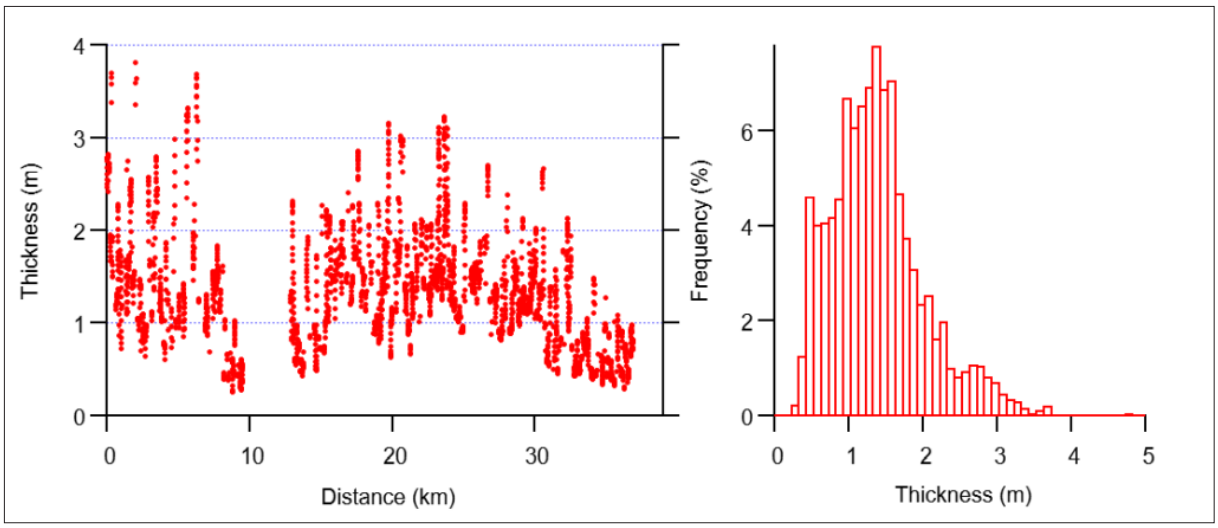

Fig. 3.3.7: Left – HEM ice thickness profile from floe north (left) to the ice edge (right) obtained on 30 July (cf. Fig. 3.2.1). Right – Ice thickness distribution of the same profile

Ship-based underway measurements

a. SIMS

The Sea Ice Monitoring System (SIMS, Section Ship-based underway measurements, above) was operated almost continuously while in the ice in the MIZ, between 11 July and 2 August. The following examples show typical gradients across the MIZ that were observed concurrently with the oceanographic TRIAXUS CTD system. Figure 3.3.8 shows a typical example of raw data from a transect from the ice edge into the closed pack ice. The first band of ice was crossed at approximately 23:30 UTC on 14 July. Northward, open water (ice thickness = 0 m) and bands of ice are crossed, until the ice cover becomes denser and thicker near the northernmost turning point at approximately 81.05 N at 04:20 UTC on 18 July. Then, a different route was taken back south, with more ice initially but much more ice later on, with only two very narrow bands of ice at 07:10 UTC and 08:15 UTC. The SIMS height above the water was measured with the sonic of the SIMS. Note that it varies a lot in the open water due to the pitching of the ship caused by swell and waves. However, as the ship sails into the ice the height variations decrease, demonstrating the dampening of swell by the sea ice. In fact, after each band of ice crossed reductions of the swell can be seen, while height variations increase again when sailing through the ice due to ship motions caused by ice breaking.

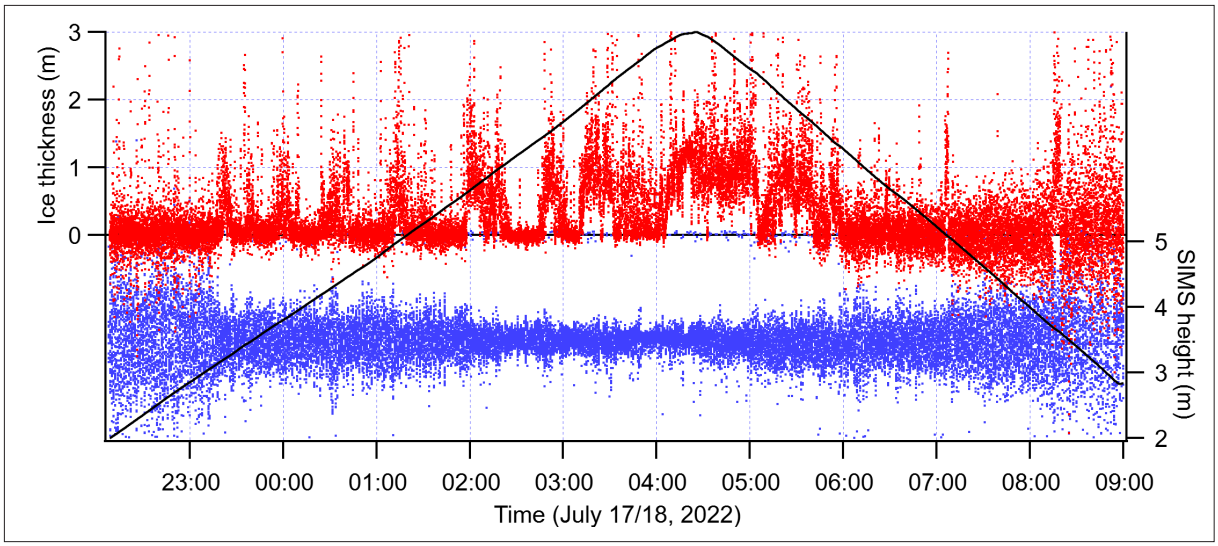

Fig. 3.3.8: Ice thickness (red) and SIMS height above water (blue) during a transect from the ice edge into the closed pack ice and back to the ice edge on 17 and 18 July; black lines show latitude, ranging from 80.55 N at 22:00 UTC to 81.05 N at 04:20 UTC.

Figure 3.3.9 shows another example, from the survey of the prominent ice filament on 1 August (see Fig. 3.3.10). The data are very noisy due to strong swell also visible in the TerraSAR image (Fig. 3.3.10). However, the crossing of the two ice bands can be seen very clearly, and there are significant differences between both. For example, the first crossing farther upstream of the filament shows more variability and is generally somewhat thinner than the second crossing farther downstream. We will investigate if these differences are due to increasing ice convergence farther downstream. In addition, the coincident ice and oceanographic gradients from the interior of the ice filament to the open water are of significant interest and will be studied with additional TRIAXUS and thermosalinograph data.

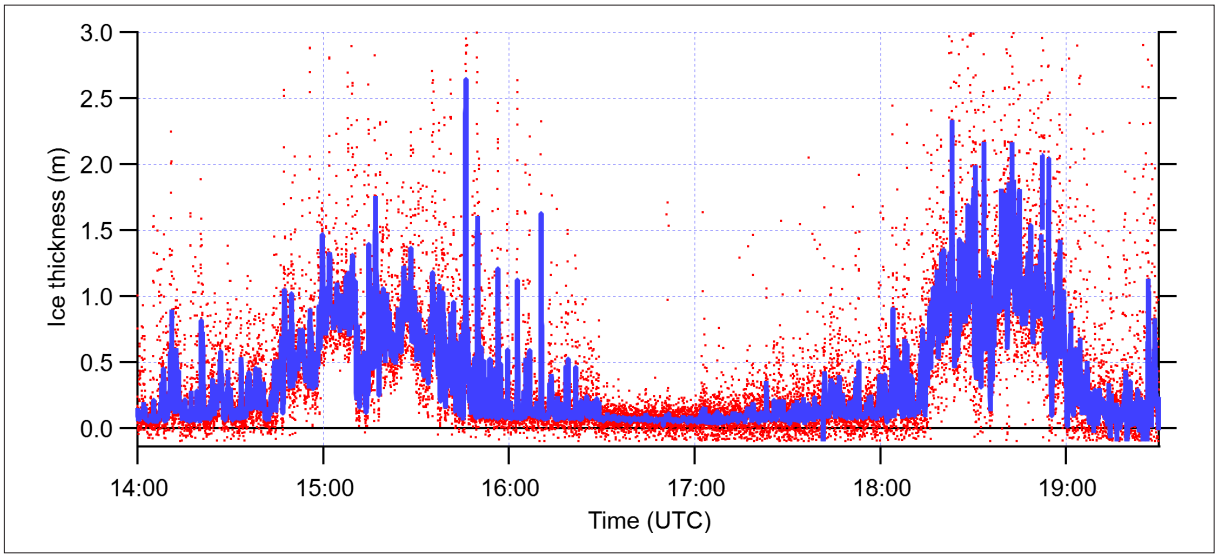

Fig. 3.3.9: SIMS ice thickness profile from the crossing of the prominent ice filament on 1 August (cf. Fig. 3.3.10); red dots show raw data and blue line shows smoothed data using a 21 point median filter.

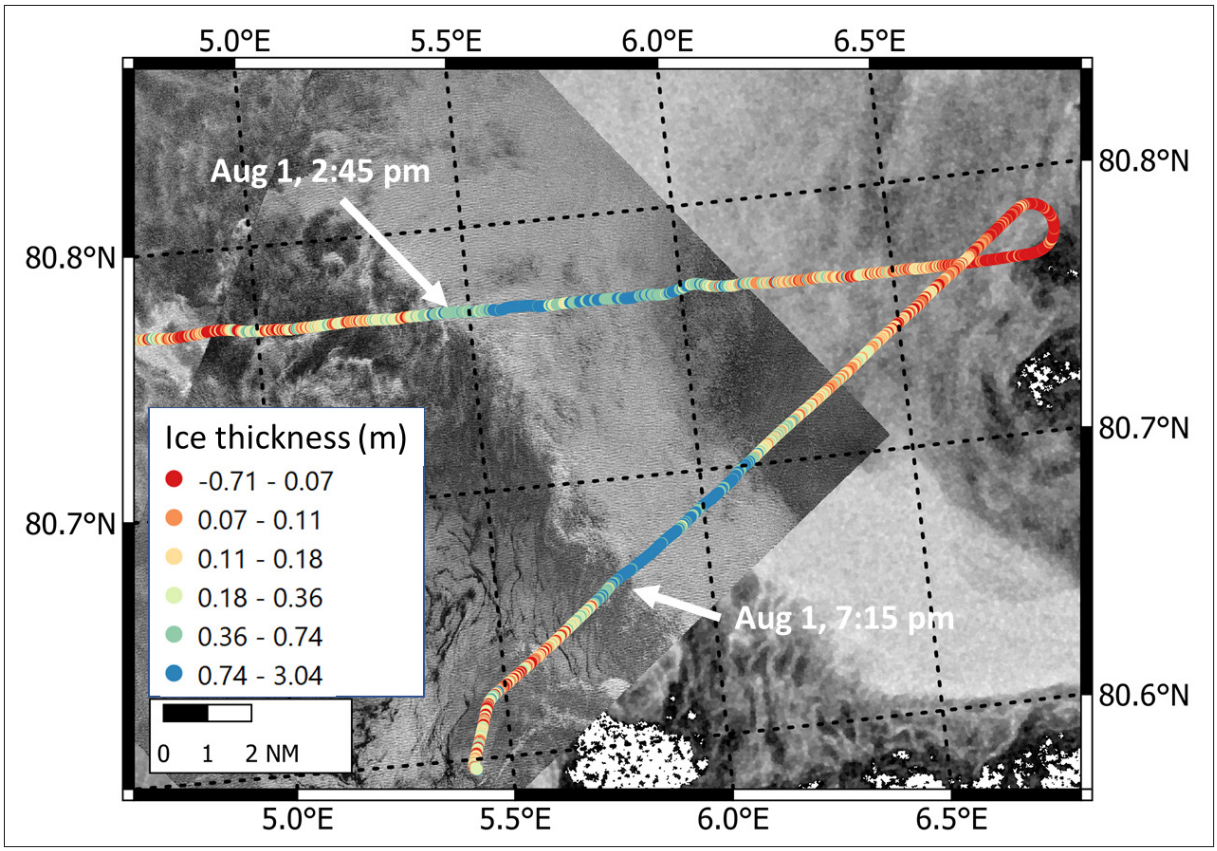

Fig. 3.3.10: SIMS ice thickness profile obtained during the survey of the prominent ice filament on 1 August. Transect started on the middle left and ended at the bottom of the map, times of first entering and last leaving the filament are indicated. Background SAR images are from Sentinel 1 (1 Aug, 07:37 UTC, right part of image) and TerraSAR-X (1 Aug, 15:09 UTC). Note that Polarstern can be seen on the TerraSAR image but is obscured by the thickness data points. Offsets between images and thickness data are due to the dynamic nature of the filament with much ice drift.

b. Laser scanner

The Velodyne laser scanner was only operated sporadically to obtain data in support of feasibility studies and for further development of processing software. Figure 3.3.11 shows an example of one laser scan, seen from the direction of the hull. Owing to the instrument's internal coordinate system, the Y axis is the direction across the ship's track, and the Z direction is the viewing direction, with the scan of the nearest laser shown in red and the farthest shown in purple. The X axis shows height. In y-direction, the example shows different ice surfaces with pressure ridges up to 2 m high. It is tilted with regard to the water level due to the fact that the ship was rolling at the time of measurement, and that the instrument was mounted in a slightly tilted way. The example also shows reflections from the SIMS with its cables and stabilizing lines at heights of 3 to 5 m above the ice. Due to the different range these measurements can be easily removed from the data sets, however, there are also shadows with no data under those obstructions. We assess the operation of the laser scanner as very successful and are confident that we will be able to identify different ice and roughness regimes as well as floe sizes, and can relate them to the motion of the ship.

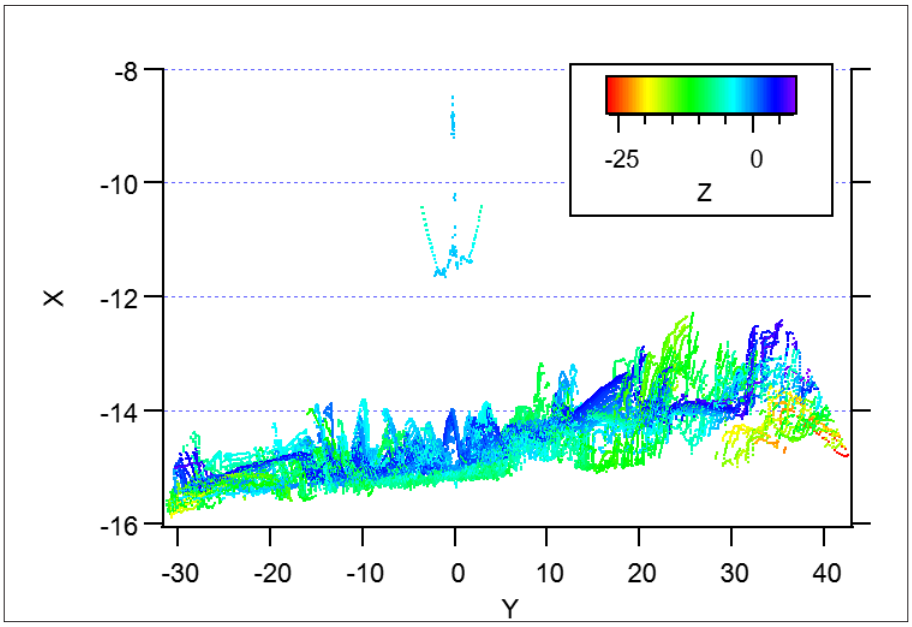

Fig. 3.3.11: Example of one scan of the laser scanner, showing the ice surface between –14 and –16 m, and the SIMS above. Axes are in meters, with the Y axis in the direction across the ship's track, the Z axis in the horizontal viewing direction from the ship forward and the X axis showing height. The laser is at Y=Z=X=0 m.

In-situ observations of ice thickness

At Floe North (Buoy site) the ice thinned from 1.93 to 1.52 m on average over the timespan of 17 days (visit 1 to visit 3), divided into –0.16 m over the first 7 days and –0.25 m over the latter 10 days.

Mean total thickness at Floe Middle (drill hole line) decreased from 1.31 to 0.84 m, with –0.31m melt over the first 7 days and –0.16 m melt over the latter 10 days. The total thickness of melt ponds reported here is the ice thickness plus water depth.

Floe South (Buoy site) mean total thickness decreased by 0.64 m over the first 7 days. This might be an overestimation of melt rates, because five of six drill holes from the first visit were on slightly thicker ice at the GEM calibration site (about 10 m away from the buoy site with the array of ablation stakes). Those were not repeated as they were located on another floe at visit 2 and 3, instead ice thickness at the ablation stakes was measured. This variation in drill hole locations explains the increase of 0.01 m from visit 2 to visit 3 – If we include only the locations at three ablation stakes that were drilled on both visits, we see a decrease from 0.87 m to 0.70 m. These ambiguities highlight the need for ice thickness distributions from spatially distributed surveys conducted with the GEM-2.

GEM-2 ice thickness profile plots were produced immediately after each transect was surveyed for the purpose of quality control and initial evaluation of ice conditions. A typical profile is shown in Figure 3.3.12. The result was corrected for ice drift and different walking speeds or periods without moving the sensor. Figure 3.3.13 shows all transects on Floe North after (approximate) colocation, together with ice thickness histograms indicating a thinning of 30 cm over the 17 days between visit 1 and visit 3. Further processing steps for the ice thickness data will be the inversion with multiple layers to account for changing electric conductivities of melt ponds, ice and sea water (see Fig. 3.3.14). For attribution of spatiotemporal changes in conductivities to different stages of pond evolution, georeferenced ortho-mosaics of the floes together with the measured pond conductivities and the under-ice CTD (Chapter 2) will be used.

In the context of the transect work, the melt pond data will mainly be used to interpret data from the GEM sensor. The results are however most relevant for the wider tasks of PS131 and will be used to characterize the evolution of melt in general.

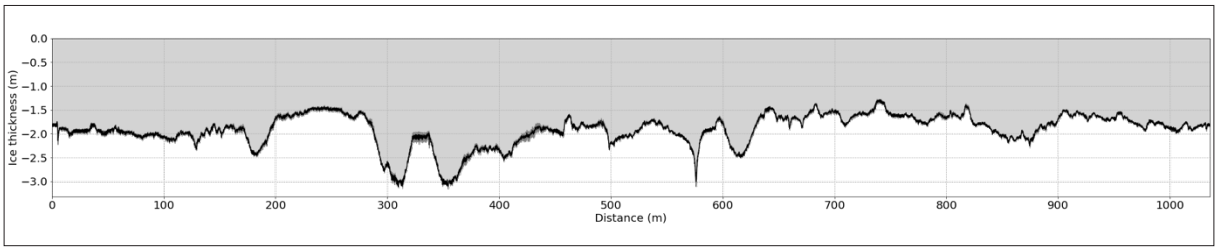

Fig. 3.3.12: Example of an ice thickness profile quicklook from GEM-2, showing repeat transect on Floe North on 13 July after drift correction.

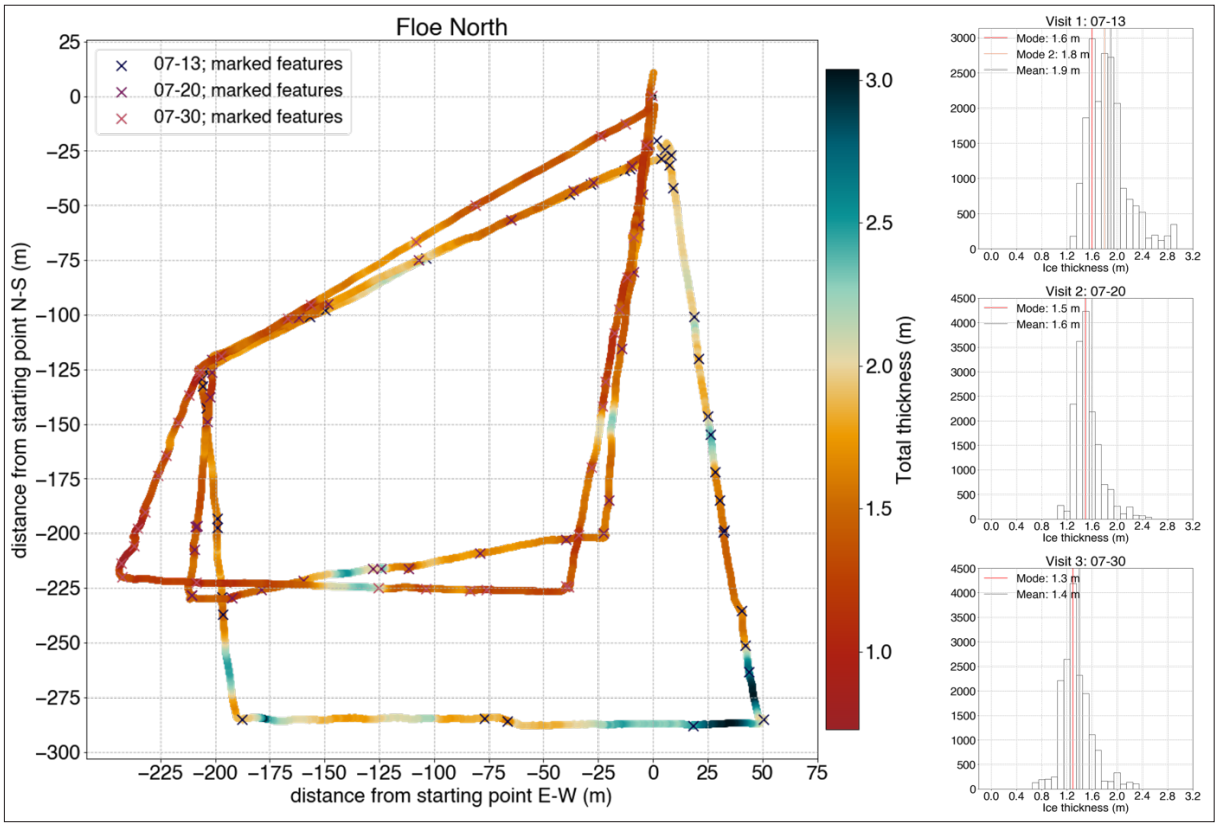

Fig. 3.3.13: Example of an ice thickness map (left panel) from GEM-2 repeat transects on Floe North after drift correction and approximate colocation; measurement locations are given in a reference frame relative to the starting point. Markers indicate features recorded along the way (mainly melt ponds). The right panel shows the corresponding histograms.

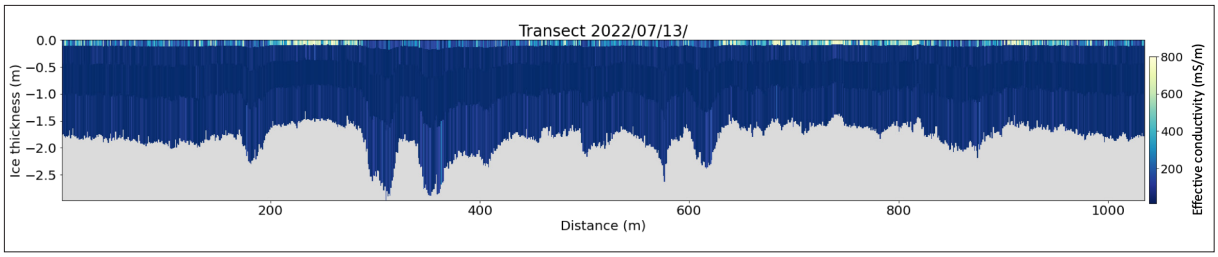

Fig. 3.3.14: Inversion with five ice layers from GEM-2 repeat transect on Floe North on 13 July (same as profile in Figure 3.3.12). The layer thickness was fixed by a forerun inversion with two layers. Ice effective conductivities were restricted to 0–800 mS/m. Sea water conductivity was fixed to 2,670 mS/m. The inversion algorithm used is Robust parameter estimation (Bárdossy and Singh, 2008). The upper layer shows the largest variations in conductivity that can be attributed to melt pond salinities, where an effective conductivity of 800 mS/m corresponds to a salinity of 4 at –1° C.

Continuous autonomous measurements

The continuous, autonomous measurements were highly successful as full data records were obtained by all instruments. They continued to operate without interruption despite strong melting conditions with strong surface ablation, and without damage by polar bears or other wildlife. All instruments were successfully recovered during the second revisit, and can be used in the next project. Only the SIMB in the outer MIZ was left in place as it drifted into an interesting region of an ice streak/filament where it melted rapidly (Fig. 3.3.17), and which was also surveyed by the SIMS (Fig. 3.3.10).

a. Automatic Weather Station (AWS)

Figure 3.3.15 shows the complete AWS data record obtained on the northern floe. While final, absolute calibration of measurements and calculation of energy terms are pending, the data suggest that the first observational period between 13 and 20 July received more energy than the second period, as there was more solar radiation due to dryer air with more clear skies and air temperatures were higher than later. This is in agreement with the general weather observations of *Polarstern's* DWD weather office and subjective experience.

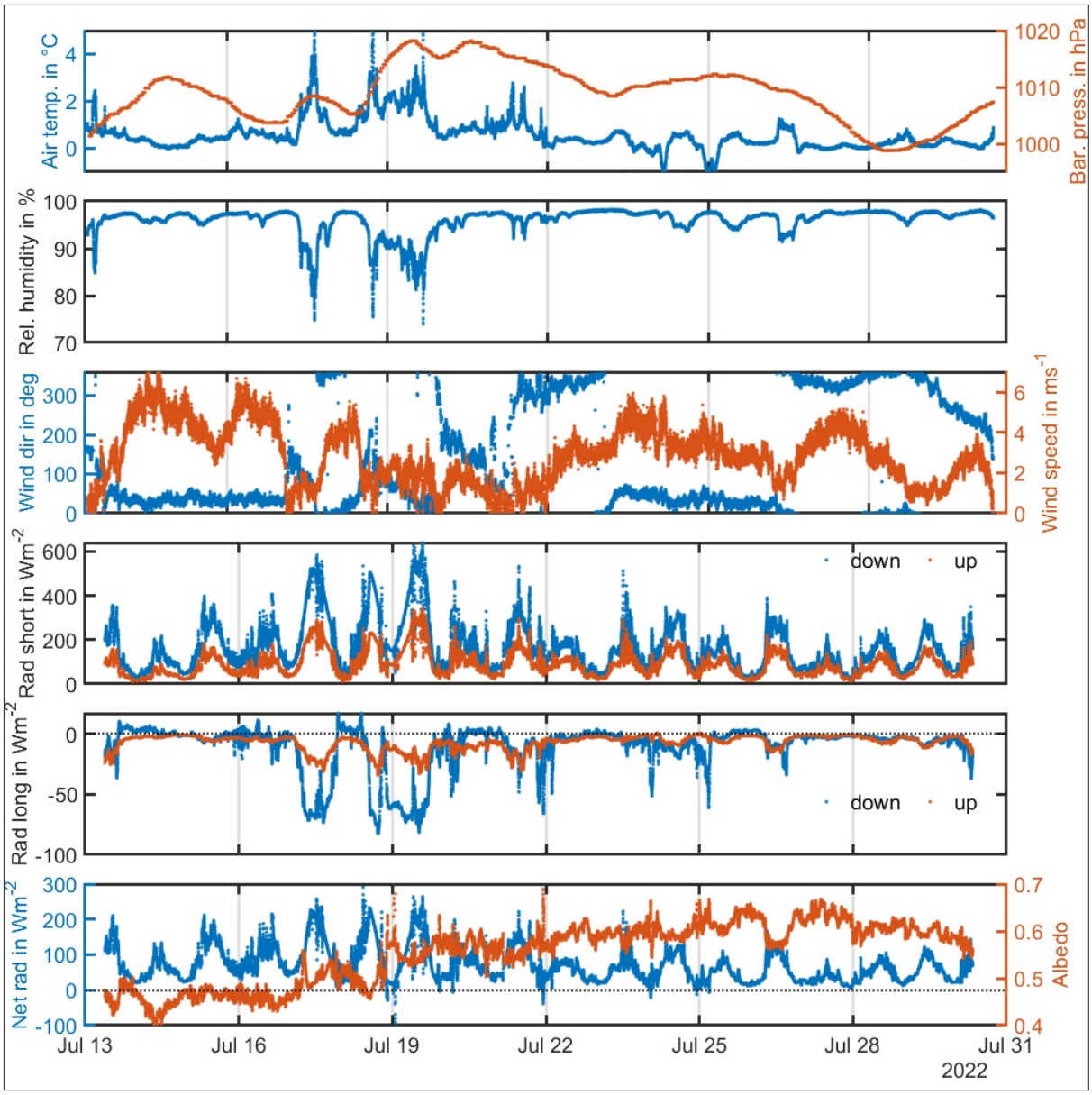

Fig. 3.3.15: Full record of meteorological data obtained by the AWS from deployment to recovery during the last visit

b. Radiation station

Figure 3.3.16 shows the complete record obtained by the radiation station on the northern floe. Results are in close agreement with the AWS (Fig. 3.3.15), showing more shortwave radiation in the first observational period before the first revisit. Sea ice transmittance shows clear temporal variations that must be related to changes of ice properties. Interpretation will be supported by photos from the Reolink SeaIceCams (Chapter 3.1), and surface scattering and ice core observations (Chapters 3.5 and 8).

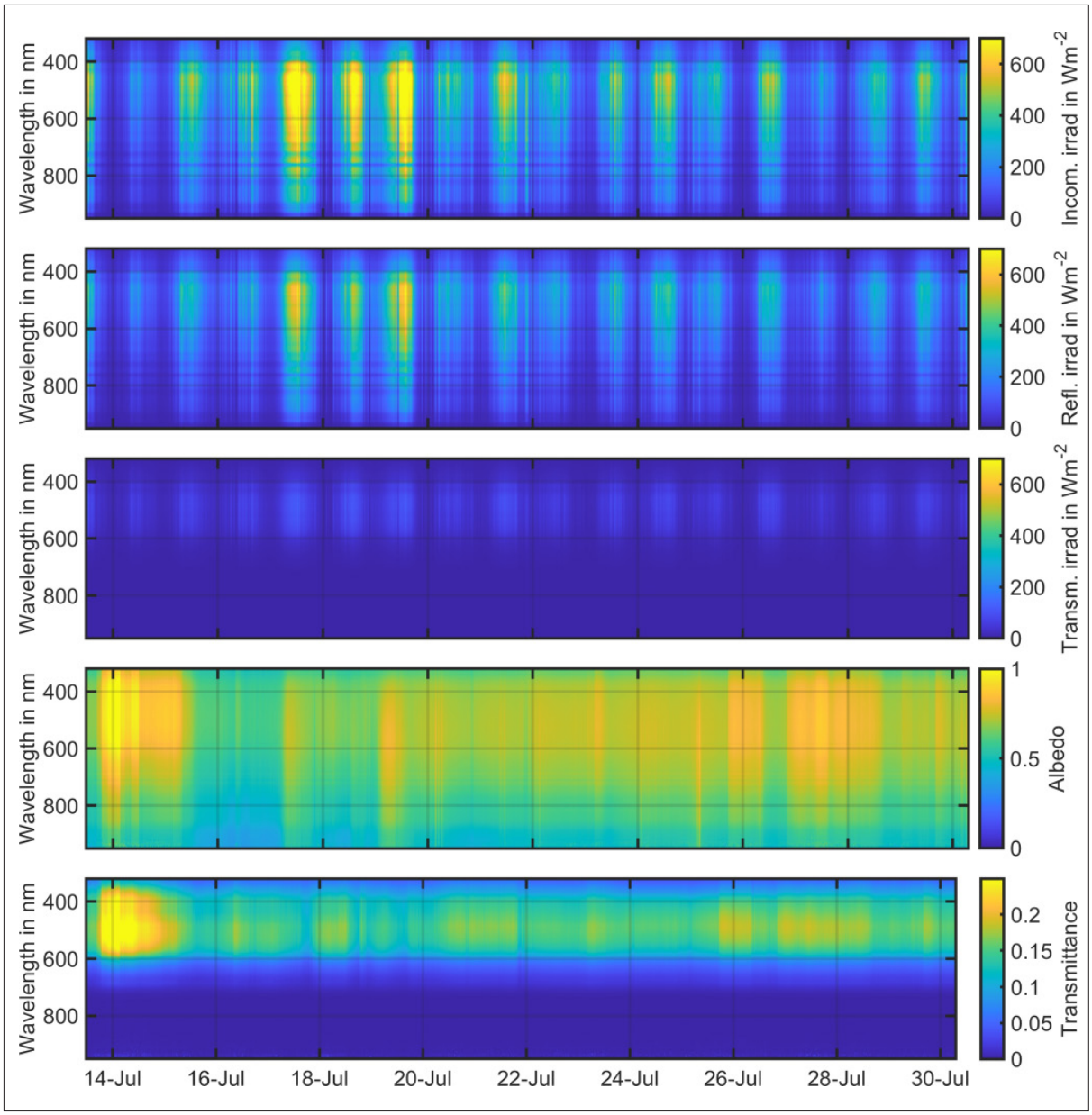

Fig. 3.3.16: Full record of radiation station data from deployment to recovery during the last visit

c. Seasonal Ice Mass Balance Buoys (SIMB)

Figure 3.3.17 shows time series observations of ice thickness change measured by the three SIMBs. The total thinning amounted to between 30 to 40 cm in 17 days, i.e. 1.8 to 2.4 cm per day. The linear fits (dotted lines) in Figure 3.3.17 suggest that the melt rate was similar across the MIZ, and that there were periods of stronger and weaker ice melt. These will be related to the weather station and oceanographic data later. However, the SIMB on the northern floe (red line) showed a strong thinning event in the beginning of observations (on 16 July) which may be related to the disappearance of a false bottom. The SIMB on the outermost floe (black line) showed some strong thinning at the end of the record. This occurred as the buoy neared the ice edge in an ice streak observed by the SIMS (Fig. 3.3.10). In fact, on 4 August the ice thickness measured by that buoy was zero (not shown here), indicating that the buoy was in water and that the ice had completely melted or broken apart. From 2 to 4 August the ice thinned by 1.46 m (73 cm per day).

Figure 3.3.17 also shows results from the ablation measurements at the location of the ablation stakes on the northern, middle, and southern floes. The stakes were observed by the Reolink SeaIceCams, and daily readings were performed visually with the midnight photos. It can be seen that surface ablation amounted to 10 to 30 cm during the observation period, with variations due to different surface conditions at the ablation stake locations. The difference of total melt from the SIMS and surface ablation from the ablation stakes can be attributed to bottom melt due to ocean heat flux.

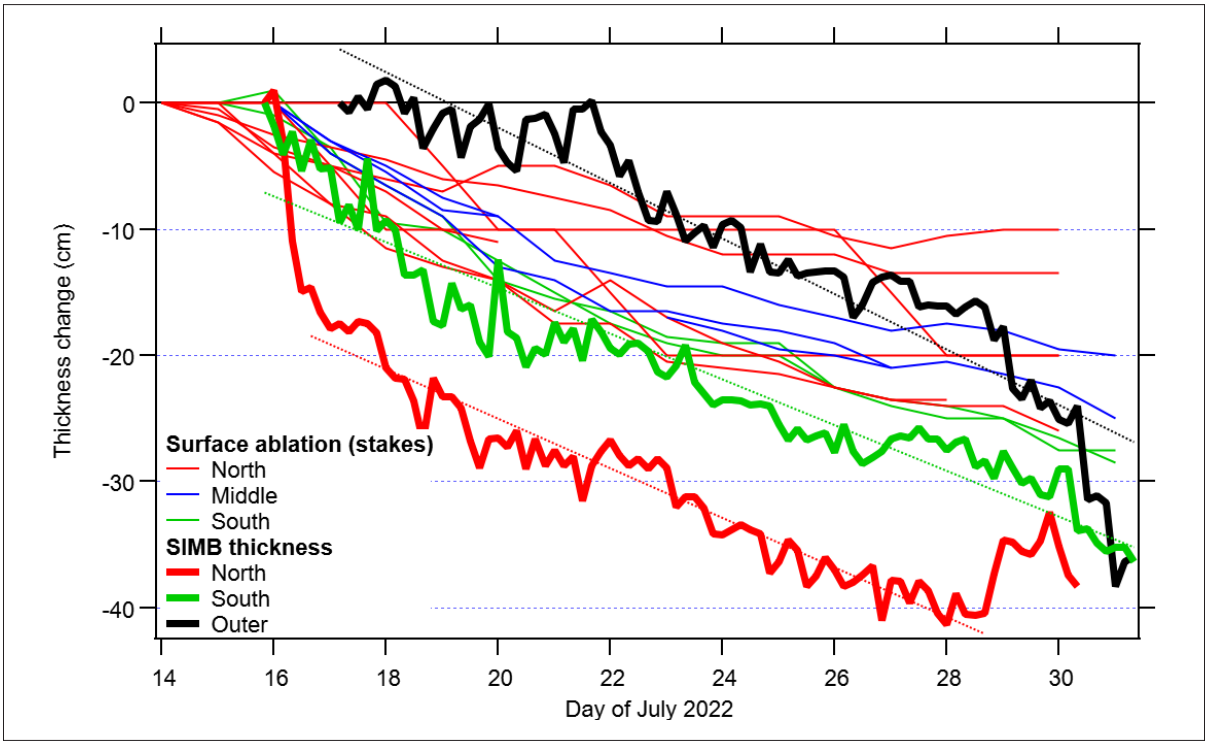

Fig. 3.3.17: Time series of ice thickness change (thinning) observed by the three SIMBs (thick lines); dotted lines are linear fits to the SIMB data. Data are compared with surface ablation observed at the ablation stakes by the Reolink SeaIceCams (thin lines). Note that there was no SIMB on the middle floe (blue), and ablation stakes were absent on the outer floe (black).

3.4 Melt pond and sea ice optical properties

Lena Buth[1], Victor Lion[3], Hannah Niehaus[2], Gunnar Spreen[2]
not on board: Gerit Birnbaum[1], Natascha Oppelt[3]

[1]DE.AWI
[2]DE.UNI-Bremen
[3]DE.CAU

Objectives

Helicopter

The helicopter sea ice surveys with optical and infrared (IR) cameras, and laser scanner extend the spatial coverage of comparable *in-situ* observation and measure geophysical parameters accessible only to airborne sensors. In addition, the helicopter observations are providing ground-truth at a higher spatial resolution than achieved by satellite remote sensing to assess the impact of sub-footprint scale variability of the ice surface on the satellite retrievals. The main geophysical parameters observed from the helicopter are (i) melt pond fraction and size distribution, (ii) melt pond optical and IR temperature properties, (iii) ice surface topography

including freeboard, (iv) open water and lead fraction, and (v) surface temperature of different ice types and the ocean. These parameters are needed to assess albedo changes, the surface energy budget and moment transfer in the atmosphere-ice-ocean system and are relevant for corresponding process studies. Improved melt pond, lead and ridge distributions as well as ice type information can be retrieved by combining measurements from different sensors.

Hyperspectral camera

During ice stations a hyperspectral (400–1,000 nm) camera was used to observe the spectral melt pond and surface scattering layer (SSL) optical properties. The hyperspectral camera measurements extend the pointwise, high-accurate Ocean Optics spectroradiometer measurements (see *Böötle* and *Stickle* below) spatially. The underlying assumption is that the spectral properties of the melt pond and ice surface type vary spatially and thus are best captured by an imaging system.

Overarching objectives are to describe the spectral properties of summer sea ice floes in the marginal ice zone. Thus, a large number of different realizations of the two surface types melt ponds and ice needed to be measured. And secondly, the temporal development of the same surface type was observed during the three visits of the same three floes. The spectral properties then will be related to physical properties like melt pond bottom ice thickness, bubble content, or grain size and type of the SSL.

The second overarching objective is to improve and develop new satellite retrievals for melt pond fraction and ice albedo. If the processes changing the spectra of melt ponds and ice surface are better understood models of the spectral properties of melt ponds (e.g., Malinka et al., 2018) can be improved. For example, while air bubbles are considered in current reflectivity models, we observed during this expedition a much higher variability in air bubbles distributions for the same ice thickness than usually assumed. After improvement such forward models can then be inverted to retrieve melt pond and ice properties from optical satellite observations (e.g., Zege et al., 2015). Retrievals are also possible on a sub-footprint scale using lower resolution satellite sensors like MERIS (Istomina et al., 2015a,b) or now OLCI on Sentinel-3, which allow daily, Arctic-wide retrievals for all cloud free regions. From these satellite observations long-term (since 2002) climate time series of ice albedo and melt pond fraction can be constructed, which will help to improve our understanding of processes like spatial variability of melt pond formation for different atmospheric forcings, melt ponds as part of the ice-albedo-feedback and climate model evaluation to increase confidence in Arctic climate projections for the future.

RAMSES under-ice spectrometer

The RAMSES under-ice spectrometer measurements are conducted to determine light transmittance through the ice and into the water column and thereby quantify the energy input into the ocean below the sea ice. By measuring the incoming irradiance on the ice surface and the light field under the ice at different depth up to 50 m deep the attenuation of transmitted radiance is measured. Sea ice variability, i.e., the abundance of melt ponds, close-by leads, ice and snow thickness, as well as ocean properties like the abundance of biological activity influence the transmittance and attenuation towards a certain depth. And thus their influence on light and energy availability can be determined by the RAMSES measurements.

Böötle & Stickle, Goniometer, and Laboratory work

The general objectives of the *Böötle & Stickle, Goniometer, and Laboratory* measurements serve the development of remote sensing-based applications to retrieve spectral ice albedo based on optical satellite data (e.g. Sentinel-2). This development is part of the research project *ArcticSense* (Development of a pre-operational application for monitoring melt ponds

in the Arctic sea ice using Sentinel-2 MSI data, funded by the German Federal Ministry of Economic Affairs and Climate Action). Moreover, the positioning of the floes will be used to validate applications for floe and floe drift detection based on Sentinel-1 and -2 data (Wang et al., 2021).

Böttle & Stickle: To support the future retrieval of melt pond parameters from optical remote sensing satellite platforms, extensive *in-situ* sampling of melt pond optical properties is necessary. The *Böötle* and *Stickle* setups allow for the retrieval of reflectance spectra in an around the visual wavelength region. Paired up with ancillary measurements of melt pond water depth, pond bottom ice thickness and water optical properties, these *in-situ* data will serve for calibration and validation of remote sensing melt pond models. *Stickle* can also be used over snow and sea ice surfaces. These measurements will help to calibrate and validate remote sensing products of sea ice albedo, as well as atmospheric correction models for the arctic region.

Goniometer: The Goniometer setup allows for the measurement of a subset of the BRDF (bidirectional reflectance distribution function) of different surfaces. The collected hemispherical-directional spectral reflectance data will be used to validate computational radiation transfer models of snow packs, as well as for the calibration of new atmospheric correction models.

Laboratory work: Lab analysis of melt pond water samples yield information about water constituents, as well as their influence on optical water properties. These data will be useful together with *Stickle* and *Böötle* measurements to separate spectral melt pond bottom signals from bulk water absorption. In conjunction with optical remote sensing data, they will be used to retrieve potentially existing CDOM (coloured dissolved organic matter) and TSM (total suspended matter) in melt ponds.

Work at sea

Helicopter

Camera and laser scanner sea ice surveys were performed with a fixed sensor installation in one, the D-HARK, of the two helicopters onboard *Polarstern*. The installation consisted of two (fisheye and 14 mm) downward-looking visual Canon cameras located in in the belly of the helicopter, and an airborne laser scanner (ALS) with Inertial Navigation System (INS), a nadir infrared camera, distribution of power and network as well as the main data acquisition systems located in the rear baggage compartment (Fig. 3.4.1). The Applanix INS contains a gyro compass coupled with two GPS receivers installed on the helicopter hull. The INS roll, pitch, speed, heading, and position data is used by all cameras and the ALS to map the sensor acquisitions on the Earth surface. All sensors were operated from the backseat in the helicopter cabin with a single display and keyboard/mouse that could connect to different industrial (ebox) PC's in the baggage compartment. An overview of the sensors is provided in Table 3.4.1. All sensors were controlled by two operators during flight. Two different flight patterns were performed: (1) long (>30 nm) flights along transect lines (e.g., along the ATWAICE transect or in triangles) and (2) floe-grid patterns over two of the ATWAICE sea ice station floes. In total 15 science plus 2 test flights were conducted with this setup. A list of all flights is summarized in Table 3.4.2.

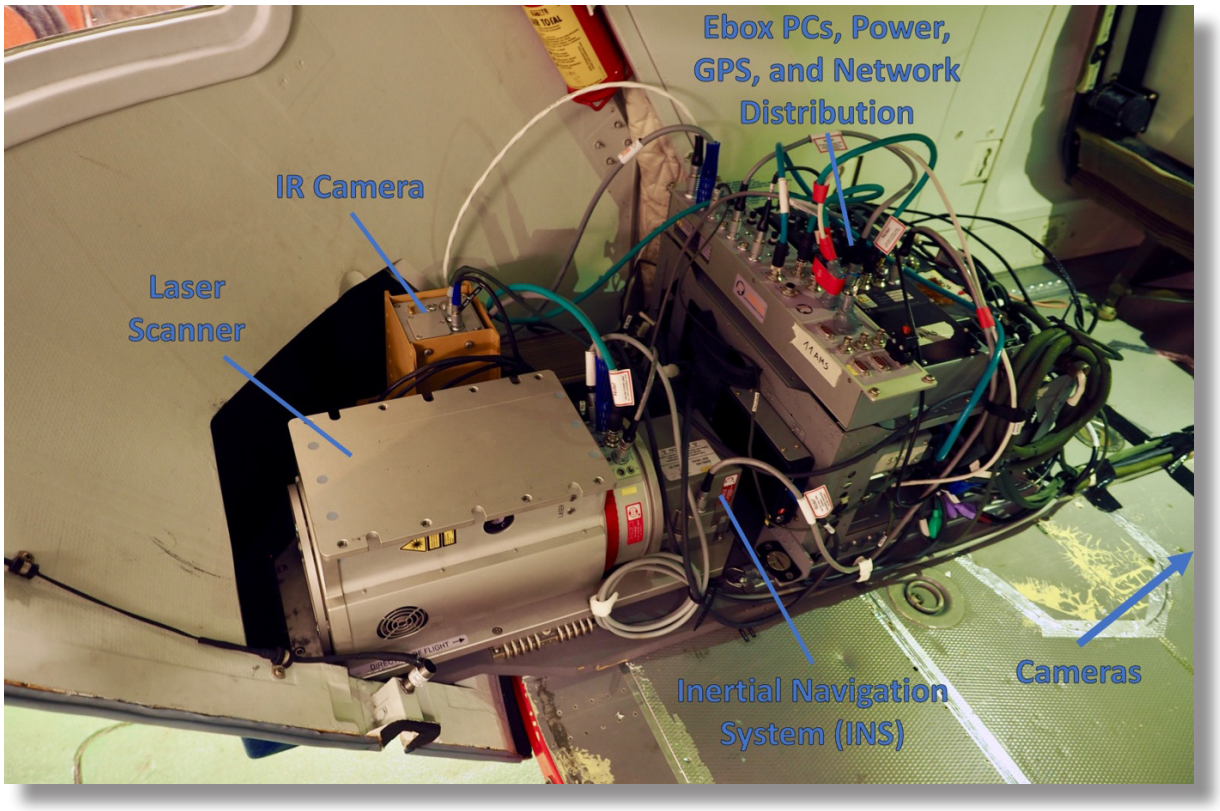

Fig. 3.4.1: Helicopter sensor installation in the rear baggage compartment of the helicopter (D-HARK). The ALS and IR camera look nadir downwards through openings in the left back door. Not on the photo are the two Canon cameras mounted in the belly panel at the front of the helicopter.

Tab. 3.4.1: Overview of sensors used for the helicopter camera and ALS sea-ice surveys

Sensor	Description	Device URN	Geophysical Parameter
Fisheye-Cam	Wide-angle nadir camera (Canon EOS-1D Mark III, Sigma fisheye 8 mm)	aircraft:heli-ps:rgbcam_fel_heli	Melt pond parameters, surface albedo
14 mm-Cam	Wide-angle nadir camera (Canon EOS-1D Mark III, Canon EF 14 mm)	aircraft:heli-ps:rgbcam_wal_heli	Melt pond parameters, surface albedo
ALS	Airborne Laser Scanner (Riegl VQ580)	aircraft:heli-ps:riegl-vq580-s9999057	Surface elevation, freeboard and roughness
IR-Cam	Nadir Infrared-Camera (Infratec Vario-CAM HD head 680)	aircraft:heli-ps:ir_variocam_02	Melt pond parameters, surface temperature distribution
INS	Applanix Inertial Navigation System (AP60-Air)	aircraft:heli-ps:applanix-ap60av-9873	position, speed, heading, roll and pitch of helicopter

Tab. 3.4.2: List of all flights performed with the cameras and ALS setup (including some combined flights with the EM-bird)

No.	Date	Type	Start Time	End Time	Sensors	Weather & comment
1	2022-07-05	test, 1,000 ft, 80 kn	10:53	11:14	Fisheye, 14 mm, INS, IR-Cam	cloud free entire flight
2	2022-07-07	test, 1,000 ft, 80 kn	13:01	13:33	Fisheye, ALS, INS, IR-Cam	cloud free entire flight (or only very thin clouds above 1000ft)
3	2022-07-13	floe north, 200 ft, 60 kn	07:53	08:01	14 mm, INS, IR-Cam	cloudy, low ceiling, partly mist
4	2022-07-13	floe north, 200 ft, 60 kn	10:45	11:05	INS, IR-Cam	cloudy, low ceiling, partly mist
5	2022-07-16	transect, 1,000 ft, 60 kn	12:33	14:09	Fisheye, 14 mm, ALS, INS	partly cloudy with some sunny areas (closer to the ship)
6	2022-07-17	EM-bird transect, 100 ft, 85 kn	07:59	09:40	IR-Cam	some mist/fog at ship; sunny further north
7	2022-07-17	transect, 1,000 ft, 80 kn	12:10	13:45	Fisheye, ALS, INS, IR-Cam	some fog at ship; sunny further north
8	2022-07-18	transect, 1,000 ft, 80 kn	08:02	08:50	Fisheye, 14 mm, ALS, INS, IR-Cam	sunny at PS, at ice edge low level fog, getting stronger north
9	2022-07-18	transect, 1,000 ft, 80 kn	14:25	15:59	Fisheye, 14 mm, ALS, INS, IR-Cam	sunny whole flight, no fog
10	2022-07-19	EM-bird, transect, 100 ft, 85 kn	07:04	08:39	IR-Cam	sunny, some clouds
11	2022-07-19	transect & floe south grid, 500-1,000 ft, 50-80 kn	10:43	12:55	Fisheye, 14 mm, ALS, INS, IR-Cam	sunny first, later broken clouds, patches of mis
12	2022-07-20	EM-bird transect, 100 ft, 85 kn	07:18	07:53	IR-Cam	
13	2022-07-24	transect, 1,000 ft, 80 kn	13:05	14:42	Fisheye, 14 mm, ALS, INS, IR-Cam	thin clouds, some sunny spots, good flight conditions
14	2022-07-30	floe north grid & transect, 500-1,000 ft, 5080 kn	04:24	05:31	Fisheye, 14 mm, ALS, INS, IR-Cam	broken clouds; fog patches; low clouds in south
15	2022-07-30	EM-bird transect, 100 ft, 85 kn	08:53	10:21	IR-Cam	broken clouds with sunny patches; good flight conditions
16	2022-07-30	transect, 1,000 ft, 80 kn	11:12	12:35	Fisheye, 14 mm, ALS, INS, IR-Cam	broken clouds, often sunny, some low level fog in the south
17	2022-08-08	transect, 1,000 ft, 80100 kn	08:43	10:29	Fisheye, 14 mm, ALS, INS, IR-Cam	sunny, no clouds, little mist

Hyperspectral camera

The 2-D hyperspectral imaging of surface areas was conducted with the S*pecim IQ* camera in a portable system setup. The *Specim IQ* records 204 spectral bands within the range of 400 to 1,000 nm with an image resolution of 512 x 512 pixel (thus the result is a 204 x 512 x 512 points data cube). However, at the applied low integration time of in most cases 1 ms, which is necessary to avoid saturation in large parts of the spectrum, the NIR range has a poor signal-to-noise ratio. Especially for > 900 nm the spectrum appears noisy and is thus not further used in the following discussion. The focal length was set to a constant value for entire measurement days, mostly to 2 m (only for the first ice station (Nothern floe, visit 1) 4 m focal length were used). The maximum opening angle of the camera and thus the field of view is 31°. The *Specim IQ* camera is installed in a Peli case to protect it from the environments (and heat it at colder temperatures) which also contains a power bank for extending the operation time. The complete setup comprises the *Specim IQ* camera mounted on a tripod, a *Panasonic Toughbook* to remotely operate the camera and a white reference plate also mounted on a tripod and placed horizontally in the lower right corner of every measured image as visible in Figure 3.4.2. A digital protractor was attached to the case of the camera to measure the viewing incidence angle. The roll angle of the camera was set to a horizontal alignment by eye. For future campaigns an additional digital protractor could be mounted on the camera setup. Also useful would be a good compass that is not affected by the drifting of the ice to note the heading of the measurement. During this campaign the heading of the measurements was estimated relatively to the ship heading which is measured accurately.

Fig. 3.4.2: Example of an RGB preview image displayed on the hyperspectral camera; the white square marks the extend of the hyperspectral measurement. In the lower right quarter the white reference plate is visible.

The hyperspectral measurements were conducted in two different modes to enable detailed analysis of melt pond spectra, and the investigation of albedo variability and mean for the entire ice floes:

1. Local Measurements: Measurements of single ponds and possibly adjacent surface scattering layer from two different perspectives (i.e., viewing directions). For each perspective at least two different viewing angles were used. The location and viewing direction of the measurements were marked with two bamboo sticks – one stick for each of the two tripods (camera and white reference).

2. Transect Measurements: Transect measurements in a straight line crossing large parts of the floe. The measurements were taken at constant distances of 5 – 20 m (estimated by footsteps) always with the same viewing angle of 50 °, perpendicular to the walking direction to the right side. In this case only the positions of the measurements were marked with bamboo sticks.

Table 3.4.3 shows a summary of all conducted measurements on the different ice floes including comments on changes in the transect lines. As described above, bamboo sticks were used to mark the measurement positions and directions to repeat measurements when revisiting the ice floes and thereby enable the investigation of melt evolution. However, there were several issues leading to loss or displacement of these markers causing difficulties in finding the same setup:

- Measurement positions were chosen too close to pond edges and were melted away
- Sticks fell over due to increased melt at the bottom of the sticks – they could be coloured white at their bottoms for the next time
- Sticks in ponds were floating up (only within transects)
- Floe instabilities disabling repetition of measurements
- Polar bears playing with the bamboo sticks

In the measurement mode (1) of single, precise pond measurements, in most cases salinity and depth of the melt ponds were measured in addition. Occasionally the imaging was accompanied by ice thickness measurements of the pond bottom.

Tab. 3.4.3: Overview of floe visits and conducted measurements

Date	Floe	Visit	Local Measurements	Transect Measurements	Transect Comment
2022-07-13	north	1	14 (3 ponds)	-	
2022-07-14	south	1	12 (3 ponds)	10 (every 20 m)	Floe breaking
2022-07-15	middle	1	17 (3 ponds)	12 (every 10 m)	
2022-07-20	north	2	20 (4 ponds)	13 (every 20 m)	
2022-07-21	south	2	14 (4 ponds)	12 (every 10 m)	Different transect than on first visit (due to floe break-up)
2022-07-22	middle	2	16 (4 ponds)	12 (every 10 m)	Measurement point 8 is shifted
2022-07-27 - 2022-07-28	24h	single	20 (4 ponds)	17 (every 20 m)	
2022-07-29	Zodiac	single	7 (2 ponds)	-	

Date	Floe	Visit	Local Measurements	Transect Measurements	Transect Comment
2022-07-30	north	3	18 (4 ponds)	11 (every 20 m)	Measurement 11 and 13 missing
2022-07-31	south	3	6 (1 pond)	10 (every 10 m)	First and third position not repeated
2022-07-31	middle	3	20 (5 ponds)	13 (every 10 m)	Both measurement 8 points from previous transects included
2022-08-06	Greenland 1	single	-	44 (every 5-10 m)	Switch from 5 to 10 m steps after measurement 34
2022-08-06	Greenland 2	single	-	34 (every 5 m)	9 m shift of line due to open melt pond after measurement point 7

RAMSES under-ice spectrometer

Two TriOS RAMSES spectral radiometers were used to measure a profile of spectral irradiance underneath the sea ice. One of them was installed on a tripod above the ice surface, facing upwards, to measure incident irradiance. The other radiometer was slowly being lowered through a hole in the ice down to 50 m depth and pulled upwards again with an average speed of about 3.3 m $(min)^{-1}$ while measuring the transmitted irradiance. Both radiometers were set on burst mode, ensuring the fastest possible series of consecutive measurements, limited by the integration time of the measurement.

On each floe, locations on level ice were chosen for the RAMSES measurements, avoiding disturbances such as melt ponds or ridges. In most cases it was not possible to use the same location or even the same hole again during consecutive visits of the North, Middle and South floe, therefore new locations were chosen.

In order to capture a potential daily cycle and other variability, a stationary site was set up at the *24h ice station*, measuring the transmitted irradiance every 5 minutes at 1 m below the ice bottom. Every 3 hours, an additional profile down to 50 m depth was measured.

An overview of the individual measurements is given in Table 3.4.4. Additionally, photos of each Ramses site were taken and are available together with the data.

Tab. 3.4.4: Overview of individual Ramses measurements on the floes.

Date	Time	Floe	Visit	Description of Ramses site
2022-07-13	12:55	north	1	level ice, between two ponds
2022-07-14	12:52	south	1	close to pond
2022-07-14	16:01	south	1	level ice, no ponds in immediate surroundings
2022-07-15		middle	1	
2022-07-20	18:58	north	2	level ice, no ponds closer than 5 m
2022-07-21	13:21	south	2	level ice, 7 m distance to ridges, 5-7 m distance to ponds, 10 m distance to ice edge

Date	Time	Floe	Visit	Description of Ramses site
2022-07-22	11:41	middle	2	level ice, interconnected ponds in all directions, minimum distance 5m to pond
2022-07-22	13:23	middle	2	level ice, interconnected ponds in all directions, minimum distance 2 m to pond
2022-07-30		north	3	
2022-08-01		middle	3	
2022-07-27 - 2022-07-28	starting 22:07	24 h	single	level ice, no ponds in vicinity
2022-08-06	08:53	Greenland 1	single	-
2022-08-06		Greenland 2	single	-

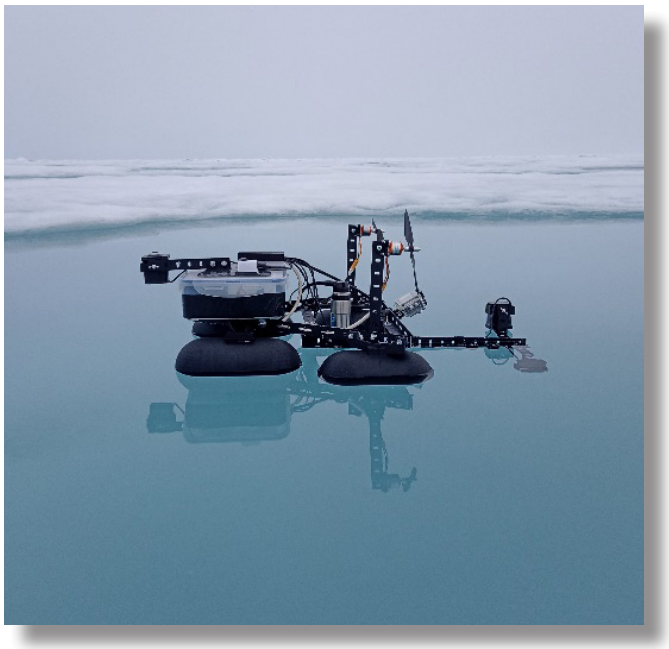

Fig. 3.4.3: Böötle swimming in Pond Nemo on the Middle Floe

Böötle

To obtain melt pond spectral characteristics the *Böötle* (Fig. 3.4.3) was used as one of two different setups. This setup consists of a self-propelled, remotely-controlled measurement platform, primarily carrying three spectroradiometers to obtain downwelling irradiance above and below the waterline, as well as upwelling radiance below the waterline. Additionally, the *Böötle* has an acoustic sensor onboard for assessing pond water depth. A temperature sensor measures temperature of the melt pond water near the waterline. The *Böötle* was always used when the melt pond depth exceeded ~15 cm. That was the case on five of twelve floes (see Tab. 3.4.5).

Stickle

In the field, another setup for obtaining melt pond spectra was used. The *Stickle* (Fig. 3.3.4) is a person-mounted monopod with two spectro-radiometers to measure down- and upwelling irradiance simultaneously. An additional spectro-radiometer for measuring upwelling radiance is also attached. All spectro-radiometers are gimbal-stabilized. When used over melt ponds, manual water depth measurements were also taken. During the last revisits of the northern and southern floe, a drill set and a thickness gauge to measure sea ice thickness along the measured points by *Stickle* finalized the procedure. The *Stickle* setup was also used on snow and ice surfaces to measure spectral albedo and reflectance. This was done by transect operations. The *Stickle* was used on eleven of twelve floes (see Tab. 3.4.5).

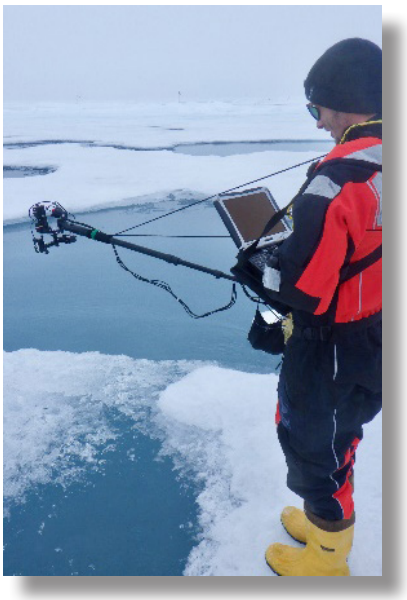

Fig. 3.4.4: Stickle in use during albedo transect

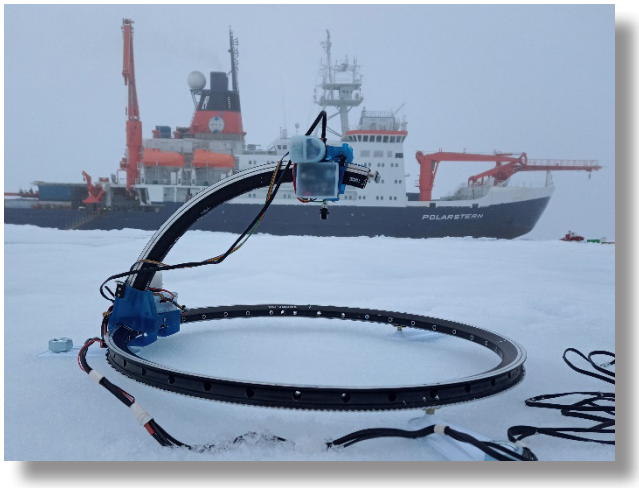

Fig. 3.4.5: Goniometer in front of Polarstern

Goniometer

The goniometer (Fig. 3.4.5) was used to collect information about BRDF (bidirectional reflectance distribution function) of snow and ice surfaces. This setup consists of one spectro-radiometer mounted onto a frame. This spectro-radiometer can be moved motor-driven to different angular positions to retrieve angular spectral backscatter of the underlying surface. A second spectro-radiometer was used to monitor downwelling spectral irradiance. The goniometer was placed on homogenous snow and ice surfaces but also on newly formed melt pond ice lids and pond bottom surfaces of drained ponds. Goniometer data are available on ten of twelve floes (see Tab. 3.4.5).

Laboratory work

Water samples of all observed melt ponds (ten of 12 floes; see Tab. 3.4.5) were taken and analyzed onboard *Polarstern* to assess optical absorption characteristics and CDOM (coloured dissolved organic matter). This is done by PSICAM (Point-Source Integrating Cavity Absorption Meter) and LWCC (Liquid Waveguide Capillary Cell) measurements. The water was also filtered by using GF-F filter pads, to later determine TSM (total suspended matter) content.w

Tab. 3.4.5: Overview of *Böötle*, *Stickle* and goniometer measurements and water samples

Date	Floe	Visit	Böötle	Stickle	Goniometer	Water sample
2022-07-13	north	1	X	X	-	X
2022-07-14	south	1	X	X	X	X
2022-07-15	middle	1	-	X	X	X
2022-07-20	north	2	-	X	X	X
2022-07-21	south	2	-	X	X	X
2022-07-22	middle	2	X	X	X	X
2022-07-27 - 2022-07-28	24h	1	X	-	X	X
2022-07-30	north	3	-	X	X	X
2022-07-31	south	3	-	X	-	X
2022-08-01	middle	3	X	X	X	X
2022-08-06	Greenland 1	1	-	X	X	-
2022-08-06	Greenland 2	1	-	X	X	-

Preliminary (expected) results

Helicopter

The full potential of the helicopter measurements setup will be achieved when the data streams from the visual and infrared cameras and from the ALS laser scanner will be combined. Preliminary analysis, however, can already be performed on the individual datasets.

Figure 3.4.6 shows examples of a threshold-based preliminary classification applied to the IR images. In these two examples melt ponds are the warmest class, the ice surface the second warmest, and the ocean the coldest class. But this is not always the case and for example the ice can be colder than the ocean and the melt pond etc. Thus, no constant IR temperature thresholds can be used. We analyze the temperature histogram of every image and apply a rule-based threshold classification based on the shape of the histogram modes. However, due to the changing surface conditions, different sections of the helicopter flights have to be manually pre-classified in the primary order of surface temperatures by class, e.g., $T_{ocean} < T_{ice} < T_{MeltPond}$. The first example in Figure 3.4.6 shows a case with a bimodal distribution dividing the colder ocean from the warmer ice and melt ponds. The second example a unimodal distribution with a more continuous temperature development between the three classes. In both cases melt ponds are identified by a threshold on the long tail of the histogram (right of the yellow line). In some cases, the ocean and melt pond temperatures are very similar and cannot be separated. In such cases they are combined in a single “water” class.

Another interesting feature in the examples in Figure 3.4.6 is the ocean surface temperature variability. We clearly can identify colder surface temperatures in the wake of the ice floes. If this is mainly ocean turbulence induced by the ice keels of the drifting floes or wind shadowing effects would need further investigation.

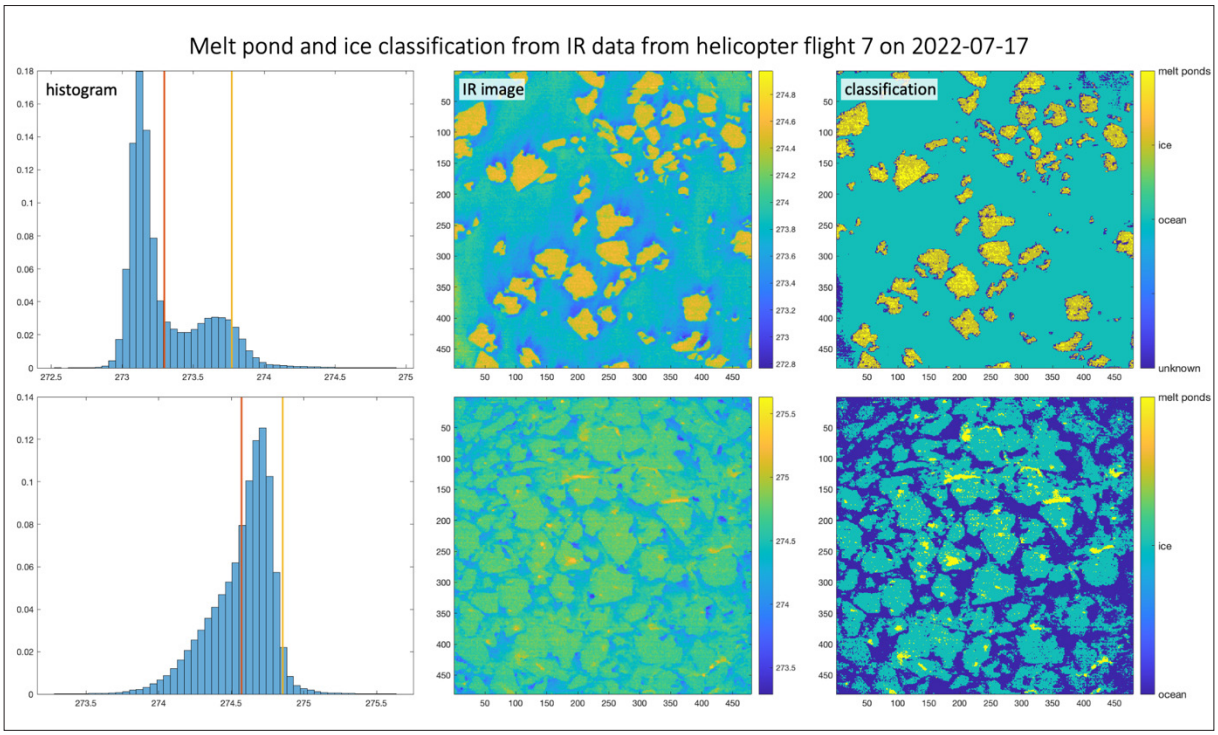

Fig. 3.4.6: Threshold-based classification of melt ponds, sea ice, and ocean from helicopter-borne IR camera images; two examples from flight 7 on 17 July 2022 are shown (row 1 and 2). Left: histogram of IR data (orange line: mean; yellow line: highest mode plus ½ mode width); middle: IR image; right: classification (mind the different colour scale for first and second example).

This histogram and threshold-based classification is applied to all IR images from helicopter flight 7 on 17 July 2022 at the beginning of the MIZ investigation and to the IR images from helicopter flight 16 on 30 July 2022 two weeks later (Tab. 3.4.2). Each flight transects covered the northern, middle, and southern floe along the ATWAICE MIZ transect. During the two-week time the floes experienced preliminary melting conditions (section 3.3). Figure 3.4.7 shows the measured IR temperatures (top) together with the classified melt pond (middle) and sea ice (bottom) fractions (without melt ponds) along the two helicopter flights. The three investigated floes (northern, middle, southern) are marked.

The surface temperatures show strong changes. While during the flight on 17 July the ice-covered part of the MIZ was warmer than the southern more ocean dominated part, this reversed during the flight on 30 July with lower temperature in the northern ice covered part and higher temperatures in the south.

The melt pond fractions from our simple classification show significant variability along the flight track. Close to the northern floe low (10–20 %) melt pond fractions prevail during both flights. The middle floe is close to an area of high (>30 %) melt pond fraction. And the melt pond fraction in that area has increased during the two weeks according to our preliminary classification. The southern floe is in an area of medium to low melt pond fraction and also here the melt pond fraction has increased between the two flights.

The sea ice fraction (excluding melt ponds) has decreased significantly in the region of the middle and southern floe according to our classification. This is in line with the increase in melt pond fraction and also the observed decrease in sea ice concentration and floe break-up in that region. However, our classification seems to overestimate the ice fraction reduction.

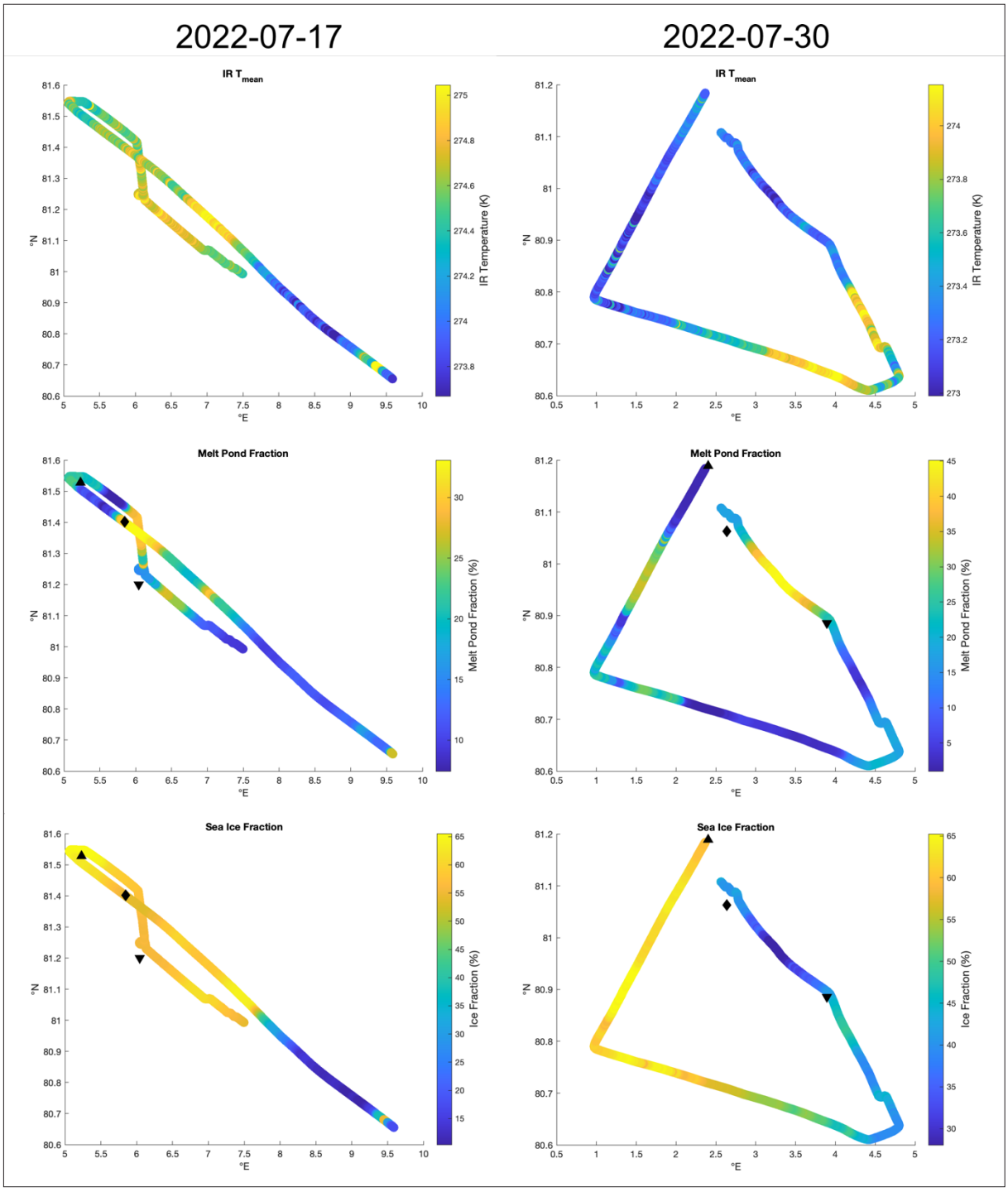

Fig. 3.4.7: Maps (lon/lat) of helicopter flights on 7 and 30 July 2022; upper row: measured IR temperatures; middle row: melt pond fraction from IR data classification; bottom row: sea ice fraction (without melt ponds) from IR data classification. Triangles and diamonds mark the northern, middle, and southern floes along the ATWAICE transect.

Thus, all classification results presented here should be considered mainly qualitative. Further evaluation and potentially a more advanced classification scheme are needed for more accurate surface type classification. Anyway, qualitatively our results show that the helicopter IR camera data can resolve changes in surfaces types and captures an increase in melt pond fraction during the two weeks, especially for the regions of the middle and southern floe. This is in line with the more detailed measurements on the ice floes presented in the next sub-section.

In addition, the IR camera is able to resolve small scale ocean surface temperature variability in the vicinity of the ice floes (Fig. 3.4.6, middle column) despite the low temperature contrast between ice and ocean during summer. This may lead to new insights in small-scale ocean and atmosphere dynamics, which will be followed up in future investigations.

Hyperspectral camera

The recorded images are saved as raw data cubes together with a dark frame and a white reference frame. Instead of using the internal created white reference frame, for each image a 20 x 20 pixel area within the white reference covered area within the image is selected and used as white reference frame. With the help of these dark and white frames the raw data is converted into reflectance data which, in case of diffuse illumination, can be assumed to be an approximation of surface albedo. Figure 3.4.8, left shows the RGB composition of an example measurement with the area used as white reference spectrum highlighted, and on the right side representative reflectance spectra of various points marked in the RGB image.

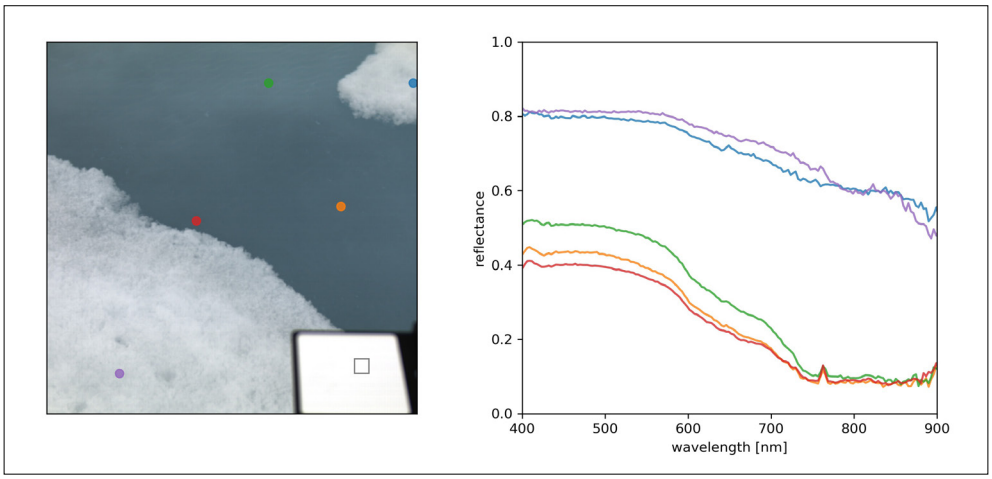

Fig. 3.4.8: RGB composite (left) of a measured hyperspectral data cube, measured on 15 July 2022 on the northern floe; the black square marks the area used as white reference to calculate the reflectance spectra shown (right) for the coloured positions, respectively.

The melt pond shows an expected lower albedo with a stronger decrease towards the near-infrared range than the surface scattering layer. Simple thresholds on reflectance bands around 400 nm and 800 nm and their reflectance difference are used to roughly divide the image into *ice* and *pond* surface areas as shown in Figure 3.4.9 to investigate the development of the reflectance of these two surface types separately. The *transition* class comprises pixels which fits neither the *ice* nor the *pond* class. The lower right quarter of the image is masked to make sure the reference target setup is not disturbing the averaging of the classes spectra.

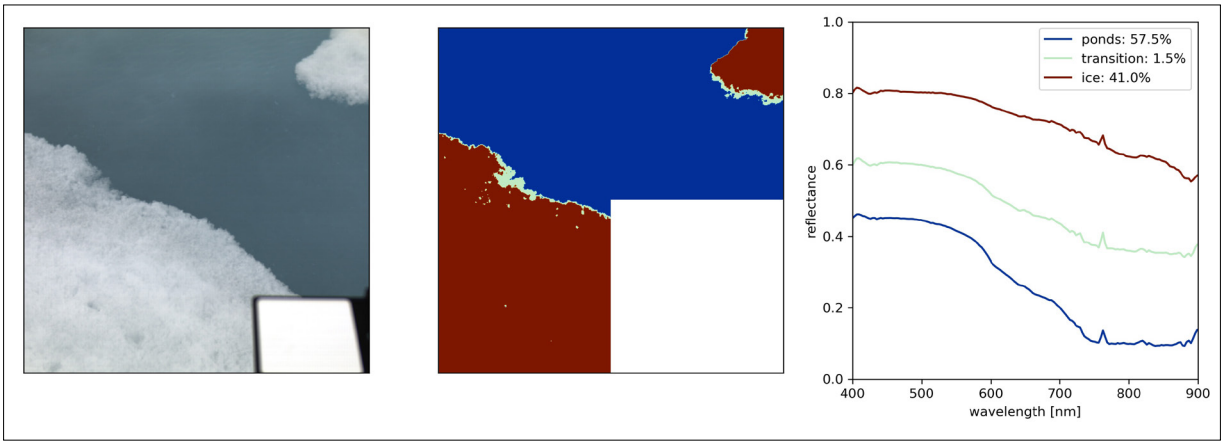

Fig. 3.4.9: RGB composite (left) and classified representation (middle) of a measured hyperspectral data cube; blue indicates a ponded surface, red indicates the ice class, the transition pixels that do not count into one of the previous classes are shown in turquoise. On the right side the averaged spectra of these three classes are shown together with their fractional values of coverage.

This classification approach is used to obtain pond and ice surface type fractions and their averaged reflectance spectra for the entire transect measurement of each floe and visit (Figure 3.4.10). We can observe that the pond fraction is increasing from the first to last visit. Overall, the melt pond reflectance is decreasing, i.e., the ponds are getting darker, which can be attributed to a thinning of the melt pond bottoms, which is in line with the observed ice thinning (and even enhanced thinning of pond bottoms) of the three ice floes (Section 3.3). The changes of the ice reflectance is not as uniform (increasing for northern and southern, and decreasing for middle floe). With a sufficient number of measurements it can be assumed that the transect averages give an approximation of the albedo and pond fraction of a floe. However, from the transect change on the southern floe that was necessary due to floe break-up it is visible in Figure 3.4.10, bottom that the number of measurements is not yet large enough to assume that each transect represents the average albedo of the floe well. The transect change causes a change especially in the appearance of the spectra for the two distinguished surface types. A detailed look into the measurements makes clear that the number of covered ponds is too small to represent the full variability of melt pond surfaces because one exceptional light pond already has a big impact on the averaged spectrum.

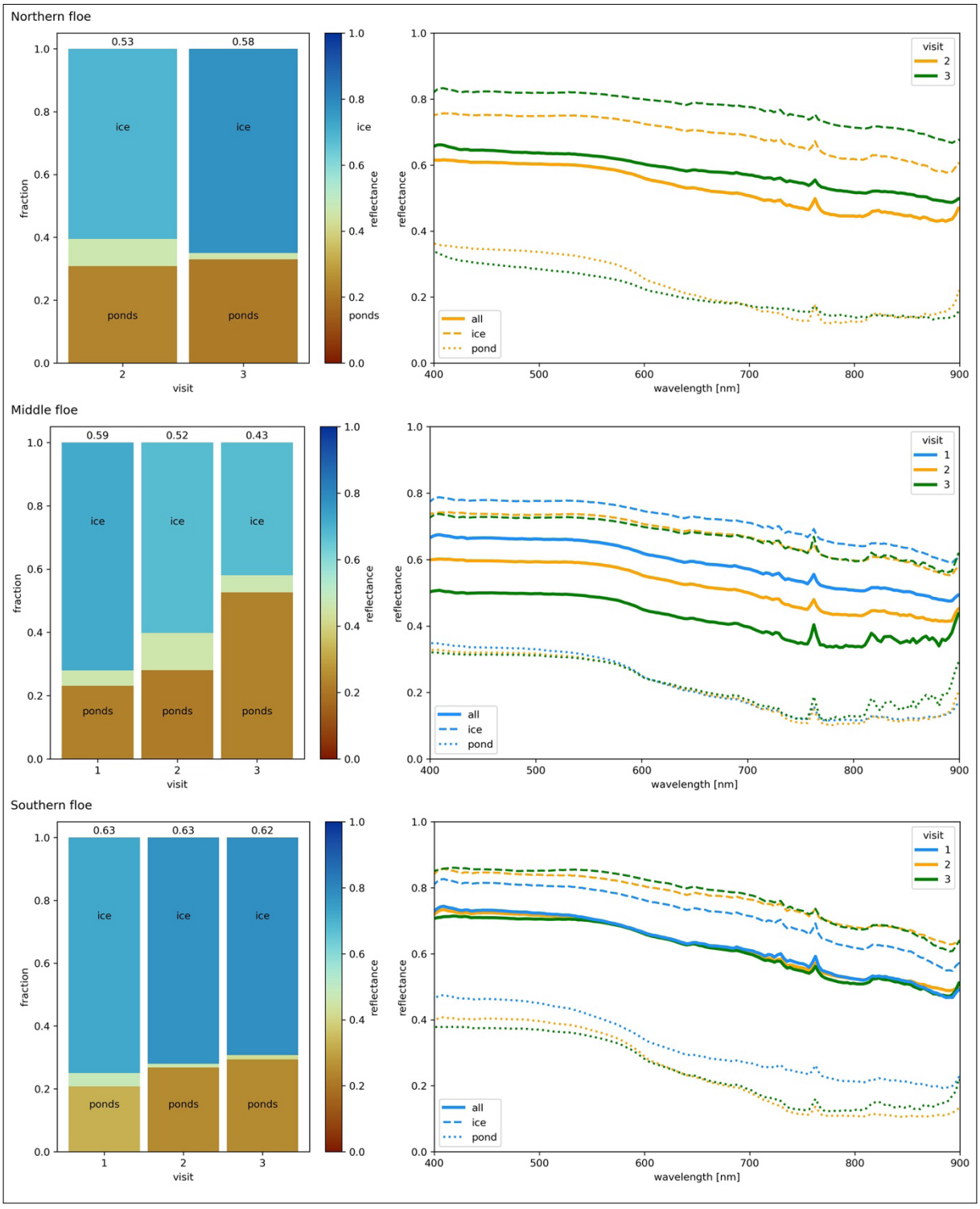

Fig. 3.4.10: Overview of averaged transect reflectances for the three main floes that were revisited; left: bar plots of the surface type fractions for each of the repeated transects per floe are visible. The colour indicates the mean reflectances, the values on top of the bars reveal the overall mean reflectance of the surfaces measured within one transect. Right: averaged spectra of all measurements (solid lines; mind that surface fraction also affect the averaged spectra) per transect line and spectra for the ice (dashed lines) and pond (dotted lines) surfaces separately. The colours indicate the number of visits.

The evaluation of the transects on the *northern floe* points out the relevance of the illumination conditions for the interpretation of the measurements. While most of the stations took place in complete overcast or even foggy conditions, the third visit of the northern floe was characterized by exceptional clear-sky conditions. The directional irradiance and thus angle dependent scattering leads locally to reflectances that are higher than the “perfect” (i.e., Lambertian) reflectance of the reference target. This leads to unphysically high reflectance values for the ice or surface scattering layer and emphasizes the difference between reflectance and albedo as in the latter case the bidirectional reflectance factor (BRF) of a surface is needed to convert the directional measurement into an albedo. Additionally, the surface orientation (of the ice surface) is very variable leading to shadows and thus lowered reflectances in some areas. This effect cannot be assumed to average out and the comparison of the two transects on the *northern floe* should be interpreted carefully. It cannot be concluded that the overall albedo of that floe was increasing in the time period between the two visits on 20 and 30 July 2022. Rather we should focus on the slight increase of melt pond fraction and the change of the reflectance spectra of the melt ponds.

The middle floe has been visited under the most constant (overcast) conditions that also allow an interpretation of the reflectance as albedo. The colours of the bar plot as well as the spectral resolved reflectances displayed in Figure 3.4.10 (middle row) show little change for the melt pond surface type throughout the timeseries. There is, however, a general decrease in reflectance <600 nm while the reflectance >800 nm is elevated during the 3rd visit. The reflectance of the ice surfaces decrease slightly between visits 1 and 2. The more important factor for the overall decrease of reflectance (solid lines) is the change of surface type fractions, which is in favour of increasing melt pond fraction and thus decreases the overall reflectance between the visits.

Figure 3.4.11 shows the results of the three additional transects measured during the *24h floe* station and on the two landfast ice stations close to the Greenland coast at about 78.5°N. It is important to note that these results are not to be interpreted as a time series and the ice conditions and properties strongly differ.

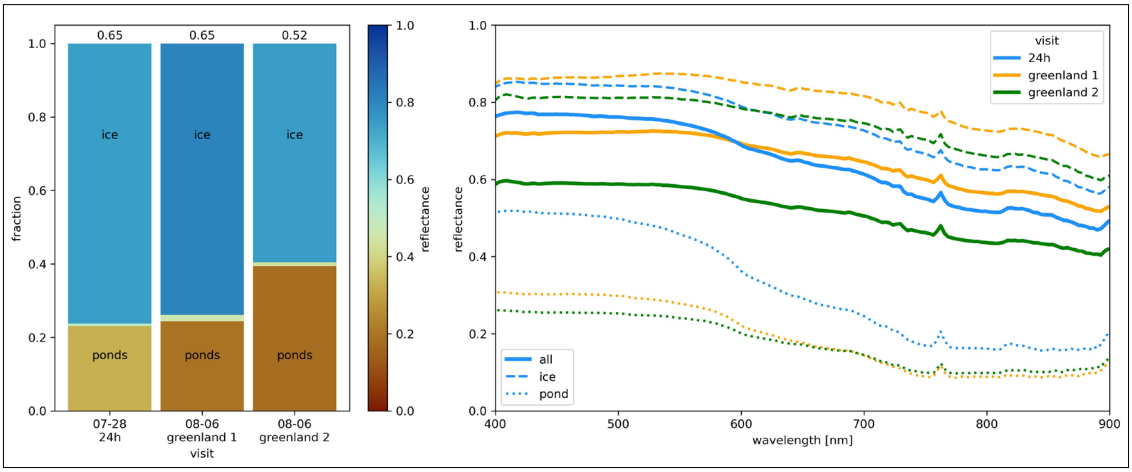

Fig. 3.4.11: Overview of averaged transect reflectances for the three additional “floes” that were visited: The 24h floe station was located on drift ice closer to the three main floes that were revisited, the Greenland 1 and 2 stations were conducted further south (~78.5°N) on landfast ice (i.e., not on ice floes in a traditional sense). Left: Bar plots of the surface type fractions for the transects on the three different “floes” – the colour indicates the mean reflectances, the values on top of the bars show the overall mean reflectance of the surfaces measured within in one transect. Right: Averaged spectra of all measurements (solid lines) per transect line and spectra for the ice (dashed lines) and pond (dotted lines) surfaces separated – the colours indicate the three different floes.

The spectral and broadband albedo of the melt ponds is significantly different between the *24h floe* (blue dotted line) and the two stations on the landfast ice (green and orange dotted lines), which implies also differences of the underlying ice and its thickness. Also remarkable is the difference in melt pond fraction between the stations *Greenland 1* and *2*, which were also visible by eye, despite that these stations were close together. However, the two station locations were intentionally chosen to reflect the different ice thickness types that were found in the region. The first station was closer to the coast and on thicker ice (1.3–2.8 m) than the second one (0.4–1.0 m), which was often melted through within in the melt ponds. This can explain the "darker" appearance of the ice surfaces (very thin ice was observed during the *Greenland 2* station) and the reduced reflectance in the blue spectrum range (<600 nm) of the melt ponds.

In Figure 3.4.12 the pond reflectance spectra are combined with under-pond ice thickness and pond depth as well as salinity measurements for one pond (number 3) on the *middle floe*. The overall reflectance of the ponds is decreasing with time but also the shape of the averaged spectrum is changing. The decrease of reflectance is most prominent at the shortest wavelengths in the blue range of the optical spectrum and is reduced towards the higher part of the visible range. Interestingly, in the near-infrared the evolution changes and the spectra are flipping order. The earlier visits feature lower reflectance measurements than the later ones. Also the observations of pond depth, ice thickness and salinity show distinct trends. The salinity is rising with time is indicating an increase of interconnections between ponds and the ocean. However, the ocean is strongly stratified and the vertical exchange is thus small and increases the salinity to at maximum 6 PSU. The pond depth on average is slightly increasing. Both of these trends are in agreement with the salinity and pond depth measurements of other ponds on the same floe which are summarized in Table 3.4.6. For this particular pond, holes were drilled in addition to measure the under-ice thickness, showing a strong decrease. This is expected to be the main driver of the decrease of pond reflectance as a higher fraction of the incoming light is transmitted into the ocean underneath. The drilled holes did not lead to an immediate increase of salinity because of high stratification that keeps the lighter fresh melt water on top of the more saline waters. The longer-term salinity changes between the visits might be due to diffusive vertical mixing of the saline ocean water or due to horizontal water transports between the ponds, which were all interconnected on the floe and thus can have contact to the ocean water in the leads on the floe sides.

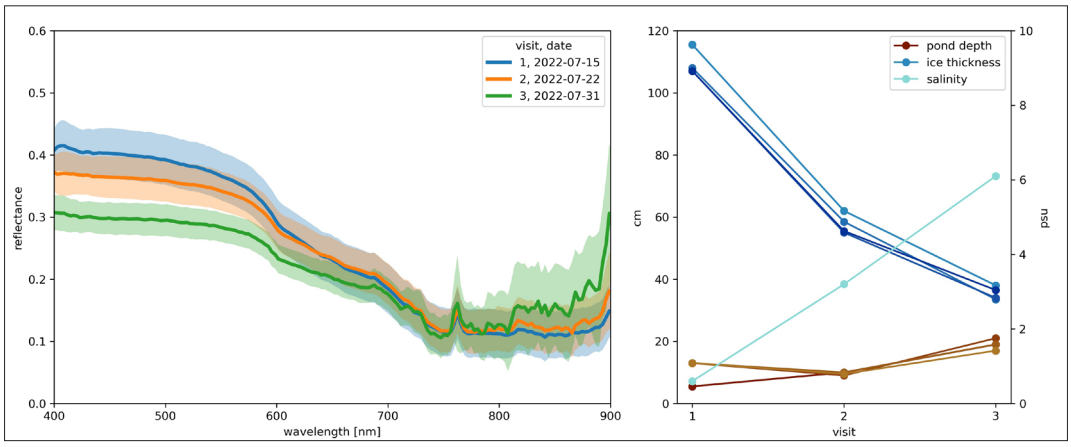

Fig. 3.4.12: Development of pond 3 on the middle floe: Left: Averaged reflectance spectra of pond surface areas for the three visits – the range of one standard deviation is shaded indicating the variability of the pond surface reflectance. Right: Pond depth measurements in red colours and under-pond ice thickness measurements at the same three locations in blue colours in cm (left axis) plotted against the visits. The turquoise line shows the evolution of pond salinity in psu (right axis).

Tab. 3.4.6: Overview of ranges of pond depth (left, in cm) and salinity (right, in psu) measurements of the single pond investigations. Grey colours indicate that there was no hyperspectral measurement taken during that visit, dark grey indicates that measurements were not possible because of pond destruction. The green colour indicates that there are under-pond ice thickness measurements available.

	Visit	Pond 1		Pond 2		Pond 3		Pond 4		Pond 5	
		depth	salinity	depth	salinity	depth	salinity	depth	salinity	depth	salinity
Northern floe (1)	1	1-17	0.1	0-2	-	0-3	-				
	2	1-18	0.1	0-3	0.3-1.0	0-3	0.2	5-8	0.1		
	3	3-20	0.9	6-10	1.4	7-10	0.6			3-5	-
Middle floe (3)	1	11-17	0.1	1-4	0.3	5.5-13	0.6	5-13	0.5		
	2	12-17	3.6	3-4	2.1	9-10	3.2	5-22	6.5		
	3	19-21	5.4	11-15	5.9	17-21	6.1	13-20	5.5	14-20	5.7
Southern floe (2)	1	1-8	-	8-12	-	11-19	2.6				
	2	1-10	4.7			13-20	14.4				
	3	9-14	13.6-15								
24h floe	1	21-24	0.7	5-11	0.6	10-14	-				

The depth of ponds features high variability (Tab. 3.4.4) but is in general slightly increasing for all three revisited floes with a stronger difference between *visits 2* and *3.* This could be related to increased melting or to the longer time period elapsed compared to the first revisit. The increasing trend for the salinity is also valid for the majority of the observations. Table 3.4.7 shows the lists of conducted under-pond ice thickness measurements for the pond/visit combinations that are marked green in Table 3.4.6.

Tab. 3.4.7: Measured under-pond ice thicknesses in cm.

	Pond	Visit	Under-pond ice thickness [cm]	
			Single measurements	Mean
Northern floe	1	3	105, 110, 116, 117, 119	113.4
	2	3	89, 94, 97, 103.5, 109, 114	101.3
	3	3	92.5, 93, 95, 98	94.6
Middle floe	1	3	73, 74, 76, 76, 78	75.4
	2	3	45, 56, 58, 63, 68	58
	3	1	107, 107, 108, 115.5	109.4
	3	2	55.5, 55.5, 58.5, 62	57.9
	3	3	33.5, 34, 36.5, 38	35.5
Southern floe	3	1	140, 142, 154, 166, 171	154.6
24h floe	1	1	61, 71, 75, 164	92.8
	2	1	94, 97, 100, 101, 113, 140, 148	113.3
	3	1	143, 157, 173, 182	163.8

The 2-D spatial resolution of the hyperspectral camera additionally enables the investigation of the dependency of the measured reflectance on the viewing incidence angle. Figure 3.4.13 shows an example where measurements were conducted at one position for four different viewing incidence angles. The spectra plotted in coloured lines are averages over pixels of one surface type class and angle which is divided into 1° steps.

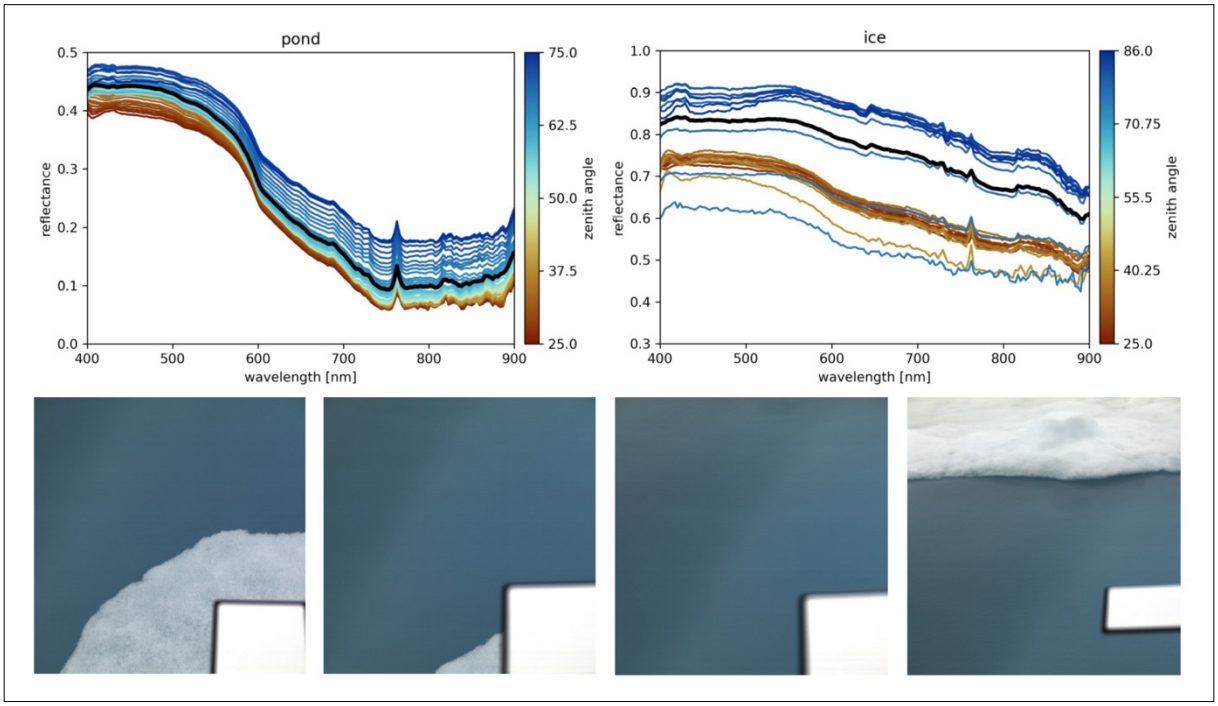

Fig. 3.4.13: Angle dependent reflectance measurements taken on 28 July 2022 on the 24h floe: Top left: Reflectance spectra of the pond pixels of all four images shown in the bottom row – the thick black line shows the average of all pond pixels, the coloured lines show the averages of the pixels subdivided with regard to the viewing incidence angle which can be seen from the colour bar. Top right: Same as top left but for the pixels classified as ice surface; note the different scales and colour scales. Bottom row: RGB composites of the measured surface – the camera is at one constant position, the viewing incidence angle is increasing from 40° to 70° in 10° steps from left to right.

The reflectance is increasing with the viewing incidence angle for both surface types throughout the entire measured spectrum while its shaped remains relatively unchanged. For the pond surface the transition is quite smooth, mainly because there is a continuous range covered by the melt pond. The spectra of the ice surface show a distinct gap which is due to the fact that there are only ice pixels below ~40 ° and above ~75 °. For future investigations it would be an idea to consider measurements with ice and pond areas side by side (in horizontal axis) for all angles for improved comparison. Additionally, there are few outliers for the ice spectra which is most probably explained by shadowing effects. Overall, the trend is not as straight forward for ice as for ponds most likely because of the higher roughness with many different surface orientations on small scales.

RAMSES under-ice spectrometer

For visualization of the transmittance, the measured spectral intensities (307–1243 nm) are integrated to obtain broadband incoming and transmitted intensities. Because of the automatically adapted integration time of measurements, the two sensors do not measure necessarily exactly at the same times. To enable the calculation of the ratio of transmitted to incoming intensity, the measurements are resampled and interpolated with a maximum

interpolation range of 10 s. Figure 3.4.14 shows an example of the total transmittance depth profiles measured during the three visits of the northern floe in a logarithmic representation. Note that the measurements were not conducted at the same locations on the floe. The dashed lines indicate the bottom of the ice, they are almost the same for the three cases and are thus barely distinguishable. For the first two visits the transmitted radiation is very similar directly underneath the ice. The strongly reduced transmittance at the top of the profile during visit 3 (green) can be explained by the ridge with larger ice thicknesses that was close by. Also it should be noted that in this case there was an additional ice layer around 1.5 m below the initial ice bottom. This could be a reason for the strong decrease of the transmitted radiation at around 4 m depth.

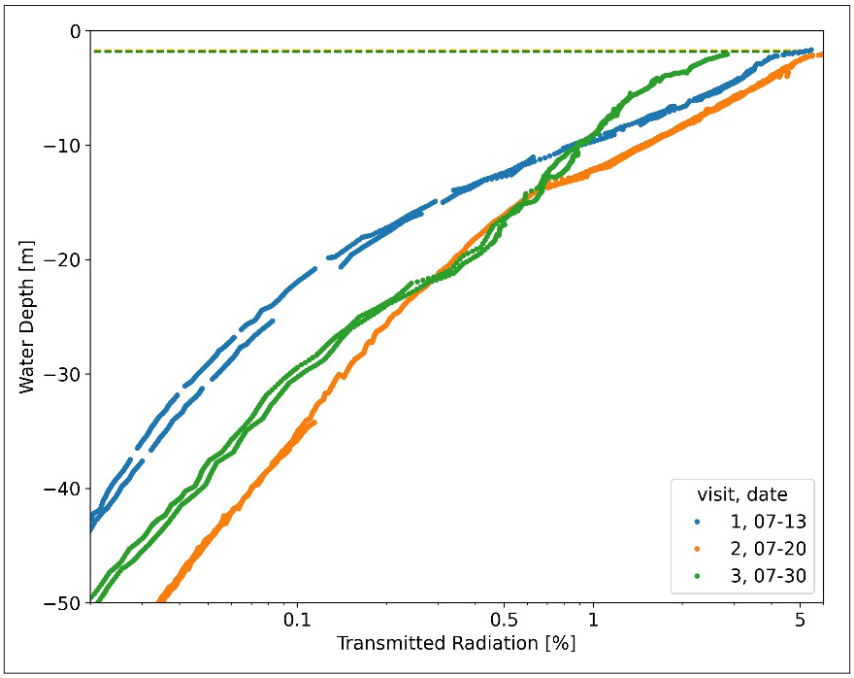

Fig. 3.4.14: Ratio of transmitted to incoming radiation with regard to the depth of the transmittance sensor for the measurements during the three visits of the northern floe: The colours indicate the number of visit and corresponding date; the coloured dashed lines mark the bottom of the ice for the respective measurements; the two slightly different lines per measurement result from the upward and downward moving measurements.

The gaps in the profile measured during visit 1 are dedicated to lowering the sensor at a speed that was not constant and too high which was adapted in the later measurements. The difference between the measuring results during the downward and upward motion of the sensor might be related to differences of the tilt of the sensor or to the different depth range that is integrated and might be an indicator of the measurement uncertainty. In the case of visit 3 from a depth of 5 m downwards the profile fits relatively well to the expected exponential decrease of transmitted radiation for homogenous water (Beer-Lambert law). The deviations from that exponential law could be linked to surface features such as melt ponds or ridges increasing or reducing the light transmittance, respectively, or changes, like algae, within the water column. In the other two cases the profiles show a stronger decrease of transmittance in the upper 15 m that is slowing down towards deeper waters.

During the 24h floe station it was possible to repeat the profiling several times at the same location. In the upper 25 m all profiles, displayed in Figure 3.4.15 (left), show the expected exponential decrease with only little deviations. For the measurements at the beginning of

the ~24 hours this behaviour is also true down to a depth of 50 m. With time evolving the transmittance is decreasing faster below 25 m depth. The minimum of transmitted radiation at constant depth reached around noon with a slight increase again afterwards. The right part of Figure 3.4.15 shows the daily cycle of incoming (dashed lines) and transmitted (solid lines) radiation. The transmitted intensity at three different depths (5, 10, 20 m) is selected and plotted against the starting time of the respective profile measurement. For reference the measurement of incoming intensity at the same time is displayed, normalized to the same initial intensity value as the transmitted measurement. The daily cycle is visible in both measurements.

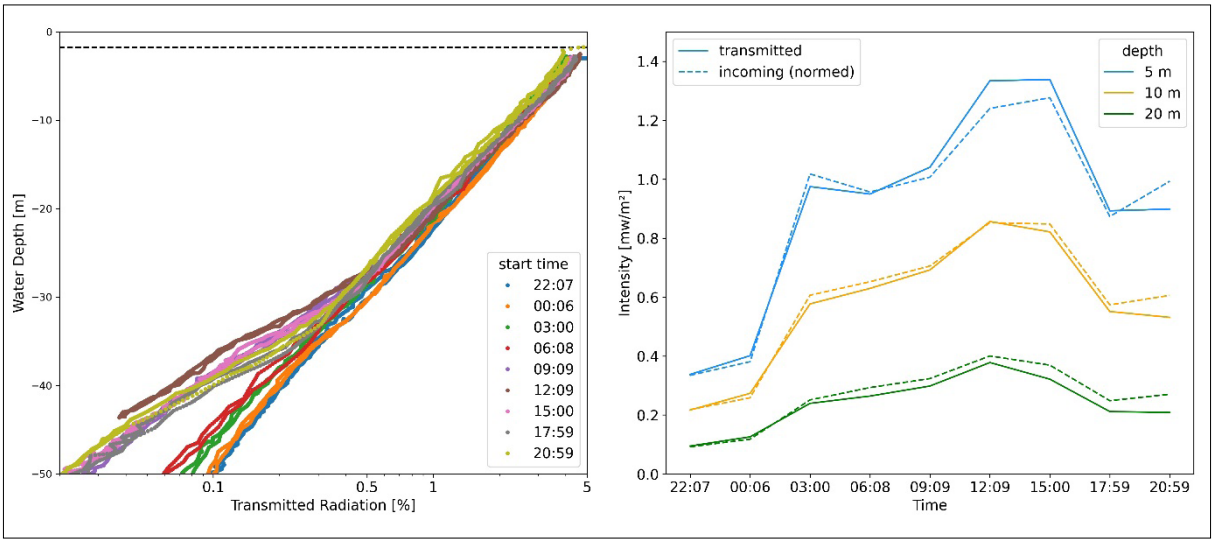

Fig. 3.4.15: Transmittance measurements conducted on the 24h floe: Left: Ratio of transmitted to incoming radiation with regard to the depth of the transmittance sensor; all profiles were measured at the same location, the colours indicate the time the profile measurements were started. The dashed lines mark the bottom of the ice. The two slightly different lines per measurement result from the upward and downward moving measurements. Right: Visualization of the daily cycle; plotted is the transmitted intensity (solid lines) at certain depths of the measured profiles throughout the 24 hours and for comparison the incoming measured intensity each normalized to the same start values as the transmitted intensities.

3.5 Microphysics of sea ice and surface scattering layer (SSL)

Janna Rückert[1], Andreas Walbröl[2], Gunnar Spreen[1]

[1]DE.UNI-Bremen
[2]DE.UNI-Köln

Microphysical examinations of the sea ice and surface scattering layer (SSL) on-top were conducted in collaboration with the “Water Vapour, Cloud Liquid Water, and Surface Emissivity” work described in Chapter 8.

Ice cores were taken at different sites on each floe (locations indicated in Fig. 3.2.3) together with microphysical descriptions (grain/needle sizes, density, salinity etc.) of the SSL. Surface roughness were determined by *Structure-from-Motion* photography and the dielectric properties of SSL and ice measured by a Stevens HydraProbe. Detailed descriptions of the measurements in the context of microphysics of sea ice and surface scattering layer (SSL) can be found in Section 8.2.

3.6 Satellite remote sensing

Christian Haas[1], Gunnar Spreen[2]

[1]DE.AWI
[2]DE.UNI-Bremen

Objectives

Information from satellite data is essentially required in support of ship navigation in the ice, for station and research planning, and for the interpretation and regional extrapolation of sea ice observations and research results. While most satellite data suffer from clouds most of the time which obscure the views of the ice, during PS131/ATWAICE we mostly relied on synthetic aperture radar (SAR) images which are not affected by clouds.

Work at sea

General

On board *Polarstern*, we have received all available Sentinel-1 and TerraSAR-X images over our study region in near-real time. Sentinel 1 is a mission of the European Space Agency (ESA) and TerraSar is a mission of the German Aerospace Center (DLR). Unfortunately image acquisitions are irregular and difficult to plan, therefore special arrangements were made prior to the cruise, as outline below.

On board, images were stored automatically such that they could immediately be viewed with *Polarstern's* MapViewer system, and overlaid with the cruise track and other information.

Sentinel-1

Sentinel-1 data acquisitions were planned prior to the cruise with AWI's FramSat acquisition system. In FramSat, two study regions were defined ("fram-strait-and-aurora" and "ne-greenland"). The system then continuously searches the ESA near-real-time archive for new images from those regions and downloads them. Once received, images are processed and converted to geotiff. The geotiff images are then provided on an ftp server which is regularly accessed and searched by the ship.

During the PS131 cruise regular Sentinel-1 acquisitions were limited to about 82°N, i.e. there were no images available over our more northern study regions and for the sailing to the Aurora field. In cooperation with ESA (special thanks to Luca Martino and Pierre Potin) the Sentinel-1 coverage could be extended up to 85°N on some days during the core time of the cruise. In total 11 extra Sentinel-1 scenes in Extra Wide Swath mode (HH/HV) were taken between 11 July and 7 August 2022. FramSat was also able to detect those and provided them to the ship in due time.

TerraSAR-X

TerraSAR-X data are usually not freely available, nor is there a systematic image acquisition plan for the Arctic. However, for ATWAICE a special contract was set up between AWI logistics and the DLR Remote Sensing Technology Institute (DLR IMF) in Bremen to plan every possible acquisition over our study region, noting that the position of the *Polarstern* is not well known 24 hours in advance of any satellite overpass when the acquisition needs to be planned at the latest. Therefore, we updated DLR regularly on our latest plans and likely position. This was somewhat simplified by the fact that our study region was small and that we did repeat the same transects several times.

Images were sent by email in png format with auxiliary geolocation files that could be read by the MapViewer and by the QGIS software.

In total 67 TerraSAR-X scenes from the ATWAICE study region were taken and received onboard. 26 of them were taken in higher resolution but smaller coverage strip mode (SM) and the majority of 41 scenes in scan SAR mode (SC). The SM acquisitions were mainly focused on the MIZ region with the repeated ATWAICE transect and ice stations. A map with all scenes is shown in Figure 3.6.1.

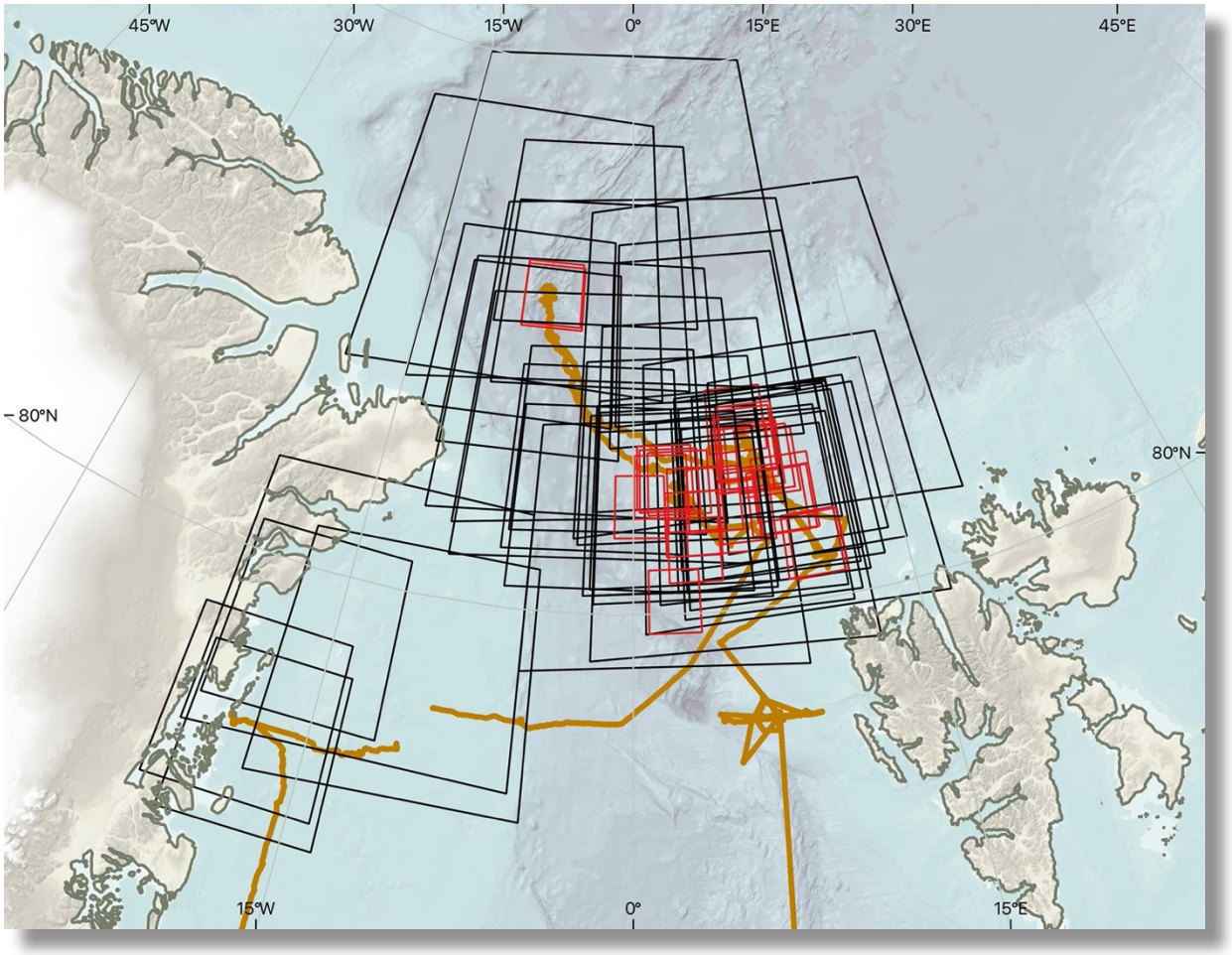

Fig. 3.6.1: Overview of the 67 TerraSAR-X scenes taken during the PS131 cruise: Red outlines mark scenes acquired in SM mode and black in SC mode. The cruise track is shown as brown line in the background.

Preliminary (expected) results

Both, Sentinel-1 and TerraSAR-X coverage and acquisitions were highly successful and updated ice information was available every one to three days. Images will be invaluable for future analysis of ice conditions and regional ice type and floe size differences, as well as for better interpreting radar backscatter. Our *in-situ*, ship-based, and airborne data will be invaluable for the validation of new SAR analysis and retrieval methods.

Of particular value were the TerraSAR-X images with their much higher pixel resolution than those of Sentinel-1. Figure 3.6.2 shows an example of a scan SAR image acquired on 31 July at 15:26 UTC. The broken track of *Polarstern* can be seen very well, as well as the ship itself (bright spot at end of track on lower right quarter of image). It is remarkable that the old tracks

several days old are still visible which indicates quite coherent ice motion with little internal deformation. The image also shows different floe size regimes in close proximity to each other.

Another example of a TerraSAR-X image that includes the ship and shows different kinds of detail is shown in Figure 3.3.10.

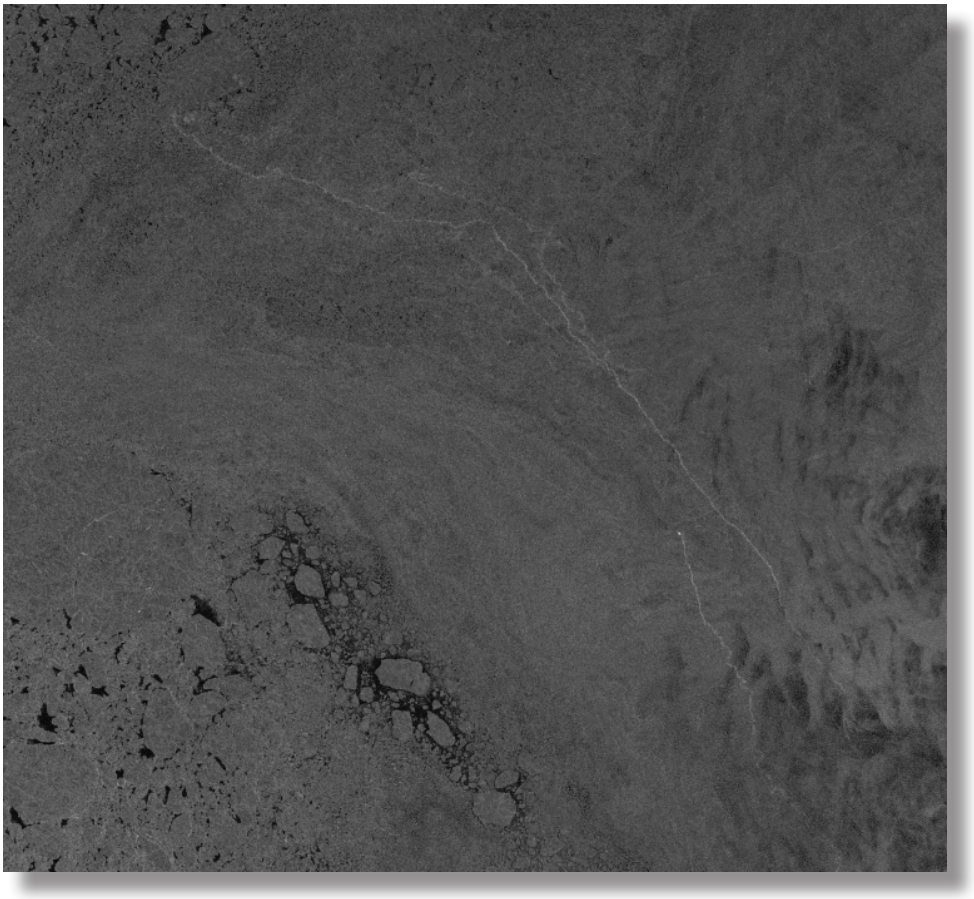

Fig. 3.6.2: TerraSAR-X scan SAR image acquired on 31 July at 15:26 UTC. Note various ship tracks as well as the ship itself (bright spot in lower right quarter of image).

Data management

After the cruise the visual ice observation data will be made openly available via the Ice Watch website hosted by the Norwegian Ice Service (https://icewatch.met.no/assist). This is a continuation of the service initiated and previously hosted at the University of Alaska Fairbanks. The Ice Watch database contains ship-based sea ice observations from all major Arctic research vessels. The provision of the ASSIST software and the database by the Ice Watch programme is gratefully acknowledged.

Within six months after the cruise, an additional copy of the sea ice observation dataset will be submitted to PANGAEA database to secure long-term storage.

All other sea ice data will be released following final processing after the cruise or depending on the completion of competing obligations (e.g. PhD projects), upon publication as soon as the data are available and quality-assessed. Data submission will be to the PANGAEA database. (https://www.pangaea.de).

This expedition was supported by the Helmholtz Research Programme “Changing Earth – Sustaining our Future” Topic 2, Subtopic 2.1.

In all publications based on this expedition, the **Grant No. AWI_PS131_02** will be quoted and the following publication will be cited:

Alfred-Wegener-Institut Helmholtz-Zentrum für Polar- und Meeresforschung (2017) Polar Research and Supply Vessel *Polarstern* Operated by the Alfred-Wegener-Institute. Journal of large-scale research facilities, 3, A119. http://dx.doi.org/10.17815/jlsrf-3-163.

References

Bárdossy A and Singh SK (2008) Robust estimation of hydrological model parameters. Hydrol. Earth Syst. Sci., 12:1273–1283. https://doi.org/10.5194/hess-12-1273-2008.

Belter HJ, Krumpen T, von Albedyll L, Alekseeva TA, Birnbaum G, Frolov SV, Hendricks S, Herber A., Polyakov I, Raphael I, Ricker R, Serovetnikov SS, Webster M, Haas C (2021) Interannual variability in Transpolar Drift summer sea ice thickness and potential impact of Atlantification. The Cryosphere, 15:2575–2591. https://doi.org/10.5194/tc-15-2575-2021.

Duarte P, Sundfjord A, Meyer A, Hudson SR, Spreen G, Smedsrud LH (2020) Warm Atlantic water explains observed sea ice melt rates north of Svalbard. Journal of Geophysical Research: Oceans, 125, e2019JC015662. https://doi.org/10.1029/2019JC015662.

Haas C (1998) Evaluation of ship-based electromagnetic-inductive thickness measurements of summer sea-ice in the Bellingshausen and Amundsen Seas, Antarctica. Cold Regions Science and Technology, 27:1–16.

Haas C, Pfaffling A, Hendricks S, Rabenstein L, Etienne JL, Rigor I (2008) Reduced ice thickness in Arctic Transpolar Drift favors rapid ice retreat. Geophys. Res. Lett., 35:L17501.

Haas C, Lobach J, Hendricks S, Rabenstein L, Pfaffling A (2009) Helicopter-borne measurements of sea ice thickness, using a small and lightweight, digital EM system. Journal of Applied Geophysics, 67(3):234-241.

Hutchings JK, Delamere J, Heil P (2018) The Ice Watch Manual, Draft 2018/06/30 for ASSIST v4.1. Draft Technical Report, University of Alaska Fairbanks, USA. http://icewatch.gina.alaska.edu/.

Istomina L, Heygster G, Huntemann M, Schwarz P, Birnbaum G, Scharien R, Polashenski C, Perovich D, Zege E, Malinka A, Prikhach A, Katsev I (2015a) Melt pond fraction and spectral sea ice albedo retrieval from MERIS data – Part 1: Validation against in situ, aerial, and ship cruise data. The Cryosphere, 9(4):1551–1566. https://doi.org/10.5194/tc-9-1551-2015.

Istomina L, Heygster G, Huntemann M, Marks H, Melsheimer C, Zege E, Malinka A, Prikhach A, Katsev I (2015b) Melt pond fraction and spectral sea ice albedo retrieval from MERIS data – Part 2: Case studies and trends of sea ice albedo and melt ponds in the Arctic for years 2002–2011. The Cryosphere, 9(4):1567–1578. https://doi.org/10.5194/tc-9-1567-2015.

Malinka, A., E. Zege, L. Istomina, G. Heygster, G. Spreen, D. Perovich, & C. Polashenski (2018). Reflective properties of melt ponds on sea ice. The Cryosphere, 12:1921–1937. https://doi.org/10.5194/tc-12-1921-2018.

Nicolaus M, Hudson SR, Gerland S, Munderloh K (2010) A modern concept for autonomous and continuous measurements of spectral albedo and transmittance of sea ice. Cold Regions Science and Technology, 62(1):14–28.

Nicolaus M, Perovich D, Spreen G, Granskog M, Albedyll L, Angelopoulos M, Anhaus P, Arndt S, Belter H, Bessonov V, Birnbaum G, Brauchle J, Calmer R, Cardellach E, Cheng B, Clemens-Sewall D, Dadic R, Damm E, Boer G, Demir O, Dethloff K, Divine D, Fong A, Fons S, Frey M, Fuchs N, Gabarró C, Gerland S, Goessling H, Gradinger R, Haapala J, Haas C, Hamilton J, Hannula H-R,

Hendricks S, Herber A, Heuzé C, Hoppmann M, Høyland K, Huntemann M, Hutchings J, Hwang B, Itkin P, Jacobi H-W, Jaggi M, Jutila A, Kaleschke L, Katlein C, Kolabutin N, Krampe D, Kristensen S, Krumpen T, Kurtz N, Lampert A, Lange B, Lei R, Light B, Linhardt F, Liston G, Loose B, Macfarlane A, Mahmud M, Matero I, Maus S, Morgenstern A, Naderpour R, Nandan V, Niubom A, Oggier M, Oppelt N, Pätzold F, Perron C, Petrovsky T, Pirazzini R, Polashenski C, Rabe B, Raphael I, Regnery J, Rex M, Ricker R, Riemann-Campe K, Rinke A, Rohde J, Salganik E, Scharien R, Schiller M, Schneebeli M, Semmling M, Shimanchuk E, Shupe M, Smith M, Smolyanitsky V, Sokolov V, Stanton T, Stroeve J, Thielke L, Timofeeva A, Tonboe R, Tavri A, Tsamados M, Wagner D, Watkins D, Webster M, Wendisch M. 2022. Overview of the MOSAiC expedition – Snow and sea ice. Elementa Science of the Anthropocene 9. https://doi.org/10.1525/elementa.2021.000046.

König M, Hieronymi M, Oppelt N (2019) Application of Sentinel-2 MSI in Arctic Research: Evaluating the Performance of Atmospheric Correction Approaches Over Arctic Sea Ice. Front. Earth Sci., 7. https://doi.org/10.3389/feart.2019.00022.

Malinka A, Zege E, Istomina L, Heygster G, Spreen G, Perovich D, Polashenski C (2018) Reflective properties of melt ponds on sea ice. The Cryosphere, 12:1921–1937. https://doi.org/10.5194/tc-12-1921-2018.

Provost C, Sennechael N, Miguet J, Itkin P, Rösel A, Koenig Z, Villacieros-Robineau N, Granskog MA (2017) Observations of flooding and snow-ice formation in a thinner Arctic sea-ice regime during the N-ICE2015 campaign: Influence of basal ice melt and storms. J. Geophys. Res. Oceans, 122:7115–7134. https://doi.org/10.1002/2016JC012011.

Rabe B, Heuze C, Regnery J, Aksenov Y, Allerholt J, Athanase M, Bai Y, Basque C, Bauch D, Baumann TM, Chen D, Cole ST, Craw L, Davies A, Damm E, Dethloff K, Divine DV, Doglioni F, Ebert F, Fang Y-C, Fer I, Fong AA, Gradinger R, Granskog MA, Graupner R, Haas C, He H, He Y, Hoppmann M, Janout M, Kadko D, Kanzow T, Karam S, Kawaguchi Y, Koenig Z, Kong B, Krishfield RA, Krumpen T, Kuhlmey D, Kuznetsov I, Lan M, Lei R, Li T, Torres-Valdes S, Lin L, Lin L, Liu H, Liu N, Loose B, Ma X, MacKay R, Mallet M, Mallett RDC, Maslowski W, Mertens C, Mohrholz V, Muilwijk M, Nicolaus M, O'Brien JK, Perovich D, Ren J, Rex M, Ribeiro N, Rinke A, Schaffer J, Schuffenhauer I, Schulz K, Shupe MD, Shaw W, Sokolov V, Sommerfeld A, Spreen G, Stanton T, Stephens M, Su J, Sukhikh N, Sundfjord A, Thomisch K, Tippenhauer S, Toole JM, Vredenborg M, Walter M, Wang H, Wang L, Wang Y, Wendisch M, Zhao J, Zhou M, Zhu J, Laukert G (2022) Overview of the MOSAiC expedition: Physical oceanography. Elementa: Science of the Anthropocene 10(1). https://doi.org/10.1525/elementa.2021.00062.

Rabenstein L, Hendricks S, Martin T, Pfaffhuber A, Haas C (2010) Thickness and surface-properties of different sea-ice regimes within the Arctic Trans Polar Drift: data from summers 2001, 2004 and 2007. J. Geophys. Res., 115: C12059.

Sirevaag A, de la Rosa S, Fer I, Nicolaus M, Tjernström M, McPhee MG (2011) Mixing, heat fluxes and heat content evolution of the Arctic Ocean mixed layer. Ocean Sci., 7, 335–349. https://doi.org/10.5194/os-7-335-2011.

Wang M, König M, Oppelt N (2021) Partial Shape Recognition for Sea Ice Motion Retrieval in the Marginal Ice Zone from Sentinel-1 and Sentinel-2. Remote Sens., 13(21):4473. https://doi.org/10.3390/rs13214473.

WMO (1989) WMO sea ice nomenclature. World Meteorological Organization, Geneva, Switzerland, WMO/OMM/BMO 259-TP-145, suppl. 5.

Worby A, Allison I (1999) A technique for making ship-based observations of Antarctic sea ice thickness and characteristics, Part 1 Observational technique and results. Cooperative research centre for the Antarctic and Southern Ocean environment. Hobart, Tasmania, Australia, 14.

Zege E, Malinka A, Katsev I, Prikhach A, Heygster G, Istomina L, Birnbaum G, Schwarz P (2015) Algorithm to retrieve the melt pond fraction and the spectral albedo of Arctic summer ice from satellite optical data. Remote Sens. Environ., 163:153–164. https://doi.org/10.1016/j.rse.2015.03.012.

4. VERTICAL TURBULENT AEROSOL PARTICLE TRANSPORT ABOVE OPEN WATER AND ICE IN THE CENTRAL ARCTIC DURING SUMMERTIME (APAICA) – AEROSOL PARTICLE SOURCES AND TRANSFORMATION IN THE ARCTIC MARINE BOUNDARY LAYER

Arun Babu Suja[1], Philipp Oehlke[1], Sabine Lüchtrath[2]
Not on board: Birgit Wehner[1], Thomas Müller[1], Laurent Poulain[1], Maik Merkel[1], Holger Siebert[1], Heike Wex[1], Manuela van Pinxteren[1], Andreas Held[2]

[1]DE.TROPOS
[2]DE.TU-BERLIN

Grant-No. AWI_PS131_04

Outline

Aerosol particles are a key component of the Arctic climate system. Depending on their optical properties, their ice nucleating properties, and their ability to form and modify Arctic clouds, aerosol particles change the radiation budget. Therefore, it is important to identify and quantify Arctic particle sources and sinks, including vertical transport, and to characterise their optical properties as well as their impact on cloud formation. However, there have only been very few surface-atmosphere particle flux measurements above open water and ice in the Central Arctic, and data on physical and chemical properties of Arctic aerosol particles are scarce. This project will focus on the turbulent flux of aerosol particles and on black carbon as well as ice nucleating particles (INP) in the air and ocean water.

Turbulent particle fluxes

To date, turbulent particle flux measurements in the Arctic and Antarctic regions have been made over snow and rock cover in Antarctica (Grönlund et al., 2002), over the Nansen Ice Sheet in Antarctica (Contini et al., 2010), over unbroken sea ice in the Canadian Hudson Bay (Whitehead et al., 2012), and in the Central Arctic Ocean (Nilsson and Rannik, 2001; Held et al., 2011a, b). Saylor et al. (2019) point out that there are not enough observations to evaluate the validity of parameterizations for particle dry deposition over snow and ice surfaces used in models, and local particle emission strengths are not well constrained. One local particle emission source are open leads, which have been described as potential sources of atmospheric particles for the first time by Scott and Levin (1972). Nilsson and Rannik (2001) measured turbulent particle fluxes by eddy covariance in the high Arctic over the open sea and over the pack ice. However, the measurement footprints over the pack ice were generally large, and Nilsson and Rannik (2001) acknowledge that most measurements were influenced by a mix of open lead and ice surfaces. Using eddy covariance and gradient measurements on the edge of an ice floe, Held et al. (2011a, b) observed a larger fraction of net emission aerosol fluxes over open leads compared to mostly net deposition over the pack ice. However, the measured aerosol fluxes could not fully explain the observed changes in particle number concentration. Thus, it is extremely important to better quantify and constrain the contribution of vertical turbulent particle fluxes and other processes to the local particle number budget in the Central Arctic boundary layer.

Black carbon

Black carbon (BC) is the most efficient atmospheric absorber of visible light (Bond et al., 2013). BC-containing particles in the Arctic can affect the radiation balance in various ways. BC particles warm the atmosphere directly by absorption of solar radiation (Haywood and Shine, 1995), and affect distribution, microphysical properties and lifetime of clouds through indirect and semidirect effects (Twomey, 1974, Ackerman et al., 2000; Jacobson, 2012; Bond et al., 2013). The mixing state plays an essential role in these processes. Studies on the mixing state in Arctic regions have been carried out by e.g., Raatikainen (2015), Zanatta (2018), and Abbatt (2019). Furthermore, BC can darken the surface and enhance absorption of radiation when deposited on snow (Quinn et al., 2011). In the airborne state, a coating on BC particles can lead to an increase in light absorption (Schwarz 2008) and also affect the ability of how well they can act as CCN (Cloud Condensation Nuclei) (e.g., Maskey et al., 2017). Motos et al. (2019) showed that externally mixed soot particles in fog with supersaturations between 0.03 % and 0.06 % do no act as CCN, while soot particles with a thick coating show a similar behaviour as soot free particles. Overall, the wet deposition for black carbon is slower than for other particles (Dlugi, 1989). Moreover, Ding et al. (2019) depicted the influence of soot on the fog formation through feedback mechanisms. Measurements of the undissolved part of refractory black carbon (rBC) in low-salinity water have been done (Bisiaux et al. 2011; Torres et al. 2014). Ohata et al. (2013) showed that rBC can be detected with modern methods (Single Particle Soot Photometer, SP2) even at low concentrations in rainwater, and measurements of soot in cloud droplets were shown in Schroder et al. (2015). There is only sparse information on the deposition of BC in the ocean (Jurado et al., 2008). Thus, collocated measurements of airborne rBC particles and rBC in fog droplets and in the ocean would improve our understanding of the mechanisms of the magnitude of rBC deposition into the ocean. However, no measurements have yet been carried out with the SP2 for ocean water with high salinity. A cross-sensitivity of the SP2 to sea salt was found in Zanatta et al. (2021) for Arctic snow samples. A desalination method was described by Zeppenfeld et al. (2020) but was not used to examine the rBC content of ocean water so far.

Ice nucleating particles

Ice nucleating particles (INP) are needed for the formation of primary ice crystals in supercooled clouds down to temperatures of ~ –38° C, the mixed phase cloud regime. The abundance of INP in the atmosphere has therefore a large effect on cloud glaciation, which then, in turn, has an effect on the cloud radiative properties, lifetime and precipitation formation. Sources for atmospheric INP, the INP abundance and possible parameterizations describing the latter have become an intensely researched field in the past years. It becomes clearer that INP concentrations at remote marine locations are comparably low (McCluskey et al., 2018a,b; Welti et al., 2020) while mineral dust particles and also biogenic particles emitted from continents contribute large fractions of the overall atmospheric INP load (Welti et al., 2020; Gong et al., 2020a, b). Based on airborne measurements from different campaigns, it was observed that mixed phase clouds in the Arctic contain larger fractions of supercooled liquid droplets, compared to clouds in midlatitudes and the tropics (Costa et al., 2017). This was assumed to originate in low INP concentrations. However, newer ground-based measurements from the Arctic show that there is a pronounced annual cycle in INP concentrations, with high concentrations observed in spring and summer months (Wex et al., 2019, Creamean et al., 2018; Tobo et al., 2019; Šantl-Temkiv et al., 2019). Sources for these cannot easily be attributed, and marine as well as terrestrial Arctic sources were suggested (Creamean et al., 2018; Wex et al., 2019). For INP active at –25° C, collected in the Canadian Arctic (in Alert) in spring, Si et al. (2019) found that INP concentrations correlated with mineral dust tracers and suggested long range transport and origin in the Gobi Desert. On the other hand, during an aircraft campaign conducted from Northern Greenland (Villum Research Station) in spring, high

INP concentrations at temperatures above –15° C were observed when flights took place at low altitudes over open leads and polynyas (Hartmann et al., 2020). For these INP, collocated measurements indicated a local marine source. In another campaign, a comparison was done for INP concentrations determined simultaneously for the Arctic Ocean water and air, and airborne concentrations were orders of magnitude above those that could be expected if sea spray was the major contributor to atmospheric INP, while, no clear source apportionment could be done, although a large number of parameters was tested (Hartmann et al., 2021).

Objectives

Overall, it is important to improve our understanding of Arctic aerosol particles and clouds, particularly mixed phase clouds, and their role in the effect of the observed strong Arctic warming (known as Arctic Amplification, Serreze and Barry, 2011), where aerosols and clouds are included in a complex web of interactions and feedbacks (Morisson et al., 2012). The cold and mixed phase in these clouds plays an important role, so sources and abundancies of INP need to be understood much better and for that, more detailed studies are needed (Solomon et al., 2018).

During the *Polarstern* cruise PS131 we aim to contribute to a better understanding of "Ocean-sea ice-atmosphere coupling in the MIZ and controls on the ecosystem" by addressing the following research questions:

- What are magnitude and sign of turbulent particle fluxes and how do they vary for different types of surface and meteorological conditions?
- What are the contributions of (i) local particle emission from the ocean and (ii) new particle formation (NPF) to the entire budget of Arctic marine boundary layer (MBL) aerosol concentration? What are the controlling factors of these processes?
- How large are BC concentrations in the air, fog and ocean?
- How is BC in surface water linked to atmospheric BC and what is the role of the mixing state for deposition?
- What are the major sources for INP in the Arctic MBL, and particularly to what extent does the ocean contribute INP to the Arctic atmosphere?

Work at sea

The atmospheric aerosol measurements were carried out from 29 June 2022 to 12 August 2022 during the expedition. This includes continuous aerosol sampling and measurement activities as well as additional intensive measurements during the selected period on the station when calm conditions allowed us to set up the instruments at the frontal outrigger and the crane. For continuous measurements of physical and chemical aerosol parameters, a laboratory container (Aerosol-Container) equipped with instrumentation (Tab. 4.1) was placed on the first deck of the ship just above the bridge (Peildeck). Continuous Aerosol-Container measurements include particle number size distributions from 9 nm to 10 µm using a combination of SMPS (Scanning Mobility Particle Sizer) and APS (Aerodynamic Particle Sizer), Optical properties, such as absorption and scattering coefficients, were continuously measured by MAAP (Multiangle Absorption Photometer), Aethalometer (AE33), and Nephelometer. The near real-time measurements of the mixing state and size distribution of airborne BC-containing particles were carried out using the Single Particle Soot Photometer (SP2). In addition, a high-volume filter sampler was installed on the roof of the container to collect aerosol particles (PM10) at a sampling regime of 24 h during the cruise to provide information on the total particle mass concentration and the chemical composition of the aerosol particles (organic and elemental

carbon, OC/EC, and water-soluble ions) as well as for the INP analysis to provide general coverage of INP concentrations throughout the whole cruise. Sea water samples were taken regularly throughout the cruise from the onboard sea water pipeline in addition to the ice samples from the ice floe stations. All filters and water samples were stored frozen on the ship for offline analysis at TROPOS after the expedition. Frequent occurrence of fog events was observed during the campaign period. During these events, fog and cloud water samples were collected with a sampler placed on top of the aerosol container. A total of 39 fog samples were collected during the expedition (details are given in Table 4.2). These samples were stored frozen right after sampling and will be analyzed offline for rBC and its mixing state, INP concentration, and basic chemical composition (water-soluble ions and water-soluble organic carbon).

Further, we have installed two systems at the bow crane for measuring vertical particle fluxes above different surfaces using the Eddy covariance and Gradient method. For estimating particle fluxes using Eddy covariance, one temperature-stabilized box equipped with an ultrasonic anemometer and a fast mixing-type condensation particle counter (MCPC) was installed at the frontal end of the bow crane's outrigger (Fig. 4.1). The data acquisition rate was 20 Hertz. These measurements were carried out under favourable meteorological conditions and ship movements. Measurements were avoided when the ship was breaking the ice due to the heavy shaking of the bow's crane. A second box equipped with an ultrasonic distance sensor and an MCPC was used to measure the vertical profiles using a winch installed at a custom-built aluminium rack mounted at the end of the crane to move them up and down. These measurements were conducted at specific field stations under favorable meteorological conditions. Each profile measurement took 30 minutes with six measurements of five minutes intervals at different heights starting from 50 cm to 12 m above the ice/ocean surface. This box was operated from a constant height when we were not conducting the profile measurements. The winch was used manually operated from the crane. Since the distance sensor only works in a range of up to 3 m, we developed and painted a bar code on our winch rope in order to know the actual height of the box when it was hanging. The first measurement with both systems was taken place on 13 July 2022, leaving the second box hanging at one height. We started arranging and optimizing the measurement at different heights in the subsequent days. Table 3 gives an overview of flux measurements during the campaign.

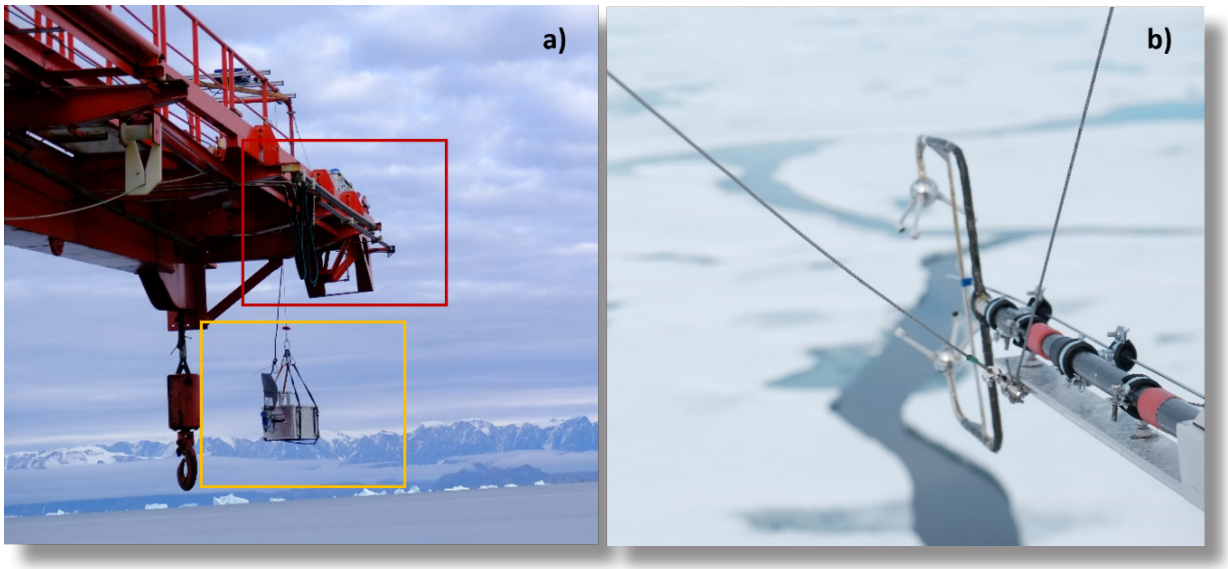

Fig. 4.1: Illustration of the two installed systems: a) One at the end of the bow crane's outrigger (red), the second underneath the crane at different heights (yellow);
b) ultrasonic wind anemometer with the integrated inlet of box 1 above the ice

Tab. 4.1: Overview of the aerosol instrumentation and parameters measured during the campaign

Instruments	Parameters measured
SMPS	Particle number size distribution (sub-micrometer size range)
APS	Particle number size distribution (0.5- 20 μm)
MAAP	eBC mass concentration
Aethalometer	Spectral Absorption coefficient
Single Particle Soot Photometer	Black carbon concentration and mixing state
Nephelometer	Light scattering coefficients and Hemispheric backscattering coefficients
High volume sampler	Chemical composition
Fog water sampler	rBC/INP concentration
Particle sampler	INP concentration
CPCs + Ultrasonic anemometer (3D)	Particle flux

Tab. 4.2: Details of fog sample collection during the expedition

Start		End	
Date and Time (UTC)	**Location**	**Date and Time (UTC)**	**Location**
04-07-2022 10:40:00	76° 19.283' N 06° 21.898' E	04-07-2022 18:54:00	77° 02.662' N 06° 30.858' E
04-07-2022 18:54:00	77° 02.834' N 06° 30.963' E	05-07-2022 07:00:00	79° 00.216' N 06° 59.225' E
09-07-2022 08:57:00	79° 00.035' N 04° 21.450' E	10-07-2022 09:00:00	79° 05.982' N 06° 39.471' E
10-07-2022 09:59:00	79° 14.330' N 06° 10.077' E	11-07-2022 07:00:00	80° 17.396' N 09° 32.992' E
12-07-2022 11:00:00	81° 22.291' N 07° 27.791' E	13-07-2022 06:00:00	81° 37.417' N 06° 49.591' E
13-07-2022 08:23:00	81° 36.588' N 06° 50.152' E	13-07-2022 20:10:00	81° 36.468' N 06° 38.435' E
13-07-2022 20:10:00	81° 36.469' N 06° 38.421' E	14-07-2022 05:00:00	81° 13.903' N 07° 55.935' E
14-07-2022 05:00:00	81° 13.897' N 07° 55.960' E	14-07-2022 16:30:00	81° 11.440' N 07° 34.962' E
14-07-2022 17:06:00	81° 11.533' N 07° 33.991' E	15-07-2022 06:00:00	81° 23.013' N 07° 05.925' E
15-07-2022 06:00:00	81° 23.005' N 07° 05.890' E	15-07-2022 18:10:00	81° 21.557' N 06° 37.216' E
15-07-2022 18:10:00	81° 21.524' N 06° 37.520' E	16-07-2022 11:00:00	80° 41.127' N 11° 55.510' E
20-07-2022 12:22:00	81° 29.917' N 06° 53.611' E	20-07-2022 21:59:00	81° 29.639' N 04° 42.927' E

Start		End	
Date and Time (UTC)	**Location**	**Date and Time (UTC)**	**Location**
20-07-2022 23:25:00	81° 29.745’ N 04° 40.991’ E	21-07-2022 11:20:00	81° 11.502’ N 05° 26.196’ E
21-07-2022 11:20:00	81° 11.502’ N 05° 26.196’ E	22-07-2022 06:40:00	81° 20.293’ N 06° 04.350’ E
22-07-2022 07:05:00	81° 20.293’ N 06° 04.350’ E	22-07-2022 17:44:00	81° 19.955’ N 05° 05.306’ E
22-07-2022 17:44:00	81° 19.955’ N 05° 05.306’ W	23-07-2022 12:35:00	81° 45.910’ N 02° 05.712’ W
23-07-2022 12:50:00	81° 45.895’ N 02° 05.880’ W	24-07-2022 04:00:00	82° 16.741’ N 04° 39.910’ W
24-07-2022 08:10:00	82° 29.211’ N 05° 27.421’ W	24-07-2022 11:45:00	82° 41.035’ N 05°59.152’ W
24-07-2022 20:10:00	82° 51.988’ N 05° 45.798’ W	25-07-2022 15:15:00	82° 53.895’ N 06° 14.959’ W
25-07-2022 06:15:00	82° 53.790’ N 06° 11.849’ W	26-07-2022 06:15:00	82° 31.117’ N 05° 58.769’ W
26-07-2022 18:44:00	81° 53.842’ N 03° 12.658’ W	27-07-2022 07:30:00	81° 25.030’ N 00° 05.928’ W
27-07-2022 08:30:00	81° 23.572’ N 00° 02.234’ E	27-07-2022 20:00:00	81° 21.982’ N 01° 26.460’ E
27-07-2022 20:00:00	81° 21.982’ N 01° 26.444’ E	28-07-2022 21:20:00	81° 18.593’ N 01° 09.747’ E
28-07-2022 20:10:00	81° 18.593’ N 01° 09.747’ E	29-07-2022 09:10:00	81° 07.14’ N 03° 02.612’ E
29-07-2022 09:10:00	81° 07.14’ N 03° 02.612’ E	30-07-2022 06:40:00	81° 11.777’ N 02° 23.106’ E
30-07-2022 17:45:00	81° 05.255’ N 03° 09.143’ E	31-07-2022 10:55:00	80° 56.008’ N 03° 52.346’ E
31-07-2022 12:55:00	80° 56.008’ N 03° 52.346’ E	31-07-2022 18:36:00	81° 04.482’ N 02° 11.503’ E
31-07-2022 18:36:00	81° 04.482’ N 02° 11.503’ E	01-08-2022 06:40:00	80° 46.139’ N 04° 17.094’ E
01-08-2022 06:40:00	80° 46.139’ N 04° 17.094’ E	01-08-2022 19:10:00	80° 38 .396’ N 05° 36.748’ E
01-08-2022 19:10:00	80° 38 .396’ N 05° 36.748’ E	01-08-2022 12:20:00	80° 29.843’ N 06° 47.604’ E
02-08-2022 12:20:00	80° 29.843’ N 06° 47.604’ E	03-08-2022 06:00:00	79° 00.405’ N 03° 08.105’ W
03-08-2022 06:00:00	79° 00.405’ N 03° 08.105’ W	03-08-2022 13:10:00	78° 59.172’ N 05° 21.710’ W
03-08-2022 13:10:00	78° 59.172’ N 05° 21.710’ W	04-08-2022 12:00:00	78 41.108’ N 10 53.391’ W

Start		End	
Date and Time (UTC)	**Location**	**Date and Time (UTC)**	**Location**
04-08-2022 19:30:00	78° 26 823' N 12° 43.872' W	06-08-2022 06:20:00	78° 26.766' N 18° 25.037' W
06-08-2022 06:20:00	78° 26.766' N 18° 25.037' W	07-08-2022 05:50:00	78° 10.711' N 15° 43.194' W
07-08-2022 05:50:00	78° 107.1' N 15° 43.194' W	08-07-2022 02:10:00	76° 36.804' N 15° 32.160' W
08-08-2022 16:30:00	74° 40.501' N 16° 33.082' W	09-08-2022 03:15:00	73° 30.146' N 17° 54.063' W
09-08-2022 03:15:00	73° 30.146' N 17° 54.063' W	10-08-2022 08:25:00	70° 54.465' N 24° 54.021' W
11-08-2022 04:44:00	70° 17.553' N 22° 41.775' W	12-08-2022 07:30:00	68° 40.501' N 15° 57.269' W

Tab. 4.3: Time and position of conducted vertical particle flux measurements. The orange rows show the measurements when both systems were running

Time and position at the start				Time and position at the end			
Date (2022)	**Time (UTC)**	**Latitude**	**Longitude**	**Date**	**Time (UTC)**	**Latitude**	**Longitude**
02.07.	14:14	68° 40.373' N	04° 45.351' E	02.07	17:49	69° 17.794' N	04° 58.845' E
07.07.	11:14	79° 00.694' N	07° 01.986' E	07.07	12:50	79° 00.049' N	06° 49.422' E
07.07.	14:59	79° 00.015' N	05° 39.979' E	0v7.07	15:29	79° 00.019' N	05° 39.964' E
08.07.	09:12	79° 10.006' N	06° 19.898' E	08.07	13:18	78° 59.989' N	07° 59.946' E
08.07	13:18	78° 59.989' N	07° 59.954' E	08.07	19:50	78° 59.420' N	06° 29.279' E
11.07.	14:28	80° 31.585' N	10° 06.990' E	12.07	06:50	81° 13.364' N	07° 57.984' E
13.07.	11:15	81° 35.733' N	06° 47.588' E	13.07	16:46	81° 35.992' N	06° 40.140' E
15.07.	13:09	81° 21.029' N	06° 45.983' E	15.07	18:47	81° 21.673' N	06° 35.716' E
16.0.7	18:20	80° 23.135' N	10° 56.437' E	16.07	20:42	80° 26.292' N	10° 20.058' E
17.07.	13:57	80° 37.216' N	09° 47.043' E	18.07	13:11	80° 37.543' N	06° 40.140' E
18.07.	14:00	80° 39.148' N	09° 38.070' E	19.07	14:32	81° 00.625' N	08° 40.110' E
19.07.	15:26	81° 03.860' N	08° 32.588' E	20.07	06:45	81° 32.427' N	07° 10.660' E
20.07.	08:10	81° 30.690' N	07° 10.969' E	20.07	13:02	81° 29.264' N	06° 28.495' E
20.07.	21:15	81° 29.645' N	04° 44.004' E	20.07	23:32	81° 29.759' N	04° 40.826' E
22.07.	10:37	81° 21.314' N	05° 09.140' E	22.07	14:34	81° 20.684' N	05° 06.467' E
24.07.	15:23	82° 50.022' N	06° 40.818' W	24.07	20:38	82° 51.872' N	05°46.152'W
24.07.	20:39	82° 51.873' N	05° 46.146' W	24.07	21:57	82° 51.770' N	05°47.057'W
25.07.	14:00	82° 54.047' N	06° 14.374' W	25.07	15:10	82° 53.930' N	06°14.840'W
29.07.	09:08	81° 12.404' N	03° 06.906 E	29.07	19:58	81° 04.806' N	03° 11.575' E
30.07.	06:47	81° 11.790' N	02° 14.297 E	30.07	14:54	81° 10.416' N	02° 26.319' E
31.07.	21:41	81° 04.029' N	02° 38.290' E	01.08	00:03	81° 03.836' N	02° 04.243' E
04.08.	11:58	78° 41.610' N	10° 04.324 'W	05.08	08:32	78° 28.743' N	05°34.226'W
06.08.	08:51	78° 26.076' N	18° 23.880 'W	06.08	11:49	78° 26.076' N	08°26.342'W

Time and position at the start				Time and position at the end			
Date (2022)	Time (UTC)	Latitude	Longitude	Date	Time (UTC)	Latitude	Longitude
08.08.	08:05	75° 57.985' N	15° 38.570 'W	08.08	16:28	74° 58.209' N	16°12.291'W
10.08.	07:14	70° 45.603' N	24° 45.603 ,W	11.08	07:36	70° 19.422' N	22°20.926'W

The filter samples for INP were collected using the system installed at the frontal outrigger. This filter sampler was operated simultaneously with the particle flux measurement systems. The collected filters were stored frozen on the ship for further analysis after the campaign. Sea water samples were also collected from the onboard sea water pipeline for INP analysis during the beginning and end of each filter sample collection at the frontal outrigger.

Preliminary results

The particle flux measurement system setup was designed for this expedition and worked out well, especially system 1 which was installed at the bows outrigger. A quality check of the data was carried out during regular intervals and it looks well. We also succeeded in doing measurements when the ship was moving, thus recording data while ice concentration was changing. That promises a great comparison of particle fluxes above different surfaces when making use of additional information about ice thickness or ice concentration. Figure 2 shows the overview of flux measurements at different locations above different surfaces. A total of 25 measurements above different surfaces like the above ocean, leads, and different ice concentrations with system 1(marked in red) were carried out. A total of five measurements were carried out on particle concentration at different heights. The in-depth analysis of the data will take place after the expedition at TROPOS and TU Berlin. Online measurements of rBC and its mixing state using the SP2 combined with offline measurements of these parameters in sea water and fog water samples will help to identify transport pathways of BC particles in the Arctic MIZ. For INP, previous studies indicated local marine sources but source apportionment is very difficult. Analysis of sea water, aerosol and fog water samples will show how INP in these compartments are connected, and, together with other analyses done in this study, will help to reveal if the ocean can be a major contributor to atmospheric INP. The parallel sampling of particulate matter, fog and cloud water, and ocean water, combined with particle flux measurements will provide a unique opportunity to better understand ocean-sea ice - atmosphere interactions in the Arctic. Regarding BC-containing particles, there is only sparse information on the deposition of BC into the ocean.

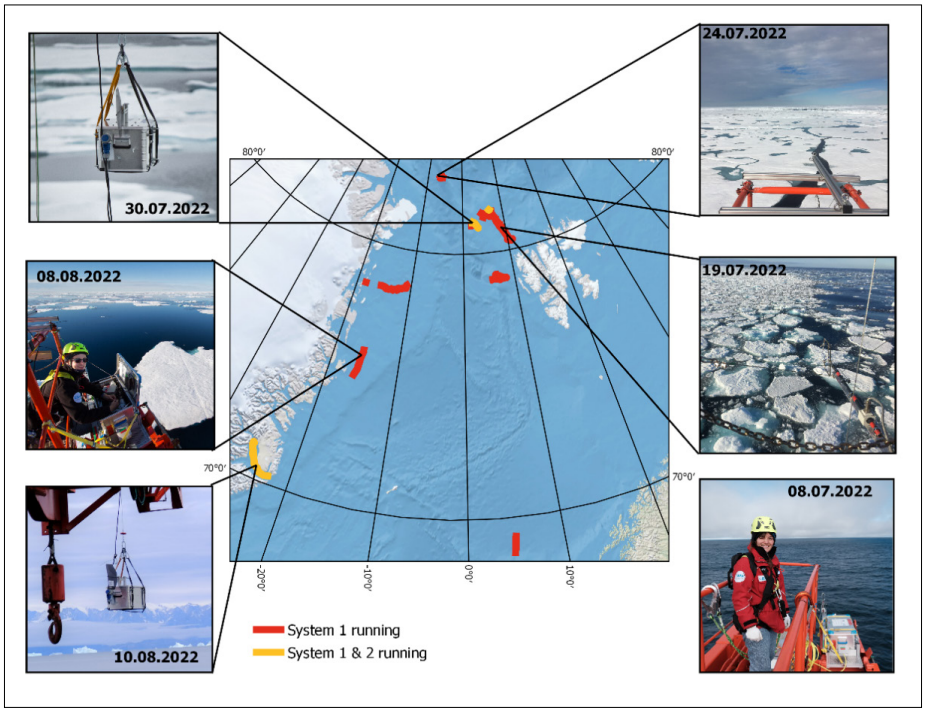

Fig. 4.2: Overview of flux measurements at different locations above different surfaces

Data management

Project results and data products will be distributed through the internet and public media for the broader community. Project results will be published in journals of the AGU (American Geophysical Union), AMS (American Meteorological Society), EGU (European Geosciences Union)/ Other reputed international journals and will be presented on major international conferences and symposia.

All project data sets will be maintained according to the FAIR (Findability, Accessibility, Interoperability, Reusability) data principles. All raw data (level 0 products) will be stored on different devices and platforms with automatic backup. Preliminary and processed data (level 1 products) are shared with the project partners and associated partners via a jointly used cloud storage server in recognised formats together with readme-files and are available to others upon request.

Environmental data will be archived, published and disseminated according to international standards by the World Data Center PANGAEA Data Publisher for Earth & Environmental Science (https://www.pangaea.de) within two years after the end of the cruise at the latest. By default, the CC-BY license will be applied.

Any other data will be submitted to an appropriate long-term archive that provides unique and stable identifiers for the datasets and allows open online access to the data. This project is supported by the German Research Foundation, DFG grants WE 2757/6-1 and HE 5214/10-1.

In all publications based on this expedition, the **Grant No. AWI_PS131_04** will be quoted and the following publication will be cited:

Alfred-Wegener-Institut Helmholtz-Zentrum für Polar- und Meeresforschung. (2017). Polar Research and Supply Vessel *Polarstern* Operated by the Alfred-Wegener-Institute. Journal of large-scale research facilities, 3, A119. http://dx.doi.org/10.17815/jlsrf-3-163.

References

Abbatt J et al. (2019) Overview paper: New insights into aerosol and climate in the Arctic. Atmos. Chem. Phys., 19:2527–2560.

Ackerman AS et al. (2000) Reduction of tropical cloudiness by soot. Science, 288, 1042–1047.

Bisiaux MM et al. (2011) Stormwater and Fire as Sources of Black Carbon Nanoparticles to Lake Tahoe. Environ. Sci. Technol., 45:2065–2071.

Bond TC et al. (2013) Bounding the role of black carbon in the climate system: A scientific assessment. J. Geophys. Res., 118:5380–5552.

Contini D et al. (2010) Deposition velocity of ultrafine particles measured with the eddy-correlation method over the Nansen Ice Sheet (Antarctica). J. Geophys. Res., 115:D16202.

Costa A et al. (2017) Classification of Arctic, midlatitude tropical clouds in the mixed-phase temperature regime. Atmos. Chem. Phys., 17:12219–12238.

Creamean JM et al. (2018) Marine and terrestrial influences on ice nucleating particles during continuous springtime measurements in an Arctic oilfield location. Atmos. Chem. Phys., 18:18023–18042.

Ding S et al. (2019) Size–Related Physical Properties of Black Carbon in the Lower Atmosphere over Beijing and Europe. Environ. Sci. Technol., 53:11112–11121.

Dlugi R (1989) Chemistry and Deposition of Soot Particles in Moist Air and Fog. Aerosol Science and Technology, 10:93–105.

Gong X et al. (2020a) Characterization of aerosol particles at Cape Verde close to sea and cloud level heights - Part 2: ice nucleating particles in air, cloud and seawater. Atmos. Chem. Phys., 20:1451 1468.

Gong X et al. (2020b), Characterization of aerosol particles at Cape Verde close to sea and cloud level heights - Part 1: particle number size distribution, cloud condensation nuclei and their origins. Atmos. Chem. Phys., 20:1431–1449.

Grönlund A et al. (2002) Aerosol dry deposition measured with eddy-covariance technique at Wasa and Aboa, Dronning Maud Land, Antarctica. Ann. Glaciol., 35:355–361.

Hartmann M et al. (2020) Wintertime airborne measurements of ice nucleating particles in the high Arctic: a hint to a marine, biogenic source for Ice Nucleating Particles. Geophys. Res. Lett., 47:e2020GL087770.

Hartmann M et al. (2021) Terrestrial or marine – indications towards the origin of Ice Nucleating Particles during melt season in the European Arctic up to 83.7°N. Atmos.Chem. Phys., 21:11613–11636.

Haywood JM, Shine KP (1995) The effect of anthropogenic sulfate and soot aerosol on the clear sky planetary radiation budget. Geophys. Res. Lett., 22:603–606.

Held A et al. (2011a) On the potential contribution of open lead particle emissions to the central Arctic aerosol concentration. Atmos. Chem. Phys., 11:3093–3105.

Held A et al. (2011b) Near-surface profiles of aerosol number concentration and temperature over the Arctic Ocean. Atmos. Meas. Tech., 4:1603–1616.

Jacobson MZ (2012) Investigating cloud absorption effects: Global absorption properties of black carbon, tar balls, and soil dust in clouds and aerosols. J. Geophys. Res., 117: D06205.

Jurado E et al. (2008) Atmospheric deposition of organic and black carbon to the global oceans. Atmos. Environ, 42:7931–7939.

Maskey S et al. (2017) Cloud Condensation Nuclei Activation of Internally Mixed Black Carbon Particles. Aerosol Air Qual. Res., 17, 867–877.

McCluskey CS et al. (2018a) Observations of Ice Nucleating Particles over Southern Ocean waters. Geophys. Res. Lett., 45:11989–11997.

McCluskey CS et al. (2018b) Marine and Terrestrial Organic Ice-Nucleating Particles in Pristine Marine to Continentally Influenced Northeast Atlantic Air Masses. J. Geophys. Res., 123:6196–6212.

Morrison H et al. (2012) Resilience of persistent Arctic mixed-phase clouds. Nat. Geosci., 5:11–17.

Motos G et al. (2019) Droplet activation behaviour of atmospheric black carbon particles in fog as a function of their size and mixing state. Atmos. Chem. Phys., 19:2183–2207.

Nilsson ED, Rannik Ü (2001) Turbulent aerosol fluxes over the Arctic Ocean: 1. Dry deposition over sea and pack ice. J. Geophys. Res., 106:32125–32137.

Ohata S et al. (2013) Evaluation of a Method to Measure Black Carbon Particles Suspended in Rainwater and Snow Samples. Aerosol Science and Technology, 47:1073–1082.

Quinn PK et al. (2011) The impact of Black Carbon on Arctic Climate. Artic Monitoring and Asessment Programme, AMAP Technical Report No. 4. Arctic Monitoring and Assessment Programme (AMAP), Oslo. 72 pp.

Raatikainen T et al. (2015) Black carbon concentrations and mixing state in the Finnish Arctic. Atmos. Chem. Phys., 15:10057–10070.

Šantl-Temkiv T et al. (2019) Biogenic sources of Ice Nucleation Particles at the high Arctic site Villum Research Station. Environ. Sci. Technol., 53: 10580–10590.

Saylor RD et al (2019) The particle dry deposition component of total deposition from air quality models: right, wrong or uncertain? Tellus B, 71:1550324.s.

Schroder JC et al. (2015) Size-resolved observations of refractory black carbon particles in cloud droplets at a marine boundary layer site. Atmos. Chem. Phys., 15:1367–1383.

Schwarz JP (2008) Measurement of the mixing state, mass, and optical size of individual black carbon particles in urban and biomass burning emissions. Geophys. Res. Lett., 35:L13810.

Scott WD, Levin Z (1972) Open channels in sea ice (leads) as ion sources. Science, 177:425–426.

Serreze MC, Barry RG (2011) Processes and impacts of Arctic amplification: A research synthesis. Global and Planetary Change, 77:85–96.

Si M et al. (2019) Concentrations, composition, and sources of ice-nucleating particles in the Canadian High Arctic during spring 2016. Atmos. Chem. Phys., 19:3007–3024.

Solomon A et al. (2018) The relative impact of cloud condensation nuclei and ice nucleating particle concentrations on phase partitioning in Arctic mixed-phase stratocumulus clouds. Atmos. Chem. Phys., 18:17047–17059.

Tobo Y et al. (2019) Glacially sourced dust as a potentially significant source of ice nucleating particles. Nat. Geosci., 12:253–258.

Torres A et al. (2014) Measuring Organic Carbon and Black Carbon in Rainwater: Evaluation of Methods. Aerosol Science and Technology, 48:239–250.

Twomey S (1974) Pollution and the planetary albedo. Atmos. Environ., 8:1251–1256.

Welti A et al. (2020) Ship-based measurements of ice nuclei concentrations over the Arctic, Atlantic, Pacific and Southern Ocean. Atmos. Chem. Phys., 20:15191–15206.

Wex H et al. (2019) Annual variability of ice nucleating particle concentrations at different Arctic locations. Atmos. Chem. Phys., 19:5293–5311.

Whitehead JD et al. (2012) Particle fluxes and condensational uptake over sea ice during COBRA. J. Geophys. Res., 117: D15202.

Zanatta M et al. (2018) Effects of mixing state on optical and radiative properties of black carbon in the European Arctic. Atmos. Chem. Phys., 18:14037–14057.

Zanatta M et al. (2021) Technical note: Sea salt interference with black carbon quantification in snow samples using the single particle soot photometer. Atmos. Chem. Phys., 21:9329–9342.

Zeppenfeld S et al. (2020) A protocol for quantifying mono- and polysaccharides in seawater and related saline matrices by electro-dialysis (ED) – combined with HPAEC-PAD. Ocean Sci., 16:817–830.

5. PLANKTON ECOLOGY AND BIOGEOCHEMISTRY IN THE CHANGING ARCTIC OCEAN (PEBCAO GROUP)

Barbara Niehoff[1], Lisa W. von Friesen[2], Christian Hohe[1], Nadine Knüppel[1], Ellen Oldenburg[1], Ovidiu Popa[1], Johanna Schüttler[3]
not on board: Astrid Bracher[1], Alexandra Gutmann[3], Katja Metfies[1], Eva-Maria Nöthig[1], Ilka Peeken[1], Lasse Riemann[2]

[1]DE.AWI
[2]DK. UCPH
[3]DE.MPI Mainz

Grant-No. AWI_PS131_05

Outline

The Arctic Ocean has gained increasing attention in recent decades due to drastic decrease in sea ice and increase in temperature, which is approximately twice as fast as the global average. It is also expected that ocean acidification will influence the chemical equilibrium and the elemental cycling in the surface ocean. The effects of such changes on the **P**lankton **E**cology and **B**iology in the **A**rctic **O**cean (PEBCAO) can be detected by long-term observations and process studies. The PEBCAO group began its studies on plankton ecology in the Fram Strait (~79°N) in 1991, intensified its efforts in 2009, and since 2014, we are part of the FRAM (Frontiers in Arctic Monitoring) Ocean Observatory team and provide information on intra- and inter-annual variations in plankton ecology, biogeochemical parameters, and microbial (prokaryotic and eukaryotic) biodiversity. In a holistic approach, we combine classical bulk measurements of biogeochemical parameters, microscopy, optical methods, satellite observations, and molecular approaches. These measurements have been complemented by dedicated process studies in the Nansen and Amundsen Basin of the Central Arctic Ocean (CAO), and by participation in the MOSAiC drift experiment. We are also involved in the development and deployment of automatic platforms and sampling technology for long-term monitoring in the Arctic Ocean with a main focus on the AWI HAUSGARTEN.

Our long-term observations in Fram Strait revealed changes in productivity and biodiversity. For instance, the chlorophyll-a (*chl-a*) values in summer increased in the eastern but not in the western Fram Strait (Nöthig et al., 2015 & 2020). This is in accordance with the increasing contributions of *Phaeocystis pouchetii* and nanoflagellates to the summer phytoplankton community. This change in community composition may have had an effect on the particulate organic carbon (POC) during summer (Engel et al., 2019) as the amount of POC decreased over the last years. We also observed that *Themisto compressa*, an invading amphipod species from temperate waters, increased in abundance (Kraft et al., 2013; Schröter et al., 2019). All this suggests that the Fram Strait ecosystem is undergoing profound changes, likely induced by climate conditions warranting sustained observation.

Sea ice is one of the major players in ecosystem processes since it affects the solar radiation fluxes due to its reflective properties, and it is a habitat and feeding ground for various organisms of the polar ecosystem. Sea ice origin even governs the community distribution of e.g. sea ice protists (Hardge et al., 2017), and thus changing transport routes and thinning sea ice

(Krumpen et al., 2019) might have major implications on the biodiversity of the sea ice biota. In addition, the changing sea ice scape increases light availability on larger and smaller scales, allowing phytoplankton to grow in previously ice-covered regions (Massicotte et al., 2019). A long-term trend towards thinner sea ice has profound implications for the timing and position of the seasonal ice zone (including MIZ) and the anticipated ice-free summers in the future will have major impact on the entire ecosystem and alter biogeochemical cycles in the Arctic.

At the interface between the atmosphere and ocean, sea ice acts as a thin, ephemeral and actively changing environment through which heat, momentum and mass are regulated (Lannuzel et al., 2020). The changes in sea ice also influence the atmospheric boundary layer, by an increase of sensible and latent heat fluxes above open water and thinner ice. A transect from temperate to the ice-covered Arctic revealed large changes of trace gases occur with e.g. highest concentrations of carbon monoxide and isoprene in the ice covered region (Tran et al., 2013). No studies currently exist about atmospheric selenium in the Arctic. The selenium cycle, and thus the global distribution of selenium resources, is thought to be driven significantly by marine emissions carried out by phytoplankton. The oceans are sinks for atmospheric selenium and these organisms can volatilize local and oxidized selenium forms by methylation and thus transfer them back from the ocean to the atmosphere. The close connection to the sulphur cycle and already observed high sulphur emissions from polar phytoplankton species suggest a significant influence of the Polar Regions on the global selenium cycle. Thus, the current cruise allows to access the role of selenium emissions on a longitudinal transect and in the ice-covered Arctic Ocean.

Primary production constituting the base of the marine food web is expected to increase in the changing Arctic Ocean. It depends, in broad terms, on a balance between stratification and mixing, the former keeping phytoplankton cells within the surface layer, where enough irradiance is available for photosynthesis, and the latter fueling the supply of new nutrients to support production. Here, nutrient availability and flux between sea ice and the upper ocean are key to understand and predict the responses of primary production to rapidly changing conditions. Nitrogen fixation, the biological conversion of N_2 to NH_3, was up until quite recently not thought to occur in the Arctic marine environment but has now been detected in several habitats of the Arctic Ocean (reviewed in Von Friesen and Riemann 2020). Knowledge about the prokaryotes responsible for nitrogen fixation (diazotrophs) in this region is however sparse, and no nitrogen fixation rates from sea ice is available.

Meltwater stratification is particularly pronounced in the marginal ice zone (MIZ) of the Arctic Ocean which is defined as an area of the ocean covered with 15 – 80 % sea ice and characterized by extensive sea ice melt (Aksenov et al., 2017; Strong and Rigor, 2013). In consequence, the MIZ is a key area of Arctic marine primary production (Gradinger and Baumann, 1981). Overall, there has been an increase in the areal extent of the MIZ reflected by low surface salinity and stratification in the seasonal ice zone of the Arctic Ocean. Observations from recent expeditions suggest, that the area impacted by sea ice melt in the Fram Strait might extend south-eastwards. This was particular obvious in summer 2021, when the sea ice edge in June extended to south of 79°N at ~ 4°E. It is currently unclear whether increased melt-water concentrations and stratification will lead to increased export of particulate organic carbon or whether the products of primary production will remain at the surface and drive a regenerating system. Arctic regions impacted by melting sea ice support specific plankton community composition (Weiss in prep.; Oldenburg in prep), and may either increase particle export (Lalande et al., 2019; Fadeev et al., 2021) or retain particles at the surface for a while, depending on the p,hysical structure of the respective water parcels at the surface (v. Appen et al., 2021). Retention rates of biomass in the upper water column might change in the future, due to expected changes in plankton communities and trophic networks in consequence to Arctic environmental change. These changes might include that small algae

gain importance in mediating element and matter turnover as well as energy fluxes in Arctic pelagic systems. However, currently cryo-pelagic coupling of microalgal communities and the role of sea-ice algae in primary production under the ice, and particularly in the MIZ has to be understood better to estimate consequences of sea ice decline on Arctic primary production and carbon cycles. A combination of measurements of classical parameter (particulate organic carbon, nitrogen, biogenic silica) and molecular biodiversity studies provided first insights into microbial distribution and *chl-a* biomass in the Arctic Ocean and suggest a high contribution of small microalgae to *chl-a* biomass in the Central Arctic Ocean (Metfies et al., 2016; Hardge et al., 2017). Many zooplankton species are affected by these changes at the base of the food web as they rely on phytoplankton as food source. Furthermore, zooplankton community composition may shift due to the increasing inflow of warmer Atlantic water into the Fram Strait. Altered zooplankton trophic interactions and community compositions will have consequences for the carbon sequestration and flux.

Comprehensive understanding of the impact of changing environmental conditions on ecosystem functions and functionality requires studying the system on different spatial and temporal scales. This can be accomplished by combining different observation approaches, providing different kinds of information: (i) satellite-based observations can provide geographically large-scale information on changes in ecosystem functions, such as *chl-a* concentrations over bigger time-scales; (ii) the deployment of sediment traps and automated water samplers for molecular biodiversity studies over extended periods of time (mainly one or two years from summer to summer) in different parts of the Arctic Ocean can provide insight into algal biodiversity and matter export during different sea ice scenarios over the annual cycle; (iii) underway sampling and towed optical plankton observations can provide high-resolution information on plankton distribution in the upper water column (Weiss et al., in prep; Sprong et al., in prep); (iv) classical CTD sampling and net-tows provide samples for vertical characterization of plankton distribution in the water column.

Objectives

The overarching objectives of PEBCAO are (1) to improve our mechanistic understanding of biogeochemical and microbiological feedback processes in the Arctic Ocean, (2) to document ongoing and long-term changes in the biotic and abiotic environment, and (3) to assess the potential future consequences of these changes. During PS131 one objective of our group therefore was to sample phyto- and zooplankton as well as seawater for measuring biogechemical parameters at our AWI-HAUSGARTEN monitoring stations (S3, HGIV, N4 and EGC) and in the MIZ north of Svalbard. To tackle plankton biodiversity and biogeography, we use traditional microscopy. However, in order to detect differences also in smallest fraction of the plankton, either among years (HAUSGARTEN monitoring) or in relation to sea ice conditions (MIZ), we apply molecular methods that are independent of cell-size and morphological features, assessing biodiversity and biogeography of Arctic prokaryotic and eukaryotic microbes based on 18S meta-barcoding.

During PS131 we also collected samples and image data to relate zooplankton biomass and biodiversity to environmental conditions, specifically sea ice coverage. For high taxonomic resolution, we use multiple net samplers, which integrate depth intervals of up to several hundred meters. These samples are preserved in formalin and studied under the microscope. Many zooplankton species are, however, associated with certain water masses, and to investigate the fine scale distribution of key species, we deployed the zooplankton recorder LOKI (light frame on-sight key species investigations), that continuously takes images during vertical casts from 1,000 m to the surface and records hydrographical parameters, i.e. salinity, temperature, oxygen concentration, and fluorescence.

To elucidate intra-annual cycles of sinking particles and phytoplankton development, we deployed and recovered several moorings, equipped with sediment traps and automated water samplers that remain in the Arctic Ocean for approx. one year, collecting material and data.

Optical measurements are used to extract the information on the overall phytoplankton biomass (indicated by *chl-a* concentration), distinctive major groups (phytoplankton functional types: PFT) and coloured dissolved organic matter (CDOM) in order to enlarge the resolution of these parameters. Satellite sensors enable to deliver information at global and high temporal (daily) scales which are not met by our sampling during the expedition. However, at high latitudes, ocean colour satellite data has sparse coverage due to the presence of sea ice, clouds and low sun elevation. To complement remote sensing data, we deployed underway spectrophotometry and hyperspectral radiometry which enable to obtain highly resolved optical data which can be processed using similar algorithms to *chl-a* and marker pigment concentrations, PFT *chl-a* and CDOM at high sampling resolution for the surface waters crossed during the entire cruise and for the underwater light profile at the CTD stations. These final biogeochemical products were verified with direct analysis of these parameters on regularly sampled discrete water enabling to quantify their uncertainties. In conjunction with satellite data, these discrete and continuously sampled data sets are important to upscale biogeochemical or phytoplankton quantities at higher resolution and better coverage for the entire expedition's transect. In addition, these data serve for validating ocean colour products from the Sentinel-3 OLCI and the Sentinel-5P TROPOMI sensors. The group of A. Bracher is part of the Sentinel-3 Validation Team and the PI of the ESA study Sentinel-5P Ocean Colour. Overall, these cruise data provide a fundamental contribution for further development of hyper- and multispectral ocean colour satellite retrievals.

During PS131, the sea ice environment was also a target habitat, where focus was placed on biodiversity, continuation of long-term monitoring of biological parameters as well as measurement of nitrogen and carbon fixation. By sampling different types of sea ice (e.g. age or melting state, marginal ice zone or land-fast ice), a better understanding of biological structure and function can be obtained. Due to the focus on the marginal ice zone that included three re-visits to three floes, our data can provide a temporal dimension of our understanding of sea-ice biology. Parameters to be analysed are pigments (HPLC), POC/PON, PBSi (particulate biogenic silica), inorganic and organic nutrients, and biodiversity of sea ice flora and fauna through molecular barcoding. Nitrogen and carbon fixation will be analysed through stable isotope tracing, and the diazotrophic communities investigated via marker gene presence (DNA) and expression (RNA).

There was also an atmospheric component in our sampling campaign. Marine phytoplankton is the biggest emitter of volatile selenium compounds. Incubations experiments have shown that some sea ice algae emit both, dimethyl selenium and dimethyl diselenium. On the expedition, environmental samples of air were taken on adsorbent cartridges to improve the understanding of the role of algae in the Arctic and the Fram Strait on the selenium biogeochemical cycling. This method can also detect other volatile organic compounds (VOCs) present in the polar marine air.

All data will not only complement our on-going time series at the AWI-HAUSGARTEN, aiming at identifying climate change induced changes in biodiversity and biochemical processes in the Fram Strait, but will also lead to a better understanding of the influence of melting sea-ice on phyto- and zooplankton and on the sea-ice algae and bacterial communities. Contributing to the general scientific aims of PEBCAO, the specific objectives on ATWAICE (PS131) were:

1. Characterize plankton distribution, biodiversity and biomass horizontally at the meso-scale with high resolution in the MIZ and adjacent areas.
2. Elucidate cryo-pelagic coupling of microbial (prokaryotic and eukaryotic) communities with respect to small scale, melt-water mediated differences in water column structuring.
3. Analyzing the abundance, biodiversity and community structure of sea ice-associated biota and quantifying ecosystem functions and their relationships with biodiversity
4. Characterization of the underwater light field and its interplay with optical constituents, such as phytoplankton and CDOM abundance and composition.
5. Measure nitrogen and carbon fixation in different sympagic habitats and characterize present and active diazotrophic communities to understand the role of nitrogen fixation in different types of sea ice
6. Develop and evaluate a method allowing biological rate measurements of intact sea ice cores (i.e. not pre-melted)

Work at sea

Protistian and Microbial Plankton

(AGs Nöthig and AG Metfies, with Nadine Knüppel, Ellen Oldenburg and Ovidiu Popa)

Seawater samples (Table 5.1) were taken at 5 – 12 depths by a CTD/rosette sampler in the HAUSGARTEN area and aliquots were filtered for analyzing biogeochemical parameters such as *chl-a* (unfractionated, and fractionated on 10 µm, 3 µm and 0.2 µm), particulate organic carbon and nitrogen (POC and PN), and biogenic silica (PbSi), respectively. At mooring stations, filtrations for seston (TPM, total particulate matter) were additional carried out. Furthermore, unfiltered CTD water samples were fixed with formalin (final concentration 0,5 – 1,0 %) for later quantitative assessment of the phytoplankton community by inverted microscopy.

Additional samples were collected from 5 depths via the CTD-rosette from the top 100 m depth for molecular analyses in order to assess microbial community compositions by 16S/18S meta-barcoding. Samples for 18S meta-barcoding analyses were fractionated by three filtrations on 10.0, 3.0 and 0.4 µm filters, while samples for prokaryotic community analyses were filtered directly on 0.2 µm filters. One additional archive sample was collected from every depth by filtration on 0.2 µm to provide a sample for future analyses methods.

To address spatial variability of microbial plankton communities we complemented sampling for molecular analyses using the CTD-rosette with sampling via the underway sampling system AUTOFIM, permanently installed on board *Polarstern* (Fig. 5.1). We used the device to collect samples on a transect from Bremerhaven to Fram Strait with a resolution of 3 h (~33 nm) on a 0.4 µm filter (Fig. 5.1). Further, to characterize plankton distribution and biomass horizontally at the meso-scale with high resolution in the MIZ, AUTOFIM samples with a resolution of 20 minutes on a 0.4 µm filter were taken in parallel to topAWI (Triaxus, McArtney) transects.

Archive sea ice cores were collected at three stations for molecular characterization of microbial sea ice communities and *chl-a*-biomass. All samples were preserved, refrigerated or frozen at – 20° C or – 80° C for storage until analyses in the laboratory (AWI, Bremerhaven).

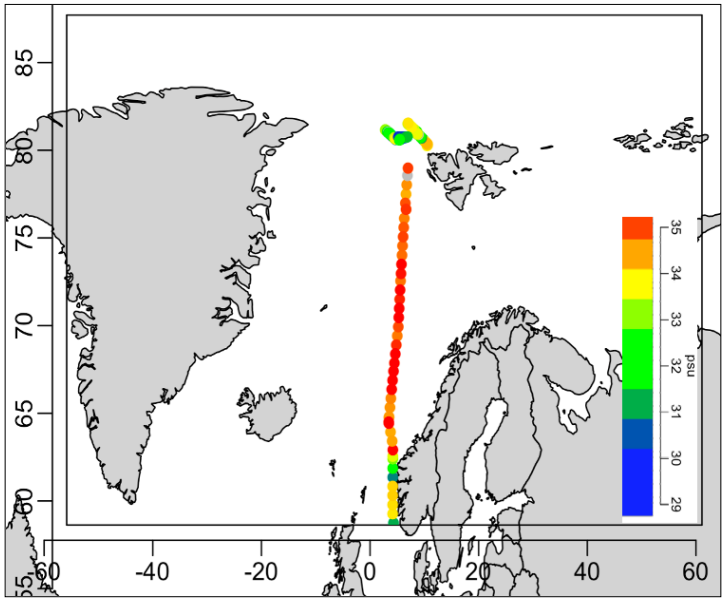

Fig. 5.1: AUTOFIM sampling during transect from Bremerhaven to Fram Strait: Dots indicate sampling locations. The colour highlights show the salinity (psu) along the sampling route.

Tab. 5.1: Overview of stations where water from deep and shallow casts with a rosette was sampled for molecular, biogeochemical and biological parameters. Euk: Eukaryota, Prok: Prokariota, POC/N: Particulate Organic Carbon/Nitrogen, PbSi: Biogenic Silicate, *Chl-a*: Chlorophyll *a*

Event Id PS131	Name	DNA Euk & Prok	Archive Filter	POC/N, PbSi, Chl_a shallow	POC/N, PbSi, deep	Seston (TPM)	Utermöhl counting
006-01	S3 deep				x	x	
006-05	S3			x		x	x
013-01	F4-S6	x	x				
027-01	HG-IV deep				x	x	
029-01	HG-IV	x	x	x		x	x
035-01	N4 deep				x	x	
035-06	N4	x	x	x		x	x
047-01	South floe (visit 1)	x					
047-02	South floe (visit 1)			x			
048-01	Middle floe (visit 1)	x		x			
048-02	Middle floe (visit 1)			x			
049-01	North floe (visit 1)	x	x	x			
049-02	North floe (visit 1)			x			
056-02	MIZ 1	x	x	x		x	x

Event Id PS131	Name	DNA Euk & Prok	Archive Filter	POC/N, PbSi, Chl_a shallow	POC/N, PbSi, deep	Seston (TPM)	Utermöhl counting
057-02	MIZ 2	x	x	x		x	x
061-02	MIZ 3	x	x	x		x	x
062-01	Yermak	x	x	x	x	x	x
065-01	MIZ 4	x	x	x		x	x
067-01	South floe (visit 2)	x	x	x			
068-01	Middle floe (visit 2)	x	x	x			
069-08	MIZ 5	x	x	x		x	x
070-01	North floe (visit 2)	x	x	x			
087-01	MIZ 6	x	x	x			x
088-01	MIZ 7	x	x	x			x
089-01	South floe (visit 3)	x	x	x			
091-01	MIZ 8	x	x	x			x
093-01	North floe (visit 3)	x	x	x			
094-01	MIZ 9	x	x	x			x
107-01	EGC deep				x	x	
107-05	EGC	x	x	x	x	x	x
108-01	Greenland north	x	x	x			
111-01	Greenland south	x	x				

Zooplankton (AG Niehoff)

Mesozooplankton biodiversity and large-scale distribution patterns were investigated at the AWI-HAUSGARTEN observatory in the Eastern Fram Strait (S3, HGIV, N4) and in the East Greenland Current (EGC, see Table 1), in the MIZ north of Svalbard, and close to Greenland using a MultiNet midi (Hydrobios, Germany, 150 µm mesh size). In the AWI-HAUSGARTEN, the net was towed vertically to sample five standard depths layers (1,500 – 1,000 – 500 – 200 – 50 – 0 m). At the EGC Station, the bottom depth was shallower than 1,500 m, and thus the depth intervals were adjusted, yielding a higher resolution of the upper water column. In the MIZ, sampling was performed associated with three ice stations and on two transects, covering different hydrographic regimes as previously determined by deploying the TRIAXUS. Here, the sampling maximum depth was 500 m, and the sampling intervals were adjusted to environmental features such as melt water layer, chlorophyll maximum and Atlantic Water influence. Thus, the sampled depth intervals varied among the stations, however, they always allow to pool the data to depth strata from 500 to 50 m and from 50 to 0 m for comparability with our long-term monitoring data from Fram Strait and the Central Arctic Ocean. All net samples were immediately preserved in 4 % formalin buffered with hexamethylenetetramine. In the laboratories at AWI, these samples will be analyzed with the optical system ZooScan (Hydroptics, France) to determine zooplankton species composition and abundance (Cornils et al., 2022).

To analyze the vertical distribution of zooplankton species with high spatial resolution, the optical system LOKI (Lightframe On-sight Key species Investigation). LOKI was equipped with a 150 µm plankton net and took images of zooplankton organisms and particles at a rate of 18 frames per second while being towed vertically through the water column. Simultaneously, depth, temperature, oxygen content and fluorescence were recorded to relate the zooplankton abundance to the environmental conditions. We deployed at 17 stations (Tab. 5.2). However, at station PS131_56 and PS131_69, both located in the MIZ (Transect 1), no image data were obtained due to technical problems, likely of the computer unit. Also, the camera apparently broke during the cast at station PS131_35, as images have only been saved for half of the haul. Therefore, after this cast the LOKI camera had to be replaced.

Tab. 5.2: List of stations of MultiNet and LOKI deployments during PS131. Names refer either to the AWI-HAUSGARTEN monitoring stations (S3, HGIV, N3, EGC) or to the location of sampling (MIZ = Marginal Ice Zone, T = Transect, Greenland = off the coast of Greenland); no data refers to LOKI casts where no images have been taken due to technical problems.

Station	Name	Date	MN	LOKI
PS131_006	S3	07.07.22		x
PS131_027	HGIV	09.07.22	x	x
PS131_035	N4	10.07.22	x	x
PS131_047	Ice floe South	13.07.22	x	x
PS131_048	Ice floe North	14.07.22	x	x
PS131_049	Ice floe Middle	15.07.22	x	x
PS131_056	MIZ T 1	17.07.22	x	no data
PS131_057	MIZ T 1	18.07.22	x	x
PS131_061	MIZ T 1	18.07.22	x	x
PS131_065	MIZ T 1	20.07.22	x	x
PS131_069	MIZ T 1	22.07.22	x	no data
PS131_087	MIZ T 2	29.07.22	x	x
PS131_088	MIZ T 2	30.07.22	x	x
PS131_091	MIZ T 2	31.07.22	x	x
PS131_094	MIZ T 2	01.08.22	x	x
PS131_107	EGC	03.08.22	x	x
PS131_108	Greenland	06.08.22	x	X

Phytoptics (AG Bracher)

For the continuous underway surface water measurements an *in-situ*–spectrophotometer (ACS; Wetlabs) was operated continuously from 3 July until 12 August 2022 in flow-through mode to obtain total and particulate matter attenuation and absorption spectra of surface water with high spectral (~3.3 nm) resolution from 400 to 800 nm. The instrument was mounted to a seawater supply taking water from about 11 m depth through the teflon tubing with a membrane pump. A flow-control with a time-programmed filter was connected to the ACS to allow alternating measurements of the total and the CDOM inherent optical properties (IOP) of the sea water. Flow-control and debubbler-system ensured water flow through the instrument with no air bubbles. The instrument is operated via the Wetlabs software COMPACT which stores the data recorded at 4 Hz every 10 min into a new file.

Tab. 5.3: Station positions and max. depth of profiling for hyperspectral upwelling and downwelling radiation in the water with the RAMSES radiometers and for hyperspectral total absorption and attenuation with the ACS spectrophotomter.

Date	Time	Lat	Lon	Max depth (m)
2022-07-06	03:52:39	78.61	5.06	100.00
2022-07-09	15:59:03	79.02	4.34	100.00
2022-07-10	23:00:37	79.72	4.43	100.00
2022-07-17	10:58:43	80.62	9.79	100.00
2022-07-17	20:36:17	80.39	10.47	100.00
2022-07-18	17:32:12	80.82	9.16	100.00
2022-07-20	0:31:15	81.52	7.03	100.00
2022-07-21	21:44:35	81.19	8.10	80.00
2022-07-29	15:32:10	81.08	3.15	8.00
2022-07-29	23:20:01	81.15	2.92	100.00
2022-07-31	2:51:49	80.72	4.44	100.00
2022-08-01	7:38:19	80.77	4.30	100.00
2022-08-03	20:07:28	78.98	-5.44	100.00

At thirteen stations (Tab. 5.3) we deployed our hyperspectral optical profiler, a profiling system to measure the optical properties vertically. It consists of a second *in-situ* spectrophotometer (ACS; WETlabs) and two TRIOS RAMSES sensors (one for measuring at high spectral resolution (10 nm, 3.3 nm sampling) the downwelling irradiance, Ed, and on for upwelling radiance, Lu), a pressure sensor, a datalogger and a battery (Fig. 5.2). The optical profiler was lowered to maximal 100 m with a continuous speed of 0.1 m/s or during daylight with additionally stops at 2, 5, 8, 10, 15, 20, 25, 30, 40, 50, 60, 70, 80, and 100 m to allow a better collection of radiometric data. The Apparent Optical Properties of water (AOPs) (mostly light attenuation through the water column) were estimated based on downwelling and upwelling irradiance measurements in the surface water profile (down to the 0.1 % light depth) from the radiometers calibrated for the incident sunlight with measurements of another RAMSES radiometer operated on the monkey deck and directly from the radiance and irradiance above water radiometry. The ACS measured the hyperspectral IOP (total attenuation, scattering and absorption) in the water profile.

A third ACS instrument and another RAMSES irradiance sensor, looking upwards and collecting downwelling irradiance data, were mounted looking upwards at the TOPAWI Triaxus system (Fig. 5.2) and operated at all Triaxus deployments (Tab. 5.4). Data were online transferred to the steering computers on the ship using for RAMSES sensor the original Trios software msda_xe and for ACS the Wetlabs COMPACT software. The second and third ACS instruments only obtained total absorption and attenuation data, since no filter could be mounted to the instruments during operation in water. All three ACS instruments were regularly calibrated by taking measurements of MilliQ water (daily for the flowthrough-ACS, after every 2 casts for the discrete station profiling ACS, before each TRIAXUS deployment for the TRIAXUS-ACS).

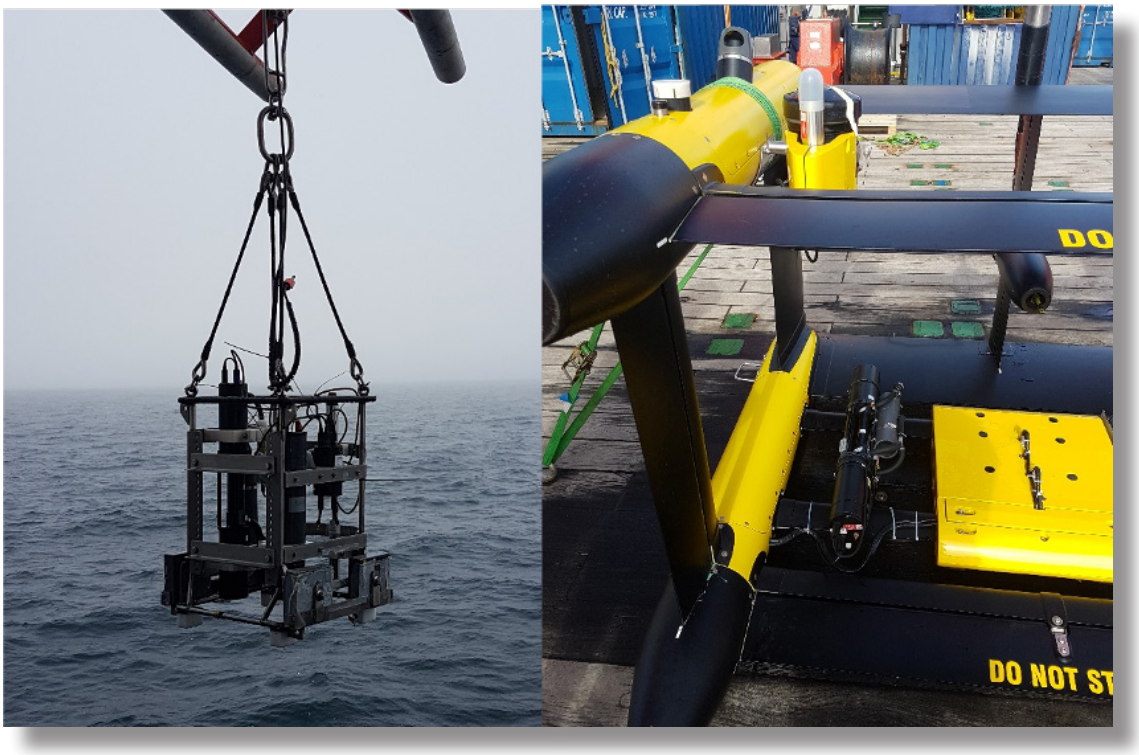

Fig. 5.2: (Left) Optical profiler operated at discrete stations down to 100 m with a hyperspectral transmissiometer and absorption spectrophotometer (ACS, Wetlabs) and hyperspectral upwelling radiance (ASC-RAMSES, Trios) and downwelling irradiance sensors ACC-(RAMSES, Trios); (right) top AWI Triaxus system with the two hyperspectral instruments ACS (Wetlabs; lower part) and downwelling irradiance sensor (ACC-RAMSES, Trios; upper part)

In order to calibrate the absorption data obtained from the ACS measurements, but also the outputs of the retrievals applied to the ACS and RAMSES derived IOP and AOP data, discrete water samples were taken and analysed for their phytoplankton pigment composition and hyperspectral absorption coefficients of CDOM and all particulates, and, for phytoplankton in particular. Surface water were sampled from the seawater pump (11m depth) on *Polarstern* with an interval of 3 hours to have a full coverage of the surface water along the whole cruise track. Further, we sampled Arctic seawater with the CTD/rosette sampler at five depths from surface to 100 m. Water samples from both, underway (Tab. 5.5) and CTD stations (Tab. 5.6, sampled stations and depths coincide with other PEBCAO samples and except for station PS131_19-1, all stations were also measured at the locations of our optical profiler deployments (Tab. 5.5)) were filtered in the laboratory to obtain the following data sets: Samples for determination of phytoplankton pigment concentrations were filtered on board immediately after sampling and then filters were thermally shocked in liquid nitrogen and stored at –80° C until the ship was back in Bremerhaven. Then they were transported directly on dry ice to AWI Bremerhaven where they are further stored until their analysis by High Performance Liquid Chromatography Technique (HPLC) following Taylor et al. (2011) but updated to our new instrumentation as described in Alvarez et al. (in revision). Samples for analysis of CDOM absorption were filtered through 0.2 µm filters, stored at 4° C until the end of PS131 and will be analyzed later at AWI with the Liquid Waveguide Capillary Cell system (LWCC, WPI) following Lefering et al. (2017). Particulate and phytoplankton absorption coefficients were determined with the quantitative filter techniques (QFT) using sample filtered onto glass-fiber filters and measuring them in a portable QFT integrating cavity setup according to Röttgers et al. (2016) immediately after filtration of the water sample on board.

Tab. 5.4: List of Triaxus transect stations with date, time, and geolocation information for starting (-s) and ending (e-) the profiling and measurements for IOP and AOP measurements by ACS and RAMSES radiometers, respectively.

Station	Time Start	Time End	Lat-s	Lat-e	Lon-s	Lon-e
PS131_18-1	07/07/2022 18:04	07/07/2022 20:24	78.9263	78.9231	6.024	6.89226
PS131_55-1	16/07/2022 19:37	17/07/2022 03:55	80.3459	81.0285	10.6154	8.64415
PS131_64-1	19/07/2022 15:15	19/07/2022 21:00	81.0132	81.5449	8.70478	6.95846
PS131_86-1	29/07/2022 08:11	29/07/2022 11:13	81.2048	80.9676	2.75745	3.64115
PS131_90-1	30/07/2022 18:06	30/07/2022 23:23	81.0578	80.6268	3.24563	4.76417
PS131_95-1	01/08/2022 13:11	01/08/2022 16:47	80.7622	80.7678	4.31059	6.84538

Tab. 5.5: Water samples collected underway during PS131 from 11 depths where hyperspectral particulate and phytoplankton absorption using the QFT technique, CDOM absorption using the LWCC technique and phytoplankton pigments using HPLC technique was measured (see details above).

Sample ID	Date UTC	Time UTC	Lat	Lon
UW1	2022-06-29	09:38:00	56.80	5.63
UW2	2022-06-29	13:32:30	57.45	5.20
UW3	2022-06-29	17:20:30	58.07	4.79
UW4	2022-06-29	21:06:30	58.69	4.35
UW5	2022-06-30	05:33:00	60.15	4.18
UW6	2022-06-30	09:31:30	60.84	4.18
UW7	2022-06-30	13:31:30	61.54	4.19
UW8	2022-06-30	17:36:00	62.25	4.19
UW9	2022-07-01	05:36:30	64.29	3.57
UW10	2022-07-01	09:29:30	64.51	3.43
UW11	2022-07-01	13:36:00	64.77	3.48
UW12	2022-07-01	17:31:00	65.16	3.63
UW13	2022-07-02	05:36:30	67.25	4.28
UW14	2022-07-02	09:34:30	67.87	4.49
UW15	2022-07-02	13:34:00	68.57	4.72
UW16	2022-07-02	17:38:00	69.26	4.97
UW17	2022-07-03	05:40:30	71.36	5.43
UW18	2022-07-03	09:31:30	72.03	5.54
UW19	2022-07-03	13:37:21	72.72	5.67
UW20	2022-07-03	17:32:22	73.33	5.77
UW21	2022-07-03	21:31:30	74.03	5.90
UW22	2022-07-04	05:29:50	75.42	6.17
UW23	2022-07-04	09:29:03	76.11	6.31
UW24	2022-07-04	13:30:25	76.65	6.67
UW25	2022-07-04	17:56:32	76.88	6.51
UW26	2022-07-04	21:29:14	77.50	6.62
UW27	2022-07-05	05:28:50	78.92	6.98
UW28	2022-07-05	09:38:52	79.02	6.92

Sample ID	Date UTC	Time UTC	Lat	Lon
UW29	2022-07-05	13:28:30	79.16	6.27
UW30	2022-07-05	17:32:48	79.00	5.67
UW31	2022-07-05	22:08:32	78.61	5.07
UW32	2022-07-06	01:30:15	78.61	5.07
UW33	2022-07-06	05:55:15	78.67	5.34
UW34	2022-07-06	09:25:50	79.01	7.01
UW35	2022-07-06	13:33:38	79.00	7.98
UW36	2022-07-06	17:53:48	78.98	7.95
UW37	2022-07-07	01:33:35	78.99	8.42
UW38	2022-07-07	05:52:22	79.00	7.00
UW39	2022-07-07	09:24:00	79.01	7.00
UW40	2022-07-07	13:24:08	79.01	6.42
UW41	2022-07-07	17:36:13	78.94	5.98
UW42	2022-07-07	21:29:04	78.98	6.91
UW43	2022-07-08	01:35:08	78.98	6.29
UW44	2022-07-08	05:28:03	79.11	6.23
UW45	2022-07-08	09:30:10	79.17	6.33
UW46	2022-07-08	13:28:48	79.00	8.00
UW47	2022-07-08	17:34:10	78.99	7.12
UW48	2022-07-08	21:29:35	79.04	5.08
UW49	2022-07-09	01:26:35	79.06	4.19
UW50	2022-07-09	05:32:30	79.06	4.19
UW51	2022-07-09	09:28:12	79.00	4.37
UW52	2022-07-09	13:26:42	79.00	4.33
UW53	2022-07-09	17:33:32	78.98	4.82
UW54	2022-07-09	21:31:35	78.98	4.82
UW55	2022-07-10	01:34:37	78.99	5.50
UW56	2022-07-10	05:53:05	79.01	6.96
UW57	2022-07-10	09:31:53	79.17	6.40
UW58	2022-07-10	13:33:00	79.72	4.43
UW59	2022-07-10	17:53:45	79.72	4.42
UW60	2022-07-10	21:29:43	79.72	4.42
UW61	2022-07-11	01:22:45	79.78	4.87
UW62	2022-07-11	05:40:05	80.15	8.48
UW63	2022-07-11	09:32:20	80.34	10.61
UW64	2022-07-11	13:27:13	80.49	10.18
UW65	2022-07-11	18:01:15	80.64	9.77
UW66	2022-07-12	09:34:27	81.31	7.59
UW67	2022-07-12	13:36:45	81.48	7.03
UW68	2022-07-12	17:49:52	81.60	6.70
UW69	2022-07-12	21:29:40	81.61	6.53
UW70_1,2,3	2022-07-13	10:16:25	81.60	6.81
UW71	2022-07-13	21:30:41	81.61	6.65

Sample ID	Date UTC	Time UTC	Lat	Lon
UW72	2022-07-14	05:31:48	81.23	7.94
UW73	2022-07-14	09:51:10	81.19	7.89
UW74	2022-07-14	22:42:42	81.16	7.56
UW75	2022-07-15	06:17:45	81.38	7.09
UW76	2022-07-15	09:39:10	81.36	6.89
UW77	2022-07-15	13:32:00	81.35	6.75
UW78	2022-07-15	21:30:51	81.37	6.53
UW79	2022-07-16	01:30:09	81.18	7.65
UW80	2022-07-16	05:42:40	80.93	8.83
UW81	2022-07-16	09:38:05	80.75	10.69
UW82	2022-07-16	13:32:55	80.63	11.86
UW83	2022-07-16	17:29:15	80.35	10.63
UW84	2022-07-16	02:31:38	80.70	9.53
UW85	2022-07-17	01:35:55	80.83	9.15
UW86	2022-07-17	05:44:53	80.93	8.81
UW87	2022-07-17	09:31:32	80.62	9.78
UW88	2022-07-17	17:54:35	80.50	10.16
UW89	2022-07-17	21:32:25	80.39	10.47
UW90	2022-07-18	01:42:46	80.40	10.19
UW91	2022-07-18	05:45:25	80.40	9.97
UW92	2022-07-18	09:24:35	80.42	10.06
UW93	2022-07-18	13:29:55	80.63	9.73
UW94	2022-07-18	21:29:22	80.83	9.14
UW95	2022-07-19	01:41:24	80.96	8.68
UW96	2022-07-19	06:16:32	80.94	8.69
UW97	2022-07-19	09:22:45	80.95	8.72
UW98	2022-07-19	13:21:30	80.97	8.68
UW99	2022-07-19	17:33:30	81.25	7.93
UW100	2022-07-19	21:28:52	81.57	7.00
UW101	2022-07-20	01:33:32	81.53	7.03
UW102	2022-07-20	06:03:40	81.54	7.16
UW103	2022-07-20	09:30:45	81.50	7.19
UW104	2022-07-20	13:55:15	81.49	5.95
UW105	2022-07-20	17:40:07	81.50	4.79
UW106	2022-07-20	21:29:20	81.49	4.73
UW107	2022-07-21	06:08:20	81.20	5.36
UW108	2022-07-21	09:35:00	81.20	5.42
UW109	2022-07-21	13:30:30	81.19	5.43
UW110	2022-07-21	17:32:42	81.18	6.48
UW111	2022-07-21	21:34:25	81.19	8.11
UW112	2022-07-22	01:26:15	81.19	7.99
UW113	2022-07-22	09:31:13	81.36	5.17
UW114	2022-07-22	13:33:17	81.35	5.12

Sample ID	Date UTC	Time UTC	Lat	Lon
UW115	2022-07-22	17:32:28	81.33	5.09
UW116	2022-07-22	02:29:13	81.45	2.73
UW117	2022-07-23	01:25:01	81.41	2.05
UW118	2022-07-23	05:34:40	81.63	0.59
UW119	2022-07-23	09:41:02	81.73	-1.19
UW120	2022-07-23	13:33:32	81.81	-2.17
UW121	2022-07-23	17:23:07	81.85	-3.01
UW122	2022-07-23	21:31:48	82.05	-4.03
UW123	2022-07-24	01:41:34	82.18	-4.06
UW124	2022-07-24	05:35:05	82.38	-4.89
UW125	2022-07-24	09:30:58	82.52	-5.70
UW126	2022-07-24	13:26:20	82.78	-6.25
UW127	2022-07-24	18:29:08	82.83	-6.18
UW128	2022-07-25	01:40:24	82.90	-6.23
UW129	2022-07-25	06:39:32	82.90	-6.20
UW130	2022-07-25	09:34:52	82.88	-6.42
UW131	2022-07-25	13:36:00	82.90	-6.23
UW132	2022-07-25	18:13:15	82.92	-6.75
UW133	2022-07-25	21:26:00	82.97	-6.22
UW134	2022-07-26	05:38:40	82.56	-6.01
UW135	2022-07-26	09:28:52	82.37	-4.50
UW136	2022-07-26	13:31:40	82.13	-3.43
UW137	2022-07-26	18:13:30	81.90	-3.23
UW138	2022-07-26	21:33:55	81.78	-3.00
UW139	2022-07-27	01:34:20	81.63	-2.07
UW140	2022-07-27	05:35:07	81.50	-0.82
UW141	2022-07-27	09:30:40	81.34	0.42
UW142	2022-07-27	13:34:28	81.37	1.18
UW143	2022-07-27	17:35:25	81.35	1.08
UW144	2022-07-27	21:30:05	81.36	1.42
UW145_1,2,3	2022-07-28	16:03:55	81.32	1.23
UW146	2022-07-28	21:29:52	81.31	1.16
UW147	2022-07-29	05:55:52	81.29	3.09
UW148	2022-07-29	09:26:50	81.10	3.12
UW149	2022-07-29	17:31:00	81.08	3.12
UW150	2022-07-29	21:28:50	81.11	3.00
UW151	2022-07-30	06:38:25	81.20	2.38
UW151	2022-07-30	06:38:25	81.20	2.38
UW152	2022-07-30	09:32:00	81.18	2.40
UW153	2022-07-30	13:33:55	81.17	2.30
UW154	2022-07-30	17:28:23	81.09	3.10
UW155	2022-07-30	21:29:55	80.78	4.22
UW156	2022-07-31	05:20:17	80.72	4.44
UW157	2022-07-31	09:31:52	80.81	4.15

Sample ID	Date UTC	Time UTC	Lat	Lon
UW158	2022-07-31	13:30:10	80.93	3.81
UW159	2022-07-31	17:35:10	81.05	2.70
UW160	2022-08-01	01:31:43	81.07	2.05
UW161	2022-08-01	05:42:15	80.82	3.93
UW162	2022-08-01	09:21:25	80.77	4.30
UW163	2022-08-01	13:32:12	80.77	4.52
UW164	2022-08-01	18:25:53	80.69	6.03
UW165	2022-08-01	21:30:25	80.71	5.12
UW166	2022-08-02	05:51:48	80.76	6.59
UW167	2022-08-02	09:21:40	80.56	7.17
UW168	2022-08-02	13:42:30	80.30	5.98
UW169	2022-08-02	17:25:58	79.78	3.81
UW170	2022-08-02	21:27:44	79.28	1.17
UW171	2022-08-03	01:28:05	79.01	-0.61
UW172	2022-08-03	05:37:27	79.00	-2.93
UW173	2022-08-03	09:24:30	78.96	-4.34
UW174	2022-08-03	13:35:30	78.99	-5.37
UW175	2022-08-03	17:25:30	79.00	-5.38
UW176	2022-08-03	21:35:53	78.98	-5.45
UW177	2022-08-04	06:06:15	79.00	-8.66
UW178	2022-08-04	09:29:30	78.96	-10.54
UW179	2022-08-04	13:31:13	78.57	-11.10
UW180	2022-08-04	17:34:50	78.47	-12.55
UW181	2022-08-05	01:32:05	78.41	-13.30
UW182	2022-08-05	05:59:30	78.44	-14.65
UW183	2022-08-05	09:25:52	78.48	-15.92
UW184	2022-08-05	13:33:10	78.48	-17.96
UW185	2022-08-05	17:31:07	78.47	-18.51
UW186	2022-08-05	21:29:40	78.47	-18.52
UW187	2022-08-06	01:27:45	78.45	-18.42
UW188	2022-08-06	06:19:27	78.45	-18.42
UW189	2022-08-06	09:24:52	78.43	-18.44
UW190	2022-08-06	13:29:23	78.43	-18.32
UW191	2022-08-06	17:33:10	78.47	-17.51
UW192	2022-08-06	21:29:57	78.42	-16.85
UW193	2022-08-07	01:33:38	78.22	-15.77
UW194	2022-08-07	06:14:43	78.18	-15.72
UW195	2022-08-07	09:26:02	78.16	-15.73
UW196	2022-08-07	13:26:50	77.84	-15.55
UW197	2022-08-07	17:31:50	77.44	-15.50
UW198	2022-08-07	21:30:50	77.11	-15.52
UW199	2022-08-08	01:37:10	76.67	-15.53
UW200	2022-08-08	05:33:53	76.23	-15.62
UW201	2022-08-08	11:05:17	75.68	-15.79

Sample ID	Date UTC	Time UTC	Lat	Lon
UW202	2022-08-08	13:36:35	75.40	-15.86
UW203	2022-08-08	17:39:42	74.79	-16.42
UW204	2022-08-08	21:29:51	74.37	-16.87
UW205	2022-08-09	01:35:10	73.79	-17.59
UW206	2022-08-09	05:40:52	73.11	-18.34
UW207	2022-08-09	09:25:37	72.48	-18.99
UW208	2022-08-09	13:40:58	71.77	-19.73
UW209	2022-08-09	17:34:05	71.08	-20.43
UW210	2022-08-09	21:29:08	70.35	-21.27
UW211	2022-08-10	01:31:38	70.32	-22.70
UW212	2022-08-10	09:31:25	71.05	-25.04
UW213	2022-08-10	13:31:47	71.23	-25.31
UW214	2022-08-10	17:20:55	71.28	-25.16
UW215	2022-08-10	21:29:05	71.30	-25.32
UW216	2022-08-11	01:34:42	70.69	-24.45
UW217	2022-08-11	06:37:27	70.29	-22.74
UW218	2022-08-11	09:32:45	70.35	-22.00
UW219	2022-08-11	13:36:15	70.36	-21.99
UW220	2022-08-11	17:30:05	70.20	-21.39
UW221	2022-08-11	21:30:45	69.78	-19.75
UW222	2022-08-12	01:35:05	69.34	-18.14
UW223	2022-08-12	05:39:13	68.89	-16.62

Tab. 5.6: List of date, time, sample depth of water samples at CTD stations during PS131 on which the same parameters were determined as stated in Table 5.5

Station	UTC Date	Time	Sampled Depth [m]
PS131_6-5	2022-07-06	4:39:00	2,23,40,50,100
PS131_19-1	2022-07-07	21:13:00	2,14,40,50,100
PS131_29-1	2022-07-09	11:00:00	2,28,40,50,100
PS131_35-6	2022-07-10	23:33:00	2,20,40,50,100
PS131_56-2	2022-07-17	10:00:00	3,32,40,50,100
PS131_57-2	2022-07-17	19:39:00	2,20,40,50,100
PS131_61-2	2022-07-18	16:29:00	2,20,40,50,100
PS131_65-1	2022-07-20	23:42:00	5,15,40,50,100
PS131_69-8	2022-07-21	02:42:00	2,25,40,50,100
PS131_87-1	2022-07-29	13:43:00	2,24,39,49,100
PS131_88-1	2022-07-29	22:18:00	2,11,40,50,100
PS131_91-1	2022-07-31	01:36:00	2,26,40,50,100
PS131_94-1	2022-08-01	06:46:00	2,27,40,50,100
PS131_107-5	2022-08-03	00:02:00	2,22,40,50,100

Exchange of moored autonomous sampling devices for biological and biogeochemical parameters
(AGs Metfies and Nöthig with Nadine Knüppel, Ellen Oldenburg and Ovidiu Popa)

The PEBCAO-team accomplished the preparation and post-deployment processing of sediment traps and automated water samplers (RAS) deployed on moorings at the stations F4, EGC and Y in the MIZ. Overall, we recovered six sediment-traps, four RAS and deployed seven sediment-traps and four RAS (Tables 5.7, 5.8, 5.9 and 5.10).

Tab. 5.7: Recovery of sediment traps during PS131

Event	Device-Name	Lat	Long	Depth [m]	Deployment period
003-01	F4S-5	N 79°00.709	E 006°57.805	194	15.06.2021 – 30.06.2022
003-01	F4S-5	N 79°00.709	E 006°57.805	603	15.06.2021 – 30.06.2022
003-01	HG IV Fevi 42	N 78°59.979	E 004°19.888	191	15.06.2021 – 30.06.2022
028-01	HG IV Fevi 42	N 78°59.979	E 004°19.888	1228	15.06.2021 – 30.06.2022
028-01	HG IV Fevi 42	N 78°59.979	E 004°19.888	2341	15.06.2021 – 30.06.2022
106-01	EGC-7	N 78°59.276	W 005°21.588	480	17.06.2021 – 30.06.2022

Tab. 5.8: Deployment of sediment traps during PS131

Event	Device-Name	Lat	Long	Depth [m]	Deployment period
030-01	HG IV Fevi 44	N 78°59.994	E 004°19.937	197	21.07.2022 – 15.06.2023
030-01	HG IV Fevi 44	N 78°59.994	E 004°19.937	2341	21.07.2022 – 15.06.2023
034-01	F4-S6	N79°00.669	E 006°57.755	202	21.07.2022 – 15.06.2023
034-01	F4-S6	N79°00.669	E 006°57.755	604	21.07.2022 – 15.06.2023
063-01	Y4-1	N 80°57.948	E 008°42.180	191	21.07.2022 – 15.06.2023
63-01	Y4-1	N 80°57.948	E 008°42.180	582	21.07.2022 – 15.06.2023
106-01	EGC-8	N 78°59.777	W 005°23.744	501	10.08.2022 – 15.06.2023

Tab. 5.9: Recovery of Remote Access Sampler (RAS) during PS131

Station	Device-Name	Lat	Long	Depth [m]	Deployment period
003-01	F4-S5	N 79°00.709	E 006°57.805	22	14.06.2021-25.06.2022
003-01	F4-S5	N 79°00.709	E 006°57.805	241	14.06.2021-25.06.2022
106-01	EGC-7	N 78°59.276	W 005°21.588	38	22.06.2021-03.07.2022
106-01	EGC-7	N 78°59.276	W 005°21.588	232	22.06.2021-03.07.2022

Tab. 5.10: Deployment of Remote Access Sampler (RAS) during PS131

Station	Device-Name	Lat	Long	Depth [m]	Deployment period
034-01	F4-S6	N79°00.669	E 006°57.755	20	13.07.2022-24.07.2023
063-01	Y4-1	N 80°57.948	E 008°42.180	250	22.07.2022-02.08.2023
063-01	Y4-1	N 80°57.948	E 008°42.180	20	22.07.2022-02.08.2023
106-01	EGC-8	N 78°59.777	W 005°23.744	52	10.08.2022-21.08.2023

Sea ice biology

(AG Peeken with Lisa W. von Friesen and Johanna Schüttler)

Sea ice cores (9 cm diameter) were collected for biological, chemical and biogeochemical analyses at 12 ice stations (Tab. 5.11, Fig. 5.3). In addition to the three main floes of the marginal ice zone that were re-visited three times each, ice stations were performed at the Aurora field, at the Yermak plateu slope and on fast ice in east Greenland. Access to the ice floes was via gangway or mummy chair. Stations were in >60 m distance from the ship except for station 72-2. Sampled sea ice water habitats were meltpond, brine (sack hole sampling, ~75 % of the ice thickness) and under-ice water (10 cm below the ice bottom). Ice condition, water, salinity and temperature, approximate ice, and meltpond coverage) were measured at each station. Light measurements along a vertical profile through the ice were also performed. The ice stations were sometimes accompanied by CTD casts from the ship (first marginal ice zone visits), and then the deep chlorophyll maximum was also sampled.

At each station, three standard cores were collected for biological and chemical analyses. The core for biological parameters was split into one top (30–45 cm), several middle (30–55 cm) and one bottom (5 cm) part/s. Two bottom parts were always pooled. Filtered seawater (<0.2 µm) from depths below 500 m was added (100 ml/cm) to prevent osmotic shock of cells during melting at 4°C in darkness for 24–72 h. Salinity, porosity (weight and melted volume) and nutrients were measured at a resolution of 10 cm (except bottom of 5 cm) through one individual core at each station after melting at 4° C in darkness for ~48 h. Samples were collected for fractionated DNA (10 µm, 3 µm and 0.4 µm), POC/PON, bPSi, HPLC (pigment analysis), microscopy and nutrients from the different matrices. Total number of samples collected for different parameters were; HPLC (113), POC/PON (106 + blanks), PbSi (106), microscopy (109), DNA (302), nutrients (242, analyzed by the group Torres-Valdes et al. onboard). Except for microscopy samples, all other samples will be analyzed within the next two years at the Polar Biological Oceanography section from the AWI.

Tab. 5.11: Overview of the sea ice stations; see section text for descriptions of the north, mid and south floes and their revisits.

Station	Latitude (N)	Longitude (E)	Floe	Visit	Cores	Algal aggregates sampled	Incubations performed
47-1	81°36.628’	006°46.552’	North	1	8		X
48-1	81°10.947’	007°45.612’	South	1	3		
49-1	81°21.024’	006°47.818’	Mid	1	8		X
67-1	81°30.010’	004°46.555’	North	2	8	X	X
68-1	81°11.430’	005°25.864’	South	2	3		
70-1	81°21.312’	005°08.505’	Mid	2	8		X
72-2	82°51.957’	-005°45.876’	Aurora	-	3	X	X
84-1	81°19.794’	001°19.533’	24h	-	3		X
89-1	81°11.245’	002°23.785’	North	3	8		X
92-1	80°55,680’	80°55,680’	South	3	0	X	
93-1	81°04.262’	002°08.608’	Mid	3	8		X
109-1	78°26.068’	-018°26.579’	GL, thick fast ice	-	3		
110-1	78°28.449’	-017°30.882’	GL, thin fast ice	-	8	X	X

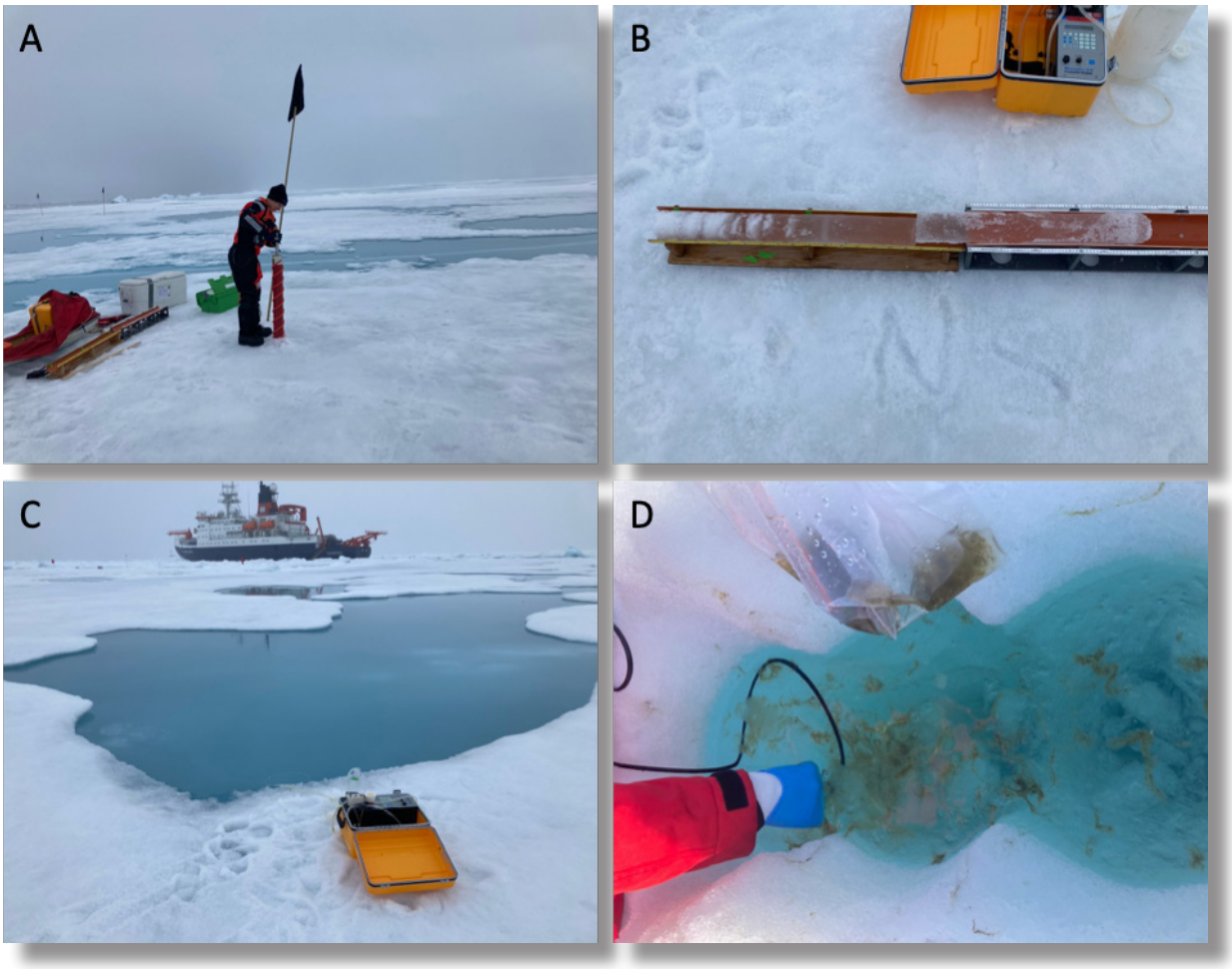

Fig. 5.3: Photos of the sampling on ice;
A: Ice coring at one of the coring sites; B: an ice core; C: water sampling from meltpond,
D: algal aggregates from below sea ice

On seven ice stations (revisit 1, 2 and 3 of the north and mid floe in the marginal ice zone and of the thin fast ice in eastern Greenland), incubations of intact (i.e. non-melted) ice core sections were performed in triplicate to determine nitrogen and carbon fixation through stable isotope tracing experiments. The sections were bottom 5 cm, the following 30 cm (from now on "mid"), and the top 30 cm. The sections were incubated as following: bottom with under-ice water (60 ml/cm), mid with brine water (~45 ml/cm) and top with meltpond water (~45 ml/cm). The water fractions were initially spiked with isotope tracers ($^{15}N_2$ and $NaH^{13}CO_3$) and pooled with its respective ice core section. Incubation took place for 24 h in an on-deck tank with a continuous throughflow of sub-surface water (~11 m) to maintain *in-situ* temperatures (Fig. 5.4). For each incubated unit, light was adjusted with black plastic mesh to simulate *in-situ* conditions. After incubation, ice cores were rapidly melted at 30° C, filtered over advantec GF75 filters and frozen at –20° C. Each experiment was accompanied by a T0 (to obtain *in-situ* d15N and d13C values) core and a DNA core (pooled with the respective water and melted in the same way as described above). RNA samples and samples for cell abundance were collected from the water fractions immediately upon sampling. Several control incubations were performed during the cruise and included a non-spiked core incubation as well as duplicate stable-isotope spiked incubations of the water fractions alone (i.e. 2x meltpond, 2x brine, 2x under-ice water).

Further, at four points when algal aggregates were encountered (Tab. 5.12, station 70-1, 72-2, 84-1, 110-1), triplicate stable isotope tracing experiments were set-up in a similar manner, pooling 100 ml of algal slurry with 100 ml of spiked water. The water was either under-ice water or meltpond water depending on where the aggregates were sampled from.

In addition, similar stable isotope tracing-incubations were performed of *chl-a* max water at eight stations during two transects through the marginal ice zone and at one station at the east Greenland shelf (Table 5.12), targeting different hydrographical regimes. These incubations also included an experimental treatment with addition of an organic carbon mix to a triplicate set of bottles to investigate potential stimulation of heterotrophic nitrogen fixation. The experiment set up from station 65-5 was deployed *in-situ* at 11 m below from the north ice floe in between revisit 2 and 3. During this time a parallel incubation was run in the onboard tank harvesting duplicate bottles at seven time points.

The originally planned incubations to tackle the impact of glacial melt on biological carbon and nitrogen fixation were not carried out, due to poor accessibility of the targeted glaciers region.

In total, 20 stable isotope tracing experiment were performed and a total of 87 DNA/RNA samples, 203 samples for EA-IRMS (elemental analyzer isotope ratio mass spectrometry), 149 samples for MIMS (membrane inlet mass spectrometry) and 138 samples for flow cytometry were collected. These samples will be analyzed at the University of Copenhagen.

Tab. 5.12: Overview of the performed stable isotope tracing experiments from *chl-a* max water.

Station	Latitude (N)	Longitude (E)	Regime
36-1	80°20.729’	10°36.554’	Atlantic
37-1	80°31.591’	10°6.866’	High melt
42-1	81°7.121’	8°14.719’	Pack-ice
56-8	80°37.210’	9°47.108’	High DCM of MIZ
57-7	80°23.401’	10°28.312’	Atlantic
61-7	80°49.573’	9°8.378’	High melt
65-5	81°32.344’	7°7.578’	Pack-ice, for *in-situ* deployment
108-1	78°26.778’	-18°25.030’	East Greenland

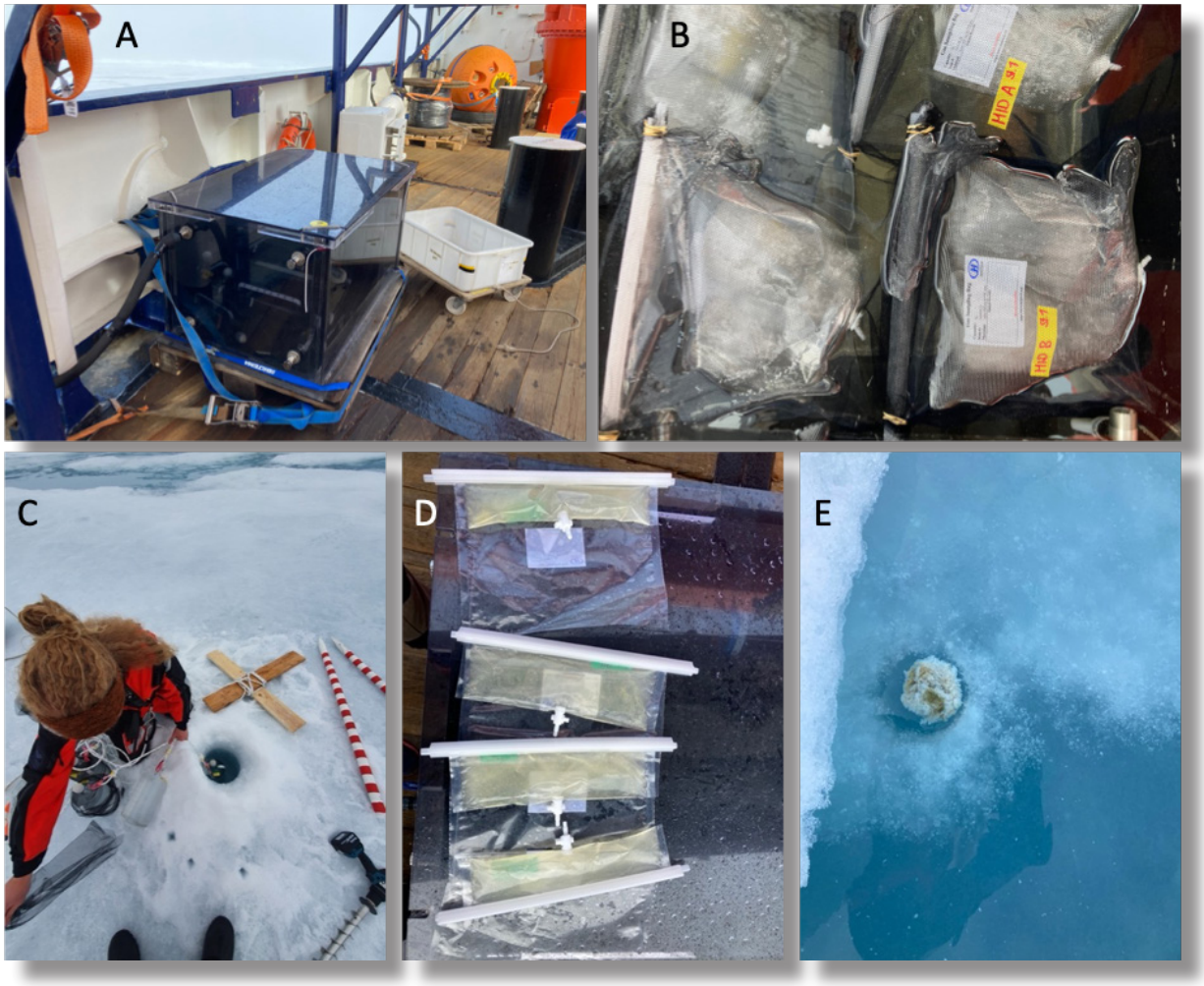

Fig. 5.4: Photos of performed stable isotope tracing work;
A: On-deck incubator with continuously flowing subsurface seawater at the aft port side of Polarstern, B: Incubation of ice core sections in gas-tight tedlar bags, light adjusted, C: Deployment of in-situ incubation of chl a max water at station 68, D: Incubation of algal aggregates in gas-tight tedlar bags, E: Algal aggregate in meltpond

For the atmospheric work, air sample cartridges were taken continuously at the crowns nest of *Polarstern* from 29 June to the 16 August (with an interruption in the waters of Iceland and Färöer Islands). At selected points, comparison samples were taken at the front of the ship using an inlet from the TROPOS research container with a handheld pump. In total 112 cartridges were taken, each for around 12 hours. The analysis will take place at the Max-Planck-Insitute in Mainz after the cruise. The focus will be on volatile selenium compounds

Additional CO_2 measurements were carried out at the same inlet point to exclude samples which were heavily influenced by the ships exhaust. Due to a leakage in the beginning of the dry, pressurized air used as a reference for the infrared sensor of the used instrument Licor 7000, the continuous CO_2 measurement has some gaps. Air canisters have been taken for comparison with the sorbent cartridges at some selected points.

For later quantification of selenium compounds dissolved in the water, underway samples from a subsurface water inlet at ~10.5 m depth were taken every 12 hours.

Fig. 5.5: Photos of atmospheric work
A: Cartridge collector at the crows nest; B: Handheld pump setup for cartridge samples in the TROPOS container; C: Inlet for CO_2 and Cartridges outside the crows nest with particle filters

Preliminary (expected) results

Protistian and Microbial Plankton

Most samples will be analyzed at AWI laboratories, and thus no data are yet available. For a preliminary view on the putative microbial plankton spatial distribution along the transect from Bremerhaven to Fram Strait as well as within the MIZ, however, we used the flow rate (f_{samp}=vol/min) from the underway sampling (AUTOFIM) as proxy for biomass. First, we calculated the flow rate using a 0.4 µm filter and clear water (f_{ref}). This value was used as a reference. We then estimated the biomass in each sample as the fold change, $-\log_2(f_{samp}/ f_{ref})$, to the reference value (Fig. 5.6). Therefore, for samples with fold change values of 2 we expected a four times higher biomass concentration compared to clear water and fold changes of 4, 16 times higher concentration. The highest fold change value (4.82) was observed for a sample taken in MIZ, the second highest (4.33) on the transect from Bremerhaven to Fram Strait. To understand the observed distribution pattern, we further analyzed the association of the fold change values in relation to salinity (psu) and *Chl-a* fluorescence measured by the *Polarstern* keel thermosalinograph and feerrybox respectively. We observed a significant but moderate correlation (rho = 0.371, pval=0.001, spearman test) with chlorophyll a concentration. Furthermore, the observed association with salinity (psu) was much stronger (rho=0.625,

pval= 1.168e-14) which is an indication that the biomass variability was linked to the different water mass profiles. This overview allows a preliminary estimation of the biomass variability associated with different water mass characteristics in the MIZ and during the transect to Fram Strait.

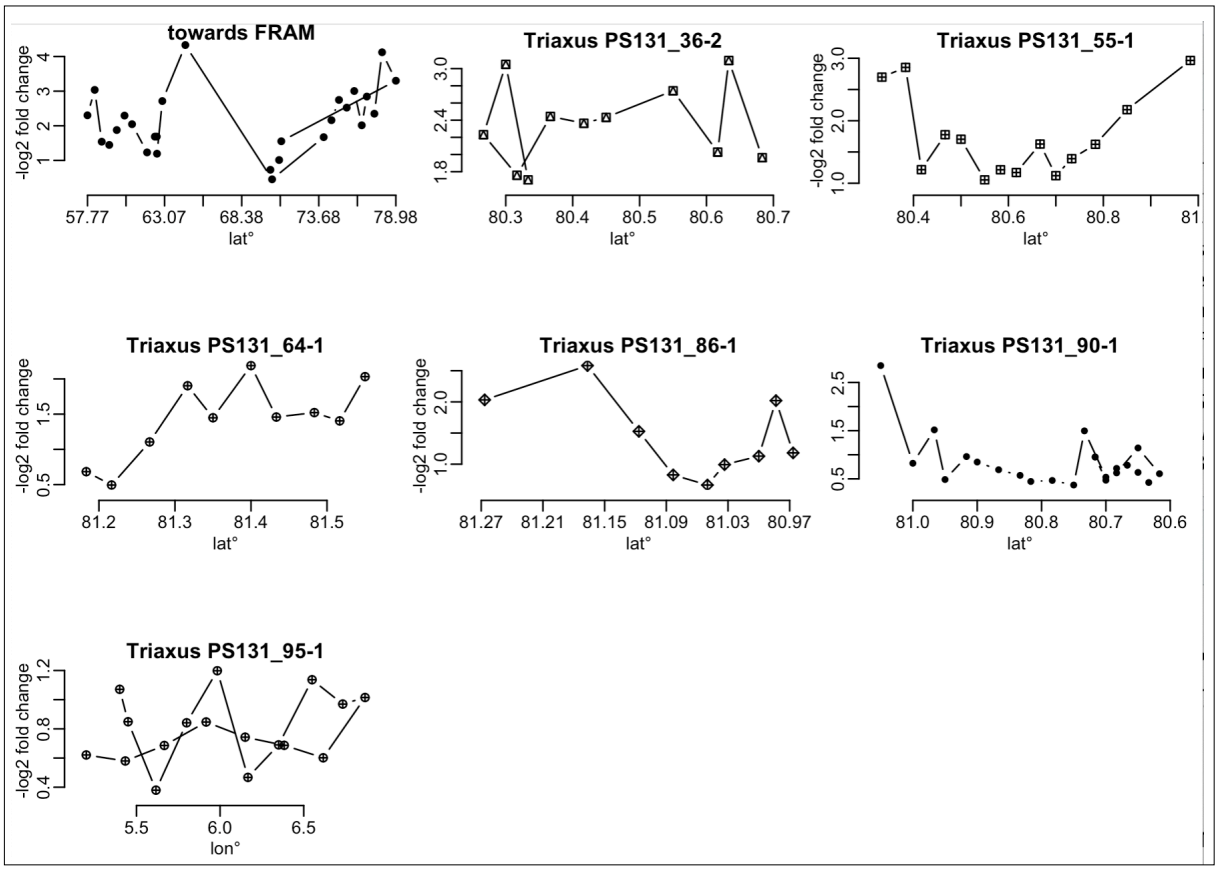

Fig. 5.6: Putative spatial distribution of biomass for several transects (coordinates on x-axis); samples were taken by the AUTOFIM in parallel to Triaxus deployments, and the panels present -log$_2$ fold changes (y-axis) of the filtered sample volumes as compared to the reference value obtained with filtered clear water.

Zooplankton

A first view on the more than 500-thousand images (Fig. 5.7) obtained from the LOKI system and on the preserved samples revealed that copepods clearly dominated the mesozooplankton community at all stations while Amphipoda, Hydrozoa, Polychaeta, Ostracoda, Siphonophora, and Chaetognatha were less abundant. Among the copepods, *Calanus glacialis* was the most frequent species in the surface layer in the MIZ while *C. finmarchicus* was the dominant large copepod species in the Eastern Fram Strait. Many female copepods were mature (Fig. 5.7b), and often large amounts of fecal pellets were found in the samples, especially in the MIZ, which could indicate that productivity was high in that area. It also appears that most organisms concentrated in the upper 50 m of the water column as to be expected during this time of the year. However, all samples and image data collected during PS131 will be analyzed in the laboratories at AWI under the stereomicroscope and using semi-automatic imaging methods to obtain detailed information on biodiversity and distribution of the zooplankton community in relation to environmental conditions (ice cover, depth, temperature, salinity, chlorophyll a concentration). These data will also continue our time series on zooplankton biomass and abundance in the Fram Strait and the Central Arctic Ocean.

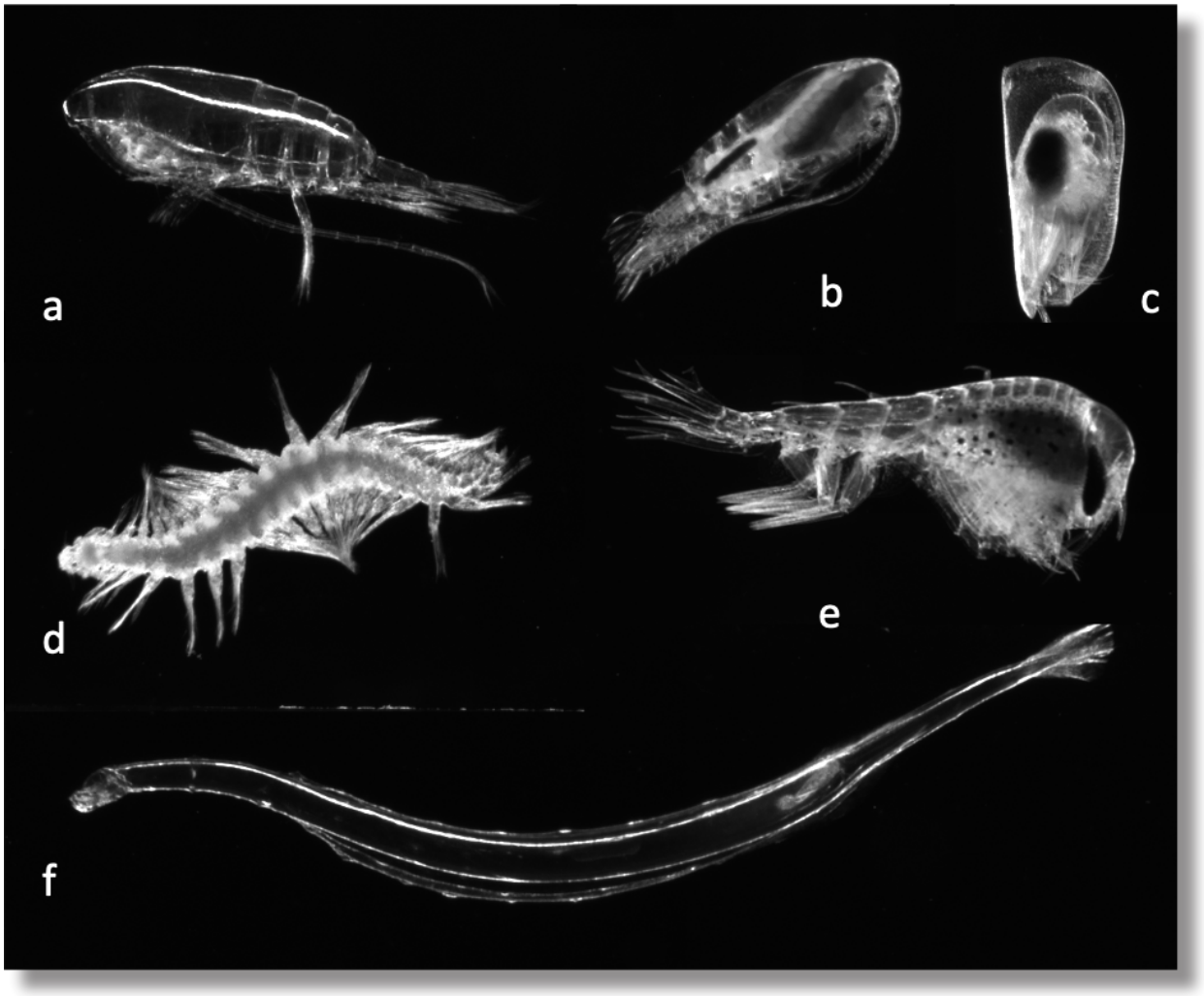

Fig. 5.7: LOKI images collected during PS 131, presenting the most abundand taxa including Copepoda (Calanus (a), Gaetanus (b)), Ostracoda (c), Polychaeta (d), Amphipoda (e), and Chaetognatha (f). Please note that the Gaetanus female (b) carries large maturing oocytes and a fecal pellet is visible in its hindgut, suggesting reproductive activity and good feeding conditions in our research areas.

Sea ice biology

In total 72 sea ice cores were collected during the twelve ice stations. Snow depth was very variable even during a single ice station and did not show any clear temporal trend during the investigation period (Fig. 5.8a). Slightly larger snow depth was found at the Aurora vent field and the Yermak slope station, where also thicker sea ice was found (Fig. 5.8b). These north south gradients are in line with the various classified ice regime with thicker and higher sea ice cover in the north (sea ice physics Chapter 3.1).

The collected biology sea ice cores during the revisiting of the three different MIZ ice floes also followed the overall pattern of decreasing sea ice thickness (see sea ice physics Chapter 3.3.). The decrease was mostly pronounced at the southernmost stations and at the third visit (Fig. 5.7). Another thick ice core was collected from the land fast ice area east of Greenland (St 109), but this was rather an exception and targeted for contrasting purposes, while the sea ice thickness of 1 m collected at station 110 was more representative of the entire area east of Greenland (sea ice physics Chapter 3.1).

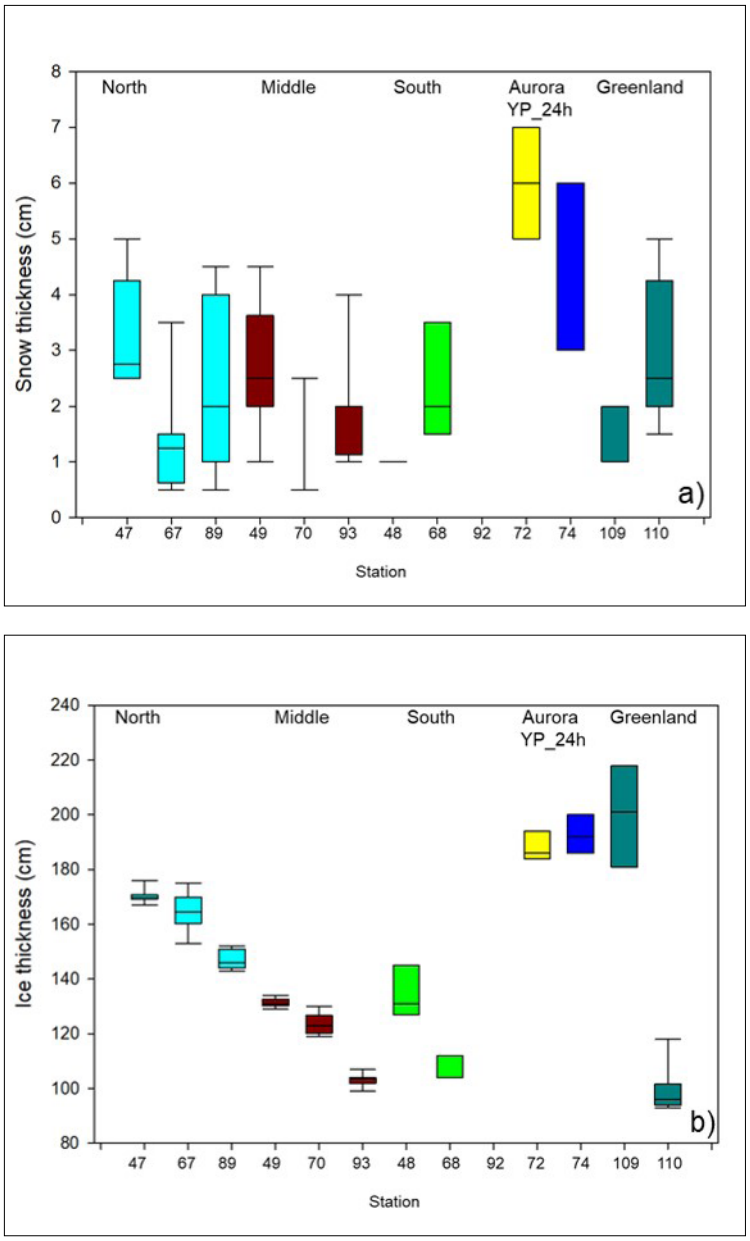

Fig. 5.8: Boxplots of snow (a) and sea ice thickness (b) of the collected ice cores for the various stations grouped by locations (Floe: North, Middle, South, Aurora vent site, 24 h station Yermak Plateau (YP) and east Greenland)

All sea ice cores collected show a reduced surface salinity caused by the meltwater flushing and indicating the influence of summer melt (Fig. 5.9). The slight deviation from this trend at the very surface indicate that the brine was also expelled upwards during sea ice growth. The decrease in salinity is mostly pronounced at the Northern floe, with decreasing surface salinity over time, which is corroborated by the only slight increase of salinity of the pond observations made by the sea ice physics team (sea ice physics Chapter 3.4 Table 3.4.4) from this ice floe. In contrast, the floes in the middle and the south rather show an increasing salinity over time suggesting a strong widening of the brine channels allowing sea water to penetrate further up in the ice floe, which is also reflected in the steep increase of melt pond salinity measured during the third visits on both floes (sea ice physics Chapter 3.4 Table 3.4.4).

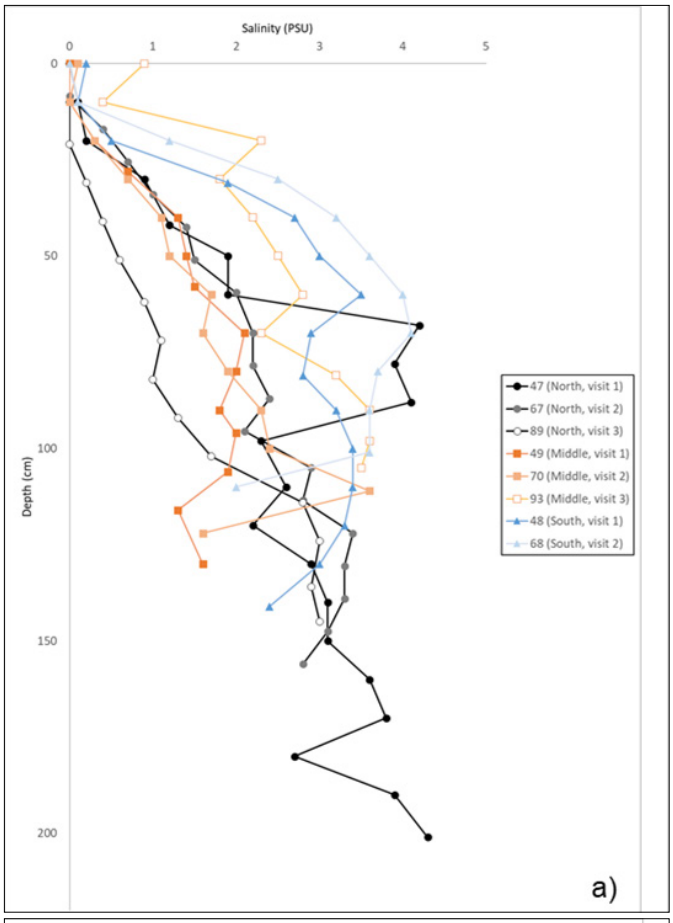

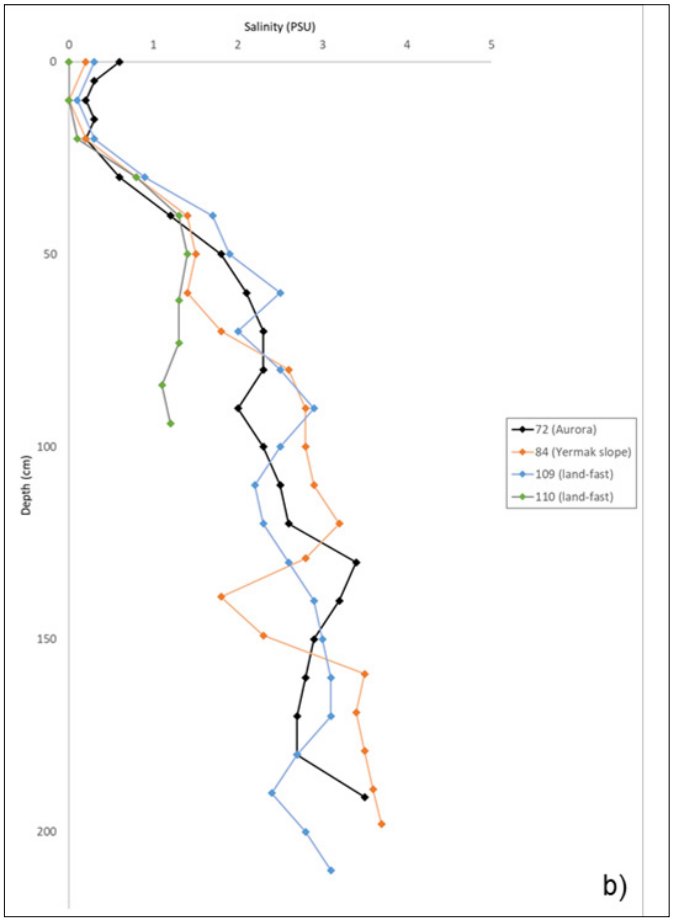

Fig. 5.9: Depth profiles of sea ice salinity at the various stations: (a) revisited ice floes at the MIZ, (b) other collection sites

The collected sea ice cores and ice water fractions reflect different ice regimes and cover melting processes in a way that enables understanding of the role of. sea ice-associated biomass to the cryo-pelagic, cryo-benthic coupling. These various sampled scenarios further allow to elucidate the role of nitrogen fixation in sea ice habitats of the Arctic Ocean and will also give a wide range of observations for possible marine Selenium emissions and any biological sources. These data can be used for modeling approaches to access the role of climate change-induced sea ice melting on the carbon and nitrogen cycle of the Arctic Ocean and allow to improve atmospheric modeling of various trace gases.

Biooptical measurements

Due to limited personnel onboard PS131 (COVID-19 testing excluded one team member), no analysis of measurements was possible on board and no preliminary results were obtained during PS131. All samples collected at discrete stations and ACS and RAMSES measurements obtained at discrete stations are listed in Tables 5.1 to 5.4. Samples for HPLC, PABS, CDOM were collected and measured for PAB on board, but will be further measured by HPLC and CDOM at AWI. All discrete sample data are analyzed to obtain phytoplankton pigment composition and concentration and absorption of particulates, CDOM and phytoplankton back at AWI. The Light profiler data logger output data will be converted for the ACS data into ascii files using Wetlabs software Wetview and RAMSES data using own written software for conversion into msda_xe formatted ascii output. Further, all ACS- and RAMSES which were collected require further processing to derive IOPs and AOPs: The RAMSES station and Triaxus data are going to be processed as in Taylor et al. (2011) and further detailed in Tilstone et al. (2020) following IOCCG protocol from 2019. The AOP data will be further analyzed to obtain phytoplankton composition and abundance in the profile using the method developed in Bracher et al. (2020). From the ACS measurements the inherent optical properties (IOPs: total attenuation, scattering and absorption) in the water profile will be derived (following Liu et al., 2018). The AOP and IOP data will be further analyzed by applying inverse radiative transfer modelling and optimal estimation approaches using spectral decomposition to derive the composition and amount of phytoplankton, other particles and CDOM (e.g., following Liu et al., 2019; Bracher et al., 2020).

The high resolution surface biogeochemical data set focusing on phytoplankton pigment and group composition and distribution will continue our time series and serve to develop optical algorithms (e.g., Xi et al., 2021), to validate satellite data (e.g., Liu et al. 2018) and to upscale other pelagic processes (e.g., Cherkaheva et al., 2014; Engel et al., 2019), in the Fram Strait.

Data management

Many of the samples (e.g., sediment trap data, molecular analyses, pigment analyses and optical measurements) will be processed and further analyzed at AWI within approximately one year after the cruise. We plan that the full data set will be available at the latest about 2–3 years after the cruise. Data will be made available to the public via PANGAEA (https://pangaea.de) in accordance with current institute data policies. Zooplankton images will be archived and made available on the website EcoTaxa (ecotaxa.obs-vlfr.fr). ACS data are foreseen to be uploaded to the FRAM data portal as raw data immediately after the cruise and as calibrated data set after carefully executing quality controls and calibrations with discrete water sample measurements.

Molecular work regarding diazotrophs will be performed at the University of Copenhagen. Molecular data (DNA and RNA data) will be archived, published and disseminated within one of the repositories of the International Nucleotide Sequence Data Collaborations (INSDC, www.insdc.org) comprising of EMBL-EBI/ENA, Genbank and DDBJ).

Any other data, such as MIMS, EA-IRMSand dual DNA/RNA samples, that will be analyzed by the University of Copenhagen, will be submitted to an appropriate long-term archive (e.g. GenBank) that provides unique and stable Identifiers for the datasets and allows open online access to the data.

All atmospheric samples are destroyed once they are analyzed. For atmospheric analysis, the cartridges are desorbed and the air in the canisters measured in the laboratory (MPI for Chemistry in Mainz). All data will be made freely accessible in the data repository PANGAEA (https://www.pangaea.de).

This expedition was supported by the Helmholtz Research Programme “Changing Earth – Sustaining our Future” Topics 2 and 6, Subtopics 2.4, 6.1 and 6.3.

In all publications, based on this cruise, the **Grant No. AWI_PS131_05** will be quoted and the following *Polarstern* article will be cited:

Alfred-Wegener-Institut Helmholtz-Zentrum für Polar- und Meeresforschung. (2017). Polar Research and Supply Vessel *Polarstern* Operated by the Alfred-Wegener-Institute. Journal of large-scale research facilities, 3, A119. http://dx.doi.org/10.17815/jlsrf-3-163.

References

Aksenov Y, Popova EE, Yool A, Nurser AJG, Williams TD, Bertino L, Bergh J (2017) On the future navigability of Arctic sea routes:High-resolution projections of the Arctic Ocean and sea ice. Mar Pol, 75:300–317.

Álvarez E, Losa S, Bracher A, Thoms S, Völker C (in revision) Impact of non-photosynthetic pigments content in the global variability of phytoplankton absorption coefficients. JAMS.

Bracher A, Xi H, Dinter T, Mangin A, Strass V H, von Appen W-J, Wiegmann S (2020) High resolution water column phytoplankton composition across the Atlantic Ocean from ship-towed vertical undulating radiometr., Frontiers in Marine Science, 7:235. https://doi.org/10.3389./fmars.2020.00235

Cherkasheva A, Bracher A, Melsheimer C, Köberle C, Gerdes R, Nöthig EM, Bauerfeind E, Boetius A (2014) Influence of the physical environment on phytoplankton blooms:a case study in the Fram Strait. J Mar Sys, 132:196–207.

Cornils A, Hase J, Hildebrand N, Auel H, Niehoff B (2022) Testing the usefulness of optical data for zooplankton long-term monitoring:Taxonomic composition, abundance, biomass and size spectra from ZooScan image analysis. Limnol. Oceanogr., 20(7):428–450.

Engel A, Bracher A, Dinter T, Endres S, Grosse J, Metfies K, Peeken I, Piontek J, Salter I, Nöthig EM (2019) Inter-Annual Variability of Organic Carbon Concentration in the Eastern Fram Strait During Summer (2009–2017). Front Mar Sci, 6:187.

Fadeev E , Rogge A, Ramondenc S , Nöthig EM , Wekerle C, Bienhold C, Salter I, Waite A, Hehemann L, Boetius A, Iversen M (2021) Sea ice presence is linked to higher carbon export and vertical microbial connectivity in the Eurasian Arctic Ocean. Communications Biol, 4:1255.

Feinberg A, Maliki M, Stenke A, Sudret B, Peter T, Winkel LHE (2020) Mapping the drivers of uncertainty in atmospheric selenium deposition with global sensitivity analysis. Atmos Chem Phys, 20:1363–1390.

Hardge K, Peeken I, Neuhaus S, Krumpen T, Stoeck T, Metfies K (2017) Sea ice origin and sea ice retreat as possible drivers of variability in Arctic marine protist composition. Mar Ecol Prog Ser, 571:43–57.

Gradinger RR, Baumann MEM (1991) Distribution of phytoplankton communities in relation to the large-scale hydrographical regime in the Fram Strait. Mar Biol, 111:311–321.

Kraft A, Nöthig EM, Bauerfeind E, Wildish DJ, Pohle GW, Bathmann UV, Beszczynska-Möller A, Klages M (2013) First evidence of reproductive success in a southern invader indicates possible community shifts among Arctic zooplankton. Mar Ecol Prog Ser, 493:291–296.

Krumpen T, Belter HJ, Boetius A, Damm E, Haas C, Hendricks S, Nicolaus M. Nöthig EM, Paul S, Peeken I, Ricker R, Stein R (2019) Arctic warming interrupts the Transpolar Drift and affects long-range transport of sea ice and ice-rafted matter. Sci Rep-Uk, 9. https://doi.org/10.1038/s41598-019-41456-y.

Lalande C, Nöthig EM, Fortier L (2019) Algal Export in the Arctic Ocean in Times of Global Warming. Geophys Res Let., 46 5959–5967.

Lannuzel D, Tedesco L, Van Leeuwe M, Campbell K, Flores H, Delille B, Miller L, Stefels J, Assmy P, Bowman J, Brown K, Castellani G, Chierici M, Crabeck O, Damm E, Else B, Fransson A, Fripiat F, Geilfus NX, Jacques, Jones H. Kaartokallio M, Kotovitch K, Meiners S, Moreau, Nomura D, Peeken I, Rintala JM, Steiner N, Tison JL, Vancoppenolle M, Van Der Linden F, Vichi M, Wongpan P (2020). The future of Arctic sea-ice biogeochemistry and ice-associated ecosystems. Nat Clim Change, 10:983–992.

Lefering I, Röttgers R, Utschig C, McKee D (2017) Uncertainty budgets for liquid waveguide CDOM absorption measurements. Applied Optics, 56(22):6357.

Liu Y, Roettgers R, Ramírez-Pérez M, Dinter T, Steinmetz F, Nöthig EM, Hellmann S, Wiegmann S, Bracher A (2018) Underway spectrophotometry in the Fram Strait (European Arctic Ocean):a highly resolved chlorophyll *a* data source for complementing satellite ocean color. Optics Express, 26(14):A678–A698.

Liu Y, Boss E, Chase AP, Xi H, Zhang X, Röttgers R, Pan Y, Bracher A (2019) Retrieval of phytoplankton pigments from underway spectrophotometry in the Fram Strait. Remote Sensing, 11:318.

Massicotte P, Peeken I, Katlein C, Flores H, Huot Y, Castellani G, Arndt S, Lange BA; TremblayJE, Babin M (2019) Sensitivity of Phytoplankton Primary Production Estimates to Available Irradiance Under Heterogeneous Sea Ice Conditions. J Geophys Res-Oceans, 124:5436–5450.

Metfies K, von Appen WJ, Kilias E, Nicolaus A, Nöthig EM (2016) Biogeography and photosynthetic biomass of Arctic marine pico-eukaryotes during summer of the record sea ice minimum 2012. PLoS ONE 11.

Nöthig EM, Bracher A, Engel A, Metfies K, Niehoff B, Peeken I, et al. (2015). Summertime plankton ecology in Fram Strait - a compilation of long- and short-term observations. Polar Res, 34:23349.

Nöthig E-M, Ramondenc S, Haas A, Hehemann L, Walter A, Bracher A, Lalande C, Metfies K, Peeken I, Bauerfeind E and Boetius A (2020) Summertime Chlorophyll a and Particulate Organic Carbon Standing Stocks in Surface Waters of the Fram Strait and the Arctic Ocean (1991–2015). Front Mar Sci, 7:35.

Röttgers R, Doxaran D, Dupouy C (2016) Quantitative filter technique measurements of spectral light absorption by aquatic particles using a portable integrating cavity absorption meter (QFT-ICAM). Opt Express, 24:1–A20.

Schröter F, Havermans C, Kraft A, Knüppel N, Beszczynska-Möller A, Bauerfeind E and Nöthig E-M (2019) Pelagic Amphipods in the Eastern Fram Strait With Continuing Presence of *Themisto compressa* Based on Sediment Trap Time Series. Front Mar Sci, 6:11.

Strong C, Rigor IG (2013) Arctic marginal ice zone trending wider in summer and narrower in winter, Geophys. Res. Lett., 40:4864–4868.

Taylor BB, Torrecilla E, Bernhardt A, Taylor MH, Peeken I, Röttgers R, Piera J, Bracher A (2011) Bio-optical provinces in the eastern Atlantic Ocean. Biogeosci, 8:3609–3629. https://doi.org/10.5194/bg-8-3609-2011.

Tilstone G, Dall'Olmo G, Hieronymi M, Ruddick K, Beck M, Ligi M, Costa M, D'Alimonte D, Vellucci V, Vansteenwegen D, Bracher A, Wiegmann S, Kuusk J, Vabson V, Ansko I, Vendt R, Donlon C, Casal T (2020) Field intercomparison of radiometer measurements for ocean colour validation. Remote Sens. 12(10):1587. https://doi.org/10.3390/rs12101587.

Tran S, Bonsang B, Gros V, Peeken I, Sarda-Esteve R, Bernhardt A, Belviso S (2013) A survey of carbon monoxide and non-methane hydrocarbons in the Arctic Ocean during summer 2010. Biogeosci 10:1909–1935.

Tran S, Bonsang B, Gros V, Peeken I, Sarda-Esteve R, Bernhardt A, Belviso S (2013) A survey of carbon monoxide and non-methane hydrocarbons in the Arctic Ocean during summer 2010. Biogeosciences, 10:1909–1935

Von Appen WJ, Waite AM, Bergmann M, Bienhold C, Boebel O, Bracher A, Cisewski B, Hagemann J, Hoppema M, Iversen MH, Konrad C, Krumpen T, Lochthofen N, Metfies K, Niehoff B, Nöthig EM, Purser A, Salter I, Schaber M, Scholz D, Soltwedel T, Torres-Valdes S, Wekerle C, Wenzhöfer F, Wietz M, Boetius A (2021) Sea-ice derived meltwater stratification slows the biological carbon pump:results from continuous observation. Nature Communications, 12:7309.

von Friesen LW and Riemann L (2020) Nitrogen Fixation in a Changing Arctic Ocean:An Overlooked Source of Nitrogen? Front Microbiol 11.

William J and Crutzen PJ (2013) Perspectives on our planet in the Anthropocene. Environmental Chemistry ,10:269–280.

Xi H, Losa SN, Mangin A, Garnesson P, Bretagnon M, Demaria J, Soppa MA, d'Andon OHF, Bracher A (2021) Global chlorophyll a concentrations of phytoplankton functional types with detailed uncertainty assessment using multi-sensor ocean color and sea surface temperature satellite products. J Geophys Res-Oceans, 126:e2020JC017127. https://doi.org/10.1029/2020JC017127.

6. PELAGIC BIOGEOCHEMISTRY: NUTRIENTS AND NET COMMUNITY PRODUCTION

Sinhué Torres-Valdés[1], Linda Rehder[1], [1]DE.AWI
Klara Köhler[1], Annika Morische[2] [2]DE.ICBM
Not on board: Daniel Scholz[1], Sebastian Rokitta[1]

Grant-No. AWI_PS131_06

Outline

Productivity in the Arctic Ocean and thus the export of carbon to depth (the biological carbon pump), are sustained by the availability of nutrients in the sunlit layer (Tremblay et al., 2015). Nutrients are supplied via rivers and coastal erosion around the Arctic coast lines (Holmes et al., 2011; Terhaar et al., 2021), and by water mass exchange from the Pacific and Atlantic Oceans through Arctic Ocean gateways (Torres-Valdés et al., 2013, 2016). Rivers and coastal erosion supply nutrients directly to the surface layers on coastal seas, where these become readily available (Terhaar et al., 2021). Oceanic nutrient transport sustains productivity either directly over inflow shallow shelves, or via physical processes (e.g., vertical mixing, eddies) when water masses are subducted (Tremblay et al., 2015). Processes involved in Arctic Ocean dynamics have been affected by climate change (e.g., sea ice extent reduction, increased river loads) and it is still unclear how this, in turn, affects nutrient availability and ultimately, primary productivity. Therefore, understanding the mechanisms of nutrient delivery to the ocean sunlit layers, quantifying nutrient supply and assessing the net primary productivity are of relevance to assess potential effects of climate change on ecosystem functioning and the biological carbon pump.

Objectives

Fram Strait is one of the main Arctic Ocean gateways, through which water masses and associated physical and biogeochemical properties are exchanged with the Nordic Seas and North Atlantic. Atlantic Water (AW) flows north within the West Spitsbergen Current and interacts with surrounding waters, thereby redistributing biogeochemical properties. For the ATWAICE (PS131) expedition, our observation programme has specific goals. One is to generate data to address the scientific aims put forward as part of the expedition project (Objective 1, Question 1 and Objective 2, Question 7 of the ATWAICE proposal). These regard the study of advection of nutrients associated with Atlantic Water, eddies and fronts as well as nutrient fluxes toward the sea ice, and the effect of these processes on Arctic Ocean productivity. A second, and linked goal, is to continue our observations within the framework of the Frontiers in Arctic Marine Monitoring (FRAM) Programme. This aims to study temporal variability of nutrient content associated with the WSC and the EGC, and their relevance to the wider Arctic Ocean nutrient budget. Therefore, measurements targeted areas where water masses of interest flow. In addition to the measurement of nutrients, this time we also measured dissolved oxygen in order to generate data to calibrate the CTD-O_2 sensors. We also deployed biogeochemical packages (Remote access samplers, plus sensors) at selected locations in Fram Strait and ATWAICE. These deployments are done in collaboration with the Microbial Observatory (Katja

Metfies, Christina Bienhold, Anja Nicolaus and Mathias Wietz) and Physical Oceanography (Wilken von-Appen, Mario Hoppmann, Matthias Monsees, Torsten Kanzow) and Deep Sea (Normen Lochtofen) groups. During PS131, RAS preparations were carried out by Ovidiu Popa and Ellen Oldenburg (from Katja Metfies group) and Mario Hoppmann (with colleagues from the mooring team), who also look after the recovery and deployment of sensors. The biogeochemical packages are intended to generate high temporal resolution measurement of biogeochemical, microbial and physical variables over a one-year cycle.

To better understand the magnitude as well as the regionality and seasonality of biogeochemical activity, we will assess concentrations of dissolved O_2 and Ar using membrane-inlet mass spectrometry (MIMS, Fig. 6.1) to determine net community production of transected water masses (Craig and Hayward, 1987). Data will be combined with hydrological data (water mass identification), chemical data (nutrient fluxes, CO_2 concentrations), biological data (phytoplankton abundance, chlorophyll abundance), and meteorological data (wind speed) to derive estimates of net community production (Kaiser et al., 2005; Ulfsbo et al., 2014).

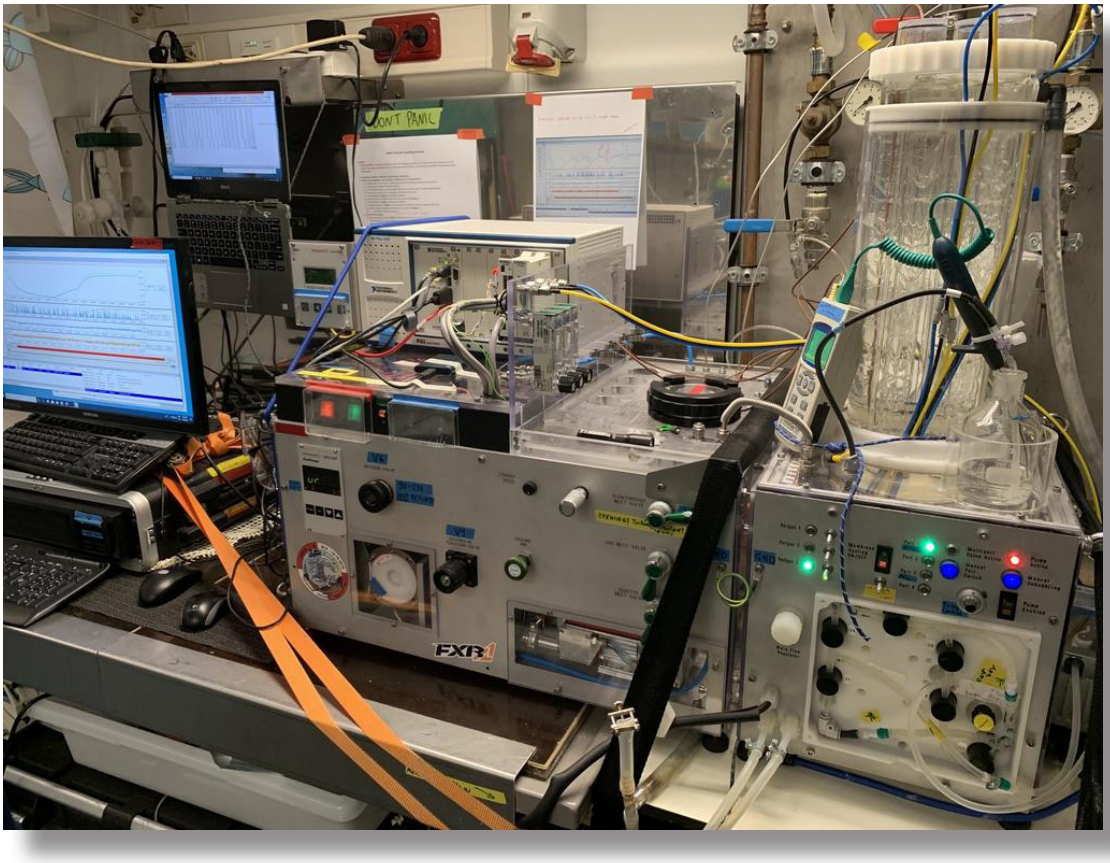

Fig. 6.1: Photo of membrane-inlet-mass-spectrometer (MIMS) as installed during the MOSAiC expedition on Polarstern Wet Lab 1; for PS 131, we had the same set up.

Work at sea

Lab set up

For PS131 a brand new 6-channel Seal Analytical AA-500 autoanalyser was set up in the chemistry lab for the analysis of micro-molar concentrations of 1) dissolved inorganic nutrients; nitrate plus nitrite (NO_3^-+NO_2^-) – hereafter referred to as nitrate –, nitrite (NO_2^-), silicate ($Si(OH)_4$), and phosphate (PO_4^{3-}), and 2) total nutrients; total phosphorus (TP) and total nitrogen (TN). Installation of the AA-500 involved the fitting of new pump tubing, a new cadmium column

for TN and new cadmium coil for nitrate. The nutrient analyser was controlled by the Seal Analytical Software AACE version 8.03 Beta15, which allows for automated and simultaneous analysis of up to 7 channels. Following analyser set up, analytical reagents (stock and working solutions), standards (stock solutions and calibrants) and lab-made quality control solutions were prepared. 'Stocks' are concentrated solutions from which 'working' reagents/standards are prepared as required by solution stability or usage. Analyses were carried out following current Seal Analytical Methods, which are based on standard and widely used colourimetric techniques for the analysis of nutrients in water and seawater. We list the methods used during PS131 here below:

1. Total dissolved nitrogen in seawater No. A-008-19 revision 1 (MT533).
2. Nitrate and nitrite in water and seawater No. A-044-19 revision 5 (MT519A).
3. Nitrite in water and seawater No. A-003-18 revision 3 (MT518).
4. Total dissolved phosphorus in seawater No. A-009-19 revision 3 (MT533).
5. Phosphate in water and seawater No. A-004-18 revision 4 (MT518).
6. Silicate in water and seawater No. A-006-19 revision 3 (MT519).

We adopted best practices procedures for the analyses of nutrients in seawater following GO-SHIP recommendations, as described in Hydes et al. (2010) and Becker et al (2020).

Calibrants

Calibration standards for the analysis were prepared using 1,000 mg/L NO_3^-, NO_2^-, PO_4^{3-} and Si MERC solutions. An intermediate standard containing 4.032, 0.152, 3.560 and 0.947 µmol/mL of nitrate, nitrite, silicate and phosphate was prepared in Milli-Q water using a 100 mL volumetric flask. Although working calibration standards are typically prepared in a saline solution or "artificial seawater" (35 g NaCl in 1 L of Milli-Q water), which is also used as a matrix for the analysis, in later years the so called "ultra clean or analytical grade reagents" have been found to be contaminated with a given nutrient (usually phosphate, nitrate and organic nitrogen, and even silicate). In our case, the analytical grade NaCl was found to be contaminated with nitrate and organic nitrogen. Therefore, standards and the analysis matrix were based on Milli-Q water instead. From the intermediate standards, five calibration standards were prepared regularly using 500 mL flasks to yield the target concentrations shown in Table 6.1.

Tab. 6.1: Set of calibration standards (*Std*) used for dissolved inorganic nutrient analysis. Concentration units are µmol L^{-1}. Concentrations in the first column are the sum of NO_3^- and NO_2^-, hence $NO_3^- + NO_2^-$. This concentration also applies for TN. Likewise, the concentration range for phosphate applies to TP.

	$NO_3^-+NO_2^-$	NO_2^-	$Si(OH)_4$	PO_4^{3-}	TN	TP
Std 1	0.469	0.017	0.399	0.106	0.469	0.106
Std 2	6.209	0.226	5.284	1.406	6.209	1.406
Std 3	11.950	0.435	10.169	2.707	11.950	2.707
Std 4	17.961	0.643	15.054	4.007	17.691	4.007
Std 5	23.431	0.852	19.939	5.307	23.431	5.307

These values were then transferred into an analysis template file of the AACE software, from which all consecutive runs were then built. For each analysis, standards were measured in triplicate, with the first measurement intended as preconditioning and thus ignored as

calibrant. It is good practice to adapt calibration concentration ranges for the particular system being measured, in this case, the Arctic Ocean. Here though, we used a rather high range for phosphate. This was determined/imposed by the method to measure TP, which is designed to work efficiently with a top standard of 5 µmol L^{-}1. A calibration range with a top standard lower than this is likely to yield high noise in the signal. However, the phosphate and TP channels were stable and linear throughout the expedition, with calibration slopes being typically 1.

All primary, secondary and working standards, CRMs and quality control solutions were kept in mosturized and dark conditions within a high-quality grade cool box when not in use and right after preparations.

Figure 6.2 shows time series of calibration standards measured through the 24 h analysis runs carried out during PS131. The cruise-mean, standard deviation and precision of the analysis at the different concentration levels are presented in Table 6.2. Calibration standards show good consistency through out the expedition. As usual, precision is reduced at low concentration levels. The limits of detection, taken as twice the standard deviation of the lowest concentration standard (cruise-long standard deviation) were: 0.14, 0.006, 0.02, 0.01, 0.09 and 0.01 µmol L^{-1} for NO_3^-+NO_2^-, NO_2^-, $Si(OH)_4$, PO_4^{3-}, TN and TP, respectively.

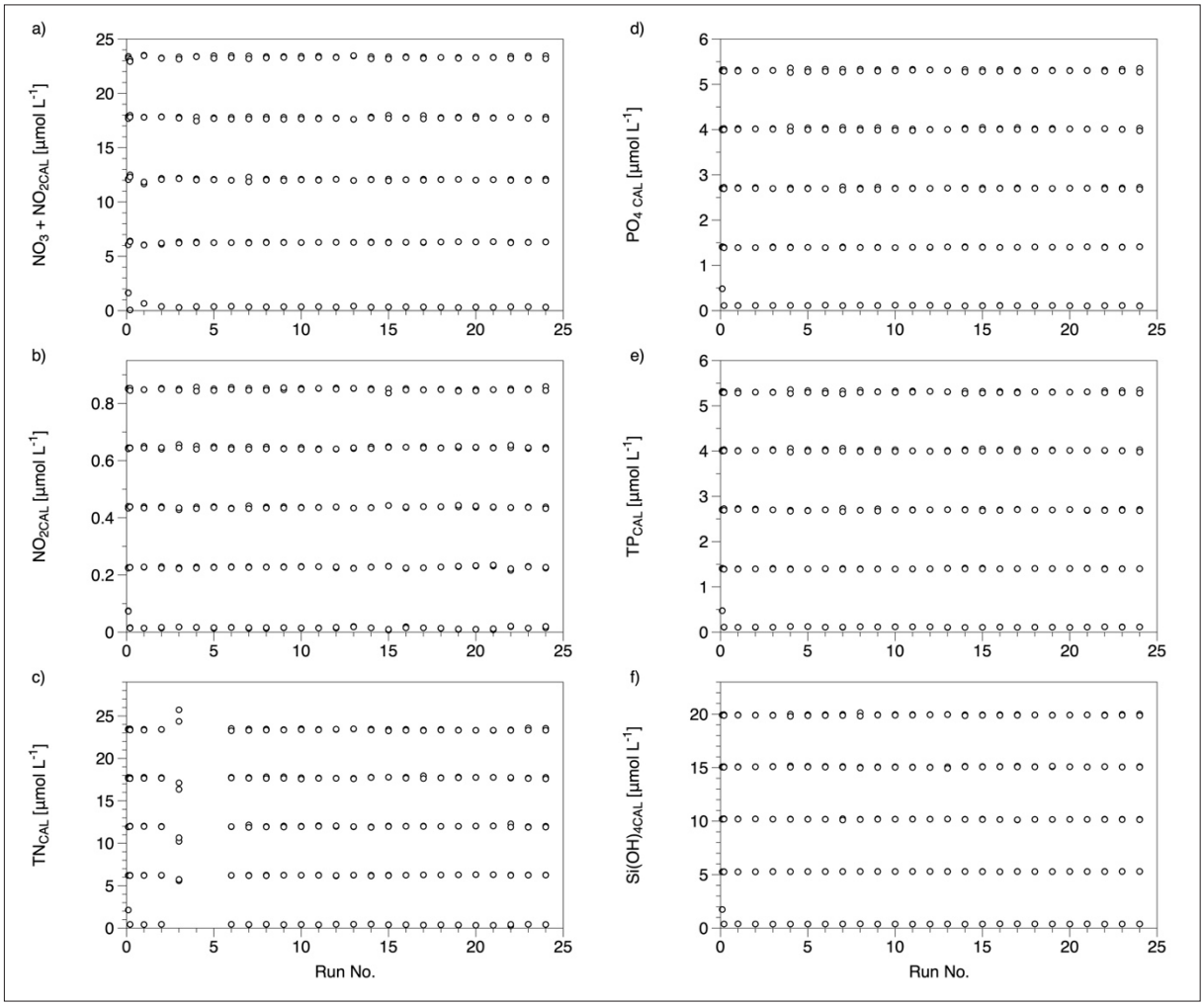

Fig. 6.2: Time series of calibration standards; with an exception of the first two test runs and some problems encountered with the measurement of TN (described later in this report), analysis yielded consistent results throughout the expedition.

Tab. 6.2: Cruise-mean, standard deviation and precision (%) of all calibration standards (Std). Concentration units are µmol L^{-1}.

	NO3-+NO2-	NO2-	Si(OH)4	PO43-	TN	TP
Std 1	0.36±0.07	0.015±0.003	0.39±0.01	0.112±0.005	0.42±0.04	0.112±0.006
Prec.	20%	21%	2.2%	4.4%	11%	5.5%
Std 2	6.28±0.07	0.227±0.003	5.29±0.01	1.400±0.007	6.22±0.13	1.400±0.007
Prec.	1.0%	1.4%	0.2%	0.5%	2.1%	0.5%
Std 3	12.05±0.10	0.437±0.003	10.17±0.03	2.702±0.014	11.92±0.34	2.701±0.014
Prec.	0.8%	0.7%	0.3%	0.5%	2.8%	0.5%
Std 4	17.74±0.10	0.645±0.004	15.07±0.04	4.011±0.02	17.67±0.24	4.014±0.019
Prec.	0.5%	0.6%	0.3%	0.5%	1.3%	0.5%
Std 5	23.33±0.09	0.849±0.004	19.92±0.05	5.308±0.022	23.46±0.39	5.307±0.021
Prec.	0.4%	0.5%	0.3%	0.4%	1.6%	0.4%

Quality controls (QCs)

There are various products and lab-made solutions that are used for quality control of the analysis; low nutrient seawater, recovery standards and certified reference materials (CRMs). Below we describe how and what we used them for. All quality control standards and CRMs were measured in duplicate in every analysis run.

Low Nutrient Seawater (LNSW) from OSIL Scientific

LNSW can have multiple uses. It can be used as a saline matrix, as a low concentration standard or, as in our case, to determine whether contamination with any given nutrient occurred during sample collection or preparation of reagents. It is expected that the signal produced is close to the baseline (i.e., blank) or above, and remain constant throughout analyses. During PS131, concentrations measured for the various nutrients, with the exception of silicate and TN, were on average within the limit of detection. In the case of silicate and TN, which are detectable, the average for the expedition was respectively, 0.65±0.03 and 3.38±0.48 µmol L^{-1}. LNSW is also useful in assessing the effect of measuring saline samples within a Milli-Q based matrix (the so-called salt effect). Seal Analytical analysers are made to account for this effect and so any impact on the analysis is minimized.

Recovery Standards: Cadmium coil and column reduction efficiency

The measurement of some nutrients such as NO_3^-+NO_2^- and TN requires continious monitoring of the reduction efficiency of the Cadmium (Cd) coil, in the former, and Cd column in the latter. The colourimetric method upon which the measurement of these two nutrients is based, relies on the chemical reaction between reagents and NO_2^-. Thus, in order to measure NO_3^-, this has to be reduced to NO_2^- (the Cd is oxidized and the NO_3^- is reduced). In the case of TN, the reaction is slightly more complicated, as all dissolved nitrogen in the water first needs to be oxidized to NO_3^-+NO_2^{--} and then reduced to NO_2^-. For TN there is thus an extra step to monitor; the oxidation efficiency, which is dealed with in the next subsection. In order to monitor the reduction efficiency, two lab-made standards containing only NO_2^- and only NO_3^- were prepared, both at a concentration of 23.31 µmol L^{-1}. The concentration yielded by measuring both recovery standards should be equal within the precision of the analyses. The reduction efficiency is the ratio of the NO_3^- standard to the NO_2^- standard in percentage. As per best practice recommendations, the Cd coil or column were reactivated or replaced when the reduction efficiency was less than 95 %. Figure 6.3 shows time series of the Cd reduction efficiency of the coil (Fig. 6.3a) and column (Fig. 6.3b). In the case of the coil, the first two

low values are results obtained from two tests runs. After these runs, the coil was reactivated twice to achieve acceptable % recoveries, with the need of two further reactivations during the expedition whenever the reduction efficiency approached 96%. The Cd column was more stable from the start, but was replaced twice during the expedition (on 12 July and on 8 August 2022). With few exceptions, recovery standards were measured in duplicate at the beginning and at the end of each run.

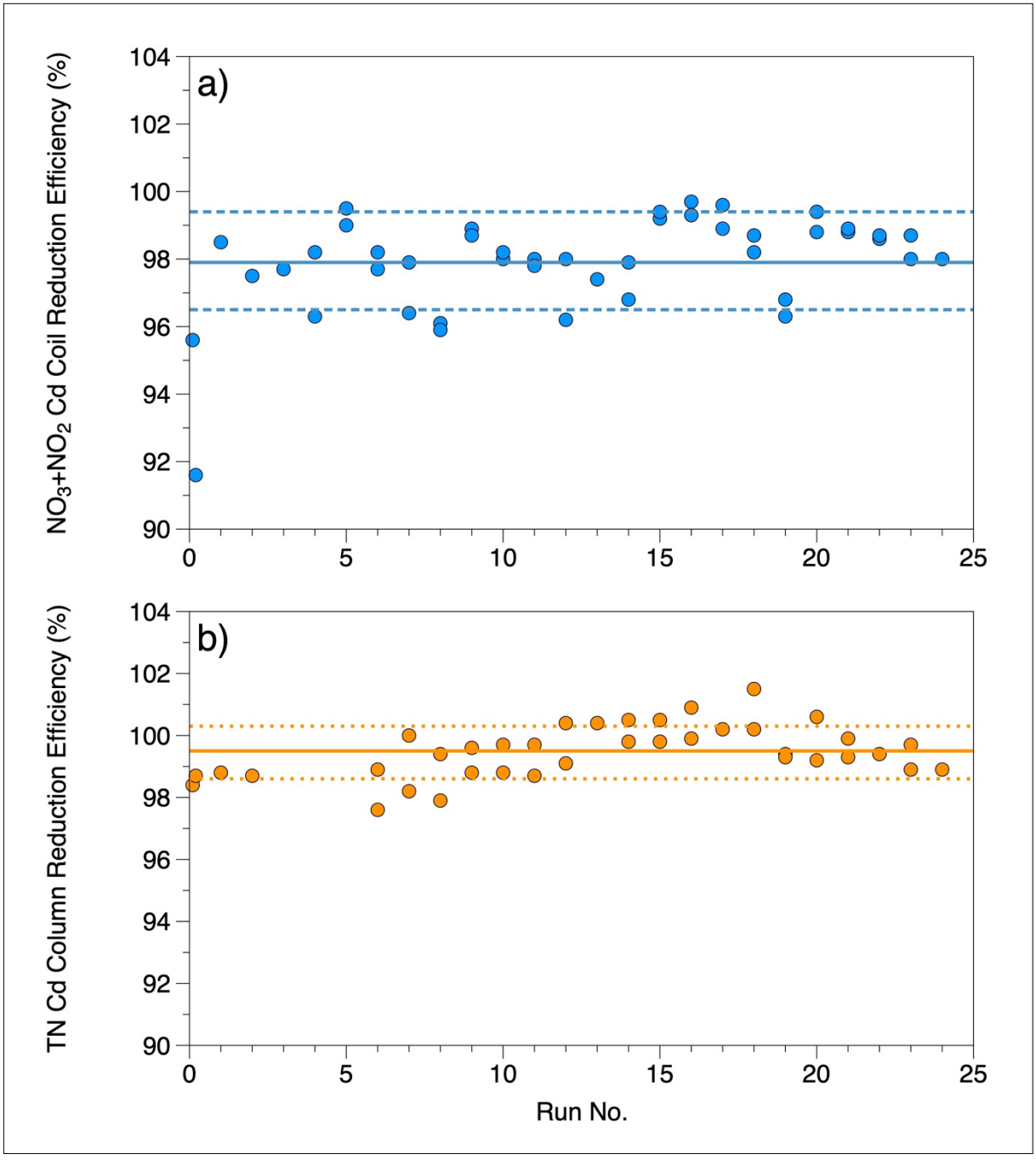

Fig. 6.3: Cd coil (a) and column (b) reduction efficiency for the measurement of NO_3^-+NO_2^- and TN during PS131. The cruise-long average reduction efficiency was 97.9±1.4% and 99.5±0.8% (shown as solid and dashed lines) for NO_3^-+NO_2^- and TN, respectively.

Recovery Standards: TN oxidation efficiency

As mentioned in the previous paragraph, the measurement of TN requires the oxidation of all nitrogenous compounds present in the sample. There are no certified reference materials available in the market to test the oxidation efficiency and the accuracy of the method. However, there are steps that can be taken. During for PS131 we used an OSIL Scientific 10 µmol L^{-1} ammonium (NH_4^+) certified standard, from which we prepared a 15 µmol-NH_4^+ L^{-1} solution. This standard was measured in duplicate in every run. Although this standard is not an organic compound, it is most useful as the NH_4^+ first needs to be oxidised to NO_3^-+NO_2^- and then reduced to NO_2^-. Figure 6.4 shows time series of the oxidation efficiency and recovery of NH_4^+. Measurements showed almost complete recovery.

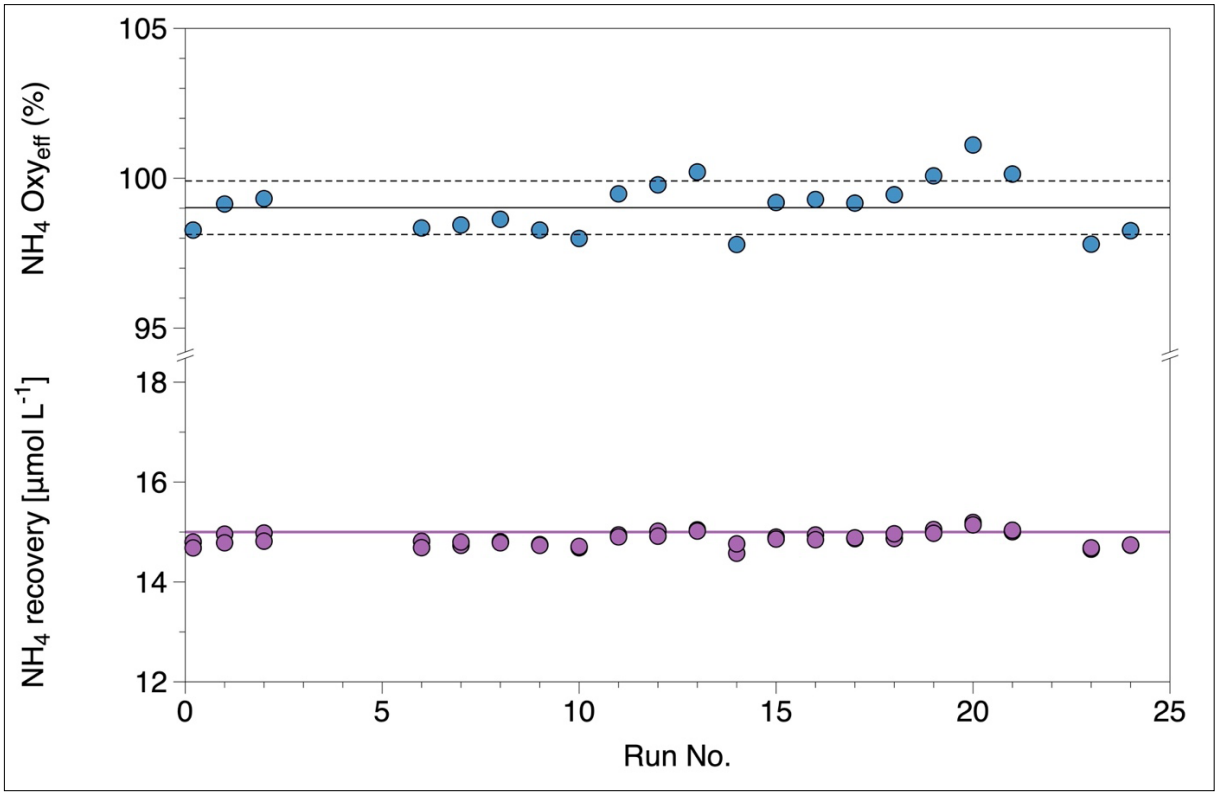

Fig. 6.4: Time series of the NH_4^+ recovery standard used during PS131 to test the oxidation efficiency of the TN channel of the nutrient analyser. The upper part of the figure shows the percent efficiency (with cruise-mean and standard deviation, 99.01±0.9%, shown as solid and dashed lines, respectively) and the lower part shows the recovery relative to the NH_4^+ standard prepared (15 µmol L^{-1}shown as a solid line). The cruise-mean NH_4^+ recovery was 14.9±0.1 µmol L^{-1}.

The oxidation efficiency also needs to be tested for TP, as phosphorous bound to organic compounds has to be oxidised to PO_4^{3-} to be measured. There is a second way in which we monitored both, the oxidation efficiency of TN and TP, and we present this in the following section.

Certified reference materials (KANSO and OSIL Scientific)

In order to assess the accuracy and consistency of the methods employed, we used two types of certified reference materials (CRMs); 1) KANSO Thechnos Co., LTD, Japan, lots CL and CJ, and 2) OSIL Scientific, UK, nutrient standards. KANSO are so called 'RMNS or reference materials for the measurement of nutrients in seawater'. These are made from natural seawater, typically by combining deep and surface water from selected ocean regions to yield

target concentrations, plus further processing (e.g., sterilisation). Certified values are reported in units of µmol kg^{-1}, so for our work we converted them to µmol L^{-1} using the reported RMNS salinity and an average lab temperature of 22°C. RMNS concentrations and salinity are shown in Table 3. For our work we use the sum of NO_3^- and NO_2^-, with the uncertainty propagated from the respective uncertainties. OSIL Scientific standards are concentrated solutions distilled-water-based and certified to 100 µmol-PO_4^{3-} L^{-1}, 100 µmol-NO_2^- L^{-1}, 1000 µmol-NO_3^- L^{-1} and 1,000 µmol-$Si(OH)_4$ L^{-1}. These concentrated solutions were used to prepare a quality control standard with concentrations equal to our top calibration standard (Table 1). With few exceptions, this standard was measured in duplicate at the beginning and at the end of each run. Table 6.4 shows the cruise-long-mean of measurements of certified materials and Figures 6.5, 6.6 and 6.7 show time series of measurements, as carried out in individual runs. The idea behind the measurement of RMNS is to assess whether the methods used are accurate or whether corrections need to be applied. As these are internationally used CRMs, the aim is to provide tracebility and render data comparable to measurements carried out by other laboratories. From our measurements it can be seen that, with the exception of NO_2^-, which was overestimated, NO_3^-+NO_2^-, PO_4^{3-} and $Si(OH)_4$ were slightly underestimated. Therefore, correction factors ($RMNS_{certified}$:$RMNS_{measured}$) were obtained to 'calibrate' the data given the accuracy as suggested by the measurement of RMNS. Correction factors were applied on a run by run basis. The main assumption or "big leap of faith" here, is that the result of the RMNS measured is representative for the whole respective run. Note that the implied correction factor is slightly different dependent on the RMNS lot used. As per best practice procedures, a CRM concentration closest to the top calibration standard should be used. Hence, for NO_3^-+NO_2^-, PO_4^{3-} and NO_2^-, measurements from RMNS lot CJ were used to obtain correction factors. In the case of $Si(OH)_4$, the certified concentration of lot CJ is well beyond our top standard (i.e., not representative of typical Arctic Ocean waters) and thus, the results from lot CL were used. In the final nutrient data for PS131, correction factors are included as well as RMNS-calibrated and uncalibrated data. The OSIL standard was used as en additional quality control, but was not considered for data adjustments as it is prepared in Milli-Q water. Although RMNS do not have certified values for TN and TP (or dissolved organic nitrogen and dissolved organic phosphorus, which is the reason why we measure TN and TP), we applied the same correction factors obtained from NO_3^- + NO_2^- and PO_4^{3-}, as TN and TP are measured as inorganic nutrients upon oxidation and/or reduction (ie., the colorimetric technique is fundamentally the same as NO_3^-+NO_2^- and PO_4^{3-}).

Tab. 6.3: RMNS certified nutrient concentrations (in µmol kg^{-1} and µmol L^{-1}) and salinity.

RMNS lot (units)	NO_3^-	NO_2^-	$Si(OH)_4$	PO_4^{3-}
CL (µmol kg^{-1})	5.47±0.15	0.015±0.006	13.80±0.30	0.425±0.019
CL (µmol L^{-1})	5.60±0.15	0.015±0.006	14.13±0.03	0.435±0.019
CL Salinity (psu)	34.685			
CJ (µmol kg^{-1})	16.20±0.2	0.031±0.007	38.50±0.40	1.190±0.20
CJ (µmol L^{-1})	16.58±0.2	0.032±0.007	39.41±0.41	1.218±0.02
CJ Salinity (psu)	34.357			

Tab. 6.4: Cruise-long-mean and standard deviation of measured CRMs for the 6 analyser channels (µmol L^{-1}).

CRMs	NO_3^-+ NO_2^-	NO_2^-	$Si(OH)_4$	PO_4^{3-}	TN	TP
CL	5.35±0.49	0.023±0.012	12.62±0.11	0.400±0.021	10.82±0.54	0.434±0.029
CJ	15.73±1.3	0.052±0.011	34.34±2.31	1.188±0.021	20.70±0.31	1.405±0.10
OSIL	22.97±0.5	0.790±0.035	19.77±0.09	5.268±0.024	23.23±0.72	5.283±0.51

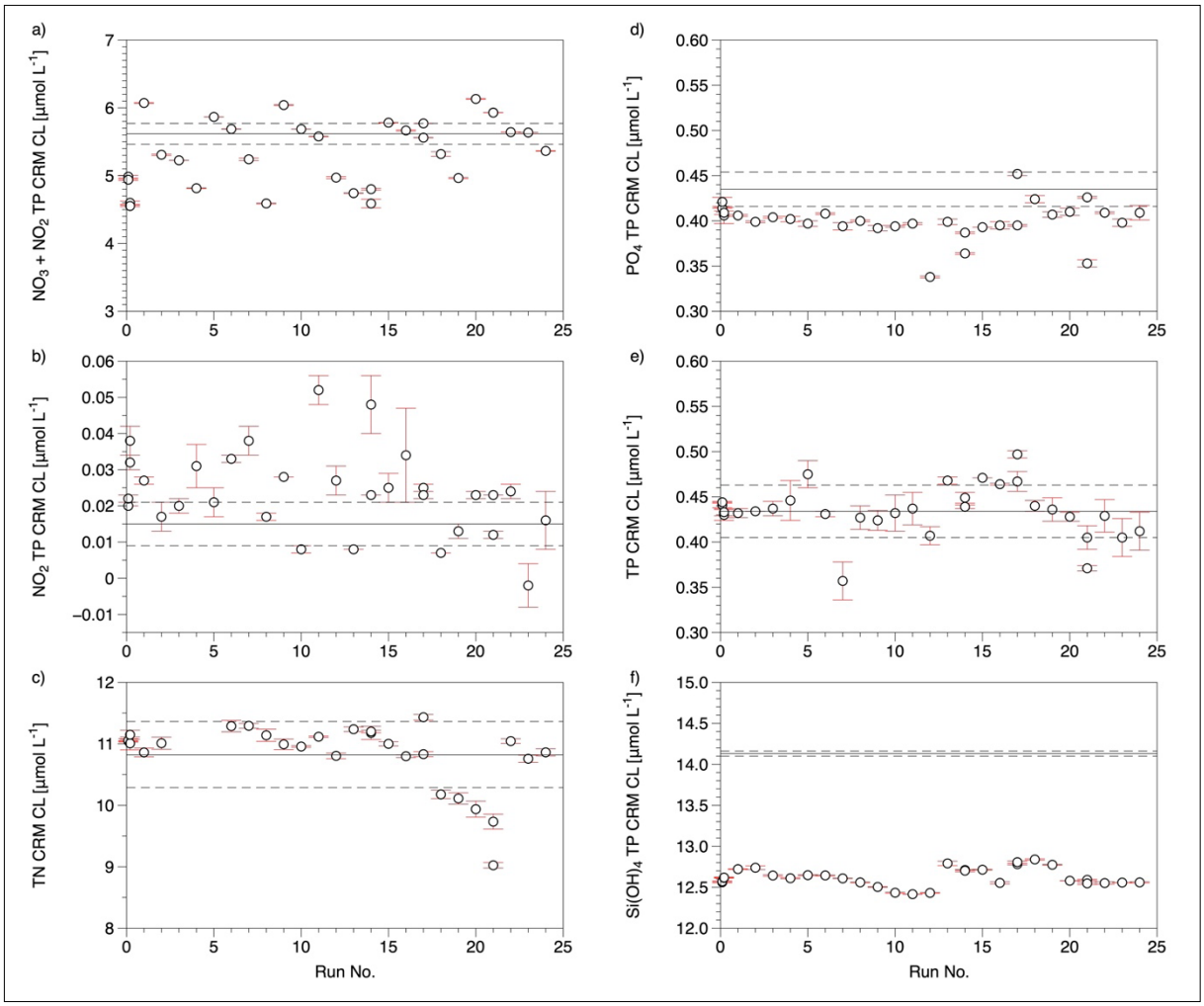

Fig. 6.5: Time series of KANSO RMNS Lot CL measured on each run through out PS131; solid and dashed lines show certified values and uncertainty, respectively, as shown in Table 6.2.

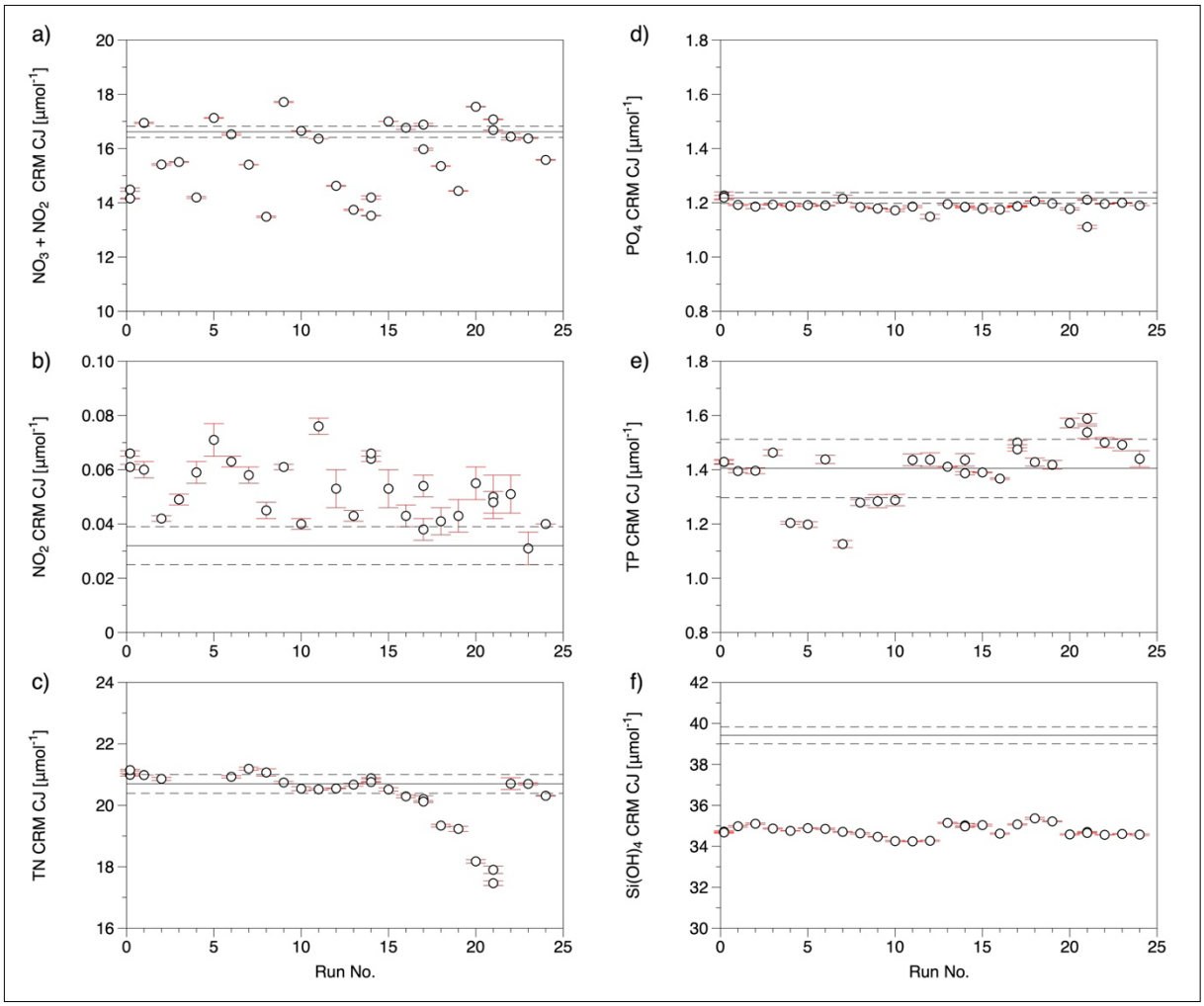

Fig. 6.6: Time series of KANSO RMNS Lot CJ measured on each run through out PS131; solid and dashed lines show certified values and uncertainty, respectively, as shown in Table 6.2.

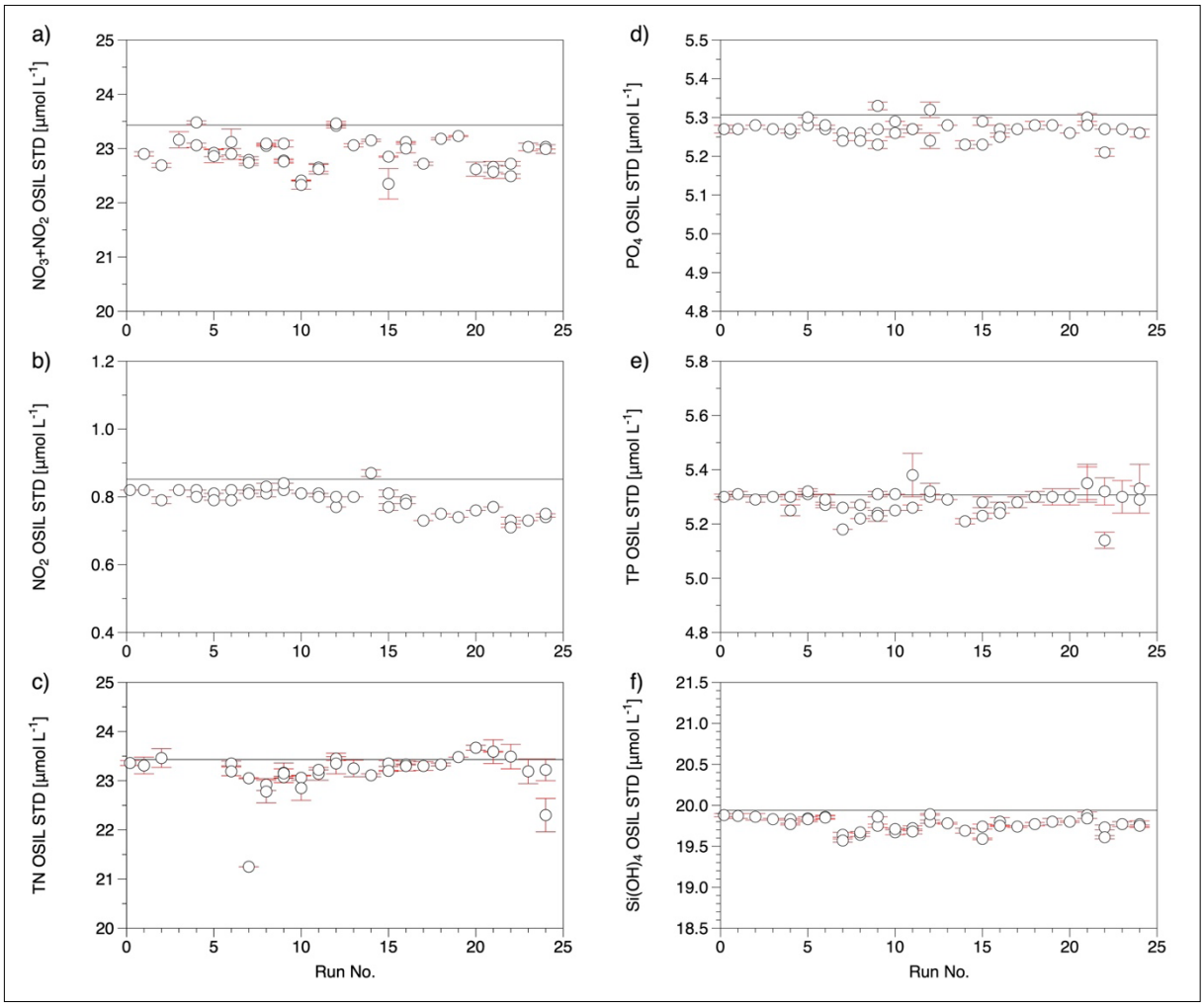

Fig. 6.7: Time series of standards prepared from OSIL Scientific concentrated CRMs; the solid line indicates the concentration at which each nutrient was prepared (top standard in Table 1).

Sample collection and analysis

40 mL samples were collected directly into 50 mL sterile Falcon tubes for the analysis of nutrients. Tubes were rinsed three times with seawater before the sample was drawn. Two duplicate samples were randomly collected from each cast. In order to optimise labwork (e.g., number of samples analysed per run) and reduce the amount chemical waste produced, analyses were carried out when a minimum of three CTD casts worth of samples were available. In most cases (in particular during hydrographic section work) samples were stored in the fridge and analysed within 12 hours of sample collection. When sampling stations were apart more than approximately 12 hours, samples were frozen until analysis took place. If this was the case, samples were defrosted over night (minimum of 18 hours) prior to analysis. Before analysis, samples were vigorously mixed. All sampling stations, with the exception of the last one at the mouth of Scoresby Sound, were sampled for the measurement of nutrients.

Attached to this document there is an excel table with our records of nutrient sample collection (Tab. 6.5). The last station was not sampled because of a combination of factors. Dangerous goods (many of our reagents) needed to be handed for storage in preparation for the freight back. We had estimated the time required for the last analysis run and left enough reagents to cover all the samples taken from hydrographic stations in Scoresby Sound, plus an extra. As

the CTD cast was planned after the recovery of a mooring there and the mooring recovery was delayed by few hours, we ran out of available reagents about 2 hours before the CTD cast took place. All samples were analysed in duplicate.

Problems encountered

In preparation for PS131 and then once on board, two tests were conducted at the AWI upon analyser installation by the manufacturer and two further tests were carried out prior to station work. The new AA-500 analyser came with new methods relative to its predecessor the AA3 analyser. During tests at the AWI and on board, all methods for inorganic nutrients yielded expected results. However, TP and TN yielded low recoveries, determined by comparison with previous analyses at the AWI using a Seal Analytical AA3 TN/TP analyser. Additionally, in the case of TN, some precipitate formed within the glass coils of the AA-500 manifold when using the new method. Initially there was confusion given that I thought I may have accidentally mixed the wrong reagents, and then I implemented the previous methods (AA3 methods) on the AA-500, thus yielding similar results.

Once on board, the TP G-439-16 revision 2 (MT33) was kept instead of the new method (listed above). In the case of TN however, we started our tests and first runs with the new method (MT533), given that the reagents prepared for PS131 were preweighted months in advance according to it. During tests, which were mostly done with standards prepared in Milli-Q water and only the RMNS being seawater, we did not experience any problems with precipitation, only low recoveries relative to previous measurements. Once we started station work though, problems with precipitating reagents occurred and for three runs we thought we would not be able to measure TN. Upon contacting the manufacturer, they confirm that the new TN method had errors and hinted towards the pH of the digestion (i.e., oxidising) reagent being the problem. This was manly driven by the use of 15 g/L of sodium hydroxide (as described in the new method), instead of 6 g/L, which they later modified to given they experience precipitation problems too. Thus, when receiving this information, rather than mixing the three reagents involved in the digestion mixture together (potassium persulfate, sodium tetraborate and sodium hydroxide), the sodium hydroxide was prepared separately and then diluted to the equivalent of 6 g/L. This solved the problem of the precipitation, but not the recoveries of the TN. Although both methods use a similar sample to digestion reagent ratio (6.1 new method *vs* 6.5 previous method), the new method uses less ammonium chloride (which helps in the reduction of NO_3^- to NO_2^- as the sample passes through the Cd column). We changed the sample to digestion reagent ratio to 4.3 and increased the amount of ammonium chloride (two lines of ammonium chloride as in the previous method vs two lines of wetting agent in the new method). This yielded recoveries similar to what we were previously obtaining in the lab using the small AA3 TN/TP analyser, and so we kept this modification.

Another problem we encountered, which is a simple flaw in the way the manufacturer connects the various reagent tubings in the analyser and a slight oversight by ourselves, relates to the colour reagent connections in the TN channel and NO_3^-+NO_2^- channel. In both cases, pump tubing and manifold tubing are joined with metal connectors. The problem is that the colour reagent contains hydrochloric acid, which reacts with metals (it dissolved them). At some point the metal connector in the TN channel dissolved and leaked reagents towards the pump, thereby corroding some parts of the tube holders and the rods/rollers of the pump. We immediateley replaced such connector with plastic connectors and the problem was solved.

Yet another problem was experienced with the measurement of NO_2^- from sea ice samples and samples taken from just under the ice. This resulted in the baseline drifting upwards to the point that in some instances, some references in the analysis that the software used to correct for such drifts, were off scale and therefore uncorrectable in few cases. Thus, some data will be affected. Whatever is it that this type of water contains seems to attached to the walls of the

glassware of the analyser, which we discovered when upon starting a new run, the baseline would drift downwards until samples and baseline were off scale (down) and data was lost. That is, the glassware seemed to clear out gradually when such samples were not many or not analysed. As we were measuring samples also for other groups, we requested them to filter the samples in preparation for analysis. After few tests, it seemed that filtration solved the problem. When NO_2^- data was affected, it was flagged accordingly.

Dissolved oxygen

As for nutrients, samples were collected for the analysis of dissolved oxygen from CTD-Rostte casts from selected depths. We also aimed to have as best vertical resolution as possible. Dissolved oxygen was measured in order to generate data to calibrate the CTD-O_2 sensors and to have reference values for the CTD-O_2 sensors attached to moorings. Whenever samples for tritium were not collected, samples for dissolved oxygen were the first drown from the Niskin bottles. Samples were collected using a tygon tube attached to the spigot of the Niskin bottles and placed directly into volume-calibrated borosilicate glass bottles with narrow necks. Care was taken to avoid bubbles inside the sampling tube and the sampling bottles. Water was left to spill over approximately three or more times the volume of the sampling bottle before the sample was drawn. A hand-held thermometer was used to measure the temperature of the seawater at the time of sample collection (i.e., fixing temperature) using a relatively fast-response temperature probe. Samples were immediately fixed by dispensing 1 mL of manganese chloride, followed by 1 mL of alkaline iodide, and then mixed thoroughly. When sampling was completed, the precipitate of the sample was let to settle to about a third of the volume (~1 hour). Then, samples were mixed thoroughly for a second time and the precipitate let to settle for a further hour or until analysis. Analysis was carried out using a brand new Metrohm Ti-Touch titration unit set up with the amperometric end point detection. Before analysis 1 mL of 5 M sulphuric acid was added to a sample for titration. We followed the method and best practices procedures as described by Langdon (2010). All hydrographic stations were sampled. However, due to having a small team (3 members) and the time required for sampling and analysis, not all CTD casts were sampled at full vertical resolution. For example, in the case of transect work and shallow (<200 m) stations, only three samples in duplicate were collected per cast. Whenever possible though, samples were collected at the same vertical resolution as for nutrients.

Soon after laboratory set up, 1 L of thiosulphate solution (titrant) was prepared (50 g/L), as it takes one to two days to stabilize. Thiosulphate calibrations were carried out using 1.667 mM OSIL Scientific certified Iodate Standards. Calibrations are done, by first measuring 5 blanks (involving 2 x 1 mL additions of iodate standard, each titrated one at a time) and then 5 standards (each with 10 mL of iodate standard). A first calibration was carried two days after the thiosulphate solution was prepared and a second calibration was carried out the following day in order to confirm the solution was stable and results from calibrations were consistent. There on, calibrations were carried out approximately every 4 days, with a total of 9 calibrations carried out during PS131.

Every time a calibration was done, calculation sheets were updated immediately with blank and standard titration volumes. Thus, the concentrations of dissolved oxygen for a given number of CTD casts were calculated with the most recent calibration results. Provided calibrations are consistent with each other and show no trend which may suggest degradation of reagents, results represent analytical ‘noise’, that is, the combination human and titration unit error associated with each analysis. We present the results from each calibration in Table 6.5 and Figure 6.8. Given there seemed to be no temporal trend, at the end of the expedition all calculation sheets were updated with the cruise-mean titration blank and standard volumes, and the dissolved oxygen concentration of all CTD casts sampled were thus recalculated. A

comparison of profiles/data calculated from individual calibrations and from the cruise mean is presented in Figure 6.9.

Last but not least, on every cast, a minimum of two randomly selected samples were collected in duplicate or better. In oder to render confidence to single measurements, in Figure 6.10 we show the absolute difference between all duplicate samples taken during the expedition, considering outliers and without outliers. In one occasion (cast 97-1), bad duplicates resulted from the fact that the valves of some Niskin bottles were not properly closed at the time of deployment. On a few more of occasions, outliers resulted from problems encountered at the time of analysis, when the titration unit did not recognise the electrode and so the sample was left opened for few minutes. On another occasion, the lid of one of the duplicates broke and the sample was lost. Of course, some other bad duplicates resulted from human error.

Tab. 6.5: Thiosulfate calibrations (titrations) done for the determination of dissolved oxygen. Blank (Blk), Standard (STD), STD minus Blk (STD-Blk) titration volume (mL), and calculated thiosulfate molarity

Date	Blank	Standard	STD-Blk	Thiosulfate Molarity
02.07.2022	0.0038	0.5008	0.4971	0.2012
03.07.2022	0.0036	0.5012	0.4976	0.2010
08.07.2022	0.0044	0.5018	0.4974	0.2011
14.07.2022	0.0055	0.5003	0.4948	0.2021
20.07.2022	0.0025	0.5009	0.4984	0.2007
24.07.2022	0.0030	0.4994	0.4964	0.2015
29.07.2022	0.0044	0.4995	0.4951	0.2020
04.08.2022	0.0035	0.4993	0.4958	0.2017
10.08.2022	0.0035	0.4990	0.4955	0.2019
Average	*0.0038*	*0.5002*	*0.4965*	*0.2015*
Stdev.	*0.0009*	*0.0010*	*0.0012*	*0.0005*

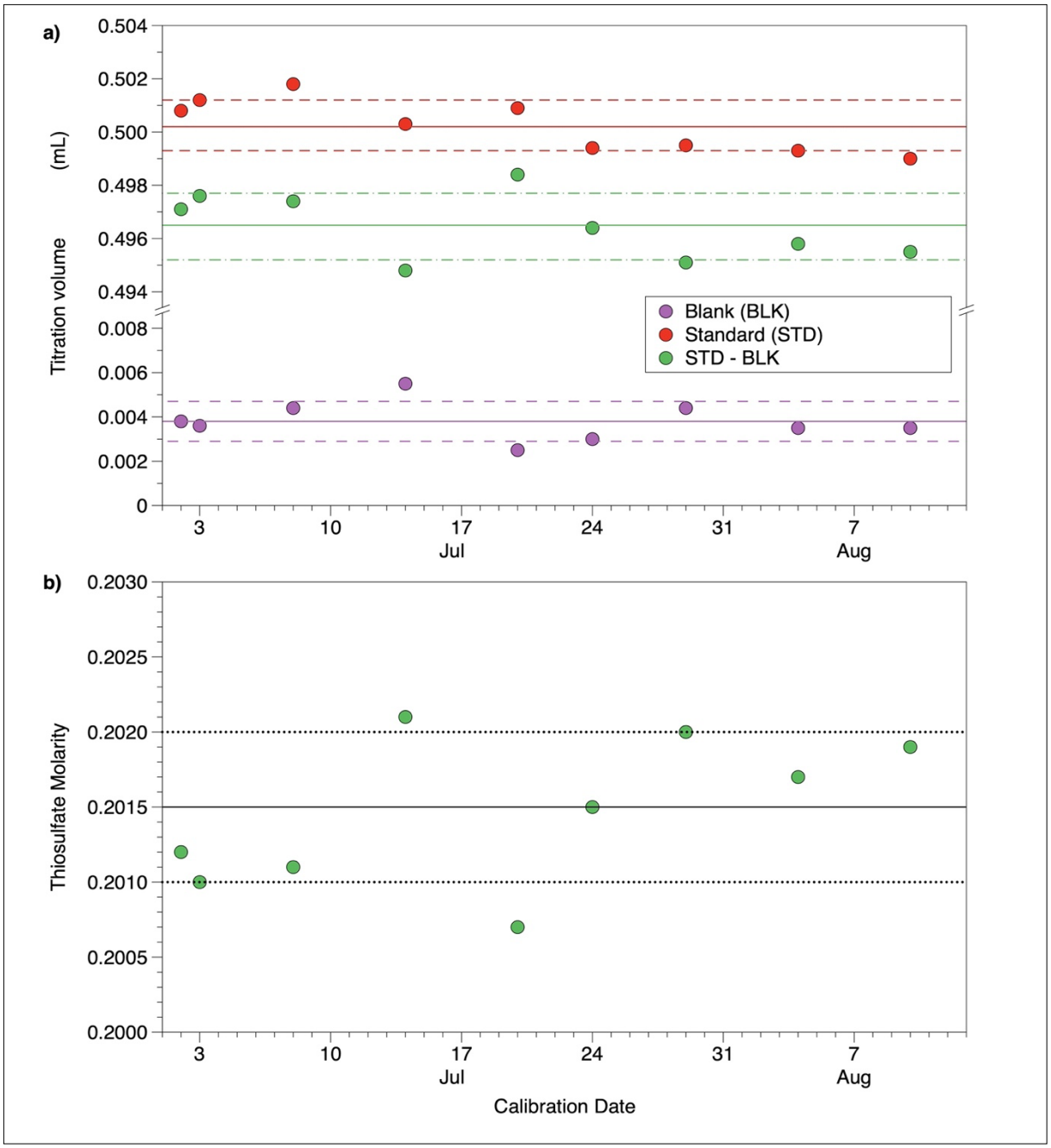

Fig. 6.8: Results from thiosulfate calibrations carried out during PS131 for the determination of dissolved oxygen in seawater; the distribution of data over time does not show any significant trend that may suggest degradation/alteration of the reagents used. Solid and dashed lines show the mean and respective standard deviation, as indicated in the two bottom rows of Table 6.5.

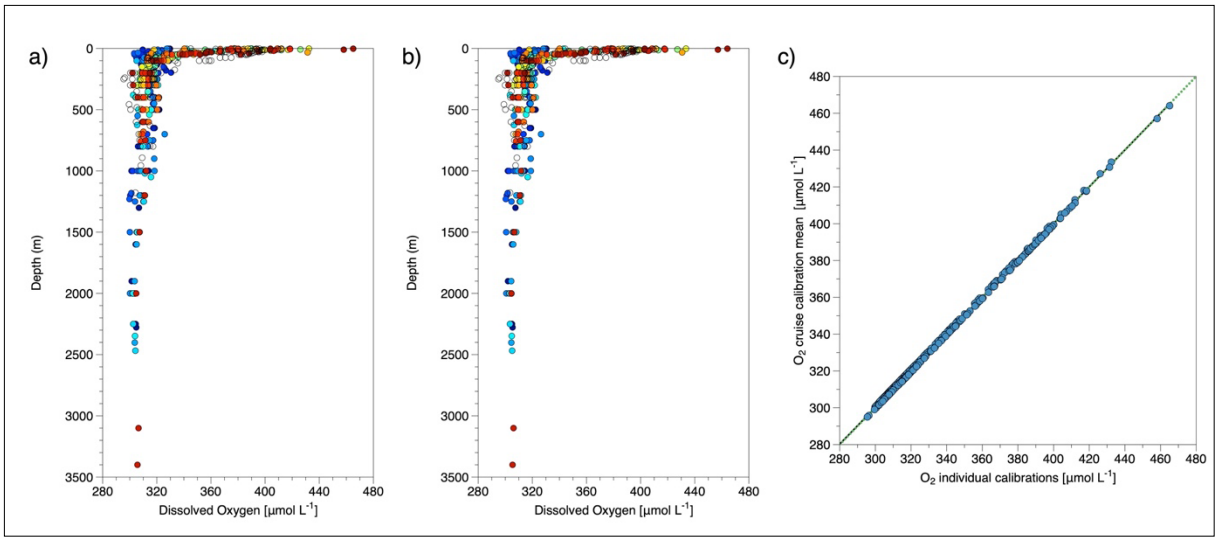

Fig. 6.9: Dissolved oxygen profiles (data from all casts) as calculated with the respective calibration results (a), dissolved oxygen profiles (all data) as calculated from the cruise-mean blank and standard titration volumes (b), and the above data plotted against each other, with the green dotted line showing the 1 to 1 relation (c). Colours represent individual casts.

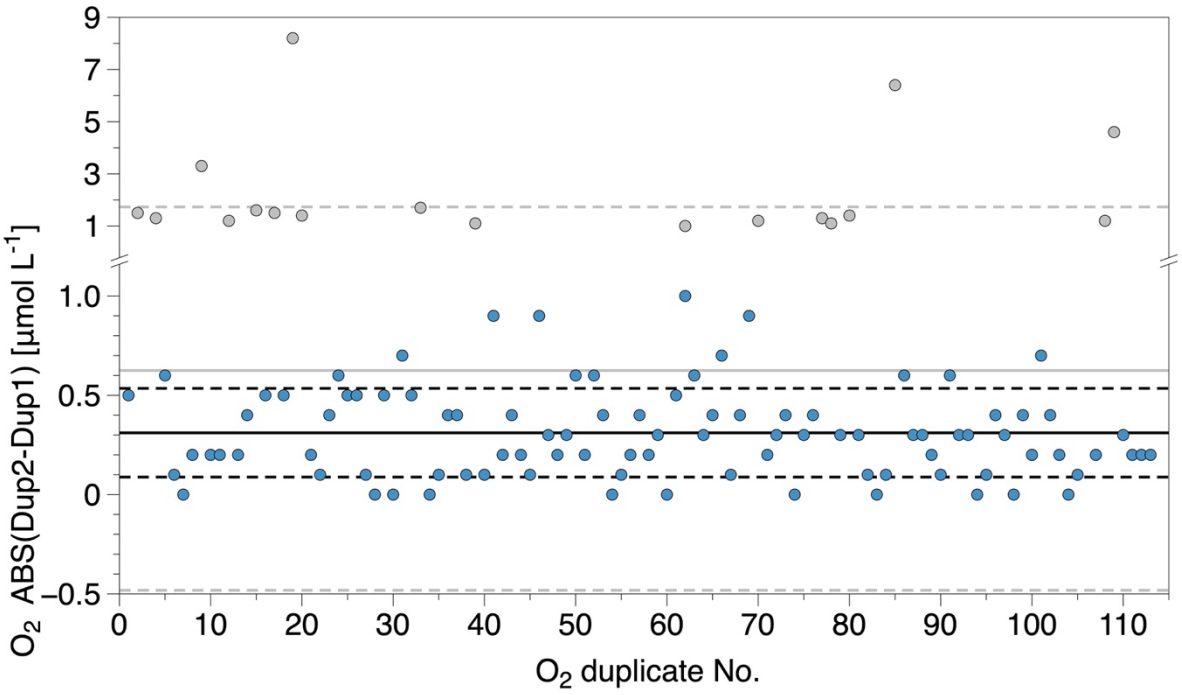

Fig. 6.10: Abolute difference between duplicate samples taken during PS131. Grey dots show outliers, here considered difference between duplicates >1 µmol L^{-1}. Solid and dashed grey lines show the mean difference of all duplicates taken (n=113; 0.63±1.1 µmol L^{-1}). Blue dots show the absolute difference of duplicates without outliers (<1 µmol L^{-1}). Solid and dashed black lines show the mean and standard deviation of the absolute difference between duplicates without outliers (n=94; 0.31±0.22 µmol L^{-1}).

Membrane-inlet-mass-spectrometry (MIMS)

For PS 131, the MIMS system established already on previous expeditions (i.e. MOSAiC) was used to continuously measure high-resolution concentrations of Oxygen (O_2), Argon (Ar) and carbon dioxide (CO_2) in surface waters (teflon in-flow system, 11 m depth). O_2 and Ar are more or less equally affected by physical parameters (i.e. temperature and salinity), hence the O_2:Ar ratio indicates biological activity of net primary production or respiration, respectively. Under atmospheric equilibrium, the O_2:Ar ratio is ~21, whereas a higher O2:Ar ratio corresponds to O_2 oversaturation, i.e. net primary production. A lower O_2:Ar ratio corresponds to O_2 undersaturation, i.e. net consumption due to respiration. We will combine our data with the output from the ship´s thermosalinograph to derive aequeous O_2 and Ar concentrations. Then we are able to estimate the biological productivity[9,10]. We expect that sea-ice coverage, light regimes, and nutrient fluxes strongly modulate patterns of net community production and the subsequent biogeochemical functioning of the ecosystem in terms of food web input, particle flux and carbon sequestration. We will correlate our obtained data with additional assessments of the mentioned parameters and attempt to quantify the contributions of such abiotic factors.

The MIMS system was deployed continuously starting in the Norwegian sea (30 June 2022) and ending when entering Icelandic waters (12 August 2022). It was calibrated using reference gases (N_2 for 0% Ar and O_2; compressed air for 1% Argon and 20.5% O_2) on a daily basis.

As an additional side project, the MIMS was newly equipped with a cuvette system to measure O_2 based physiological rates of photosynthesis and respiration of dicrete algal community samples. Therefore, algal biomass from under ice water, CTD casts or zooplankton multinet tows were concentrated on a 3 µm pore size polycarbonate filter and transferred into a temperature-controlled cuvette system. After the inlet pressure was stabilized, O_2 evolution and consumption (corresponsing to net photosynthesis and mitochondrial respiration, respectively) were measured during consecutive light-dark phases. After the assay, samples for chlorophyll extraction and microscopy were taken and will be analyzed at AWI at a later time. Data will be combined with chlrophyll a data from the water column.
The measurement of net photosynthesis in discrete field samples with the MIMS showed principally worked, but little and/or unproductive biomass and an unstable inlet pressure prevented measurements with the desired resolution. Especially the fluctuating inlet pressures need to be improved for further expeditions to hopefully measure in-situ physiological activity on future cruises.

Preliminary (expected) results

All dissolved nutrient and dissolved oxygen results were processed within the expedition time.

Two days before leaving the ship the dissolved oxygen data, quality controlled and flagged accordingly, was handed to the physical oceanography team for CTD-O_2 calibrations. The whole data set can be already seen in Figure 9 above. The nutrient data was also fully processed and quality controlled before leaving *Polarstern*. An example is presented here below in Figure 11, which shows the distribution of NO_3^-+NO_2^-, TN, PO_4^{3-} and $Si(OH)_4$ across a hydrographic section carried out over the Yermak plateau. Interesting features include the NO_3^-+NO_2^- and PO_4^{3-} depleted surface waters, which is to be expected as we surveyed the region late in the productive season. However, what it is conspicuous, is the fact that in the case of $Si(OH)_4$, residual concentrations occur in the south part of the section. This is consistent with observations made on board by biology groups, indicating that the south part was dominated by Phaeocystis, a group phytoplankton that does not require $Si(OH)_4$ to grow. Instead, the northern part of the section was dominated by diatoms, a phytoplankton group that does require this nutrient to generate their protective frustules. Also of interest is the distribution of surface TN. The difference between TN and dissolved inorganic nitrogen

species represents the dissolved organic nitrogen pool (DON), of which little is know about in the Arctic. Observations made on board suggest that the DON pool may either be used as a nutrient source, it may reflect the different water mass regimes encountered (yet to be investigated), or most likely, a combination of both. Also, towards depth, isopleths (lines of equal nutrient concentration) hint to the occurrance of mesoscale features (e.g., and eddy), with nutrients being pushed towards the surface between kilometres 50 and 75 of the section, where this can further fuel primary production if enough light and viable cells are available.

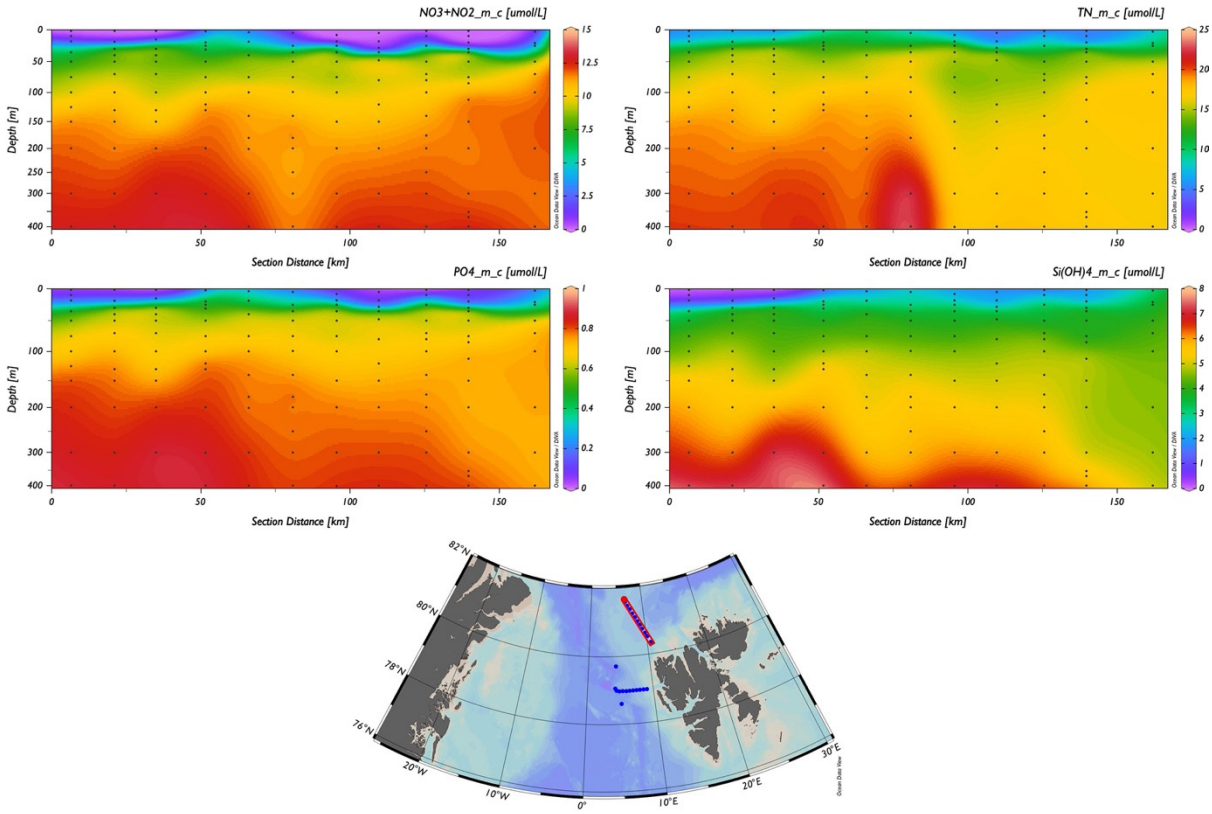

Fig. 6.11: Nutrient distribution (NO_3^-+NO_2^-, TN, PO_4^{3-} and $Si(OH)_4$) across a 400 m depth section over the Yermak Plateau, with section hydrigraphic stations highlited in red in the map.

All MIMS results (continuous O_2:Ar measurements and physiological activity) will be processed in the upcoming months. Measurements, that were synchronized to Triaxus activity, will be combined with Triaxus data. However, it can already be said, that O_2:Ar ratios during the expedition changed clearly: Whereas the open water areas of the Fram Strait showed low ratios, indicating little primary production, which was expected for the relatively late time of the season. In the marginal ice zone, the ratio changed fast between equilibrated oxygen concentrations to local oversaturation, indicating significant local primary production.

Data management

Dissolved nutrients, dissolved oxygen and MIMS derived data will be archived, published and disseminated according to international standards by the World Data Center PANGAEA Data Publisher for Earth & Environmental Science (https://www.pangaea.de) within 12 months after the end of the cruise at the latest. A 2-year moratorium will be requested in order to analyse the data for scientific purposes and publishing of results. By default, the CC-BY license will be applied.

This expedition was supported by the Helmholtz Research Programme “Changing Earth – Sustaining our Future” Topics 2 and 6, Subtopics 2.1 and 6.3.

In all publications based on this expedition, the **Grant No. AWI_PS131_06** will be quoted and the following publication will be cited:

Alfred-Wegener-Institut Helmholtz-Zentrum für Polar- und Meeresforschung (2017) Polar Research and Supply Vessel *Polarstern* Operated by the Alfred-Wegener-Institute. Journal of large-scale research facilities, 3, A119. http://dx.doi.org/10.17815/jlsrf-3-163.

References

Becker S., Aoyama M, Woodward EMS, Bakker K, Coverly S, Mahaffey C, Tanhua T (2020) GO-SHIP Repeat Hydrography Nutrient Manual: The precise and accurate determination of dissolved inorganic nutrients in seawater, using continuous flow analysis methods. Frontiers in Marine Science, 7:581790. https://doi.org/10.3389/fmars.2020.581790.

Craig H, Hayward T (1987) Oxygen Supersaturation in the Ocean: Biological Versus Physical Contributions. Science, 235:199–202. https://doi.org/10.1126/science.235.4785.199.

Holmes RM, McClelland JW, Peterson BJ, et al. (2011) Seasonal and Annual Fluxes of Nutrients and Organic Matter from Large Rivers to the Arctic Ocean and Surrounding Seas. Estuaries and Coasts, 35:369–382. https://doi.org/10.1007/s12237-011-9386-6.

Hydes DJ., Aoyama M, Aminot A, Bakker K, Becker S, Coverly S, Daniel A, Dickson AG, Grosso O, Kerouel R, van Ooijen J, Sato K, Tanhua T, Woodward EMS, Zhang JZ (2010) Determination of dissolved nutrients (N, P, Si) in seawater with high precission and inter-comparability using gas-segmented continuous flow analysers. GO-SHIP Repeat Hydrography Manual: A collection of expert reports and guidelines. IOCCP report #14, ICPO Publications series no. 134, Version 1.

Kaiser J, Reuer MK, Barnett B, Bender ML (2005) Marine productivity estimates from continuous O2/Ar ratio measurements by membrane inlet mass spectrometry. Geophys Res Lett, 32:n/a-n/a. https://doi.org/10.1029/2005gl023459.

Langdon C (2010) Determination of dissolved oxygen in seawater by Winkler titration using the amperometric technique. GO-SHIP Repeat Hydrography Manual: A collection of expert reports and guidelines. IOCCP report #14, ICPO Publications series no. 134, Version 1.

Terhaar J, Lauerwald R, Regnier P, et al. (2021) Around one third of current Arctic Ocean primary production sustained by rivers and coastal erosion. Nature Communications, 12(169): https://doi.org/10.1038/s41467-020-20470-z.

Torres-Valdés S, Tsubouchi T, Bacon S, et al. (2013) Export of nutrients from the Arctic Ocean. Journal of Geophysical Research, 118:1625–1644. https://doi.org/10.1002/jgrc.20063.

Torres-Valdés S, Tsubouchi T, Davey E, et al. (2016) Relevance of dissolved organic nutrients for the Arctic Ocean nutrient budget. Geophysical Research Letters, 43:6418–6226. https://doi.org/10.1002/2016gl069245.

Tremblay J-E, Anderson LG, Matrai P, et al. (2015) Global and regional drivers of nutrient supply, primary production and CO2 drawdown in the changing Arctic Ocean. Progress In Oceanography, 139:171–196. https://doi.org/10.1016/j.pocean.2015.08.009.

Ulfsbo A, Cassar N, Korhonen M, et al. (2014) Late summer net community production in the central Arctic Ocean using multiple approaches. Global Biogeochemical Cycles, 28:1129–1148. https://doi.org/10.1002/2014gb004833.

7. GEOPHYSICAL AND OCEANOGRAPHIC EXPLORATION OF AURORA VENT FIELD

Vera Schlindwein[1,2], Henning Kirk[1] [1]DE.AWI
Not on board: Maren Walter[2] [2]DE.Uni Bremen

Grant-No. AWI_PS131_03

Objectives

Polarstern cruise PS137, ALOIS, in 2023 is devoted to a detailed exploration of the geological setting of Aurora vent field at western Gakkel Ridge, the provenance of its hydrothermal fluids and the biota living around the so far only known hydrothermal vent location in the Arctic Ocean. In particular, it is unknwon from where the vent mines heat to drive vigorous circulation. Gakkel Ridge belongs to the melt-starved slowest spreading ridges on Earth but exhibits surprisingly active hydrothermalism (Edmonds et al., 2003). Aurora vent field is located on a basalt mound, but the composition of the vent fluids indicates a circulation through mantle rocks. These must therefore either be situated at shallow levels below the basaltic crust or circulation must be deep reaching.

In order to investigate the hydrothermal circulation system, we will record microseismic activity around the vent location for the duration of one year and in parallel monitor the physical properties of its hydrothermal plume. Seismic activity may change circulation paths of the hydrothermal system and hence affect the output of the vent. Furthermore, seismic tremor has proved a suitable tool to study subsurface fluid flow (Meier and Schlindwein, 2018). Microearthquakes around the vent will also be used as source of seismic rays for a three-dimensional seismic tomography of the subsurface structure of Aurora vent field. Cruise PS137 will follow up with active seismic surveying of the crust-mantle structure and acquisition of potential field data to complete the geophysical exploration of the vent setting.

Work at sea

We deployed a network of 8 ocean bottom seismometers (OBS) in an area of approximately 15 km x 15 km surrounding the vent field (Fig. 7.1). OBS were deployed in free-fall mode and were tracked with the Posidonia positioning system either to full depth (OBS 4 and 8, Fig. 7.2), or for some part of the water column (Tab. 7.1). The position of OBS02 at the seafloor was determined upon a revisit of the deployment site. This failed for OBS03, whose Posidonia transponder did not reply from the seafloor location.

All OBS will record ground motion at a sampling rate of 100 Hz until recovery during cruise PS137 in July 2023. Further recording parameters are summarized in Tables 7.2 and 7.3.

A planned full-depth CTD cast was further away from the vent site than originally proposed, due to the challenging local sea ice conditions. The respective cast 075_01 (see Chapter 2 for further information) was performed with a turbidity sensor designed to detect the expected particle size in the non-buoyant plume of the hydrothermal vent. The sensor was successfully tested on board; however, likely due to the distance to the vent site, no plume was found during the cast. Furthermore, water samples for Helium and Tritium were taken from this CTD cast, regarding which the reader may also be referred to Chapter 2 for more detailed information.

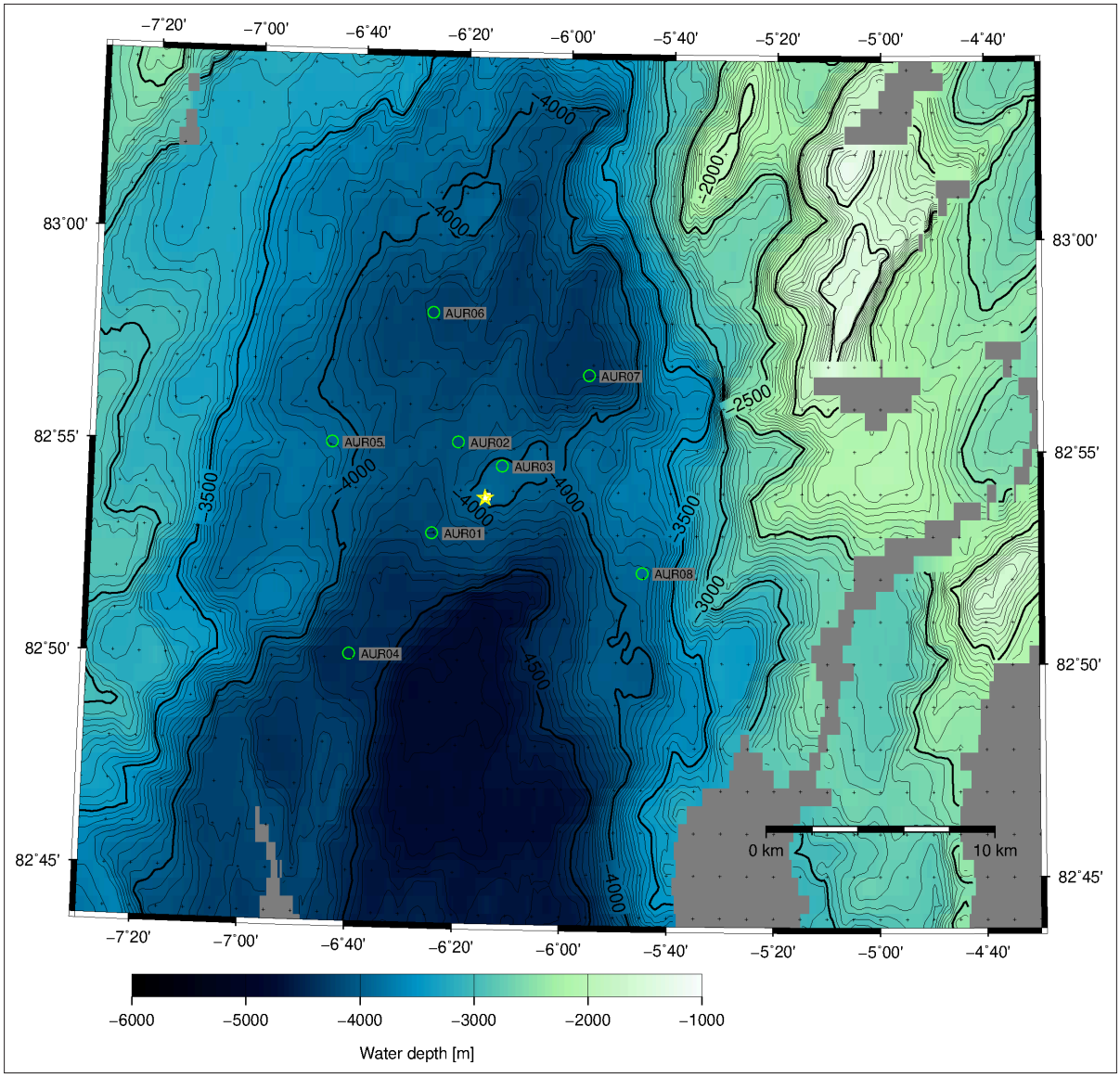

Fig. 7.1: Deployment positions at seasurface of OBS network (circles) around Aurora vent site (star) with location of mooring (square)

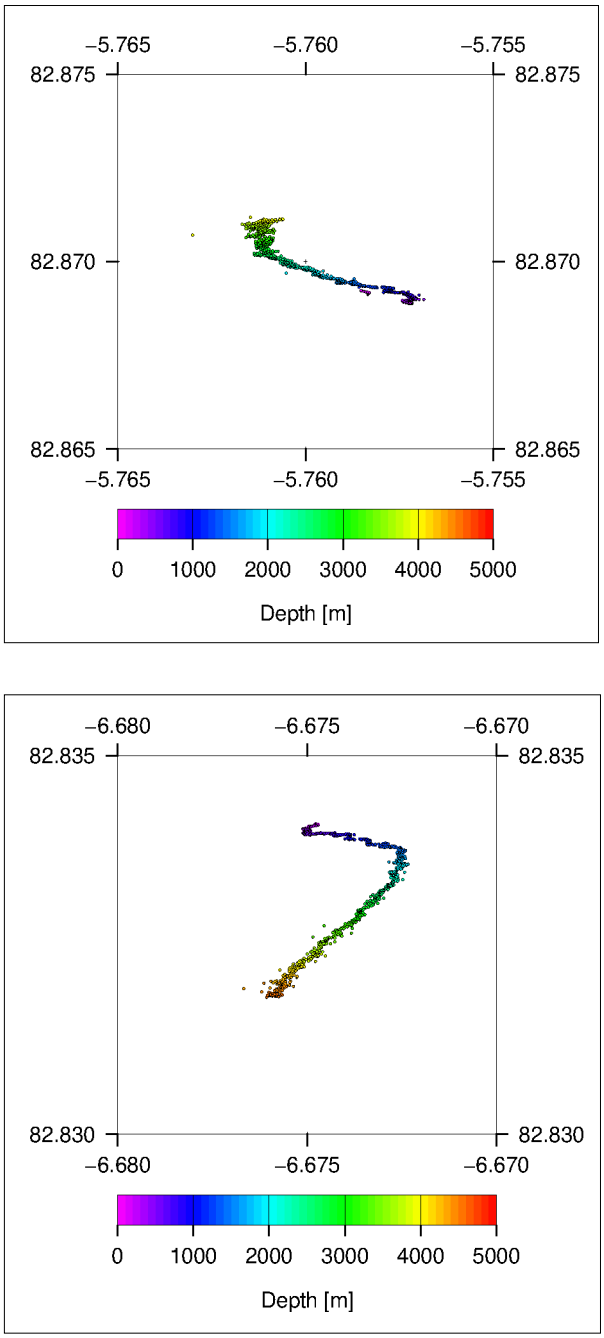

Fig. 7.2: Posidonia track of OBS AUR04 (left) and AUR08 (right) to the seafloor

Tab. 7.1: Deployment positions of OBS Network

	Deployment		Deployment Position at surface			Deepest Posidonia position		
Station	**Date**	**Time UTC**	**Latitude**	**Longitude**	**Depth [m]**	**Latitude**	**Longitude**	**Depth [m]**
AUR01	25.07.2022	09:53	82° 52.979‘ N	06° 25.383‘ W	4215	82° 53.059‘ N	06° 24.778‘ W	1565
AUR02	25.07.2022	00:05	82° 55.131‘ N	06° 20.667‘ W	4155	82° 55.248‘ N	06° 20.166‘ W	4183

	Deployment		Deployment Position at surface			Deepest Posidonia position		
Station	**Date**	**Time UTC**	**Latitude**	**Longitude**	**Depth [m]**	**Latitude**	**Longitude**	**Depth [m]**
AUR03	24.07.2022	23:25	82° 54.589‘ N	06° 12.218‘ W	3988	82° 54.569‘ N	06° 12.124‘ W	317*
AUR04	24.07.2022	16:48	82° 50.100‘ N	06° 40.500‘ W	4408	82° 49.911‘ N	06° 40.547‘ W	4511
AUR05	25.07.2022	17:19	82° 55.072‘ N	06° 44.413‘ W	3900	82° 55.021‘ N	06° 44.405‘ W	2052
AUR06	25.07.2022	19:50	82° 58.167‘ N	06° 26.032‘ W	4250	82° 58.124‘ N	06° 26.304‘ W	1567
AUR07	25.07.2022	22:14	82° 56.753‘ N	05° 55.852‘ W	4354	82° 56.772‘ N	05° 56.313‘ W	1527
AUR08	24.07.2022	19:44	82° 52.112‘ N	05° 45.272‘ W	3917	82° 52.268‘ N	05° 45.637‘ W	3943

Tab. 7.2: Recording parameters of OBS network

Station	**Recording Start time**	**Sample Rate (Hz)**	**Gain**	**Seismo-meter**	**Hydro phone**	**Recorder6d6**	**Tempera-ture sensor**
			HXYZ	**Type**	**Inverted (I)**	**SN**	**SN**
AUR01	25.07.2022 00:37:51	100	2 1 1 1	Trillium 6000	I	61607189	yes
AUR02	24.07.2022 21:21:38	100	2 1 1 1	Trillium 6000	H	61607092	yes
AUR03	24.07.2022 20:40:46	100	2 1 1 1	Trillium 6000	H	61607090	1854377
AUR04	24.07.2022 13:33:51	100	2 1 1 1	Trillium 6000	H	61607069	No
AUR05	25.07.2022 16:33:45	100	2 1 1 1	Trillium	H	61607195	185437?
AUR06	25.07.2022 18:59:59	100	2 1 1 1	Trillium	H	61607083	1854370
AUR07	25.07.2022 20:52:45	100	2 1 1 1	Trillium 6000	H	61607078	No
AUR08	24.07.2022 16:37:28	100	2 1 1 1	Trillium	H	61607073	1854372

Tab. 7.3: Clock and releaser parameters of OBS network

	Synchronisation		Auto release		Release Code	Posidonia
Station	**Date**	**Time UTC**	**Date**	**Time UTC**		**SN**
AUR01	25.07.2022	00:37:51	24.07.2023	16:00	445164	1017
AUR02	24.07.2022	21:21:26	24.07.2023	20:00	231056	1014
AUR03	24.07.2022	20:38:51	24.07.2023	12:00	444421	1018
AUR04	24.07.2022	13:32:40	25.07.2023	04:00	443366	1015
AUR05	25.07.2022	16:33:45	25.07.2023	00:30	224722	1106
AUR06	25.07.2022	18:59:59	25.07.2023	12:00	424361	1019
AUR07	25.07.2022	20:52:45	25.07.2023	16:00	225267	1016
AUR08	24.07.2022	16:37:18	25.07.2023	08:00	427374	1122

The oceanographic mooring was deployed about 100 m northeast of the vent location (Fig. 7.3).

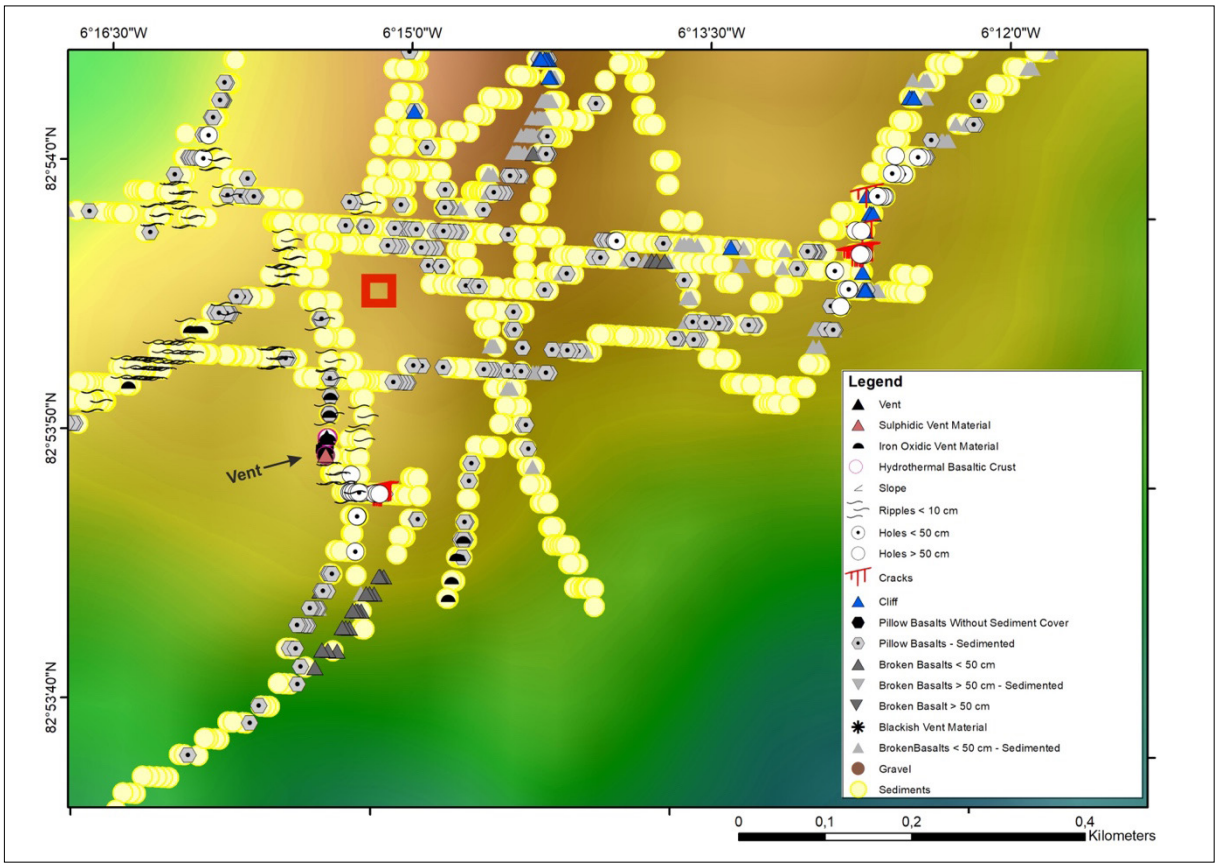

Fig. 7.3: Approximate position of the mooring (red square) relative to known geological features logged from OFOS camera footage (M. Doll, 2017 pers. comm.)

Preliminary (expected) results

Data will only become available upon recovery of the instrumentation in 2023.

Data management

Mooring data will be archived, published and disseminated according to international standards by the World Data Center PANGAEA Data Publisher for Earth & Environmental Science (https://www.pangaea.de) within two years after the end of the cruise at the latest. By default, the CC-BY license will be applied.

Raw seismological data will be archived and published in PANGAEA. Time-corrected miniseed archives of the seismological data will be submitted to GEOFON from where they are accessible with seismological data base query tools.

This expedition was supported by the Helmholtz Research Programme “Changing Earth – Sustaining our Future” Topic 2, Subtopic 3.

In all publications based on this expedition, the **Grant No. AWI_PS131_03** will be quoted and the following publication will be cited:

Alfred-Wegener-Institut Helmholtz-Zentrum für Polar- und Meeresforschung (2017) Polar Research and Supply Vessel *Polarstern* Operated by the Alfred-Wegener-Institute. Journal of large-scale research facilities, 3, A119. http://dx.doi.org/10.17815/jlsrf-3-163.

References

Edmonds HN, Michael PJ, Baker ET, Connelly DP, Snow JE, Langmuir CH, Dick HJB, Mu R, German CR, Graham DW (2003) Discovery of abundant hydrothermal venting on the ultraslow-spreading Gakkel ridge in the Arctic Ocean. Nature, 421. https://doi.org/10.1038/nature01351.

Meier M, Schlindwein V (2018) First In Situ Seismic Record of Spreading Events at the Ultraslow Spreading Southwest Indian Ridge. Geophysical Research Letters, 45. https://doi.org/10.1029/2018GL079928.

8. WATER VAPOR, CLOUD LIQUID WATER AND SURFACE EMISSIVITY

Janna Rückert[1], Andreas Walbröl[2], [1]DE. UNI-Bremen
Gunnar Spreen[1] (Co-PI) [2]DE.UNI-Köln
Not on board: Kerstin Ebell[2] (PI), Mario Mech[2] (Co-PI)

Grant-No. AWI_ PS131_11

Outline

Water vapor, cloud liquid water, and microwave surface emissivity were measured and analyzed as part of the *Polarstern* secondary-use project *Water Vapor, Cloud Liquid Water, and Surface Emissivity over the Arctic Marginal Ice Zone in Summer* (WALSEMA). This work enhances the observational data base of key climate variables in the Arctic, i.e., atmospheric integrated water vapor (IWV) and liquid water path (LWP). Clouds and water vapor play a crucial role in the Arctic climate system and are closely interwined with the complex feedback mechanisms resulting in the so-called Arctic Amplification, i.e., the enhanced increase in Arctic near-surface air temperature compared to the global mean temperature rise. However, large uncertainties still exist in the processes governing Arctic Amplification, which can be partly attributed to a lack of reliable observations. While ground-based reference observations are performed at a few Arctic land sites, observations over the Arctic Ocean and sea ice are even more limited. With the measurements collected during PS131 we are able to better characterize summertime atmospheric water vapor and liquid water path in the Fram Strait and western Nansen Basin over open ocean, marginal sea ice, and pack ice and complement observations from past expeditions in the Arctic Ocean.

We operated two microwave (MW) radiometers as well as infrared and visual cameras (sky and surface) on board of *Polarstern* and launched additional radiosondes (60 in total). As a next step these measurements will be used to evaluate satellite MW retrievals of IWV and LWP for the challenging region of the transition zone from open ocean to pack ice. To allow the evaluation of surface contributions to the microwave signals received from the satellites, the MW radiometers were occasionally pointed away from the sky to the ocean and ice surfaces. The measurements along the transects through the marginal ice zone (MIZ) conducted during PS131 allow to investigate gradients in the atmospheric variables related to the varying surface conditions.

Objectives

Objective 1: Water vapor in the summertime Arctic

We continuously measured atmospheric water vapor, i.e., IWV and the vertical water vapor profile, in the Fram Strait and the adjacent Arctic Ocean/sea ice region. The impact of different surface conditions, i.e., open ocean, marginal sea ice zone, ice pack, on the atmospheric water vapor are assessed and potential gradients in water vapor analyzed. The research questions are:

Q1: What is the spatio-temporal variability of summertime integrated water vapor and of the water vapor profile in the Fram Strait and the adjacent Arctic Ocean/sea ice region?

Q2: How do surface conditions, i.e., open ocean, marginal sea ice zone, and sea ice, influence the atmospheric water vapor content? Can we identify a surface signal or is the coupling to the surface rather masked by large-scale transport mechanisms of water vapor?

To tackle these two questions, we synergistically exploit the measurements of both MW radiometers, the IR/visual cameras and also combine them with radiosonde and satellite information. Objective 1 is also closely coupled to the research question Q4 of ATWAICE: "How does sea ice heterogeneity in turn affect the turbulent heat fluxes in the atmospheric boundary layer along the ice edge […]". Here, we focus on the impact of turbulent heat fluxes of water vapor in the atmospheric boundary layer.

Objective 2: Variability of summertime Arctic liquid-bearing clouds

With objective 2, we aim to improve our understanding of liquid-containing clouds over the Fram Strait and Western Nansen Basin. Long-term LWP measurements are already provided at the research station AWIPEV in Ny-Ålesund (Svalbard). However, we expect that the liquid cloud characteristics were quite different over the open ocean during PS131 and also are impacted by the underlying surface. The research questions thus are:

Q3: What is the spatio-temporal variability of LWP of summertime Arctic clouds in the Fram Strait and Western Nansen Basin?

Q4: How is LWP coupled to the surface conditions and water vapor availability? (link to Q2)

In this way, we also complement the atmospheric studies within ATWAICE (by TROPOS, Leipzig), which focused on aerosols (concentration/properties) with a special interest on new particle formation and the origin and source of cloud condensation nuclei (see Chapter 4). The infrared and optical sky cameras together with the meteorological measurements from *Polarstern* are helping to evaluate the sky conditions.

Objective 3: Surface emissivity in the microwave spectrum

We performed regular measurements of the surface emissivity by downward looking *HATPRO* and *MiRAC-P* MW radiometers in connection with measurements by IR and visual cameras to characterize the surface properties.

Q5: What is the spatio-temporal variability of MW emissivity of sea ice and ocean in the Fram Strait and adjacent Arctic Ocean/sea ice region?

Q6: How much does the variability in surface emissivity caused by different surface conditions, i.e., open ocean, marginal sea ice zone and ice pack influence, the MW radiometer satellite retrievals of IWV?

This objective is also closely linked to **Q2** "How do surface conditions, i.e., open ocean, marginal sea ice zone and sea ice, influence the atmospheric water vapor content?". In addition to the upward looking IWV microwave radiometer measurements also downward looking radiometer measurements and observations of the surface conditions by IR/visual cameras were performed to characterize the surface conditions.

8.1 Atmospheric measurements

Work at sea

Two microwave radiometers (*RPG-HATPRO*, *RPG-LHUMPRO-243-340-G4* (*MiRAC-P*)) and upward (sky) and downward (surface) infrared (IR) and visual cameras were operated on board of *Polarstern* (surface camera IR: *InfraTec VarioCAM HDx 625*; visual: *GoPro Hero 9 Black*; including an inertial motion unit (MiniIMU) for pitch and roll angle measurements). In upward looking mode the radiometers measure radiance emitted by the atmosphere (mainly related to water vapour, oxygen and liquid water content) as brightness temperatures (BTs) in the microwave spectrum.

Installation

The radiometers were installed at the railing on the *Peildeck* of *Polarstern* (the highest deck on top of the bridge) to have unobstructed sky and side views (for incidence angles 10° – 70°) on the ocean/sea ice (Fig. 8.1). Before leaving Bremerhaven, the mirrors were attached by which the radiometers can observe the ocean/sea ice. Due to insufficient amount of liquid nitrogen onboard *Polarstern*, both radiometers could not be calibrated before departure. Instead, we already installed the sky camera (*Mx-S16B-S1 camera* and *Mx-O-SMA-TS-R079 Therm sensor module*) in the evening of 28 June 2022. On 30 June 2022, we started setting up the surface cameras (IR and visual) on a tripod next to *MiRAC-P* (see Fig. 8.1). The sampling of the IR surface camera was initiated on 3 July 2022 16:00 UTC, taking an IR image every 10 seconds. On 3 July 2022, we noticed that, against expectations, water condensed on the inside of the visual part of the sky camera. At first, we tried to dry it with a heat gun pointed at the lens, but the condensed water did not evaporate or diffuse out of the housing. Subsequently, the camera was unmounted to dry off inside for three days. During reinstallation on 6 July 2022, we lost the original visual camera module of the sky camera and replaced it by a *GoPro Hero 10 Black*, which we attached to the sky camera housing next to the IR sensor. Both the IR and visual sky cameras took photos of the sky every 60 seconds.

Liquid nitrogen calibration

After an attempt of liquid nitrogen calibration on 1 July 2022, which ended prematurely because we could not completely fill the required calibration container, we experienced problems with *MiRAC-P*. The highest frequency channel (340 GHz) appeared to be unable to measure any radiance. We tried to fix the issue also contacting the manufacturer but remained unsuccessful. The issue persisted throughout the expedition so that one of eight *MiRACP* frequencies did not provide any data.

A combination of fair weather (no fog or precipitation) and sufficient amount of liquid nitrogen did not allow us to perform the calibration before the morning of 7 July 2022. Data obtained before that date needs to be corrected for offsets, which is possible using the calibration coefficients obtained on 7 July. To ensure high quality measurements, we performed another liquid nitrogen calibration for both MWRs in the morning of 30 July 2022 before the third visit of the *Northern Floe*. During our second calibration we had to use a common hair dryer to remove condensed water from the calibration target's surface because of colder temperatures and high relative humidity (but no fog at the ship).

Daily work

During the transit from Bremerhaven to the *Hausgarten* stations west of Svalbard, we cleaned the radomes and lenses of the instruments as a daily routine. From 9 July 2022 on, we stopped cleaning the radomes because pouring water over *MiRAC-P*'s radome caused BT anomalies

that required at least 45 minutes to dry in fair weather conditions. Further north with foggy conditions and relatively little sea spray (especially when surrounded by sea ice) daily cleaning proved no longer beneficial. We continued to clean the camera lenses at least once per day and checked if the mirrors (for the surface observations) were dry throughout the entire cruise. Ideally, the mirrors should be prepared with a hydrophobic substance before the next campaign if possible. We also found it necessary to restart the radiometer measurements each day to synchronize the atmosphere/ice observations (more details below) of *HATPRO* and *MiRAC-P*. We extracted the memory card of the *GoPro Hero 10 Black*, transferred the images taken to our computers, cleared the memory card and manually restarted the recording. The restart of the recording was always synchronized with the IR camera part as good as possible. Temporal offsets should always be less than two seconds. An extra hard drive for backups of BT and sky camera measurements would have been useful.

Preparing the instruments for sea ice operation

On 10 July 2022 14:30 UTC (16:40 UTC), the radiometers (surface camera) were prepared for observations in the sea ice. Henceforth, the radiometers alternated between *Atmospheric Mode* (upward looking, for objectives 1 and 2) and *Surface-Mode* (downward looking, for objective 3) instead of permanent *Atmospheric Mode*. The recording rate of the surface camera was increased to every 5 seconds (from 10 s before) and the camera angle was adjusted to cover the MWRs' footprints on the surface.

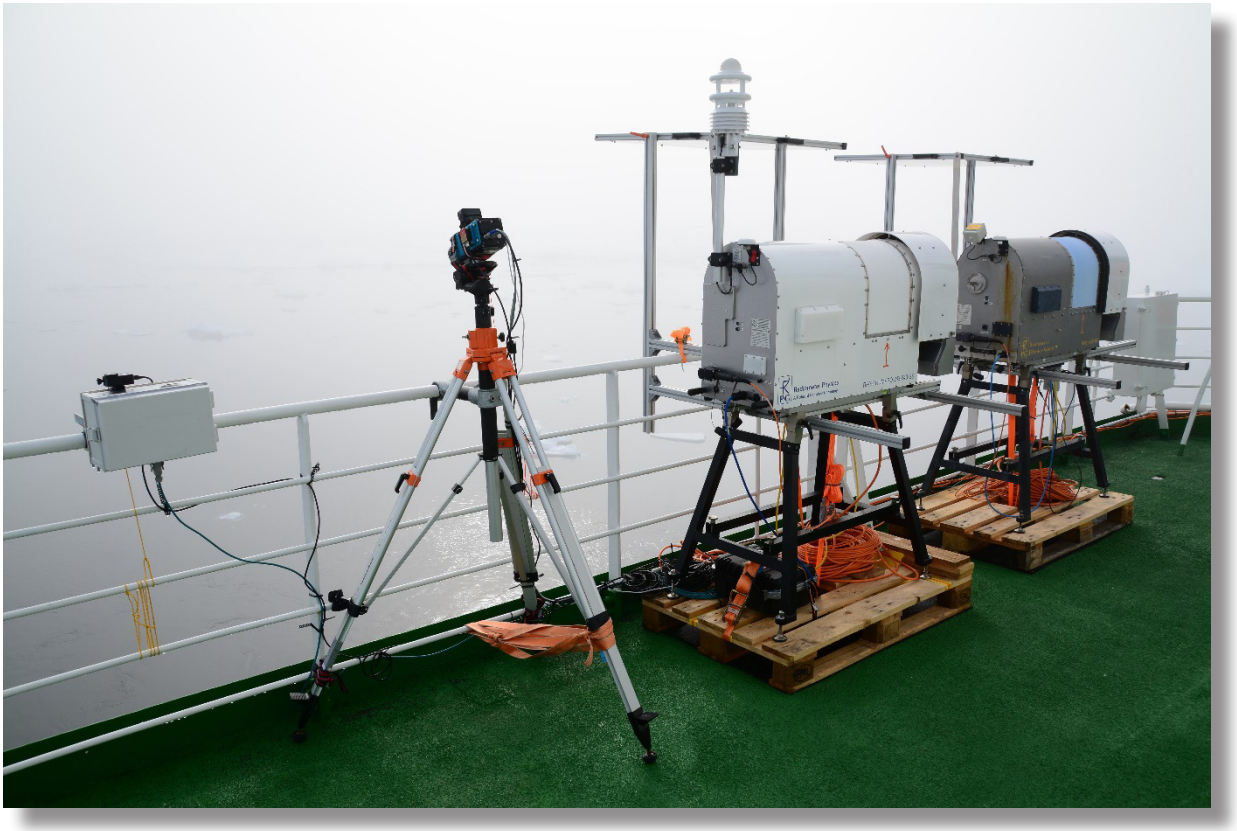

Fig. 8.1: IR & visual sky cameras and surface cameras, MiRAC-P and HATPRO microwave radiometers (left to right) were mounted on or at the deck rail on Peildeck. The metal mirrors for observing the surface can be seen behind the radiometers.

Atmospheric measurements

In *Atmospheric Mode*, which was set to a duration of 45 minutes and was always followed by 15 minutes of *Surface-Mode*, the MWRs pointed in zenith direction (elevation angle 90°). *HATPRO* performed an additional boundary layer scan every 30 minutes to improve the resolution of low-level temperature profiles by sampling the elevation angles 90, 14.4, 11.4, 8.4, 6.6 and 5.4°.

A preliminary data analysis of the MWRs and sky camera data was performed during the expedition (see also *Preliminary results* section below). A simple regression retrieval was created in *Python* based on the original *IDL* code. It was applied on *HATPRO* data collected during the expedition and we retrieved IWV, LWP and coarse water vapour profiles from BTs between 22.24 and 31.4 GHz, and coarse temperature profiles from BTs between 51.26 and 58.00 GHz. The MWR measurements were monitored and compared to simulations with the PAMTRA (Passive and Active Microwave Radiative Transfer) forward simulator tool (Mech et al., 2020) based on the radiosonde ascents performed during the cruise. After the expedition, we will develop more sophisticated retrievals, combining *HATPRO* and *MiRAC-P* BTs for improved water vapour profiling and IWV estimates.

Since the retrieved temperature and water vapor profiles provide vertical information only with a coarse resolution (but temporally highly resolved with 1 s sampling rate), they were complemented by radiosonde measurements. Radiosondes are also used for evaluation of the retrieval. Radiosondes yield highly resolved vertical profiles but have a low temporal resolution. In addition to the regular daily sounding at 12 UTC (launch time always about 65 minutes earlier) by the German Weather Service (DWD), more soundings were performed as part of our WALSEMA project. On 4 July 2022, when we reached the southern Fram Strait, we began with one additional sounding at 00 UTC. From 6 July 2022 on, the DWD started launching another sonde at 06 UTC due to helicopter flight operations. Thus, all transects from the ocean to the inner ice pack and all other cruise time in the ice have at least three radiosondes per day. From 15 to 18 July 2022, a warm air intrusion with high amounts of humidity reached *Polarstern* so that we increased the sounding rate to up to 3-hourly. Between the end of the warm air intrusion and 27 July 2022, 3 radiosondes were launched per day (00, 06, and 12 UTC). At this time, the weather forecast did not predict any more significant warm/moist air intrusions or cold/dry air outbreaks during the remaining time of the cruise, which would have justified another 3-hourly intense observation period. However, because we had enough remaining radiosondes available we decided to increase the daily sampling to 4 soundings (00, 06, 12 and 18 UTC), always keeping an eye on the forecast for potential strong humidity gradients or moist/dry events. We were able to maintain the 6-hourly sampling rate until 8 August 2022. On 9 August 2022, on our way to *Scoresby Sund*, only two radiosondes (00 and 12 UTC) were launched. The final additional radiosondes (at 00 and 06 UTC) were launched on 10 and 11 August 2022. For the remaining part of PS131, only the 12 UTC radiosonde was launched by DWD but at that time we were already outside our target area for the WALSEMA project.

The additional sky camera (*Mx-S16B-S1 camera*, later replaced by *GoPro Hero 10 Black,* and *Mx-O-SMA-TS-R079*) next to the radiometers provided information about the sky conditions throughout the expedition. Automatic cloud coverage from the camera images will be extracted after the expedition.

Data availability

Regarding *HATPRO* and *MiRAC-P*, all data before the first liquid nitrogen calibration (on 7 July 2022) must be considered with care and require post processing to compute BT offsets (marked yellow in Tab. 8.1). The respective offsets are also translated to the derived products (e.g. in Fig. 8.2 or 8.3) but are presented nonetheless. We do not show any data of *MiRAC-P*'s

340 GHz channel because it was broken almost throughout the entire expedition. Between 1 and 7 July 2022, we restarted *MiRAC-P* several times, attempting to fix the issue with the 340 GHz channel. Testing scans and changing radiometer settings caused data gaps for *HATPRO* and *MiRAC-P* on 8 and 9 July 2022. Additionally, *HATPRO* was restarted on 9 July 2022, attempting to eliminate receiver instabilities that caused BT drifts in between automatic internal calibrations. Unfortunately, we could not solve the issue and there were receiver instabilities above a threshold of 0.05 K set by the manufacturer on each day of the expedition. However, these instabilities rarely caused notable BT drifts, which we will correct after the expedition if necessary. Occasionally, without any indications of problems in the housekeeping data, *MiRAC-P*'s BTs in all 183 GHz channels showed a clear offset (we could exclude an atmospheric signal as cause) for about 5 minutes in between two internal calibrations. A first look at the raw data showed that this occurred on 15, 18, and 20 to 24 July 2022. We will also try to correct these temporary offsets after the expedition. A delayed manual start of the default *Atmospheric* and *Surface Mode* observations on 1 August 2022 after surface scans caused a measurement gap from 00:00 to 01:30 UTC. *HATPRO*'s 51.26 GHz channel suffered from noise throughout the expedition, causing BT jumps of several Kelvin.

Sky camera data is not available from 3 July 2022 14:24 UTC to 6 July 2022 08:31 UTC due to the water that condensed inside *Mx-S16B-S1 camera* (see Tab. 8.1). Gaps in the *GoPro Hero 10 Black* data were related to power or configuration issues. While manually restarting the *GoPro Hero 10 Black* on 13 July 2022, apparently the wrong recording configuration was set so that a video instead of one image was taken every 60 seconds. Therefore, the memory card was full after a few hours and no data available from the *GoPro Hero 10 Black* between 13 July 2022 05:27 UTC and 14 July 2022 07:24 UTC. The power cable (USB-C) caused problems from 15 to 16 July 2022 and was, for unknown reasons, no longer recognized by the camera after 29 July 2022 07:13 UTC. After ice stations, we had time to exchange the power cable on 2 August 2022 09:11 UTC. The IR part of the sky camera (*Mx-O-SMA-TS-R079 Therm sensor module*) lost connection on 7 August 2022 14:42 UTC. We re-established the connection by unplugging the power/network cable for 60 seconds on 8 August 2022 07:54 UTC.

More details about the data availability for the surface cameras can be found in Section 8.2. However, the data availability overview is included in Table 8.1.

Tab. 8.1: Data availability chart for each instrument (*MiRAC-P*, *HATPRO*, visible (VIS) and infrared (IR) part of the sky camera and surface camera, radiosondes, and *MiniIMU*). Red (orange) entries indicate that more (less) than 50 % of the day's data is lost. Yellow entries indicate a small data gap exists or corrupted but repairable data. Green entries show a (nearly) complete data set for that day.

Dates	MiRAC-P		HATPRO		Sky camera		Surface camera			Radiosonde
	G-band	243	K-band	V-band	IR	VIS	IR	VIS	MiniIMU	
2022-06-28										
2022-06-29										
2022-06-30										
2022-07-01										
2022-07-02										
2022-07-03										
2022-07-04										
2022-07-05										
2022-07-06										

Dates	MiRAC-P		HATPRO		Sky camera		Surface camera			Radiosonde
	G-band	243	K-band	V-band	IR	VIS	IR	VIS	MiniIMU	
2022-07-07										
2022-07-08										
2022-07-09										
2022-07-10										
2022-07-11										
2022-07-12										
2022-07-13										
2022-07-14										
2022-07-15										
2022-07-16										
2022-07-17										
2022-07-18										
2022-07-19										
2022-07-20										
2022-07-21										
2022-07-22										
2022-07-23										
2022-07-24										
2022-07-25										
2022-07-26										
2022-07-27										
2022-07-28										
2022-07-29										
2022-07-30										
2022-07-31										
2022-08-01										
2022-08-02										
2022-08-03										
2022-08-04										
2022-08-05										
2022-08-06										
2022-08-07										
2022-08-08										
2022-08-09										
2022-08-10										
2022-08-11										
2022-08-12										

Preliminary results

An existing, but newly implemented and preliminary regression retrieval, which was trained with Ny-Ålesund radiosondes from 2006 to 2017, was applied to *HATPRO* BT measurements. Through this we were able to preliminarily analyse IWV, LWP, humidity and temperature profiles during the expedition. BT data from *MiRAC-P*, which will be combined with *HATPRO* after the expedition, could not be converted directly to IWV or humidity profiles because it requires more

extensive processing. We were not able to apply existing retrievals to *MiRAC-P* data (i.e., those used for MOSAiC data) because of the broken 340 GHz channel.

In the following, we provide a preliminary evaluation of IWV between *HATPRO* and radiosondes (Fig. 8.2). We will also show an atmospheric overview of PS131 from radiosonde data and *HATPRO* (Fig. 8.3) and an example including also raw data from *MiRAC-P* and the sky camera (Fig. 8.4).

During PS131, the IWV was mainly between 10 and 22 kg m^{-2} but also increased to 35 kg m^{-2} (see Fig. 8.2). Before the LN2 calibration on 7 July 2022, IWV derived from *HATPRO* was offset by about 2.5 kg m^{-2} compared to radiosondes (Fig. 8.2). Once the BTs were calibrated, also the derived IWV agreed very well with radiosondes with a standard deviation of 0.48 kg m^{-2} and a mean difference from the radiosondes ("bias") of 0.11 kg m^{-2}. Figure 8.2 demonstrates that *HATPRO*'s IWV estimates are reliable and can be taken as a general truth for time steps when no radiosonde was launched. Besides an imperfect retrieval, differences between radiosondes and *HATPRO* might be caused by horizontal drifts of the radiosonde or averaging *HATPRO* BT data over 30 minutes for this comparison (especially if close to humidity gradients).

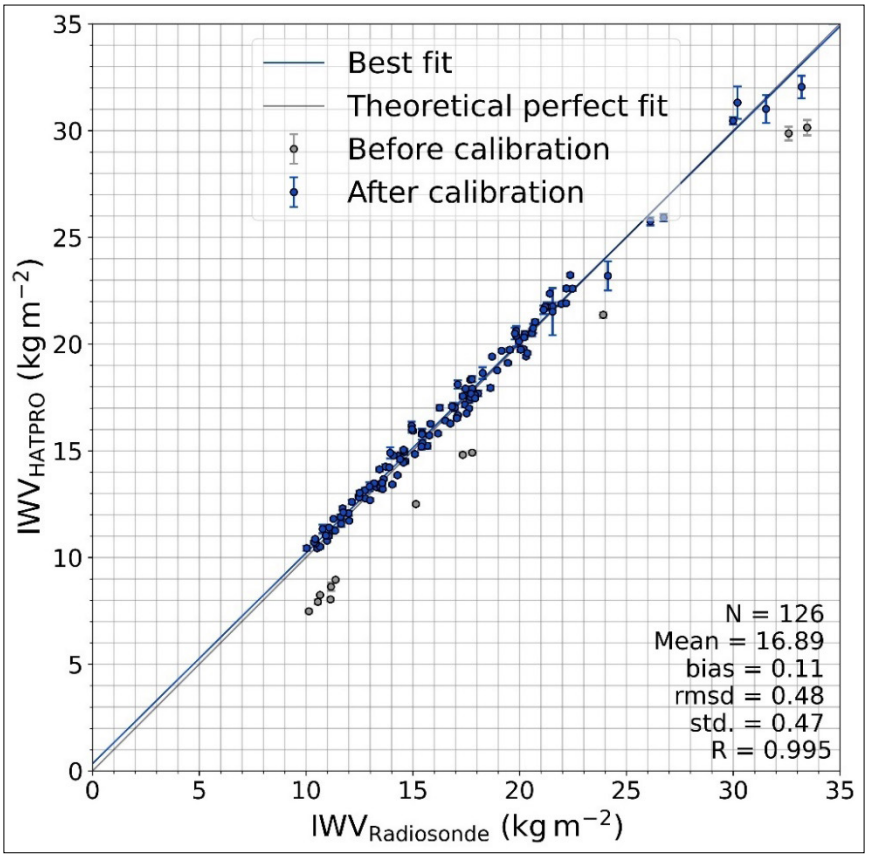

Fig. 8.2: Scatter plot comparing the IWV derived from HATPRO BT data before (grey) and after the first liquid nitrogen calibration (blue) with the IWV computed from radiosonde humidity measurements; the data points cover the period 28 June 2022 12 UTC to 12 August 2022 00 UTC. HATPRO IWV was averaged over 30 minutes starting from sonde launch time and the error bars show the standard deviation over that time window. Additionally, a linear fit ("Best fit", blue), and the one-to-one line (grey) are shown for orientation. The number of radiosondes samples (N), bias, root mean squared deviation (rmsd), standard deviation (std.) and Pearson correlation coefficient (R) with the HATPRO IWV after the first calibration are given on the lower right.

The atmospheric overview given in Figure 8.3 covers the period 7 July 2022 00 UTC (Fram Strait) to 12 August 2022 00 UTC (transit to Bremerhaven). The warm conditions during the transit from Bremerhaven to the southern Fram Strait have been excluded. From 7 to 9 July 2022, weak temperature inversions were present at 200 to 500 m altitude and the boundary layer was only rarely saturated with water vapour (mostly low cloud cover). Below the temperature inversion, temperatures remained close to ocean surface temperatures (2 - 5 °C).

On 13 and 14 July 2022, air with a higher moisture content was advected to *Polarstern* by an occluded warm front connected to a low-pressure system over the North Atlantic. It was also accompanied by warmer temperatures above the surface inversion (7 °C in 600 m altitude) and precipitation. This event was followed by two strong warm/moist air intrusions (15 to 17 and 17 to 19 July 2022) caused by a low-pressure complex around Svalbard and northern Scandinavia and high pressure over the Kara Sea. Strong south-easterly winds transported high amounts of humidity to Svalbard and beyond, but lee effects from Svalbard suppressed low clouds and precipitation at *Polarstern*. The second of the warm/moist air intrusion was stronger with IWV peaking at 35 kg m^{-2} in the evening of 17 July 2022, when also the highest freezing level of about 3,800 m was observed. The maximum temperature of 18 °C at 650 m altitude occurred in the morning of 18 July 2022. This delay of warm lower tropospheric temperatures reflects the typical warm front characteristic of upgliding warm air. After the event, a remarkably strong moisture gradient passed over *Polarstern*, decreasing IWV by 15 kg m^{-2} in less than 3 hours according to *HATPRO*. Even with 3-hourly radiosonde, the moisture gradient is smoothed to 15 kg m^{-2} in 6 hours in the radiosonde data. The extreme intrusion of warm and moist air likely had a strong impact on the sea ice surface scattering layer of the three floes between the first and second visit.

A third, weaker warm air intrusion without a distinct increase in humidity followed on 19 July 2022. As we went back to ice stations on 20 to 22 July 2022, near surface temperatures were in the range 0 - 1 °C with 100 % relative humidity (fog/mist). At the surface, radiosondes again detected shallow humidity and temperature inversions. Two precipitation events, one on 22 and 23 July 2022, and one on 27 and 28 July 2022, probably also strongly affected the surface scattering layer. During the first event, more humid, but not warmer air saturated the air mass and led to deeper clouds (see LWP in Fig. 8.3). Drizzle and rain were observed at *Polarstern*. The other precipitation event also featured graupel in between with temperatures below 0° C in a deeper layer (0 - 600 m).

Warmer and more humid air (IWV increased from 14 to 22 kg m^{-2}) got advected to *Polarstern* in the evening of 30 July 2022, forming again a stronger temperature inversion with 0 to 1°C at the surface and 5°C a few hundred meters above. At the beginning of the transit to the east coast of Greenland (2 to 4 August 2022), even warmer air was recorded above *Polarstern* with temperatures up to 8°C in 850 m height. Temperatures remained close to 0 °C with fog at 100 % relative humidity. During the second part of the transit (4 and 5 August 2022), temperatures were below 0°C at the surface and fog existed in patches around *Polarstern*. On 5 to 8 August 2022, colder and drier air from the coast caused the lowest 850 hPa temperature of the campaign with -6.1°C and IWV of 10 - 12 kg m^{-2} on 7 August 2022 06 UTC.

The occlusion front observed on 8 August 2022 during the transit to Scoresby Sund is also shown in Figure 8.4. The occluded warm front was accompanied by clouds in various layers, starting with thin clouds at high altitudes (see *GoPro* image at 14:37 UTC in Fig. 8.4). Over time, the clouds' thickness increased and cloud base height descended (see *GoPro* image at 16:08 UTC in Fig. 8.4). Similarly, moisture first increased in high altitudes and later also at the surface when higher altitudes were already drier again. IWV increased from 10 to 23 kg m^2 within 9 hours. Apparently, the cold front had already sufficiently cooled down the warm sector air mass so that only a weak warming signal could be seen in the radiosonde data above

1,500 m altitude. Despite the strong precipitation in the evening of 8 August 2022, *HATPRO* seemed to yield reliable IWV estimates when compared to the radiosonde observations.

On 10 August 2022 in Scoresby Sund, *Polarstern* was under the influence of warmer but relatively dry air with 7°C close to the surface and IWV of 13 kg m^{-2} (see Fig. 8.3). As opposed to many days in the sea ice or northern Fram Strait, no distinct surface temperature inversion was present, and the relative humidity remained below 100 %.

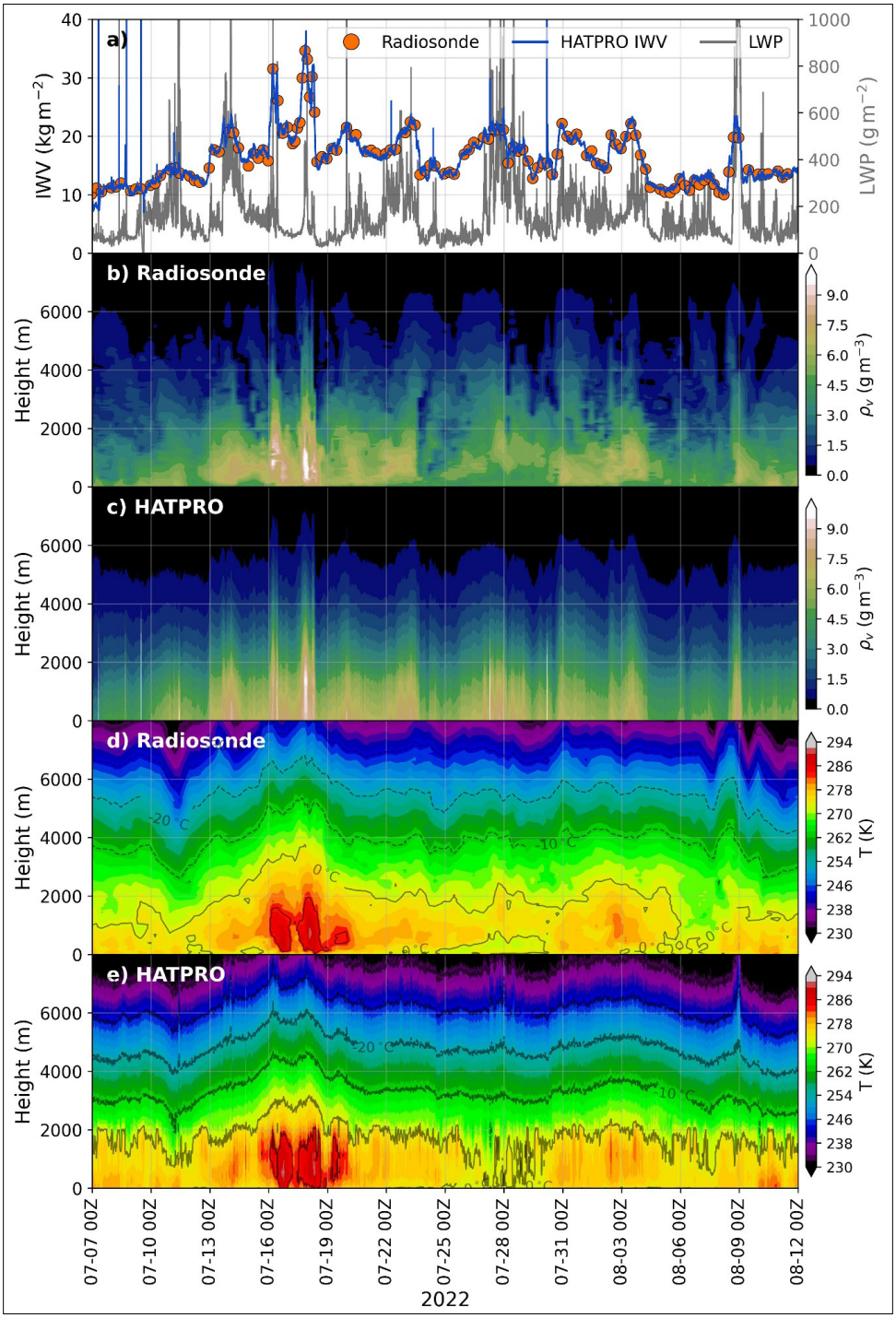

Fig. 8.3: Atmospheric overview over the campaign showing the IWV (LWP) from HATPRO as blue (black) line, IWV computed from radiosonde humidity measurements as orange circles (a), the absolute humidity profile from radiosondes (b) and HATPRO (c), as well as temperature profiles from radiosondes (d) and HATPRO (zenith and boundary layer scans) (e).

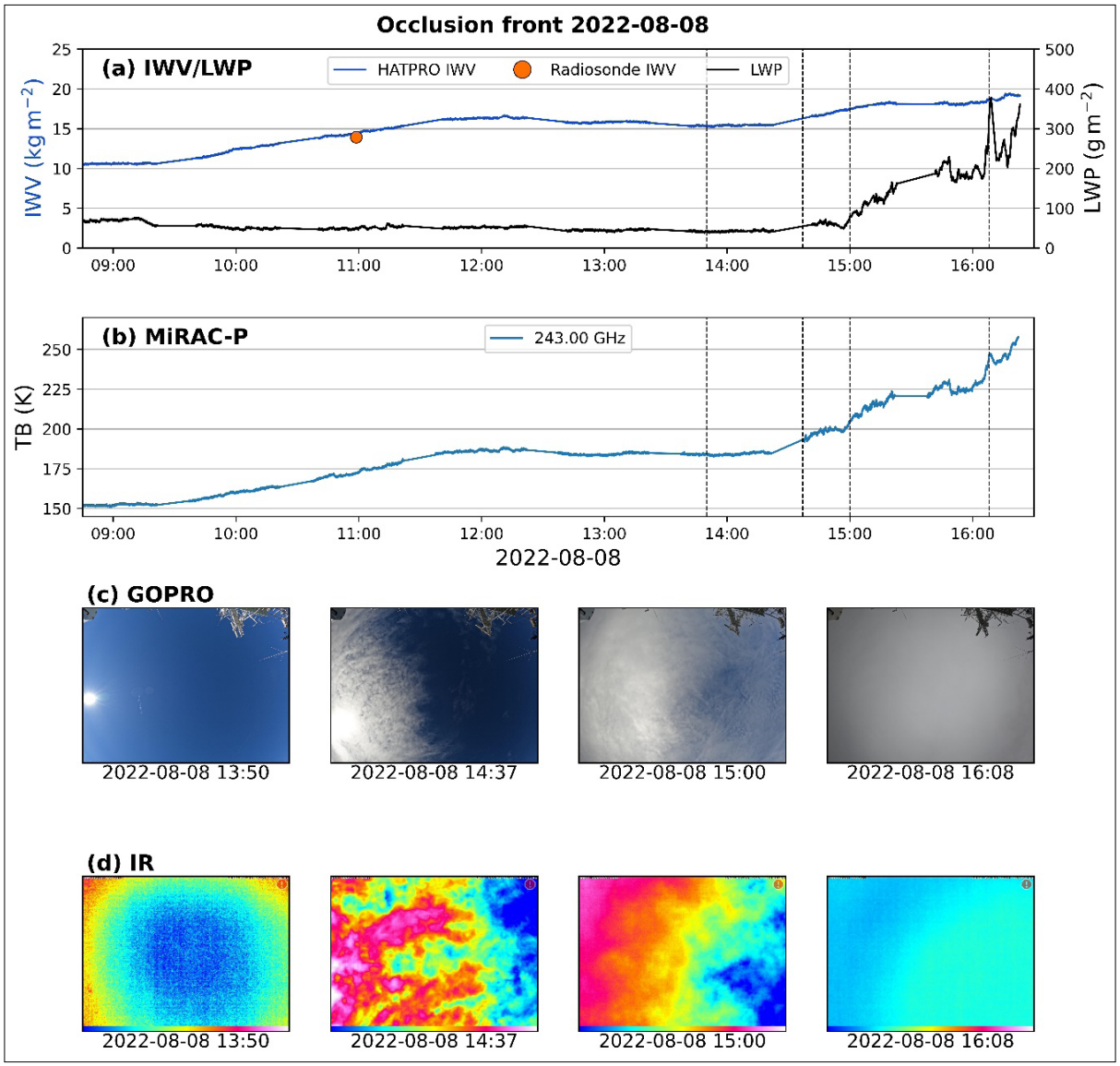

Fig. 8.4: Example overview showing the IWV and LWP from HATPRO (blue and black lines) and IWV from radiosondes (orange circles) in (a), brightness temperatures (TB) from MiRAC-P at 243 GHz in (b), sky camera images at four selected times in the visible and infrared spectrum ((c) and (d)) for an occlusion front reaching Polarstern on 8 August 2022. Mind the different opening angles of the visual and IR camera in (c) and (d). The IR data covers only a small section of the visual images towards the centre; the IR colour scale varies between the images and provides only qualitative cold to warm temperature information.

8.2 Ice surface measurements

Work at sea

Ship-based

Measurements with the regular radiometers and camera setup started on 10 July 2022 (see Section 8.1 above). From then on the surface was measured for 15 minutes every hour by *HATPRO* and *MIRAC-P*. For that, the elevation angle of the radiometers was set to 140° so that they were facing the horizontally placed (91.5°) mirrors, resulting in an effective incidence angle of 53°.

Whenever we noticed water (droplets) on the mirrors, we cleaned them during daily maintenance. For future campaigns, the cleaning procedure could be improved, including bringing proper cleaning equipment, like wipers.

A visual *GoPro Hero 9 Black* camera as well as an inertial motion unit *MiniIMU* (WitMotion Shenzen Co., Ltd) were fixed on the *VarioCam HD* infrared (IR) camera that was installed on a tripod, which we attached to the railing on the *Peildeck* (see Figure 8.1). The IR camera was connected to an industrial mini PC stored in a *Pelicase* underneath the radiometers. This setup was connected by an ethernet cable to our office on A deck of *Polarstern*, two floors below the *Peildeck*, so that the IR camera could be operated remotely using the *IRBIS vision* software. The *MiniIMU* was calibrated in the beginning, using the acceleration calibration and magnetic field calibration included in the firmware. The calibration of pitch and roll angles was successful. Despite several attempts, we were not able to calibrate the z-angle (yaw), so that this data is not available. However, in our setup with the camera fixed to the railing, we assume this angle to be stable relative to *Polarstern's* heading. In our daily routines, we restarted the recording and corrected the time of the *MiniIMU* every morning.

The *GoPro* visual camera was attached on top of the IR camera to measure at the same incidence angle. However, the *GoPro* has a larger opening angle and thus captures more of the surroundings. Every morning, we exchanged the memory SD card and saved the data. As we experienced a failure of both *GoPro* cameras in the end of July, possibly related to the camera software, we then also started to remove the battery when exchanging the memory SD card to fully restart the camera.

From 10 July, 16:00 UTC, the two surface cameras were operated with a sampling rate of 0.2 Hz, taking a picture every 5 s. The incidence angle was set to approximately 50° in order to both contain the radiometer footprint but also the horizon. On 8 August, 8:11, the angle was adjusted by –5° to cover more of the surface.

At least once per day the lenses were cleaned with a tissue and often ethanol. Due to mild temperatures, there was hardly any freezing.

In addition to the regular microwave brightness temperature measurements at 53°, we performed extensive scans of the surface at up to 7 different incidence angles from 10° to 70° in steps of 10° by adjusting the mirrors manually and measuring for 5 minutes at each incidence angle. This was done five times during the cruise (plus one test scan), see Table 8.2. For these scans, the incidence angle of the camera setup was changed to 60° to cover the range of footprints.

Data availability

The surface camera data availability is summarised in Table 8.1. The IR camera data is available starting 3 July and *GoPro* images are available starting 11 July, 11:00. The thermal infrared data is missing on 24 July from 7:09-19:22 and on 7 August from 17:16-21:20 when the recording was stopped due to unknown/software issues.

GoPro data is missing from 17 July, 8:52 to 18 July, 7:05 due to a full memory card, on 25 July from 16:55 - 18:13 for unknown reasons (maybe failure during data transfer), from 31 July, 10:16 to 1 August, 10:52 due to power loss and from 2 August, 8:20 to 3 August, 9:42 possibly due to a software failure.

The *MiniIMU* software was not always recording reliably, so that there are gaps in the data, see Table 8.1.

Tab. 8.2: Overview of extensive surface scans with varying incidence angles performed during the cruise

Start time	End time	HATPRO incidence angles	MiRAC-P incidence angles	Ice conditions	Weather conditions
2022-07-07 15:24	2022-07-07 16:06	test scan: 10, 20, 60, 70	test scan: 10, 20, 60, 70	open ocean	cloud free
2022-07-09 11:40	2022-07-09 11:50	atmospheric test scan	-	open ocean	8/8 thin stratus, dissolving to 7/8
2022-07-09 12:14	2022-07-09 13:15	10, 20, 30, 40, 50, 60	-	open ocean	6/8 to 8/8 thin stratus
2022-07-12 20:21	2022-07-12 21:21	10, 20, 30, 40, 50, 60	10, 20, 30, 40, 50, 60	Ship position and ice not stable; small ice floes (10 m diameter) moving in and out of footprint	1/8 - 3/8 stratus and altocumulus
2022-07-24 20:14	2022-07-24 21:32	10, 20, 30, 40, 50, 60	10, 20, 30, 40, 50, 60	Rather stable ship position (relative to ice), open ocean for small angles, melt pond signature in footprint for some angles possible, Aurora ice station: ice core data available	7/8 - 8/8 stratus and altocumulus
2022-07-25 17:41	2022-07-25 18:46	10, 20, 30, 40, 50, 60	10, 20, 30, 40, 50, 60	Rather stable ship position (relative to ice), melt pond signature in footprint for some angles possible	6/8 - 8/8 stratus and altocumulus
2022-08-06 07:47	2022-08-06 09:00	10, 20, 30, 40, 50, 60, 70	10, 20, 30, 40, 50, 60, 70	Stable ship position (relative to ice), 100% SIC, Greenland 1 station: ice core + snow data available	5/8 - 8/8 stratocumulus and stratus

Ice stations

During the 12 ice stations (for a description of the sites see Chapter 3.2) measurements of the surface properties that effect microwave emissions were performed. That included ice cores to obtain temperature, density and salinity profiles, snow pits to study the surface scattering layer, surface roughness measurements of the surface by photogrammetry and dielectric permittivity measurements. Under-water videos were also recorded to observe the topography of the ice under water. On each floe, two to four different sites were studied to account for local variability. For the three floes that were revisited, the same sites were sampled at each visit (if possible), to study temporal changes. The positions of the sites on the floe are marked in Figure 3.2.3 and additional sea ice physics work is presented in Chapter 3.

The sites were numbered and if a second snow pit or core was taken very close by during revisits, it got a corresponding extension, e.g., site 1.2. An overview about the work conducted on the ice at the different sites is given by Table 8.3.

Due to logistical reasons, ice stations were mostly done on portside, so that sampling in the footprint of the remote sensing observations on starboard was rarely possible, but still done two times explicitly in the footprint (indicated in Table 8.3). For these two cases, the footprint was approximately found by peaks in the brightness temperatures of the MWRs triggered by people walking in and out of the footprint.

To obtain the ice cores, a 9 cm *Kovacs* corer was used. For the first two ice stations (13 and 14 July), two cores per site were taken: one to measure temperatures at different depths and the other for density and salinity (Greisinger G1410 salinometer) measurements. From 15 July onwards, only one core per site was taken and used together for temperature, density, and salinity analyses. Usually, the upper 20 cm were sampled in 4 cm steps, while the lower, remaining part was sampled in 10 cm steps (see Table 8.4 for typical total ice thicknesses between 0.4 to 2.9 m). This was done to achieve a higher vertical resolution for the upper part, which dominates the influence on the microwave signal. The cores were cut and weighted on the ice and then taken to the ship for salinity measurements. The distinction between ice and the icy surface scattering layer was not always clear. At least one full core per floe was taken, while for some of the additional sites on a floe only the upper 20 to 40 cm were sampled. Table 8.3 lists all sites, where cores were taken and sites where a core was fully sampled are indicated in the Table by a grey background colour. All in all, 33 ice cores were taken and analysed, while for 13 of them only the upper 20 to 40 cm were measured. Additionally, ice thickness measurements were performed in the core holes and often additional ice thickness drillings close to the coring sites.

Tab. 8.3: Overview of measurements during the ice stations. Grey background indicates full length ice cores (for the remaining only the upper 20 or 40 cm were sampled).

Date	Floe	Visit	Site/# cores	Snow pit	Surface roughness	Hydra Probe
2022-07-13	north	1	1/1	yes	2	SSL
			2/1	yes	3	SSL + ice
			2.2/1	no		
2022-07-14	south	1	1/1	yes	2	Instrument failure
			2/1	yes	2	
			3/1	none	none	
2022-07-15	middle	1	1/1	yes	3	SSL
			2/1	yes	2	SSL + ice
			2.2/1	no		
2022-07-20	north	2	1/1	yes	2	SSL + ice
			1.2/1	no		
			2/1	yes	4	SSL + ice
			3/1	yes	1	SSL + ice
2022-07-21	south	2	1/1	yes	2	SSL
			1.2/1	yes		
2022-07-22	middle	2	1/1	yes	2	SSL + ice
			2/1	yes	2	SSL + ice
			3/1	yes	2	SSL + ice
2022-07-27 – 2022-07-28	24h	single	1/1	yes	2	SSL + ice
			1.2/1	yes		
			2/1	yes	2	SSL + ice
2022-07-29	Zodiac	single, 2 floes	1/none	Only grain size	1	none
			2/none	Only grain size	2	none
2022-07-30	north	3	1/1	yes	2	SSL + ice
			2/1	yes	4	SSL + ice
			3/1	yes	2	SSL + ice

Date	Floe	Visit	Site/# cores	Snow pit	Surface roughness	Hydra Probe
2022-07-31	south	3	1/1	yes	2	SSL + ice
			1.2/1	yes	1	SSL + ice
2022-07-31	middle	3	1/1	yes	2	SSL + ice
			2/1	yes	1	SSL + ice
			3/1	yes	2	SSL + ice
			4/1 (footprint)	yes	1	SSL + ice
			4.2/none	yes	1	
2022-08-06	Greenland 1	single	1/1 (footprint)	yes	2	SSL + ice
			1.2/none	yes		
2022-08-06	Greenland 2	single	1/1	yes	2	SSL + ice
			2/1	yes	1	SSL + ice

The snow/surface scattering layer analysis consisted of temperature measurements at different depths and assessing the hardness, as well as grain size and shape of the crystals. We did not encounter any new snow during our ice stations and had surface melting conditions. Thus, all surfaces can best be categorized as surface scattering layer (SSL; even if in the following we sometimes mention or term it snow). Photos were taken of observed snow/ice crystals and a plate with a 2 mm grid was used to determine crystal sizes. With a wooden ruler, the height of the SSL layer was determined. Usually, 10 height measurements in 1 m radius around the snow pit were taken to account for locally variable snow heights. With a density cutter of 3 cm height (100 cm^3) 5 to 10 measurements of density were performed at each snow pit to account for variability and the higher uncertainty of the density cutter for harder, icy layers. Additionally, samples of the surface layer were taken and later analyzed for their salinity content on board.

Close to the coring site, around ten photos of the surface were taken with an *Olympus E-M5* digital camera from different angles to be analysed with photogrammetry software. Coded targets on a wooden frame were placed within the photos, so that the images contain information about distances. From this the surface topography and roughness can be retrieved, which is an important parameter for the microwave emission and scattering. The number in Table 8.3 in the column *surface roughness* indicates the number of measurements at each site. To increase contrast, we experimented with an IR lens with a bandpass of 760 nm to 860 nm and with a 6200 lumen LED lamp but did not find any significant improvements. Except for the third visit of the Northern floe we always had overcast conditions so that shadows were not an issue.

The real and imaginary part of the permittivity at 50 MHz was measured with a *Stevens HydraProbe* Soil Sensor. Depending on the thickness of the SSL layer, the instrument was either horizontally or vertically placed. In order to deploy the probe in a hard surface scattering layer or ice, 5 mm holes were drilled with the help of a template for the four tines of the instrument. The drilling could possibly have affected the ice structure of the probed site but we did not find clear evidence of that. The instrument was placed for a few minutes each at different sites around the snow pit in the surface scattering layer, usually within distances of 20 cm to 30 cm to the previous placement. Often, the instrument was additionally placed in the ice surface and in the bottom piece of the ice core taken for density and salinity measurements when it was already in the melt pot to avoid brine loss by drilling.

Preliminary results

Ship-based

For the microwave radiometer measurements in surface mode, we can combine the visual, infrared and microwave measurements to get a comprehensive picture of the sea ice and ocean

emissions. In some cases, this can even be directly combined with footprint measurements of the ice and surface layer, as shown exemplarily in Figure 8.5 and Figure 8.6. Figure 8.5 shows the surface brightness temperatures at 53° incidence angle and three surface camera images during these measurements at the Greenland 1 station. At this station we also performed measurements at different incidence angles. Figure 8.6 c) shows the average brightness temperature over five minutes measured at each incidence angle with corresponding standard deviation. Figure 8.6 a) and b) gives an overview of the ice core and snow pit measurements taken within the footprint.

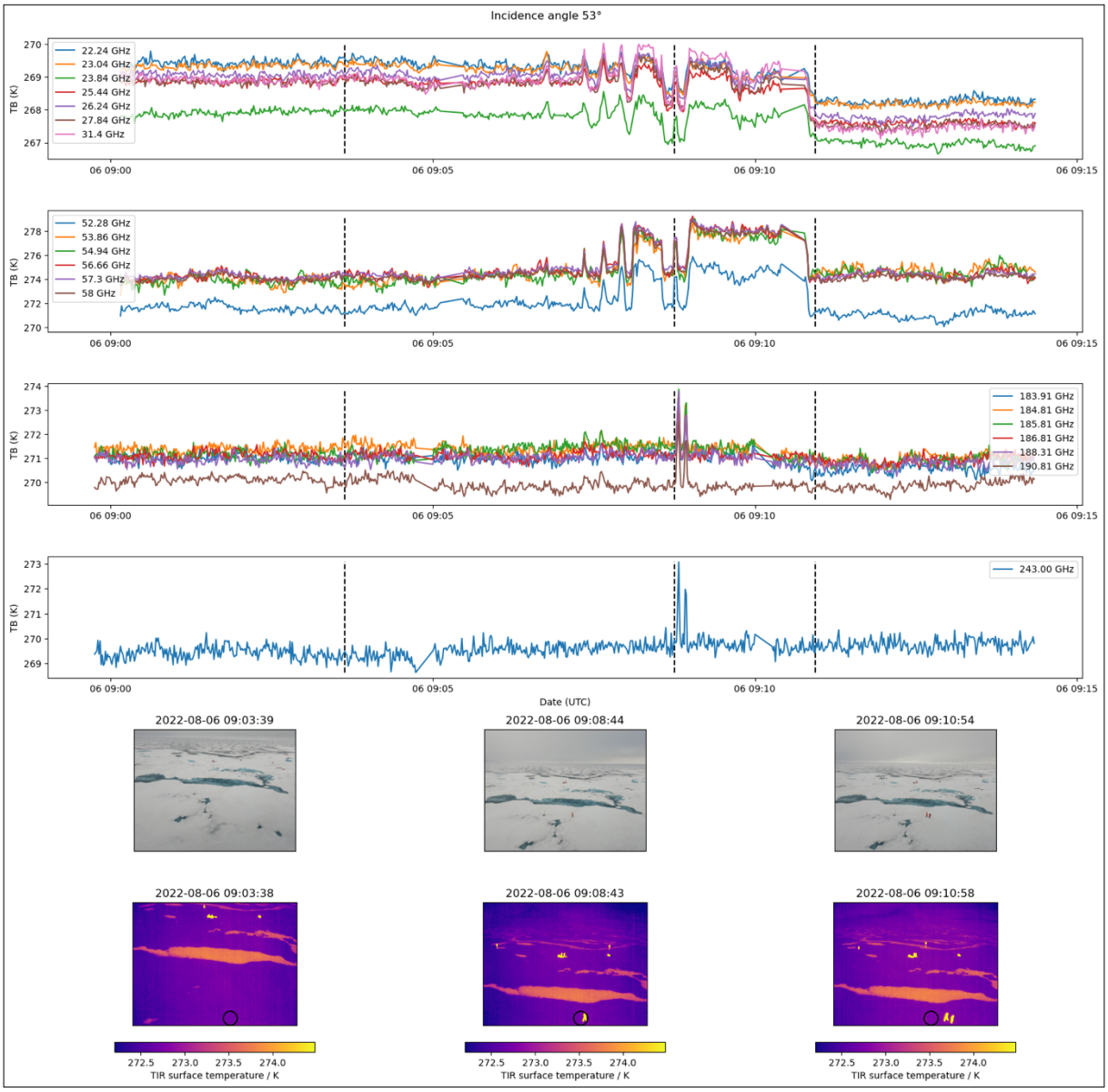

Fig. 8.5: Brightness temperature data from HATPRO (first two rows) and MiRAC-P (third and fourth row) in surface mode (incidence angle 53°) during the Greenland 1 station on 6 August 2022. For clarity the channel at 51.26 GHz is excluded due to larger noise. The peaks in the vicinity to the second vertical dashed line are people walking in the footprint, which allowed us to find the footprint later for ice core and surface scattering layer measurements. The reason for the decrease of TB in K-Band (upper row) after people walked in the footprint is unclear at the moment. The fifth and sixth row shows visual and thermal infrared images taken at three times, indicated by the vertical dashed lines in the first four rows. The circle in the thermal infrared image is a rough estimate of the radiometer footprint. Shortly before this measurement, the surface was measured at different incidence angles by changing the mirror angle, which is shown in Figure 8.6c.

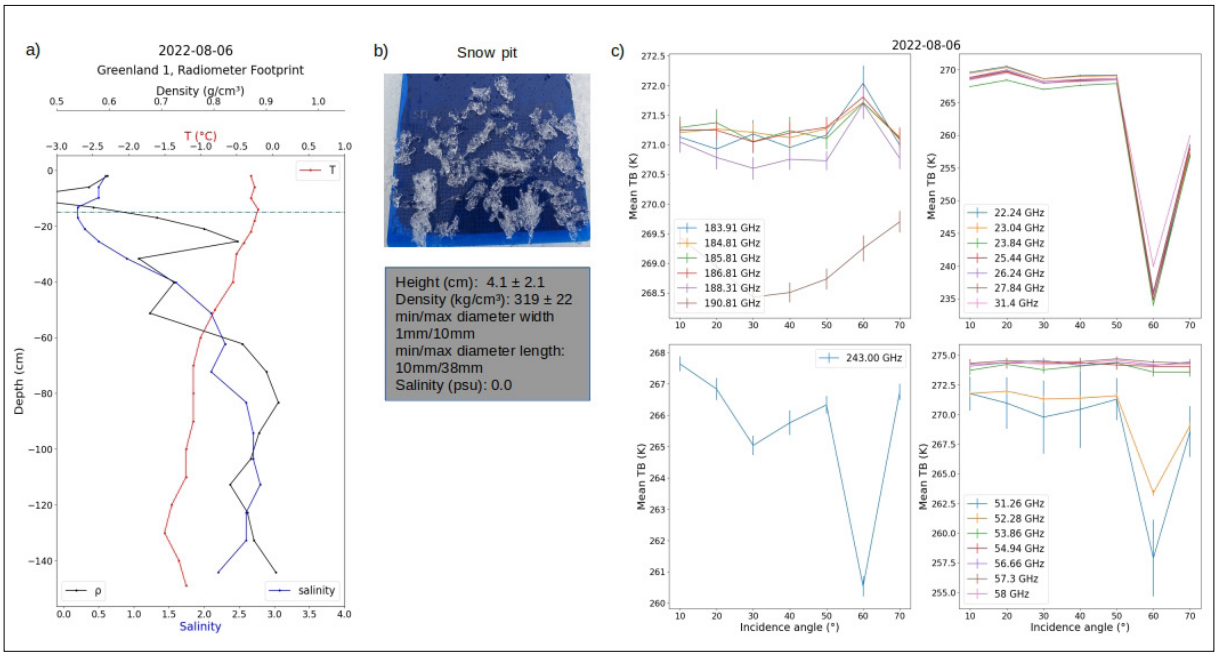

Fig. 8.6: a) Ice core taken in the radiometer footprint at 53° on ice station Greenland 1, 6 August 2022 (see also Fig. 8.5); b) snow pit data from same footprint site; c) shows the dependence of the brightness temperatures on the incidence angle measured at that station by adjusting the mirror angle.

Ice stations

Table 8.4 gives an overview of all ice thickness measurements conducted during ice stations by this project (see Chapter 3 for more ice thickness measurements). Those obtained in ice core holes are indicated in bold fonts. The other measurements were done by normal drilling.

The underwater images obtained from the coring sites reveal the different topographies below the ice. While on some sites, the ice was more or less smooth, it could strongly differ in thickness at other sites. The small-scale local variability should be kept in mind when interpreting thickness data.

When taking the ice cores there was often no distinct boundary between the ice and the icy surface layer, thus especially the measurements of salinity and density for the upper 5 cm to 10 cm need to be treated with care. All in all, little gradients in temperature and only low (<4 psu) gradients in salinity values were observed.

When averaging the upper 40 cm of the 27 cores taken on the three floes in the marginal ice zone (North, South, Middle), we get a mean temperature of –0.3°C, a mean bulk salinity of 0.52 psu, and a mean density of 768 kg cm^{-3}. The average profile is shown in Figure 8.7.

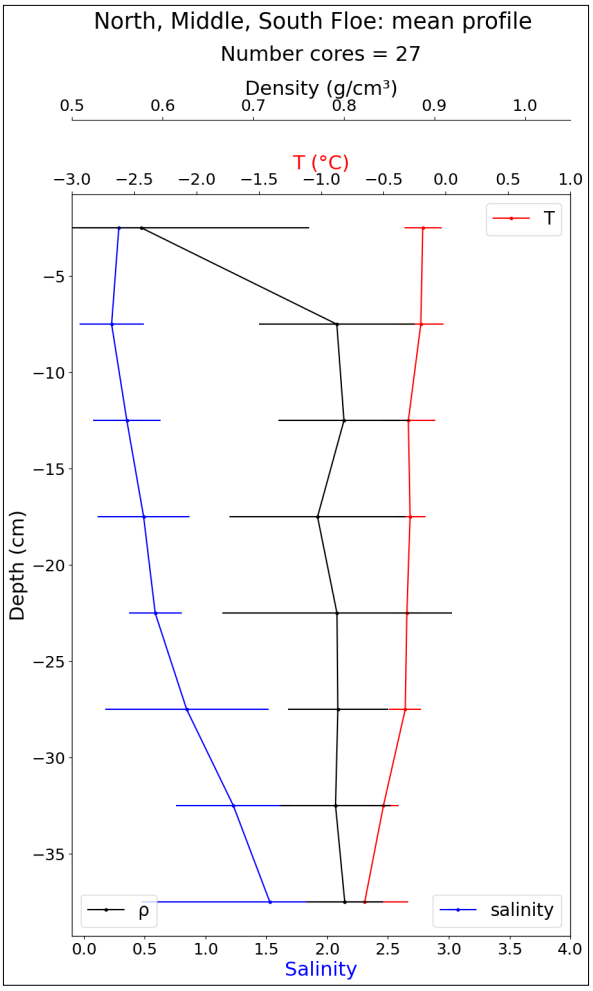

Fig. 8.7: *Average profile of temperature (red), salinity (blue), and density (black) of all ice cores taken during the three visits of each of the three floes in the marginal ice zone, the standard deviations are given as error bars.*

Tab. 8.4: Ice thickness and freeboard measurements from all ice stations. Bold font indicates measurements from ice cores, the others are from drilling. NA indicates that a particular measurement was not taken. However, SSL depth was usually measured within 2 m to the coring hole as part of the snow pit data.

Date	Floe	**Visit**	**Site**	**Ice thickness [cm]**	**Freeboard [cm]**	**SSL depth [cm]**
2022-07-13	north	1	1	211, **190, 185**	21, NA, NA	6, NA, NA
			2	**173**	NA	NA
			2.2	NA		
2022-07-14	south	1	1	143, **128, 133**	14, NA, NA	1, NA, NA
			2	114	NA	NA
			3	200	26	4
2022-07-15	middle	1	1	144, **137**	23, NA	2, NA
			2	**132**	11	4
			2.2	NA		

Date	Floe	**Visit**	**Site**	**Ice thickness [cm]**	**Freeboard [cm]**	**SSL depth [cm]**
2022-07-20	north	2	1	**179**, 180, 192	21, 19, 23	NA, NA, 1
			1.2	NA		
			2	**169**	19	2
			3	202	39	6
2022-07-21	south	2	1	114, 222, **126**	13, 27, 14	2, 1.9, 5
			1.2	209, **267**	22, NA	1.3, 5
2022-07-22	middle	2	1	**108,** 106	19, 19	3,4
			2	**104**	NA	NA
			3	**87**	NA	NA
2022-07-27 – 2022-07-28	24h	single	1	169, **193**	18, 17.5	2.2, NA
			1.2	275, **290**	27, 30	3, NA
			2	**170**	12	3
2022-07-30	north	3	1	**158**, 156	13, 11	4.2, 3.9
			2	**162**	19	3
			3	**184**	29	5
2022-07-31	south	3	1	**104**	12	2
			1.2	**233**	25	5
2022-07-31	middle	3	1	**93**, 110, 106, 96	16, 9, 19, 16,	4, 3, 3.4, 2.3
			2	92	11	4
			3	79	10.5	3
			4	96	12	3
2022-08-06	Greenland 1	single	1	**150**, 144, 146, 147, 147, 135, 155, 158	20, 15, 15.5, NA, 16, 1, 12.5, 18.5, 41.6, 22.7, 14.6	5, NA
2022-08-06	Greenland 2	single	1	**99**	12	6
			2	**41**	5.5	2

In the 31 sampled snow pits we could see a wide variety of grain sizes and shapes. Notably, needle-like structures were observed most of the times, often vertically oriented, with a minimum width of 1 mm and a maximum length of up to 70 mm. However, also round grains and platelet structures were found and could sometimes be related to the topography of the ice: the round grains were more often found close to or on ridges. Also, we could observe how rain on snow directly affected the surface structures within a few hours, thus changes between the revisits of the floes were expected.

The hardness of the pits varied between “2F” and “knife”.

Averaging all 31 snow pits we obtained a mean SSL height of 3.4 cm ± 1.6 cm with a minimum and maximum of 1.1 cm and 6.3 cm, respectively. Note that the standard deviation of the height measurements of the surface scattering layer could vary by up to 2.3 cm (or about 50%) at one snow pit.

We inferred a mean density of the surface scattering layer of 404.5 kg cm^{-3} with a standard deviation of 94.9 kg cm^{-3} for all 31 snow pits, with minimum and maximum values of 275.0 kg cm^{-3} and 679.0 kg cm^{-3}, respectively. Note that the density at one site could vary by up to 16%. However, these values are to be treated with caution, as the snow density cutter was intended

to be used in snow. The studied surfaces were often very icy and hard so that the use of the density cutter might affect the density of the sample.

Regarding the surface roughness measurements from photogrammetry, preliminary analysis shows that 3D mesh grids with defined distances can be generated using the *Agisoft metashape* software, see Figure 8.8. After the cruise, this data will be further explored to obtain mean surface heights and correlation lengths from these grids.

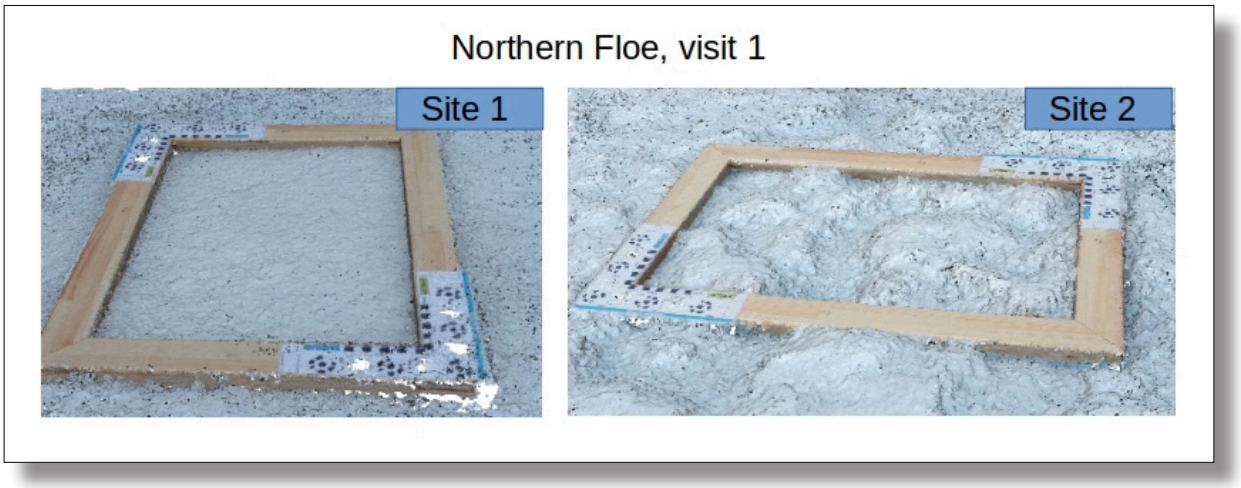

Fig. 8.8: Snapshots of surface topography maps generated with the Agisoft software of surface measurements taken at two different sites during the first visit of the Northern floe. The scale bars on one site of the frame are 10 cm long. While the surface of site 1 was rather smooth, site 2 showed a lot more roughness at the centimetre scale.

A first look at the relative permittivity data by the *Stevens HydraProbe* reveals stable measurements at placements in the surface scattering layer of about 2–3 for the real part of the permittivity and 0.2 for the imaginary part and values higher than 3 (real part) and higher than 1.2 (imaginary part) for ice cores. We also observe increases in both real and imaginary part when the instrument was placed in moister areas or more saline ice cores, which is the expected behaviour.

Data management

The processed radiometer, camera, and radiosonde data will be uploaded to the World Data Center PANGAEA Data Publisher for Earth & Environmental Science (https://www.pangaea.de) when processing and quality checking has been completed (about 6-9 months after the cruise). The metadata will be openly visible, but the processed sensor data will be given a 1-year moratorium to allow publication of the scientific results by the applicants. Data will be made directly available to the ATWAICE team and other collaborating partners. In particular, the time series of the atmospheric measurements will be provided as “quicklooks” which are open to the public.

This WALSEMA project is supported by the Deutsche Forschungsgemeinschaft (DFG, German Research Foundation) through the Transregional Collaborative Research Centre TRR-172 “ArctiC Amplification: Climate Relevant Atmospheric and SurfaCe Processes, and Feedback Mechanisms (AC)³” (grant 268020496).

In all publications based on this expedition, the **Grant No. AWI_PS131_11** will be quoted and the following publication will be cited: Alfred-Wegener-Institut Helmholtz-Zentrum für Polar- und Meeresforschung (2017) Polar Research and Supply Vessel *Polarstern* Operated by the Alfred-Wegener-Institute. Journal of large-scale research facilities, 3, A119. http://dx.doi.org/10.17815/jlsrf-3-163.

References

Mech M, Maahn M, Kneifel S, Ori D, Orlandi E, Kollias P, Schemann V, Crewell S (2020) PAMTRA 1.0: The Passive and Active Microwave radiative TRAnsfer tool for simulating radiometer and radar measurements of the cloudy atmosphere. Geoscientific Model Development, 13, 4229–4251. https://doi.org/10.5194/gmd-13-4229-2020.

9. GREENHOUSE GAS FLUXES AT THE OCEAN-SEA ICE – INTERFACES IN THE ARCTIC OCEAN (FLUX-ON-SITE)

The group has cancelled the participation on the expedition.

10. ICEJELLY: INFLUENCE OF SEA-ICE AND SUB-MESOSCALE OCEANOGRAPHY ON JELLY DISTRIBUTIONS AND COMMUNITIES

Ayla Murray[1], Meret Jucker[1], [1]DE.AWI
Charlotte Havermans[1] (not on board)

Grant-No. AWI_PS131_ 10

Outline

Gelatinous zooplankton (GZP) or "jellies" are a broad group of taxa, comprised of *ctenophores*, *cnidarians* and *tunicates*. They are largely understudied despite hypotheses of recent increases in biomass throughout the World's Oceans. This phenomenon, referred to as "ocean jellification", is likely a result of the complex interplay of climate change, overfishing and other anthropogenic factors. Environmental changes are occurring at an unprecedented pace in the Arctic Ocean, urgently highlighting the need for a large-scale understanding of Arctic marine biodiversity. Pioneering work has shown GZP to be particularly abundant in Arctic waters, including under-ice environments. GZP species are also known to aggregate at hydrographic features as a result of their affinities to particular water masses. However, little is known about GZP diversity, abundances and community structure in the Arctic in general, and even less at the sub-mesoscale. Hence, the ICE-Jelly project aims to investigate GZP diversity and small-scale distribution patterns along a sea-ice gradient and at mesoscale and sub-mesoscale spatial scales. We have a focus on particular features such as the halocline, fronts and ice regimes in the marginal ice zone (MIZ). To do so, we combine net catches with optical and environmental DNA (eDNA) surveys and environmental data. These integrative studies proposed will significantly boost our understanding of GZP dynamics, ecology and allow us to improve predictions on the future Arctic ecosystem.

Objectives

In the Arctic, environmental changes are occurring at an unprecedented pace. The Arctic Ocean is undergoing pronounced sea-ice thinning (Krumpen et al., 2015) and a decline of the overall summer sea ice extent, with a prediction of nearly ice-free summers within the next 25 years (Overland & Wang, 2009). There has been a growing influence of warmer Atlantic water, entering the Arctic via the eastern Fram Strait and the Barents Sea, a phenomenon referred to as "Atlantification" (Polyakov et al., 2017). This warm-water inflow carries along nutrients and advected Atlantic-boreal species (Wassmann et al., 2015). As a result, the AO has already experienced noticeable changes in species composition as well as poleward range expansions of species of Atlantic origin (e.g., Neukermans et al., 2018; Schröter et al., 2019; Haug et al., 2017). Hence, a large-scale understanding of Arctic marine biodiversity is particularly pressing. Accurate distribution records and community assessments, combining traditional and molecular methods, are needed to predict and monitor community shifts and potential invaders in the Arctic Ocean (Lacoursière-Roussel et al., 2018).

GZP are fragile, soft-bodied organisms that lack an exoskeleton or hard body parts. It groups together a number of phylogenetically very distant taxa: *ctenophores, scyphomedusae,*

hydromedusae (including colonial *siphonophores*) and pelagic tunicates (e.g. *appendicularians*). In contrast to crustacean zooplankton, relatively little is known about Arctic GZP beyond records of occurrence and regional species lists (e.g., Kosobokova et al., 2011). As a rule, rather than the exception, jellies are discarded from quantitative plankton surveys and when included in pelagic studies, data are limited to coarse taxonomic levels (Geoffroy et al., 2018). Hence, comparable regional abundance data of GZP in the Arctic are missing, let alone temporal datasets over several years to monitor potential gelatinous regime shifts as those witnessed in the Antarctic, with the notorious krill-to-salp shift (Atkinson et al., 2019). Nonetheless, pioneering work with underwater imaging and under-ice trawls showed ctenophores and hydromedusae to be particularly abundant in several Arctic Ocean basins (Raskoff et al., 2005, 2010; Purcell et al., 2010; David et al., 2015). *Appendicularians* are among the highest biomass of non-copepod zooplankton taxa, and thrive at the margins of *polynyas* and at the ice edge (Deibel et al., 2005, 2017). They significantly contribute to vertical carbon export with their discarded houses and faecal pellets (Deibel et al., 2005). These observations further corroborate the importance of this faunal group in the Arctic ecosystem, which may well be a jelly-dominated ecosystem.

How further warming and sea-ice thinning will affect Arctic GZP communities will critically depend on whether dominant species are cold-adaptive or bound to sea ice as habitat, for shelter or for food supply (through the sea-ice algal production). Large populations of jellies, in particular ctenophores, have been observed under the ice in the Fram Strait (PS107, C. Havermans, pers. obs.) and the central Arctic region (MOSAiC ROV videos). We can currently not explain these high abundances under the ice because of a lack of knowledge on Arctic jelly ecology (e.g., behaviour, feeding habits, potential overwintering strategies). Therefore, it is essential to evaluate the role of sea ice in structuring GZP communities and shaping their distributions in order to make reliable predictions on the impact of further sea-ice decline.

Variation in distribution and abundance of GZP often relate to physical water properties and features. GZP are known to aggregate horizontally as a result of their affinities to particular water masses (Graham et al., 2001), with highest densities of GZP often occurring at fronts or halo/thermoclines (Raskoff et al., 2005). Pioneering studies using ROV, SCUBA diving and depth-stratified nets could link species distributions with the complex and multi-origin water layers typical of the AO, characterized by strong discontinuities in temperature and salinity (Raskoff et al., 2005; Purcell et al., 2010). The interaction of warm, salty Atlantic Water and cold, fresher Polar Water, as well as meltwater from sea-ice melt, generates sharp sub-mesoscale fronts (von Appen et al., 2018). Since fronts and eddies are ubiquitous in the near-surface AO, it is important to determine the interaction between physical oceanography and GZP small-scale distributions for determining the environmental niche of the different species and identifying the variation in GZP community composition.

The overarching goal of the ICE-Jelly research programme is to establish a comprehensive baseline knowledge of jelly diversity and distributional patterns and their link to oceanographic patterns and sea ice. We aim to collect species-level GZP data along a sea-ice gradient, from open ocean across the Marginal Ice Zone (MIZ) to the pack ice. We will focus also on the submesoscale, by testing for differences in pelagic community structure along particular oceanographic features such as the halocline, fronts and eddies (see Fig. 10.1). To do so, we apply integrative jelly surveys, combining depth-stratified net sampling with non-invasive methods including environmental DNA (eDNA) and optical (imaging) surveys with the Underwater Vision Profiler (UVP) and video footage under the ice. These surveys will allow us to study how jelly aggregations, distributions and feeding habits change in different regions and water masses, and from open ocean across the Marginal Ice Zone (MIZ) to the pack ice. These datasets of unprecedented spatial resolution will significantly improve our understanding of GZP dynamics, ecology and allow us to improve predictions on future GZP communities.

The objectives of the ICE-Jelly project are:

- Study species richness, community composition and small-scale distributions of GZP and link these to environmental parameters. Species distributions will be assessed vertically and along sea-ice and sub-mesoscale hydrographic gradients – plankton net catches, DNA barcoding, eDNA metabarcoding, UVP surveys, under-ice GoProTM footage;
- Obtain and compare GZP abundance data from different sampling methods across different hydrographic and sea-ice gradients – plankton net catches, UVP surveys;
- Elucidate the trophic role of dominant jellies in local Arctic food webs and their reliance on sea-ice associated food sources – plankton net catches, biomarker and molecular diet analyses;
- Identify GZP “bioregions” based on data from the different sampling methods in the various sampling areas of open water, MIZ, and pack ice – species distribution and community distribution modelling;
- Compare GZP species composition at the same localities over several years and link this to local hydrography and other environmental parameters – eDNA time series at several LTER-HAUSGARTEN stations (2019-2022), plankton net catches.

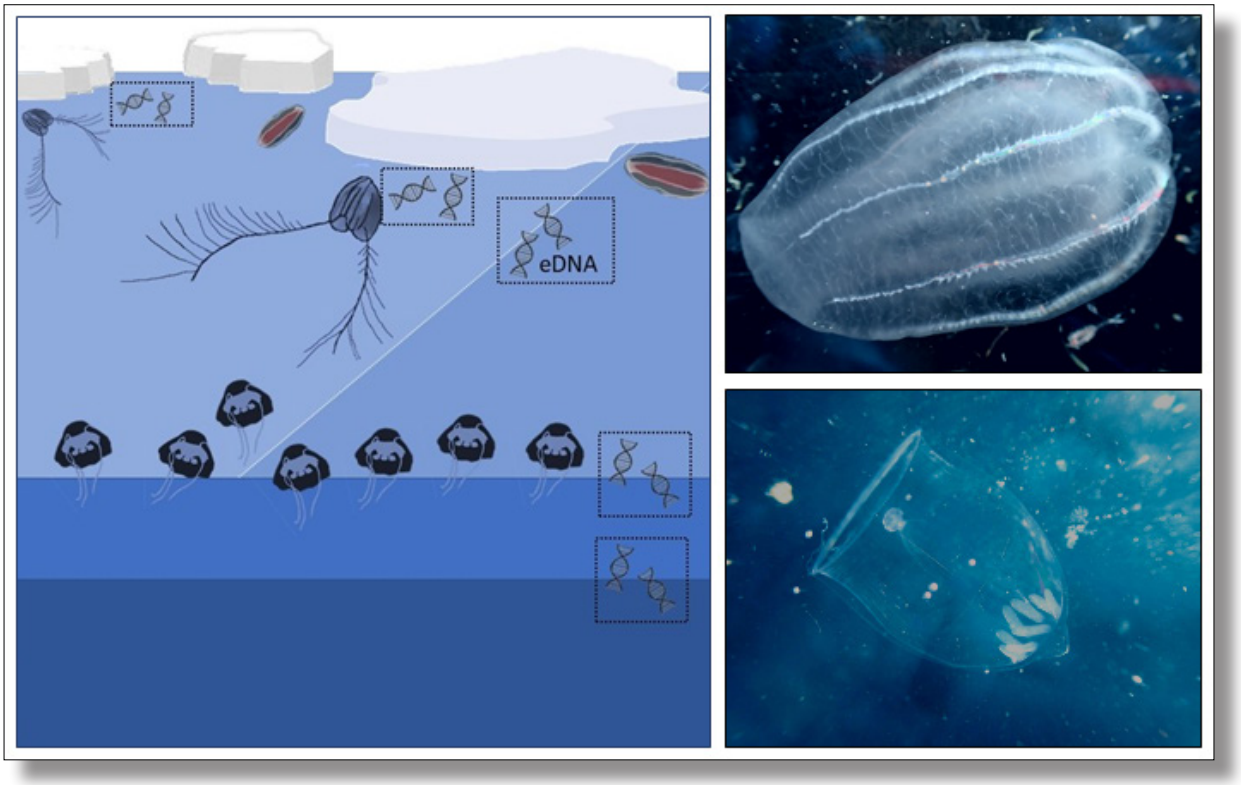

Fig. 10.1: Left: A schematic drawing illustrating the small-scale distributions of GZP we aim to assess with the ICE-Jelly programme (Drawing: Charlotte Havermans)
Right: Arctic GZP species known to be abundant under the ice: the ctenophore Beroe cucumis and the hydrozoan Aglantha digitale (Photos: Charlotte Havermans)

Work at sea

The working area during PS131 consisted of different target regions: i) the West Spitsbergen Current in Fram Strait, ii) the transition from open waters to the MIZ and the pack ice on the Yermak Plateau, iii) the Aurora Vent field iv) the East Greenland Shelf and v) Scoresby Sound. In total, 23 pelagic stations and 13 ice stations were comprehensively sampled for the ICE-Jelly project. Zooplankton were sampled with the Multi-Net at 13 sites, while eDNA samples were collected from CTD casts at 23 pelagic sites, and with a hand Niskin at 11 ice stations. Optical surveys were conducted with the UVP at 58 sites and with the GoPro at all 11 ice stations.

Pelagic sampling during PS131

We conducted Midi-Multinet (Midi-MN) deployments at three LTER-HAUSGARTEN stations (S3, HG-IV, N4), and sampled water at specific depth intervals from the surface to above the seafloor for eDNA studies from the CTD rosette (see Fig. 10.2 and Tab. 10.1). The species diversity revealed with depth-stratified net sampling will be compared with the results of the eDNA analyses of water sampling from the CTD, at a range of corresponding depths. Vertical distribution of smaller-sized GZP will also be characterized with the UVP profiles obtained at CTD stations, with the UVP attached to the CTD rosette. This HAUSGARTEN dataset will allow us to carry on a time series of eDNA characterization over several years (2019 – PS121, 2020 – MSM95, 2021 – PS126), which will allow us to assess inter-annual variation of Arctic GZP communities.

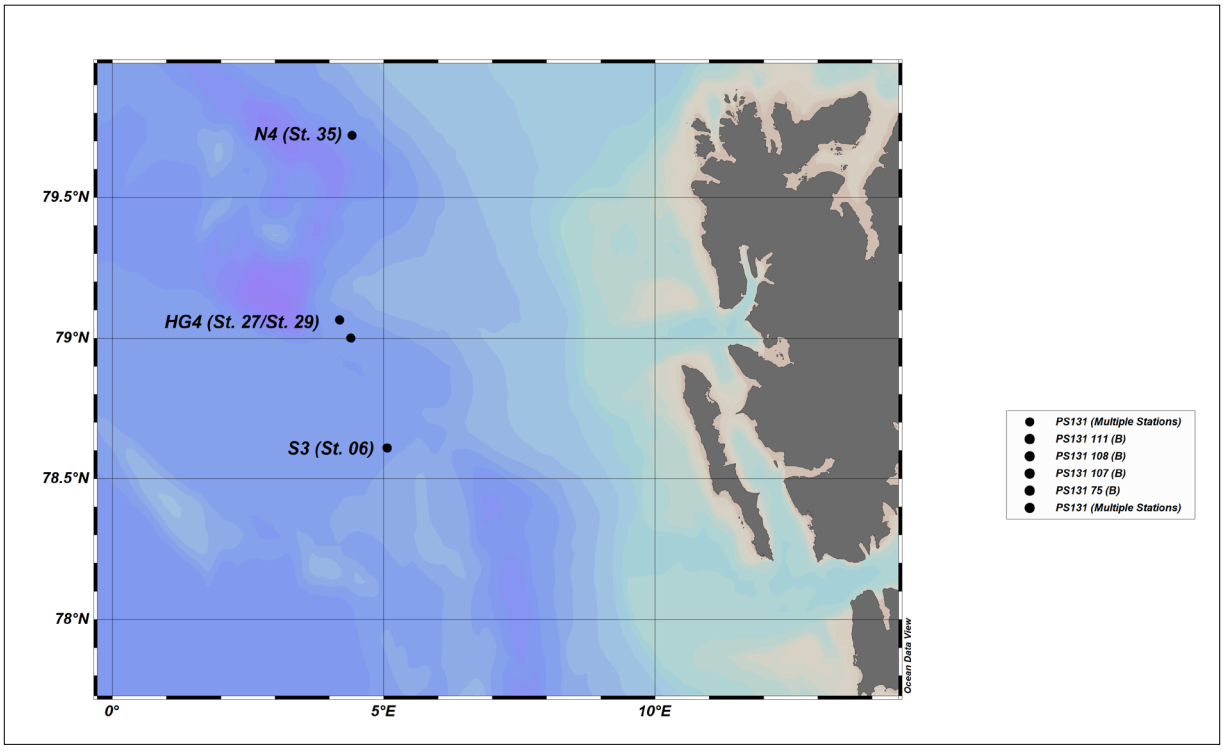

Fig. 10.2: Map of LTER-HAUSGARTEN stations sampled for the ICE-Jelly programme during PS131

In order to investigate small-scale (mesoscale and sub-mesoscale) distributions of GZP and identify potential aggregations of different species according to oceanographic features, sampling has been carried out based on mesoscale features detected with the TopAWI (as described in TopAWI Chapter 2). These included two transects from open water into the MIZ and the second across an ice tongue feature at the edge of the MIZ. The sampling transects were identified based on TopAWI profiles and according to sea-ice distribution patterns. At

these locally identified gradients, we carried out depth-stratified sampling of the shallower layers with Midi-MN deployments where possible, water from the CTDs for eDNA analyses, and UVP surveys (see Tab. 10.1 and Fig 10.3).

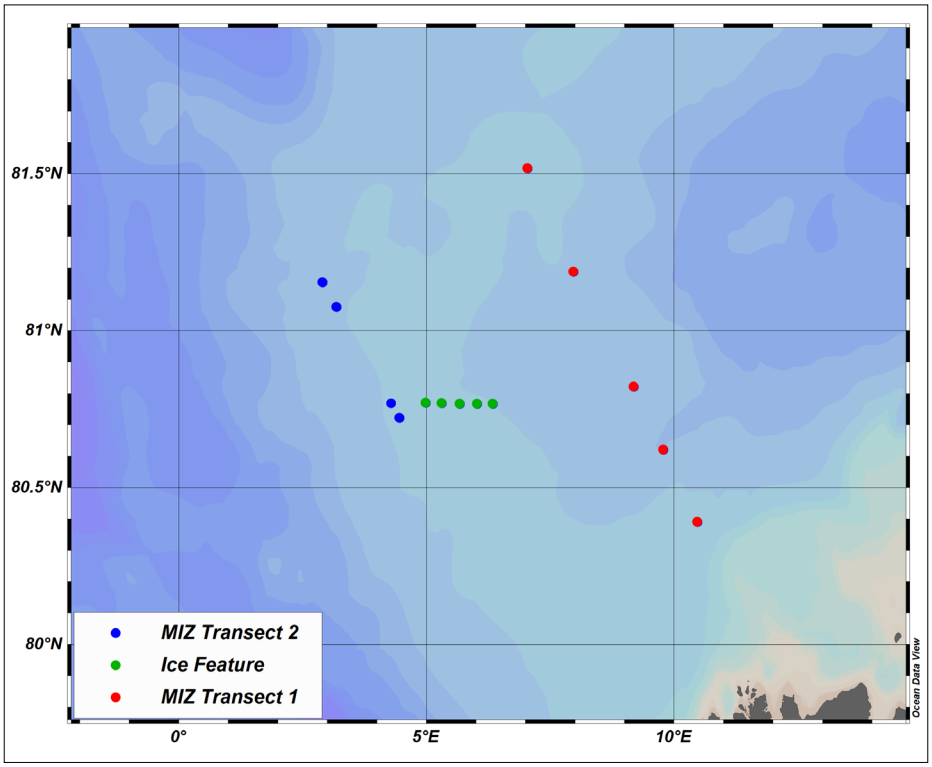

Fig. 10.3: Map of transect stations based on Top-AWI deployments across the MIZ, sampled during the ICE-Jelly programme

Stations on the East Greenland Shelf and coast were also sampled comprehensively with eDNA, UVP and Midi-MN where possible (depending on ice conditions). One LTER-HAUSGARTEN station on the slope of the EG shelf (EGVI), two coastal stations in fast-ice near the 79°N glacier and two station in Scoresby Sound were sampled in this area (see Tab. 10. 1 and Fig. 10. 4). The influences of the East Greenland Current on GZP biodiversity and distribution will be analysed, as well as the differences to the central Fram Strait stations and GZP community composition in Scoresby Sound.

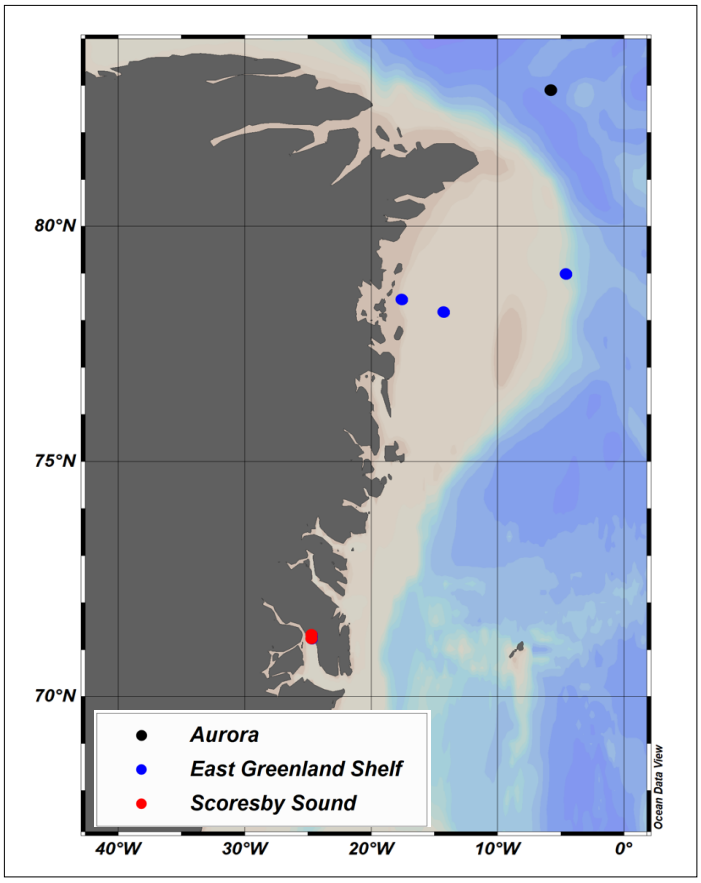

Fig. 10.4: Map of East Greenland, Aurora Vent Field and Scoresby Sound pelagic sites sampled for the ICE-Jelly project

Ice-based work during ICE-Jelly programme

In order to characterize GZP diversity and distribution under the ice; ice stations were conducted on the three focus ice floes (see Chapter 3 describing ice floes) at each of the three visits. Additional ice stations were sampled at the Aurora Vent Field and over the Yermak Plateau (24-hour ice station) (see Fig. 10.5). At all ice stations, water sampling was carried out in through drill holes. The location of the holes was chosen within close vicinity or in the same hole as the under-ice CTD sampling (see Chapter 2 describing ice CTD). Water sampling for eDNA studies was done by deploying a 2.5L Hydrobios Niskin bottle. 6L of water was taken from the under-ice interface and at 5 m depth, and immediately taken back on board to be filtered over 0.2 µm Sterivex filters (2L per filter). We conducted visual surveys in each eDNA ice-hole with a GoProTM camera, in order to capture footage of any GZP aggregations under the ice. At three ice-floe stations (North Floe – visit 3, Middle Floe – visit 3 and the 24-hour station), eDNA samples and GoPro surveys were conducted in three holes (50 m – 100 m apart) across the floe to investigate within-floe variation in eDNA distribution.

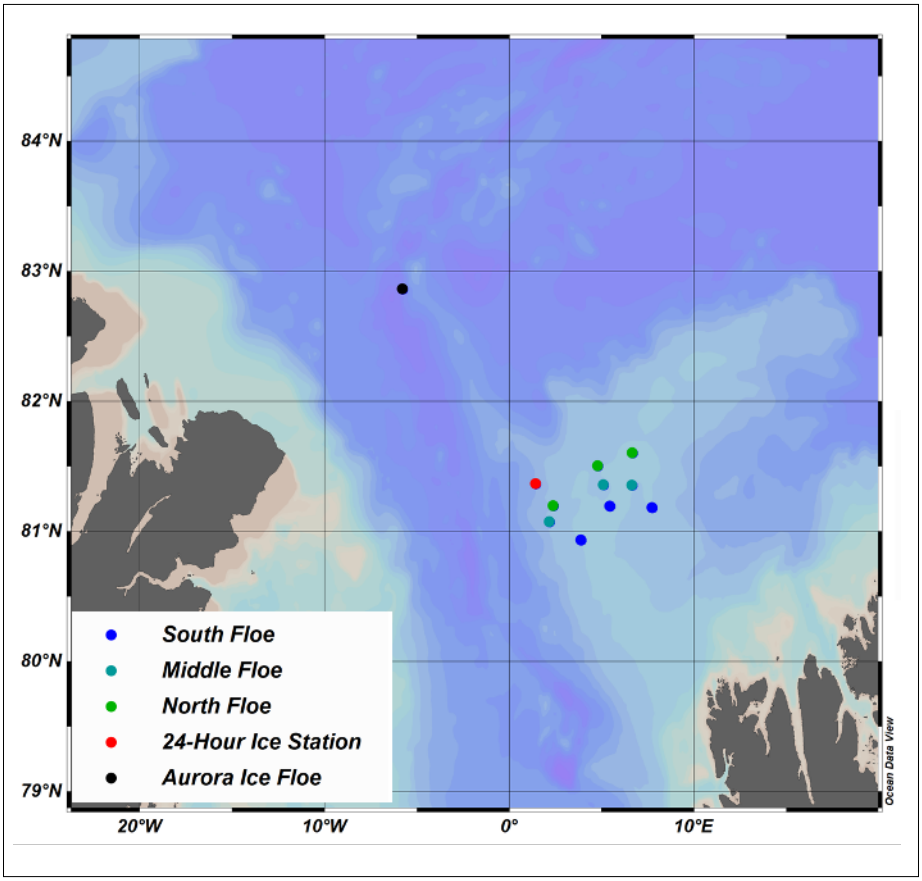

Fig. 10.5: Map of ice stations sampled during the ICE-Jelly programme on PS131

Zooplankton sampling

GZP samples for species identification, molecular and biomarker analyses were collected using Midi-MN deployments. Vertical deployments (0.25 m^2 mouth opening, mesh sizes 100/150 µm) were conducted vertically in the water column. Hauls were made at a speed of 0.5 m/s with five different opening and closing nets for depth-stratified sampling. All catches were immediately sorted in a cool lab into different taxonomic groups. GZP specimens were individually photographed, identified to species level when possible, and frozen at -80°C or preserved in 96% undenatured ethanol. Very abundant GZP taxa were preserved in bulk with 96% undenatured ethanol. Abundances will be calculated based on the volume of water sampled and the number of jellies counted per species. Other macrozooplankton species, including *amphipods* (e.g. *Themisto spp*), *chaetognaths*, and *pteropods* were also isolated and subsequently preserved in ethanol (see Fig. 10.5).

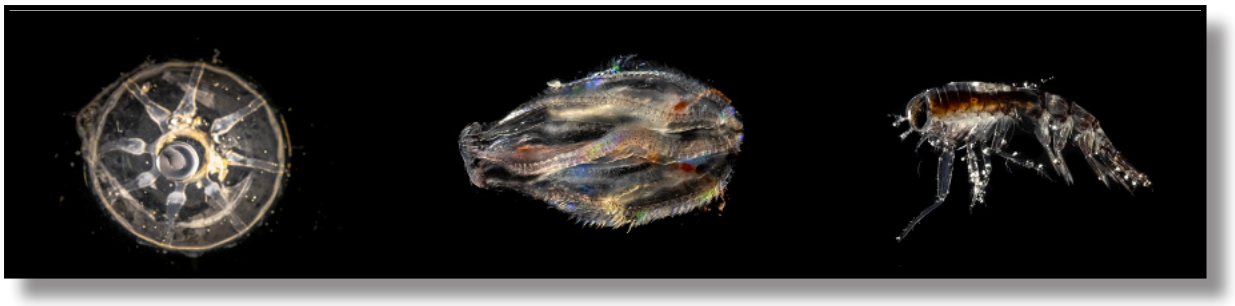

Fig 10.6. Zooplankton catches from Midi-MN during PS131;
left to right: Botrynema brucei, cyddipid ctenophore, Themisto libellula (Photos: Mario Hoppmann)

eDNA metabarcoding analyses of water samples

We sampled water from the CTD rosette for eDNA analyses at 23 stations across Fram Strait, the MIZ and Greenland (see Tab. 10.1) and 11 ice stations (see Tab. 10.2). These eDNA samples will used to study zooplankton (metazoan) diversity, with strong focus on GZP diversity and distribution. This will be achieved through DNA metabarcoding using universal primer sets for the mitochondrial cytochrome c oxidase subunit I (COI) marker and the 18S rRNA nuclear marker. In order to achieve an eDNA pelagic time series at the HAUSGARTEN stations S3, HG-IV, N4, we sampled water from four different depths: surface, Chlorophyll maximum layer (Chl-a max), 50 m, 100 m, 200 m, 400 m, 500 m, 750 m, 1,000 m, 1,300 m, 1,600 m, 2,000 m, 2,500 m and above bottom. At both the pelagic station and the transects across the features, we sampled water from the rosette at shallower depths, ranging from the surface to 200 m (see Tab. 10.1). At these stations where the Midi-MN was deployed and UVP casts were obtained, we will be able to compare the pelagic diversity and community structures revealed by eDNA with physical and optical data. At the under-ice stations, eDNA results will be compared with optical data sets collected during GoPro deployments in the same ice hole the water was collected in. For each depth at every station, triplicates of 2L were sampled and filtered over 0.2 µm Sterivex filters. A blank of MilliQ water was included for each filtration to test for potential contamination.

Optical profiles with the Underwater Vision Profiler and underwater video camera

The Underwater Vision Profiler (UVP) images, enumerates and measures zooplankton (>0.5 mm), as well as particle aggregates (>60 µm) such as marine snow, quantifying their vertical distribution in situ (Picheral et al., 2010) (see Fig. 10.6). It was mounted on the CTD-rosette, imaging the plankton during its descent, hence each image is associated with the environmental variables at corresponding depths. This allows a quantitative assessment of smaller-sized GZP abundances. The UVP consists of a pressure-safe housing and two LED lights, coupled to a camera. It efficiently images smaller-sized plankton and particles of ca. 0.1 to 10 mm, each time illuminating a volume of approximately 1L, when being deployed vertically in the water column (Picheral et al., 2010). Six to eleven images are taken per second, which are immediately processed during the downcast, i.e. objects are counted, sized and saved, together with depth and other information.

At the sea-ice stations, a GoProTM underwater camera was immediately before or after the water was sampled. These deployments ranged from 2 minutes to 45 minutes, depending on ice and temperature conditions. Where possible, the GoProTM was deployed in nearby ice holes and over the edge of the ice floe. The maximum depth of the deployments was 4 m under the ice. Jellies observed on these under-ice visual surveys will be used to validate eDNA results.

Tab. 10.1: ICE-Jelly pelagic sampling on board PS131

Site	Station	Sampling	Depth intervals
S3	006/01	Multinet-Midi vertical	0-50m, 50-100m, 100-300m, 300-500m, 500-1500m
	006/05	CTD rosette for eDNA	Surface, Chl-a max, 50m, 100m, 200m
	006/01	CTD rosette for eDNA	400m, 500m, 1000m, 1300m, 1600m, 2000m, 2250m
	006/01, 006/05	UVP casts for optical surveys	Surface – 2278m
Surface – 250m			
HG-IV	027/03	Multinet-Midi vertical	0-50m, 50-100m, 100-300m, 300-500m, 500-1500m
	027/03	CTD rosette for eDNA	400m, 500m, 1000m, 1300m, 1600m, 2000m, 2250m, Above Bottom
	029/01	CTD rosette for eDNA	Surface, Chlorophyll maximum, 50m, 100m, 200m
	027/03, 029/01	UVP casts for optical surveys	Surface – 2402m
Surface – 250m			
N4	035/04	Multinet-Midi vertical	0-50m, 50-100m, 100-300m, 300-500m, 500-1500m
	035/01	CTD rosette for eDNA	400m, 500m, 1000m, 1300m, 1600m, 2000m, 2250m, Above Bottom
	035/06	CTD rosette for eDNA	Surface, Chlorophyll maximum, 50m, 100m, 200m
	035/01		
035/06	UVP casts for optical surveys	Surface – 2677m	
Surface – 250m			
Top-AWI transect 1, Station 1	056/04	Multinet-Midi vertical	0-50m, 50-100m, 100-200m, 200-600m, 600-1200m
	056/02	CTD rosette for eDNA	Surface, Chl-a max, 50m, 100m, 200m
	056/02	UVP casts for optical surveys	Surface – 500m
Top-AWI transect 1, Station 2	057/04	Multinet-Midi vertical	0-50m, 50-100m, 100-200m, 200-300m, 300m-400m
	057/02	CTD rosette for eDNA	Surface, Chl-a max, 50m, 100m, 200m
	057/02	UVP casts for optical surveys	Surface – 472m
Top-AWI transect 1, Station 3	061/04	Multinet-Midi vertical	0-50m, 50-100m, 100-200m, 200-300m, 300-650m
	061/02	CTD rosette for eDNA	Surface, Chl-a max, 50m, 100m, 200m

Site	Station	Sampling	Depth intervals
	061/02	UVP casts for optical surveys	Surface – 500m
Top-AWI transect 1, Station 4	065/03	Multinet-Midi vertical	0-50m, 50-100m, 100-200m, 200-300m, 300m-400m
	065/01	CTD rosette for eDNA	Surface, Chl-a max, 50m, 100m, 200m
	065/01	UVP casts for optical surveys	Surface – 476m
Top-AWI transect 1, Station 5	069/04	Multinet-Midi vertical	0-50m, 50-100m, 100-200m, 200-300m, 300m-550m
	069/08	CTD rosette for eDNA	Surface, Chl-a max, 50m, 100m, 200m
	069/08	UVP casts for optical surveys	Surface – 500m
Aurora Vent Field	075/07	CTD rosette for eDNA	Surface, Chl-a Max, 50m, 100m, 200m, 400m, 600m, 750m, 1000m, 1500m, 2000m, 2600m, 3000m, 3500m, Above Bottom
	075/07	UVP cast UVP casts for optical surveys	Surface – 3943m
Top-AWI transect 2, Station 1	087/05	Multinet-Midi vertical	0-50m, 50-100m, 100-200m, 200-300m, 300-750m
	087/01	CTD rosette for eDNA	Surface, Chl-a max, 50m, 100m, 200m
	087/01	UVP casts for optical surveys	Surface – 500m
Top-AWI transect 2, Station 2	088/01	CTD rosette for eDNA -Midi vertical	Surface, Chl-a max, 50m, 100m, 200m
	088/01	UVP casts for optical surveys	Surface – 500m
Top-AWI transect 2, Station 3	091/04	Multinet-Midi vertical	0-50m, 50-100m, 100-200m, 200-300m, 300-650m
	091/01	CTD rosette for eDNA	Surface, Chl-a max, 50m, 100m, 200m
	091/01	UVP casts for optical surveys	Surface – 500m
Top-AWI transect 2, Station 4	094/04	Multinet-Midi vertical	0-50m, 50-100m, 100-200m, 200-300m, 300-650m
	094/01	UVP casts for optical surveys	Surface – 506m
Mesoscale ice feature transect, Station 1	096/01	CTD rosette for eDNA	Surface, Chl-a max, 50m
	096/01	UVP casts for optical surveys	Surface – 250m
Mesoscale ice feature transect, Station 2	097/01	CTD rosette for eDNA	Surface, Chl-a max, 50m

Site	Station	Sampling	Depth intervals
	097/01	UVP casts for optical surveys	Surface – 250m
Mesoscale ice feature transect, Station 3	098/01	CTD rosette for eDNA	Surface, Chl-a max, 50m
	098/01	UVP casts for optical surveys	Surface – 250m
Mesoscale ice feature transect, Station 4	100/01	CTD rosette for eDNA	Surface, Chl-a max, 50m
	100/01	UVP casts for optical surveys	Surface – 250m
Mesoscale ice feature transect, Station 5	101/01	CTD rosette for eDNA	Surface, Chl-a max, 50m
	101/01	UVP casts for optical surveys	Surface – 250m
EGI-I	107/03	Multinet-Midi vertical	0-50m, 50-100m, 100-200m, 200-500m, 500-900m
	107/05	CTD rosette for eDNA	Surface, Chl-a max, 50m, 100m, 200m
	107/05	UVP casts for optical surveys	Surface – 956m
EG Coast 1	108/02	Multinet-Midi vertical	0-50m, 50-100m, 100-200m, 200-300m, 300-400m
	108/01	CTD rosette for eDNA	Surface, Chl-a max, 50m, 100m, 200m
	108/01	UVP casts for optical surveys	Surface – 250m
EG Coast 2	111/01	CTD rosette for eDNA	Surface, Chl-a max, 50m, 100m, 200m
	111/01	UVP casts for optical surveys	Surface – 351m
Scoresby Sound 1	114/03	CTD rosette for eDNA	Surface, Chl-a Max, 50m, 100m, 200m, 400m, 600m, Above Bottom
	114/03	UVP UVP casts for optical surveys	
Scoresby Sound 2	116/01	CTD rosette for eDNA	Surface, Chl-a Max, 50m, 100m, 200m, 400m, 600m, 800m, 1000m, Above Bottom
	116/01	UVP casts for optical surveys	Surface – 1196m

Tab. 10.2: ICE-Jelly sea-ice sampling on board PS131

Site	Station	Site description	Deployments
North Floe, Visit 1	047/01	Single ice hole	

Site	Station	Site description	Deployments
	Hand Niskin bottles for eDNA (Under ice, 5m) GoProTM camera deployment		
South Floe, Visit 1	048/01	Single ice hole	
	Hand Niskin bottles for eDNA (Under ice, 5m) GoProTM camera deployment		
Middle Floe, Visit 1	049/01	Single ice hole	
	Hand Niskin bottles for eDNA (Under ice, 5m) GoProTM camera deployment		
North Floe, Visit 2	067/01	Single ice hole	
	Hand Niskin bottles for eDNA (Under ice, 5m) GoProTM camera deployment		
South Floe, Visit 2	068/01	Single ice hole	
	Hand Niskin bottles for eDNA (Under ice, 5m) GoProTM camera deployment		
Middle Floe, Visit 2	088/01	Single ice hole	
	Hand Niskin bottles for eDNA (Under ice, 5m) GoProTM camera deployment		
North Floe, Visit 3	089/01	Three ice holes on floe, separated by 50-100m distance	Hand Niskin bottles for eDNA (Under ice, 5m) GoProTM camera deployment
South Floe, Visit 3	092/01	Single ice hole	
	Hand Niskin bottles for eDNA (Under ice, 5m) GoProTM camera deployment		
Middle Floe, Visit 3	093/01	Three ice holes on floe, separated by 50-100m distance	Hand Niskin bottles for eDNA (Under ice, 5m) GoProTM camera deployment
24-hour Ice station	084/01	Three ice holes on floe, separated by 50-100m distance	Hand Niskin bottles for eDNA (Under ice, 5m) GoProTM camera deployment
Aurora Ice Floe	072/02	Single ice hole	
	Hand Niskin bottles for eDNA (Under ice, 5m) GoProTM camera deployment		

Preliminary (expected) results

Diversity, abundances and distribution patterns of gelatinous zooplankton from net catches

We sampled GZP with the Midi-MN at 13 different stations at depths ranging from surface to 1500m. Individuals will have their morphological identifications confirmed in the home laboratory, and uncertain identifications will be validated with molecular barcoding (COI or 18s markers). Abundances will be calculated based on the number of individuals per volume of water filtered through the MN (flow meter). These results will then be compared between stations and linked to environmental gradients such as temperature and salinity. The most abundant species encountered during this cruise and at most respective stations were the hydrozoan Aglantha digitale, the hydrozoan *Sminthea arctica* and the siphonophore *Dimophyes arctica* (see Fig. 10.1). Based on preliminary results, the East Greenland Shelf stations exhibited more species richness than the other stations, including the hydrozoan species *Aeginopsis laurentii* and the scyphozoan genus *Atolla*. More than 300 GZP were collected during this cruise, the majority of which was photographed and frozen or preserved individually. Many more bulk samples of the most common species were also collected and will be counted in the home laboratory. Species composition and abundance data will be linked with oceanographic features and sea ice patterns in order to identify key drivers for distribution patterns. The results on diversity and abundances from net catches will be compared with those obtained with eDNA analyses and optical datasets.

eDNA metabarcoding analyses

eDNA metabarcoding will be carried out using universal primer sets, which could include i) the mitochondrial COI (Leray primer), ii) the 18S rDNA universal primer sets (V1-V2 or V4) and 16S primers. As these universal primer sets target metazoan diversity, our analyses will allow to compare pelagic communities at the vertical and spatial scale, with a particular focus on GZP. The necessary DNA will be isolated in the home laboratory, from the Sterivex filters used for water filtrations throughout the cruise. The efficiency of eDNA to provide semi-quantitative estimates of species will also be assessed, by comparing the relative read abundances of the metabarcoding analyses with abundance data obtained from optical datasets and net casts for different depths.

eDNA time series in Fram Strait

Repeated eDNA sampling has been carried out in Fram Strait at several of the LTER-HAUSGARTEN stations, which has been continued during PS131. These samples have been collected by collaborators (2019 by H-J Hoving on PS121, 2020 by V. Merten on MSM95) and in 2021 by the ARJEL team during PS126 (FramJelly project). Comparison of community composition data obtained from eDNA metabarcoding analyses (described above) will allow us to identify interannual variation, as so far, our sample set spans over four consecutive years, and potentially link this to varying environmental conditions (e.g., sea-ice cover). These data will also contribute to modelling efforts and may serve as a baseline for future long-term monitoring of GZP range shifts, in the context of the FRAM initiative.

Optical datasets

Images obtained with the UVP are automatically screened with a custom software routine to extract objects larger than 100 pixels (ca. 0.5 mm); most of the organisms cannot be reliably identified below that size because of the low resolution of the image (Stemman et al., 2008). Further processing will be done with the ZooProcess software (Gorsky et al., 2010), in order to calculate morphological descriptors (e.g., size, gray level distribution) for each object/specimen (Vilgrain et al., 2021). Images, their metadata, and morphological descriptors will be stored in

the EcoTaxa web application (https://ecotaxa.obs-vlfr.fr/; Picheral et al., 2017). Morphological descriptors will be used to train a random forest (RF) algorithm (Breiman, 2001) that suggests a taxonomic classification for each object into final categories. The categories comprising GZP will be selected for validation or correction by visual (human) annotation. This will be followed by a numerical analysis including vertical binning of each profile and assessment of variability in the community structure, using multidimensional-scaling (MDS) analysis and the ANOSIM procedure (Clarke & Warwick, 2001) to assess the significance of the within site variability against the among-sites variability.

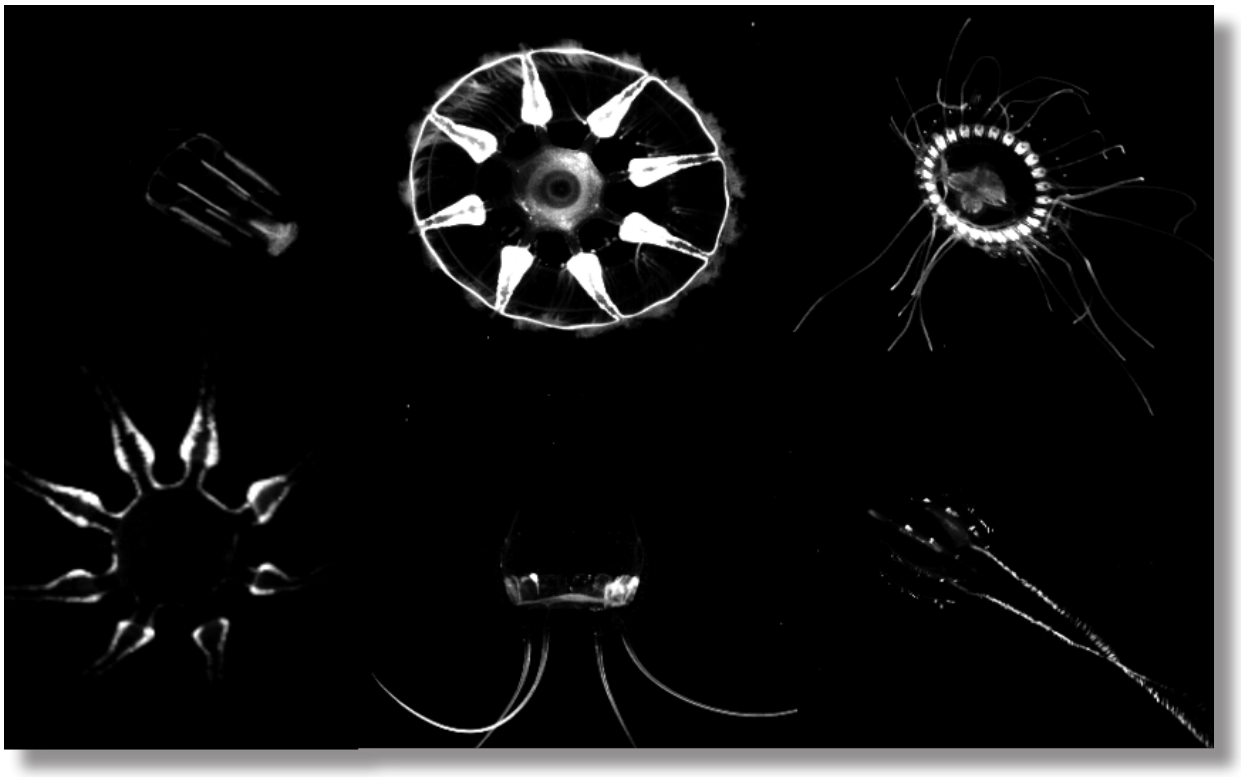

Fig 10.7: Gelatinous zooplankton taxa captured on the UVP (not to scale). Top left to Bottom right: Aglantha digitale, Botrynema sp., Atolla sp., Hydrozoan, Aeginopsis laurentii, cyddipid ctenophore

Joint species distribution modelling

Based on the data from the nets and optical datasets, (joint) species distribution models will be conducted using the "HMSC" (Hierarchical modelling of Species Communities) package following Ovaskainen et al. (2020). Hierarchical Modelling of Species Communities (HMSC), is a hierarchical joint species distribution model with Bayesian inference. This modelling framework will allow us, where possible, to link data on species abundance (or presence/absence), ecological conditions, species traits, and phylogenetic relationships to community-assembly processes (Ovaskainen et al., 2020). The HMSC package will allow us to perform predictions over continuous environmental gradients (Ovaskainen et al., 2020) and further perform spatial predictions over unsampled areas based on the oceanographic models/atlases. Grouping the predicted communities in a discrete set of bioregions will allow us to shed light on the variation in community composition. In addition, we will also apply model-based approach Regions of Common Profile (RCP), which allows us to identify bioregions in a probabilistic form (Foster et al., 2013). A combination of the HMSC and RCP approaches will allow us to determine whether open water, marginal ice, and pack ice zones can be treated as distinct biogeographical regions of GZP. The trained models will be coupled with climate

change scenarios (from CMIP6) that will allow us to forecast potential changes in ecosystems, predict future range expansions and identify climate change winners and losers among the jelly species and bioregions in the surveyed regions.

DNA barcoding and phylogeography

A subset of the GZP specimens sampled will be genetically characterized (or “barcoded”) by sequencing different markers, depending on the taxon, such as the COI, 16S rDNA and 18S rDNA. By doing so, we will complement existing reference databases and our own Fram Strait barcode dataset (based on PS126 samples) and assess the regional genetic variability of morphospecies. For widespread species, we will combine these sequence datasets with sequences of species collected elsewhere in the Arctic region during previous sampling campaigns such as, amongst others, the HE560 (2020) and HE605 (2022) expeditions targeting Svalbard fjords, and PS122 (MOSAiC) in the central Arctic. These will allow to carry out phylogeographic studies on key Arctic GZP species, as well as on Atlantic species that are commonly advected into and abundant in the Arctic Ocean.

Molecular diet and biomarker analyses

In order to investigate the importance of sea ice in terms of food supply (ice-associated carbon sources) and determine the variation in prey spectrum under different environmental conditions, we will carry out biomarker and molecular diet analyses. The results of these analyses on dominant jelly species will allow us to elucidate longer-term dietary signals (including those characteristic of ice algae versus pelagic flagellates with marker fatty acids) as well as a full characterization of prey spectrum analysis at species level (DNA metabarcoding of gastric pouch contents). For the molecular analyses, DNA will be isolated from the stomach contents in the AWI laboratories, and investigated with DNA metabarcoding using universal primers, similar to the eDNA metabarcoding procedure described above.

Data management

Zooplankton samples will be archived and stored at the AWI. DNA extracts of GZP and other zooplankton as well as eDNA filters will be stored at -80°C in the AWI for up to ten years after publication of the results (according to the DFG guidelines for good scientific practice). A voucher collection of GZP specimens, linked to their DNA extracts by unique sample identifiers, will be kept in a repository at the AWI. Geo-referenced datasets including species inventories and distribution records from net catches will be submitted to the World Data Center PANGAEA Data Publisher for Earth & Environmental Science (https://www.pangaea.de) as soon as the data are available (within two years after the cruise at the latest), possibly with an embargo period until publications have been finalized. By default, the CC-BY license will be applied.

Acquired optical datasets will be archived in IT storage infrastructures of the AWI, and metadata will be made accessible in PANGAEA, within six months after completion of the expedition. The image datasets from the UVP will be submitted to EcoTaxa (https://ecotaxa.obs-vlfr.fr/), and released as soon as the results are published (up to three years after the expedition). Molecular data (DNA data) will be archived, published and disseminated within one of the repositories of the International Nucleotide Sequence Data Collaboration (INSDC, www.insdc.org), comprising EMBL-EBI/ENA, GenBank and DDBJ. Results on eDNA metabarcoding analyses will be published in peer-reviewed journals within three years after the cruise. Any other data will be submitted to an appropriate long-term archive that provides unique and stable identifiers for the datasets and allows open online access to the data.

This expedition was supported by the Helmholtz Research Programme "Changing Earth – Sustaining our Future" Topic 6, Subtopic 1”.

In all publications based on this expedition, the **Grant No. AWI_PS131_10** will be quoted and the following publication will be cited:

Alfred-Wegener-Institut Helmholtz-Zentrum für Polar- und Meeresforschung (2017) Polar Research and Supply Vessel *Polarstern* Operated by the Alfred-Wegener-Institute. Journal of large-scale research facilities, 3, A119. http://dx.doi.org/10.17815/jlsrf-3-163.

References

von Appen WJ, Wekerle C, Hehemann L, Schourup-Kristensen V, Konrad C, Iversen M (2018) Observations of a submesoscale cyclonic filament in the marginal ice zone. Geophysical Research Letters.

Atkinson A, Hill SL, Pakhomov EA, Siegel V, Reiss CS, Loeb VJ, Steinberg DK, Schmidt K, Tarling GA, Gerrish L, Sailley SF (2019) Krill (*Euphausia superba*) distribution contracts southward during rapid regional warming. Nature Climate Change 9:142-147.

Breiman L (2001) Random forests. Machine Learning 45:5-32.

Clarke KR. Warwick R (2001). Change in Marine Communities: An Approach to Statistical Analysis and Interpretation, 2nd edn. Ntural Environmental Research Council, Plymouth, UK.

David C, Lange B, Rabe B, Flores H (2015) Community structure of under-ice fauna in the Eurasian central Arctic Ocean in relation to environmental properties of sea-ice habitats. Marine Ecology Progress Series, 522:15-32.

Deibel D, Saunders PA, Acuna JL, Bochdansky AB, Shiga N, Rivkin RB (2005) The role of appendicularian tunicates in the biogenic carbon cycle of three Arctic polynyas. In: Gorsky G, Youngbluth MJ, Deibel D (eds) Reponse of marine ecosystems to global change: Ecological impact of appendicularians. Gordon and Breach, Paris, pp. 327-356.

Deibel D, Saunders P, Stevens C (2017) Seasonal phenology of appendicularian tunicates in the North Water, northern Baffin Bay. Polar Biology, 40:1289-1310.

Doyle TK, Houghton JDR, McDevitt R, Davenport J, Hays GC (2007) The energy density of jellyfish: estimates from bomb-calorimetry and proximate consumption. Journal of Experimental Marine Biol ogy and Ecology, 343:239-252.

Foster SD, Givens GH, Dornan GJ, Dunstan PK, Darnell R (2013) Modelling biological regions from multi-species and environmental data. Environmetrics, 24(7):489-499.

Geoffroy M, Berge J, Majaneva S, Johnsen G, Langbehn TJ, Cottier F, Mogstad AA, Zolich A, Last K (2018) Increased occurrence of the jellyfish Periphylla periphylla in the European high Arctic. Polar Biology, 41:2615-2619.

Graham WM, Pagès F, Hamner WM (2001) A physical context for gelatinous zooplankton aggregations: a review. Hydrobiologia 451: 199-212.

Hays GC, Doyle TK, Houghton JD (2018) A paradigm shift in the trophic importance of jellyfish? Trends in Ecology and Evolution, 33:874-884.

Haug T, Bogstad B, Chierci M, Gjosaeter H, Hallfredsson EH, Age S, Hoines A, Hoel H, Ingvaldsen RB, Jorgensen L, Knutsen T, Loeg H, Naustvoll LJ Rottingen I, Sunnana K (2017) Future harvest of living resources in the Arctic Ocean north of the Nordic and Barents Seas: a review of possibilities and constraints. Fisheries Research, 188:38-57.

Hosia A, Falkenhaug T, Baxter EJ, Pagès F (2017) Abundance, distribution and diversity of gelatinous predators along the northern Mid-Atlantic Ridge: A comparison of different sampling methodologies. PLoS ONE, 12:e0187491.

Kosobokova KN, Hopcroft RR, Hirche HJ (2011) Patterns of zooplankton diversity through the depths of the Arctic's central basins. Marine Biodiversity, 41:29-50.

Krumpen T, Gerdes R, Haas C, Hendricks S, Herber A, Selyuzhenok V, Smedsrud L, Spreen G (2015) Recent summer sea ice thickness surveys in the Fram Strait and associated volume fluxes. The Cryosphere Discussions, 9: 5171-5202.

Lacoursière-Roussel A, Howland K, Normandeau E, Grey EK, Archambault P, Deiner K, Lodge DM, Hernandez C, Leduc N, Bernatchez L (2018) eDNA metabarcoding as a new surveillance approach for coastal Arctic biodiversity. Ecology and Evolution, 8:7763–7777.

Licandro P, Blackett M, Fischer A, Hosia A, Kennedy J, Kirby RR, Raab K, Stern R, Tranter P (2015) Biogeography of jellyfish in the North Atlantic, by traditional and genomic methods. Earth System Science Data, 7:173-191.

Neukermans G, Oziel L, Babin M (2018) Increased intrusion of warming Atlantic water leads to rapid expansion of temperate phytoplankton in the Arctic. Global Change Biology. https://doi.org/10.1111/gcb.14075.

Ovaskainen O, Abrego N (2020) Joint species distribution modelling: with applications in R. Cambridge University Press.

Overland JE & Wang M (2009) A sea ice free summer Arctic within 30 years? Geophysical research letters, 36(7).

Picheral M, Guidi L, Stemmann L, Karl DM, Iddaoud G, Gorsky G (2010) The underwater vision profiler 5: An advanced instrument for high spatial resolution studies of particle size spectra and zooplankton: Underwater vision profiler. Limnology and Oceanography Methods, 8:462-473.

Picheral M, Colin S, Irisson JO (2017) EcoTaxa, a tool for the taxonomic classification of images. http://ecotaxa.obs-vlfr.fr.

Polyakov, IV, Pnyushkov, AV, Alkire MB, Ashik IM, Baumann TM, Carmack EC, Goszczko I, Guhrie J, Ivanov V, Kanzow T, Kirshfield R (2017) Greater role for Atlantic inflows on sea-ice loss in the Eurasian Basin of the Arctic Ocean. Science, 356(6335):285-291

Purcell E, Hopcroft RR, Kosobokova KN, Whitledge TE (2010) Distribution, abundance, and predation effects of epipelagic ctenophores and jellyfish in the western Arctic Ocean. Deep Sea Research II: Topical Studies in Oceanography, 57:127-135.

Raskoff KA, Hopcroft RR, Kosobokova KN, Youngbluth MJ, Purcell JE (2010) Jellies under ice: ROV observations from the Arctic 2005 Hidden Ocean Expedition. Deep-Sea Res. II, 57:111-126.

Raskoff KA, Purcell JE, Hopcroft RR (2005) Gelatinous zooplankton of the Arctic Ocean: in situ observations under the ice. Polar Biol., 28:207-217.

Schröter F, Havermans C, Kraft A, Knüppel N, Beszczynska-Moeller A, Bauerfeind E, Nöthig EM (2019) Evidence of continuing presence of a temperate amphipod in the Fram Strait based on sediment trap time series. Front Mar Sci, 6:311.

Stemmann L, Hosia A, Youngbluth MJ, Soiland H, Picheral M, Gorsky G (2008) Vertical distribution (0–1000m) of macrozooplankton, estimated using the Underwater Video Profiler, in different hydrographic regimes along the northern portion of the Mid-Atlantic Ridge. Deep Sea Res Part 2 Top Stud Oceanogr., 55:94-105.

Vilgrain L, Maps F, Picheral M, Babin M, Aubry C, Irisson JO, Avata SD (2021) Trait-based approach using in situ copepod images reveals contrasting ecological patterns across an Arctic ice melt zone. Limnology & Oceanography. https://doi.org/10.1002/lno.11672.

Wassmann P (2015) Overarching perspectives of contemporary and future ecosystems in the Arctic Ocean. Progress in Oceanography, 139:1-12.

Weydmann A, Carstensen J, Goszczko I, Dmoch K, Olszewska A, Kwasniewski S (2014) Shift towards the dominance of boreal species in the Arctic: Inter-annual and spatial zooplankton variability in the West Spitsbergen Current. Mar Ecol Progr Ser, 501:41-52.

11. GEODETIC-GLACIOLOGICAL INVESTIGATION OF ZACHARIAE ISSTRØM, NORTH-EAST GREENLAND

Katrina Bartek[1], Erik Loebel[2]
Not on board:
Mirko Scheinert[2], Matthias Braun[1]

[1]DE. FAU
[2]DE. TU-Dresden

Grant-No. AWI_PS131_09

Objectives

The Greenland Ice Sheet (GrIS) is sensitive to changes in atmospheric and oceanic conditions that occur as a consequence of climate change. Meltwater percolates into and drains the glaciers and finally enters the ocean which influences both global and regional sea levels as well as oceanic circulation patterns. While the mass balance was still close to equilibrium in the 1990s, significant mass losses set in thereafter, reaching values above 300 Gt/a in the years 2010 to 2012 and weakening slightly again in the following years (Shepherd et al. 2019, Pörtner et al. 2021). In the period 2005 – 2015, the GrIS alone contributed to about 20 % of global mean sea level rise. About half of the mass decreases resulted from a decrease in the surface mass balance (SMB) and half to an acceleration of glacier flow (Shepherd et al. 2019, Mouginot et al. 2019).

In the working area, the ice sheet is dominated by the Northeast Greenland Ice Stream (NEGIS), which is devided into the three main streams Nioghalvfjerdsbræ, Zachariae Isstrøm and Storstrømmen. Since the beginning of the 21st century, dynamically induced mass loss has been observed for Nioghalvfjerdsbræ and Zachariae Isstrøm (about 10 Gt/a between April 2006 and April 2012, Khan et al. 2014). The glacier tongue of Nioghalvfjerdsbræ lost 30 % of its thickness between 1999 – 2014 (Mayer et al. 2018). Even greater mass losses occurred at Zachariae Isstrøm. Mouginot et al. (2015) describes the further accelerated retreat of this glacier since 2012 as a result of the extensive dissolution of its offshore ice shelf.

These ice mass changes occurring over the course of glaciation history, especially since the last glacial maximum, cause a glacial isostatic adjustment (GIA) of the solid Earth (Whitehouse et al. 2018, Caron et al. 2018). Today, the GIA effect is reflected in a long-term linear trend, with the effective elastic lithosphere thickness and upper mantle viscosity being crucial for the focusing and decay behaviour, respectively. In addition, there is an instantaneous response to changes in ice loading on short time scales which may be in the same order of magnitude as, or even larger than the GIA effect. The combined effect of GIA and present-day deformation can be measured by permanent and/or repeated geodetic GNSS recordings with an accuracy at the level of 1 mm/a (Kappelsberger et al. 2021).

Temporal variations of supraglacial lakes are an important indication of the meltwater processes. Knowing the lake volume, it is possible to better quantify the temporal dynamics of meltwater input to the glacier bed and ultimately also to the ocean. While their area can be measured quite well based on time series from optical and radar satellite missions (Hochreuther et al. 2021), the lake depth is still difficult to retrieve. Lake depth measurements are required to integrate this information with the lake area for an estimate of the melt water volume. Together

with the drainage geometry and system, this enables to provide information where and how much melt water approximately drains into the glacier.

During the *Polarstern* cruise PS131 we will focus on repeated and permanent GNSS measurements at western Lambert Land (LAMW). Measurements to infer the depth and further parameters of supraglacial lakes will have to be focused on specific lakes at Nioghalvfjerdsbræ and Zachariae Isstrøm due to the accessibility by the helicopter flights from *Polarstern*.

Work at sea

Work along and on the coast of Northeast Greenland was planned for the several days prior to the return transit to Bremerhaven. Upon leaving the marginal ice zone, the sea ice condition around the coast of Greenland was assessed in order to create an optimal ship route to the research areas. Unfortunately, the sea ice extended further from the coast than anticipated and concerns over the difficulty of ice-breaking led to the decision to only visit one glacier outlet, as a cruisealong the entire coast would have been too difficult and time consuming. It was decided that approaching Zachariae Isstrøm from the south would allow for an overall maximized research opportunity, with the disadvantage that the recovery of the HOLM GNSS station would no longer be possible as it would be out of helicopter flying range.

While the ship eventually managed to approach the coast of Northeast Greenland and was within flying range of the LAMW GNSS station and the surrounding supraglacial lakes, unrelenting fog and low cloud cover rendered flying to the glacier with the helicopter impossible. After evaluating the weather forecast for the following days and determining that the atmospheric situation only appeared as if it would worsen, the decision was made to move on to other oceanographic work further south in Scoresby Sound. By leaving this region, the recovery of both GNSS stations was abandoned.

The opportunity to measure supraglacial lake depths still persisted, as an impromptu evaluation of the glaciers surrounding Scoresby Sound determined that there were many areas with lakes present, some within flying distance of the ship's planned routes. After gaining the required extensions of research permissions, two flights were able to be conducted. Unexpectedly, the surface layer of the lakes was found to be frozen, which was not perceivable from the satellite images. We landed at the first supraglacial lake on Brede Glacier and evaluated that the thick surface slush, presumably caused by a recent heavy snowfall, was impassable for our remote controlled depth-surveying boat. The second flight to the southern branch of the Eielson Glacier revealed many supraglacial lakes, all with frozen surfaces. Due to this, no lake depth information was acquired.

Preliminary (expected) results

Due to the poor sea ice and weather conditions around Northeast Greenland, none of the GNSS data could be recovered, thus no results will be produced from this part of the mission.

While supraglacial lake flights could be made in Scoresby Sound, no depth information could be gathered. However, valuable insights into the freezing process of supraglacial lakes and the perceivability of the lake's freezing process from satellite images were collected. The survey flights have been mapped and the comparison of the lakes in satellite images and helicopter images is shown in Figures 11.1 and 11.2, which will be used for future understanding of lake condition evaluation and the limitations of a satellite-based lake depth algorithm.

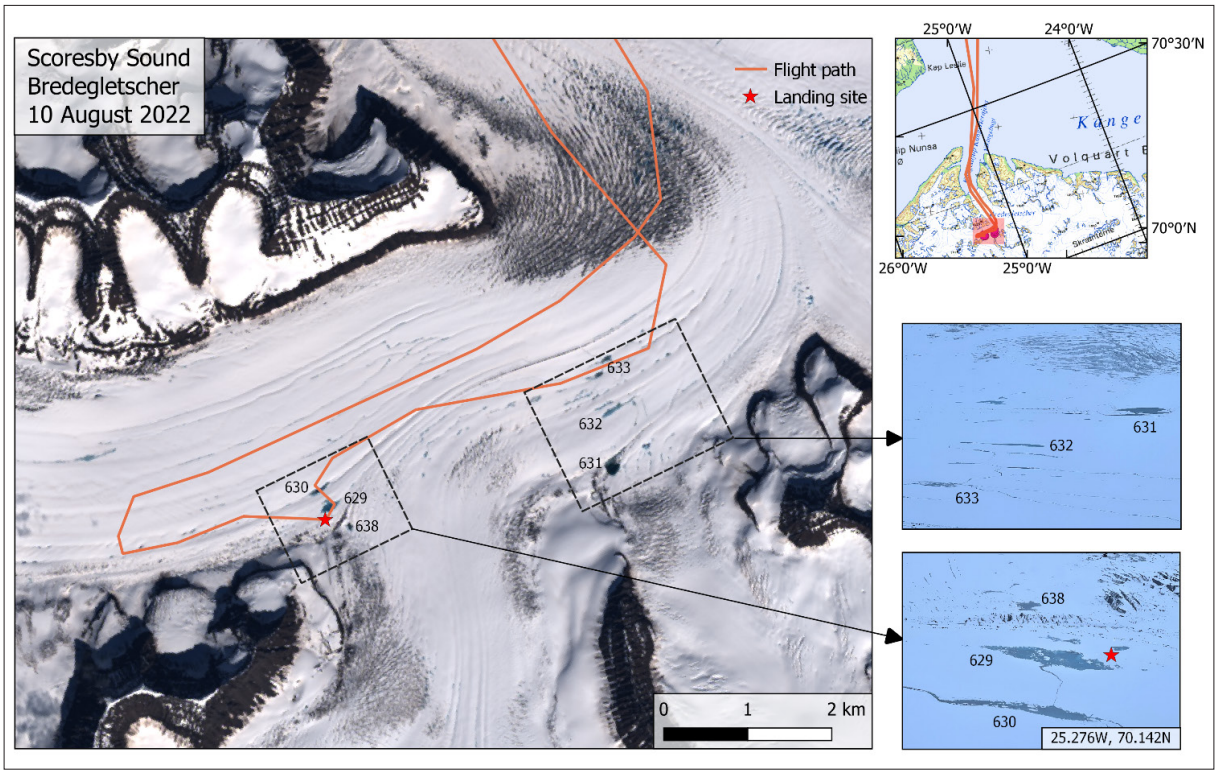

Fig. 11.1: Flight path of the supraglacial lake survey on Brede Glacier along with acquired in-situ images geolocated on a recent optical satellite image

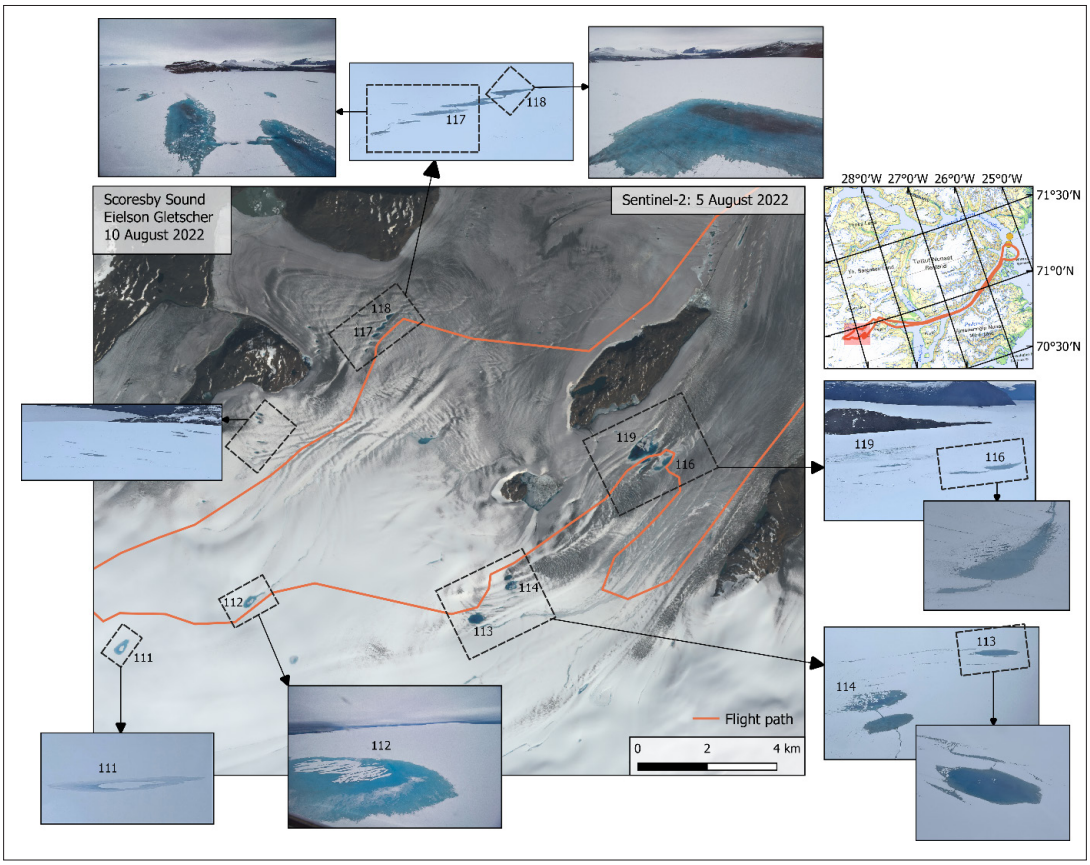

Fig. 11.2: Flight survey for supraglacial lakes on Eielson Glacier along with acquired in-situ images geolocated on a recent optical satellite image

Data management

As no data were recorded, no data from this sub-project will be published.

References

Caron L, Ivins ER, Larour E, Adhikari S, Nilsson J, Blewitt G (2018) GIA model statistics for GRACE hydrology, cryosphere, and ocean science. Geophysical Research Letters, 45:2203– 2212. https://doi.org/10.1002/2017GL076644.

Hochreuther P, Neckel N, Reimann N, Humbert A, Braun M (2021) Fully Automated Detection of Supraglacial Lake Area for Northeast Greenland Using Sentinel-2 Time-Series. Remote Sensing, 13(2):205. https://doi.org/10.3390/rs13020205.

IPCC (2019) IPCC Special Report on the Ocean and Cryosphere in a Changing Climate [Pörtner H-O, Roberts DC, Masson-Delmotte V, Zhai P, Tignor M, Poloczanska E, Mintenbeck K, Alegría A, Nicolai M, Okem A, Petzold J, Rama B, Weyer NM (eds)] Cambridge University Press, Cambridge, UK and New York, NY, USA, 755 pp. https://doi.org/10.1017/9781009157964.

Kappelsberger MT, Strößenreuther U, Scheinert M, Horwath M, Groh A, Knöfel C, Lunz S, Khan SA (2021) Validating surface-deformation predictions in north-east Greenland using refined estimates of contemporary ice-mass change and densified GNSS measurements. Journal of Geophysical Research: Earth Surface, 126:e2020JF005860. https://doi.org/10.1029/2020JF005860.

Kappelsberger M, Strößenreuther U, Scheinert M, Horwath M, Groh A (2021a) Gridded rates of ice-mass change in north-east Greenland from a combination of satellite gravimetry and satellite altimetry. https://doi.pangaea.de/10.1594/PANGAEA.922884.

Khan SA, Kjær KH, Bevis M, Bamber JL, Wahr J, Kjeldsen KK, Bjørk AA, Korsgaard NJ, Stearns LA, van den Broeke MR, Liu L, Larsen KN, Muresan IS (2014) Sustained mass loss of the northeast Greenland ice sheet triggered by regional warming. Nature Climate Change, 4:292–299. https://doi.org/10.1038/nclimate2161.

Mayer C, Schaffer J, Hattermann T, Floricioiu D, Krieger L, Dodd PA, Kanzow T, Licciulli C, Schannwell C (2018) Large ice loss variability at Nioghalvfjerdsfjorden Glacier, Northeast-Greenland. Nature Communication, 9(2768). https://doi.org/10.1038/s41467-018-05180-x.

Mouginot J, Rignot E, Scheuchl B, Fenty I, Khazendar A, Morlighem M, Buzzi A, Paden J (2015) Fast retreat of Zachariae Isstrøm, northeast Greenland. Science, 350(6266):1357–1361. https://doi.org/10.1126/science.aac7111.

Shepherd A, Ivins ER, Rignot E, Smith B, van den Broeke M, Velicogna I, Whitehouse P, Briggs K, Joughin I, Krinner G, Nowicki S, Payne T, Scambos T, Schlegel N, A G, Agosta C, Ahlstrøm A, Babonis G, Barletta VR, Bjørk AA, Blazquez A, Bonin J, Colgan W, Csatho B, Cullather R, Engdahl ME, Felikson D, Fettweis X, Forsberg R, Hogg AE, Gallee H, Gardner A, Gilbert L, Gourmelen N, Groh A, Gunter B, Hanna E, Harig C, Helm V, Horvath A, Horwath M, Khan S, Kjeldsen KK, Konrad H, Langen PL, Lecavalier B, Loomis B, Luthcke S, McMillan M, Melini D, Mernild S, Mohajerani Y, Moore P, Mottram R, Mouginot J, Moyano G, Muir A, Nagler T, Nield G, Nilsson J, Noël B, Otosaka I, Pattle ME, Peltier WR, Pie N, Rietbroek R, Rott H, Sandberg Sørensen L, Sasgen I, Save H, Scheuchl B, Schrama E, Schröder L, Seo K, Simonsen SB, Slater T, Spada G, Sutterley T, Talpe M, Tarasov L, van de Berg WJ, van der Wal W, van Wessem M, Vishwakarma BD, Wiese D, Wilton D, Wagner T, Wouters B, Wuite J (The IMBIE Team) (2019) Mass balance of the Greenland Ice Sheet from 1992 to 2018. Nature, 579:233-239, https://doi.org/10.1038/s41586-019-1855-2.

Whitehouse PL (2018) Glacial isostatic adjustment modelling: historical perspectives, recent advances, and future directions. Earth System Dynamics, 6(2):401–429. https://doi.org/10.5194/esurf-6-401-2018.

APPENDIX

A.1 TEILNEHMENDE INSTITUTE / PARTICIPATING INSTITUTES

A.2 FAHRTTEILNEHMER:INNEN / CRUISE PARTICIPANTS

A.3 SCHIFFSBESATZUNG / SHIP'S CREW

A.4. STATIONSLISTE / STATION LIST

A.1 TEILNEHMENDE INSTITUTE / PARTICIPATING INSTITUTES

Affiliation	Address
DE.AWI	Alfred-Wegener-Institut Helmholtz-Zentrum für Polar- und Meeresforschung Postfach 120161 27515 Bremerhaven Germany
DE.CAU	Christian-Albrechts-Universität zu Kiel Christian-Albrechts-Platz 4 24118 Kiel Germany
DE.DRF	DRF Luftrettung gAG Rita-Maiburg-Straße 2 70794 Filderstadt Germany
DE.DWD	Deutscher Wetterdienst Seewetteramt Bernhard Nocht Str. 76 20359 Hamburg Germany
DE.FAU	Friedrich-Alexander-Universität Erlangen-Nürnberg Institute of Geography Wetterkreuz 15 91058 Erlangen Germany
DE.GEOMAR	GEOMAR Helmholtz-Zentrum für Ozeanforschung Wischhofstraße 1-3 24148 Kiel Germany
DE.HHU	Heinrich-Heine-Universität Düsseldorf Universitätsstraße 1 40225 Düsseldorf Germany
DE.MPIC	Max-Planck-Institut für Chemie (Otto-Hahn-Institut) Hahn-Meitner-Weg 1 55128 Mainz Germany

Affiliation	Address
DE.NHC	Northern HeliCopter GmbH Gorch-Fock-Straße 103 26721 Emden Germany
DE.TROPOS	Leibniz Institut für Troposphärenforschung Permosserstraße 15 4318 Leipzig
DE.TU-Berlin	Technische Universität Berlin Straße des 17. Juni 135 10623 Berlin
DE.TU-Dresden	Technische Universität Dresden Institut für Planetare Geodäsie 01062 Dresden Germany
DE.UNI-Bremen	Universität Bremen Bibliothekstraße 1 28359 Bremen Germany
DE.UNI-Köln	Universität zu Köln Albertus-Magnus-Platz 50923 Köln Germany
DE.UNI-Oldenburg	Carl von Ossietzky Universität Oldenburg Ammerländer Heerstraße 114-118 26129 Oldenburg Germany
DK.KU	Københavns Universitet Nørregade 101165 København Denmark
FR.SHOM	Naval Hydrographic and Oceanographic Service 13 rue du Chatellier 29200 Brest France
JP.UTOKYO	University of Tokyo 5-1-5, Kashiwa-no-ha 277-8564 Kashiwa Japan

Affiliation	Address
NO.METNo	Norwegian Meteorological Institute Henrik Mohns plass 1 0313 Oslo Norway
NO.UIB	Universitetet i Bergen 5007 Bergen Norway
UW	University of Washington 1503 NE Boat St Box 357940 98195-7940 Seattle Unites States

A.2 FAHRTTEILNEHMER:INNEN / CRUISE PARTICIPANTS

Name/ Last name	Vorname/ First name	Institut/ Institute	Beruf/ Profession	Fachrichtung/ Discipline
Allerholt	Jacob	Alfred-Wegener-Institut	Technician	Oceanography
Babu Suja	Babun	Leibniz Institut für Troposphären-forschung	Scientist	Physics
Bartek	Katrina Marie	Friedrich-Alexander-Universität Erlangen-Nürnberg	PhD Student	Glaciology
Becker	Hauke	Alfred-Wegener-Institut	Engineer	Oceanography
Brauer	Jens	Northern HeliCopter GmbH	Pilot	Heli Service
Buth	Lena	Alfred-Wegener-Institut	PhD Student	Physics
Colias Blanco	Manuel	Northern HeliCopter GmbH	Technician	Heli Service
Elliott	Fiona	Universitetet Bergen	Technician	Oceanography
Fer	Ilker	Universitetet Bergen	Scientist	Oceanography
Graupner	Rainer	Alfred-Wegener-Institut	Technician	Oceanography
Haas	Christian	Alfred-Wegener-Institut	Scientist	Glaciology
Hofmann	Zerlina	Alfred-Wegener-Institut	PhD Student	Oceanography
Hohe	Christian Klaus	Alfred-Wegener-Institut	Technician	Biology
Hoppmann	Mario	Alfred-Wegener-Institut	Scientist	Oceanography
Jucker	Meret Nia	Alfred-Wegener-Institut	Student (Master)	Biology
Kanzow	Torsten	Alfred-Wegener-Institut	Scientist	Oceanography
Kirk	Henning	Alfred-Wegener-Institut	Technician	Geophysics
Knüppel	Nadine	Alfred-Wegener-Institut	Technician	Biology
Koehler	Klara	Alfred-Wegener-Institut	Student (Master)	Oceanography
Lion	Victor	Christian-Albrechts-Universität zu Kiel	Student (Master)	Other Geophysics Sciences

Name/ Last name	Vorname/ First name	Institut/ Institute	Beruf/ Profession	Fachrichtung/ Discipline
Lochthofen	Normen	Alfred-Wegener-Institut	Engineer	Engineering Sciences
Loebel	Erik	Technische Universität Dresden	Scientist	Glaciology
Lüchtrath	Sabine	Technische Universität Berlin	PhD Student	Other Geophysics Sciences
Mathieu	Laura	Alfred-Wegener-Institut	Doktorandin	Oceanography
McPherson	Rebecca	Alfred-Wegener-Institut	Scientist	Oceanography
Miehe	Kai	DRF Luftrettung gAG	Technician	Heli Service
Monsees	Matthias	Alfred-Wegener-Institut	Technician	Oceanography
Morische	Annika	Carl von Ossietzky Universität Oldenburg	Student (Master)	Other Geophysics Sciences
Murray	Ayla Rosina Cherrington Sealey	Alfred-Wegener-Institut	PhD Student	Biology
Neudert	Mara	Alfred-Wegener-Institut	PhD Student	Physics
Niehaus	Hannah Maria	Universität Bremen	Doktorandin	Physics
Niehoff	Barbara	Alfred-Wegener-Institut	PhD Student	Biology
Oehlke	Philipp Wilhelm	Leibniz Institut für Troposphären-forschung	Student (Master)	Engineering Sciences
Oldenburg	Ellen	Heinrich Heine Universität Düsseldorf	PhD Student	Biology
Ovidio	Popa	Heinrich Heine Universität Düsseldorf	Scientist	Biology
Rehder	Linda	Alfred-Wegener-Institut	PhD Student	Biology
Reifenberg	Simon Felix	Universität Bremen	PhD Student	Oceanography
Rohleder	Christian	DWD	Weather technician	Meteorology
Rückert	Janna Elisabeth	Universität Bremen	PhD Student	Physics
Schlindwein	Vera	Alfred-Wegener-Institut	Scientist	Geophysics
Schüttler	Johanna	Max-Planck-Institut für Chemie	Student (Master)	Chemistry

Name/ Last name	Vorname/ First name	Institut/ Institute	Beruf/ Profession	Fachrichtung/ Discipline
Sebastian	Archana	GEOMAR Helmholtz-Zentrum für Ozeanforschung	Student (Master)	Oceanography
Spreen	Gunnar	Universität Bremen	Scientist	Physics
Suter	Patrick	Deutscher Wetterdienst	Scientist	Meteorology
Torres-Valdés	Sinhué	Alfred-Wegener-Institut	Scientist	Oceanography
Vaupel	Lars	Northern HeliCopter GmbH	Pilot	Heli Service
von Appen	Wilken-Jon	Alfred-Wegener-Institut	Scientist	Oceanography
Walbröl	Andreas	Universität zu Köln	PhD Student	Meteorology
Winberg von Friesen	Lisa	Københavns Universitet	PhD Student	Biology

A.3 SCHIFFSBESATZUNG / SHIP'S CREW

No.	Nachname	Voname	Position
1	Langhinrichs	Moritz	Master
2	Lauber	Felix Thomas	C/Mate
3	Strauss	Erik	2nd Mate 1
4	Eckenfels	Hannes	2nd Mate 2
5	[tbn]		2nd Mate 3
6	Ziemann	Olaf	Chief Eng
7	Rusch	Torben	2nd. Eng
8	Fiedler	Alexander	2nd. Eng 1
9	Ehrke	Tom	2nd. Eng 2
10	Hofmann	Joerg Walter	Elec./Eng Komm.
11	Frank	Gerhard Ansgar Leon	Elec./Eng. Brücke
12	Schwedka	Thorsten	Elec./Eng. Labor
13	Zohrabyan	David Rubeni	Elec./Eng. Labor
14	Pommerencke	Bernd	Elec./Eng. Set
15	Winter	Andreas	Elec./Eng. System
16	Krueger	Lars	Elec./Eng. Winde
17	Brueck	Sebastian	Bosun
18	Schade	Tom	MP Rating/D1
19	Weiss	Daniel	MP Rating/D 2
20	Möller	Falko	MP Rating/D 3
21	Decker	Jens	MP Rating/D 4
22	Buchholz	Joscha	MP Rating/D 5
23	Lutz	Johannes Paul	MP Rating/D 6
24	Lello	Ants	MP Rating/D 7
25	Fink	Anna-Maria	MP Rating/D 8
26	Waterstradt	Felix	MP Rating/M 1
27	Clasen	Nils	MP Rating/M 2
28	Arnold - Becker	André	MP Rating/M 3
29	Hansen	Jan Nils	MP Rating/M 4
30	[tbn]		MP Rating/M 5
31	Keller	Jürgen Eugen	Carp. 1
32	Niebuhr	Tim	AB 1
33	Plehn	Marco Markus	Fitter/E 1
34	Cook 1	Schnieder	Sven

No.	Nachname	Voname	Position
35	Martens	Michael	2nd Cook 1
36	Matter	Sebastian Udo	2nd Cook 2
37	Wartenberg	Irina Marion	C/Stwd. 1
38	Ilk	Romy	Stwd./KS
39	Hettwer	Kathrin	2nd Stwd. 1
40	Witusch	Petra	2nd Stwd. 2
41	Golla	Gerald	2nd Stwd. 4
42	Shi	Wubo	2nd Stwd. 4
43	Hu	Guo Yong	2nd Stwd. 5
44	Chen	Quanlun	2nd Stwd. 6
45	Guba	Klaus	Doc

A.4 STATIONSLISTE / STATION LIST PS131

**Station list of expedition PS131 from Bremerhaven to Bremerhaven;
the list details the action log for all stations along the cruise track.**

See https://www.pangaea.de/expeditions/events/PS131 to display the station (event) list for expedition PS131.
This version contains Uniform Resource Identifiers for all sensors listed under https://sensor.awi.de. See https://www.awi.de/en/about-us/service/computing-centre/data-flow-framework.html for further information about AWI's data flow framework from sensor observations to archives (O2A).

Event label	Optional label	Date/Time	Latitude	Longitude	Depth [m]	Gear	Action	Comment (cut.)
PS131-track		2022-06-28T00:00:00	53.568	8.555		CT	Station start	Bremerhaven - Bremerhaven
PS131-track		2022-06-28T00:00:00	53.568	8.555		CT	Station end	Bremerhaven - Bremerhaven
PS131_0_Underway-14		2022-06-28T11:30:00	53.561	8.560		NEUMON	Station start	
PS131_0_Underway-14		2022-06-28T11:30:00	53.564	8.559		NEUMON	Station end	
PS131_0_Underway-6		2022-06-28T11:30:30	53.561	8.560		MYON	Station start	
PS131_0_Underway-6		2022-06-28T11:30:30	53.564	8.559		MYON	Station end	
PS131_0_Underway-29		2022-06-28T11:32:18	53.561	8.560		SWEAS	Station start	
PS131_0_Underway-29		2022-06-28T11:32:18	53.564	8.559		SWEAS	Station end	
PS131_0_Underway-16		2022-06-28T12:35:00	53.558	8.559	2.3	CAME	Station start	
PS131_0_Underway-16		2022-06-28T12:35:00	53.564	8.559		CAME	Station end	
PS131_0_Underway-23		2022-06-28T17:36:13	54.199	7.478	26.7	TSG	Station start	
PS131_0_Underway-23		2022-06-28T17:36:13	68.673	-15.949		TSG	Station end	
PS131_0_Underway-24		2022-06-28T17:36:48	54.200	7.477	26.9	TSG	Station start	
PS131_0_Underway-24		2022-06-28T17:36:48	68.673	-15.949		TSG	Station end	
PS131_0_Underway-1		2022-06-29T06:49:25	56.336	5.932	32.3	ADCP	Station start	

Event label	Optional label	Date/Time	Latitude	Longitude	Depth [m]	Gear	Action	Comment (cut.)
PS131_0_Underway-1		2022-06-29T06:49:25	68.675	-15.954		ADCP	Station end	
PS131_0_Underway-18		2022-06-29T15:13:46	57.723	5.015	88.5	pCO2	Station start	failure of Sinus-pump due to ice condition
PS131_0_Underway-18		2022-06-29T15:13:46	68.675	-15.954		pCO2	Station end	failure of Sinus-pump due to ice condition
PS131_0_Underway-7		2022-06-29T15:14:04	57.723	5.015	88.7	FBOX	Station start	failure of Sinus-pump due to ice condition
PS131_0_Underway-7		2022-06-29T15:14:04	68.673	-15.949		FBOX	Station end	failure of Sinus-pump due to ice condition
PS131_0_Underway-2		2022-06-29T15:30:00	57.767	4.985	94	AFIM	Station start	
PS131_0_Underway-2		2022-06-29T15:30:00	67.644	-13.012		AFIM	Station end	
PS131_0_Underway-12		2022-06-30T06:23:25	60.297	4.176	289	GRAV	Station start	
PS131_0_Underway-12		2022-06-30T06:23:25	68.673	-15.949		GRAV	Station end	
PS131_0_Underway-22		2022-06-30T06:24:44	60.301	4.176	289	SNDVELPR	Station start	
PS131_0_Underway-22		2022-06-30T06:24:44	68.675	-15.954		SNDVELPR	Station end	
PS131_1-1		2022-07-01T07:56:08	64.515	3.434	2191.9	CTD-RO	max depth	
PS131_1-2		2022-07-01T09:16:00	64.515	3.433	2192	MSN	Station start	
PS131_1-2		2022-07-01T09:16:00	64.515	3.434	2192	MSN	Station end	
PS131_0_Underway-13		2022-07-01T09:51:52	64.515	3.434			Station start	
PS131_0_Underway-13		2022-07-01T09:51:52	69.623	-19.152			Station end	
PS131_1-3		2022-07-01T12:14:00	64.766	3.484	1693	CTD-RO	max depth	Test
PS131_1-6		2022-07-01T13:41:00	64.765	3.484	1693	CTD-RO	max depth	Test
PS131_0_Underway-17		2022-07-02T07:54:55	67.588	4.392	1228.3	pCO2	Station start	failure of Sinus-pump due to ice condition

** Comments are limited to 130 characters. See https://www.pangaea.de/expeditions/events/PS131 to show full comments in conjunction with the station (event) list for expedition PS131*

Event label	Optional label	Date/Time	Latitude	Longitude	Depth [m]	Gear	Action	Comment (cut.)
PS131_0_Underway-17		2022-07-02T07:54:55	68.675	-15.954		pCO2	Station end	failure of Sinus-pump due to ice condition
PS131_2-1	F4-20	2022-07-05T06:06:44	78.995	6.991	1206.9	MOOR	max depth	recovered?
PS131_3-1	F4S-5	2022-07-05T08:33:35	79.008	6.952	1225.9	MOOR	max depth	recovered?
PS131_4-1	F4-OZA-2	2022-07-05T11:49:42	79.167	6.332	1422.7	MOOR	max depth	not recovered
PS131_5-1	F5-19	2022-07-05T14:47:28	78.997	5.659	2118.9	MOOR	max depth	
PS131_6-1		2022-07-05T21:29:22	78.609	5.067	2296.1	CTD-RO	max depth	
PS131_6-2		2022-07-05T23:55:38	78.609	5.066	2295.7	MSN	Station start	
PS131_6-2		2022-07-05T23:55:38	78.609	5.064	2296.6	MSN	Station end	
PS131_6-3		2022-07-06T02:22:20	78.609	5.067		LOKI	Station start	
PS131_6-3		2022-07-06T02:22:20	78.609	5.067		LOKI	Station end	
PS131_6-4		2022-07-06T03:52:39	78.609	5.065		RAMSES	Station start	
PS131_6-4		2022-07-06T03:52:39	78.610	5.067		RAMSES	Station end	
PS131_6-5		2022-07-06T04:53:20	78.609	5.066		CTD-RO	max depth	
PS131_7-1	F4W-3	2022-07-06T09:00:23	79.012	7.034		MOOR	max depth	
PS131_8-1	F3-19	2022-07-06T13:28:43	78.998	7.985		MOOR	max depth	
PS131_9-1	F2-20	2022-07-06T16:00:52	78.996	8.336		MOOR	max depth	
PS131_10-1		2022-07-06T17:54:23	78.980	7.944		GLD	Station start	
PS131_10-1		2022-07-06T17:54:23	78.998	7.903		GLD	Station end	
PS131_11-1		2022-07-06T20:24:45	78.984	7.949		CTD-RO	max depth	
PS131_12-1		2022-07-06T23:07:38	78.983	9.000		CTD-RO	max depth	
PS131_13-1		2022-07-07T00:45:42	78.984	8.478		CTD-RO	max depth	
PS131_14-1		2022-07-07T03:27:25	78.983	7.431		CTD-RO	max depth	
PS131_15-1	F4-21	2022-07-07T05:59:13	79.000	6.999		MOOR	max depth	
PS131_16-1	F4-W-4	2022-07-07T10:47:51	79.012	7.033		MOOR	max depth	
PS131_17-1	F5-20	2022-07-07T14:35:06	79.000	5.667		MOOR	max depth	
PS131_18-1		2022-07-07T18:00:19	78.929	6.017		TOPR	max depth	
PS131_19-1		2022-07-07T21:45:46	78.983	6.908		CTD-RO	max depth	

Event label	Optional label	Date/Time	Latitude	Longitude	Depth [m]	Gear	Action	Comment (cut.)
PS131_20-1		2022-07-08T00:24:07	78.983	6.384		CTD-RO	max depth	
PS131_21-1		2022-07-08T03:11:04	78.984	5.862		CTD-RO	max depth	
PS131_22-1	F4-OZA-2	2022-07-08T05:59:14	79.164	6.384		MOOR	max depth	
PS131_23-1	F4-OZA-3	2022-07-08T08:30:28	79.167	6.332		MOOR	max depth	
PS131_24-1	F3-20	2022-07-08T11:53:50	79.008	7.954		MOOR	max depth	
PS131_25-1	F2-21	2022-07-08T14:27:25	79.000	8.333		MOOR	max depth	
PS131_26-1	UIB_VMP500_ SN420	2022-07-08T17:30:41	78.985	7.124		VMP	max depth	
PS131_27-1		2022-07-08T23:39:00	79.064	4.189		CTD-RO	max depth	
PS131_27-2		2022-07-09T00:53:51	79.064	4.188		MSN	Station start	
PS131_27-2		2022-07-09T00:53:51	79.064	4.189		MSN	Station end	
PS131_27-3		2022-07-09T03:21:27	79.064	4.188		MSN	Station start	
PS131_27-3		2022-07-09T03:21:27	79.064	4.188		MSN	Station end	
PS131_27-4		2022-07-09T05:35:41	79.064	4.189		LOKI	Station start	
PS131_27-4		2022-07-09T05:35:41	79.064	4.189		LOKI	Station end	
PS131_28-1	FEVI-42	2022-07-09T07:39:11	79.002	4.352		MOOR	max depth	
PS131_29-1		2022-07-09T11:11:25	79.000	4.395		CTD-RO	max depth	
PS131_30-1	FEVI-44	2022-07-09T12:02:18	79.000	4.333		MOOR	max depth	
PS131_31-1		2022-07-09T15:57:03	79.017	4.336		RAMSES	Station start	
PS131_31-1		2022-07-09T15:57:03	79.015	4.339		RAMSES	Station end	
PS131_32-1		2022-07-09T17:18:01	78.983	4.820		POS	max depth	
PS131_32-2		2022-07-09T20:40:13	78.983	4.816		CTD-RO	max depth	
PS131_33-1		2022-07-09T22:54:53	78.983	5.339		CTD-RO	max depth	
PS131_34-1	F4-S-6	2022-07-10T05:56:57	79.012	6.962		MOOR	max depth	
PS131_35-1		2022-07-10T14:49:03	79.721	4.421		CTD-RO	max depth	
PS131_35-2		2022-07-10T16:52:31	79.721	4.420		MSN	Station start	
PS131_35-2		2022-07-10T16:52:31	79.721	4.423		MSN	Station end	
PS131_35-3		2022-07-10T19:14:00	79.721	4.422		LOKI	Station start	

Event label	Optional label	Date/Time	Latitude	Longitude	Depth [m]	Gear	Action	Comment (cut.)
PS131_35-3		2022-07-10T19:14:00	79.721	4.420		LOKI	Station end	
PS131_35-4		2022-07-10T20:46:36	79.721	4.420		MSN	Station start	
PS131_35-4		2022-07-10T20:46:36	79.721	4.426		MSN	Station end	
PS131_35-5		2022-07-10T22:57:17	79.721	4.426		RAMSES	Station start	
PS131_35-5		2022-07-10T22:57:17	79.720	4.428		RAMSES	Station end	
PS131_35-6		2022-07-10T23:48:17	79.718	4.434		CTD-RO	max depth	
PS131_36-1		2022-07-11T08:54:37	80.345	10.610		CTD-RO	max depth	
PS131_36-2		2022-07-11T09:56:07	80.341	10.609		TOPR	max depth	
PS131_0_Underway-30		2022-07-11T13:13:00	80.470	10.238		ICERAD	Station start	
PS131_0_Underway-30		2022-07-11T13:13:00	70.229	-21.491		ICERAD	Station end	
PS131_37-1		2022-07-11T14:21:10	80.527	10.115		CTD-RO	max depth	
PS131_38-1		2022-07-11T17:12:51	80.641	9.787		CTD-RO	max depth	
PS131_39-1		2022-07-11T19:56:52	80.768	9.346		CTD-RO	max depth	
PS131_40-1		2022-07-11T22:34:09	80.886	9.075		CTD-RO	max depth	
PS131_41-1		2022-07-12T01:05:36	81.001	8.638		CTD-RO	max depth	
PS131_42-1		2022-07-12T04:04:08	81.119	8.255		CTD-RO	max depth	
PS131_43-1		2022-07-12T07:43:37	81.236	7.874		CTD-RO	max depth	
PS131_44-1		2022-07-12T10:42:14	81.372	7.467		CTD-RO	max depth	
PS131_45-1		2022-07-12T12:52:55	81.477	7.056		ZODIAC	max depth	
PS131_45-2		2022-07-12T13:34:22	81.478	7.028		CTD-RO	max depth	
PS131_46-1		2022-07-12T17:45:23	81.602	6.700		CTD-RO	max depth	
PS131_47-1		2022-07-12T20:52:48	81.609	6.531		ICE	max depth	
PS131_47-1_1	PS131_47-1, Floe North Visit 1	2022-07-13T11:08:00	81.355	6.470		MSSP	max depth	
PS131_47-1_2	PS131_47-1, Floe North Visit 1	2022-07-13T11:28:00	81.355	6.470		MSSP	max depth	

Event label	Optional label	Date/Time	Latitude	Longitude	Depth [m]	Gear	Action	Comment (cut.)
PS131_47-1_3	PS131_47-1, Floe North Visit 1	2022-07-13T11:47:00	81.355	6.470		MSSP	max depth	
PS131_47-1_4	PS131_47-1, Floe North Visit 1	2022-07-13T14:49:00	81.355	6.424		MSSP	max depth	
PS131_47-1_5	PS131_47-1, Floe North Visit 1	2022-07-13T15:08:00	81.355	6.420		MSSP	max depth	
PS131_47-1_6	PS131_47-1, Floe North Visit 1	2022-07-13T15:09:00	81.355	6.420		MSSP	max depth	
PS131_47-1_7	PS131_47-1, Floe North Visit 1	2022-07-13T15:29:00	81.356	6.416		MSSP	max depth	
PS131_47-2		2022-07-13T18:15:29	81.604	6.657		CTD-RO	max depth	
PS131_47-3		2022-07-13T19:22:01	81.606	6.649		MSN	Station start	
PS131_47-3		2022-07-13T19:22:01	81.608	6.640		MSN	Station end	
PS131_47-4		2022-07-13T20:31:09	81.609	6.636		LOKI	Station start	
PS131_47-4		2022-07-13T20:31:09	81.611	6.635		LOKI	Station end	
PS131_48-1_1	PS131_48-1, Floe South Visit 1	2022-07-14T12:22:00	81.110	7.453		MSSP	max depth	
PS131_48-1		2022-07-14T12:30:00	81.182	7.737		ICE	max depth	
PS131_48-1_2	PS131_48-1, Floe South Visit 1	2022-07-14T12:43:00	81.110	7.442		MSSP	max depth	
PS131_48-1_3	PS131_48-1, Floe South Visit 1	2022-07-14T13:05:00	81.110	7.430		MSSP	max depth	

Event label	Optional label	Date/Time	Latitude	Longitude	Depth [m]	Gear	Action	Comment (cut.)
PS131_48-1_4	PS131_48-1, Floe South Visit 1	2022-07-14T13:27:00	81.110	7.419		MSSP	max depth	
PS131_48-1_5	PS131_48-1, Floe South Visit 1	2022-07-14T13:53:00	81.110	7.407		MSSP	max depth	
PS131_48-1_6	PS131_48-1, Floe South Visit 1	2022-07-14T14:15:00	81.113	7.395		MSSP	max depth	
PS131_48-1_7	PS131_48-1, Floe South Visit 1	2022-07-14T14:29:00	81.113	7.393		MSSP	max depth	
PS131_48-1_8	PS131_48-1, Floe South Visit 1	2022-07-14T14:47:00	81.112	7.386		MSSP	max depth	
PS131_48-1_9	PS131_48-1, Floe South Visit 1	2022-07-14T15:07:00	81.113	7.379		MSSP	max depth	
PS131_48-1_10	PS131_48-1, Floe South Visit 1	2022-07-14T15:27:00	81.113	7.372		MSSP	max depth	
PS131_48-1_11	PS131_48-1, Floe South Visit 1	2022-07-14T15:47:00	81.114	7.367		MSSP	max depth	
PS131_48-1_12	PS131_48-1, Floe South Visit 1	2022-07-14T16:06:00	81.115	7.362		MSSP	max depth	
PS131_48-1_13	PS131_48-1, Floe South Visit 1	2022-07-14T16:25:00	81.115	7.357		MSSP	max depth	
PS131_48-2		2022-07-14T18:44:36	81.190	7.475		CTD-RO	max depth	
PS131_48-3		2022-07-14T19:48:10	81.190	7.419		MSN	Station start	

Event label	Optional label	Date/Time	Latitude	Longitude	Depth [m]	Gear	Action	Comment (cut.)
PS131_48-3		2022-07-14T19:48:10	81.191	7.356		MSN	Station end	
PS131_48-4		2022-07-14T21:10:31	81.192	7.339		LOKI	Station start	
PS131_48-4		2022-07-14T21:10:31	81.194	7.306		LOKI	Station end	
PS131_49-1		2022-07-15T11:24:27	81.353	6.818		ICE	max depth	
PS131_49-1_1	PS131_49-1, Floe Middle Visit 1	2022-07-15T12:38:00	81.210	6.474		MSSP	max depth	
PS131_49-1_2	PS131_49-1, Floe Middle Visit 1	2022-07-15T12:58:00	81.210	6.467		MSSP	max depth	
PS131_49-1_3	PS131_49-1, Floe Middle Visit 1	2022-07-15T13:17:00	81.210	6.461		MSSP	max depth	
PS131_49-1_4	PS131_49-1, Floe Middle Visit 1	2022-07-15T13:34:00	81.210	6.456		MSSP	max depth	
PS131_49-1_5	PS131_49-1, Floe Middle Visit 1	2022-07-15T13:51:00	81.210	6.451		MSSP	max depth	
PS131_49-1_6	PS131_49-1, Floe Middle Visit 1	2022-07-15T14:09:00	81.210	6.448		MSSP	max depth	
PS131_49-1_7	PS131_49-1, Floe Middle Visit 1	2022-07-15T14:32:00	81.210	6.441		MSSP	max depth	
PS131_49-1_8	PS131_49-1, Floe Middle Visit 1	2022-07-15T14:50:00	81.210	6.434		MSSP	max depth	
PS131_49-1_9	PS131_49-1, Floe Middle Visit 1	2022-07-15T15:07:00	81.211	6.429		MSSP	max depth	

Event label	Optional label	Date/Time	Latitude	Longitude	Depth [m]	Gear	Action	Comment (cut.)
PS131_49-1_10	PS131_49-1, Floe Middle Visit 1	2022-07-15T15:27:00	81.211	6.423		MSSP	max depth	
PS131_49-1_11	PS131_49-1, Floe Middle Visit 1	2022-07-15T15:45:00	81.211	6.418		MSSP	max depth	
PS131_49-1_12	PS131_49-1, Floe Middle Visit 1	2022-07-15T16:02:00	81.211	6.413		MSSP	max depth	
PS131_49-1_13	PS131_49-1, Floe Middle Visit 1	2022-07-15T16:20:00	81.212	6.406		MSSP	max depth	
PS131_49-2		2022-07-15T18:29:49	81.361	6.609		CTD-RO	max depth	
PS131_49-3		2022-07-15T20:00:18	81.366	6.565		MSN	Station start	
PS131_49-3		2022-07-15T20:00:18	81.369	6.541		MSN	Station end	
PS131_49-4		2022-07-15T21:12:36	81.370	6.535		LOKI	Station start	
PS131_49-4		2022-07-15T21:12:36	81.372	6.523		LOKI	Station end	
PS131_50-1		2022-07-16T04:22:09	81.001	8.516		WRIDER	max depth	
PS131_51-1		2022-07-16T06:20:36	80.910	8.925		WRIDER	max depth	
PS131_52-1		2022-07-16T09:15:57	80.768	10.547		TOPR	max depth	
PS131_53-1		2022-07-16T11:57:18	80.678	12.029		CTD-RO	max depth	
PS131_53-2	Arvor-I_22DE010	2022-07-16T12:56:07	80.679	12.027		ARGOFL	max depth	
PS131_53-3	Arvor-I_22DE011	2022-07-16T13:00:00	80.679	12.038		ARGOFL	max depth	
PS131_54-1	UIB_VMP500_SN420	2022-07-16T13:52:45	80.608	11.786		VMP	max depth	
PS131_55-1		2022-07-16T17:30:24	80.345	10.630		TOPR	max depth	
PS131_56-1	UIB_VMP500_SN420	2022-07-17T09:05:05	80.620	9.786		MSSP	max depth	

Event label	Optional label	Date/Time	Latitude	Longitude	Depth [m]	Gear	Action	Comment (cut.)
PS131_56-1_1	PS131_56-1, 56_01	2022-07-17T09:15:00	80.372	9.471		MSSP	max depth	
PS131_56-1_2	PS131_56-1, 56_01	2022-07-17T09:20:00	80.372	9.470		MSSP	max depth	
PS131_56-2		2022-07-17T10:16:01	80.620	9.786		CTD-RO	max depth	
PS131_56-3		2022-07-17T10:53:54	80.620	9.785		RAMSES	Station start	
PS131_56-3		2022-07-17T10:53:54	80.620	9.785		RAMSES	Station end	
PS131_56-4		2022-07-17T11:35:21	80.620	9.786		MSN	Station start	
PS131_56-4		2022-07-17T11:35:21	80.620	9.785		MSN	Station end	
PS131_56-5		2022-07-17T13:44:30	80.620	9.785		MSN	Station start	
PS131_56-5		2022-07-17T13:44:30	80.620	9.786		MSN	Station end	
PS131_56-6		2022-07-17T15:00:08	80.620	9.786		LOKI	Station start	
PS131_56-6		2022-07-17T15:00:08	80.620	9.786		LOKI	Station end	
PS131_56-7		2022-07-17T15:42:46	80.620	9.786		LOKI	Station start	
PS131_56-7		2022-07-17T15:42:46	80.620	9.787		LOKI	Station end	
PS131_56-8		2022-07-17T16:42:46	80.620	9.787		CTD-RO	max depth	
PS131_57-1	UIB_VMP500_ SN420	2022-07-17T18:46:07	80.391	10.468		MSSP	max depth	
PS131_57-1_1	PS131_57-1, 057_01	2022-07-17T18:53:00	80.235	10.278		MSSP	max depth	
PS131_57-2		2022-07-17T19:56:18	80.390	10.472		CTD-RO	max depth	
PS131_57-3		2022-07-17T20:33:23	80.390	10.471		RAMSES	Station start	
PS131_57-3		2022-07-17T20:33:23	80.390	10.471		RAMSES	Station end	
PS131_57-4		2022-07-17T21:12:15	80.390	10.472		MSN	Station start	
PS131_57-4		2022-07-17T21:12:15	80.390	10.473		MSN	Station end	
PS131_57-5		2022-07-17T22:11:27	80.390	10.471		MSN	Station start	
PS131_57-5		2022-07-17T22:11:27	80.390	10.471		MSN	Station end	
PS131_57-6		2022-07-17T23:17:13	80.390	10.473		LOKI	Station start	

Event label	Optional label	Date/Time	Latitude	Longitude	Depth [m]	Gear	Action	Comment (cut.)
PS131_57-6		2022-07-17T23:17:13	80.390	10.472		LOKI	Station end	
PS131_57-7		2022-07-18T00:17:41	80.390	10.473		CTD-RO	max depth	
PS131_57-8	UIB_VMP500_SN420	2022-07-18T00:42:46	80.390	10.478		MSSP	max depth	
PS131_57-8_1	PS131_57-8, 057_08	2022-07-18T00:43:00	80.234	10.287		MSSP	max depth	
PS131_58-1		2022-07-18T02:44:46	80.401	10.060		CTD-RO	max depth	
PS131_58-2	Y1-1	2022-07-18T06:23:14	80.402	10.059		MOOR	max depth	
PS131_59-1	Y2-1	2022-07-18T08:24:04	80.417	10.058		MOOR	max depth	
PS131_60-1		2022-07-18T12:13:57	80.629	9.764		OBS	Station start	
PS131_60-1		2022-07-18T12:13:57	80.625	9.720		OBS	Station end	
PS131_61-1	UIB_VMP500_SN420	2022-07-18T15:47:23	80.816	9.206		MSSP	max depth	
PS131_61-1_1	PS131_61-1, 061_01	2022-07-18T15:49:00	80.489	9.123		MSSP	max depth	
PS131_61-2		2022-07-18T16:47:08	80.822	9.181		CTD-RO	max depth	
PS131_61-3		2022-07-18T17:32:12	80.827	9.156		RAMSES	Station start	
PS131_61-3		2022-07-18T17:32:12	80.833	9.138		RAMSES	Station end	
PS131_61-4		2022-07-18T18:18:05	80.835	9.131		MSN	Station start	
PS131_61-4		2022-07-18T18:18:05	80.842	9.104		MSN	Station end	
PS131_61-5		2022-07-18T19:55:01	80.824	9.157		MSN	Station start	
PS131_61-5		2022-07-18T19:55:01	80.827	9.132		MSN	Station end	
PS131_61-6		2022-07-18T20:57:27	80.826	9.139		LOKI	Station start	
PS131_61-6		2022-07-18T20:57:27	80.826	9.135		LOKI	Station end	
PS131_61-7		2022-07-18T21:58:57	80.826	9.141		CTD-RO	max depth	
PS131_61-8	UIB_VMP500_SN420	2022-07-18T22:20:20	80.825	9.130		MSSP	max depth	
PS131_61-8_1	PS131_61-8, 061_08	2022-07-18T22:25:00	80.495	9.076		MSSP	max depth	

Event label	Optional label	Date/Time	Latitude	Longitude	Depth [m]	Gear	Action	Comment (cut.)
PS131_62-1		2022-07-19T00:48:31	80.954	8.688		CTD-RO	max depth	
PS131_62-2	Y3-1	2022-07-19T06:00:04	80.939	8.678		MOOR	max depth	
PS131_63-1	Y4-1	2022-07-19T10:59:12	80.966	8.703		MOOR	max depth	
PS131_63-2		2022-07-19T11:24:17	80.966	8.701		ZODIAC	max depth	
PS131_64-1		2022-07-19T14:46:36	81.013	8.705		TOPR	max depth	
PS131_65-1		2022-07-19T23:59:43	81.519	7.032		CTD-RO	max depth	
PS131_65-2		2022-07-20T00:31:15	81.521	7.026		RAMSES	Station start	
PS131_65-2		2022-07-20T00:31:15	81.524	7.024		RAMSES	Station end	
PS131_65-3		2022-07-20T02:19:08	81.530	7.037		MSN	Station start	
PS131_65-3		2022-07-20T02:19:08	81.533	7.051		MSN	Station end	
PS131_65-4		2022-07-20T03:08:41	81.533	7.056		MSN	Station start	
PS131_65-4		2022-07-20T03:08:41	81.536	7.079		MSN	Station end	
PS131_65-5		2022-07-20T05:20:02	81.539	7.131		CTD-RO	max depth	
PS131_65-6		2022-07-20T06:00:46	81.540	7.154		LOKI	Station start	
PS131_65-6		2022-07-20T06:00:46	81.540	7.176		LOKI	Station end	
PS131_65-7	UIB_VMP500_SN420	2022-07-20T06:54:52	81.540	7.182		MSSP	max depth	
PS131_65-7_1	PS131_65-7, 065_07	2022-07-20T06:55:00	81.324	7.110		MSSP	max depth	
PS131_66-1	Y5-1	2022-07-20T10:28:31	81.504	7.159		MOOR	max depth	
PS131_67-1		2022-07-20T17:00:52	81.503	4.788		ICE	max depth	
PS131_67-1_1	PS131_67-1, Floe North Visit 2	2022-07-20T18:33:00	81.301	4.466		MSSP	max depth	
PS131_67-1_2	PS131_67-1, Floe North Visit 2	2022-07-20T18:52:00	81.300	4.464		MSSP	max depth	

Event label	Optional label	Date/Time	Latitude	Longitude	Depth [m]	Gear	Action	Comment (cut.)
PS131_67-1_3	PS131_67-1, Floe North Visit 2	2022-07-20T19:13:00	81.299	4.461		MSSP	max depth	
PS131_67-1_4	PS131_67-1, Floe North Visit 2	2022-07-20T19:31:00	81.299	4.459		MSSP	max depth	
PS131_67-1_5	PS131_67-1, Floe North Visit 2	2022-07-20T19:58:00	81.299	4.454		MSSP	max depth	
PS131_67-1_6	PS131_67-1, Floe North Visit 2	2022-07-20T22:08:00	81.297	4.423		MSSP	max depth	
PS131_67-1_7	PS131_67-1, Floe North Visit 2	2022-07-20T22:25:00	81.298	4.419		MSSP	max depth	
PS131_67-1_8	PS131_67-1, Floe North Visit 2	2022-07-20T22:43:00	81.298	4.415		MSSP	max depth	
PS131_68-1		2022-07-21T10:46:49	81.193	5.435		ICE	max depth	
PS131_68-1_1	PS131_68-1, Floe South Visit 2	2022-07-21T12:26:00	81.113	5.260		MSSP	max depth	
PS131_68-1_2	PS131_68-1, Floe South Visit 2	2022-07-21T12:48:00	81.113	5.259		MSSP	max depth	
PS131_68-1_3	PS131_68-1, Floe South Visit 2	2022-07-21T13:15:00	81.112	5.259		MSSP	max depth	
PS131_68-1_4	PS131_68-1, Floe South Visit 2	2022-07-21T13:36:00	81.111	5.258		MSSP	max depth	

Event label	Optional label	Date/Time	Latitude	Longitude	Depth [m]	Gear	Action	Comment (cut.)
PS131_68-1_5	PS131_68-1, Floe South Visit 2	2022-07-21T14:01:00	81.111	5.258		MSSP	max depth	
PS131_68-1_6	PS131_68-1, Floe South Visit 2	2022-07-21T14:21:00	81.110	5.257		MSSP	max depth	
PS131_68-1_7	PS131_68-1, Floe South Visit 2	2022-07-21T14:39:00	81.109	5.257		MSSP	max depth	
PS131_68-1_8	PS131_68-1, Floe South Visit 2	2022-07-21T14:41:00	81.109	5.257		MSSP	max depth	
PS131_69-1	UIB_VMP500_SN420	2022-07-21T20:20:42	81.199	8.101		MSSP	max depth	
PS131_69-1_1	PS131_69-1, 069_01	2022-07-21T20:23:00	81.119	8.062		MSSP	max depth	
PS131_69-1_2	PS131_69-1, 069_01	2022-07-21T20:41:00	81.118	8.063		MSSP	max depth	
PS131_69-2		2022-07-21T21:19:09	81.194	8.105		CTD-RO	max depth	
PS131_69-3		2022-07-21T21:44:35	81.192	8.102		RAMSES	Station start	
PS131_69-3		2022-07-21T21:44:35	81.190	8.094		RAMSES	Station end	
PS131_69-4		2022-07-21T22:59:46	81.187	8.070		MSN	Station start	
PS131_69-4		2022-07-21T22:59:46	81.186	8.043		MSN	Station end	
PS131_69-5		2022-07-22T00:22:25	81.186	8.019		MSN	Station start	
PS131_69-5		2022-07-22T00:22:25	81.186	7.998		MSN	Station end	
PS131_69-6_1	PS131_69-6, 069_06	2022-07-22T01:37:00	81.112	7.591		MSSP	max depth	
PS131_69-6	UIB_VMP500_SN420	2022-07-22T01:37:19	81.186	7.983		MSSP	max depth	
PS131_69-7		2022-07-22T02:21:44	81.187	7.972		WRIDER	max depth	

Event label	Optional label	Date/Time	Latitude	Longitude	Depth [m]	Gear	Action	Comment (cut.)
PS131_69-8		2022-07-22T02:57:52	81.189	7.968		CTD-RO	max depth	
PS131_70-1		2022-07-22T09:48:20	81.357	5.161		ICE	max depth	
PS131_70-1_1	PS131_70-1, Floe Middle Visit 2	2022-07-22T11:46:00	81.213	5.083		MSSP	max depth	
PS131_70-1_2	PS131_70-1, Floe Middle Visit 2	2022-07-22T12:54:00	81.211	5.076		MSSP	max depth	
PS131_70-1_3	PS131_70-1, Floe Middle Visit 2	2022-07-22T13:20:00	81.210	5.073		MSSP	max depth	
PS131_70-1_4	PS131_70-1, Floe Middle Visit 2	2022-07-22T13:38:00	81.210	5.071		MSSP	max depth	
PS131_70-1_5	PS131_70-1, Floe Middle Visit 2	2022-07-22T14:55:00	81.207	5.064		MSSP	max depth	
PS131_70-1_6	PS131_70-1, Floe Middle Visit 2	2022-07-22T15:20:00	81.207	5.062		MSSP	max depth	
PS131_70-1_7	PS131_70-1, Floe Middle Visit 2	2022-07-22T15:38:00	81.206	5.061		MSSP	max depth	
PS131_71-1		2022-07-24T14:45:22	82.835	-6.674		OBS	Station start	
PS131_71-1		2022-07-24T14:45:22	82.831	-6.695		OBS	Station end	
PS131_72-1		2022-07-24T19:43:29	82.869	-5.757		OBS	Station start	
PS131_72-1		2022-07-24T19:43:29	82.909	-6.205		OBS	Station end	
PS131_72-2		2022-07-24T20:03:27	82.867	-5.763		ICE	max depth	
PS131_73-1		2022-07-24T23:22:26	82.910	-6.203		OBS	Station start	
PS131_73-1		2022-07-24T23:22:26	82.909	-6.205		OBS	Station end	

Event label	Optional label	Date/Time	Latitude	Longitude	Depth [m]	Gear	Action	Comment (cut.)
PS131_74-1		2022-07-25T00:00:01	82.919	-6.342		OBS	Station start	
PS131_74-1		2022-07-25T00:00:01	82.918	-6.346		OBS	Station end	
PS131_75-1		2022-07-25T05:54:09	82.897	-6.198		CTD-RO	max depth	
PS131_76-1		2022-07-25T09:39:54	82.884	-6.421		OBS	Station start	
PS131_76-1		2022-07-25T09:39:54	82.881	-6.425		OBS	Station end	
PS131_77-1	AURORA1	2022-07-25T12:36:31	82.903	-6.230		MOOR	max depth	
PS131_78-1		2022-07-25T17:19:56	82.918	-6.745		OBS	Station start	
PS131_78-1		2022-07-25T17:19:56	82.916	-6.745		OBS	Station end	
PS131_79-1		2022-07-25T19:46:30	82.969	-6.433		OBS	Station start	
PS131_79-1		2022-07-25T19:46:30	82.967	-6.434		OBS	Station end	
PS131_80-1		2022-07-25T22:16:43	82.946	-5.934		OBS	Station start	
PS131_80-1		2022-07-25T22:16:43	82.945	-5.929		OBS	Station end	
PS131_81-1		2022-07-26T18:13:21	81.901	-3.230		WRIDER	max depth	
PS131_82-1		2022-07-27T09:46:49	81.333	0.507		MBES	Station start	
PS131_82-1		2022-07-27T09:46:49	81.343	1.207		MBES	Station end	
PS131_83-1	UIB_Moo-ring_Y7	2022-07-27T12:55:45	81.373	1.199		MOOR	max depth	
PS131_84-1		2022-07-27T20:20:50	81.366	1.437		ICE	max depth	
PS131_84-1_1	PS131_84-1, Floe 24h	2022-07-27T22:20:00	81.213	1.236		MSSP	max depth	
PS131_84-1_2	PS131_84-1, Floe 24h	2022-07-27T22:38:00	81.213	1.233		MSSP	max depth	
PS131_84-1_3	PS131_84-1, Floe 24h	2022-07-27T22:40:00	81.213	1.233		MSSP	max depth	
PS131_84-1_4	PS131_84-1, Floe 24h	2022-07-27T22:59:00	81.212	1.230		MSSP	max depth	
PS131_84-1_5	PS131_84-1, Floe 24h	2022-07-27T23:42:00	81.211	1.224		MSSP	max depth	

Event label	Optional label	Date/Time	Latitude	Longitude	Depth [m]	Gear	Action	Comment (cut.)
PS131_84-1_6	PS131_84-1, Floe 24h	2022-07-28T00:13:00	81.211	1.220		MSSP	max depth	
PS131_84-1_7	PS131_84-1, Floe 24h	2022-07-28T00:30:00	81.211	1.218		MSSP	max depth	
PS131_84-1_8	PS131_84-1, Floe 24h	2022-07-28T00:47:00	81.211	1.217		MSSP	max depth	
PS131_84-1_9	PS131_84-1, Floe 24h	2022-07-28T01:13:00	81.211	1.215		MSSP	max depth	
PS131_84-1_10	PS131_84-1, Floe 24h	2022-07-28T01:27:00	81.211	1.214		MSSP	max depth	
PS131_84-1_11	PS131_84-1, Floe 24h	2022-07-28T02:07:00	81.211	1.213		MSSP	max depth	
PS131_84-1_12	PS131_84-1, Floe 24h	2022-07-28T02:23:00	81.211	1.213		MSSP	max depth	
PS131_84-1_13	PS131_84-1, Floe 24h	2022-07-28T02:38:00	81.211	1.214		MSSP	max depth	
PS131_84-1_14	PS131_84-1, Floe 24h	2022-07-28T02:53:00	81.211	1.214		MSSP	max depth	
PS131_84-1_15	PS131_84-1, Floe 24h	2022-07-28T03:07:00	81.211	1.215		MSSP	max depth	
PS131_84-1_16	PS131_84-1, Floe 24h	2022-07-28T03:22:00	81.211	1.215		MSSP	max depth	
PS131_84-1_17	PS131_84-1, Floe 24h	2022-07-28T03:37:00	81.211	1.216		MSSP	max depth	
PS131_84-1_18	PS131_84-1, Floe 24h	2022-07-28T03:51:00	81.211	1.217		MSSP	max depth	
PS131_84-1_19	PS131_84-1, Floe 24h	2022-07-28T04:08:00	81.211	1.218		MSSP	max depth	
PS131_84-1_20	PS131_84-1, Floe 24h	2022-07-28T04:28:00	81.211	1.219		MSSP	max depth	

Event label	Optional label	Date/Time	Latitude	Longitude	Depth [m]	Gear	Action	Comment (cut.)
PS131_84-1_21	PS131_84-1, Floe 24h	2022-07-28T04:46:00	81.211	1.220		MSSP	max depth	
PS131_84-1_22	PS131_84-1, Floe 24h	2022-07-28T05:06:00	81.211	1.221		MSSP	max depth	
PS131_84-1_23	PS131_84-1, Floe 24h	2022-07-28T05:34:00	81.210	1.222		MSSP	max depth	
PS131_84-1_24	PS131_84-1, Floe 24h	2022-07-28T05:50:00	81.210	1.223		MSSP	max depth	
PS131_84-1_25	PS131_84-1, Floe 24h	2022-07-28T06:16:00	81.209	1.223		MSSP	max depth	
PS131_84-1_26	PS131_84-1, Floe 24h	2022-07-28T06:35:00	81.209	1.223		MSSP	max depth	
PS131_84-1_27	PS131_84-1, Floe 24h	2022-07-28T06:40:00	81.209	1.223		MSSP	max depth	
PS131_84-1_28	PS131_84-1, Floe 24h	2022-07-28T06:58:00	81.208	1.223		MSSP	max depth	
PS131_84-1_29	PS131_84-1, Floe 24h	2022-07-28T07:00:00	81.208	1.223		MSSP	max depth	
PS131_84-1_30	PS131_84-1, Floe 24h	2022-07-28T07:17:00	81.208	1.223		MSSP	max depth	
PS131_84-1_31	PS131_84-1, Floe 24h	2022-07-28T07:34:00	81.207	1.222		MSSP	max depth	
PS131_84-1_32	PS131_84-1, Floe 24h	2022-07-28T07:49:00	81.206	1.221		MSSP	max depth	
PS131_84-1_33	PS131_84-1, Floe 24h	2022-07-28T08:04:00	81.206	1.220		MSSP	max depth	
PS131_84-1_34	PS131_84-1, Floe 24h	2022-07-28T08:20:00	81.205	1.218		MSSP	max depth	
PS131_84-1_35	PS131_84-1, Floe 24h	2022-07-28T08:35:00	81.204	1.217		MSSP	max depth	

Event label	Optional label	Date/Time	Latitude	Longitude	Depth [m]	Gear	Action	Comment (cut.)
PS131_84-1_36	PS131_84-1, Floe 24h	2022-07-28T08:51:00	81.204	1.215		MSSP	max depth	
PS131_84-1_37	PS131_84-1, Floe 24h	2022-07-28T09:07:00	81.203	1.213		MSSP	max depth	
PS131_84-1_38	PS131_84-1, Floe 24h	2022-07-28T09:23:00	81.202	1.210		MSSP	max depth	
PS131_84-1_39	PS131_84-1, Floe 24h	2022-07-28T09:40:00	81.201	1.207		MSSP	max depth	
PS131_84-1_40	PS131_84-1, Floe 24h	2022-07-28T09:43:00	81.201	1.207		MSSP	max depth	
PS131_84-1_41	PS131_84-1, Floe 24h	2022-07-28T09:58:00	81.201	1.204		MSSP	max depth	
PS131_84-1_42	PS131_84-1, Floe 24h	2022-07-28T10:13:00	81.200	1.202		MSSP	max depth	
PS131_84-1_43	PS131_84-1, Floe 24h	2022-07-28T10:31:00	81.199	1.198		MSSP	max depth	
PS131_84-1_44	PS131_84-1, Floe 24h	2022-07-28T10:52:00	81.198	1.194		MSSP	max depth	
PS131_84-1_45	PS131_84-1, Floe 24h	2022-07-28T11:10:00	81.198	1.191		MSSP	max depth	
PS131_84-1_46	PS131_84-1, Floe 24h	2022-07-28T11:28:00	81.197	1.188		MSSP	max depth	
PS131_84-1_47	PS131_84-1, Floe 24h	2022-07-28T12:09:00	81.196	1.179		MSSP	max depth	
PS131_84-1_48	PS131_84-1, Floe 24h	2022-07-28T12:26:00	81.196	1.175		MSSP	max depth	
PS131_84-1_49	PS131_84-1, Floe 24h	2022-07-28T12:51:00	81.195	1.170		MSSP	max depth	
PS131_84-1_50	PS131_84-1, Floe 24h	2022-07-28T13:07:00	81.195	1.167		MSSP	max depth	

Event label	Optional label	Date/Time	Latitude	Longitude	Depth [m]	Gear	Action	Comment (cut.)
PS131_84-1_51	PS131_84-1, Floe 24h	2022-07-28T13:22:00	81.195	1.164		MSSP	max depth	
PS131_84-1_52	PS131_84-1, Floe 24h	2022-07-28T13:42:00	81.195	1.160		MSSP	max depth	
PS131_84-1_53	PS131_84-1, Floe 24h	2022-07-28T13:57:00	81.194	1.157		MSSP	max depth	
PS131_84-1_54	PS131_84-1, Floe 24h	2022-07-28T14:12:00	81.194	1.154		MSSP	max depth	
PS131_84-1_55	PS131_84-1, Floe 24h	2022-07-28T14:26:00	81.194	1.152		MSSP	max depth	
PS131_84-1_56	PS131_84-1, Floe 24h	2022-07-28T15:04:00	81.194	1.145		MSSP	max depth	
PS131_84-1_57	PS131_84-1, Floe 24h	2022-07-28T15:23:00	81.194	1.142		MSSP	max depth	
PS131_84-1_58	PS131_84-1, Floe 24h	2022-07-28T15:40:00	81.193	1.139		MSSP	max depth	
PS131_84-1_59	PS131_84-1, Floe 24h	2022-07-28T15:55:00	81.193	1.137		MSSP	max depth	
PS131_84-1_60	PS131_84-1, Floe 24h	2022-07-28T16:10:00	81.193	1.134		MSSP	max depth	
PS131_84-1_61	PS131_84-1, Floe 24h	2022-07-28T16:27:00	81.193	1.132		MSSP	max depth	
PS131_84-1_62	PS131_84-1, Floe 24h	2022-07-28T17:14:00	81.192	1.125		MSSP	max depth	
PS131_84-1_63	PS131_84-1, Floe 24h	2022-07-28T17:33:00	81.191	1.123		MSSP	max depth	
PS131_84-1_64	PS131_84-1, Floe 24h	2022-07-28T17:50:00	81.191	1.120		MSSP	max depth	
PS131_84-1_65	PS131_84-1, Floe 24h	2022-07-28T18:06:00	81.190	1.118		MSSP	max depth	

Event label	Optional label	Date/Time	Latitude	Longitude	Depth [m]	Gear	Action	Comment (cut.)
PS131_84-1_66	PS131_84-1, Floe 24h	2022-07-28T18:24:00	81.190	1.116		MSSP	max depth	
PS131_84-1_67	PS131_84-1, Floe 24h	2022-07-28T18:41:00	81.189	1.113		MSSP	max depth	
PS131_84-1_68	PS131_84-1, Floe 24h	2022-07-28T18:56:00	81.189	1.112		MSSP	max depth	
PS131_84-1_69	PS131_84-1, Floe 24h	2022-07-28T19:10:00	81.189	1.110		MSSP	max depth	
PS131_84-1_70	PS131_84-1, Floe 24h	2022-07-28T19:24:00	81.188	1.109		MSSP	max depth	
PS131_84-1_71	PS131_84-1, Floe 24h	2022-07-28T19:38:00	81.188	1.107		MSSP	max depth	
PS131_84-1_72	PS131_84-1, Floe 24h	2022-07-28T19:52:00	81.187	1.105		MSSP	max depth	
PS131_84-1_73	PS131_84-1, Floe 24h	2022-07-28T20:08:00	81.187	1.104		MSSP	max depth	
PS131_84-1_74	PS131_84-1, Floe 24h	2022-07-28T20:22:00	81.186	1.102		MSSP	max depth	
PS131_85-1	UIB_Moo-ring_Y8	2022-07-29T04:00:41	81.317	3.122		MOOR	max depth	
PS131_86-1		2022-07-29T08:09:50	81.205	2.757		TOPR	max depth	
PS131_87-1		2022-07-29T13:58:18	81.076	3.178		CTD-RO	max depth	
PS131_87-2		2022-07-29T14:48:29	81.076	3.160		ZODIAC	max depth	
PS131_87-3		2022-07-29T15:02:59	81.076	3.154		MSSP	max depth	
PS131_87-3_1	PS131_87-3, 087_03	2022-07-29T15:03:00	81.046	3.093		MSSP	max depth	
PS131_87-4		2022-07-29T15:32:10	81.077	3.147		RAMSES	max depth	
PS131_87-5		2022-07-29T16:40:53	81.080	3.132		MSN	Station start	
PS131_87-5		2022-07-29T16:40:53	81.080	3.114		MSN	Station end	
PS131_87-6		2022-07-29T18:18:56	81.080	3.113		MSN	Station start	

Event label	Optional label	Date/Time	Latitude	Longitude	Depth [m]	Gear	Action	Comment (cut.)
PS131_87-6		2022-07-29T18:18:56	81.081	3.108		MSN	Station end	
PS131_87-7		2022-07-29T19:20:37	81.081	3.106		LOKI	Station start	
PS131_87-7		2022-07-29T19:20:37	81.086	3.098		LOKI	Station end	
PS131_87-8		2022-07-29T20:33:49	81.086	3.097		MSSP	max depth	
PS131_87-8_1	PS131_87-8, 087_08	2022-07-29T20:34:00	81.052	3.057		MSSP	max depth	
PS131_88-1		2022-07-29T22:36:57	81.154	2.905		CTD-RO	max depth	
PS131_88-2		2022-07-29T23:20:01	81.155	2.919		RAMSES	Station start	
PS131_88-2		2022-07-29T23:20:01	81.155	2.933		RAMSES	Station end	
PS131_88-3		2022-07-30T00:02:34	81.155	2.937		MSN	Station start	
PS131_88-3		2022-07-30T00:02:34	81.157	2.957		MSN	Station end	
PS131_88-4_1	PS131_88-4, 088_04	2022-07-30T01:10:00	81.096	2.583		MSSP	max depth	
PS131_88-4	UIB_VMP500_SN420	2022-07-30T01:10:48	81.159	2.973		MSSP	max depth	
PS131_88-5		2022-07-30T01:50:41	81.161	3.001		LOKI	Station start	
PS131_88-5		2022-07-30T01:50:41	81.164	3.038		LOKI	Station end	
PS131_89-1		2022-07-30T06:12:46	81.197	2.372		ICE	max depth	
PS131_89-1_1	PS131_89-1, Floe North Visit 3	2022-07-30T08:16:00	81.113	2.235		MSSP	max depth	
PS131_89-1_2	PS131_89-1, Floe North Visit 3	2022-07-30T08:35:00	81.112	2.234		MSSP	max depth	
PS131_89-1_3	PS131_89-1, Floe North Visit 3	2022-07-30T08:50:00	81.112	2.233		MSSP	max depth	
PS131_89-1_4	PS131_89-1, Floe North Visit 3	2022-07-30T09:05:00	81.111	2.232		MSSP	max depth	

Event label	Optional label	Date/Time	Latitude	Longitude	Depth [m]	Gear	Action	Comment (cut.)
PS131_89-1_5	PS131_89-1, Floe North Visit 3	2022-07-30T09:19:00	81.110	2.231		MSSP	max depth	
PS131_89-1_6	PS131_89-1, Floe North Visit 3	2022-07-30T09:41:00	81.110	2.228		MSSP	max depth	
PS131_89-1_7	PS131_89-1, Floe North Visit 3	2022-07-30T09:58:00	81.109	2.225		MSSP	max depth	
PS131_89-1_8	PS131_89-1, Floe North Visit 3	2022-07-30T10:15:00	81.108	2.221		MSSP	max depth	
PS131_89-1_9	PS131_89-1, Floe North Visit 3	2022-07-30T10:50:00	81.108	2.214		MSSP	max depth	
PS131_89-1_10	PS131_89-1, Floe North Visit 3	2022-07-30T11:07:00	81.107	2.210		MSSP	max depth	
PS131_89-1_11	PS131_89-1, Floe North Visit 3	2022-07-30T11:23:00	81.107	2.206		MSSP	max depth	
PS131_89-1_12	PS131_89-1, Floe North Visit 3	2022-07-30T11:37:00	81.106	2.203		MSSP	max depth	
PS131_89-1_13	PS131_89-1, Floe North Visit 3	2022-07-30T11:52:00	81.106	2.199		MSSP	max depth	
PS131_89-1_14	PS131_89-1, Floe North Visit 3	2022-07-30T12:12:00	81.106	2.193		MSSP	max depth	

Event label	Optional label	Date/Time	Latitude	Longitude	Depth [m]	Gear	Action	Comment (cut.)
PS131_89-1_15	PS131_89-1, Floe North Visit 3	2022-07-30T12:27:00	81.105	2.189		MSSP	max depth	
PS131_89-1_16	PS131_89-1, Floe North Visit 3	2022-07-30T12:43:00	81.105	2.184		MSSP	max depth	
PS131_89-1_17	PS131_89-1, Floe North Visit 3	2022-07-30T12:58:00	81.105	2.180		MSSP	max depth	
PS131_89-1_18	PS131_89-1, Floe North Visit 3	2022-07-30T13:13:00	81.105	2.176		MSSP	max depth	
PS131_89-1_19	PS131_89-1, Floe North Visit 3	2022-07-30T13:37:00	81.105	2.170		MSSP	max depth	
PS131_89-1_20	PS131_89-1, Floe North Visit 3	2022-07-30T13:51:00	81.105	2.166		MSSP	max depth	
PS131_89-1_21	PS131_89-1, Floe North Visit 3	2022-07-30T13:53:00	81.105	2.166		MSSP	max depth	
PS131_89-1_22	PS131_89-1, Floe North Visit 3	2022-07-30T14:08:00	81.105	2.163		MSSP	max depth	
PS131_90-1		2022-07-30T17:40:18	81.090	3.147		TOPR	max depth	
PS131_91-1		2022-07-31T01:54:16	80.726	4.475		CTD-RO	max depth	
PS131_91-2		2022-07-31T02:51:49	80.719	4.444		RAMSES	Station start	
PS131_91-2		2022-07-31T02:51:49	80.721	4.483		RAMSES	Station end	
PS131_91-3		2022-07-31T03:27:35	80.721	4.496		MSSP	max depth	
PS131_91-3_1	PS131_91-3, 091_03	2022-07-31T03:28:00	80.433	4.299		MSSP	max depth	

Event label	Optional label	Date/Time	Latitude	Longitude	Depth [m]	Gear	Action	Comment (cut.)
PS131_91-3_2	PS131_91-3, 091_03	2022-07-31T03:34:00	80.433	4.304		MSSP	max depth	
PS131_91-4		2022-07-31T04:18:10	80.720	4.431		MSN	Station start	
PS131_91-4		2022-07-31T04:18:10	80.722	4.508		MSN	Station end	
PS131_91-5		2022-07-31T05:28:23	80.718	4.431		MSN	Station start	
PS131_91-5		2022-07-31T05:28:23	80.718	4.488		MSN	Station end	
PS131_91-6		2022-07-31T06:24:57	80.718	4.509		LOKI	Station start	
PS131_91-6		2022-07-31T06:24:57	80.718	4.554		LOKI	Station end	
PS131_91-7		2022-07-31T07:22:59	80.717	4.578		MSSP	max depth	
PS131_91-7_1	PS131_91-7, 091_07	2022-07-31T07:23:00	80.431	4.347		MSSP	max depth	
PS131_91-8		2022-07-31T08:05:53	80.712	4.606		WRIDER	max depth	
PS131_92-1		2022-07-31T11:00:25	80.934	3.874		ICE	max depth	
PS131_92-1_1	PS131_92-1, Floe South Visit 3	2022-07-31T13:31:00	80.557	3.490		MSSP	max depth	
PS131_92-1_2	PS131_92-1, Floe South Visit 3	2022-07-31T13:49:00	80.556	3.484		MSSP	max depth	
PS131_92-1_3	PS131_92-1, Floe South Visit 3	2022-07-31T14:06:00	80.556	3.478		MSSP	max depth	
PS131_92-1_4	PS131_92-1, Floe South Visit 3	2022-07-31T14:22:00	80.556	3.472		MSSP	max depth	
PS131_92-1_5	PS131_92-1, Floe South Visit 3	2022-07-31T14:36:00	80.556	3.467		MSSP	max depth	
PS131_93-1		2022-07-31T19:03:26	81.073	2.178		ICE	max depth	

Event label	Optional label	Date/Time	Latitude	Longitude	Depth [m]	Gear	Action	Comment (cut.)
PS131_93-1_1	PS131_93-1, Floe Middle Visit 3	2022-07-31T20:21:00	81.043	2.086		MSSP	max depth	
PS131_93-1_2	PS131_93-1, Floe Middle Visit 3	2022-07-31T20:35:00	81.042	2.083		MSSP	max depth	
PS131_93-1_3	PS131_93-1, Floe Middle Visit 3	2022-07-31T20:52:00	81.042	2.079		MSSP	max depth	
PS131_93-1_4	PS131_93-1, Floe Middle Visit 3	2022-07-31T21:07:00	81.042	2.075		MSSP	max depth	
PS131_93-1_5	PS131_93-1, Floe Middle Visit 3	2022-07-31T21:27:00	81.041	2.071		MSSP	max depth	
PS131_93-1_6	PS131_93-1, Floe Middle Visit 3	2022-07-31T21:42:00	81.041	2.067		MSSP	max depth	
PS131_93-1_7	PS131_93-1, Floe Middle Visit 3	2022-07-31T22:00:00	81.040	2.063		MSSP	max depth	
PS131_93-1_8	PS131_93-1, Floe Middle Visit 3	2022-07-31T22:17:00	81.040	2.059		MSSP	max depth	
PS131_93-1_9	PS131_93-1, Floe Middle Visit 3	2022-07-31T22:31:00	81.040	2.056		MSSP	max depth	
PS131_93-1_10	PS131_93-1, Floe Middle Visit 3	2022-07-31T22:47:00	81.039	2.053		MSSP	max depth	

Event label	Optional label	Date/Time	Latitude	Longitude	Depth [m]	Gear	Action	Comment (cut.)
PS131_93-1_11	PS131_93-1, Floe Middle Visit 3	2022-07-31T23:01:00	81.039	2.050		MSSP	max depth	
PS131_93-1_12	PS131_93-1, Floe Middle Visit 3	2022-07-31T23:16:00	81.039	2.047		MSSP	max depth	
PS131_93-1_13	PS131_93-1, Floe Middle Visit 3	2022-07-31T23:28:00	81.039	2.044		MSSP	max depth	
PS131_93-1_14	PS131_93-1, Floe Middle Visit 3	2022-07-31T23:49:00	81.039	2.040		MSSP	max depth	
PS131_93-1_15	PS131_93-1, Floe Middle Visit 3	2022-08-01T00:03:00	81.039	2.038		MSSP	max depth	
PS131_93-1_16	PS131_93-1, Floe Middle Visit 3	2022-08-01T00:17:00	81.039	2.036		MSSP	max depth	
PS131_94-1		2022-08-01T06:29:26	80.769	4.272		CTD-RO	max depth	
PS131_94-2		2022-08-01T07:38:19	80.769	4.305		RAMSES	Station start	
PS131_94-2		2022-08-01T07:38:19	80.768	4.306		RAMSES	Station end	
PS131_94-3_1	PS131_94-3, 094_03	2022-08-01T08:20:00	80.461	4.181		MSSP	max depth	
PS131_94-3		2022-08-01T08:20:47	80.768	4.303		MSSP	max depth	
PS131_94-4		2022-08-01T08:51:24	80.767	4.297		MSN	Station start	
PS131_94-4		2022-08-01T08:51:24	80.765	4.303		MSN	Station end	
PS131_94-5		2022-08-01T09:59:12	80.767	4.286		MSN	Station start	
PS131_94-5		2022-08-01T09:59:12	80.765	4.280		MSN	Station end	
PS131_94-6		2022-08-01T11:01:59	80.764	4.267		LOKI	Station start	
PS131_94-6		2022-08-01T11:01:59	80.762	4.238		LOKI	Station end	

Event label	Optional label	Date/Time	Latitude	Longitude	Depth [m]	Gear	Action	Comment (cut.)
PS131_94-7_1	PS131_94-7, 094_07	2022-08-01T11:51:00	80.457	4.143		MSSP	max depth	
PS131_94-7		2022-08-01T12:00:08	80.761	4.233		MSSP	max depth	
PS131_94-7_2	PS131_94-7, 094_07	2022-08-01T12:01:00	80.457	4.139		MSSP	max depth	
PS131_95-1		2022-08-01T12:57:15	80.756	4.242		TOPR	max depth	
PS131_96-1		2022-08-01T22:30:51	80.770	4.968		CTD-RO	max depth	
PS131_97-1		2022-08-02T00:10:18	80.769	5.291		CTD-RO	max depth	
PS131_98-1		2022-08-02T01:57:59	80.767	5.669		CTD-RO	max depth	
PS131_99-1		2022-08-02T02:35:09	80.768	5.659		DRIFT	max depth	
PS131_100-1		2022-08-02T03:34:09	80.767	6.019		CTD-RO	max depth	
PS131_101-1		2022-08-02T05:03:15	80.767	6.335		CTD-RO	max depth	
PS131_102-1		2022-08-02T06:25:17	80.767	6.666		CTD-RO	max depth	
PS131_103-1		2022-08-02T07:03:53	80.762	6.696		TSG	Station start	
PS131_103-1		2022-08-02T07:03:53	80.587	7.481		TSG	Station end	
PS131_104-1		2022-08-02T09:48:36	80.553	7.108		GLD	Station start	
PS131_104-1		2022-08-02T09:48:36	80.532	6.936		GLD	Station end	
PS131_105-1	EGC-7	2022-08-03T13:11:41	78.986	-5.362		MOOR	max depth	
PS131_106-1	EGC-8	2022-08-03T16:14:38	79.002	-5.337		MOOR	max depth	
PS131_107-1		2022-08-03T18:57:17	78.983	-5.416		CTD-RO	max depth	
PS131_107-2		2022-08-03T20:07:28	78.982	-5.436		RAMSES	Station start	
PS131_107-2		2022-08-03T20:07:28	78.983	-5.445		RAMSES	Station end	
PS131_107-3		2022-08-03T20:42:40	78.983	-5.446		MSN	Station start	
PS131_107-3		2022-08-03T20:42:40	78.983	-5.457		MSN	Station end	
PS131_107-4		2022-08-03T22:08:50	78.983	-5.460		MSN	Station start	
PS131_107-4		2022-08-03T22:08:50	78.977	-5.479		MSN	Station end	
PS131_107-5		2022-08-04T00:15:32	78.977	-5.481		CTD-RO	max depth	
PS131_107-6		2022-08-04T00:51:36	78.976	-5.488		LOKI	Station start	

Event label	Optional label	Date/Time	Latitude	Longitude	Depth [m]	Gear	Action	Comment (cut.)
PS131_107-6		2022-08-04T00:51:36	78.974	-5.512		LOKI	Station end	
PS131_108-1		2022-08-06T00:06:29	78.446	-18.417		CTD-RO	max depth	
PS131_108-2		2022-08-06T00:45:04	78.446	-18.417		MSN	Station start	
PS131_108-2		2022-08-06T00:45:04	78.446	-18.417		MSN	Station end	
PS131_108-3		2022-08-06T01:32:30	78.446	-18.417		MSN	Station start	
PS131_108-3		2022-08-06T01:32:30	78.446	-18.417		MSN	Station end	
PS131_108-4		2022-08-06T02:35:46	78.446	-18.417		LOKI	Station start	
PS131_108-4		2022-08-06T02:35:46	78.446	-18.417		LOKI	Station end	
PS131_108-5		2022-08-06T03:47:39	78.446	-18.417		CTD-RO	max depth	
PS131_109-1		2022-08-06T07:37:38	78.435	-18.439		ICE	max depth	
PS131_109-1_1	PS131_109-1, Floe Fast-ice	2022-08-06T08:38:00	78.261	-19.333		MSSP	max depth	
PS131_109-1_2	PS131_109-1, Floe Fast-ice	2022-08-06T09:02:00	78.261	-19.333		MSSP	max depth	
PS131_109-1_3	PS131_109-1, Floe Fast-ice	2022-08-06T09:27:00	78.261	-19.334		MSSP	max depth	
PS131_109-1_4	PS131_109-1, Floe Fast-ice	2022-08-06T09:50:00	78.261	-19.334		MSSP	max depth	
PS131_109-1_5	PS131_109-1, Floe Fast-ice	2022-08-06T10:13:00	78.261	-19.333		MSSP	max depth	
PS131_109-1_6	PS131_109-1, Floe Fast-ice	2022-08-06T10:34:00	78.261	-19.333		MSSP	max depth	
PS131_109-1_7	PS131_109-1, Floe Fast-ice	2022-08-06T10:59:00	78.261	-19.334		MSSP	max depth	
PS131_110-1		2022-08-06T15:58:23	78.475	-17.515		ICE	max depth	
PS131_111-1		2022-08-07T05:24:13	78.179	-15.721		CTD-RO	max depth	
PS131_112-1	IdF3-2	2022-08-07T06:20:03	78.179	-15.719		MOOR	max depth	
PS131_113-1		2022-08-07T07:03:28	78.177	-15.724		WRIDER	max depth	
PS131_114-1	SCO2-1	2022-08-10T10:46:15	71.228	-25.305		MOOR	max depth	

Event label	Optional label	Date/Time	Latitude	Longitude	Depth [m]	Gear	Action	Comment (cut.)
PS131_114-2		2022-08-10T10:51:24	71.228	-25.304		ZODIAC	max depth	
PS131_114-3		2022-08-10T13:04:27	71.232	-25.302		CTD-RO	max depth	
PS131_115-1	SCO1-1	2022-08-10T15:28:39	71.279	-25.167		MOOR	max depth	
PS131_115-2		2022-08-10T17:17:58	71.282	-25.164		CTD-RO	max depth	
PS131_116-1		2022-08-10T19:55:00	71.316	-25.283		CTD-RO	max depth	
PS131_117-1		2022-08-11T04:36:32	70.321	-23.451		TOPR	max depth	
PS131_118-1	SCO3-1	2022-08-11T08:31:03	70.355	-22.005		MOOR	max depth	
PS131_118-2		2022-08-11T15:11:55	70.353	-22.006		CTD-RO	max depth	

** Comments are limited to 130 characters. See https://www.pangaea.de/expeditions/events/PS131 to show full comments in conjunction with the station (event) list for expedition PS131*

Abbreviation	Method/Device
ADCP	Acoustic Doppler Current Profiler
AFIM	AutoFim
ARGOFL	Argo float
CAME	Camera
CT	Underway cruise track measurements
CTD-RO	CTD/Rosette
DRIFT	Drifter
FBOX	FerryBox
GLD	Glider
GRAV	Gravimetry
ICE	Ice station
ICERAD	Ice radar
LOKI	Light frame on-sight keyspecies investigation
MBES	Multibeam echosounder
MOOR	Mooring
MSN	Multiple opening/closing net
MSSP	Microstructure Profiler
MYON	DESY Myon Detector
NEUMON	Neutron monitor
OBS	Ocean bottom seismometer
POS	Posidonia positioning system
RAMSES	RAMSES hyperspectral radiometer
SNDVELPR	Sound velocity probe
SWEAS	Ship Weather Station
TOPR	Towed Ocean Profiler
TSG	Thermosalinograph
VMP	Vertical microstructure profiler
WRIDER	Waverider
ZODIAC	Rubber boat, Zodiac
pCO2	pCO_2 sensor

Die **Berichte zur Polar- und Meeresforschung** (ISSN 1866-3192) werden beginnend mit dem Band 569 (2008) als Open-Access-Publikation herausgegeben. Ein Verzeichnis aller Bände einschließlich der Druckausgaben (ISSN 1618-3193, Band 377-568, von 2000 bis 2008) sowie der früheren **Berichte zur Polarforschung** (ISSN 0176-5027, Band 1–376, von 1981 bis 2000) befindet sich im electronic Publication Information Center **(ePIC)** des Alfred-Wegener-Instituts, Helmholtz-Zentrum für Polar- und Meeresforschung (AWI); see https://epic.awi.de. Durch Auswahl "Reports on Polar- and Marine Research" (via "browse"/"type") wird eine Liste der Publikationen, sortiert nach Bandnummer, innerhalb der absteigenden chronologischen Reihenfolge der Jahrgänge mit Verweis auf das jeweilige pdf-Symbol zum Herunterladen angezeigt.

The **Reports on Polar and Marine Research** (ISSN 1866-3192) are available as open access publications since 2008. A table of all volumes including the printed issues (ISSN 1618-3193, Vol. 377-568, from 2000 until 2008), as well as the earlier **Reports on Polar Research** (ISSN 0176-5027, Vol. 1–376, from 1981 until 2000) is provided by the electronic Publication Information Center **(ePIC)** of the Alfred Wegener Institute, Helmholtz Centre for Polar and Marine Research (AWI); see URL https://epic.awi.de. To generate a list of all Reports, use the URL http://epic.awi.de and select "browse"/"type" to browse "Reports on Polar and Marine Research". A chronological list in declining order will be presented, and pdf-icons displayed for downloading.

Zuletzt erschienene Ausgaben:

Recently published issues:

770 (2023) The Expedition PS131 of the Research Vessel POLARSTERN to the Fram Strait in 2022, edited by Torsten Kanzow

769 (2023) The Expedition TRITON2021 of the Hendes Dansk Majestæt Skib TRITON to the Atlantic Ocean in 2021, edited by Rebecca McPherson, Carina Engicht and Torsten Kanzow

768 (2022) Mit Erich von Drygalski in die Ostantarktis – Paul Björvigs Tagebuch von der ersten deutschen Südpolarexpedition 1901-1903. Aus dem Norwegischen übersetzt von Volkert Gazert und herausgegeben von Cornelia Lüdecke

767 (2022) Expeditions to Antarctica: ANT-Land 2021/22 Neumayer Station III, Kohnen Station, Flight Operations and Field Campaigns, edited by Christine Wesche and Julia Regnery with contributions of the participants

766 (2022) The Expedition West-Alaska 2016 of the ERC group PETA-CARB to permafrost regions in western Alaska in 2016, edited by Josefine Lenz, Matthias Fuchs, Ingmar Nitze, Jens Strauss, Guido Grosse

765 (2022) The Expeditions PS130/1 and PS130/2 of the Research Vessel *Polarstern* to the Atlantic Ocean in 2022, edited by Simon Dreutter and Claudia Hanfland with contributions of the participants

764 (2022) The Expedition PS128 of the Research Vessel *Polarstern* to the Weddell Sea, Lazarew Sea, Riiser-Larsen Sea, Cosmonaut Sea, and Cooperation Sea in 2022, edited by Ralf Tiedemann and Juliane Müller with contributions of the participants

763 (2022) The MOSES Sternfahrt Expeditions of the Research Vessels ALBIS, LITTORINA, LUDWIG PRANDTL, MYA II and UTHÖRN to the Elbe River, Elbe Estuary and German Bight in 2021, edited by Ingeborg Bussmann, Norbert Anselm, Holger Brix, Philipp Fischer, Götz Flöser, Elisabeth von der Esch, Norbert Kamjunke

762 (2022) 28th International Polar Conference Polar Regions, Climate Change and Society, Potsdam, 01 – 05 May 2022 German Society for Polar Research, edited by H. Kassens, D. Damaske, B. Diekmann, F. Flisker, G. Heinemann, J. Herrle, U. Karsten, N. Koglin, F. Kruse, R. Lehmann, C. Lüdecke, C. Mayer, B. Sattler, M. Scheinert, C. Spiegel-Behnke, and R.Tiedemann

ALFRED-WEGENER-INSTITUT
HELMHOLTZ-ZENTRUM FÜR POLAR-
UND MEERESFORSCHUNG

BREMERHAVEN

Am Handelshafen 12
27570 Bremerhaven
Telefon 0471 4831-0
Telefax 0471 4831-1149
www.awi.de

HELMHOLTZ